Metallogeny of the Loch Tay area (Central Scotland) from gold compositional variations, vein parageneses and structural constraints

Lucia Savastano

Submitted in accordance with the requirements for the degree of Doctor of Philosophy

The University of Leeds
School of Earth and Environment

January 2026

''We shall not cease from exploration
And the end of all our exploring
Will be to arrive where we started
And know the place for the first time.''

{T.S. Eliot, from Little Gidding}

I confirm that the work submitted is my own, except where work which has formed part of jointly authored publications has been included. My contribution and the other authors' to this work have been explicitly indicated below. I confirm that appropriate credit has been given within the thesis where reference has been made to the work of others.

Chapters 6 and 7 of this thesis include some of the work that has appeared in the publication: Chapman, R., Torvela, T., Savastano, L. Insights into Regional Metallogeny from Detailed Compositional Studies of Alluvial Gold: An Example from the Loch Tay Area, Central Scotland. Minerals 2023c, 13, 140. https://doi.org/10.3390/min13020140

The gold compositional data from the Group 1 and Group 2 localities (as classified in the publication) have been analysed and interpreted in the thesis alongside supplementary gold data from the same and different localities, to enhance the arguments presented in Chapman et al., 2023a and generate new insights.

Author Contributions to the publication: Conceptualization, R. C. and T. T.; methodology, R. C., T. T., L. S.; formal analysis, L. S., R. C.; investigation, R. C., L. S., T. T.; data curation, R. C.; writing—original draft preparation, R. C., T. T.; writing—R. C., T. T., L. S.; visualization, R. C., T. T.

Chapters 5 and 7 frequently refer to the work that has appeared in the publication: Webb, S., Torvela, T., Chapman, R., Savastano, L. Textural mapping and building a paragenetic interpretation of hydrothermal veins, with a case study from an Au-Cu-Zn-Pb vein in Glen Almond, Loch Tay, Scotland. Geol. Soc., London, Special Publications 2024, 541 (1) https://doi.org/10.1144/SP541-2023-1

Author contributions: R. C. & L. S. carried out the original vein sample selection for the study; the paragenetic analysis of the Almond Vein, as presented in this thesis, is the result of data acquisition and interpretation conducted dominantly (credited when otherwise) by LS. Similarly, the paragenetic analysis of the Almond vein in Webb et al., 2024 (in the second part of the publication) was developed mostly independently of LS' one. Consequently, both studies arrived at compatible - although slightly different - results.

Webb et al., 2024. S. W.: conceptualization (equal), data curation (equal), formal analysis (equal), visualization (supporting), writing – original draft (equal), writing – review & editing (supporting); T. T.: conceptualization (equal), data curation (equal), formal analysis (supporting), supervision (lead), visualization (lead), writing – original draft (equal), writing – review & editing (lead); R. C.: conceptualization (supporting), data curation (supporting), formal analysis (equal), visualization (supporting), writing – original draft (supporting), writing – review & editing

(supporting); L. S.: data curation (supporting), formal analysis (equal), writing – review & editing (supporting).

This copy has been supplied on the understanding that it is copyright material and that no quotation from the thesis may be published without proper acknowledgement. The right of Lucia Savastano to be identified as Author of this work has been asserted by Lucia Savastano in accordance with the Copyright, Designs and Patents Act 1988

Acknowledgements

I would like to start by expressing my gratitude to NERC (Natural Environment Research Council) and IoM^3 for having provided generous funding to make this research and the associated activities possible.

Then, I'd like to thank my Supervisors, Dr Taija Torvela and Dr Rob Chapman, for the constructive guidance and criticism provided throughout this journey to always help me improve my work. Especially, thank you Rob, for your patience. Huge thanks also to the Examiners, Dr Dan Morgan and Dr Norman Moles, for the invaluable feedback and insights provided in reviewing this thesis.

Thanks a lot to Dr Richard Walshaw, for the support and precious guidance he constantly gave me during my electron-optics sessions, and to Harri Wyn Williams for his amazing work in preparing my thin sections - also, your "musical" lab is such a fun!

Green Glen Minerals and their Staff are hugely thanked for their help during fieldwork activities, and also for providing data and samples.

Thank you to the Turkish colleagues (Drs Nuri, Fatma, Namik and the others) for their warm hospitality in their Istanbul Lab and their professional advice and help. To this end, thanks to Dr David Banks for providing me with the opportunity to meet them (and also for 'Silling' my laser data).

Thanks a lot to Dr Steve Hollis for carrying out the Pb isotope analyses for me.

Special thanks to Milena and Rachel (Leeds) for having made the final stages of this whole PhD journey come true (literally). Thank you so much.

Sincere thanks to my friends - probably don't need to list nicknames but - particularly, thanks to Lisa, Junia (& Latinas), Emi, Georgian and Genny, who were with me through this. And to the fabulous Golden Guys (OMG Leeds) for being so supportive of each other, IAG group, Friday drinks and the Zumba Crew at the Edge. And to my two "special friends" during the PhD/Leeds life. Sincere thanks also go to the Berlin crew and Electronic music, which pulled me through the writing phase, and to those lovely people who wished me luck. And to the new Brno friends.

Most importantly, I could never thank my family enough for having been there throughout. You guys truly are the most precious thing I have. And Pulce.

Finally, I would like to thank myself for being so embarrassingly stubborn not to let myself give up all of this (…at least, so far).

To Anthony.

Abstract

Deciphering the metallogeny of auriferous mineralisation in orogenic belts can often be challenging, due to the potential interplay of genetically distinct hydrothermal processes associated with it and complications that might arise from the discontinuity or lack of visible mineralised outcrops at the exploration stage.

The Loch Tay area of Central Scotland is a host of both gold-bearing hydrothermal veins and widespread placer gold populations. However, the genetic relationships between these types of auriferous occurrences as well as the associated mineralization style(s) have been long unresolved. This can be achieved by combining gold compositional signatures and hydrothermal vein paragenetic histories with an understanding of the local structural/tectonic context. The proposed approach has been implemented to understand the metallogeny of the area and facilitate predicting the nature of possible undiscovered auriferous mineralisation.

In situ mineralization at Calliachar Burn, River Almond and Coire Buidhe records the temporal overlap of separate fluid pulses and at least two gold input events. At the Lead Trial, vein textures and internal variations in the gold alloy composition support the hypothesis of a low-sulphidation epithermal system and evolving nature of the mineralising fluids. In all cases, the range of compositional signatures (alloy and inclusion suites) exhibited by particle populations from alluvial localities is larger than that observed in local eluvial and in situ samples, suggesting subtle variation in mineralogy within geographically proximal and genetically related vein systems. Additionally, the compositional signatures of gold populations from the South of the area (e.g., Glen Lednock and Keltie Burn, for which only placer samples were analysed) indicate derivation from porphyry and low-sulphidation epithermal environments, respectively.

The multi-scale and multivariate approach that is adopted for this study may find successful application in other similar ore-related settings worldwide.

Contents

Chapter 1. Introduction 1-1

1.1 Thesis Rationale 1-1

1.2 Aim and objectives 1-5

1.3 Thesis structure 1-6

Chapter 2. Literature Review and Background 2-7

2.1 Introduction 2-8

2.2 Vein-hosted gold in orogenic belts: an overview 2-8

2.2.1 Parameters controlling the composition and assemblage of gold mineralisation .. 2-8

2.2.2 Hydrothermal veining – Definition, microstructure and main genetic processes. 2-19

2.2.3 Orogenic gold deposits and magmatic-related deposits 2-28

2.3 Characterisation of gold deposits via gold compositional studies 2-36

2.3.1 Gold alloy 2-37

2.3.2 Mineral inclusions in gold particles 2-38

2.3.3 Genetic environments of gold formation 2-38

2.4 Lead isotope studies 2-41

2.4.1 Model ages 2-41

2.5 Geological background of the study area 2-44

2.5.1 The Caledonian Orogeny 2-45

2.5.2 Geology of the Loch Tay area 2-52

2.6 Research questions 2-54

Chapter 3. Methodology 3-55

3.1 Introduction 3-56

3.2 Fieldwork and data collection 3-56

3.2.1 Sampling rationale and collection 3-57

3.3 Sample preparation 3-59

3.4 Analytical techniques 3-60

3.4.1 SEM Imaging Techniques 3-60

3.4.2 Electron Probe Microanalysis on gold particles 3-63

3.4.3 LA-ICP-MS on gold particles 3-64

3.4.4 Pb Isotope analyses 3-67

3.5 Visualisation and presentation of the datasets 3-67

3.5.1 Structural data display 3-67

3.5.2 Gold data representation 3-68

Chapter 4. Structures and textures at outcrop and their significance 4-77

4.1. Introduction 4-78
4.2 Field observations 4-78
4.2.1 Calliachar-Urlar Burn 4-79
4.2.2 River Almond 4-89
4.2.3 Lead Trial 4-92
4.2.4 Coire Buidhe 4-97
4.2.5 Loch Tay area South 4-100
4.3 Interpretation of the structural data 4-101
4.3.1 Possible localisation of the veins in dilational or Riedel shear zones 4-101
Chapter 5. Paragenesis of the hydrothermal veins near Loch Tay 5-105
5.1 Introduction 5-106
5.2 Quartz-bearing veins, BSE and CL characteristics 5-106
5.2.1 Calliachar and Urlar Burn 5-106
5.2.2 (Glen) Almond Vein 5-123
5.2.3 Lead Trial 5-131
5.2.4 Coire Buidhe 5-151
5.3 Vein paragenetic interpretations 5-161
5.3.1 Calliachar - Urlar Veins 5-161
5.3.2 Almond Vein 5-169
5.3.3. Lead Trial Veins 5-171
5.3.4 Coire Buidhe 5-179
5.4 Pb Isotope data 5-180
Chapter 6. Gold compositional signatures in the Loch Tay area 6-183
6.1 Introduction 6-184
6.2 Gold (physical and) compositional characteristics 6-184
6.2.1 Calliachar Burn 6-184
6.2.2 River Almond 6-191
6.2.3 Lead Trial and Ardtalnaig 6-196
6.2.4 Loch Tay South 6-198
6.2.5 Glen Quaich 6-202
6.2.6 Composition of gold at the trace element level 6-204
6.3 Gold compositional signatures 6-209
6.3.1 Calliachar Burn 6-209
6.3.2 River Almond 6-212
6.3.3 Lead Trial and Ardtalnaig 6-215
6.3.4 Loch Tay South 6-216

6.3.5 Critical evaluation of the trace element data 6-217

Chapter 7. Discussion & Synthesis 7-224

7.1 Introduction 7-224

7.2 Discussion 7-225

7.2.1 Comparisons between vein systems across the Loch Tay area 7-225

7.2.2 (Vein-hosted) gold mineralising history 7-233

7.2.3 Genetic comparison of placer gold signatures in the Loch Tay area (and potential for undiscovered mineralisation) 7-240

7.2.4 Regional structural/tectonic context of the mineralisation 7-254

A potential model for the formation of the Calliachar-Urlar veins 7-255

7.3 Regional synthesis 7-260

Chapter 8. Conclusions and Future work 8-267

References 270

Appendix 1. 308

Appendix 2. 313

Appendix 3. 320

Appendix 4. 326

Appendix 5. 328

Figures

Figure 1.1. Geological map (with the main lithologies) of the Loch Tay area of Central Scotland. The localities with gold occurrences (vein-hosted and placer), investigated for this study, are also indicated. Modified from Digimap, Edina, 2023. 1-3
Figure 2.1 From Williams-Jones et al., 2009: "Gold solubility (in parts per billion; solid lines) and speciation at 500 bar and 250°C as a function of log fO2 and pH in a solution containing 1 m NaCl with ΣS = 0.01 m". "The dashed lines separate regions of predominance of H2S, HS-, SO42- and HSO4-. Regions of high solubility are highlighted" (Williams-Jones et al 2009). The stability constants for gold species are from Stefánsson and Seward (2004), and thermodynamic data for other species are from the SUPCRT92 database (Johnson et al. 1992).....2-10
Figure 2.2 "Gold solubility (in terms of molality, m, and parts per billion) and speciation at 1 Kbar as a function of temperature for an aqueous solution containing 1.5 molal (m) NaCl and 0.5 m KCl, with pH buffered by the assemblage K-feldspar–muscovite–quartz" (Williams-Jones et al. 2009). (A) "ΣS (total S) = 0.01 m and f O2 (oxygen fugacity) is buffered by the assemblage hematite–magnetite. (B) ΣS and fO2 are buffered by the assemblage pyrite–pyrrhotite–magnetite; the maximum value of ΣS is 0.1 m. The black dashed line (ΣAu) indicates the total solubility of gold. The stability constants for gold species are from Stefánsson and Seward (2004), and thermodynamic data for other species are from the SUPCRT92 database (Johnson et al. 1992)". From Williams-Jones et al., 2009). 2-12
Figure 2.3 Schematic display (from Hastie et al., 2020) of CDR reactions and textures forming at different stages of the process (using concepts from Putnis, 2009)." Py1a is a hybrid phase between the first-generation pyrite (Py1) and the replacement pyrite (Py2)" Hastie et al., 2020. 2-16
Figure 2.4 a) From Saunders and Burke 2017; b) from Rhys et al., 2020. a) Organization of fractal dendrites in epithermal systems - progression from dissolved Au ions to nanoparticles, to self-organized fractal dendrites (Saunders & Burke 2017); b) Platy-dendritic electrum intergrown in quartz-adularia veinlet (Rhys et al., 2020).....2-17
Figure 2.5 Schematic representation of the relationship between vein type (e.g., antitaxial, syntaxial, stretched crystals), internal crystal morphology and number of crack-seal events against the growth plane localisation (from Bons et al. 2012). 2-20
Figure 2.6 a) Numerical simulation of growth competition (Bons, 2001a) – The "fast growth" direction is indicated by shading; dark crystals are quickly overgrown by the brighter ones (Bons et al, 2012); b) Micrograph of a syntaxial calcite vein showing strong growth competition in the direction of growth (black arrow). Adapted from Bons et al., 2012.....2-21
Figure 2.7 Micrographs (a= cross-polarized and b) plane-polarised) of a stretching vein in quartzite (from Bons et al., 2012).....2-22
Figure 2.8 From Shimizu, 2014: (a) Comb texture. (b) Microcrystalline/colloform texture, with dsseminated ore minerals locally precipitated (c) Colloform texture. The colloform quartz is often associated with Au-Ag minerals. (d) Cockade texture (e) Platy texture. The sample contains groups of platy quartz that are parallel within a group and show local radial elongation.....2-26
Figure 2.9 Elements from the quartz textural classification of Dong et al., 1995. The textures were classified based on three main categories (i.e., Primary, Recrystallisation and Replacement) and include definitions from Lindgren (1899), Schrader (1912), Rogers (1917), Adams (1920), Morgan (1925) Schieferdecker (1959), Boyle (1979), Lovering (1972), Sanderand Black (1988), Saunders (1990). Adapted from Dong et al., 1995. 2-27
Figure 2.10 Adapted from Sillitoe, 2020. Schematic regional context of the principal gold deposit types, inspired by Robert et al. (2007). Depth is expressed on a logarithmic scale. "CRD = carbonate-replacement deposit, HS = high sulfidation, IS = intermediate sulfidation, IOCG = iron oxide copper-gold, LS = low sulfidation, and VMS = volcanogenic massive sulfide"- Sillitoe, 2020. 2-28
Figure 2.11 From Groves et al., 2018: Schematic map of the Denali-Tintina Fault Zone, showing high-angle cross faults, in an "domino" like array within the major Fault Zone. The rotation within blocks was produced by opposite motion on either side of the blocks by faults with the same sense of motion

(Sanchez et al., 2014). Allan et al., (2013) reported some of the localities (Fort Knox, Pogo) in the figure as 'RIRG (Reduced Intrusion-Related Gold deposits)'.'.....2-34
Figure 2.12. Adapted from Zartman & Doe, 1981: Lead isotope evolution models, 206Pb/204Pb versus 207Pb/204Pb. The diagrams show changes in lead isotope composition in a hypothetical two-stage model. The Earth is assumed to be isotopically homogeneous until 3.5 Ga, at which time a crust-differentiating event generates two reservoirs that evolve separately. 2-43
Figure 2.13 Adapted from Shaw et al., 2022. Timeline of the main thermo-tectonic events in the Caledonian Orogeny. 2-46
Figure 2.14 From Tanner, 2014b. Structural map (a) and sketch section (b) of the Grampian Terrane. The Tay Nappe is indicated.....2-48
Figure 2.15. From Tanner, 2014a. Regional-scale faults in the Grampian Terrane. 2-49
Figure 2.16. Adapted from Tanner, 2014a. Gold-bearing mineralisation (specific localities are indicated 1 to 7) in the Grampian Terrane of Scotland. References: 1-2: Ixer et al., 1997; 3-4: Treagus, 1991; 5-6: Parnell et al., 2000; 7: Aherne, Reynolds & Burke, 1992.....2-51
Figure 2.17. Geological map (with main lithologies) of the Loch Tay area of Central Scotland. The localities with gold occurrences (vein-hosted and placer), investigated for this study, are also reported. Modified from Digimap, Edina, 2023. 2-52
Figure 3.1. Examples of particle mount set-ups for polished blocks, RJC 97 and RJC 98 (i.e., gold particles are distributed across populations depending on their sampling localities and relative grain sizes).....3-60
Figure 3.2 From Gotze, 2021. Quartz imaging at the micron scale (crossed polars – a) and CL (b) - from Kemmlitz (Germany); different quartz generations are distinguishable by different CL emission bands (c): (1) blue CL = primary quartz phenocryst, (2) red CL = volcanic quartz of a second generation, (3) yellow-CL = secondary microcrystalline quartz (hydrothermal); the circles in (b) indicate the locations of spectral CL analyses (Gotze, 2021). 3-62
Figure 3.3 a) Tescan SEM; b) JEOL 8230 Electron Microprobe (EPMA). 3-63
Figure 3.4 a) LA-ICP-MS instrument and equipment. Photo credit to Dr Fatma Sisman. b) Particle surface selection to target LA spots analysis (LHS), element signals produced by gold ablation (RHS). 3-65
Figure 3.5 a) Silver profiles from Chapman et al., 2000, indicating the relationships between Ag content of gold populations and volume of mineralized material (Chapman et al., 2000). B) Examples of silver profiles from different gold sample types (from Calliachar Burn and Glen Almond in the Loch Tay area). Gold liberated from multi-sourced material generally shows a wider compositional range, reflected in the gradient of the plot (e.g., Chapman et al. 2000).....3-69
Figure 3.6 a) Ag-Hg and b) Ag-Cu bivariate plots of different gold samples (i.e., placer gold in a), used to estimate the element covariance; b) from Chapman et al., 2016 (Klaza epithermal deposit, Yukon); gold compositional fields are further depicted by specific symbology.....3-70
Figure 3.7 a) Steps in the methodology used to describe inclusion assemblages via radar diagrams (by Chapman, 2019); a) typical orogenic-related inclusion assemblage, indicated by the presence of base metal components; magmatic-related inclusion assemblage, as indicated by the presence of Bi-Ag-Te components.....3-71
Figure 3.8 a) Spider diagram highlighting the distribution (based on the proportions) of different mineral inclusions in a gold population; b) and c) Examples of inclusion assemblages (grouped by localities) of different minerals within the overall assemblage (from Chapman et al. 2018).....3-72
Figure 3.9 From Chapman et al., 2016. Comparative matrix of vein-hosted gold mineralisation and mineral inclusion suites of adjacent placer samples. The shaded areas indicate Pd-bearing minerals. 3-73
Figure 3.10 a), c), d) Silver profiles and b) Mercury profiles of initial and augmented gold samples from Calliachar Burn and River Almond. The data from 2022 incorporates the data from samples collected during previous field campaigns across the same locations. Sample sizes (= number of particles) are also indicated.....3-74
Figure 3.11 From Chapman et al., 2021. Trace element abundances in a study of 1100 gold particles by quadrupole-LA-ICP-MS. a: Element abundances in the entire population, b: Element abundance distribution according to hydrothermal systems. 3-75
Figure 4.1 Geological map with an overview of the locations that were targeted for primary field investigations. LTF = Loch Tay Fault; HBF = Highland Boundary Fault (modified after the BGS geological

map from https://digimap.edina.ac.uk/). Full lithological legend available on https://digimap.edina.ac.uk. 4-78
Figure 4.2 Geological map of Calliachar and Urlar Burn, with details on the structural data collected across the area (modified after the BGS geological map from https://digimap.edina.ac.uk/).....4-81
Figure 4.3 Stereographic projections of the structural data collected across the Calliachar-Urlar area. Pole projections have been calculated for all the measure types and rose diagrams represent statistical estimations of the original plane measurements.....4-82
Figure 4.4 Geological map highlighting the vein outcrops which are most important for this study. These were personally investigated over the two field campaigns of 2019 and 2021 (modified after the BGS geological map from https://digimap.edina.ac.uk/).....4-83
Figure 4.5 'Discovery Vein' field outcrop. a) Contextualization across the stream; b) Detail on the actual vein surface.....4-84
Figure 4.6 V9 Vein outcrop. a) Main vein; b) parallel ~3cm thick vein.....4-84
Figure 4.7 G Vein (a) and V9 Vein (b) hand specimens.....4-85
Figure 4.8. a) V3 Vein outcrop, where a possible sigmoidal geometry is also visible. b), c), d) Main textural and mineralogical features of the V3 Vein, highlighting the abundance of galena mineralisation. 4-86
Figure 4.9 General and in-detail features around the V3 and LS veins. a) and b) LS Vein; c) and d) V3 Vein; e) and f) LS vein structural markers.....4-87
Figure 4.10 Float (a) and b)) and in situ (c)) quartz-bearing specimens from Urlar Burn that have also been used for SEM-CL investigations.....4-88
Figure 4.11 Panoramic photograph of the Glen Almond catchment, taken during fieldwork activity. ..4-90
Figure 4.12 Map displaying (deducted) fault and vein occurrences across River Almond (modified after the BGS geological map from https://digimap.edina.ac.uk/). 4-90
Figure 4.13. a) The Glen Almond Vein in its host-rock; b) in-situ mineral evidence on one the Almond vein(s) surfaces; c) Detail on quartz texture and sulphide mineralisation in the Glen Almond Vein. Photographs in a) and c) were taken by Rob Chapman.....4-91
Figure 4.14 Geological map of the Lead Trial area, inclusive of sample locations (modified after the BGS geological map from https://digimap.edina.ac.uk/).....4-92
Figure 4.15 Lead Trial outcrops at the main site. a) and b) In situ gold-bearing main veining; physical relationships between the main local lithologies (rhyolite and schists); c) detail on silification evidence at the contact between quartz and schist. 4-94
Figure 4.16 Additional outcrop features at the Lead Trial. a) in situ schist reporting evidence of schistosity planes; b) quartz veinlet in rhyolites; c) minor vein in rhyolite, for which internal (syntaxial) crystal growth has been observed.....4-95
Figure 4.17b Lead Trial main textures. a) Polymictic/polyphase breccia (photo source: Erris Gold Resources, 2021); b) Hydrothermal breccia with bladed barite (Ba); c) microcrystalline, white quartz and sulphides; d) weathered quartz with sulphides and rhyolite.....4-97
Figure 4.18 Geological map highlighting the Corrie Buidhe site locations (modified after the BGS geological map from https://digimap.edina.ac.uk/).....4-98
Figure 4.19 a) In-situ quartz and galena vein exposure at the Coire Buidhe mine sites; b) Zoomed in detail of 4.19a; c) and d) Quartz textures at one of the Coire Buidhe sites (NN 70452 34031); areas selected for petrographic thin sections are also indicated.....4-99
Figure 4.20 Photographs of rock specimens from the WNW Coire Buidhe mine site, indicating the typical mineral associations. a) LSCB; b) LScb..... 4-100
Figure 4.21 Geological map showing the distribution of the placer gold samples from the Southern Loch Tay area (modified after the BGS geological map from https://digimap.edina.ac.uk/. 4-101
Figure 4.22 a), b). Structural markers in Calliachar Burn (a) horse-tail structures; b) qtz vein passive marker. c), d). Riedel-shear model accounting for both the Urlar and the Loch Tay Fault. The yellow arrows represent the dextral sense of motion of both the structural markers and the Riedel Shear planes. 4-104
Figure 5.1 SEM-CL images of the LSCG block. a) BSE-mode montage map, where specific sub-areas in Figures 5.1 and 5.2 are also located (5.1b-c and 5.2a); b) and c) BSE and CL Blue modes of the same

section area. Quartz (Qtz), pyrite (Py) and sphalerite (Sph) are displayed as mineralogical components. Multiple quartz generations are visible in CL Blue mode (c)..... 5-108
Figure 5.2 SEM-CL images of the LSGC block. a) and b) BSE and CL Blue modes of the same section area; c) and d) BSE mode pictures that highlight the presence of gold grains in specific sections of the block (pictures taken by Rob Chapman)..... 5-109
Figure 5.3 BSE-mode (a, b, c) and CL-blue mode (d) images of the LSGV (the image in a) was taken by Rob Chapman). The context of a) and b) is given by figure c), where relevant areas are highlighted; gold (Ag content also displayed) is visible alongside the other mineral components in figures a) and b). Images c) and d) were taken on the same area of the section using two different detectors (BSE and CL) – multiple quartz generations are visible in d). 5-110
Figure 5.4 CL-color mode images of LSGV (section sub-areas). Multiple quartz generations (QA_gv, QB_gv, QC_gv) are visible, as well as minor intra-crystal fractures and crystal boundaries. Pyrite and arsenopyrite are the two sulphides identified in these sample areas. Figure b) displays clearly the relationship between quartz and pyrite, which occurs together with QC; the prominent rhomb-shaped void may suggest weathered-out dolomite. 5-112
Figure 5.5 SEM-CL analysis of LSCL2. a), b), c), and e) CL Blue mode photographs of different sub-areas of the thin sections, that indicate the different quartz stages, their inter-relationships and their relationships with the two identified sulphides; in particular, arsenopyrite (ApyC_ls) occurs aslongside QC and pyrite (PyE_ls) and dolomite (DoE_ls) occur as later phases (figures b and e); d) BSE mode photograph that zooms into arsenopyrite mineralisation in quartz. Full montage maps of LSCL2 are available in both BSE and CL Blue modes in Appendix 2. 5-114
Figure 5.6 SEM-CL analysis of LSCV3. a) full montage map in the BSE mode, where the main mineral phases are visible; b) detail of galena mineralisation in void – secondary products (s1= cerussite) fill cracks in galena; c) and d) BSE and CL Blue modes pf the same sub-area in the thin section (also indicated in 27a); e) partial CL-Color mode montage (the full one is available), that highlights the three quartz stages identified and their relationship with the galena mineralisation. 5-115
Figure 5.7 SEM-CL analysis of LSCV9. a) and e) BSE mode photographs of different sub-areas of the thin section; c), d) SE mode photographs highlighting specific mineral phases; b) and f) CL-Blue mode photographs highlighting the different quartz generations. Full montage maps of LSCV9 are available in both BSE and CL Blue modes. 5-117
Figure 5.8 Analysis of LSCDV in sole Cl Blue mode. a) Overview-montage map, that indicates the occurrence of quartz and its physical interaction with the wall-rock (weathered area); b) sub-area of the overview map (as labelled in 29a) where QA and QB are well visible; c) sub-area of the section where QA, QB and QC are visible. 5-118
Figure 5.9 SEM-CL analysis of LSCL3. a) full montage map in CL Blue mode. A sub-area (b) which is also presented in further detail in Figure 5.9, is marked; b) and c) CL Blue mode pictures of sub-areas of the full montage, highlighting the spatial relationships between quartz and galena; d) and e) BSE mode of two other sub-areas of the same thin section, where sulphides and secondary products (i.e., cerussite) are visible. 5-120
Figure 5.10 CL Color mode overview map of LS4B thin section, displaying the relationships between galena (GaC_ub), chalcopyrite (CpyC_ub), CL lighter quartz (QA_ub), and CL darker quartz (QB_uc). The two sulphides fill fractures across QA_ub and QB_ub; galena is, in turn, crosscut by minor fractures. 5-121
Figure 5.11 Rock specimens used for the extraction of the Almond Vein sections/blocks, before being processed. One of the two thin section traces is indicated in Figure 5.11a, where sulphide mineralisation is visible. 11b shows a section of the vein thickness, where the elongated (comb) morphology of the quartz crystals can be observed..... 5-123
Figure 5.12 BSE mode images of one of the polished blocks used for the optical characterisation of the Almond Vein. 5.12a and 5.12b represent two sub-areas of the overview montage map (SEM images taken by Rob Chapman), represented in 5.12c. The images provide a preliminary overview of the mineral composition (Qtz, Dol, Ga, Sph and Cpy) of the analysed block. 5-125
Figure 5.13 BSE mode image that shows the spatial relationships between sphalerite, galena, chalcopyrite, quartz and dolomite in the Almond Vein. 5-126

Figure 5.14 a), c), d) and e) BSE mode images of specific sub-sections of the Almond Vein samples that highlight the physical features of gold in sulphides; b) SE mode image that shows internal compositional variations in a pyrite grain; e) CL Blue mode image that highlights the physical relationships between galena, two quartz phases (qA and qB) and the Dolomite. SEM images in a) to d) taken by Rob Chapman. 5-127
Figure 5.15 CL Blue mode images (Figures a, c, and f) and BSE mode images (Figures b, d, e) three different sub-sections s in the Almond Vein, to highlight the relationships between quartz and sulphides. 5-128
Figure 5.16 a) Full montage BSE map of one of the 'Almond' polished blocks; b) and c) CL Blue and BSE modes, respectively, of two sub-areas in one of the Almond blocks; d) and e) BSE mode images of two close sub-areas in one of the Almond blocks, which emphasizes the spatial relationships between gold, sulphides and fracturing..... 5-129
Figure 5.17 BSE mode images that represent specific minerals from the pan-concentrate and their physical interactions (SEM images taken by Georgian Manuc); a silver-rich gold particle can be observed in 5.17a. The sample was prepared by simply fixing the material on a stub, prior to SEM analysis... 5-130
Figure 5.18 Typical quartz textures and mineral assemblages observed in the Lead Trial samples. a) LSLTA; b) 28641-2; c) 28861-2; d) RX30781. See also Table 5.3. The sample cuts highlight the distinctive quartz textures – vuggy, microcrystalline – the morphology of some of the crystals, and the physical relationships between quartz and sulphides. In figure 5.18c a physical scale is placed beneath the sample..... 5-132
Figure 5.19 LSLTA. a) BSE-mode; b)-d) CL-Blue mode; e) CL-Color mode. A) and b) are images acquired on the same section area. Quartz, sulphides (i.e., galena and sphalerite), baryte and micas (chlorite and sericite) are visible as mineralogical components, alongside zinc secondary products. Pictures 5.19b to 5.19d are especially useful in distinguishing zonation and the first two quartz generations (QA_lt and QB_lt); the larger scale of 5.19e enables view on QC_lt as well. The red lines in c) and e) help distinguishing two quartz pluses in QA_lt (namely, QA_lt1 and QA_lt2). 5-134
Figure 5.20. Gold in LSLTA. a), c) and d) BSE mode; b) and e) CL Blue mode. d) and e) are images acquired on the same section area..... 5-135
Figure 5.21 CL Blue mode image from the LS1b thin section. Three quartz textures are evident (qa_lt1 ; qa_lt2 ; qb_lt) alongside galena and sphalerite..... 5-137
Figure 5.22 LS1b thin section. a) CL Blue mode, with emphases on the quartz phases, their mutual relationships and their relationships with the sulphides; b) BSE mode; c) Color CL mode, highlighting the galena and sphalerite intra-relationships..... 5-138
Figure 5.23 CL Blue mode image extracted from the LS1b thin section analysis, especially showing the relationships between galena and sphalerite. Galena also occurs in sphalerite fractures. 5-139
Figure 5.24 Relationships between quartz textures (qa_at1; qa_at2; qb_at) and sulphides (Ga and Sph) in the 28641 thin section. CL Blue mode..... 5-141
Figure 5.25 Textural and mineralogical characteristics in the 28861-2 thin sections. a) CL-Blue mode; b), c), d) f) CL-Color mode; e) BSE mode. Figure 5.25b shows a zoomed-in area of 5.25a, where the euhedral morphology of the QA_ch1 (quartz) crystals is clearly visible. In 5.25c, fractures tend to accommodate the original crystal boundaries; QA_ch1 and QA_ch2 can be distinguished within the crystals. Sphalerite (dominantly) and galena are the two sulphides visible in these sections..... 5-142
Figure 5.26 28641. Textural and mineralogical details in sections 28641-2. The observed mineralogical species are quartz, sphalerite, galena and baryte. Images a), b) and e) were captured using the CL blue channel, to highlight characteristic quartz textural features (e.g., plumose texture) and distinguish between mineralisation events; some of these features are also displayed in 5.26c, obtained using the CL color channel..... 5-143
Figure 5.27. Thin sections RX30781 (a, b, c) and LSLTD (d, e, f). b), d), e) are in BSE mode.; a), c), f) are in CL Blue mode. SEM-CL imaging of these samples has illuminated the morphology of quartz crystals (5.27a and 5.27c), helped underpin the relationships between quartz and baryte (5.27a), and detected the presence of molybdenite and gold (5.27e and 5.27f, respectively). 5-145
Figure 5.28 RX30781. All images are in the CL Blue mode, except 5.28b, which is in the BSE mode. Besides quartz, mica schist fragments appear in figures b) and c), while baryte, filling quartz intercristal

spaces, can be distinguished from the bright coloration in c). The characteristic "comb" shape of the crystals can be distinguished in 5.28c. QS_rx indicates the fine-grained quartz interspersed with mica-schist fragments..... 5-147
Figure 5.29 RX30781-2 thin sections. A), d), e) SEM-BSE mode; b) and c) CL Blue mode. Comb morphologies are visible in c). 5-148
Figure 5.30. a) and b) "fresh-cut" quartz surfaces across the LSBOIL and LSCB rock samples to extract the respective thin sections; c) and d) LS1 in-situ vein and derived rock sample..... 5-151
Figure 5.31 investigation of the LSBOIL2 thin section. 5.31a and b are BSE and CL Blue overviews (respectively) of two section areas and of the same section area, where the two images overlap (the underlaying area of the BSE map is visually mostly homogeneous due to the dominant presence of quartz; full view available in the Appendix; c) is a detail of 5.31b (still CL Blue mode), and d) is the BSE equivalent of the same section area. 5-153
Figure 5.32 a) and b) BSE and CL Blue mode images, respectively, of the same section area in LSBOIL2; c) and d) are BSE and CL Panchro mode images, respectively, of two different areas of LSBOIL1; e) and f) are, respectively, CL Blue and SE mode images of the section area in LS1, where galena and quartz relationships can best be appreciated..... 5-154
Figure 5.33 LSCB1. a) and b) BSE mode; c) CL Blue mode. Fragmented pyrrhotite (Po) and brecciated chalcopyrite (Cpy) are well visible as sulphides in LSCB1a and LSCB1b; Biotite (Bt) is also visible in all three figures, appearing in physical contact with chalcopyrite and quartz..... 5-156
Figure 5.34 Mineralogical components in LSCB1 & LSCB2. a) to d) BSE mode; f) Color CL mode. 5.34a and 5.35b respectively display sphalerite blemishes and galena inclusions in pyrite; gold in a pyrite fracture is shown in 5.34b. The sample contest (in BSE) of 5.34b is provided in 5.34c..... 5-157
Figure 5.35 LSCB2 thin section. a), b), d) and e) CL Blue mode; c) BSE mode. a) shows an almost full thin section scan in CL. The relationships between quartz and pyrrhotite (Po) are clarified in b) and e), where the "uncertain" QC_cb phase is also evident. Minor veinlets and fractures are visible in d)..... 5-158
Figure 5.36. LSCB1 & LSCB2. a), c), e), g) BSE mode; d) CL Color mode; f) CL Blue mode - the bright Au response is a BSE artifact, not a true CL response. Au appears to fill cavities in most of these cases displayed in this figure. The context of c), where the gold particle is located on a QB_cb margin, is indicated in b). 5-159
Figure 5.37 SEM-CL (a) and BSE (b) images of a section area from the G Vein, where the relationships between the Py3 cataclastic pyrite and the quartz stages (Q3_v3, Q2 and Q1) are visible. The rhombic void indicates the original presence of a carbonate (dolomite or ankerite) crystal..... 5-164
Figure 5.38 Some specific paragenetic relationships (i.e., between quartz and sulphides) in the Calliachar and Urlar Burn veins..... 5-165
Figure 5.39 Calliachar and Urlar Burn overarching, schematic paragenetic table. 5-168
Figure 5.40. Schematic paragenetic table for the (Glen) Almond Vein. 5-170
Figure 5.41. Characteristic textural features in Lead Trial vein samples. a) Plumose texture in quartz, partly overgrown by sphalerite; b) Q3_LT crosscuts Q1_LT(1and 2) and Q2_LT..... 5-173
Figure 5.42. Model for interpretation of the quartz textures at the Lead Trial, in the ideal scenario of precipitation in a single vein/widening fracture. Ga = galena; Sph = sphalerite. a), b), d) quartz euhedral crystals; c) quartz comb crystals. Different quartz crystal morphologies (e.g., sub-spherical and plumose) can be observed in the vein centre, along with galena and sphalerite..... 5-175
Figure 5.43. Quartz textures from some Lead Trial vein samples (LSLTD2, RX30781 and 2864) showing evidence of sector zoning. 5-176
Figure 5.44. a) Gold particle from the Lead Trial crushed-ore (photo credit – Rob Chapman); b) tiny gold particle on euhedral quartz in one of the Lead Trial vein samples (LSLTA); c) three main CL quartz generations in one of the Lead Trial vein samples (LSLTA)..... 5-177
Figure 5.45 Geological map (modified after the BGS geological map from https://digimap.edina.ac.uk/) correlating the Pb model ages to the respective rock sample sites. 5-181
Figure 5.46 Plot of all the (corrected, Yuan et al. 2016) Pb Isotope data. 5-182
Figure 6.1 Map of Calliachar Burn showing the gold sample locations described in this section (modified after the BGS geological map from https://digimap.edina.ac.uk/). 6-184

Figure 6.2 wt% vs cumulative% plots for Calliachar_6, Calliachar_7 and Calliachar_8. Silver (a) and mercury (b) contents in the gold alloy. LOD = Limit Of Detection; LOQ = Limit Of Quantification. 6-186
Figure 6.3 %Hg and %Ag bivariate plots that account for gold in gossan and in-situ samples from Calliachar Burn..... 6-187
Figure 6.4 Inclusion suite observed for Calliachar 6 and 7. a) Mineralogical composition '10' and '08' indicates the total number of inclusions reported for each sample; b) Elemental composition. '18' indicates the total of inclusions reported for this sample..... 6-188
Figure 6.5 wt% vs cumulative% plots for Calliachar_1 to Calliachar_5. Silver (a) and mercury (b) contents in the gold alloy. LOD = Limit Of Detection. LOQ = Limit Of Quantification. 6-189
Figure 6.6 Radar diagrams indicative of the elemental inclusion components in gold samples from Calliachar Burn, downstream (Calliachar 1) to upstream (Calliachar 5). The numbers on top-RHS indicate the total of inclusions reported for each sample..... 6-190
Figure 6.7 Spider diagrams indicative of the inclusion mineral species (respective amounts) in gold samples from Calliachar Burn, downstream (Calliachar 1) to upstream (Calliachar 5)..... 6-190
Figure 6.8 Map of River Almond showing the gold sample locations described in this section (modified after the BGS geological map from https://digimap.edina.ac.uk/). 6-191
Figure 6.9 Compositional characteristics of the in-situ gold from River Almond. a) wt% Ag vs cumulative% plots; b) Almond_6b complementary paragenetic information. 6-192
Figure 6.10 wt% Ag vs cumulative% plots relating to the placer gold samples from River Almond.... 6-193
Figure 6.11 Radar diagrams indicative of the elemental inclusion components in gold samples from River Almond, downstream (Almond_1) to upstream (Almond_5). The numbers on top-RHS indicate the total of inclusions reported for each sample. 6-194
Figure 6.12 Spider diagrams indicative of the inclusion mineral species (respective amounts) in gold samples from Glen Almond, downstream (a) to upstream (b). The numbers to the right of the legend elements in b) indicate the total of inclusions reported for each sample..... 6-195
Figure 6.13 a) and b) SEM pictures of gold particles from the Lead Trial (a) was taken by Rob Chapman; c) Ag vs cumulative% plots relating to the gold samples from Lead Trial/Ardtalnaig. 6-196
Figure 6.14 Inclusion assemblages in the Lead Trial gold samples. The numbers on the Top-right of each diagram indicate the total of inclusions reported for each sample. 6-197
Figure 6.15 Geological map of the South of the Loch Tay area with gold sampling locations (modified after the BGS geological map from https://digimap.edina.ac.uk/). 6-198
Figure 6.16 %Ag versus cumulative% plots accounting for gold samples from the Southern Loch Tay area. Figure 6.16b – Logarithmic scale..... 6-199
Figure 6.17 Cu-Ag binary plots for gold samples from the Southern Loch Tay area. LOQ= Limit of quantification LOD= Limit of detection..... 6-199
Figure 6.18 Radar diagrams indicative of the inclusion chemistry in gold samples from the Southern Loch Tay area. The numbers on the Top-right of each diagram indicate the total of inclusions reported for each sample. 6-200
Figure 6.19 Spider diagrams indicative of the inclusion mineral species (respective amounts) in gold samples from the Southern Loch Tay area..... 6-201
Figure 6.20. Wt.% vs cumulative% plots for the Glen Quaich placer gold sample. Silver (a) and mercury (b) contents in the gold alloy..... 6-202
Figure 6.21. Inclusion suite in the Glen Quaich placer gold sample. a) mineral inclusions; b) inclusion chemistry. Inclusion count in the Glen Quaich sample: 37. 6-203
Figure 6.22. Ag (ppm; a) and Au (ppm; b) vs cumulative percentages plots of LA-ICP-MS and EPMA data obtained for the Calliachar 02 and Lead Trial gold populations (30 particles were used for each of the datasets). EPMA (wt%) values were converted into ppm units to facilitate graphical comparison with LA-ICP-MS values..... 6-204
Figure 6.23 Box and whisker plots indicating the distribution in the abundances (ppm) of Au, Ag, Hg, and Cu for Calliachar Lower, Upper Almond, Invergeldie, Lead Trial, and Ardtalnaig, measured by LA-ICP-MS. The diagrams were built upon the analyses (Au197, Ag107, Hg202 and Cu63) from the same set of particles (30 in total) for each location, except Ardtalnaig (for which only 18 analysed particles were available)..... 6-206

Figure 6.24 Radar displays of the trace element abundances (ppm) by average in the investigated sample sets..... 6-207
Figure 6.25 Schematic representation of the hydrothermal veins and gold sample localities in Calliachar Burn downstream; the projection of the V3 strike towards the G Vein outcrop is also indicated..... 6-211
Figure 6.26 Partition of the inclusion suite in the gold from the Lead Trial based on silver content classes (<29.5% and > 29.5% Ag)..... 6-215
Figure 6.27 a) Te-Ag binary plot for the Lead Trial gold sample (introduced in 6.2.6); b) Mo-Bi vs Ag plot for the Lead Trial gold sample within a specific range of values (full Mo range in ppm is available in Appendix 3). The original Ag content values in ppm have been converted into wt.% to facilitate data visualization on these graphs..... 6-218
Figure 6.28 Te-Mo Binary plots for the Lead Trial gold sample; data in b) are a sub-set of the range displayed in a) - i.e., highlighted by the green rectangle in a)..... 6-219
Figure 6.29. Box and whisker plots indicating the distribution in the abundances (ppm) of Mo (a) and Te (b) across the Lead Trial gold sample (data available in Appendix 3), measured by LA-ICP-MS..... 6-220
Figure 6.30. Multivariate plots of trace elemental concentrations for a) Ag-Mo in the Lead Trial sample; b) and d) Ag-Pb-Zn in the Lead Trial sample ("d" represents a sub-set of the range shown in "b"); c) Ag-Bi-Te from Ardtalnaig..... 6-221
Figure.7.1. Schematic representation of the main textural and mineralogical associations in the Calliachar-Urlar, Glen Almond (e.g., Webb et al., 2024) and Lead Trial Vein systems. 'S1 to S5' are used to indicate the possible stages of the parageneses in an 'encompassing' sense. To be noted that the Lead Trial system has been interpreted in relation to separate genetic processes..... 7-229
Figure 7.2 Cumulative percentile of the number of particles vs increasing wt.% Ag plots, for the examined gold samples. V=VEIN HOSTED. Calliachar_6G = Calliachar 6 in previous sections (also "gossan-derived"); Almond 6H = Almond 6a in previous sections..... 7-235
Figure 7.3. Distribution of the inclusion species (relative abundance) by gold particle (wt.% Ag) classes in the Calliachar_6 (gossan-derived) sample..... 7-236
Figure 7.4. Distribution of the inclusion suite in the gold from River Almond based on silver content classes (up to ~27% and between ~33 and 42% Ag)..... 7-237
Figure 7.5 Graphical comparison of the mineral (spider plots) and elemental (radar plots) inclusion suites of the placer gold samples from Calliachar Burn (Upstream and Downstream), River Almond (Upstream) and Glen Quaich (tot. inclusion number forming the Glen Quaich sample: 37). Chapman et al. (2023c) employs the same datasets presented here; however, the sub-sets relevant to some of the localities (e.g., Calliachar 1, 3, 5 and Almond 4, 5) have been merged in the paper (e.g., "Calliachar Burn", "Glen Almond"), and Almond 1 is regarded as "Sma Glen"..... 7-243
Figure 7.6. Graphical comparison of the gold alloys (Hg and Ag Cumulative%) from the Calliachar Burn, River Almond and Glen Quaich placer samples..... 7-244
Figure 7.7 Simplified geological map of the Calliachar-Urlar Burn, Glen Quaich and Glen Almond area, highlighting the local presence of reported and interpreted (inferred) faults (modified after the BGS geological map from https://digimap.edina.ac.uk/)..... 7-245
Figure 7.8 Conceptual model illustrating how the inclusion signature of the placer gold populations may vary across a stream section (i.e., from upstream to downstream) receiving contributions from the 'upper' gold occurrences..... 7-247
Figure 7.9 Histogram depictions and comparisons of the mineral components (actual quantities) of the inclusion assemblages in the Almond 3, Invergeldie, Glen Lednock and Almond 2 placer gold samples... 7-252
Figure 7.10 Graphical comparison of gold compositional data from the Invergeldie Burn and localities from both Group 1 and Group 2. a) Ag% vs cumulative plots; b) trace element (ppm) radar diagrams. .. 7-253
Figure 7.11. Faults (reported and interpreted) in the central region of the Loch Tay area. Modified from Digimap, Edina, 2021..... 7-259
Figure 7.12. Schematic localisation and distribution of the genetic types of deposits identified in the Loch Tay area. The relative sizes of the polygons are indicative, and inclusive of the potential areas of

"influence" of the relevant hydrothermal systems. Basemap from Digimap (BGS source), Edina (2022). 7-261
Figure 7.13 Projection of the $^{207}Pb/^{204}Pb$ and $^{206}Pb/^{204}Pb$ ratios calculated for the Loch Tay samples on graphical databases (modified after Standish et al., 2014 (a) and Torvela et al., 2022 (b; references therein), respectively. 7-265

Tables

*Table 2.1 Adapted from Torvela et al., (2022); continues to the next pages. Overarching genetic features of some main gold deposit types (namely: Orogenic, Porphyry, Epithermal, Carlin-type and Placer). *''Unmixing due to depressurization can lead to separation of high v. low saline fluids''. Torvela et al., 2022 and references therein: (1) Goldfarb and Groves (2015); (2) Groves et al. (1998); (3) Goldfarb et al. (2001); (4) Gebre-Mariam et al. (1995); (5) Cline et al. (2005); (6) Thompson et al. (1999); (7) Baker (2002); (8) Hart (2007); (9) Sillitoe (2000); (10) Sillitoe (2020) 11) Hannington et al., 1999; 12) Dubé et al., 2007; 13) Galley et al., 2007; 14) Slingerland, 1984; 15) Garnett and Bassett, 2005; 16) Boyle, 1979; 17) Chapman et al., 2023b.....2-29*
Table 2.2. Compositional characterisation of gold according to microchemical signatures and mineralisation styles. From Chapman et al., 2023b – and references therein).....2-40
Table 4.1. Vein and faults measured across the Coire Buidhe outcrops.....4-98
Table 5.1. Polished thin sections from the Calliachar and Urlar Burn veins that have been used for SEM-CL characterisation..... 5-107
Table 5.2. Summary of the textural features and crosscutting relationships in and between the Calliachar-Urlar vein samples..... 5-122
Table 5.3 Thin section IDs and textural, mineralogical features of the Lead Trial rock samples.'' indicates the samples provided by Erris Gold Resources..... 5-131*
Table 5.4. Summary of the textural features and crosscutting relationships in and between the Lead Trial vein samples..... 5-150
Table 5.5 Thin section IDs and textural, mineralogical features of the Coire Buidhe rock samples.'' indicates that the sample was provided by Erris Gold Resources. 5-151*
Table 5.6. Summary of the textural features and crosscutting relationships in the Coire Buidhe vein samples (Figures refs relative to each description to be added)..... 5-160
Table 5.7 Table summarising Pb isotope sample IDs, corresponding rock samples in the Loch Tay area, and the calculated Model ages and Mu values. Raw data, inclusive of the absolute errors, are available in the Appendix..... 5-182
Table 6.1 Gold particle samples from Calliachar Burn and respective details..... 6-185
Table 6.2. Calliachar_8 gold: morphological, compositional and paragenetic characteristics. 6-186
Table 6.3 Gold particle samples from River Almond and respective details..... 6-191
Table 6.4. Gold particle samples from the Lead Trial and Ardtalnaig, with respective details..... 6-196
Table 6.5 Gold particle samples from the South of the Loch Tay area with respective details..... 6-198
Table 6.6. Gold particle sample from Glen Quaich; relevant details and grid reference. 6-202
Table 6.7. LA-ICP-MS elemental (Ag, Au, Pb, Mo) concentrations from two ablation spots in the same gold particle (RJC-134-21-19). 6-221
Table.7.1. Comparative paragenetic Table for the Loch Tay vein systems investigated in this study. The Almond Vein paragenesis partially incorporates the interpretation by Webb et al. 2024; the darker boxes in the 'Quartz' row correspond to the darker CL, overprinting paragenetic stages..... 7-225
Table 7.2. Comparative assessment of the compositional signatures relating to the vein-hosted, gossan and placer gold from Calliachar Burn. The total number of particles hosting inclusions is specified bottom-right..... 7-234
Table 7.3. Comparative assessment of the compositional signatures relating to the in-situ and placer gold samples from River Almond..... 7-238

List of Abbreviations

Apy Arsenopyrite

Ba Baryte

BSE Back Scattered Electron

CC Chalcocite

CL Cathodoluminescence

Cpy Chalcopyrite

EPMA Electron Probe Micro Analyser

Ga Galena

GGF Great Glen Fault

HBF Highland Boundary Fault

LA-ICP-MS Laser Ablation Inductively Coupled Plasma Mass Spectrometry

LOD Limit of Detection

LOQ Limit of Quantification

LS Low-Sulphidation

LTF Loch Tay Fault

Mo Molybdenum

Moly Molybdenite

nA Nanoamps

Po Pyrrhotite

Ppm Parts Per Million by mass

Py Pyrite

Qtz Quartz

REE Rare Earth Elements

SEM Scanning Electron Microscopy

Sph Sphalerite

Wt. % Percentage by weight (of an element in a gold particle composition)

Chapter 1. Introduction

1.1 Thesis Rationale

Beyond having been defined as the noblest metal (e.g., Williams-Jones et al., 2009), gold is also one of the softest and heaviest, and can be preserved in nature in native form due to its high non-reactivity to liquid and gases. Thanks to its excellent conductivity of both heat and electricity, malleability, resistance to corrosion and optical reflectivity (Corti and Holliday, 2004; Energy & Mining, 2023) gold has been frequently employed in modern society for industrial, technological, medical and aesthetic uses. Moreover, it has formed part of the human culture for thousands of years due to its universally recognised monetary value. Also worthy of notice is that a large proportion (10-15%) of the global gold is retrieved as a byproduct of copper, zinc and nickel – critical metals – production (Berkeley College of Natural Resources, 2023; Ferron, 2016).

Native gold is a solid solution of pure gold and silver (which may occur in variable proportions) and, in some cases, other metals. In this work, this is referred to as gold alloy (e.g., Chapman et al., 2021). The purity of gold is generally expressed as gold fineness and measured as (Au × 1000)/ (Au + Ag), where Au and Ag are expressed as weighted percentages (Morrison et al., 1991; Chapman et al. 2021); therefore the value of 1000 (parts per thousands – by mass) stands for the highest degree of gold purity by mass (Energy & Mining, 2023). The term electrum is classically used to indicate gold-silver alloys with (bulk) Au/Ag ratios between 0.2-0.8 (e.g., Gammons and Williams-Jones, 1995).

Gold occurs naturally in various geological environments, and it can be deposited from either magmatic-related or metamorphic fluids, their mutual combination, or their interaction with other fluids in the Earth's crust. Different types of ore deposits are the result of physical and chemical processes that acted over a wide range of temporal scales and from surficial to mid-crustal paleodepths (e.g., McCuaig et al., 2010; Joly et al., 2015, Sillitoe 2020). The most important criteria for their genetic distinction include the characterisation of the nature of their precipitation fluids, mechanisms of metal transport and environment of deposition (e.g., Herrington and Wilkinson, 1993; Williams-Jones et al., 2009; Phillips and Powell, 2010; Zhong et al., 2015).

Certain deposit types are classically recognised and comprise orogenic, porphyry and epithermal (high- and low-sulphidation) systems (e.g., Groves et al., 1998; Ridley and Diamond, 2000; Sillitoe, 2000; 2010; Goldfarb et al., 2005; Simmons et al., 2005). The main characteristics of these deposits are summarised as follows:

- Orogenic: These (high temperature) deposits are typically hosted in quartz-bearing veins in metamorphic terranes and formed over a broad age range (i.e., Precambrian to Phanerozoic) from relatively high temperature (e.g., 250-350 °C) near neutral pH and low-salinity fluids (e.g., Goldfarb et al., 2001). Common mineral associations include: pyrite, pyrrhotite and arsenopyrite.
- Porphyry: these are typically hosted in stockwork and/or breccia or can manifest as disseminated mineralisation. Precipitate from high temperature (e.g., up to 700 °C), oxidised and hypersaline fluids. Common mineral association include: chalcopyrite, chalcocite, molybdenite, bornite, pyrite, tennantite, and tetrahedrite.
- Epithermal (low-sulphidation): generally structurally controlled deposits, these are hosted in fracture-controlled veins and tens of metre scale faults (e.g., Torvela et al., 2022 and references therein). The mineralising fluids are low-temperature and low-salinity, oxidised and near-neutral pH (Sillitoe, 2020). Typical mineral associations include: galena, sphalerite, pyrite, arsenopyrite, and silver.

As such, gold deposits are often found within orogenic belts where they can partially share fluid sources or physically overlap without being genetically related (e.g., Lang & Baker, 2001). Unravelling the metallogeny of auriferous occurrences in orogenic contexts can thus prove challenging; this may be further complicated by the discontinuity (or lack) of visible in-situ mineralisation during the exploration stage.

The Grampian Terrane of the British Caledonides is a crustal-scale strike-slip system hosting both lode (vein-hosted) and placer (alluvial) gold, occurrences for which the in-situ hosts are poorly known. Based on a classical understanding of local gold deposits, it appears that a large part of the regional mineralisation is located in second-order faults of major, left-lateral, transcurrent systems (e.g., Treagus, 1999; Tanner, 2014a), while some of it experienced a magmatic pulse (e.g., Cononish mineralisation, Spence-Jones et al., 2018). In the Grampian Terrane of Central Scotland, the “Loch Tay area” is bounded by the Loch Tay Fault and the Highland Boundary Fault and hosts NNW-SSE sulphide-bearing quartz veins associated with gold mineralisation (Figure 1.1; Mason, 1990; Ixer et al., 1997); these have been identified at targeted locations but often

show poor exposure due to vegetation and overburden. Additionally, gold occurs in the form of widespread alluvial particles in glens and rivers (Figure 1.1). This makes the Loch Tay area a natural laboratory to gain more insights into the local gold mineralisation mechanisms.

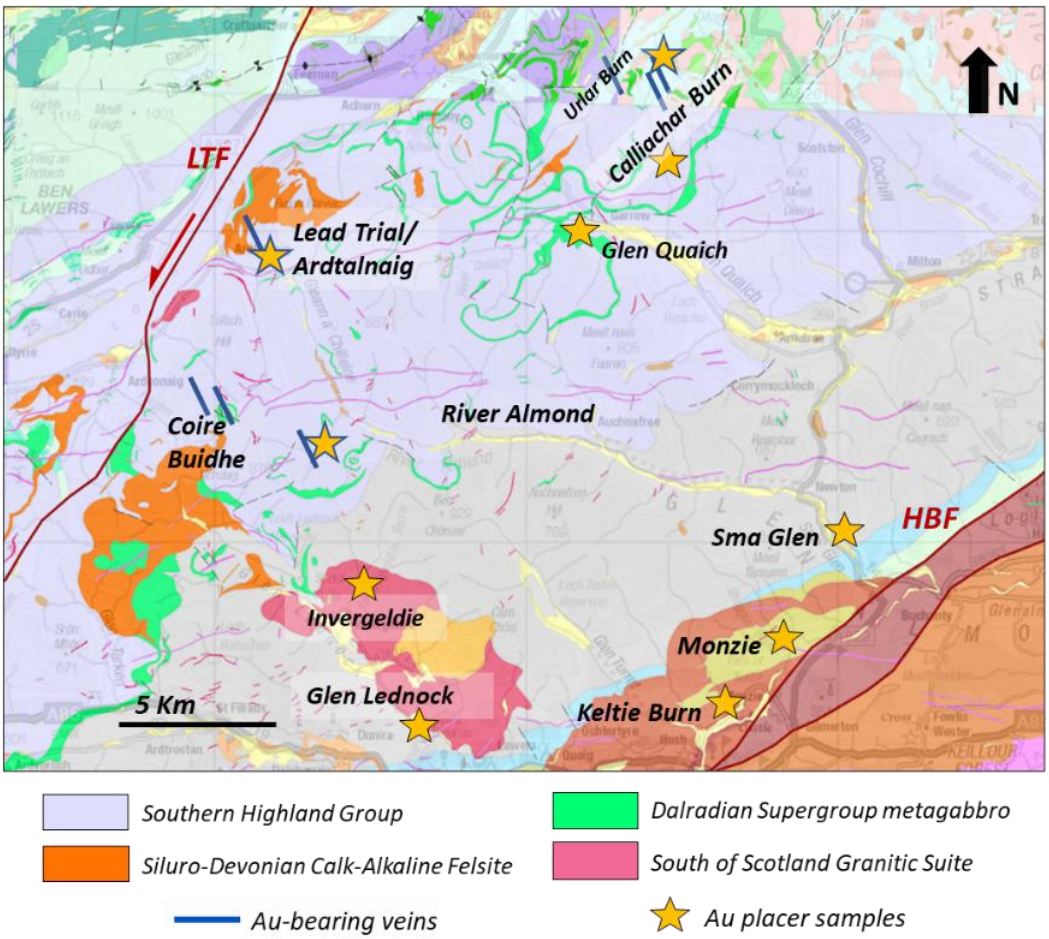

Figure 1.1. Geological map (with the main lithologies) of the Loch Tay area of Central Scotland. The localities with gold occurrences (vein-hosted and placer), investigated for this study, are also indicated. Modified from Digimap, Edina, 2023.

Crustal deformation processes, implying variations in local and regional stress fields, strongly control the porosity and permeability rates in crystalline rocks, where epigenetic gold deposits are typically located (e.g., Sibson et al. 1988; Cox et al., 2001; Micklethwaite et al. 2010). Permeable structures need to generate enough connectivity to link fluid source rocks and reservoirs to ore deposition sites in fracture-dominated hydrothermal systems (Cox, 2005) and, in strike-slip systems, porosity preferentially develops near releasing bends and within dilational jogs (Mount and Suppe, 1992). Tanner (2014a) suggested a repetition of the same structural style to interpret the pattern of gold-bearing quartz veins in the Grampians – as hosted in second-order Riedel fractures of primary transcurrent faults resulting from roughly N–S-

compression. However, the work of Tanner (2014a) didn't focus entirely on mineralisation around Loch Tay (Perthshire), for which only partial structural datasets existed (e.g., Ixer et al 1997). Besides, the interaction of gold-bearing hydrothermal fluids with reactive lithologies plays a determinant role in both the deposition and final chemistry of mineralisation. Therefore, more local structural and lithological controls on the gold-bearing mineralisation need to be considered and explored in the context of the study area.

Earlier ore-focused research carried out near Loch Tay (Ixer et al., 1997; Corkhill et al., 2010) was systematically constrained by the limited vein-hosted, mineralised evidence and relied on classical petrography techniques in spite of more sophisticated instrumentation (e.g., SEM-CL), which became gradually more accessible later. Consequently, the outcomes were inconclusive in terms of deeper implications of the metal associations and fluid nature in the gold mineralising history and of holistic insights into mineralisation styles on a regional scale. Furthermore, new sulphide- and gold-bearing vein occurrences were discovered over the past few years (e.g., Lead Trial prospect and Glen Almond Vein; Lavelle, 2020a, b; Webb et al., 2024) for which sectional interpretations were developed outside of this work.

Compositional studies of gold populations from across the area were previously conducted by Leake et al. (1997a, b) and Chapman et al., (2000a) but utilised many fewer gold particles than the ones forming the current, comprehensive database (produced in the course of this research) of gold samples from central Scotland. Nevertheless, these (and other) authors highlighted the effectiveness of placer-lode relationships in Scotland and Ireland upon the evidence of placer gold being retrieved in proximity to bedrock mineralisation and showing mineralogical similarities with these (Chapman et al., 2000b); the possible effect of glacial processes in gold mineralisation was also taken into account, since the area underwent multiple glaciation events. In these cases, the relative size of a gold population can be evaluated alongside the mineral signature(s) of heavy mineral concentrates, to establish the likelihood that a deposit was transported or dispersed after glaciation processes (Moles and Chapman, 2019).

Gold compositional studies implemented a methodology reliant on the microchemistry of gold, which combines EPMA and SEM investigations of alloys and opaque inclusion suites, respectively (e.g., Chapman et al., 2000a) of gold particle populations, to discriminate their genetic source(s) as either orogenic or magmatic-related and possibly inform the paragenetic context of gold (e.g., Spence-Jones, 2021). The principle governing this technique resides in the use of mineral inclusions as primary source indicators, alongside gold alloy components.

The novel application of LA-ICP-MS on gold particles (e.g., Banks et al., 2018; Chapman et al., 2021), to be integrated into the pre-existent technique, represents a pivotal development in deciphering the nature of possible Au-bearing fluids – especially in light of an enhanced understanding of gold microchemistry achieved over the past (several) years of dedicated research.

Interdisciplinary approaches are necessary to elucidate gold mineralisation processes at multiple stages and scales of the ore-forming system(s). However, the in-depth relationships between gold compositional variations and the (paragenetic) evolution of their potential lode system were previously investigated only by a limited number of studies (e.g., Spence-Jones, 2021), and mineralisation in the Loch Tay area was never a target of these. Furthermore, the combination of detailed compositional studies of detrital gold with an understanding of the local structural-tectonic controls is still somewhat novel and, critically, a non-invasive (e.g., not involving drilling campaigns) exploration approach.

1.2 Aim and objectives

This work aims to build the first metallogenic framework for the Loch Tay area by gaining an understanding of the types of possible hydrothermal system(s) responsible for gold-bearing mineralisation at several localities, and the geological factors controlling them. The approach undertaken, consisting of the main following aspects, could also be exported into other similar ore-related settings worldwide.

1) Investigate the relationships between multi-scale faults, fractures and hydrothermal veins within (and if necessary, around) the study area, to understand local and regional structural controls/stress fields on the gold-bearing mineralisation;

2) Reconstruct detailed paragenetic sequences for gold and sulphide-bearing veins from multiple auriferous localities in the Loch Tay area and cross-compare them, to determine the paragenetic context of the vein-hosted gold mineralisation and the relative chronology of hydrothermal fluid events during vein formation;

3) Establish gold compositional signatures by combining alloy composition and inclusion suite datasets for hypogene, eluvial and placer gold populations from different localities, then evaluate the in-situ (including vein-hosted) gold signatures alongside those of their proximal eluvial and placer expressions, to

I. Underpin the gold mineralising history within the paragenetic interpretations of the auriferous veins (= insights into the compositional variations of gold between paragenetic stages, where the hypogene source is known).

II. Interpret the source mineralisation of placer gold and determine possible gold deposit types (magmatic vs orogenic-related) and their extent on a regional scale.

More insights into the gold genetic signatures and their variations at the trace element level will be achieved from LA-ICP-MS analysis of particles from the same populations.

4) Combining the outcomes from 1, 2 and 3 to deduce the hydrothermal fluid nature and variability against lithological and structural factors in the Loch Tay area (how does this vary across mineralisation styles regionally?) and identify potential, undiscovered in-situ auriferous sources.

1.3 Thesis structure

For these main objectives to be constructively addressed, three chapters (4, 5 and 6) of this thesis focus on the respective, individual research areas – field investigations, hydrothermal vein paragenesis, gold compositional signatures – in terms of data that this project has generated and their interpretation, whilst an ultimate discussion chapter (7) synthesises and evaluates the outcomes from all of them. A literature background overview is provided in Chapter 2, while the methodology applied is described in Chapter 3. To conclude, some ideas moving forward are proposed in Chapter 8, after the main conclusions (Conclusions and Future Work).

Chapter 2.

Literature Review and Background

2.1 Introduction

This chapter introduces (and reviews) the current understanding of gold-bearing deposits in orogenic belts, emphasising the genetic processes related to their formation, their mode of occurrence and evolution, the textural products of the associated hydrothermal veining and structural mechanisms of vein development. The research is focused on interpreting the composition of gold particles in terms of the style of source mineralization. As such, understanding how conditions of gold precipitation can vary in and between deposit types is crucial, and will be primarily discussed in section 2.2.1. The identification of specific hydrothermal vein features plays an important role in gold exploration strategies, therefore the most relevant vein textures and associated genetic/structural mechanisms are described in section 2.2.2. Section 2.2.3 provides an overview of different possible deposit types in an orogenic belt, with a focus on orogenic gold mineralisation. The principles behind gold compositional studies and their application in targeting deposit types are incorporated and discussed in 2.3, to highlight the relevance and potential of this approach to the project. Lead isotope studies, also of relevance to this project, are introduced in 2.4.

An account of the geodynamic and geological setting of the target area of this study is presented in the second part of the chapter (2.5) in an attempt to frame the known gold-bearing occurrences within the possible geological evolution of the area.

In view of the theoretical and geological background provided, specific research questions are raised towards the end of the Chapter (in 2.6) to refine the work objectives.

2.2 Vein-hosted gold in orogenic belts: an overview

2.2.1 Parameters controlling the composition and assemblage of gold mineralisation

Gold is a noble metal whose unique physical properties and economic potential have been recognised and exploited for thousands of years. While native gold is universally known to be highly insoluble (i.e., even in strong acids), its concentration to profitable levels can be achieved by transport and deposition via crustal fluids where this element can first be available in the form of dissolved species (e.g., Williams-Jones et al., 2009). The development of high-grade deposits may be enhanced by specific modes of transport and focus (e.g., Petrella et al., 2020; Voisey et al., 2020) and/or the contribution of gold remobilisation mechanisms coming into effect at a later stage (e.g., Hastie et al., 2020). The following paragraphs will explore some first

and second-order parameters and processes involved in the sourcing, concentration, and distribution of gold mineralisation in orogenic belts.

2.2.1.1 Aqueous chemistry of gold in natural systems

Gold concentration by transport and deposition would require a factor of 1000 – 10,000 from its average crustal abundance of 1ppb to achieve economically important mineralisation (Phillips and Powell, 2010, Pokrovski et al., 2014). Hydrothermal processes are subordinated to the dissolution of gold from a source rock prior to transport and deposition in a specific site. Oxidation of Au to either $Au^{+}_{(aq)}$ or $Au^{3+}_{(aq)}$ only occurs at artificially high values of Eh (oxidation potential), andthe complexation of gold facilitates Au metal dissolution in natural systems. According to the "hard-soft" classification introduced by Pearson (1963), native gold behaves as a "soft" metal, thus favouring bonding with "soft" ligands (e.g., hydrosulphide and chloride; Pearson, 1963; Williams-Jones et al., 2009). Additionally, the atomic structure of gold is characterised by a delocalisation of its outer electron cloud, enabling electron transfer and weak connections with other atoms. This results in the agglomeration of (mostly) negatively charged surfaces that tend to repel each other (Williams-Jones et al., 2009).

Figure 2.1 shows the solubility of gold hydrosulphide ($Au(HS)_2^-$ and $AuHS^o$) and gold chloride ($AuCl_2^-$) at temperatures typical of orogenic gold systems. Fluids from such environments typically contain CO_2 and pH is buffered around 7 (Ridley and Diamond, 2000), therefore the hydrosulphide complexes are the dominant species (Stefánsson and Seward 2004, Williams-Jones et al. 2009). The hydrogen bisulphide complex forms under reducing conditions as $Au(HS)_2^-$, according to equation 1 (Phillips and Powell, 2010):

$$(2) \qquad Au(s) + H_2S + HS^- = Au(HS)_2^- + 0.5H_2$$

The activity of HS^- may be lowered due to boiling mechanisms, recurrent in epizonal and epithermal (i.e., "low-sulphidation") systems. These would produce H_2S fractionation into the vapour via the following reaction (Williams-Jones et al., 2009):

$$(2) \quad HS^- + H+ = H_2S$$

As a result, the solution pH will increase, galvanising gold precipitation (Williams-Jones et al., 2009). Chloride complexes are only capable of carrying gold at very low pH (in acidic environments) or at temperatures higher than those normally associated with orogenic systems (Figure 2.2, Gammons and Williams-Jones, 1997). At higher temperatures, electrostatic

interactions are favoured by a decrease in the dielectric constant of water and allow the Au^+ ions to bond with the harder Cl^- or OH^- ions (Williams-Jones et al., 2009). Thus, the $AuCl_2^-$ species will be dominant in the high-temperature field associated with acid and oxidizing conditions, typical of magmatic-related (e.g., porphyry) hydrothermal systems (Stefánsson and Seward 2004). Elevated gold concentrations (~500 ppb) in the fluid can result from strongly oxidizing and strongly acidic chloride solutions, in response to pronounced hydrolytic leaching in magmatic "high-sulphidation" epithermal settings (Simmons et al., 2020).

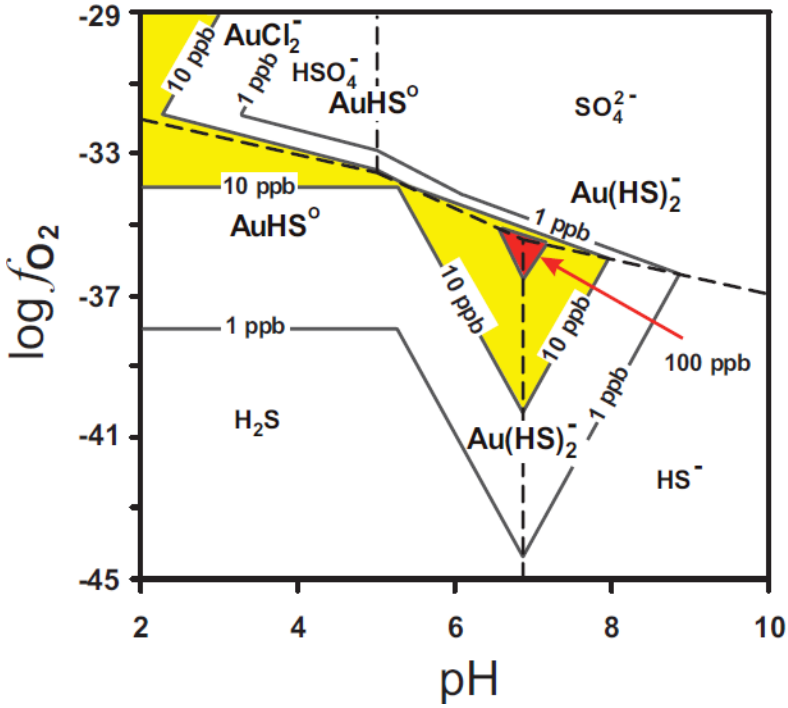

Figure 2.1 From Williams-Jones et al., 2009: "Gold solubility (in parts per billion; solid lines) and speciation at 500 bar and 250°C as a function of log fO2 and pH in a solution containing 1 m NaCl with ΣS = 0.01 m". "The dashed lines separate regions of predominance of H2S, HS-, SO42- and HSO4-. Regions of high solubility are highlighted" (Williams-Jones et al 2009). The stability constants for gold species are from Stefánsson and Seward (2004), and thermodynamic data for other species are from the SUPCRT92 database (Johnson et al. 1992).

2.2.1.2 Transport and destabilisation mechanisms

Transport of gold in metamorphic and magmatic-related hydrothermal systems requires both fluid availability and a source for sulphur. Investigations were conducted by Zhong et al. (2015), who simulated auriferous fluid production during prograde metamorphism, by quantifying the gold, sulphur, and base metals released from pelites during devolatilization. It was concluded that metamorphic 2-10evolatilization processes would be essential in providing both the metals and fluids necessary for orogenic gold deposit formation. Gold solubility and transport are dependent upon reduced sulphur, which may be supplied by the reaction of pyrite transforming into pyrrhotite (equation 3; e.g., Thomas et al., 2011, Finch and Tomkins, 2017). The pyrite-

pyrrhotite transition takes place under greenschist metamorphic facies (at 450° to 600° C) and is connected to chlorite dehydration (Sahoo and Venkatesh, 2015).

$$(3)\ FeS_2 + H_2O = FeS + H_2S + 0.5O_2$$

One of the limitations of the metamorphic 2-11evolatilization model is the difficulty in determining whether metamorphic fluids alone would be capable of extracting sufficient amounts of gold from the hosting lithologies (Zhong et al., 2015). Other models have been proposed to explain gold-sourcing mechanisms, which account for external hydrothermal fluids (and sources) such as magmatic, mantle-derived and meteoric ones (e.g., de Ronde et al., 2000, 2019sib; Mao et al., 2008; Jenkin et al., 1994). Magmatic fluids are generally assumed to be the product of fractional crystallisation (e.g., Tomkins, 2013b). However, for these fluids to constitute the unique triggers of gold mineralisation in orogenic belts, spatial and temporal relationships with the associated gold deposits are necessary. Since direct relationships are often absent (Goldfarb and Groves, 2015), gold mineralisation in such contexts can be interpreted as a result of the interplay between magmatic and orogenic-related fluids (e.g., Mortensen et al., 2022).

The potential of a fluid to transport gold as different species varies in proportion to specific parameters, which include Eh (oxidation potential), pH, and T. The behaviour of gold solubility (Σau) is illustrated in Figure 2.2, according to the relative prevalence of the different (bisulphide and chloride) ligands against fluid temperature (T) (Williams-Jones et al. 2009). In general, chloride speciation is favoured at temperatures higher than 350˚C; sulphide minerals reduce the potential of gold solubility as bisulphide complexes at low temperatures although an increase in solubility may be observed for constant total sulphur (Figure 2.1a, Williams-Jones et al., 2009). Au transportation as bisulphide complexes (e.g., Benning and Seward, 1996; Zezin et al., 2011) has generally proven more efficient (e.g., Pokrovski et al., 2014).

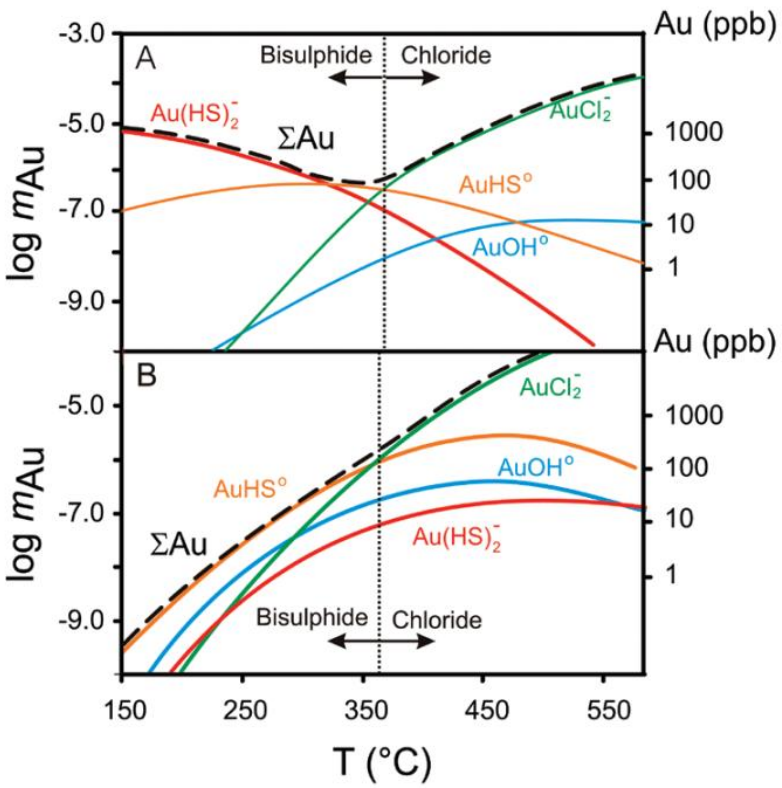

Figure 2.2 ''Gold solubility (in terms of molality, m, and parts per billion) and speciation at 1 Kbar as a function of temperature for an aqueous solution containing 1.5 molal (m) NaCl and 0.5 m KCl, with pH buffered by the assemblage K-feldspar–muscovite–quartz'' (Williams-Jones et al. 2009). (A) ''ΣS (total S) = 0.01 m and f O2 (oxygen fugacity) is buffered by the assemblage hematite–magnetite. (B) ΣS and fO2 are buffered by the assemblage pyrite–pyrrhotite–magnetite; the maximum value of ΣS is 0.1 m. The black dashed line (ΣAu) indicates the total solubility of gold. The stability constants for gold species are from Stefánsson and Seward (2004), and thermodynamic data for other species are from the SUPCRT92 database (Johnson et al. 1992)''. From Williams-Jones et al., 2009).

The stability of the gold hydrosulphide complex is a function of the relationship in Equation 2. The transport of gold is operated by fluids in physio-chemical equilibrium with the lithologies involved. Interaction of such fluids with rocks of mafic nature typically generates a series of reactions yielding a common mineral assemblage – pyrite forms in response to the sulphidation of iron-bearing minerals in the wall rock, implying a reduction of HS^- concentration (equations 4 and 5; Williams-Jones et al., 2009). Pyrite minerals are generated by the reaction of hydrogen sulphide with either Fe oxides or silicates (Phillips and Powell, 2010):

(4) FeO (as silicate) + $2H_2S = FeS_2 + H_2O + H_2$

and

(5) Fe_3O_4 (oxide form) + $6H_2S = 3FeS_2 + 4H_20 + 2H^2$

The typical gold-pyrite association is to be attributed to the bisulphide complex destabilisation from the hydrothermal fluid by a redox reaction with the (iron-bearing) host rocks, precipitating

both pyrite and free gold (Stefánsson and Seward, 2004; Phillips and Powell, 2010; Pearce et al 2015). Enhanced levels of CO_2 in the fluid enable the retention of pH values favourable to gold solubility (e.g., McInnes et al., 2008), whilst CO_2-poor fluids favour gradual solubility variations in response to rock-buffered pH control and early pyrite precipitation, inducing less focused gold deposition (Petrella et al., 2022). Iron, magnesium and calcium, liberated by the decomposition of mafic minerals may react with the CO_2- bearing fluids to generate carbonates (Kerrich and Fyfe 1981). Thus, the common association of pyrite, carbonates and native gold is a consequence of progressive changes in a complex chemical environment, and this assemblage is commonly encountered as a microchemical signature in orogenic gold (Chapman et al. 2009). Furthermore, Petrella et al. (2021) show that host-rock oxidation mechanisms yield high-grade gold deposition, typically associated with vein-hosted mineralisation, whereas sulphidation mechanisms are responsible for lower-grade, disseminated, gold mineralisation. Therefore, the nature of the host rock as well as the CO_2 content of the fluid contribute greatly to the effectiveness of gold deposition processes (e.g., Petrella et al, 2021 and 2022). Destabilization of the hydrosulphide ion can also happen in response to phase separation, which can be caused either by upward migration of fluids in epizonal/epithermal systems or by pressure release at depth due to tectonic activity. Phase separation in epithermal systems is achieved by boiling mechanisms (Herrington and Wilkinson, 1993) and has an effect on gold-complex destabilization analogous to the one observed in mesothermal systems (e.g., Spooner et al., 1987).

Fault valve model and implications

The “fault valve” model was proposed by Sibson et al. (Sibson, 1981, Sibson et al., 1988) to explain the mechanism of gold deposition in response to upward migration of metal-bearing fluids and lithostatic-hydrostatic pressure fluctuations. When the pressure of the rising fluids builds up until reaching supra-lithostatic conditions, it leads to a pre-failure stage and the development of a high-seismicity zone in the brittle domain. The subsequent failure domain produces propagating rupture and fracture permeability draining the fluids from the underlying reservoir. The rapid release of fluids within the brittle domain, results in instantaneous pressure decrease and the fluids being injected into fractures where minerals are precipitated (Sibson et al., 1988, McCuaig and Kerrich, 1998). The deposition of mineralisation (post-failure stage) seals the permeability, induces stress re-accumulation and the makes whole process repeat cyclically (Sibson et al., 1988; Hodkiewicz et al., 2005). The fault valve model implies significant fluid pressure drop and adiabatic cooling after failure (Sibson et al. 1988). A fluid pressure drop of the order of 1.3 kbar has been observed in relatively recent orogenic terrains, in association with phase separation and vein formation (Vrolijk and Myers, 1990, Herrington and Wilkinson,

1993). Assuming an aqueous nature of the fluid, depressurization can lead to fluid supersaturation in amorphous silica (Herrington and Wilkinson, 1993). Although this mechanism of mineralisation is considered valid for orogenic systems (e.g., Simmons et al., 2020), the process of phase separation due to pressure release may be strictly related to epizonal orogenic mineralisation in areas characterised by rapid tectonic uplift (Craw et al. 2010).

2.2.1.3 Colloidal transport of gold

The transport in hydrothermal solutions of gold as colloids was first proposed by Saunders (1990) and Herrington and Wilkinson (1993) to justify scenarios where the traditionally accepted gold ligands - chloride and sulphur species - are thermodynamically unstable (Saunders, 1990). Colloidal transport was also postulated by Pearce et al. (2015), many years later, to explain the apparent imbalance between the amount of gold recovered in the Junction Gold Deposit (Western Australia) and the solubility of the metal in a small volume of fluid. The former authors suggested that gold may not be deposited right after destabilisation but may stay suspended in the fluid phase due to mutual surface interaction with other species (and be deposited at a later stage). According to Saunders (1990) and as re-proposed by Williams-Jones (2009), if gold-bearing solutions reach supersaturation conditions (e.g., due to a sharp drop in temperature), negatively charged colloidal particles may be nucleated; these would repeal each other, making the gold stay in suspension and available for further transport. Gartman et al. (2018) were the first to record colloidal gold in black smoker fluids exhaled into the seawater. They demonstrated that Au colloids can remain in suspension after boiling, showing that the colloid accumulation in boiled liquids can eventually result in gold concentrations that exceed saturation values. Bozkaya and Banks (2015) investigated gold-metal mineralisation from an LS-IS epithermal deposit in western Turkey and found that slightly saturated hydrothermal fluids produced well-developed quartz crystals by a slow, gentle mechanism of cooling, whereas extremely oversaturated fluids led to the deposition of colloidal aggregates or gels by instantaneous pressure drop. Based on the mineral assemblages and element concentrations observed, amorphous silica bands were therefore regarded as indicators of a much more effective mechanism of Au-Ag-base metal deposition than the well-developed quartz.

Colloidal gold also holds the potential to be adsorbed onto positively charged mineral (e.g., arsenian pyrite) surfaces (Williams-Jones, 2009). Experimental investigations were undertaken by various authors (e.g., Pokrovski et al., 2019) to quantify invisible gold incorporation (ppm) in

arsenic-rich pyrite and highlighted a direct, positive relationship between gold enrichment and the arsenic content of pyrite (e.g., Hastie et al., 2020; Simmons et al., 2020).

While colloidal gold has frequently been reported in active hydrothermal systems (e.g., Gartman et al., 2018; Hannington et al., 2016), it is not commonly recognised as a feature of the orogenic-related ones, where the colloidal structure may be destroyed during post-deposition gold coarsening (amalgamation) mechanisms at greater depths (Herrington and Wilkinson, 1993; Petrella et al. 2020). Such textural disruption may however be prevented by the interaction of gold with silica colloids, potentially favouring a high-grade gold enhancement even in mesothermal systems (Petrella et al, 2020).

2.2.1.4 Electrum nanoparticles

The nucleation and aggregation of gold (electrum) nanoparticles are considered determinant stages towards gold deposition from supersaturated solutions (Figure 2.3 a, e.g., Saunders et al., 1994; Saunders and Burke 2017; Hastie et al., 2021). As such, hydrothermal fluids need to reach ''far-from-equilibrium'' conditions for nanoparticles to be formed (Saunders and Burke 2017). While nanoparticles are characterised by an atomic structure which can vary as a function of their size (10^{-9} to10^{-7}), colloids typically have diameters of $<10^{-6}$ m and are (by definition) dispersed in another medium (e.g., an aqueous solution) (Hochella et al., 2008; Saunders and Burke, 2017). Gold transport by nanoparticle suspension has recently been proposed by Petrella et al. (2022) to explain the formation of narrow high-grade gold-bearing veins, for which the action of large volumes (and/or multiple injections) of hydrothermal fluids could not be accounted for. In such cases, the wallrocks show minimal alteration, supporting the argument for a single pulse of fluid depositing high-grade gold. Since the low solubility of gold would not be compensated by the restricted volume of fluid during the generation of gold mineralisation (e.g., Pearce et al., 2015 - see earlier paragraph), their model examines the percolation of a solution pre-concentrated in gold nanoparticles that would enable enrichment to economic levels. The focused precipitation of gold - from solution and as suspended nanoparticles - along with silica and carbon-rich phases is deemed to be the result of phase separation plus physicochemical changes (e.g., of the H_2CO_3 pH buffer) in the hydrothermal fluid. The model proposed by Petrella et al. (2022) would not conflict with the one suggested by Hastie et al. (2020) to justify the mechanism of gold remobilisation and consequent mineralisation upgrade in some orogenic contexts. The ideal scenario described by Hastie et al. (2020) accounts for the fundamental role of gold nanoparticles during coupled dissolution–reprecipitation (CDR) reactions (illustrated in Figure 2.3), which would liberate gold and trace elements from former,

auriferous (100–5,000 ppm) pyrite. These types of reactions would require the activity of an initial fluid (T between 250˚and 400˚) to enable Au "extraction", and possible mediation by polymetallic melts in contributing to the auriferous upgrade. Therefore, this whole process would critically dismiss the mechanisms of gold transport as dissolved species (i.e., $Au(HS)^{2-}$ or $AuCl^{2-}$). Further to this, Hastie et al., (2021) supported the role of nanoparticles in determining the coarsening of gold mineralisation, in conjunction with the change of variables (e.g., pH) affecting the properties of the hydrothermal fluids involved in their transport.

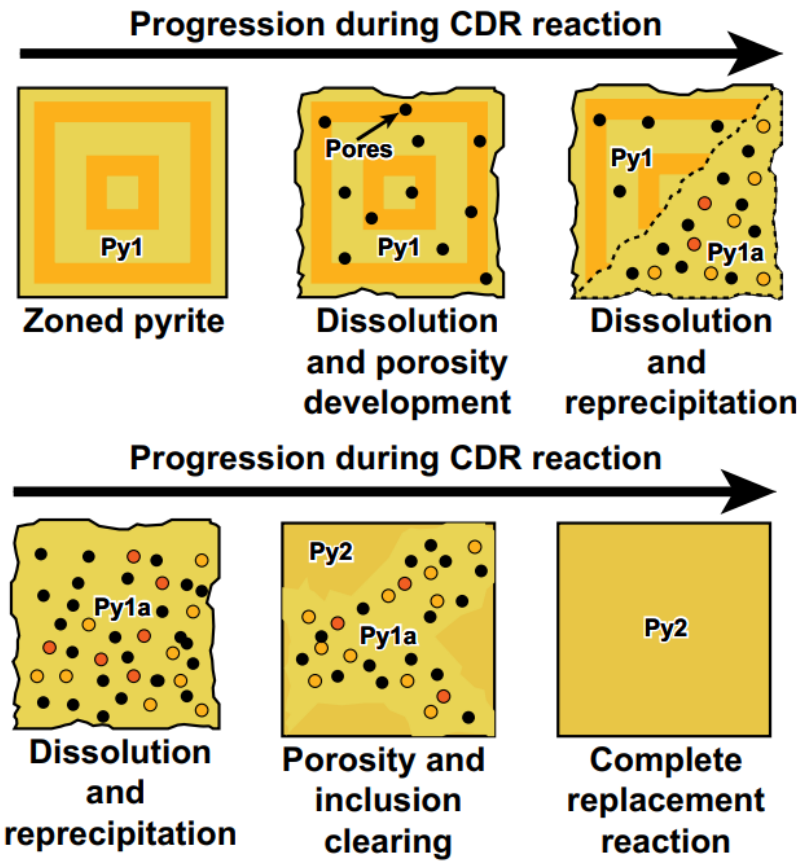

Figure 2.3 Schematic display (from Hastie et al., 2020) of CDR reactions and textures forming at different stages of the process (using concepts from Putnis, 2009).'' Py1a is a hybrid phase between the first-generation pyrite (Py1) and the replacement pyrite (Py2)'' Hastie et al., 2020.

Gold (electrum) nanoparticles have been invoked to explain gold mineralisation upgrading in orogenic settings also by other authors (e.g., Voisey et al., 2020) and are frequently employed to justify gold deposition mechanisms in epithermal systems. In the second case, electrum nanoparticles can either derive from boiling and subsequently agglomerate on-site, or originate at depth and be transported upwards, where they can aggregate after boiling (Saunders and Burke, 2017). Fractal electrum dendrites (Figure 2.4) have been documented in several

"bonanza" epithermal deposits as indicators of nanoparticle agglomeration during ore-forming processes (Saunders et al., 1995 and 2011). These dendrites are normally incorporated in gangue (e.g., silica) minerals (e.g., Herrington and Wilkinson 1993; Saunders and Burke, 2017).

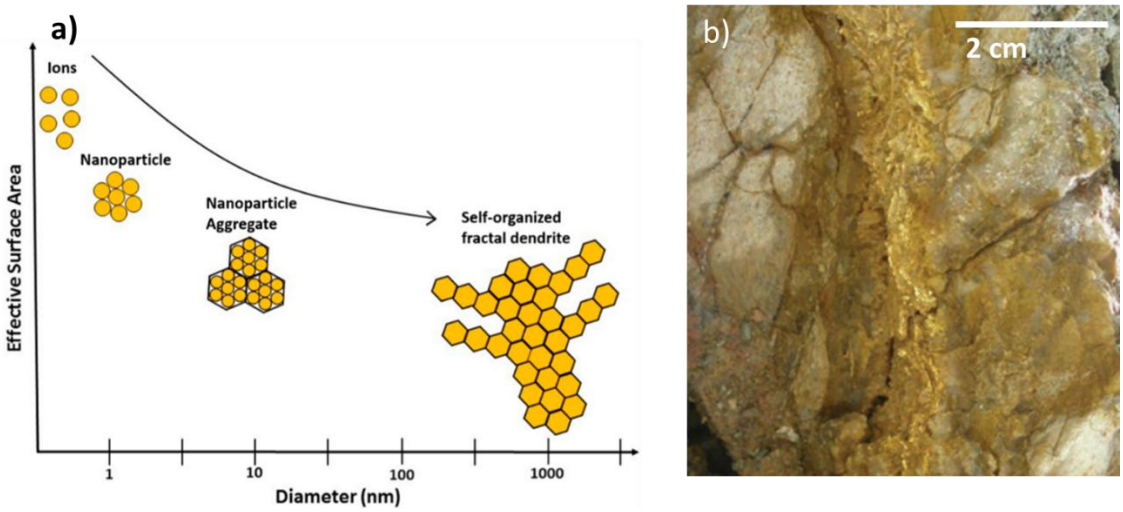

Figure 2.4 a) From Saunders and Burke 2017; b) from Rhys et al., 2020. a) Organization of fractal dendrites in epithermal systems - progression from dissolved Au ions to nanoparticles, to self-organized fractal dendrites (Saunders & Burke 2017); b) Platy-dendritic electrum intergrown in quartz-adularia veinlet (Rhys et al., 2020).

2.2.1.5 Implications for the microchemistry of gold

In hydrothermal systems, gold almost never precipitates as a pure metal and is usually alloyed with silver (e.g., Bolyle 1979). The variable physicochemical conditions of different depositional environments influence the relationships of equilibrium between Au and Ag, which in turn control the gold alloy composition (Gammons and Williams-Jones 1995). In fact, the Au/Ag ratio is governed by both the temperature and chemistry of the fluid (e.g., pH, fS_2, fCl_2, Au/Ag_{aq}; Gammons and Williams-Jones 1995). While Gammons and Williams-Jones (1995) were among the first to model the behaviour of electrum (gold-silver alloy) against the variability of these parameters, some previous experimental work (e.g., by Shikazono 1985, Gammons et al. 1988, Spycher and Reed 1989, Krupp and Weiser 1992) stressed the importance of Au-Ag solid solutions in ore-forming systems, introducing the theoretical basis to later allow interpretation of the parageneses of gold alloys.

Gold alloy and inclusion suites of particulate gold are primary precipitation features (Chapman et al. 2000a, Chapman et al. 2021). A modification of the primary gold alloy may take place by interaction with hydrothermal solutions with which the original Au composition is not in equilibrium (Chapman et al., 2021). These processes may occur in the gold hypogene environment (i.e., during the late stages) or more superficially in the system, and are generally

evidenced by Ag-rich patches or tracks (e.g., Hough et al. 2009; Hancock and Thorne 2011; Chapman et al., 2021). An increase in the silver proportion of a gold alloy may be also dictated by fluid cooling (e.g., Gammons and Williams-Jones, 1995; Chapman et al., 2021), and when a large portion of original alloy is replaced by a more Ag-rich one, it is likely the conditions of the mineralising system experienced an evolving continuum (Chapman et al., 2021). Therefore, textural and compositional changes in individual gold particles, reflected by Au/Ag ratio variations, can be used as ''paragenetic'' indicators in the evolution of gold mineralisation (e.g., Spence-Jones, 2021).

In the mineralising conditions typical of orogenic systems (low-salinity, near neutral pH, aqueous-carbonic fluid), gold is transported in solution predominantly as a bisulphide ($Au(HS)_2^-$) ion, whilst silver occurs as a chloride complex (Huston et al., 1992). As such, the usual parameters controlling the Au content in the alloy are accompanied by αS_2 (Gammons and Williams-Jones, 1995). Epizonal orogenic mineralisation shows commonalities with low-sulphidation epithermal mineralisation, which may be recorded by the associated suite of minerals (Allan et al. 2013). This concept also applies to other types of gold environments (e.g., magmatic-related) and the mineralogical similarities may be reflected in the compositional signature of particulate gold, where they are inherited in the form of mineral inclusions (e.g., Chapman and Mortensen 2006, Chapman et al., 2009; Wrighton, 2013; Chapman et al., 2017). In many cases, mineral inclusions represent components of ore assemblages (Chapman et al. 2000a, Chapman et al. 2021). The compositional signature of a gold population is defined by the combination of its alloy composition and mineral inclusion content (Leake et al., 1991; Chapman et al. 2000a) and can transmit important information on the genetic source of mineralisation (e.g., whether this is orogenic or magmatic-related), when investigated quantitatively. More insights on this topic will be provided in section 2.3.3.2 and Chapter 3 (Methodology).

2.2.2 Hydrothermal veining – Definition, microstructure and main genetic processes

Veins and, specifically, hydrothermal veins are typically the product of a range of natural processes. Several authors (e.g., Hilgers et al., 2004; Bons et al., 2012) define the veins as mineral aggregates that precipitate from fluids in dilational sites or, more specifically, as the "hydrothermal material filling up the space" created and delimited by fracture walls (e.g., Ramsay and Huber, 1987). This definition does not extend to dikes and leucosomes (Passchier and Trouw, 2005). The material within dilatant sites is generally polycrystalline and may consist of either equigranular or subparallel and elongated crystals (Passchier and Trouw, 2005). Vein microstructure is due to a range of microscale parameters and processes, involving fluid transport rate, local deformation rates, anisotropic growth kinetics, and the feedback mechanisms between mineral crystallisation/growth and vein wall separation (e.g., Hilgers et al., 2004).

An essential condition for any vein formation (and development) is the action of fluid circulation within the hosting lithologies. Fluid pressure values in rocks are typically placed between hydrostatic (=pressure of a water column at a given depth) and the minimum principal stress tensor (σ3; Passchier and Trouw, 2005). The pore fluid pressure (P_f) increases until it reaches a critical value (P_c, "confining pressure"), as illustrated by the following relationship (e.g., Passchier, 2005):

$$(6) \quad P_f = P_c = \sigma_3 - T_s$$

where "T_s" is the tensile strength of the rock along pre-existing planes of weakness. Elevated fluid pressures ($P_f = P_{lithostatic}$) are generally necessary to generate fracturing (e.g., Cox, 2010) and are controlled by low permeability values. The intrinsic variables contributing to a decrease in permeability and an increase in pore fluid pressure are deformation rates, dehydration reactions and reduction of pore volume. Though indirectly, the combination of all these factors ultimately impacts the potential of a fluid to precipitate mineralisation in the newly formed fracture(s) (Phillips and Powell, 2010; Passchier and Trouw, 2005).

2.2.2.1 Vein growth mechanisms

The "crack-seal" theory was formulated by Ramsay (1980) to explain the structural mechanism of vein formation, especially in relation to veins comprised of elongated and "fibrous" crystals. The theory relies on the concept that a fresh, narrow fracture may be infilled by crystalline

material; a vein is thus formed, and the event may repeat cyclically as the vein re-opens, allowing injection of new material and timely re-seal (Ramsay, 1980; Dietrich and Ramsay, 1980). However, later work (e.g., by Bons and Jessel, 1997; Oliver and Bons, 2001; Wiltschko and Morse, 2001) suggested that not all the veins originate from this mechanism as some of them can virtually keep growing without the need for further fracturing (e.g., the "antitaxial veins'', see next paragraphs). Bons et al. (2012) classified possible vein types by correlating the number of crack-seal events with the localisation of growth planes (Figure 2.5). These are additionally described as follows.

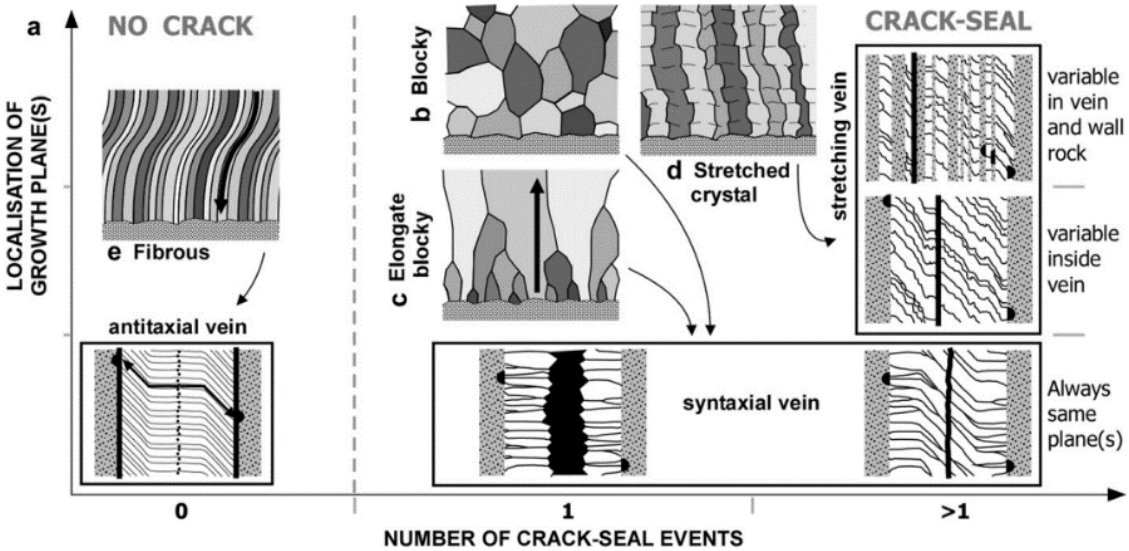

Figure 2.5 Schematic representation of the relationship between vein type (e.g., antitaxial, syntaxial, stretched crystals), internal crystal morphology and number of crack-seal events against the growth plane localisation (from Bons et al. 2012).

Syntaxial veins

The "syntaxial'' veins (Durney & Ramsay, 1973) form when the vein-filling crystals grow in an outward direction from the vein wall-rock. The material is added by overgrowth along the direction of the main crystal axes on both sides of a medium plane ("growth plane'', Bons, 2000), and typically on both the fracture walls (Bons, 2000). This results in the formation of elongated crystals (Bons et al., 2012) which can be either symmetric or asymmetric to the growth plane (Fisher & Byrne, 1990; Fisher & Brantley, 1992). Growth competition occurs when the crystals themselves show different growth rates, causing the preferential growth of some at the expense of others (e.g., Bons, 2001b; Hilgers and Urai, 2002a; Nollet et al., 2005; Okamoto and Sekine, 2011; Figures 2.6).

Syntaxial veins can result from the crack-seal mechanism when the growth interface of the inward-growing crystals becomes the imaginary surface of repeated cracking (Ramsay, 1980; Urai et al., 1991). In the case of an irregularly sealed crack, subsequent failure is more likely to take place, leading to crystal growth across the following crack-seal cycle (Holland and Urai, 2010; Bons et al, 2012).

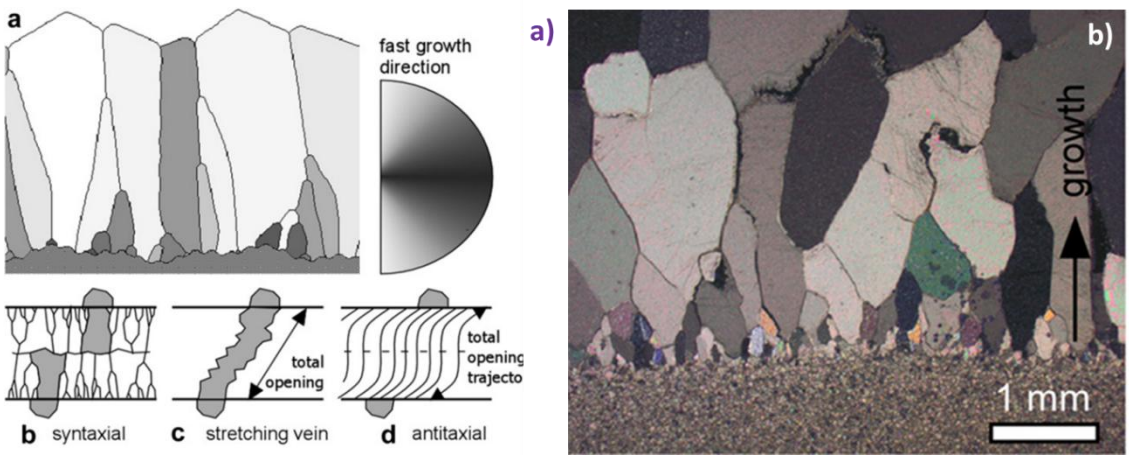

Figure 2.6 a) Numerical simulation of growth competition (Bons, 2001a) – The ''fast growth'' direction is indicated by shading; dark crystals are quickly overgrown by the brighter ones (Bons et al, 2012); b) Micrograph of a syntaxial calcite vein showing strong growth competition in the direction of growth (black arrow). Adapted from Bons et al., 2012.

Antitaxial veins

As opposed to syntaxial veins, the ''antitaxial'' ones are characterised by two growth planes (instead of just one) lying on the outer surface of the vein, at contact with the wall rock (Bons 2000; Bons et al., 2012), where the new crystallising material is simultaneously and gradually added. As a consequence, the core of these veins is constituted of the ''older'' precipitating material, whereas the ''youngest'' material is external (Bons, 2000). The imaginary interface for antitaxtial growth is represented by the ''median zone'' (Oliver and Bons, 2001) and the internal crystals are usually narrow and elongated (sometimes showing very elevated length/width ratios; Bons et al., 2012). These crystallographic characteristics indicate that the mutual growth competition is, in general, largely inhibited (Mügge, 1925, 1928). The absence of growth competition in these types of veins has been seen by some authors (Bons, 2001b; Hilgers et al., 2001) as evidence of ''zero-width'' fracturing to allow vein growth, albeit it has been more commonly accepted that these veins develop in response to crack-seal mechanisms (e.g., Cox et al., 1987; Passchier and Trouw, 2005; Barker et al., 2006).

Stretching veins

The "stretching" veins (Ramsay & Huber, 1983), also called "ataxial" veins by Passchier & Trouw (1996) are, as their nomenclature suggests, characterised by a typical stretched morphology of the crystals (Figure 2.7a and b). These form in response to crack-sealing along a dynamic fracture plane (e.g., Ramsay, 1980; Renard et al., 2005). As such, the fracture (crack) surface of stretched veins can crosscut previously crystallised material and also propagate in the wall rock (Bons et al., 2012), making these veins different from the syntaxial ones where the crack surface is represented by the "growth" front towards which the mineralisation converges from the walls (Bons et al., 2012). Stretching veins are consequently characterised by extremely elongated crystals (also named "fibres") that show no mutual growth competition and develop according to non-established patterns (Bons et al., 2012).

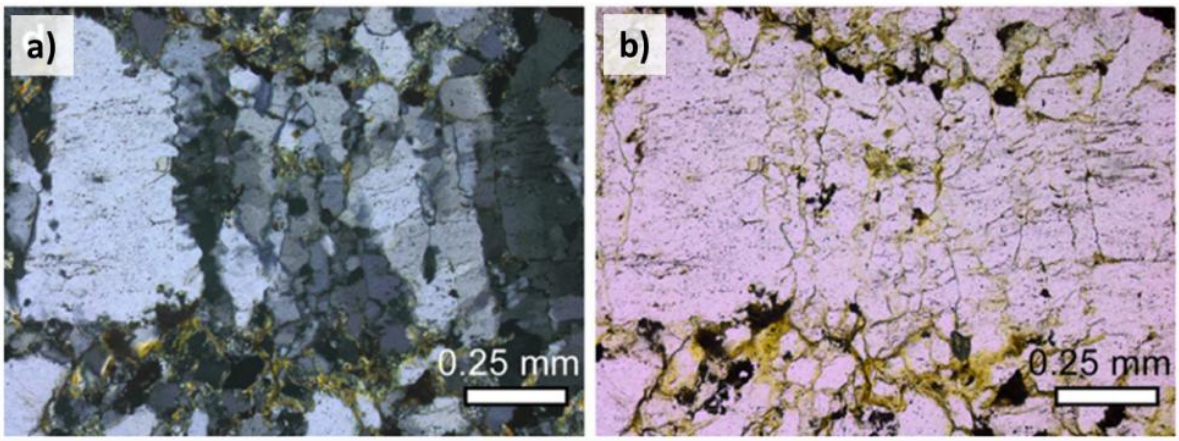

Figure 2.7 Micrographs (a= cross-polarized and b) plane-polarised) of a stretching vein in quartzite (from Bons et al., 2012).

<u>*2.2.2.2 Main crystal morphologies and vein textures*</u>

The vein textural characteristics are designed by the size, shape and crystallography of the minerals that form them (e.g., Cox and Etheridge, 1983; Fisher and Brantley, 1992; Oliver and Bons, 2001; Hilgers and Urai, 2002a; Passchier and Trouw, 2005; Van Noten et al., 2011). Bons (2000) classified the veins according to four main texture types (*blocky, elongate-blocky, stretched crystal and fibrous;* see Figure 2.5), although intermediate-composite types - e.g., where more than a texture coexists in the same vein - can often be observed in nature (Passchier and Trouw, 2005; Okamoto et al., 2011). The two end members are probably represented by the *blocky* and *fibrous* textures. The former can be noted in veins where the internal crystals are

roughly equidimensional and randomly oriented (Bons, 2000) and interpreted to be the product of continuous nucleation/growth or recrystallisation (e.g., Oliver and Bons, 2001; Okamoto and Tsuchiya, 2009). Fibrous textures, as anticipated, can be identified from vein crystals with extremely high length/width ratios and smooth boundaries (Bons et al., 2012) which experienced almost no growth competition between themselves (e.g., Bons 2000). The term "fibrous" is, however, commonly misused under a broader meaning (Bons et al., 2012). Elongated-blocky and stretched crystals can easily occur within the same vein (Okamoto et al., 2008); as such, these features have often been ascribed to composite textures whose internal variations were not dictated by temperature control (Okamoto and Sekine, 2011).

2.2.2.3 Hydrothermal veins in ore-bearing systems

Chemical and physical variables of the fluid

The precipitation of minerals and metals from hydrothermal solutions, in order to generate ore-bearing veins, is a function of several parameters (pressure, pH, chemical reduction, cooling, dilution) and of the way these interact with each other in a complex and evolving system. As a general rule, all minerals tend to become more soluble with increasing pressures (e.g., Rutter, 1983) while fluid supersaturation and crystal growth are facilitated at shallower levels of the system, where much lower pressure gradients and lower temperatures can be achieved (e.g., Tosdal et al., 2009; Newton and Manning, 2010; Bons et al., 2012). The relationships between mineral solubility and fluid temperature are typically more complex and variable according to the properties of the mineral species (for instance, calcite has "retrograde" solubility; Dolejs and Manning, 2010); besides, mineral solubility is also strongly dependent on the chemistry (i.e., pH, Eh, ion concentration) of the fluid (Bons et al., 2012). For example, quartz and carbonate solubilities are highly susceptible to pH control – quartz occurs in solution in the form of silicic acid (H_4SiO_4) whilst calcite dissolves in acid solutions (Bons et al., 2012). Also, sulphide is liberated from H_2S or HS^- due to a pH increase, determining sulphide mineral precipitation (Reed and Palandri, 2006). The redox (or oxidation) potential Eh is another fundamental parameter in defining the equilibrium of a fluid, as some elements are highly sensitive to it. Sulphur is one of these and can form a strong acid under oxidising conditions (H_2SO_4) and a weak acid (H_2S) under reducing conditions (Bons et al., 2012). In this way, the Eh may affect the identity of other dissolved species and indirectly alter the pH of the fluid. In ore-forming processes, this has implications on the role of different sulphur complexes with possible consequences on gold deposition (see section 2.2.1.1). Interaction of the fluid with the host rock

can also significantly change the chemical properties of the hydrothermal solution (Mikucki, 1998; Zheng and Hoefs, 1993). For instance, when acid hydrothermal fluids encounter carbonates and feldspars in wall rocks, the pH increases, as well as when CO_2 is volatilised from a fluid due to boiling (Reed and Palandri, 2006). Finally, the mechanism of dilution can determine cooling of the fluid by input of external cold water, which may be enhanced by heat conduction into cold wall rocks (Reed and Palandri, 2006).

Because of these equilibria, hydrothermal fluids are characterised by transient conditions of temperature and chemistry, which may evolve in response to phase separation prior to mineral precipitation (e.g., Quilichini et al., 2016; Webb et al., 2024). These conditions influence the pattern of precipitation of different mineralogical phases during a fluid event. For instance, chalcopyrite and galena are characterised by a lower degree of solubility with decreasing temperature than sphalerite, therefore will tend to precipitate slightly earlier in a mineralising sequence (e.g., Barrett and Anderson 1988; Kamilli 1988; Leach et al., 2001). Similar principles apply to the precipitation of gold from Au-H_2S complexes (as discussed in section 2.2.1.2) which, in hydrothermal veins, is often found in association (e.g., incorporated as inclusions) with sulphide mineralisation (e.g., Liu et al., 2010).

Gangue mineralisation in ore-bearing veins

Quartz and carbonates are common gangue minerals in ore-bearing vein systems and can crystallise over a relatively large range of conditions (Bons et al. 2012). Calcite veins – and especially the ones with a fibrous nature - generally show lower temperatures of formation than those of quartz veins which, in contrast, have appeared to be independent of the mineral's internal microstructure (Bons et al., 2009; Bons et al., 2012). Quartz has been widely investigated due to its capacity to reflect various fluid properties and parameters and, consequently, its potential to help understand the conditions and evolution of the hydrothermal system responsible for the mineralisation (e.g., Saunders, 1994; Dong and Zhou, 1996; Shimizu et al., 1998; Moncada et al., 2012). In addition, quartz is chemically more stable than calcite and tolerates post-crystallisation weathering (e.g., Bons et al., 2012; Shah et al., 2022). Because of the recurrent euhedral morphology (often observed in hydrothermal veins), quartz is usually interpreted as the first mineral to originate in a sequence as a result of unimpeded growth; this assumption may, however unjustified when the mineralisation is precipitated into earlier vugs (Wilson, 1994; Ahmed et al., 2009; Webb et al., 2024).

Quartz textures

One of the main characteristics of ore-bearing hydrothermal veins is the large variety of quartz textures that they can exhibit, as a function of the physicochemical characteristics of the fluid(s) and pressure and temperature conditions under which quartz formed. Therefore, specific textural features can be used, along with other types of investigation, to constrain the environment of deposition and crystallisation of the ores. Because hydrothermal veins may result from less or more complex interactions of multiple episodes of fluid flow and mineral precipitation, the deriving quartz textures can reflect mechanisms of fracturing, dissolution and recrystallisation (Rusk, 2012). The SEM-cathodoluminescence technique has the unique potential to illuminate the chronological sequence of these textural events by establishing their relative crosscutting relationships. However, an account of the principles behind the application of this tool is beyond the purpose of this section and will be appositely presented in Chapter 3 (Methodology; paragraph 3.4.1.1). Gold-bearing epithermal systems are arguably the ones that display the greatest variety of quartz textures, as these reflect the dynamic nature of fluid evolution around the deposits, while other types of hydrothermal systems (i.e., orogenic) are characterised by a more limited range of textural features within their vein expressions. Textual investigations of hand specimens from epithermal deposits have systematically revealed a transition from coarsely crystalline (at depth) to fine-grained and microcrystalline morphology towards more surficial levels of the system (Dowling and Morrison, 1989; Hedenquist et al., 2000; Simmons et al., 2005; Shimizu, 2014). Quartz from orogenic (especially) and porphyry deposits, in contrast, tend to appear much more homogeneous due to the higher temperatures and pressures involved in the vein formation (e.g., Rusk, 2012; Rottier and Casanova, 2021). Shimizu (2014) proposed a revised classification of quartz vein textures in epithermal ores, identifying six textures (*crustiform, comb, microcrystalline, colloform, cockade and platy;* Figure 2.8) through hand specimen observation and previous literature work (e.g., Roger, 1917; Adams, 1920; Lindgren, 1933; Dong et al., 1995; Moncada et al., 2012). Their features are summarised as follows.

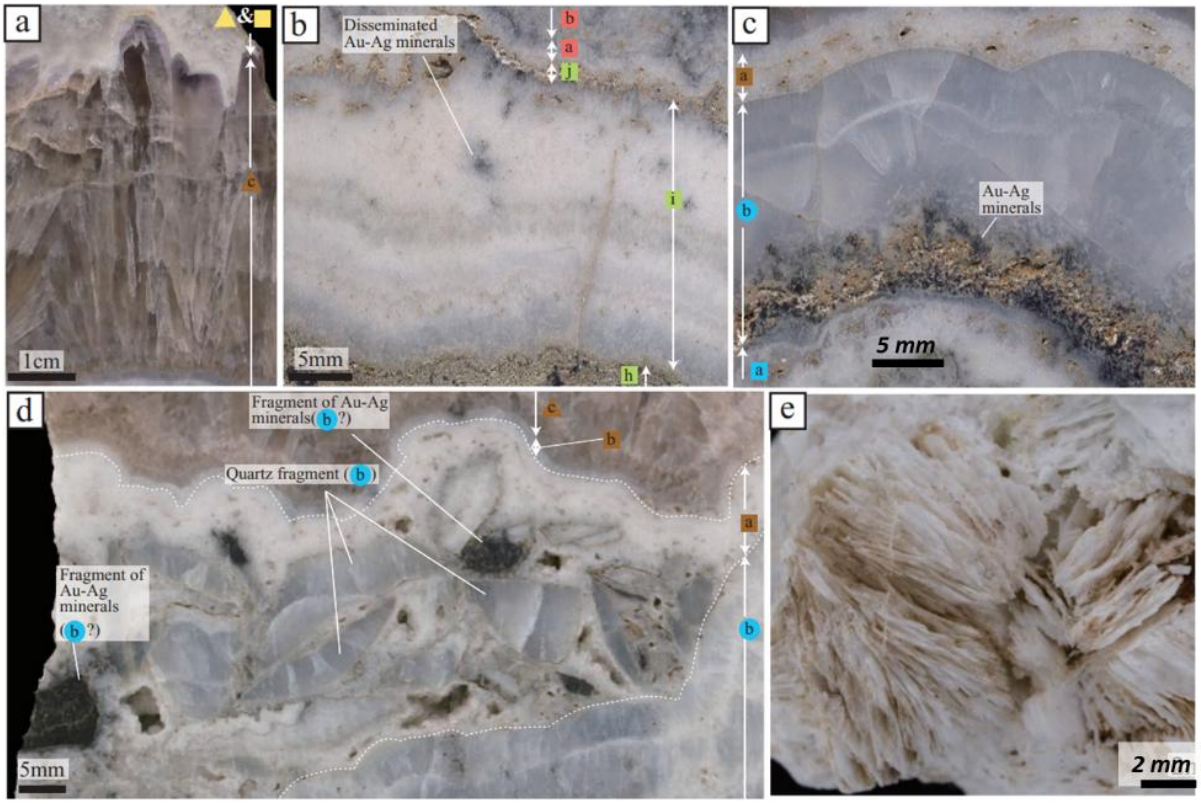

Figure 2.8 From Shimizu, 2014: (a) Comb texture. (b) Microcrystalline/colloform texture, with dsseminated ore minerals locally precipitated (c) Colloform texture. The colloform quartz is often associated with Au-Ag minerals. (d) Cockade texture (e) Platy texture. The sample contains groups of platy quartz that are parallel within a group and show local radial elongation.

Crustiform textures are primary depositional textures formed of subparallel, relatively thin (up to a few centimetres) "crusty" layers of minerals and are typically symmetric to the footwall and the hanging wall of the veins (Shimizu, 2014);

Comb textures (Figure 2.8a) are primary textures formed of parallel (or subparallel) euhedral quartz crystals elongated perpendicularly to the vein walls and adjacent to each other. This texture is commonly interpreted to be the product of slightly supersaturated silica fluids, therefore, of slowly fluctuating physicochemical conditions of the solution (Fournier, 1985). Such configuration derives from an adaptation of crystal growth and morphology to compete for space (Grigor'ev, 1965), implying that the direction of the maximum growth rate coincides with the crystal "major" axis, as discussed in section 2.2.2.1.

The *Colloform* texture (Fig. 2.8c) is a composite texture formed of mineral aggregates with mixed morphologies - spherical, botryoidal, reniform - that are strictly connected to Au-Ag mineralisation (example in paragraph 2.2.1.3). This texture is indicative of a high degree of silica supersaturation, resulting in rapid crystal precipitation (Fournier, 1985; Shimizu, 1994).

Cockade textures (Figure 2.8d) can be observed when quartz grows outwards from rock fragments during early veining stages, giving rise to patterns of concentric bands (Shimizu, 2014).

The *Platy* texture (Figure 2.8e) is composed of quartz crystals distributed in bladed morphologies (e.g., Dong et al., 1995), resembling pseudo-acicular aggregates under a microscope (Shimizu et al., 1998 and 2014)

Microcrystalline textures (Figure 2.8b) are formed of anhedral quartz crystals and agglomerates that typically appear homogeneous and either vitreous or milky in hand specimen. Microcrystalline bands are associated with a high degree of silica supersaturation, forming amorphous silica (Fournier, 1985; Dong et al., 1995). As such, they are often accompanied by Au-Ag mineralisation and *colloform* textures (Shimizu, 2014).

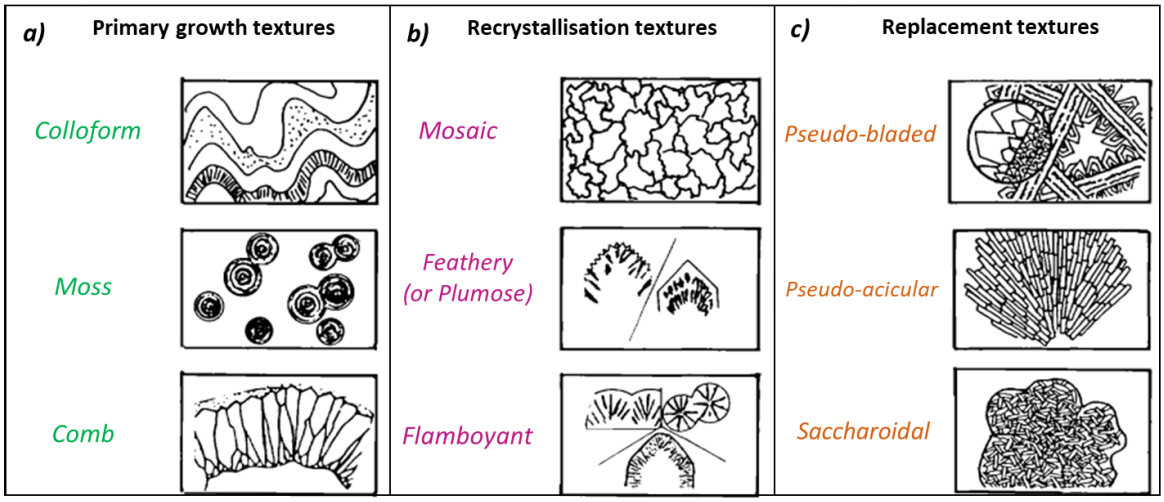

Figure 2.9 Elements from the quartz textural classification of Dong et al., 1995. The textures were classified based on three main categories (i.e., Primary, Recrystallisation and Replacement) and include definitions from Lindgren (1899), Schrader (1912), Rogers (1917), Adams (1920), Morgan (1925) Schieferdecker (1959), Boyle (1979), Lovering (1972), Sanderand Black (1988), Saunders (1990). Adapted from Dong et al., 1995.

A former textural classification for epithermal quartz, compiled by Dong et al. (1995), included other sub-types of textures (exemplified in Figure 2.9) which were later incorporated by Shimizu (2014) under the nomenclature presented in this section. Among these, the *Moss texture* was inferred to originate from silica gel, requiring a high degree of fluid supersaturation with respect to amorphous silica (Fournier, 1985). Moss textures were often found alongside colloform textures in siliceous sinters within active geothermal systems (e.g., White et al., 1956; Herzig et al., 1988; Fournier et al., 1991). The two texture types were differentiated based on the mode of occurrence of their initial nuclei: adherent to the wall-rock in a scenario of colloform texture

formation, and suspended in silica gel as precursors of moss textures (Dong et al., 1995). Shimizu (2014) demonstrated that for certain epithermal systems a firm linkage between intense boiling conditions, silica supersaturation and precious metal precipitation can be deduced, as proven by the concentration of Au- and Ag-bearing mineralisation within colloform and microcrystalline quartz textures. However, gentle boiling - around temperatures of 243° to 268°C and inferred from the presence of comb quartz crystals - has been shown to play a significant role in the physical transport and deposition of precious metals.

2.2.3 Orogenic gold deposits and magmatic-related deposits

Gold mineralisation can form in a variety of geological environments, which can possibly encompass an indefinite number of hydrothermal scenarios. These involve precipitation from magmatic, mantle-derived and metamorphic - which can additionally be mixed with meteoric – fluids. As such, the associated mechanisms of gold transport, destabilisation and trapping are a function of the geodynamic context, which in many cases entails subduction and collision in an accretionary setting (Sillitoe, 2020; Table 2.1). A universal and univocal classification of gold deposit types has been so far unachievable, since certain occurrences may exhibit equivocal traits and/or the overprint of later deformation and metamorphic events (Sillitoe, 2020). Furthermore, multiple deposits may spatially overlap (e.g., Liu et al., 2021b; Torvela et al., 2022, Figure 2.10), for example, in the proximity of intrusive bodies which may have an actual genetic relationship with only some of them (Lang & Baker 2001), leading to their misinterpretation.

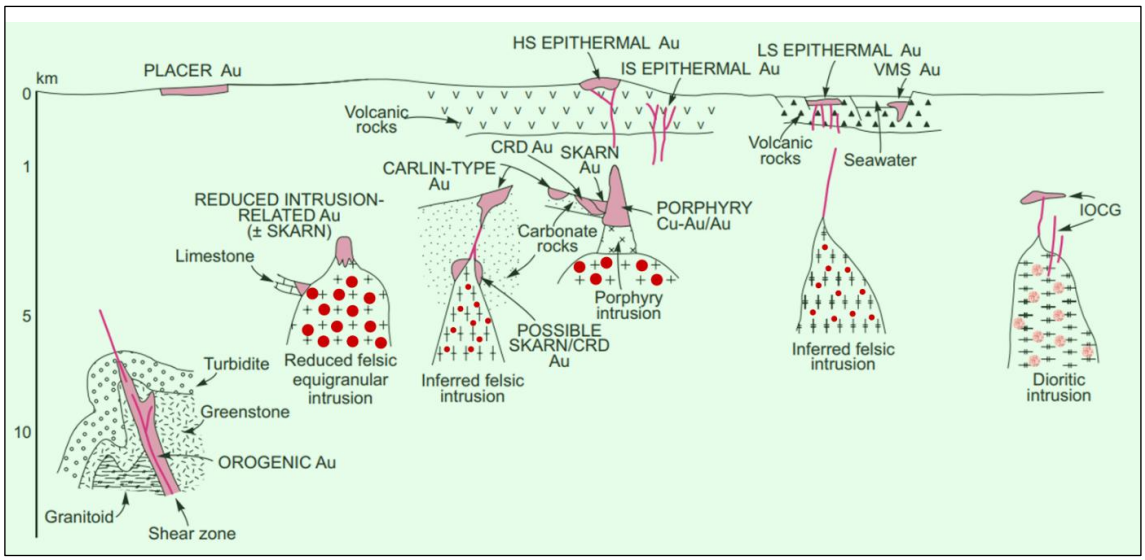

Figure 2.10 Adapted from Sillitoe, 2020. Schematic regional context of the principal gold deposit types, inspired by Robert et al. (2007). Depth is expressed on a logarithmic scale. ''CRD = carbonate-replacement deposit, HS = high

sulfidation, IS = intermediate sulfidation, IOCG = iron oxide copper-gold, LS = low sulfidation, and VMS = volcanogenic massive sulfide''- Sillitoe, 2020.

As anticipated in Chapter 1, some major categories of deposit types are generally recognised over others (namely orogenic, epithermal, porphyry and carlin-type), whose main characteristics are reported in Table 2.1 (by Torvela et al., 2022, plus references therein), although other types (and subtypes) also occur globally - e.g., placer and paleoplacer, Volcanogenic Massive Sulfide (VMS), Reduced Intrusion-related (RIGS), Figure 2.10. The following paragraphs will provide an account of the main genetic and structural features of orogenic gold deposits and, particularly, the Phanerozoic ones, as these were "classically'' associated with the type of mineralisation occurring in the area object of this study (located in the Grampian Highlands of Scotland).

*Table 2.1 Adapted from Torvela et al., (2022); continues to the next pages. Overarching genetic features of some main gold deposit types (namely: Orogenic, Porphyry, Epithermal, Carlin-type and Placer). *''Unmixing due to depressurization can lead to separation of high v. low saline fluids''. Torvela et al., 2022 and references therein: (1) Goldfarb and Groves (2015); (2) Groves et al. (1998); (3) Goldfarb et al. (2001); (4) Gebre-Mariam et al. (1995); (5) Cline et al. (2005); (6) Thompson et al. (1999); (7) Baker (2002); (8) Hart (2007); (9) Sillitoe (2000) ; (10) Sillitoe (2020) 11) Hannington et al., 1999; 12) Dubé et al., 2007; 13) Galley et al., 2007; 14) Slingerland, 1984; 15) Garnett and Bassett, 2005; 16) Boyle, 1979; 17) Chapman et al., 2023b.*

Gold deposit type	Trap/mineralization type	Host type	Tectonic setting	Crustal palaeodepth	Temperature of ore-forming fluids	Mineralogical and/or alteration zonation
Orogenic gold	Quartz ± carbonate veins and breccias in lower-order structural traps (veins, faults, shear zones, fold hinges) near major crustal faults; typically showing evidence of progressive deformation and multiple fluid pulses (e.g. 1)	Variable metamorphic and magmatic rocks (e.g. 1)	Orogenic belts: late to post-peak metamorphism; form typically, but not always, during the late stages of the orogeny (2)	Variable: <5 km to >15 km; typically 5–7 km (2; 3)	Variable but up to 650–700°C; typically *c.* 350°C (2; 3; 4)	Alteration not systematic: any alteration and its type depends on the effective chemical gradient between fluid and host; nugget effect common in gold grade (1)
Oxidized intrusion-related gold systems (Porphyry Au (-Cu) systems)†	Typically in breccias and veins, stockwork and dissemination; also in fracture zones, sheeted veins, skarns/replacement ore distal to intrusion. Major deformation post-deposition rare (9). Au grades usually low (<1.5 g t^{-1}; e.g. 10)	Accretionary wedge or back-arc basinal sedimentary rocks (9)	(Locally) extensional sites in continental and island volcanic arcs at convergent margins; usually pre-collisional, syn-subduction (9)	Typically 1–2 km (9)	500–700°C proximal to intrusion; <350°C distally (9)	Yes: zoned alteration, albeit often overprinting by successive magmatic fluids: proximal potassic to propylitic, intermediate pyrite-rich phyllic, to outer argillic zones in the epithermal parts of the system (9)
Carlin-type	Anticlinal traps and similar structural culminations within reactive, permeable calcareous host rocks capped by non-reactive siliciclastics (5)	Non-metamorphic calcareous and pyritic sedimentary rocks (5)	N/A: traps form along orogenic thrust fronts but mineralization post-orogenic extension and/or strike slip (5)	<5 km (5)	*c.* 180–240°C (5)	Not systematic (5)
Epithermal deposits Au(-Ag) (low-, intermediate- and high-sulfidation types: LS/IS/HS)†	100 m-scale fault- and fracture-controlled veins; low- and intermediate-sulfidation types can be very rich with >30 g t^{-1} Au; colloform banding and vugs very common (10)	Volcanic host but fluids derived from buried intrusion(s) of variable compositions (10)	Volcanic arcs and orogenic belts (10)	<1 km	200–300°C (10)	Yes: pervasive silicification and argillic alteration (10)
Fluvial placer deposits	Physical deposition of detrital particles controlled by variations in hydrodynamic setting at all scales (14)	Fluvial sediments (15, 16)	Various, according to interplay of geological and geomorphological setting (15, 16)	Contemporary erosion level	N/A	N/A

Gold deposit type	Syn-ore magmatism	Other typical metals/elements	Fluid type	Fluid CO_2 content	Fluid salinity (NaCl equiv.)
Orogenic gold	Can occur but no universal association with magmatism in time or space (1)	As, B, Bi, Sb, Te, W; low base-metal contents (1)	Aqueous-carbonic, 'metamorphic' fluids injected during multiple seismic cycles (1)	5–20 mol% (1)*	3–7 wt% (1)
Oxidized intrusion-related gold systems (Porphyry Au (-Cu) systems)†	Yes: typically crustal melts of intermediate composition, low-K calc-alkaline, oxidized, magnetite-rich, sulfur-poor; not highly fractionated granitic magmas (9, 10). In composite intrusions, high grades usually with early magmas only (9, 10)	Cu very common and often dominant; Zn, Ag, Pb, Mo, Te; occasional PGEs; low As and Hg except in the most proximal epithermal parts of the system (9)	Oxidized magmatic fluids (9)	25–30 mol% in intial magmatic fluids (9)	40–60 wt% in initial magmatic fluids; 5–20 wt% in later fluids* (9)
Carlin-type	Probably none, although some of the fluids may have magmatic origins (5)	As, Sb, Tl, Hg, Ba, F; low base metal and Ag contents; some U (5)	Aqueous-carbonic from a variety of sources ± fluid mixing (5)	<4 mol% (5)	2–3 wt% (5)
Epithermal deposits Au(-Ag) (low-, intermediate- and high-sulfidation types: LS/IS/HS)†	Yes; igneous intrusions at depth; HS and IS above shallow intrusions; LS above deeper intrusions of up to 10 km depth (10)	Ag common; base metals occur in many IS and HS type deposits; LS types related to alkaline magmas can be high in Te (10)	Vapour-rich magmatic fluids: HS fluids acidic; IS and LS fluids near-neutral (10)	Variable (10)	Usually low especially in LS but can be higher in IS/HS (10)
Fluvial placer deposits	N/A	Can be significant: governed by compositional characteristics of source (17)	N/A	N/A	N/A

Previous attempts were made to decipher the mineralisation styles that acted across the Loch Tay area of Central Scotland, some of which led to the interpretation of deep-seated

mantle/magmatic inputs contributing to the auriferous mineralisation at Calliachar and Urlar Burn (Ixer et al., 1997), and of a porphyry-related style at the Tomnadashan and Coire Buidhe localities (Pattrick, 1984). However, due to the complexity in classifying different deposit types, as previously stated in this paragraph, and the systematic lack of outcrop exposure in the area, no well-constrained hypothesis could be made. Recent work from Chapman et al. (2023c) highlighted and supported the possible occurrence of more deposit types (i.e., orogenic, porphyry and low-sulphidation epithermal) upon the analysis of placer gold particles from several localities. Some of the dataset employed by Chapman et al. (2023c) is presented in this thesis as parts of Chapters 6 and 7.

2.2.3.1 Orogenic gold deposits: An overview

Beyond representing the most ubiquitous source of gold mineralisation globally, orogenic gold deposits (OGDs) can also be placed among the most profitable ones (Mortensen et al., 2022). These deposit types are deemed to form at shallow to discrete crustal depths (5 to 15 Km) from metamorphic fluids with little or no magmatic input (e.g., Tomkins, 2013b; Gaboury, 2019). The genesis of OGDs covers an exceptionally long temporal range, inclusive of the major thermal and tectonic changes that the Earth experienced (e.g., Cawood and Hawkesworth, 2014).

It has recently become widely recognised that the potential of OGDs is not just limited to the vein-hosted Au mineralisation but critically extends to the disseminated occurrences (e.g., Craw et al., 1999; Goldfarb et al., 2005; MacKenzie et al., 2010; Allibone et al., 2018). In fact, these deposits also source most of the greatest alluvial (placer) gold deposits in the world, which contribute to their economic importance (Mortensen et al., 2022). The accumulation of placer gold is largely a consequence of orogen uplift and exhumation, taking place post-lode mineralisation (Mortensen et al., 2022).

Precambrian and Phanerozoic Orogenic Gold Deposits

Previous extensive research in the field has highlighted that significant differences between several Phanerozoic OGDSs and the Precambrian OGDs do exist (Mortensen et al., 2022). In principle, most Archean deposits are sited within volcanic-dominated rock sequences (greenstones) and BIF units. Although this is roughly the case for many Proterozoic deposits as well, a significant fraction of these is hosted by thicker sedimentary rock sequences (Groves and Goldfarb, 2015). Suture zones, expressions of fossil subduction zones due to the amalgamation of continents and microcontinents, are usually considered key to the tectonic scenario

responsible for Precambrian OGDs (Goldfarb et al., 2021; Groves & Santosh, 2015). On the contrary, most models for Phanerozoic OGDs have relied on their location along convergent margins and accretionary terranes, associating their hydrothermal activity with plate subduction and/or lithospheric delamination (e.g., Landefeld, 1988; Goldfarb et al., 1988; Haeussler et al., 1995; Groves et al., 2000).

Phanerozoic orogenic gold deposits can be framed in a precise paleogeographic context, designed by the collision of Gondwana and Laurentia and the subsequent closure of the Tethys Ocean (from Ordovician to Carboniferous times). As such, these types of deposits span across the North American Appalachian and the European Caledonides (Goldfarb et al., 2005). Mortensen et al., (2022) suggested an eventual classification for them, alongside the hypothesis that almost all these subtypes could be sourced from restricted middle or upper crust reservoirs. The four proposed subtypes are i) crustal-scale fault (CSF) related, referring to vein arrays and associated crustal-scale strike slip faults; ii) sediment-hosted orogenic gold (SHOG), within turbiditic sediments and including both extensive veining and disseminated mineralisation; iii) forearc (FA), referring to clastic sedimentary sequences hosting vein arrays; and iv) syn- and late tectonic dispersed (SLTD) subtype, typically unrelated to any major structures but characterised by a strong lithological control on Au distribution.

According to Mortensen et al., 2022, the Au-bearing deposits hosted in the Grampians of Scotland, Ireland and Northern Ireland do not belong to any of these four main categories, but to a different and currently unclassified style. This conclusion was based on the outcomes reported previously for the Cononish deposit of Scotland (Spence-Jones et al., 2018) and the Curraghinalt (plus other) deposit(s) in Northern Ireland (e.g., Rice et al., 2016; Shaw et al., 2022). In the former case, evidence of an early hydrothermal-magmatic pulse (possibly connected to local granitic bodies) was inferred to have affected the mineralisation, in principle considered wholly orogenic and partly reconcilable to remobilisation from SEDEX (exhalative) horizons. In the latter case, the structure-hosted gold-bearing deposits were interpreted as orogenic and linked to transtensional shearing mechanisms.

Structural controls on Orogenic Gold Deposits

Over the last decades, the possible structural mechanisms controlling gold mineralisation in orogenic belts have been the target of investigations for several workers (e.g., Goldfarb et al., 2005; Tanner, 2014a; Deng et al., 2015; Groves et al., 2018). According to Groves et al., (2018), orogenic gold deposits show several repetitive features associated with ore-bearing fluid flux and gold deposition sites. A first-order control on globally important orogenic gold provinces is

represented by the adjacent, crustal to lithospheric-scale, faults and shear zones (Groves et al., 2000; Goldfarb et al., 2005; Robert et al., 2005; Groves et al., 2018). These major structural features usually accommodate lamprophyre and dyke intrusions, enabling the introduction of deeper fluids into the crust, due to their common mantle derivation (e.g., Perring et al., 1989; Deng et al., 2017, Groves et al., 2018). In many cases, OGDs are primarily controlled by subduction in collisional systems and, ideally, a fertile lower crust/upper mantle (Kerrich and Wyman, 1990; Bierlein et al., 2009; Hronsky et al., 2012). It is now widely accepted that, in these types of scenarios, the precious mineralisation is deposited within networks of second and third-order faults, fractures and/or dilatant zones by means of originally deeper fluids that are transferred by the crustal-scale discontinuities into the upper crust (e.g., Mueller et al., 1988; Neumayr et al., 2000, Cox, 2005; Tanner, 2014a; Groves et al., 2018). The largest deposits (province to district scale) particularly appear to have been conveyed within jogs that host fault arrays oriented at 70˚ to the main, belt-parallel, lithospheric-scale features (Figure 2.11; Weinberg et al., 2018, Groves et al., 2018) albeit these arrays have also been ascribed to later, post-mineralisation (D3-D4) events in a D1-D4 deformation sequence (Boulter et al., 1987; Bateman and Hageman, 2004; Gauthier et al., 2004; Weinberg et al., 2005). Regardless, the (repeated) reactivation of pre-existing faults and discontinuities due to far-field stress variations may justify the occurrence of multiple episodes of mineralisation in several OGDs worldwide (Groves et al., 2020).

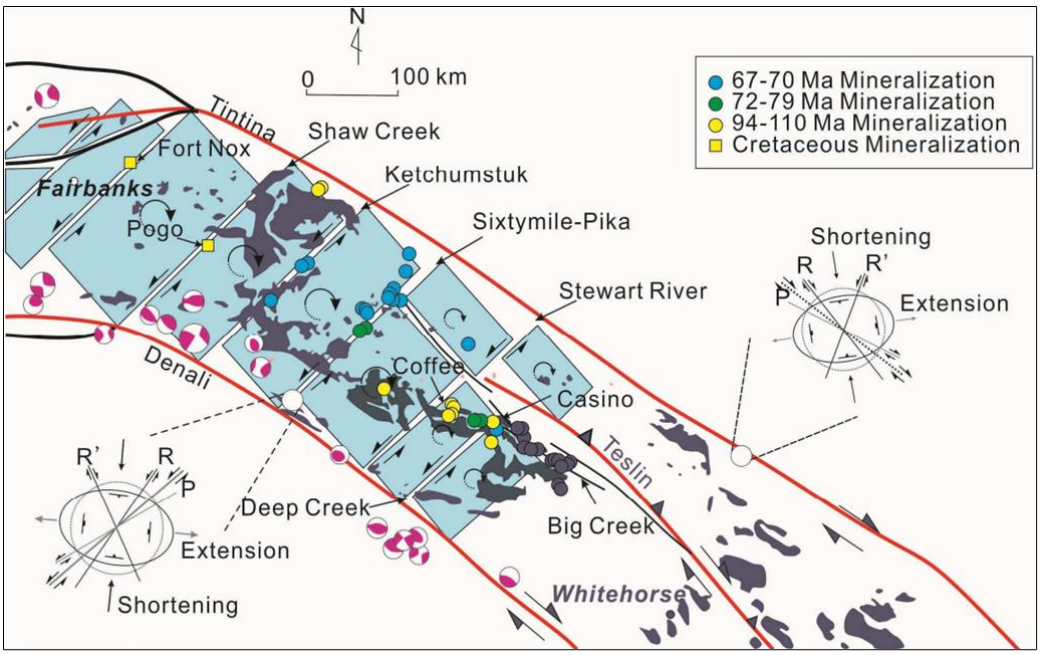

Figure 2.11 From Groves et al., 2018: Schematic map of the Denali-Tintina Fault Zone, showing high-angle cross faults, in an ''domino'' like array within the major Fault Zone. The rotation within blocks was produced by opposite motion on either side of the blocks by faults with the same sense of motion (Sanchez et al., 2014). Allan et al., (2013) reported some of the localities (Fort Knox, Pogo) in the figure as 'RIRG (Reduced Intrusion-Related Gold deposits)'.'

Lawley et al. 2013 support the hypothesis of pore fluid pressure cycling and variable degrees of weakening, indicated by a coefficient of friction (μ) <0.6 (Jefferies et al., 2006b; Holdsworth et al., 2011, cf. Byerlee, 1978), being the main structural controls on Au- bearing veins of different nature and style along non-Andersonian faults and shear zones in transpressional domains. Conversely, Andersonian (i.e., based on Andersen's assumption that at least one of the principal stress axis σ_1, σ_2, σ_3 behind faulting mechanisms is vertical, Anderson; E.M., 1905, 1951) relationships of regional strike-slip faults with the major stress axes, were accounted for by Tanner (2014a) to locate Au-Ag bearing veins in secondary Riedel fractures of orogen-parallel faults in the Grampians of Scotland. Their model would however need to consider that large-displacement strike-slips faults are not perfectly planar; consequently, a compressional regime is normally associated with local restraining bends and contractional jogs, and an extensional regime with releasing bends and dilational jogs (Mount and Suppe 1992). Critically, gold-bearing mineralisation tends to concentrate in these latter areas of enhanced porosity; deflections and variations in local stress fields would not account for Andersonian relationships with regional σ1 trajectories.

Fluid chemistry, transport and trapping mechanisms in OGDs

Transportation of gold by a fluid is an essential mechanism to allow the element mobilisation and subsequent concentration (e.g., see section 2.2.1.2). In these types of settings, the fluids may be either externally sourced or produced synchronously to gold dissolution (Phillips and Powell, 2010). The source and chemistry of the fluids connected to gold deposition in orogenic belts were reviewed by several authors (e.g., Ridley and Diamond 2000, Groves et al., 2003) who report fluid inclusion data indicating low-salinity and mixed aqueous-carbonic fluids. The majority of OGDs is characterised by fluid temperatures of ~250˚to 450˚C, pressures in the range of 500 to 1500 bars, and salinities typically of ≤ 3 wt% (NaCl equivalent), near neutral pH and elevated CO_2 and H_2S contents (Petrella et al., 2022). These features differ substantially from the ones typical of magmatic-hydrothermal systems, associated with porphyry and epithermal mineralisation styles (see Table 2.1); however, the OGD fluid type(s) may be fairly close to the ones attributed to reduced intrusion systems (i.e., "carbonic" fluids).

The nature of the lithological sequences plays a determinant role in both structural and geochemical transport and trapping of the Au mineralisation (reviews by Groves et al., 2000, 2016; Goldfarb et al., 2005; Robert et al., 2005, Groves et al., 2018). In general, only the most competent rock units favour an enhanced permeability for fluid flow and mineral deposition. In many cases, gold precipitation in quartz-carbonate veins would require pressure fluctuations

during hydrofracturing, accompanied by phase separation to destabilize aqueous sulphur complexes of gold (Herrington and Wilkinson, 1993) although there may be many more concurring physicochemical factors, some of which increase whereas others decrease gold solubility (Mikucki, 1998; section 2.2.1). Evidence that orogenic gold mineralisation sits in the amphibolite facies domain has suggested that the ore-bearing fluids likely derive from depths coincident with those of peak metamorphism (Ridley et al., 2000).

The classic genetic model for OGD formation, particularly the Phanerozoic ones, implies that they are generated by metamorphic devolatilization (Phillips and Powell 2010). Sedimentary and volcanic sequences of the greenschist facies are "devolatilised" across the greenschist-amphibolite boundary within a temperature range of ~440-520 C° (Elmer et al., 2006, Phillips and Powell, 2010; Yardley and Cleverley, 2013), and the volume of fluid liberated is a function of the abundance of hydrous and carbonate minerals. In brief, as the newly formed (i.e., by prograde metamorphism) auriferous fluid releases sulphur – an essential component for both solubility and transport of gold (see section 2.2.1.2) - it ascends through the crust until it reaches sites suitable for the deposition of both gold and metals (e.g., Stuwe, 1998; Garofalo and Ridley, 2014, Sahoo and Venkatesh, 2015). Worthy of notice is that, in the metamorphic model, the "fluid-transported" gold is dissolved at the onset of devolatilization (e.g., section 2.2.1.2), and not supplied by some other lithologies along the fluid pathways (Phillips and Powell, 2010). However, uncertainty and debate still exist around the mechanisms driving the migration of fluids from the metamorphic sequences into regional-scale faults (e.g., Ferry 1994, Ord and Oliver 1997; Groves & Santosh 2015). Another key issue with this model is that the peak metamorphism is frequently postdated by the gold mineralisation (e.g., up to million years; Nesbitt, 1991; Wilson et al., 2013). As such, alternative mechanisms (e.g., gold concentration by nanoparticles - see section 2.2.1.4, and references therein) were recently proposed to explain the occurrence of high-grade mineralisation in orogenic gold deposits.

2.3 Characterisation of gold deposits via gold compositional studies

Particulate gold is physically and chemically stable in most surface settings and holds compositional features that can be descriptive of its environment of precipitation. Datasets of gold alloy and inclusion suites have been used to classify gold populations in terms of source mineralisation styles, based on compositional criteria (e.g., Chapman et al., 2023b).

2.3.1 Gold alloy

As described in paragraph 2.2.1.5, the gold alloy composition reflects the physicochemical parameters of the mineralising fluid at the point of precipitation (Gammons and Williams-Jones 1995), therefore, different alloy compositions indicate variations in the conditions of gold precipitation. Natural gold alloy almost always contains Ag as a subordinate component, but may also contain minor amounts of Cu, Pd or Hg.

Higher silver contents are generally recorded in gold precipitated from relatively low-temperature fluids and late in the mineralising history (Gammons and Williams-Jones, 1995; Chapman et al., 2021). Alluvial gold populations are typically formed of particles having different origins and often exhibit wide ranges in silver content (Chapman et al., 2000a); these may reflect either a single Au-bearing mineralising system, experiencing large physicochemical variations during its evolution, or the mixing of gold from different mineralised sources (e.g., Chapman et al., 2023c). Consequently, a characterisation of the Au/Ag ratios of particles from single or multiple mineralizing episodes yields the potential to inform the evolution of the hydrothermal system(s) involved (e.g., Chapman et al. 2010a; Spence-Jones 2021). One of the limitations of this approach, however, is that gold alloy compositions may not be exclusive to specific deposit types.

In some cases, an association between lower temperatures and Hg-rich gold alloys was also reported and attributed to the high volatility of mercury (Gas'kov, 2017). Chapman et al., (2010a) investigated the parameters controlling the Hg concentration in some gold alloys but robust linkages to specific mineralisation conditions were not observed. Also, Mackenzie and Craw (2007) noted that the composition of Au-Ag-Hg alloys from several veins in the Otago Schists were unrelated to specific depth gradients. However, a quantification of the mercury content in gold can sometimes be more informative than that of the silver content as it can more easily reveal variations among gold types (Leake et al., 1997b, 1998; Chapman et al 2000; Moles et al., 2013).

Higher Cu contents in gold alloys (e.g., up to 5 wt%, Chapman et al., 2017) have been associated with higher temperatures in the primary environment of formation; evidence was found in the composition of gold from magmatic-related systems (e.g., porphyry; Antweiler and Campbell, 1977; Morrison et al., 1991; Chapman et al., 2017, 2018). The mutual behaviour of Cu and Ag in the gold composition was investigated by several authors who identified an inverse relationship between these components (Chapman et al., 2017; Dongmo et al., 2018), although it is uncertain whether the frequently observed <0.5 wt% Cu in gold particles may often be a result

of the hydrothermal fluid composition more than the role of Ag content in the alloy (Chapman et al., 2021).

2.3.2 Mineral inclusions in gold particles

Inclusions suites are paired with gold alloy compositions to identify and distinguish source mineralisation styles (e.g., Chapman et al., 2017; Chapman et al., 2018). Deposit types show distinctive ore mineral assemblages, which can be incorporated by gold in the form of tiny inclusions, making the quantification of their species an informative tool. While individual inclusion species are generally not regarded as exclusive indicators of a deposit style, combinations or groups of inclusions have proved diagnostic to interpret gold genetic environments (e.g. Chapman et al. 2017; Chapman et al., 2023b). Relatively large numbers of gold particles are typically required to establish a genetic signature because inclusions are often only observed in a small proportion, typically 20% of them (Chapman et al., 2010; Chapman et al., 2021a). Mineral species, such as pyrrhotite - suggesting low redox state (e.g., Chapman and Mortensen, 2006)- and calcite – suggesting neutral to alkaline pH - may also be considered to infer compositional stability fields and help predict gold mineralising conditions (e.g., Chapman and Mortensen, 2006).

2.3.3 Genetic environments of gold formation

Gold signatures and genetic environments are schematised in Table 2.2 (Chapman et al., 2023b). Gold from orogenic systems forms an overarching group which mainly comprises mineralisation deriving from fluids of a metamorphic nature but with, in some cases, a magmatic-related component (Goldfarb and Groves, 2015). Most gold populations analysed in previous studies (e.g., Chapman et al., 2021 and references therein) are from younger (i.e., Phanerozoic) orogenic systems. These typically exhibit relatively large ranges of gold alloy compositions and inclusion species and often show higher Ag contents than gold from Archean and Proterozoic orogenic settings. Cu normally occurs below the LOD; however, values of at least 0.8% were observed in placer gold from these systems (e.g., Moles et al., 2023). Hg is rarely detectable but can reach percent values in certain cases (e.g., Chapman et al., 2023c). Generic traits in the inclusion signatures of gold from Phanerozoic orogenic systems are represented by non-metal components, sulphides and, in some cases, Sb, As and Te (Chapman et al., 2023b). Mineralogical similarities, in the form of a pronounced Ag-Te signature, can be observed between gold compositions from certain epithermal and orogenic systems; these may be the result of similar mineralising conditions in epizonal and epithermal settings (e.g., Chapman et al., 2023ba). Distinctive Bi-Te signatures are characteristic of Archean orogenic gold and suggest that the

composition of the fluid from which it precipitated was affected by the presence of igneous rocks (Chapman et al., 2021 and Chapman 2023b).

Magmatic hydrothermal systems comprise porphyry (both calc-alkalic and alkalic) systems, skarn, high- and low-sulphidation epithermal systems, intrusion-related and (late-stage) ultrabasic-related gold mineralisation. Chapman et al. (2017 and 2018) developed effective compositional templates to characterise gold from porphyry environments based on their genetic signatures (Bi-Pb-Te-S association). Porphyry systems are known to be characterised by higher temperatures and pressures than epithermal ones, which also affect the alloy compositions of their gold mineralisation. For example, gold from the former systems commonly contains Cu at levels above the limit of detection (LOD).

The typical inclusion assemblage of gold from calc-alkalic porphyry systems (e.g., from the Canadian Cordillera; Chapman et al., 2018) is formed of Bi–tellurides, galena, altaite, tetradymite and cosalite, which are reflected into the elemental Pb–Bi–Te–S signature mentioned above. Molybdenite is common in all porphyry systems as well as chalcopyrite, which can be accompanied by Cu sulphides (e.g., Chapman et al., 2021). Additionally, alkalic porphyry systems are often characterised by Pd-Hg gold signatures with detectable (>0.3) Hg values (Chapman et al., 2023b).

Gold from epithermal environments generally exhibits a wider spectrum of compositions, due to the greater variations in pressure, temperature and chemistry in the associated hydrothermal systems (Chapman et al. 2018; 2021). Especially in the low-sulphidation deposits, gold alloys are characterised by large silver content ranges (e.g., 1-50 wt%; Table 2.2). Inclusion signatures generally contain base metals and Te or Se components, sometimes accompanied by Bi tellurides. Cu contents are lower than in the metallic signatures of gold from porphyry environments (Chapman et al., 2021). Relatively high Cu contents associated with Cu sulphide inclusions in alluvial gold particles were reported by Moles et al., 2013 and thought to have formed in a high-sulphidation epithermal environment. On the other hand, the Pb (±Zn) component tends to increase at the transition from porphyry to epithermal (low-sulphidation) systems, similarly to Ag (Chapman et al., 2018).

Table 2.2. Compositional characterisation of gold according to microchemical signatures and mineralisation styles. From Chapman et al., 2023b – and references therein)

Style of mineralization	Mineralization/Microchemical signature				Comments
	Alloy compositions		Inclusion suite		
	Ag range (wt%)	Other metals	Chemistry	Typical mineralogy	
Orogenic: Phanerozoic[1–7]	4–30	Occasional Hg to 10%	(i) S, (ii) S + As (iii) S + Te ± As ± Ag (iv) Pb + S + Sb ± As	(i) py, ga, cpy, sph (ii) py, ga, cpy, sph, apy (iii) py, ga, cpy, sph, hs, apy (iv) ja, ga, apy, py	Simple sulfide inclusion suites are the most common. Te usually present as hs.
Orogenic: Precambrian[8,9,10,11]	5–50, but many <10	Cu to 2% common Occasional Hg to 3%	S, ± As, ± (Te + Bi)	py, ga, cpy, sph, apy ± BiTe	The majority of alloy compositions are in the 1–10 wt% Ag range
Epithermal: Low sulfidation[12,13,14]	1–50	Occasional Hg to 10%	S, ± As, + Te, + Ag, Bi,	py, ga, cpy, sph, BiTe ± apy	Large variation in Ag ranges in populations from different localities but often small variation between particles from a single locality. Cu normally below LOD by EPMA (0.02 wt%)
Epithermal High Sulfidation[15,16]	1–14	Cu to 1 wt%	Cu + Pb + Zn + S + As ± Te	bn, cc, cpy, ga, sph	Limited data available
Calc alkalic Porphyry[14]	5–50	Cu usually > 0.02 wt% (LOD by by EPMA)	Bi + Pb + Te + S		
Alkalic porphyry[17]	5–40	Hg, Pd to 11 wt% in around 4% of particles	Hg + Pd + Pb + Bi + Te + Cu	tem, PdTe, PdAs, py, cpy, bn, cc,	
Skarn[18]	>11		Pb + Ag + Te + Bi + S		Limited data available
Oxidizing chloride hydrothermal: low temperature (T < 120°C)[19]	0–6	Pd or Hg to 12%, Rare Cu to 4%	Se ± Te + wide range of metals	Selenides and tellurides of Pd, Hg, Cu, Bi, Pb. pt	Ag often extremely low. Au–Pd alloys common. Sulfides absent from high Au and Au–Pd alloys
Ultrabasic intrusion association[20]	0–20	Cu commonly to 10 wt%	Au,Cu	Au–Cu intermetallics, cc, po	Common exsolution texture of Au–Cu intermetallics from Au–Ag–Cu alloy. Often extreme heterogeneity so ascribing a Ag value is problematic

Elevated Cu contents (i.e., to percent levels) are commonly associated with gold mineralisation related to ultramafic lithologies and, less frequently, to gold originated in low-temperature oxidising chloride hydrothermal systems (Knight and Leitch, 2001; Chapman et al., 2023b). Low-temperature oxidising chloride auriferous systems (OCAS) show a somewhat peculiar signature, with palladium-rich, low-silver (<10 wt%) alloys formed in response to Au and Pd co-transport as chloride complexes (Mountain and Wood 1988).

2.4 Lead isotope studies

Lead occurs in nature as four stable isotopes: ^{204}Pb, ^{206}Pb, ^{207}Pb, and ^{208}Pb. Among these, ^{204}Pb is not produced by radioactive decay (Jaffey, 1971; Woodhead & Hergt, 2000; Huston & Champion, 2023). In recent decades, lead isotope analysis has become an important tool in both metallogenic research and mineral exploration (e.g., Milot et al., 2021; Mortensen et al., 2022; Webb et al., 2025). While it is primarily employed to identify metal source regions through isotopic fingerprinting, variations in lead isotope ratios at the district scale can serve as vectors toward ore bodies, help distinguish different mineralization styles within a province, and, in some cases, indicate deposit fertility (Goldhaber et al., 1995; Tosdal et al., 1999; Bao et al., 2017, Huston & Champion, 2023).

The Pb isotope signatures of galena reflects several key controls: the origin of lead (with upper crustal sources generally more radiogenic than mantle sources), potential mixing of different lead reservoirs during fluid–rock interaction, and isotopic ratios modifications during hydrothermal alteration (Cannon et al., 1961; Mühe et al., 1997; Carranza, 2012; Mortensen et al., 2022; Webb, 2024).

2.4.1 Model ages

Because several lead isotopes are products of uranium and thorium decay, they are widely employed for calculating model ages (Huston & Champion, 2023). These ages are derived from mathematical models describing the evolution of Pb isotopic compositions through geological time, based on assumptions about the sample's initial lead content (Stacey & Kramers, 1975; Cumming & Richards, 1975; Milot et al., 2021; Huston & Champion, 2023). The approach assumes that the sample originated from a single reservoir, such as the mantle, upper crust, or ore-forming fluid, and evolved from an initial composition without experiencing later disturbance. Model ages are indicative of the amount of time since the lead separated from a given source (Stacey and Kramers, 1975; Albarède et al., 2012; Huston and Champion, 2023).

Model Pb ages are determined by comparing measured lead isotope ratios in a sample to theoretical models of Pb isotope evolution through time, which can be represented as an isochron indicating the time elapsed since the source formed (Holmes, 1946; Huston & Champion, 2023). Galena typically contains both radiogenic and non-radiogenic (common) Pb, making its separation challenging (Townsend et al., 1998). Pb isotope studies normalize radiogenic ratios to the non-radiogenic isotope ^{204}Pb, i.e.:

^{206}Pb/^{204}Pb, ^{207}Pb/^{204}Pb and ^{208}Pb/^{204}Pb

^{204}Pb is not a product of radioactive decay, therefore it is considered to remain constant over time (Holmes, 1946; Stanton & Russell, 1959; Cannon et al., 1961; Huston & Champion, 2023). These models assume that the accumulation of radiogenic Pb isotopes is dependent on the elapsed time, the decay constants of U and Th, and their initial abundances at Earth's formation at 4.54 Ga (Tatsumoto et al., 1973). Pb isotope values from mineralization events of different ages often display considerable variability (Mortensen et al., 2022). Younger events are typically characterized by higher proportions of radiogenic lead, consistent with ongoing uranium and thorium decay over geological time (Huston & Champion, 2023).

2.4.1.1 Single-stage and two-stage models

Models describing Pb isotope evolution are generally classified as *single-stage* or *two-stage* (Huston & Champion, 2023). Single-stage models assume continuous fractionation of Pb from U and Th without later disturbance (Stanton & Russell, 1959; Tera & Carlson, 1999; Maltese & Mezger, 2020). In contrast, two-stage models account for early geological events that fractionated U, Th, and Pb following Earth's formation (Wedepohl & Hartmann, 1994; Palme & O'Neill, 2003). In this context, mantle-crust differentiation created reservoirs with distinct Pb isotope signatures; the process was driven by density contrasts, with lighter silicate phases migrating toward the surface (Agee & Walker, 1988). Uranium, being lithophile, preferentially partitioned into the crust (Andersen et al., 2015; Huston and Champion, 2023); this mechanism led to progressively higher concentrations of radiogenic Pb isotopes (^{206}Pb, ^{207}Pb, and ^{208}Pb) in the crust, as a consequence of radioactive decay.

Single-stage and two-stage models both rely on assumptions about Earth's initial Pb isotopic composition - commonly based on the Canyon Diablo meteorite - as well as initial values of μ (Mu; ^{238}U/^{204}Pb), κ (Kappa; ^{232}Th/^{238}U), and ω (Omega; ^{232}Th/^{204}Pb). These parameters describe the relative abundances of uranium, thorium, and lead in a reservoir and control the production of radiogenic Pb isotopes over time. High μ values indicate U enrichment and lead to greater

accumulation of ^{206}Pb, while κ influences the balance between ^{208}Pb (from Th) and Pb derived from U decay. ω reflects absolute Th enrichment relative to Pb and affects long-term ^{208}Pb growth (Stacey & Kramers, 1975; Wedepohl & Hartmann, 1994; Browning et al., 1987; Huston & Champion, 2023). Among these, μ is particularly useful as a visual indicator of Pb isotope variability across regions and in metallogenic research (Browning et al., 1987; Blitchert-Toft et al., 2016; Huston et al., 2017; Huston & Champion, 2023; Webb, 2024).

Single-stage models attempt to track the reservoir evolution using the assumed initial isotopic ratios and applying decay constants to predict changes over time (Stanton & Russell, 1959; Tera & Carlson, 1999; Maltese & Mezger, 2020). These models are generally unrealistic at smaller scales because they do not account for later geological events that fractionate U and Th relative to Pb. Two-stage models aim to address this limitation by introducing a point of geochemical differentiation, such as mantle-crust separation (at 3.5 Ga, Figure 2.12), after which two reservoirs evolve along distinct isotopic trajectories (Zartman & Doe, 1981; Wedepohl & Hartmann, 1994; Palme & O'Neill, 2003). The widely used Stacey and Kramers (1975) model is a two-stage approach that simulates terrestrial Pb evolution following early geochemical differentiation. These models provide reasonable global-scale approximations of lead evolution; however, the geological complexity of the processes that create isotopic reservoirs should be noted (Huston & Champion, 2023).

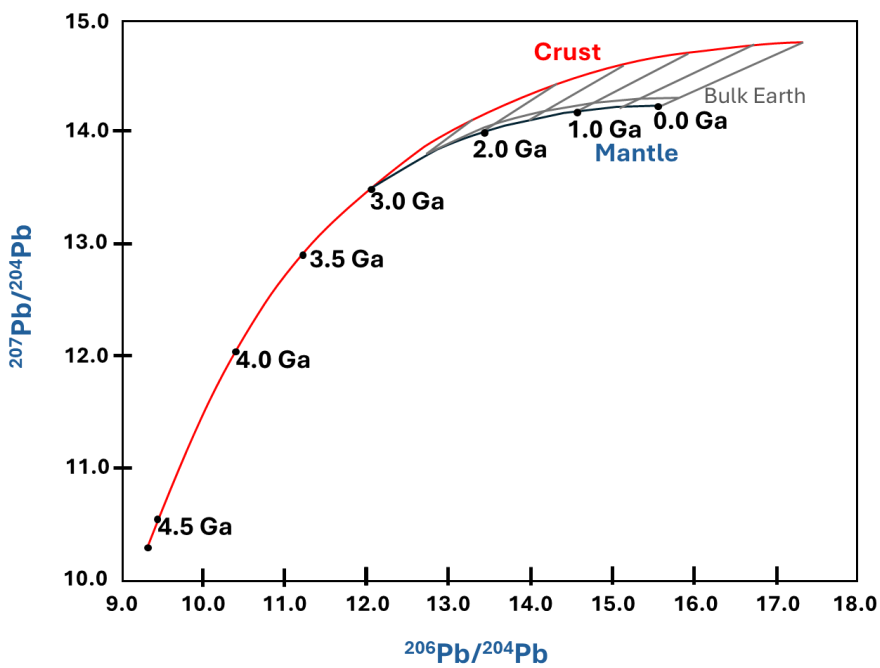

Figure 2.12. Adapted from Zartman & Doe, 1981: Lead isotope evolution models, 206Pb/204Pb versus 207Pb/204Pb. The diagrams show changes in lead isotope composition in a hypothetical two-stage model. The Earth is assumed to be isotopically homogeneous until 3.5 Ga, at which time a crust-differentiating event generates two reservoirs that evolve separately.

2.4.1.2 Advantages and limitations of Pb model ages

The use of uranogenic isotopes ^{206}Pb, ^{207}Pb offers considerable advantages when generating model ages in U–Pb geochronology. Both isotopes are stable end-products of uranium decay - ^{206}Pb comes from ^{238}U, and ^{207}Pb comes from ^{235}U - and do not undergo further radioactive transformation, preserving the time-integrated decay history of their parent isotopes (Holmes, 1946; Huston & Champion, 2023). Their decay constants enable cross-checking between two independent chronometers, improving accuracy and revealing disturbances such as Pb loss or U gain (Stacey & Kramers, 1975; Tera & Carlson, 1999). Furthermore, since initial Pb values are assumed to be negligible in the U-Pb system, normalization to non-radiogenic ^{204}Pb can be applied, making this approach suitable for dating the oldest rocks (Stanton & Russell, 1959; Huston & Champion, 2023).

Despite the aforementioned advantages, global lead evolution models - such as Stacey and Kramers (1975) – still need to account for certain limitations. For instance, they are based on assumptions about the timing of mantle–crust differentiation, which may not have been synchronous for all regions, as well as universal initial Pb compositions (Carr et al., 1995; Sun et al., 1996). Additionally, these approaches would demand that the mineral has remained a closed system since crystallization; however, processes such as recrystallization, hydrothermal alteration, or later mineralizing events can reset or mix lead isotopic signatures, producing ages that do not reflect initial formation (Huston & Champion, 2023). All these aspects need to be considered when endeavouring to generate model ages of galena samples from ore bodies at the district scale.

2.5 Geological background of the study area

The present study has focused on a sub-region of the Grampian Highlands of Scotland, delimited by the regional-scale Highland Boundary Fault and the Loch Tay Fault. The area (''Loch Tay area'') sits on meta-sedimentary sequences intruded by mafic and felsic igneous bodies (e.g., Chapman et al., 2023c), and thoroughly crosscut by minor faults. The geodynamic configuration of the Loch Tay area is rooted in the wider processes that led to the development of the Scottish Caledonides. As such, the most important tectono-metamorphic and metallogenic events associated with the Caledonian Orogeny and – particularly - the Grampian Terrane, will be illustrated in the following paragraphs, ahead of local geological observations in and around the Loch Tay area itself.

2.5.1 The Caledonian Orogeny

The Caledonian orogen can be mapped across a territory that extends to both sides of the North Atlantic Ocean for several thousand kilometres, including part of the Arctic. The orogen formed by collisional processes that incorporated rock sequences of diverse nature, originally belonging to the Laurentia, Baltica and Avalonia continental blocks (Corfu et al., 2014). Their convergence took place in Palaeozoic times. The first collisional phase (Grampian event, Figure 2.12) of the Caledonian Orogeny was NW-SE oriented and involved thrust tectonics with consequent crustal thickening, roughly placed at ~475–465 Ma (e.g., Roberts and Treagus 1977; Oliver et al. 2008; Chew et al., 2008; Tanner 2014a). The second convergent Caledonian phase (Scandian event, Figure 2.12; McKerrow et al., 2000; Stephenson et al., 2013) can be reconciled to a transpressional, orogen-parallel, tectonic stage (e.g., Dewey and Strachan 2003; Tanner 2014b) which determined the final closure of the Iapetus Ocean, placed at ~435–410 Ma (e.g., Dewey and Mange 1999; Leslie et al., 2008; Chew and Strachan 2013). The Grampian and Scandian main events were separated by a~20 Ma stage of tectonic uplift and collapse (e.g., Dempster 1985; Rice et al., 2016; Oliver 2001).

The final stages of the Caledonian Orogeny comprise Early-Mid Devonian, brittle tectonic events and strike-slip tectonics along regional-scale faults, such as the Great Glen Fault (GGF) of Scotland and the Billefjorden Fault Zone in the Svalbard's (Corfu et al., 2014). The NNE-SSW trending Loch Tay Fault also developed during these times (e.g., Chew and Strachan 2013) and is roughly parallel to other structures crosscutting the Grampian Terrane, which similarly show left-lateral movement along their strikes (Treagus, 1991). The amount of displacement along these regional-scale structures has been the subject of continuous debate (Corfu et al., 2014), having an impact on deriving palaeogeographical interpretations (e.g., Harland & Wright 1979; Soper et al. 1992). Particular attention has also been given to the regional transition from transpression to transtension (Dewey and Strachan 2003), assumed to coincide with the emplacement of the "Newer Granites" around Early Devonian times (e.g., Rice et al., 2016). The transtensional phase was dictated by a WSW-ENE-oriented extension, which enabled the creation of pull-apart basins in the Grampians of Scotland (Dewey and Strachan 2003).

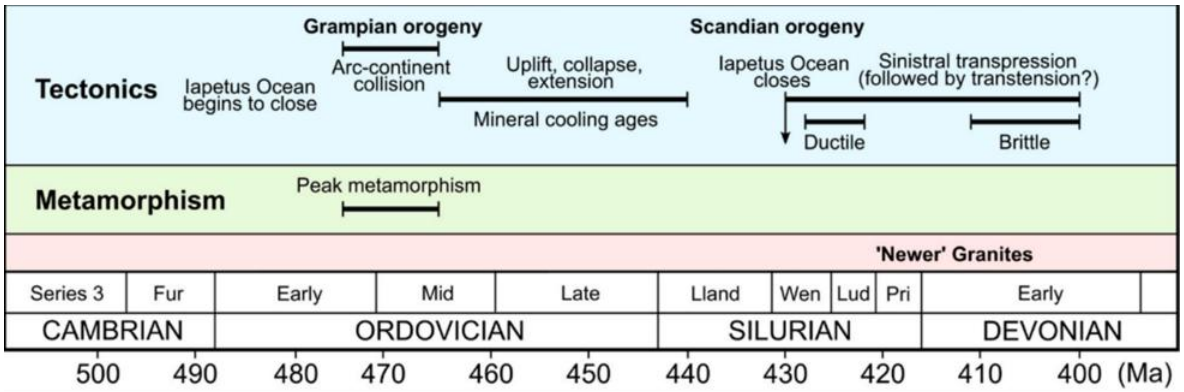

Figure 2.13 Adapted from Shaw et al., 2022. Timeline of the main thermo-tectonic events in the Caledonian Orogeny.

The British and Irish Caledonides have been the focus of detailed research for centuries, due to their high potential to act as a natural laboratory for testing many key geological theories - e.g., concerning stratigraphic and tectonic concepts (e.g., Peach et al. 1907; Coward, 1980; Corfu et al., 2014). Additionally, the Caledonian orogenic belt has frequently been analysed alongside the Himalayan-Alpine one due to their comparable scales and driving mechanisms (e.g., Milnes 1998; van Staal et al. 1998; Labrousse et al. 2010; Corfu et al. 2014).

2.5.1.1 The Grampian Terrane

The Grampian Terrane is formed of metamorphosed sequences which lie between the Northern Highlands Terrane (to the NW) and the Midland Valley Terrane (to the SW), respectively delimited by the Great Glen Fault (GGF) and the Highland Boundary Fault (HBF). The Grampian orogenesis resulted from the obduction of part of the Dalradian basin floor alongside the recently active ridge onto the Laurentian passive margin (Tanner, 2014b). Subduction polarity was, at this stage, flipped to the NW and stayed unchanged for the rest of the tectonic evolution (Tanner, 2014b). It is generally accepted that NW-directed subduction proceeded until ~426 Ma (Atherton & Ghani, 2002; Neilson, Kokelaar & Crowley, 2009) when the process ended due to slab break-off and emplacement of the 'Newer Granites', involving acid to intermediate magmatism. The structural evolution of the Grampian Terrane was defined by a 426 Ma limit, which not only signified the switch from left-lateral transpression to left-lateral transtension during regional-scale crustal fracturing (Dewey & Strachan, 2003) but also coincided with the sub-division of the Terrane in NE-SW oriented compartments separated by transcurrent faults (Tanner, 2014a).

The Dalradian Supergroup forms the Laurentian cover sequence of the Grampian Terrane, whereas evidence of basement rocks is provided by the Annagh Gneiss Complex in NW Ireland,

the Rhinns Complex in SW Scotland, and the xenoliths found in Permo-Carboniferous igneous rocks within Midland Valley Terrane (; Stephenson and Gould, 1995; Chew and Strachan, 2013; Badenszki et al., 2019 and references therein).

The Dalradian Supergroup

The Dalradian sequence was deposited between the Mid Neoproterozoic Era (Cryogenian) and the Mid Cambrian Period on the developing Laurentian eastern passive margin (Tanner & Sutherland, 2007; Stephenson et al., 2013). The Supergroup has a complex lithostratigraphic succession, with four Groups identified: Grampian Group, Appin Group, Argyll Group and Southern Highland Group. Both the Argyll and Southern Highland Groups, ranging in age from late Neo-Proterozoic to Mid Cambrian, outcrop in the Loch Tay area. In turn, the Argyll Group includes the Ben Eagach Schist, Ben Lawers Schist, Farragon Volcanics, Ben Lui Schist and Loch Tay Limestone Formations; the Southern Highland Group includes the Pitlochry Schists and the Ben Ledi Grit Formations. The Darladian lithological sequence indicates shallow to deep marine deposition and the subsequent action of turbidity currents, reflected in submarine fans, channels, lobes and basin plains (e.g., Stephenson and Gould, 1995; Rooney et al., 2011). Sills, dikes, and lamprophyre bodies were emplaced into the Dalradian sequence post-D4 (deformation) phase (Tanner, 2012).

The rocks of the Dalradian Supergroup only experienced a single metamorphic episode, making the Grampian Highlands a suitable territory to investigate the prime causes of regional metamorphism (Blake and Jones, 2003). The epidote-amphibolite facies in the southwest underwent metamorphism at c. 450 °C and 700-900 MPa, recording some of the highest pressures despite being the 'coldest' facies. Rocks from the north-east region experienced similar temperatures but at considerably lower pressures (Blake and Jones, 2003). Further heat supply is required to explain the typical Barrovian-type (medium-pressure) metamorphism observed in the middle region (e.g., Stephenson et al., 2013). In the Loch Tay area, metamorphic processes are evident from the Green Beds within the Pitlochry Schist Formation. A strong contribution from volcaniclastics has been taken into account to explain the chloritic nature of much of the bedrock lithologies (e.g., Stephenson et al., 2013; Armstrong, 2021); however, it was additionally noted that chlorite is the index mineral of the lowest-grade facies in the Barrovian metamorphic sequence.

Structure of the Grampian Highlands

The Grampian Orogeny took place in early Ordovician times and was a short-lived event (5–15 Ma; Dewey 2005), with at least four major deformation phases (D1 to D4) of regional significance (e.g., Tanner, 2014b; The Blake and Jones, 2003). The earliest structures and associated fabrics are represented by large-scale synclines and anticlines (e.g., the Ardrishaig Anticline, Loch Awe Syncline and Islay Anticline). Prolonged crustal shortening led to the formation of ductile fold nappes and to a series of associated ductile thrusts and shear zones (e.g., the Fort William Slide and the Boundary Slide). The Tay Nappe (Fig. 2.14) is of regional importance and maintains a NE-SW orientation across the entire Terrane. However, in contrast to other coeval major folds, this structure is SE-facing, posing an interesting structural debate (Blake and Jones, 2003). According to Tanner (2014b), the Tay Nappe is the major early structure, with an axial trace parallel to the margin of the Grampian Terrane, the right-way-up limb forming a 2-4 km wide outcrop NW of the Highland Boundary Fault and an extensive lower limb. The latter is affected by D2 deformation and pervasive cleavage, increasing with depth (Tanner, 2014b).

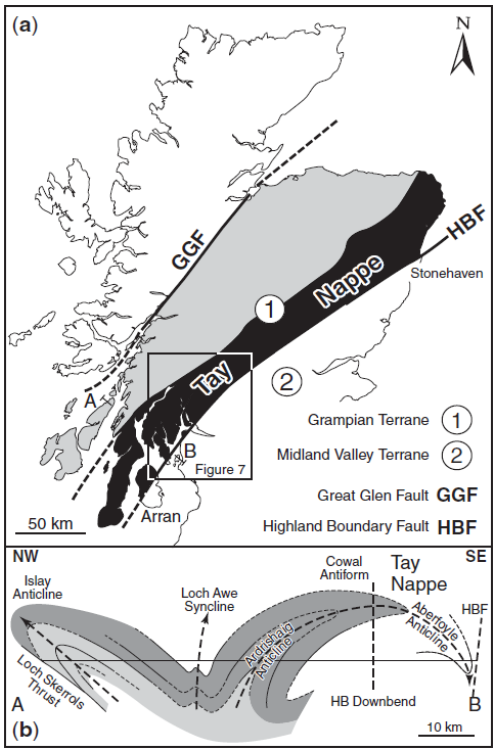

Figure 2.14 From Tanner, 2014b. Structural map (a) and sketch section (b) of the Grampian Terrane. The Tay Nappe is indicated.

The D3 and D4 major phases of the Grampian Orogeny deformed the D1-D2 features but were less intense than the former phases. Their products are NE-SW-trending structures which include open upright folds and structural domes (Blake and Jones, 2003).

Regional-scale faults

The Grampian Terrane is bounded by two major faults, the Great Glen Fault (GGF) and the Highland Boundary Fault (HBF). Another five faults are sub-parallel to these (Figure 2.15; Ericht–Laidon, Tyndrum, Garabal, Killin and Loch Tay) and notably influenced the lithostratigraphic boundaries of the Daladian sequences (Treagus 1991; Tanner, 2014a)). Sinistral strike-slip displacement with a normal component has been recorded for these faults in relation to the transtensional phase (e.g., Treagus, 1991).

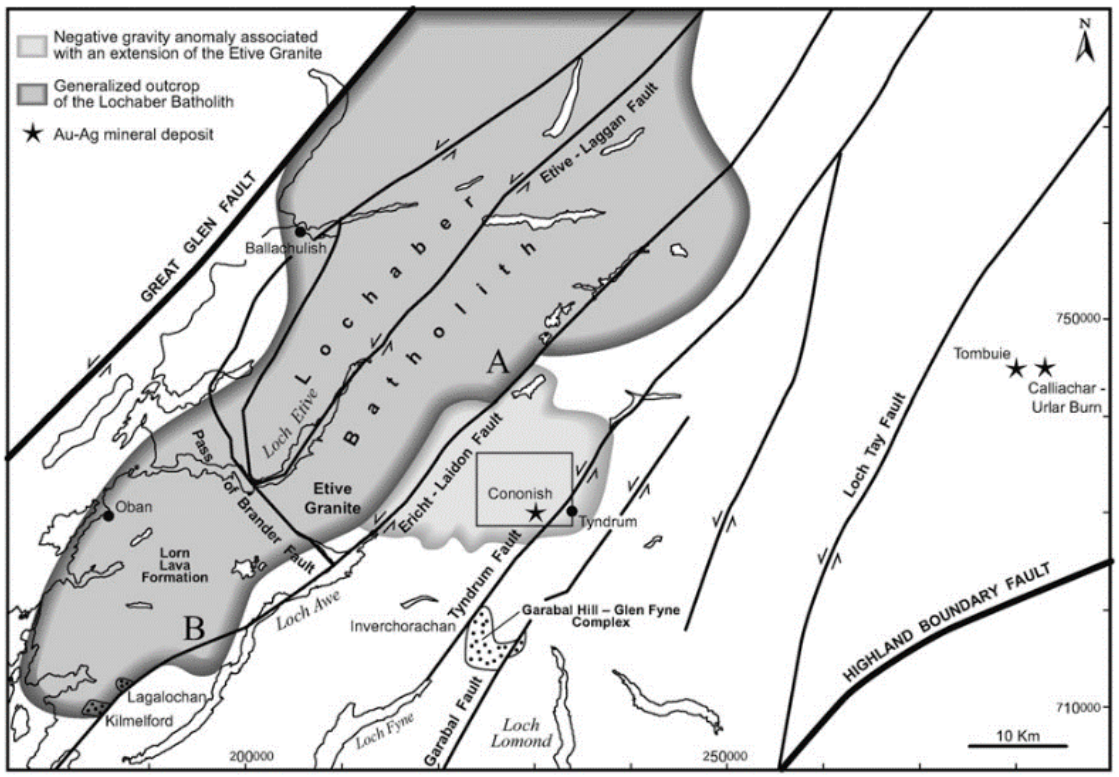

Figure 2.15. From Tanner, 2014a. Regional-scale faults in the Grampian Terrane.

The Great Glen Fault is a crustal-scale, reactivated strike-slip fault, trending NNE–SSW and showing left-lateral movement (e.g. Hutton & McErlean 1991; Soper et al. 1992; Stewart et al. 2000), which developed in Ordovician to Early Devonian times (e.g. Hutton & McErlean 1991; Soper et al. 1992; Stewart et al. 2000, 2001; Mendum & Noble 2010). Dewey and Strachan (2003), argue for a major left-lateral displacement along the Great Glen Fault and associated transcurrent structures to take place in the time between c. 425 Ma and 410 Ma.

The HBF is a major terrane boundary (e.g., Bluck, 1984) that can be traced across Scotland for ~240 km, defining the northern margin of the Midland Valley. It is currently a steep, NW-dipping reverse fault (Tanner, 2008). The development of this fault has been interpreted to span from the Ordovician to the Middle Devonian including reactivation (Tanner, 2008). A determinant phase of sinistral strike-slip movement along the HBF was interpreted to be of Silurian age (Ryan et al. 1995).

The Tyndrum Fault can be traced over a 60 km strike length and is a left-lateral, strike-slip fault with a displacement of ~4 km and a vertical downthrow of ~2 km to the SE (Treagus, 1991). Fractures and splays can be observed in a ~1.5 km wide zone on the NW side of the fault plane (Treagus et al. 1999). The fault experienced a late-stage movement under a transtensional

regime dominated by a sinistral component (Treagus et al. 1999) between 429-412 Ma (Clayburn et al. 1983; Rogers & Dunning 1991; Treagus et al. 1999).

Several workers acknowledged the causal relationship between the emplacement of the Newer Granite suite, for example the Lochaber Batholith (Fig. 2.15), and these major faults (Watson, 1984, Hutton, 1987; Jacques & Reavy, 1994; Neilson, Kokelaar & Crowley, 2009).

Gold deposits (resources) in the Grampian Terrane

The Grampian Terrane of Scotland is the host of polygenetic, gold-bearing mineralisation (e.g., Corkhill et al., 2010) which has been reported in the form of Au–Ag deposits at Calliachar–Urlar Burn, Tombuie, Cononish (Tyndrum area) in Scotland and Curraghinalt, Cavanacaw (Omagh mine), Croagh Patrick, Cregganbaun and Bohaun in Ireland (Figure 2.16, Tanner, 2014a). Despite being distributed over hundreds of kilometres parallel to the strike of the Caledonide belt, most of these deposits share the same mineralogical features (Tanner, 2014a). The greatest gold resources of the UK are hosted in the Dalradian sequences at Curraghinalt and Cavanacaw (Northern Ireland), previous resource estimates respectively accounted 2,700,000 and 438,000 oz Au (Dalradian Resources Inc. 2012; Galantas Gold Corporation 2013). Several gold prospects are located in the Tyndrum area, and most of the mineralisation is within a 10 km radius of Cononish (Hill et al. 2011; Tanner, 2012; Spence-Jones, 2021). The Cononish mine recorded total metal resources of 266,000 oz Au and 1,096,000 oz Ag as of 2015 (Scotgold Resources, 2023).

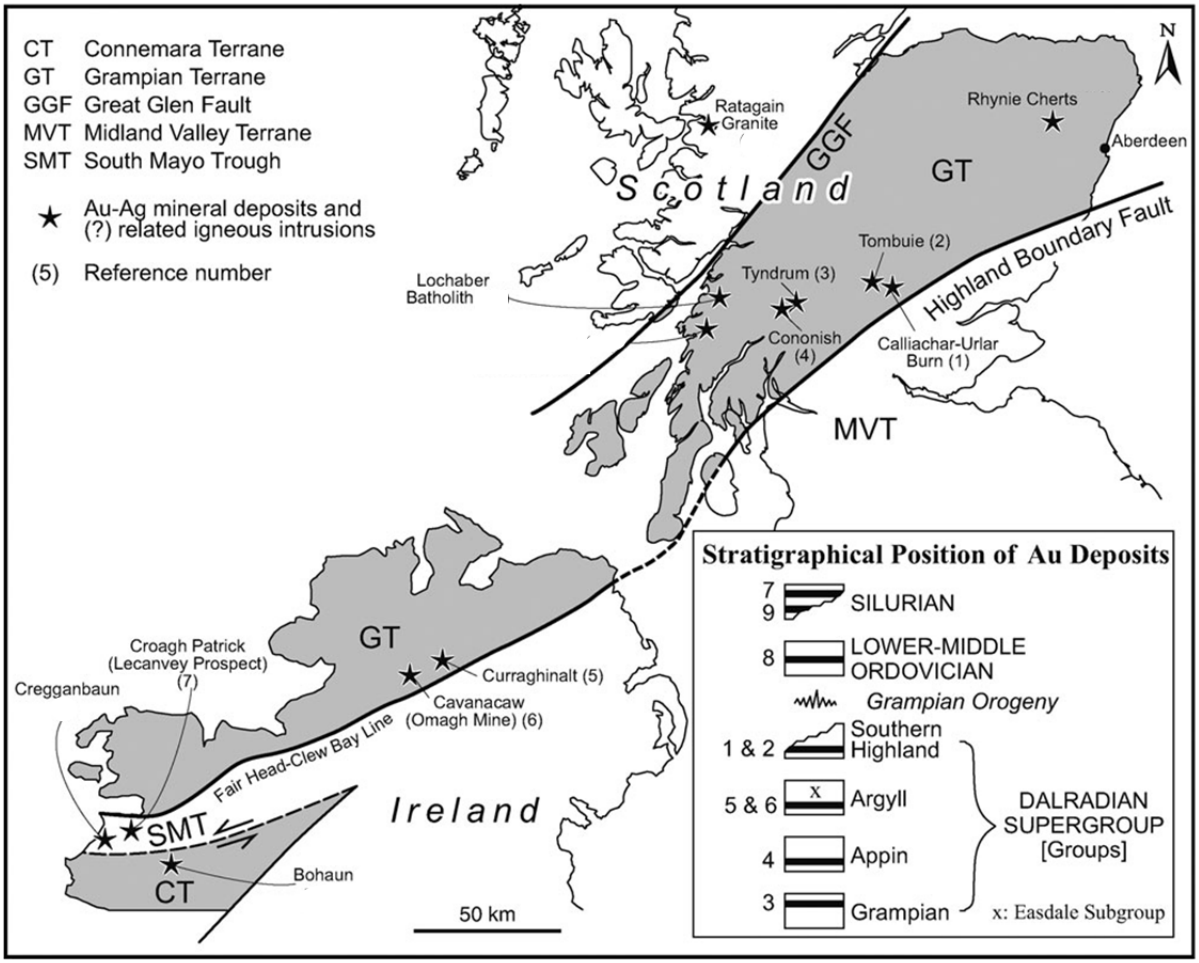

Figure 2.16. Adapted from Tanner, 2014a. Gold-bearing mineralisation (specific localities are indicated 1 to 7) in the Grampian Terrane of Scotland. References: 1-2: Ixer et al., 1997; 3-4: Treagus, 1991; 5-6: Parnell et al., 2000; 7: Aherne, Reynolds & Burke, 1992.

2.5.2 Geology of the Loch Tay area

The study has focused on a sub-area of the Grampian Highlands of Scotland, which is bounded by the regional-scale Highland Boundary Fault and Loch Tay Fault (Fig. 2.17). These are, in turn, crosscut by minor faults. Figure 2.17 shows a geological map of the area of interest, where the main localities (and relevant gold occurrences) investigated for this study are also indicated.

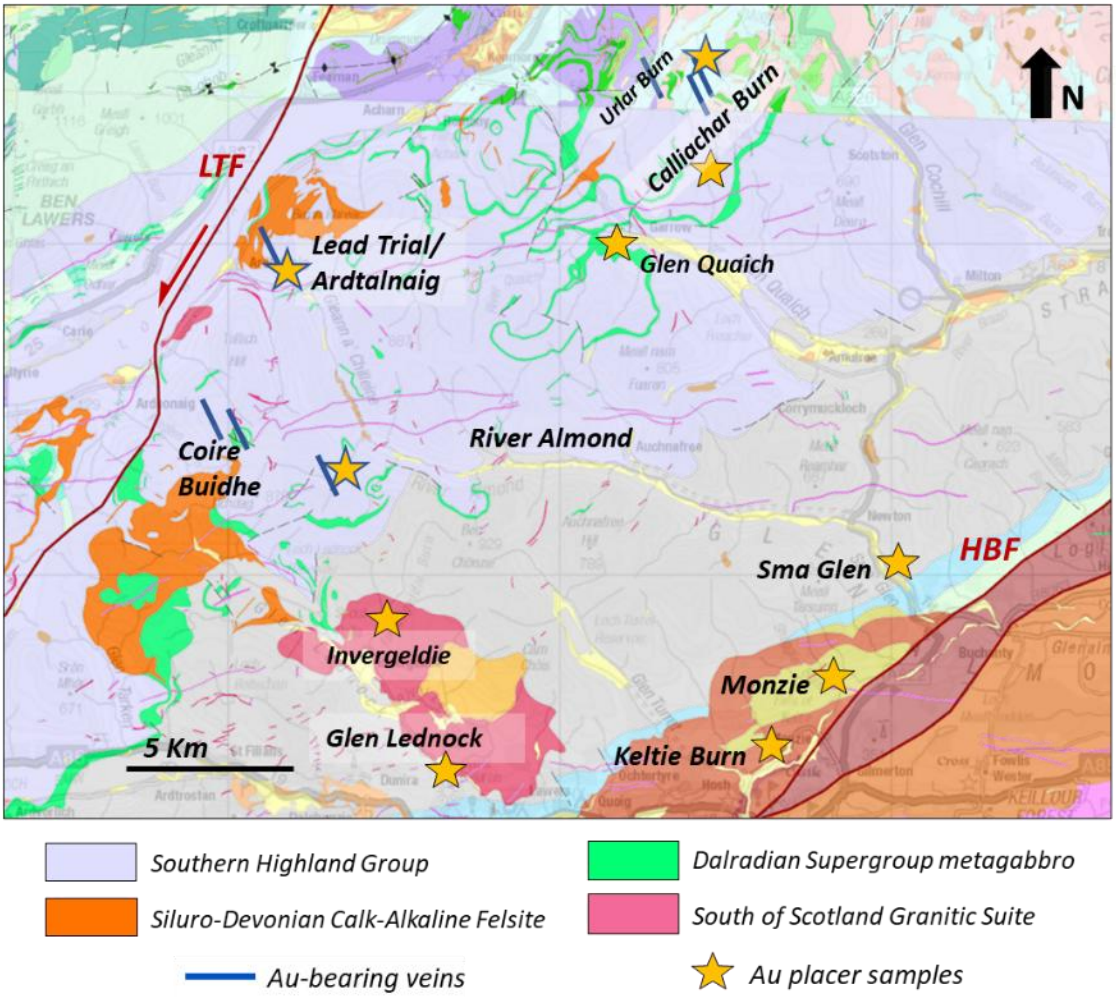

Figure 2.17. Geological map (with main lithologies) of the Loch Tay area of Central Scotland. The localities with gold occurrences (vein-hosted and placer), investigated for this study, are also reported. Modified from Digimap, Edina, 2023.

The Grampian Terrane metamorphic rocks are mainly represented by horizontal to shallow dipping layer packages of psammites and pelites, intercalating with amphibolite and biotite-chlorite schists. The Pitlochry Schist Formation dominates at the Ardtalnaig with pelites to mica shists, dipping 8°-20° to the E, and minor psammite and greywacke layers (Stephenson and Gould, 1995). Local mineralisation includes cm-scale veins crosscutting rhyolite (in the Siluro-Devonian Felsite) or mica schist, consisting of brecciated and massive quartz. Across the Calliachar Burn drainage (Figure 2.17), psammites occur more densely downstream than

upstream where, in contrast, pelites are more common. A fine to medium-grained dyke of dolerite to micro-gabbro is exposed ~20m downstream of the so called (Ixer et al. 1997) Discovery Vein (Erris Resources, 2020). The measures of the bedding across Calliachar Burn consistently record a dominant dip of 10°-20° to the S or SW. In the Urlar Burn these are more variable, although the recurrent dip direction is to the W at shallow angles (10°-15°). Movement along the Urlar Fault has been reported as sinistral (Ixer et al. 1997).

The Southern Grampian Suite comprises felsic to intermediate, calc-alkaline intrusions (Stephenson and Gould, 1995) which outcrop in the Ardtalnaig area as minor felsite bodies and, specifically, a felsite sill which shallowly dips to the E. A similar body (fine-grained with coarser-grained biotite, quartz and k-feldspar) has been identified in the vicinity of the Lower Calliachar Burn, ENE of the V3 vein structure (Erris Resources, 2020).

2.6 Research questions

In light of the literature background provided in the previous sections, some specific research questions can be formulated to guide this PhD study:

1) *What is the nature of the gold mineralisation in the Loch Tay area?*
2) *Are the local auriferous occurrences genetically related or unrelated? For example – are the Calliachar Burn, Urlar Burn and Coire Buidhe veins (Figure 2.17) genetically linked themselves? How do the more recently discovered ones (Lead Trial, Glen Almond Vein) map onto those occurrences?*
3) *How do the placer gold deposits correlate to auriferous veins – do the mineralogical associations in the hydrothermal veins show similarities with the gold mineralogical (i.e., inclusions) composition?*
4) *In which paragenetic stages of the respective vein system does the auriferous mineralisation fit in, and how does it vary in composition? Can variations in the silver content of the gold alloy inform on whether single or multiple fluid events took place?*
5) *Are there auriferous mineralised sources yet to be discovered in the Loch Tay area? If yes, how would this relate to the known ones?*
6) *Is it possible to establish the role of minor and major faults on the distribution of the gold mineralisation in light of its compositional nature? Would there be shared hydrothermal systems/fluid types?*
7) *Is it possible to identify different gold mineralisation styles that can be linked to deposit types?*
8) *Can the Loch Tay metallogenic system be compared to other similar systems in the Grampian Terrane of Scotland (i.e., Cononish)?*

Chapter 3. Methodology

3.1 Introduction

The driving concept of this PhD research is in enabling the prediction of gold mineralisation styles as well as of the location of gold mineralised occurrences in an area - within the Grampians of Central Scotland - characterised by poor outcrop exposure. The proposed methodological approach combines gold compositional studies with detailed petrographic analysis of hydrothermal veins (where available), and with an assessment of the vein structural orientations alongside fault and fracture plane measurements.

The correlation of compositional signatures (alloy and mineralogical assemblage) of gold from specific paragenetic stages with those of eluvial and alluvial gold occurrences, particularly, can illuminate the possible origin of the alluvial (i.e., placer) gold. In this context, previous work on the gold alloy composition has contributed to the interpretation of paragenetic sequences in several hydrothermal systems (e.g., Parnell et al., 2000; Arif and Baker., 2004; Spence-Jones et al., 2018), while the analysis of Au-hosted opaque inclusions of ore minerals can especially help the distinction between mineral assemblages and gold deposit styles (e.g., Chapman and Mortensen, 2016; Chapman et al., 2017; Chapman et al., 2023b). As such, this work has developed around relating ”classical” paragenetic investigations of lode deposits with detailed compositional characterisation of particulate gold, and placing this information in possible tectonic scenarios (i.e., fault and vein stress fields) which assume that local faults acted as conduits for hydrothermal fluid flow.

To this end, this Chapter describes the field, analytical and visualisation techniques and tools aimed at the project accomplishment.

3.2 Fieldwork and data collection

The field campaigns were designed for the main purposes of collecting geological and structural data and sampling both veins/bedrock and gold occurrences. These were conducted during the summers of 2019-2021 and principally involved LS, Dr Rob Chapman (RC) and Dr Taija Torvela (TT). Support was received from an exploration company committed to local field surveys and sampling campaigns (Green Glen Minerals Ltd, formerly Erris Gold Resources), who also provided part of the rock samples and the structural data. One of these field campaigns was designed to take place during the summer of 2020, however, due to prolonged COVID-19 restrictions (University of Leeds) the fieldwork capability was not extended to LS.; gold particle collection was undertaken by RC during July 2020 to partially mitigate the issue.

Geological fieldwork was carried out in the study area (''Loch Tay area'', Perthshire, Scotland) to inspect lithological and structural features, examine the texture and mineralogy of hydrothermal veins at the macro-scale, identify possible structural linkages between faults, fractures and veining, measure their respective orientations and estimate the general trend of the foliation/schistosity of the rock sequences at outcrop. Data were collected for each of the main localities upon sufficient outcrop exposure, which (unfortunately) was not in all cases achievable. Details and GPS coordinates are provided in Chapter 4, section 4.2.

In principle, the choice of locations was informed by previous literature work and survey reports around the area, relevant to the research target(s) set for this type of study (see Chapter 2, section 2.4; e.g., Mason, 1990; Ixer et al., 1997; Leake et al., 1997a; Tanner et al., 2014a). Later on, it was guided by the increasing availability of suitable gold and vein samples as well as data analyses, which progressively helped refine the most critical sites for investigation.

3.2.1 Sampling rationale and collection

3.2.1.1 Hydrothermal vein samples

Vein specimens were collected for any of the metallic, quartz-bearing, hydrothermal veins noted during the field activity. When this was rendered impossible by the too hard nature of the host-rock, analogous float samples were retrieved in the immediate proximity of the vein(s). All these veins, including their sampling locations (GPS coordinates), are described in Chapter 5 (section 5.2). Besides, several quartz-bearing veins were sampled around locations for which gold-bearing mineralisation was reported (e.g., Calliachar Burn, particularly downstream; Glen Lednock). However, upon inspection of fresh cut material which, in some cases, did not reveal any note-worthy feature (e.g., a hydrothermal quartz texture or sulphide mineralisation), a few rock samples were excluded from further investigation.

The vein samples from the Lead Trial prospect (Lavelle, 2020b) were selected in an attempt to provide a structured, broadly sequential coverage of the main outcrop area. Auxiliary information was gained by studying drill cores and rock sample databases from Green Glen Minerals, which helped mitigate the outcrop-scale visual complexity due to the interaction between multi-generational veins, structures and host-rock. Although only a couple of in-situ hand specimens were obtained, quartz and sulphide-bearing float samples showing reconcilable textural and mineralogical features were retrieved from the main auriferous vein location (see section 5.2.3) to complement their petrography. Additional hydrothermal vein samples were collected from a few nearby locations where Au mineralisation was specifically reported to occur

(e.g., Table 5.3), but which show distinctive textural and mineralogical character. The ultimate purpose of vein sample selection and collection was to estimate the style and evolution of mineralisation.

In the case of other localities (e.g., Calliachar-Urlar Burn, Upper Glen Almond), due to the generally lower vein thicknesses and textural complexities observed at outcrop, a potentially higher level of sample representativeness was achieved by collecting one or two specimens for each in-situ vein.

3.2.1.2 Gold samples

Alluvial gold populations were recovered in stream sediments from several rivers and glens, sampled at different points of a stream section (e.g., upstream, midstream, downstream) and - where these were observed - in proximity of metallic hydrothermal veins (Figure 2.17). Gold is a dense metal, as such, it tends to concentrate at the bottom of the sediments. Sampling was possible via initial sediment sluicing, allowing progressive mechanical separation of gold and heavy metals from the rest of the fluvially transported material, and subsequent hand panning to isolate the gold particles from the panned concentrate (e.g., Leake et al., 1997a).

Eluvial gold populations were only recovered in the Calliachar Burn (downstream) from gossans zones sited on top of two sulphide-bearing quartz veins, mostly by hand panning of the sedimentary material and consequent heavy metal separation. Hypogene-derived (i.e., "in-situ") material was obtained by progressive crushing of metal-bearing vein samples and subsequent hand panning of the finer concentrate to isolate gold and other heavy minerals. In both cases (eluvial and in-situ gold), the smallest gold particles (diameters ≤50 µm) were lost during the panning procedure. The detrital gold samples obtained were used to complement the compositional information of vein-sited (i.e., not extracted) gold mineralisation, due to the limited occurrences that are generally observable for the latter.

Gold particle collection aimed for a minimum of 60 particles for each sampling location, expanding upon original considerations by Leake et al. (1997a) which recommended at least 30 gold particles to allow compositional characterisation. A solid standard protocol was implemented for gold particle labelling, due to their overall high quantity - comprising populations from several localities, multiple samplers, and multiple field campaigns – and to additionally account for the number of EPMA and LA-ICP-MS spot analyses and SEM optical analyses, conducted not simply for each sample population but also for some individual gold particles. An example of raw data, plus particle numbering, labelling, respective locations etc.

has been included in the Appendix. Details and sampling locations (GPS coordinates) of all the gold populations incorporated in this study are reported in Chapter 6 (section 6.2).

3.3 Sample preparation

Petrographic thin sections

As a general rule, at least two orthogonal thin sections were obtained from each of the hydrothermal vein samples to be microscopically analysed, in order to reproduce as much as possible a three-dimensional perspective of their (typical) internal microtextures and mineralogical assemblages. Polished thin sections (47mm x 26mm) were produced at the dedicated University of Leeds facility, following an established technical procedure. Diamond lapidary saws were used to cut the samples to size, while subsequent grinding was achieved utilizing Buehler Motopol rotating wheels (i.e., 40µm and 10µm diamond-impregnated disks). Hand lapping, accompanied by optical estimation of the quartz birefringence, allowed the 30µm standard thickness of thin sections to be reached. The thin sections were finally polished on a rotating plate, first impregnated with 1µm diamond paste and ultimately with a "Gamma alumina", in a BuehlerTM Automat 250 apparatus.

Gold particle mounts on polished blocks

Gold particles were inspected using a binocular microscope before individual mounting on resin blocks. These blocks generally host gold populations distributed in rows of 5 or more particles each. Gold particles with roughly similar size are usually kept together within the same block (example in Figure 3.1) and fixed on double-sided adhesive tape before being set in resin; particle diameters range from <10 to >1000 microns. The blocks (25 mm or 30 mm in diameter) are polished via the same procedure adopted for thin sections (e.g., eventually using Gamma alumina).

Figure 3.1. Examples of particle mount set-ups for polished blocks, RJC 97 and RJC 98 (i.e., gold particles are distributed across populations depending on their sampling localities and relative grain sizes).

Polished thin sections and blocks were always carbon-coated prior to SEM imaging and analysis, to allow sufficient material conductivity and minimize charging in vacuum conditions.

Sample solutions for Pb isotope analysis

Powdered galena was obtained from selected hand specimens (from the 2019 field season) of the Loch Tay veins using a Dremel drill. These powder samples were transferred into vials and subsequently sent to the National Centre for Isotope Geochemistry at University College Dublin (UCD) for analysis. Sample preparation for Pb isotope analysis was taken further by Dr Steve Hollis, following the same procedure reported in Yesares et al., 2019. Approximately 5–10 mg of galena was digested using 2.5 ml of 6 M HCl and 250 µl of 70% HNO_3. The resulting solutions were evaporated to dryness on a hotplate at ~120 °C and subsequently re-dissolved in a mixture of 19 ml deionised water and 1 ml of 70% HNO_3. A 10 µl aliquot was then collected, centrifuged, diluted with 2.5 ml of 3% HNO_3, and spiked with 25 µl of a thallium standard solution with a known $^{203}Tl/^{205}Tl$ ratio to correct for instrumental mass bias.

3.4 Analytical techniques

3.4.1 SEM Imaging Techniques

The Scanning Electron Microscope (SEM) includes several tools (i.e., BSE, EDS or EDX, CL), all designed for micron-scale phase mapping and analysis, but each with a specific function. Among these, the Back-Scatter Electron (SEM-BSE) analysis utilises electrons - emitted during the

sample scanning - to display the spatial configuration of different elements in a material; it reflects the mean electron density of the target mineral, a function of atomic number and mineral density, generating high-resolution imaging and enabling visualisation of the material contrast. The Energy Dispersive X-ray Spectroscopy (SEM-EDS) enables the acquisition of semi-quantitative compositional information (i.e., in terms of element chemistry) on any mineralogical phase. The Cathodoluminescence technique (SEM-CL) allows the visualisation and differentiation of intrinsic textural features (e.g., in quartz), which would be otherwise indistinguishable – e.g., through standard SEM analysis in the BSE mode (Rusk et al., 2008b; Götze, 2012). The CL detection mechanism relies on the emission of photons from a material in response to electron bombardment (Marshall, 1988; Götze, 2009). Due to the importance of this tool in the methodological approach to vein sample analysis used in this study, some key theoretical principles are described in the next paragraph.

3.4.1.1 Principles of SEM-Cathodoluminescence

The chemistry and mineralogy of quartz are mainly dictated by its crystal lattice and defects in its structure (Gotze et al., 2021). These, along with fluid micro-inclusions and minerals, can be assimilated into quartz during crystallisation under variable thermodynamic conditions and secondary processes (Götze, 2009). As such, quartz luminescence has been attributed to multiple factors (e.g., lattice defects, vacant lattice sites, mechanical deformation and localised impurities; Lehmann et al., 2009, Rusk et al., 2011). These features were more broadly classified as intrinsic and extrinsic defects (Frelinger et al., 2015). Particularly intrinsic defects, generated by vacancies in the quartz lattice and trace element (e.g., aluminium, titanium) substitution, can give clues on the physiochemical conditions during crystal growth (Müller et al., 2003; van den Kerkhof et al., 2004; Götze, 2009; Hamers and Drury, 2011). Since these determine the ''defect luminescence'' of a solid, the variation in a quartz cathodoluminescence (CL) response (Figure 3.2) can be exploited as indicator of its physicochemical environment of formation and evolution (Baele et al., 2019, Götze, 2012 and 2021). Metamorphic quartz is typically identified upon a homogeneous CL response, mostly deriving from annealing processes (Rusk, 2012) due to the redistribution of lattice defects and, to some extent, trace elements (Sprunt et al. 1978; Spear and Wark 2009). Hydrothermal quartz displays a wide range of CL textures resulting from physiochemical changes at different scales, associated with hydrothermal veining, micro-fracturing and mineral precipitation (Rusk et al., 2014). In principle, assuming that the same analytical parameters are set, low-luminescence quartz appears darker than quartz emitting high luminescence (e.g., Rusk, 2012; Sales de Oliveira et al., 2017). In hydrothermal veins, SEM-cathodoluminescence has the capability of illuminating both separate quartz mineralising

events and internal zoning. While the former information is critical in reconstructing vein paragenetic histories, different types of mineral zoning (e.g., normal, oscillatory and sectorial) may help track the stability conditions of the crystallising fluid (e.g., Northrup & Reeder, 1994; Onasch & Vennemann, 1995; Shah et al., 2022).

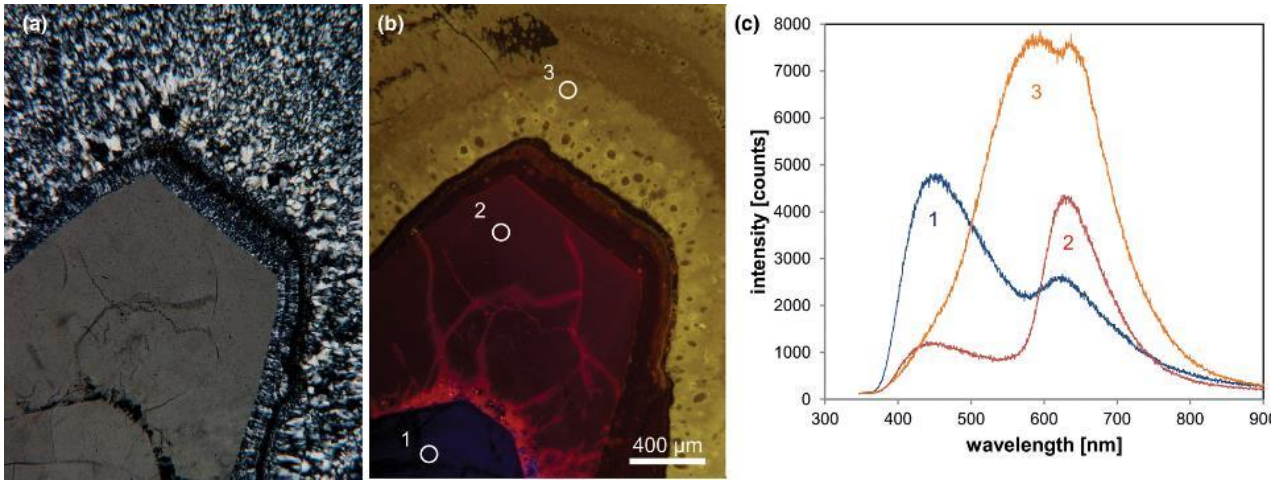

Figure 3.2 From Gotze, 2021. Quartz imaging at the micron scale (crossed polars – a) and CL (b) - from Kemmlitz (Germany); different quartz generations are distinguishable by different CL emission bands (c): (1) blue CL = primary quartz phenocryst, (2) red CL = volcanic quartz of a second generation, (3) yellow-CL = secondary microcrystalline quartz (hydrothermal); the circles in (b) indicate the locations of spectral CL analyses (Gotze, 2021).

3.4.1.2 Data acquisition

SEM-CL analyses were performed at the LEMAS (Leeds) facilities, using a Tescan VEGA3 XM (Figure 3.3a) equipped with a panchromatic CL detector (RGB filtered). The photograms were acquired via multiple CL channels - i.e., CL Grey, CL Blue, CL Red, CL Panchro, Color CL - applying an acceleration voltage of 20kV and a beam intensity of 19-20 (corresponding to a measured beam current of ~5 nA). The working distance (from the sample surface) was normally set at ~15 mm, and imaging was adapted to field-of-view ranges from 2 mm to 100 µm. Parallel SEM-BSE images were almost always obtained by lowering the beam intensity to ≤15. CL and BSE (automated) panorama maps of the thin sections were produced through overnight runs for several samples, exploiting the Image Snapper tool of the Tescan software and a slightly increased working distance. SEM-EDS (elemental) analyses were undertaken using an Oxford Instruments X-max 150 and visualised in the Aztec energy software. In very few cases, the thin sections were inspected before SEM-CL imaging by reflected light microscopy, to locate specific mineral features.

To estimate and record the nature and number of mineral inclusions in gold, the resin blocks with mounted particles were scanned with a FEI Quanta 650 FEG-ESEM (Scanning Electron Microscope), and individual inclusions were analysed by an operator (credit to RC) using the EDS (Energy Dispersive X-ray Spectroscopy) system of the same apparatus. This method (e.g., Chapman et al, 2000a) generally provides semi-quantitative information on the chemical composition of minerals, although mineral speciation is usually detectable.

3.4.2 Electron Probe Microanalysis on gold particles

The alloy composition (in terms of Au, Ag, Cu, Hg and Pd wt. %; Chapman et al., 2000a) of individual gold particles was obtained quantitatively using a JEOL 8230 electron probe microanalyzer (EPMA; Figure 3.3b). The analytical conditions used an excitation voltage of 20kV with a beam current of 50nA, and an on-off peak count time totalling 1 minute per element. Cu and Pd generally had limits of detection (LOD) around 200 ppm and 900 ppm, respectively. The spots for analyses were chosen in each particle on free of defects/inclusions surfaces by screen navigation (SE and optical microscope). The results can be considered reliable when the values of the returned totals are within the ~98-102% range. Both automated and manual (real-time) analyses were run, including a standard sample at the beginning, in the middle, and at the end of each cycle (~250 positions for automated and ~40 positions for manual analyses). Over 6500 positions on more than 6000 particles were stored in total.

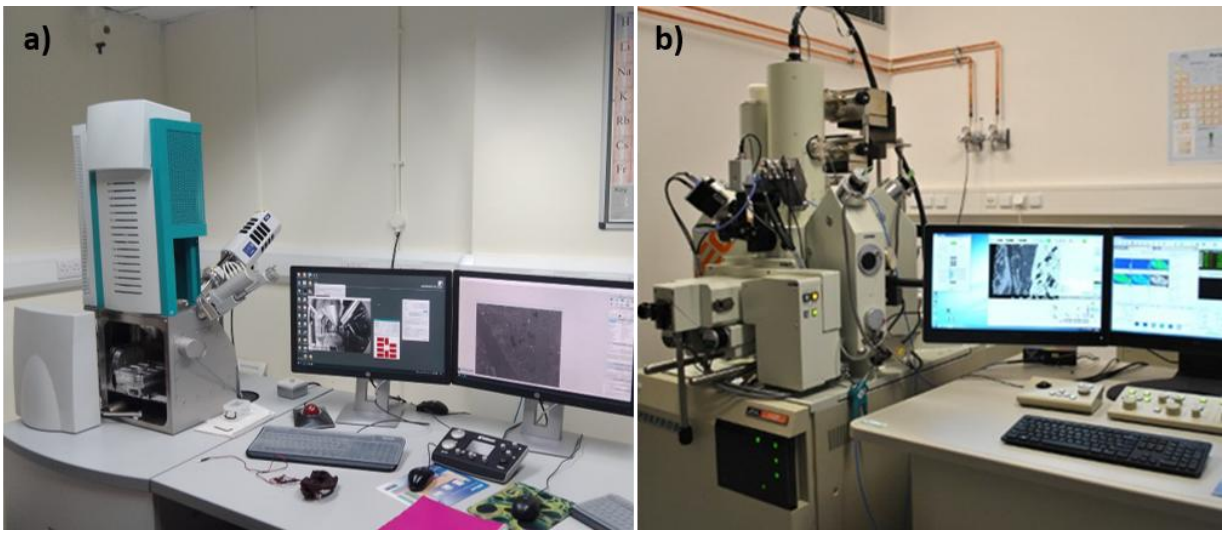

Figure 3.3 a) Tescan SEM; b) JEOL 8230 Electron Microprobe (EPMA).

3.4.3 LA-ICP-MS on gold particles

A common issue with the approach described in the previous paragraphs - entailing EPMA on gold alloy to establish part of the compositional signature - resides in the quality of the resulting Cu and Hg datasets, as some of the measured values can get close to the limit of detection (LOD) of the electron microprobe. In fact, although the microprobe is analytically accurate, an alternative analytical method, such as Laser Ablation Inductively Coupled Plasma Mass Spectrometry (LA-ICP-MS), offers the advantage of being more sensitive and can deliver high precision results, despite its lower accuracy. Also, although the combined investigation of gold alloy and mineral inclusion suites should render a distinction between gold populations - deriving from separate mineralizing events and different source styles of mineralization possible - this would still be dictated by the availability of sufficiently large populations to mitigate the usual inclusion scarcity in individual gold grains (e.g., Chapman et al 2010; Chapman et al., 2023b). The LA-ICP-MS has proven advantageous in employing more restricted gold populations for analyses to make detrital gold a more effective mineral indicator (Banks et al. 2018, Chapman et al., 2021). This technique is however limited by its characteristic of being destructive, since it requires the mineral to be ablated (i.e., partly destroyed) while being analysed. As such, during "single-spot" analyses, the measured compositions are strictly dependent on the spot size and location(s).

The LA-ICP-MS technique enables a quantification of the elemental composition of samples in the form of trace element abundances, expressed in parts per million by weight (ppm) (e.g., Pochon et al., 2021; Liu & Beaudoin, 2021; Liu et al., 2021a). The obtained elemental composition may not exclusively reflect elements incorporated in the gold alloy as trace lattice impurities (i.e., in solid solution; Antweiler and Campbell, 1977). Trace elements can also occur in gold alloys as heterogeneous, localised concentrations, indicating micro-inclusions of minerals which are generally undetectable by conventional means (e.g., Liu et al., 2021a; Banks et al., 2018; Gas'kov, 2017; Spence-Jones, 2021). Beyond the major alloying elements (Au, Ag, Cu, Hg and Pd), multiple additional components can thence be recorded in gold, namely: Si, Al, S, Ti, V, Cr, Mn, Fe, Co, Ni, Zn, Ga, Ge, As, Se, Y, Nb, Mo, Rh, Cd, In, Ir, Sn, Sb, Te, La, W, Pt, Pb, Bi, Th and U (e.g., Liu et al., 2021a; Banks et al., 2018; Spence-Jones, 2021). Among these, Bi, Te, Pb, Zn, and Mo are common components of accessory phases (e.g., sulphides) associated with gold mineralisation (e.g., Chapman et al., 2021). As such, it can be challenging to identify their contributions to the trace-element composition of gold as potential lattice-bound constituents

rather than micron- to sub-micron-scale mineral inclusions, accidentally co-ablated with the gold (Banks et al., 2018; Chapman et al., 2023b).

The potential of using LA-ICP-MS for this specific study is in providing an additional and distinct measure of gold composition besides the other two "standard" techniques, to improve the understanding of the genetic environment of gold particle formation, and to allow more subtle fluid source distinctions (e.g., magmatic-related or not) to be proposed.

3.4.3.1 Analytical procedure

Single-spot LA-ICP-MS analysis on a selected suite of gold samples from this PhD project was carried out in the ICP-MS laboratory at the Istanbul University-Cerrahpasa, with support from Dr Fatma Sisman; the sample list is reported in Table 3.1. The instrument used is a quintupled Nd: YAG laser equipped with a safety interlock system (Figure 3.4).

The adopted analytical protocol demands that the individual Au particle surfaces are ablated through laser pulses with a 50µm spot size (e.g., Watling et al. 1994). Normally, one (or two, exceptionally) position per particle was selected for ablation, on inclusion-free surfaces away from silver-depleted rims. The instrument was set on 200 pulses at 5Hz (ablation time of 40 seconds). 30 seconds of gas blank were included before ablation (~every ten samples). The standardisation required AuRm-2 std, NIST 80/20 Au/Ag wire, Mass-1 and NIST 610, with typically 3 ablation spots run on each standard, and on AURM-2 and NIST at more regular intervals during daily runs. Elements and isotopes analysed were S32, V51, Cr53, Mn55, Fe57, Co59, Ni60, Cu63, Zn66, As75, Se82, Mo95, Ag107, Cd111, Sn118, Sb121, Te125, Au197, Hg202, Tl205, Pb208, Bi209, Th232, U238 (at a counting time of 10 milliseconds) and Rh103, Pd105, Re187, Ir193, Pt195 (at a counting time of 20 milliseconds).

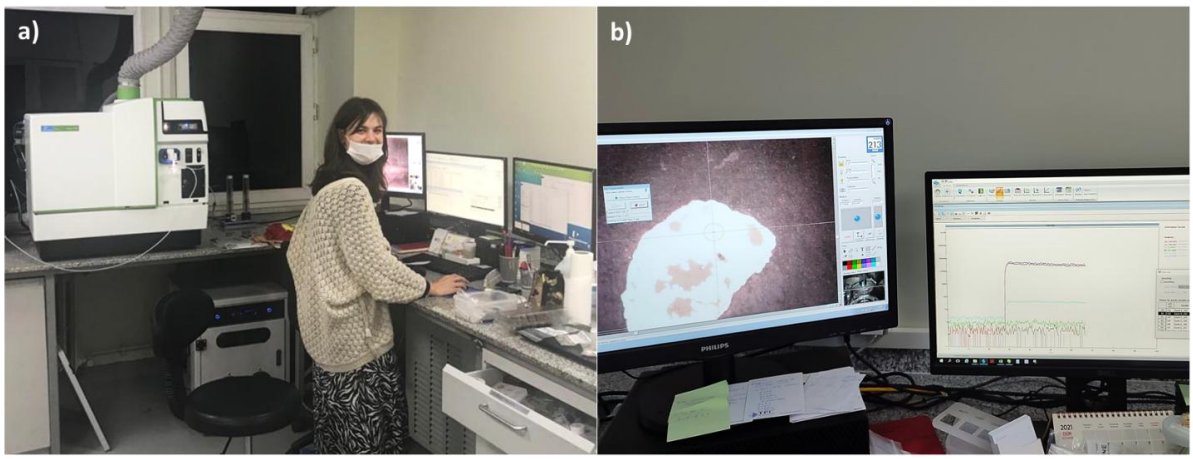

Figure 3.4 a) LA-ICP-MS instrument and equipment. Photo credit to Dr Fatma Sisman. b) Particle surface selection to target LA spots analysis (LHS), element signals produced by gold ablation (RHS).

Table 3.1. Sample set of gold particles (organised by locality) analysed at the Istanbul University-Cerrahpasa. Particles with Hg-rich alloys were removed from the selection as this would have compromised the instrument's functioning. "Population on block" indicates the specific gold population number on that block.

Location	Block	Population on block	Number of particles	Notes
Calliachar Lower	RJC136	14	06	Particles with higher Hg were deselected
Calliachar Lower	RJC137	12	11	Particles with higher Hg were deselected
Calliachar Lower	RJC137	11	14	Particles with higher Hg were deselected
Upper Calliachar	RJC137	10	07	Particles with higher Hg were deselected
Upper Calliachar	RJC138	03	19	Particles with higher Hg were deselected
Lead Trial	RJC134	20	24	
Lead Trial	RJC134	21	10 (11 to 20)	
Ardtalnaig	RJC134	10	1 to 6	
Ardtalnaig	RJC135	18	05	
Ardtalnaig	RJC138	01	02	
Upper Almond	RJC136	07	15	
Upper Almond	RJC135	15	16	
Almond @hydro	RJC137	01	16	
Almond Trib	RJC135	17	04	
Almond Trib	RJC136	13	06	
Almond Auchnafree	RJC137	04	11	
Lower Almond	RJC138	06	10	
Invergeldie	RJC138	05	21	

These ICP-MS systems typically measure the trace element concentrations in relation to a standard element (of established concentration) internal to the material. Therefore, it is essential to determine the major element concentrations for each gold particle (e.g., with EPMA) before any ablation (Chapman et al. 2021).

Data acquisition during the ablation process is first recorded as signal-type outputs. The signal morphology of any of the measured elements may be indicative of whether under-surface inclusions in gold were hit by the laser during data acquisition, and of the possible size of these (e.g., Banks et al., 2018). Inclusions are generally identifiable from an irregular shape of the ablation profile of that element. For instance, if the Fe profile shows a "spiky" morphology -

instead of a nearly flat one - that is highly suggestive of the influence of multiple pyrite micro-inclusions below the gold particle surface. Reduction of the raw LA-ICP-MS data outputs (time-resolved) was performed via the software Sills (credit to Dr David Banks; Allan et al., 2008). Further information regarding calculation of the LODs (limits of detection) is available in Appendix 3.

3.4.4 Pb Isotope analyses

Analytical procedure

Sample solutions, obtained from the procedure described in 3.3, were analysed (credit to Dr David Van Acken and Dr Steve Hollis) using a Thermo Scientific Neptune multi-collector inductively coupled plasma mass spectrometer (MC-ICP-MS) at the National Centre for Isotope Geochemistry, University College Dublin (UCD). During the analysis period, the mean values obtained for the NIST NBS 981 standard were $^{206}Pb/^{204}Pb$ = 16.9352, $^{207}Pb/^{204}Pb$ = 15.4900, and $^{208}Pb/^{204}Pb$ = 36.6939. Results were corrected against the NIST NBS 981 standard, following the isotopic ratios as reported by Yuan et al. (2016). The reproducibility (2σ) for NBS 981 was 0.0027% for $^{206}Pb/^{204}Pb$, 0.0032% for $^{207}Pb/^{204}Pb$, and 0.0037% for $^{208}Pb/^{204}Pb$. Raw data and relevant conditions are reported in Appendix 4.

3.5 Visualisation and presentation of the datasets

3.5.1 Structural data display

The measured orientations and dips of fault planes, and of fractures and veins - all stored as MS Excel datasets - were plotted as stereographic projections using the Stereonet software (v. 11) by Richard W. Allmendinger, when the total measured values in a dataset were generally ≥15. Rose-diagrams (in equal-angle stereo-net formats) were found useful in displaying the strike orientation values statistically. Additional pole projections (with Kamb contouring) were calculated for all the measurements and displayed on the same diagrams.

Multi-scale geo-structural maps of the study area were built upon digital (geological and OS) base-maps downloadable from Digimap (https://digimap.edina.ac.uk) via the Inkscape open-source software. This has been used to project structural and geochemical data and to plot sample occurrences, as a valid alternative of ArcMap, which was temporarily inaccessible due to restrictions of services on campus. Google Earth Pro was chosen to allow the identification of

further structural features, specifically faults, due to the high-quality satellite photography provided.

3.5.2 Gold data representation

3.5.2.1 Gold alloy and inclusion suite

Gold compositional signatures are best illustrated via a graphical representation of the alloy composition and the associated inclusion assemblages. 'Cumulative percentile vs. increasing Ag' plots (e.g., Chapman et al., 2000a; Leake et al., 1997a) have been adopted to indicate the silver contents of the studied gold samples, where the Ag% measure of each particle is expressed by an individual data point on the profile (Figure 3.5). These types of plots facilitate a visual comparison between gold populations having different sizes and multiple origins, as the gradients and overall shape of the silver profiles describe the nature of the samples (Fig. 3.5b). Breaks in the curve or changes in the gradient within a single population are generally interpreted as evidence of the presence of particles from separate fluid events or even sources, particularly when the silver content variability can be correlated with different mineral inclusion assemblages (Chapman et al., 2000a). As such, when the distribution of the silver contents of several gold particles translates in a plateau or a flat horizon on the profile, it is suggesting a univocal or shared source for that gold (e.g., Chapman et al., 2000a and 2021). Roughly coincident plots observed for gold from adjacent sampling sites may indicate a similarity in the gold fluid source, or - when this is noted for the silver profiles of separate placer gold populations – similarity of multiple contributing sources or in the evolution of whole mineralising events (e.g., Chapman et al., 2023c; Chapman et al., 2023d).

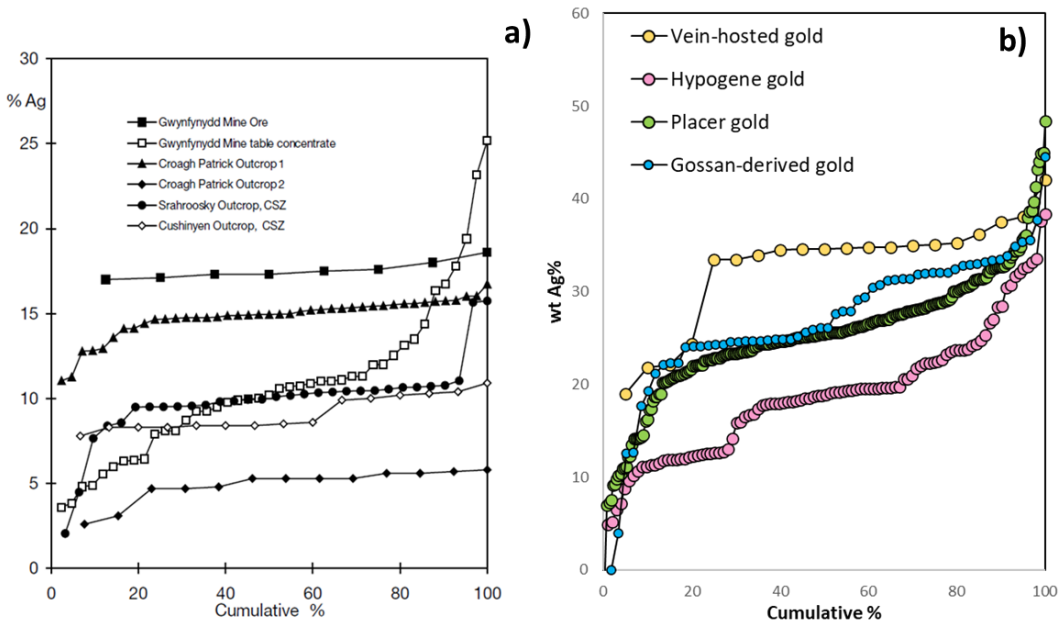

Figure 3.5 a) Silver profiles from Chapman et al., 2000, indicating the relationships between Ag content of gold populations and volume of mineralized material (Chapman et al., 2000). B) Examples of silver profiles from different gold sample types (from Calliachar Burn and Glen Almond in the Loch Tay area). Gold liberated from multi-sourced material generally shows a wider compositional range, reflected in the gradient of the plot (e.g., Chapman et al. 2000).

The same graphical approach, cumulative-percentile based, can also be used to illustrate the content of other elements (e.g., Hg and Cu) in various gold alloys. However, the datasets of minor alloying elements are always evaluated with respect of the element LOD (Limit of Detection) and LOQ (Limit of Quantification, or LOD x 3), meaning that those elements may not occur (i.e., in gold alloy) in amounts that would allow their quantitative appreciation. When this is otherwise possible, binary plots of Ag vs Hg (e.g., example in Figure 3.6a) or Ag vs Cu (e.g., Chapman et al. 2017 and 2021) can be appropriate to assess the element covariances. These types of diagrams are helpful in highlighting gold compositional fields and can also be used for multivariate analysis – for instance, by incorporating symbols which represent other characteristics of the analysed gold, or the presence of inclusions (Figure 3.6b; Chapman et al 2023b).

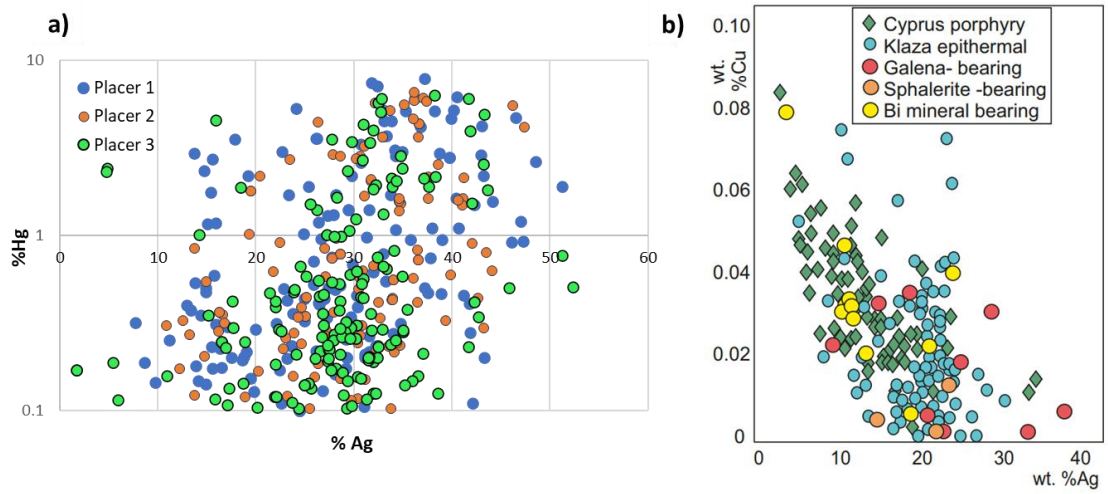

Figure 3.6 a) Ag-Hg and b) Ag-Cu bivariate plots of different gold samples (i.e., placer gold in a), used to estimate the element covariance; b) from Chapman et al., 2016 (Klaza epithermal deposit, Yukon); gold compositional fields are further depicted by specific symbology.

The inclusion suites of gold populations are defined by counting the particles in a population which host specific inclusion species (Chapman and Mortensen 2016), regardless of the number of inclusions of the same species in an individual particle. These datasets may be represented graphically in several ways (e.g., Chapman et al., 2023b) and rely on the mutual proportions of different components in a sample of inclusions. For this study, two main graphical approaches - which enable a quantification in gold particles of the inclusions as both mineral and chemical identities - have been preferred over others.

A specific methodology describing the inclusion assemblages as elemental datasets has been adopted recently (e.g., Chapman et al 2021 and 2023b) and accounts for the inclusion metal and non-metal content. In this context, radar diagrams (in logarithmic scale) offer an effective visual tool that allows immediate comparison of gold signatures from different sites. The method (schematically explained in Figure 3.7) is based on a scoring system which requires the total 'metal' value and the total 'non-metal' value of an inclusion to be each equal to 1 (Chapman et al., 2023b). Scoring is irrespective of chemical stoichiometry and the total score of each element is established by summing the same element contributions in an inclusion sample set. Mineralogical speciation may be lost in some cases - for instance, pyrite inclusions score the same as pyrrhotite inclusions, with Fe = 1, S = 1 (Chapman et al., 2023b) - however, this approach is helpful in emphasizing the contributions of minor elemental components to the inclusion assemblage (e.g., Sb and Te; Chapman et al., 2023b).

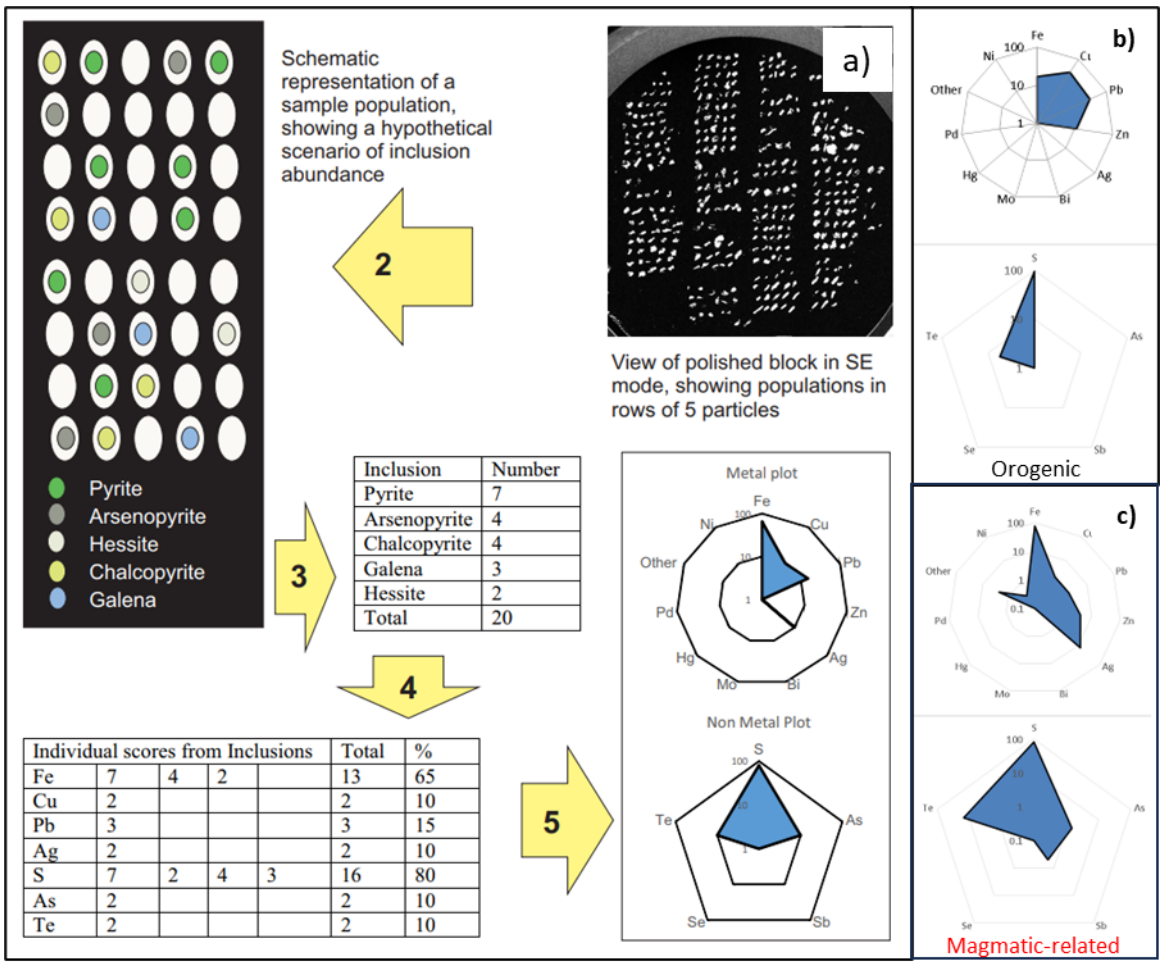

Figure 3.7 a) Steps in the methodology used to describe inclusion assemblages via radar diagrams (by Chapman, 2019); a) typical orogenic-related inclusion assemblage, indicated by the presence of base metal components; magmatic-related inclusion assemblage, as indicated by the presence of Bi-Ag-Te components.

Spider diagrams to depict the inclusion mineralogy of several gold populations were introduced by Chapman et al. (2018). This system, critical for highlighting the occurrence of distinctive mineral species as inclusions in gold, proved particularly successful in acknowledging minerals (i.e., within the Pb-Bi-S-Te system) as discriminators in the calc-alkalic porphyry environment (example in Figure 3.8). Clarity can however be compromised by more than three-line plots per diagram.

Combining radar plots with spider diagrams has been particularly beneficial to the present project, since it has permitted an overarching elemental comparison of the inclusion suites from multiple populations regionally alongside an ad-hoc evaluation of the relative proportions of specific mineral components in certain samples (e.g., Chapman et al., 2023c, Chapman 2023d). In cases where the inclusion abundance in detrital gold samples from the Loch Tay area was not sufficient (i.e., ≥ 15 inclusions) to robustly interpret compositional signatures, samples from 2

or 3 different locations were amalgamated based on both geographical and - after preliminary analysis - genetic criteria.

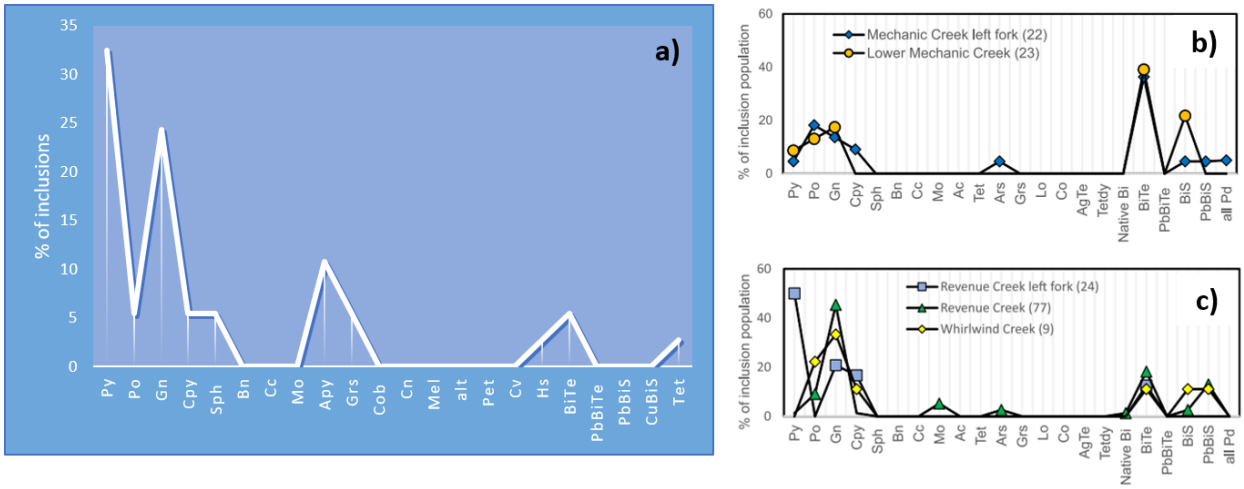

Figure 3.8 a) Spider diagram highlighting the distribution (based on the proportions) of different mineral inclusions in a gold population; b) and c) Examples of inclusion assemblages (grouped by localities) of different minerals within the overall assemblage (from Chapman et al. 2018).

As anticipated above, a correlation of alloy compositions and inclusion suites of gold particles may also be presented as annotated binary plots – displaying alloying metals and corresponding inclusion mineralogy - defining distinct compositional fields (e.g., Chapman et al. 2017). Consideration of placer-lode gold relationships usually demands the correlation of inclusion assemblages of detrital gold populations with the mineralogy of a potential lode source. In these cases, a matrix of inclusion species occurrences against vein mineralogy (Example in Figure 3.9), as proposed by Chapman et al., 2016, can be informative.

Mineral Species	Late stage subepithermal veins				Inclusion assemblages of placer populations						Mineralogy of ore stage					
	Mt M Vb veins [1]	Friday . Ck veins [2,3,4]	Afton and Mt M [5,6]		Cherry . Ck [7]	King .Richard Ck[7]	Whipsaw Ck[7]	Friday Ck[7]	Similkameen . R[7]		Mt M. Early Veins[8]	Cu Mt 1[2]	Cu Mt 2[2]	Whipsaw Porphyry [9]	Wood[10]	Afton Pit [6,11,12]
Chalcopyrite	■	■			■		■	■	■		■	■	■	■	■	■
Bornite		■					■	■	■		■		■		■	■
Pyrite	■	■			■	■	■		■		■	■		■		■
Carbonate	■	■				■	■		■							■
Cu sulphosalts	■					■			■				■			■
Chalcocite/covellite		■			■		■	■	■				■			■
Ag- tellurides	■	■			■		■		■			■				■
Galena	■								■			■				
Bi-tellurides	■				■			■	■							
Arsenopyrite	■								■							
Sphalerite	■								■			■	■	■		
Pyrrhotite							■	■	■			■				
Molybdenite					■		■	■	■					■	■	■
Other As- bearing								■	■							
Sperrylite			■				■									■
Merenskyite/ Kolutskite	■	■	■				■	■	■			■				
Temagamite	■	■	■		■				■							■
Mertieite II					■				■			■				■
Stibiopalladinite			■					■	■							

Figure 3.9 From Chapman et al., 2016. Comparative matrix of vein-hosted gold mineralisation and mineral inclusion suites of adjacent placer samples. The shaded areas indicate Pd-bearing minerals.

3.5.2.2 Accuracy of the alloy data from Calliachar Burn and River Almond

The number of gold particles sampled at specific sites from two main locations (Calliachar Burn and River Almond) was increased throughout different field campaigns, providing an opportunity to integrate the alloy and inclusion data of the respective gold populations after each sampling stage. A few considerations have been made upon the comparison between initial and enhanced datasets. After having analysed a larger number of grains i) the overall silver contents tend to remain stable for the placer gold samples and to increase for the gold from gossan-derived samples (Figure 3.10 a, c, d); the overall mercury content recorded for gossan-derived gold from Calliachar tends to increase slightly for one of the two populations and to decrease for the other (Figure 3.10b); the mercury contents increase for placer gold.

In terms of data reproducibility, these observations suggest that the availability of a larger sample can generally be more helpful to the depiction of mercury rather than silver, and more informative for gossan-derived rather than placer gold. It is thus confirmed that any evaluation of the relative amounts of alloy components in different gold samples needs to account for the number of particles involved.

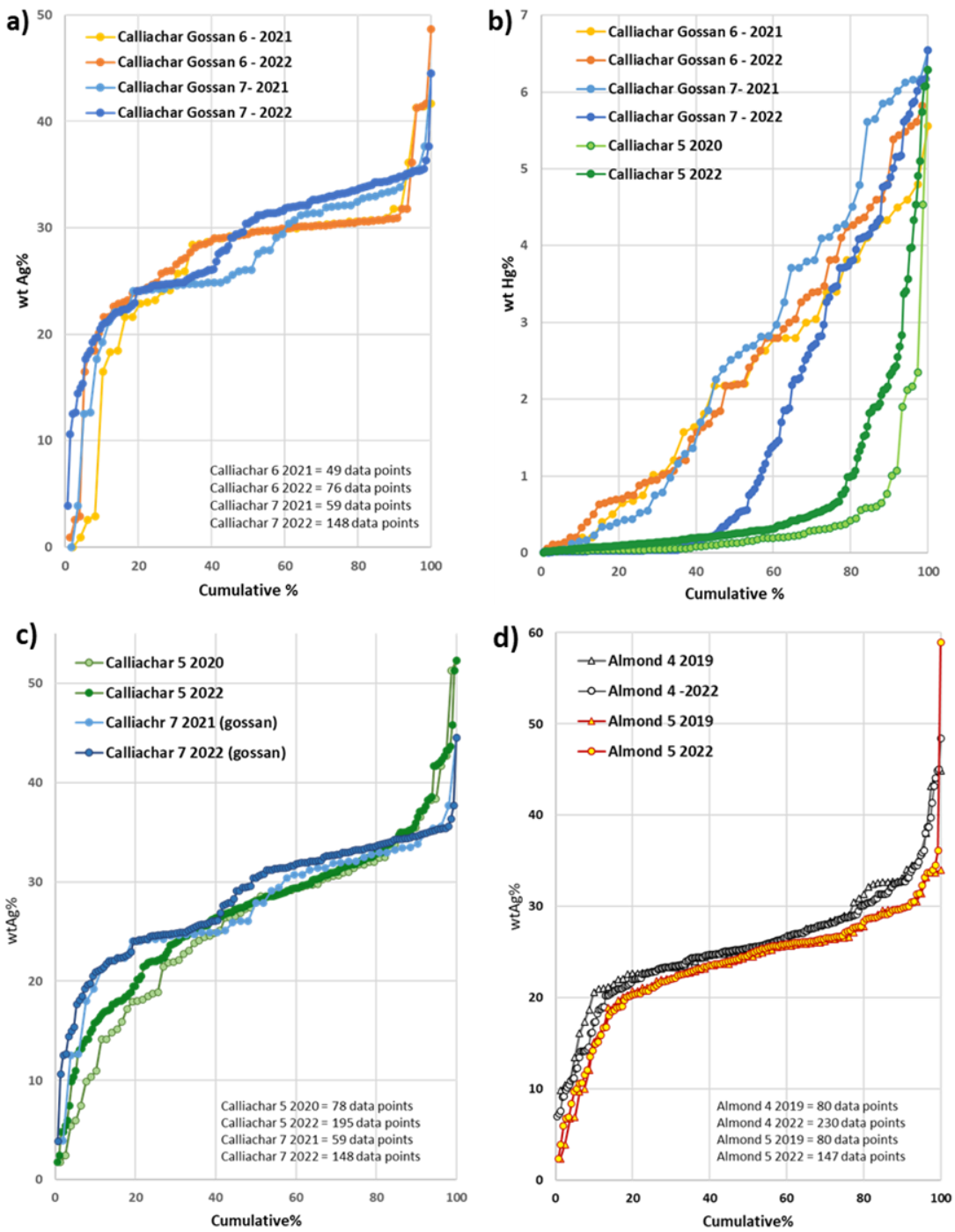

Figure 3.10 a), c), d) Silver profiles and b) Mercury profiles of initial and augmented gold samples from Calliachar Burn and River Almond. The data from 2022 incorporates the data from samples collected during previous field campaigns across the same locations. Sample sizes (= number of particles) are also indicated.

3.5.2.3 Trace elements in gold

The representation of trace element data obtained by LA-ICP-MS investigation on gold particles has been attempted, to date, by Watling et al. (1994), Banks et al. (2018). Chapman et al. (2021 – some references therein) and Spence-Jones (2021). An approach commonly adopted by these authors consisted of indicating the abundance of gold particles in a sample set which show specific element concentrations above the detection limit (example in Figure 3.11; Chapman et al., 2021); quantification of the trace element data by box and whiskers diagrams, instead, was found effective in helping distinguish the datasets with respect of their associated gold deposit type (e.g., orogenic; alkalic porphyry; Banks et al., 2018). In all cases, preliminary comparison of the major alloy elements in gold measured with LA-ICP-MS and EPMA was performed to assess the reliability of LA-ICP-MS analyses.

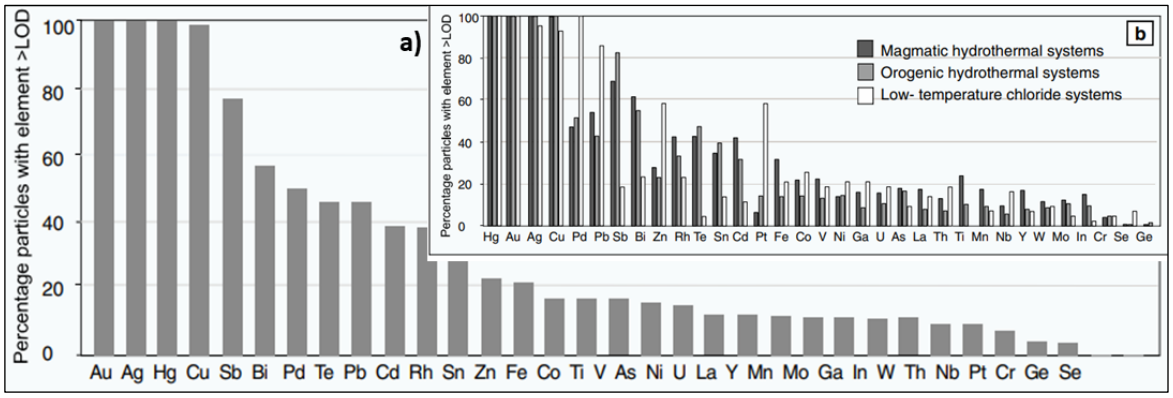

Figure 3.11 From Chapman et al., 2021. Trace element abundances in a study of 1100 gold particles by quadrupole-LA-ICP-MS. a: Element abundances in the entire population, b: Element abundance distribution according to hydrothermal systems.

The visual approach proposed in this study entails representation of the trace element data via radar and binary plots. The dataset used only includes the elemental values above the limit of detection (LOD).

Radar plots were constructed for each sample population, accounting for the average concentrations of specific trace elements in it. The average values were calculated by dividing the total element concentration (in an established gold population, measured in ppm) by the number of just the particles in which the element was detected (i.e., not the total number of particles analysed from that population). In this way, only element abundances above the LOD are used for the calculation of the averages (and subsequent data display), since the elemental concentrations were gathered from a dataset filtered by limit of detection (i.e., all the "less than values" = values below the LOD; see Appendix 3). This method was chosen in order to allow a

straightforward, overarching comparison between gold populations from different sampling sites and, possibly, a subsequent comparison of these trace element datasets with some equivalent elemental components recorded by the inclusion suites of the same samples. A limitation of this approach, however, is given by the variability in the number of particles (and respective element abundances) used to obtain the mean values indicated in the plots – for example, if any of the datasets included an individual point for which an unusual value of elemental concentration was measured, this would possibly bias the final (calculated) average concentration. This aspect will be further discussed upon presentation and evaluation of the LA-ICP-MS dataset utilized for this study (e.g., section 6.2.6).

On the other hand, binary (i.e., bivariate) plots were found useful in evaluating the mutual occurrences (concentrations in ppm) of specific elements (e.g., Te-Ag; Mo-Ag; Bi-Mo) in a gold population on a particle basis – particularly in gold samples for which a magmatic-related origin was hypothesised. Box and whisker diagrams were additionally employed to visualize the distribution of the concentrations of major elements (Au, Ag, Cu and Hg) across gold samples from the main localities investigated. Although such an approach is particularly effective in displaying the median and outlier abundances of a certain element for multiple samples simultaneously, it may be inconvenient to adopt when many measured elements occur in different populations with very variable concentration ranges (ppm), due to the difficulty in visualizing these altogether across close scale values.

Chapter 4.

Structures and textures at outcrop and their significance

4.1. Introduction

This chapter provides a detailed account of the geological features examined within the study area, organized by locality, together with their potential interpretations. The descriptions mostly entail structural data and mineralisation patterns, which formed the basis for the sampling strategy and subsequent analytical work. To provide context, a comprehensive geographical and geological overview of the four main areas that were investigated is introduced ahead of a more in-depth characterisation of each of them.

4.2 Field observations

Field investigations were conducted at specific localities across an area of ~200 Km^2 (Figure 4.1) and focussed on the locations of Calliachar-Urlar Burns, Lead Trial/Ardtalnaig, Coire Buidhe and the River Almond catchment. The primary purposes of these campaigns were to explore hydrothermal vein outcrops (e.g., textures, mineralogy) and associated structural features, and to evaluate drainage geometries and water flow to collect potential placer gold samples. Publicly available digital geological maps were obtained prior to fieldwork from https://digimap.edina.ac.uk/, an official online repository for maps and data of Great Britain from the British Geological Survey.

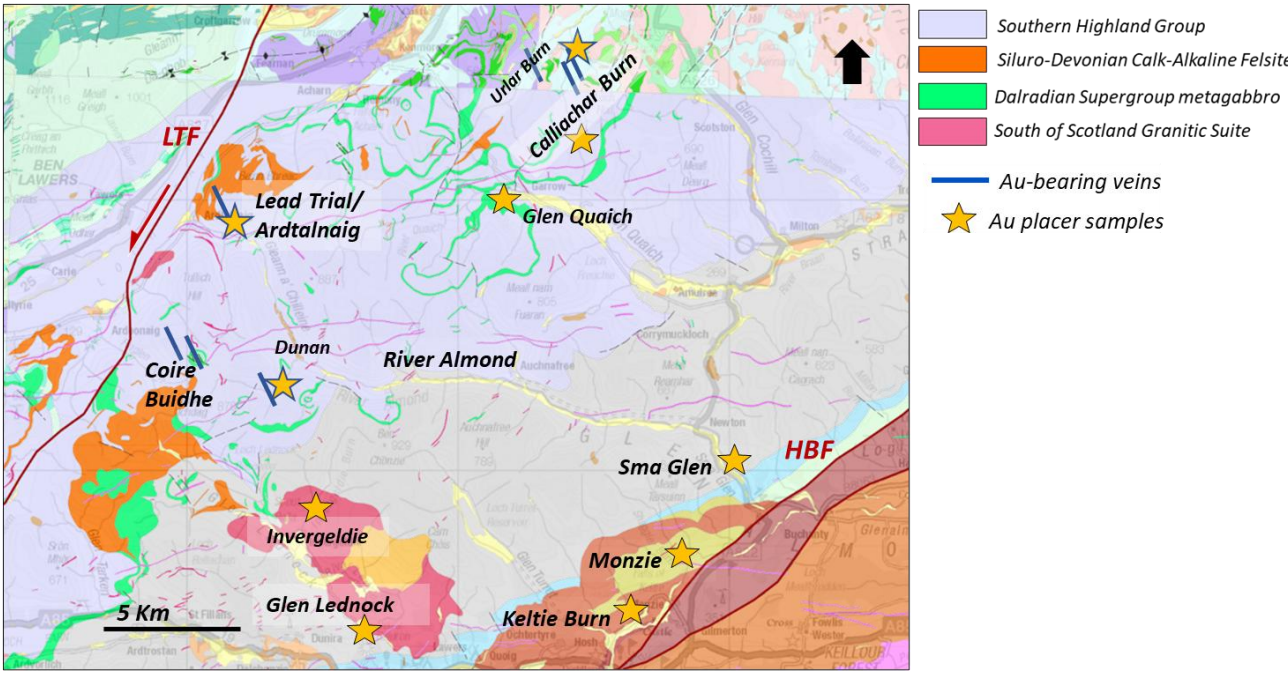

Figure 4.1 Geological map with an overview of the locations that were targeted for primary field investigations. LTF = Loch Tay Fault; HBF = Highland Boundary Fault (modified after the BGS geological map from https://digimap.edina.ac.uk/). Full lithological legend available on https://digimap.edina.ac.uk.

Calliachar Burn and Urlar Burn are located ~4 Km south-west of Aberfeldy, where they mostly cross part of the Pitlochry Schist Formation (psammites and semi pelites) in the Southern Highland Group (semi pelites). These locations were among the first targets to be selected for field investigations, to explore the documented hydrothermal veining and gold placer occurrences in relation to the local structural setting. The Almond area extends for ~20 Km in an east-west direction, where River Almond flows through the Southern Highland Group from the Dunan to Sma Glen localities. Mica schists are the local dominant rock type, in which thin sulphide-bearing quartz veins were identified by recent field and exploration campaigns; placer gold can be recovered throughout the catchment in relatively high abundances. The 'Lead Trial' prospect (Erris Resources, 2020) is located immediately to the East of the Loch Tay Fault, in a restricted area associated with the hydrothermal-magmatic activity; this extends for >4 Km in the W-E direction and for a couple of kilometres in the N-S direction. Rhyolites are the main lithology, and host quartz veins which typically contain variable amounts of galena, sphalerite and barite. The Coire Buidhe mine sites are located approximately 5 km south of the Lead Trial ones. The southernmost region of the Loch Tay area ('Loch Tay South') covers approximately 15 Km^2. Igneous bodies outcrop at Invergeldie and Glen Lednock, specifically the Early Devonian granitic suite, and near Keltie Burn (Devonian andesite/basalts) in the Ben Ledi Grit Formation. Due to the nature of the landscape - gentle topography mostly due to glacial modification and few bedrock exposures - the collection of structural data by field activity has proved somewhat challenging; the existence of a few faults has been deduced by digitally interpolating local lithologies and topography, in addition to the ones reported on historical maps. Placer gold occurs in Keltie Burn, Glen Lednock, Invergeldie and Monzie.

Due to the structural data (e.g., fault, fracture and vein orientations) being available in variable amounts depending on the relevant site of collection, slightly different approaches have been adopted for their presentation - in particular, stereonets have only been used where the number of measurements to feed into the plot format (i.e., dip values required) is equal or greater than 10. More detailed, zoomed-in maps for each locality will be presented alongside the relevant descriptive section in the following paragraphs.

4.2.1 Calliachar-Urlar Burn

4.2.1.1 Overview of the structural data

A large number of structural measurements was gained after careful inspection of the different sections of the Calliachar Burn catchment (from north to south: downstream, midstream and upstream); these were explored in the course of different field campaigns, particularly during

Summer 2019 and 2021. A similar approach was adopted for the structural investigation of the adjacent Urlar Burn drainage, although over more limited occasions (Figure 4.2). The structural data include fault, fracture and joint orientations, vein orientations, and evidence of passive structural markers (when observed). Field pictures relevant to different sections of Calliachar Burn are additionally available in Appendix 1.

Figure 4.3 displays the statistical distribution (in equal-angle stereo-net formats) of measurement orientations from the Calliachar-Urlar area, where sufficient data is available to provide a robust estimation. The only exception is represented by the sulphide-bearing veins (Figures 4.2 and 4.3f) for which the number of available measures is <10. These have equally been plotted due to the criticality of sulphide-bearing vein orientations in the local structural analysis, especially in relation to the 'barren veins' (= with no sulphide mineralisation) and the joint/fracture distribution. Pole projections have been calculated for all the datasets (from 3a to 3f) included in Figure 4.3. Individual measurements of the strikes were used for the calculation; in addition, rose diagrams were chosen to provide statistical estimations of the original plane measurements, to highlight the local dominant trends instead of displaying the individual strikes. In such cases, these are visually grouped into angular bins (i.e., intervals of 10°) whose length depends on the proportion of measurements recording the same strike.

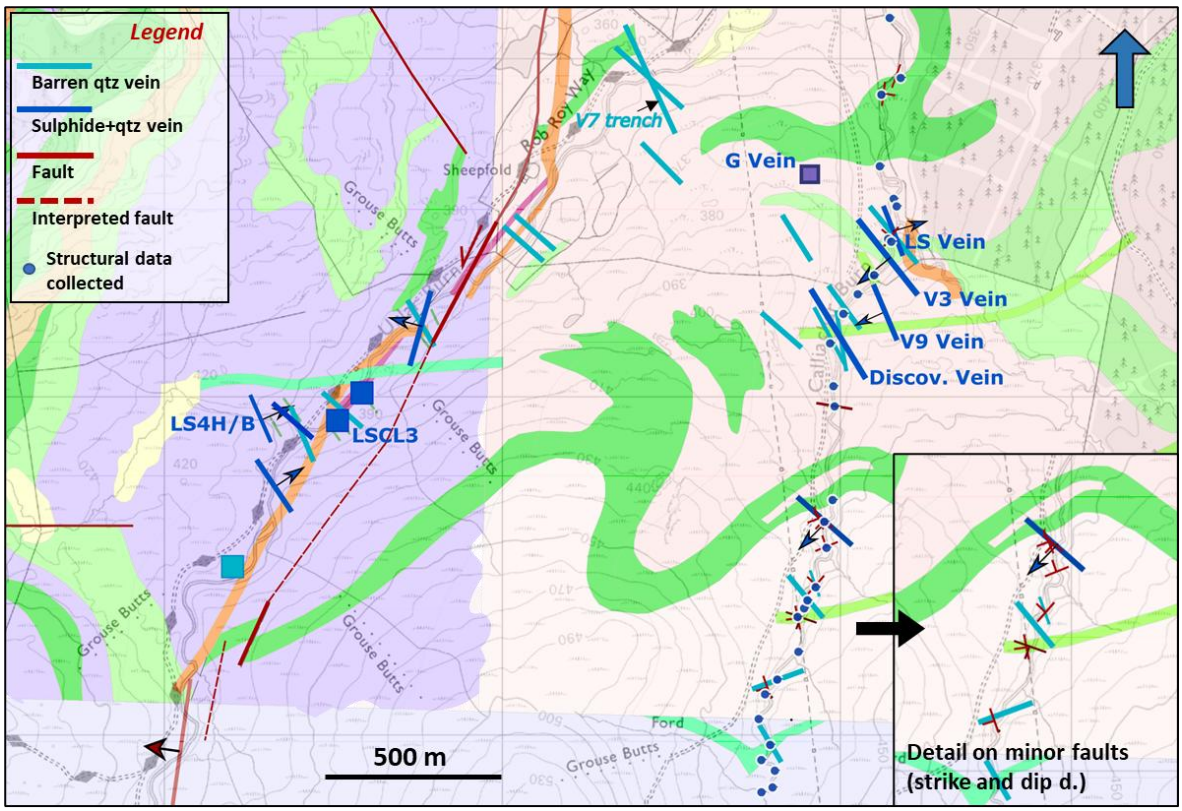

Figure 4.2 Geological map of Calliachar and Urlar Burn, with details on the structural data collected across the area (modified after the BGS geological map from https://digimap.edina.ac.uk/).

All the vertical joint measurements collected across different sections of the Calliachar Burn (Upper, Mid and Lower, Figure 4.3a, b, c) and the Urlar Burn (~ 40 measures available overall, Figure 4.3c) display a dominant NW-SE trend. Joints filled with quartz mineralisation, identified throughout the area, have been included in the analysis, resulting in a preferential 150˚ orientation. The NW-SE trend is in large part preserved by the orientation of barren and sulphide-bearing veins (Figures 4.2, 4.3e, f). However, the distribution of minor fault orientations obtained for the Calliachar catchment shows no preferential trend (Figures 4.2 and 4.3d). The Urlar Fault locally represents a major, almost vertical structural feature, striking NNE-SSW with a dominant sinistral sense of shear.

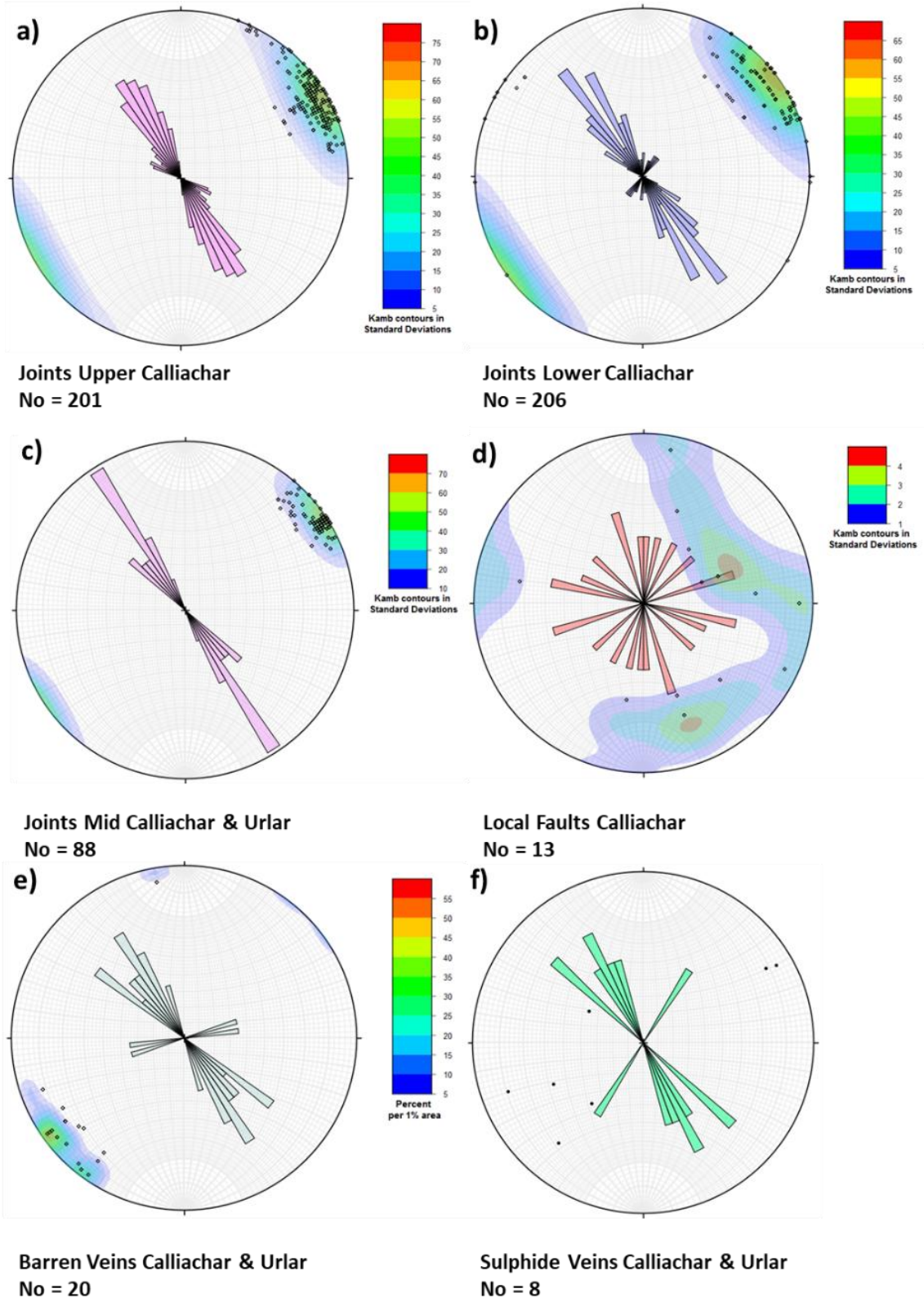

Figure 4.3 Stereographic projections of the structural data collected across the Calliachar-Urlar area. Pole projections have been calculated for all the measure types and rose diagrams represent statistical estimations of the original plane measurements.

4.2.1.2 Hydrothermal vein characterisation

Quartz-bearing veins were identified throughout the Calliachar and Urlar Burns. The sulphide- and, in some cases, Au-bearing, hydrothermal ones only outcrop across restricted segments of the two catchments. In the first instance, investigations were focused on veins for which important preliminary information on texture, mineralogy and ore grade is available from literature and reports (e.g., Ixer et al. 1997). A map is provided to help visualise these occurrences (Figure 4.4), which are individually described below, from downstream to upstream. Five main hydrothermal veins can be located across the downstream (northernmost) section of Calliachar Burn, and a couple across the midstream section of Urlar Burn.

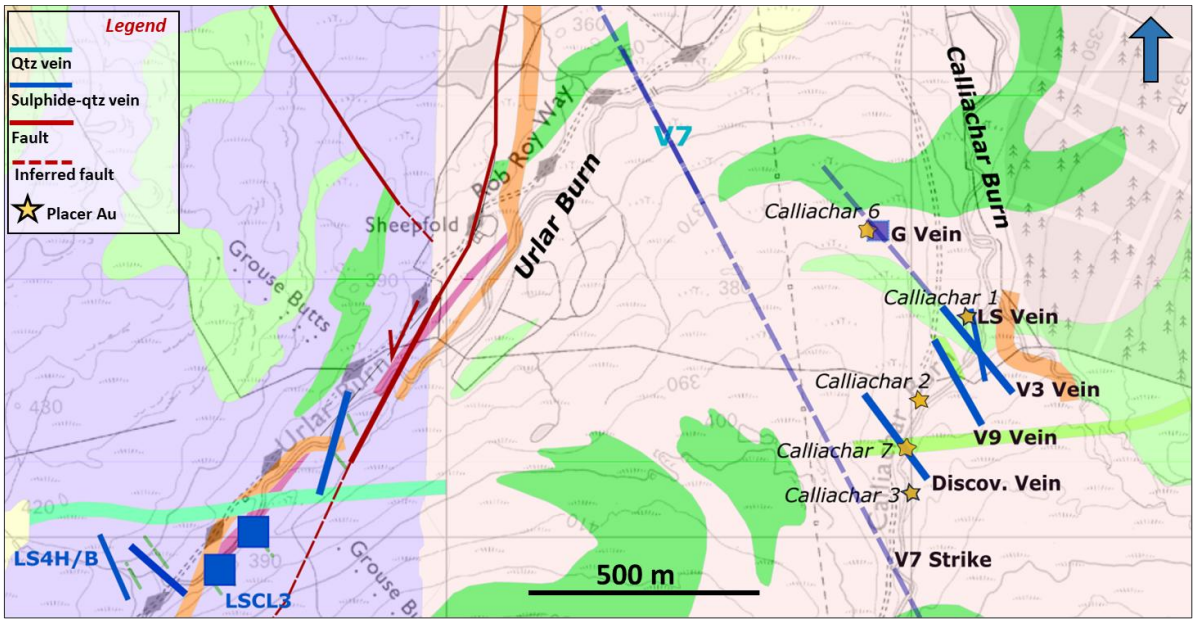

Figure 4.4 Geological map highlighting the vein outcrops which are most important for this study. These were personally investigated over the two field campaigns of 2019 and 2021 (modified after the BGS geological map from https://digimap.edina.ac.uk/).

The Discovery Vein outcrops at NN 84000 45175, and trends N 149/80 in a ~ 60cm wide zone Figure 4.5a). It is hosted in soft mica-schists which are locally silicified and fractured (Figure 4.5b) and surrounded by limonitic gouge. The vein gangue is formed of white quartz and subordinate carbonate; quartz comes as irregular prismatic aggregates. Additional minor veins (~1 cm thickness) were observed along N 154˚, 169˚and 168˚strikes; open-space quartz textures were observed within these veins (Erris Resources, 2020). A set of joint strikes (N 138˚- 148˚- 150˚, dominant values) was recorded in the vicinity of the vein. Abundant gossan material also features in the uppermost part of the outcrop (Figure 4.5a). Sporadic pyrite mineralisation (mm-scale) was identified locally, but not directly on the vein surface.

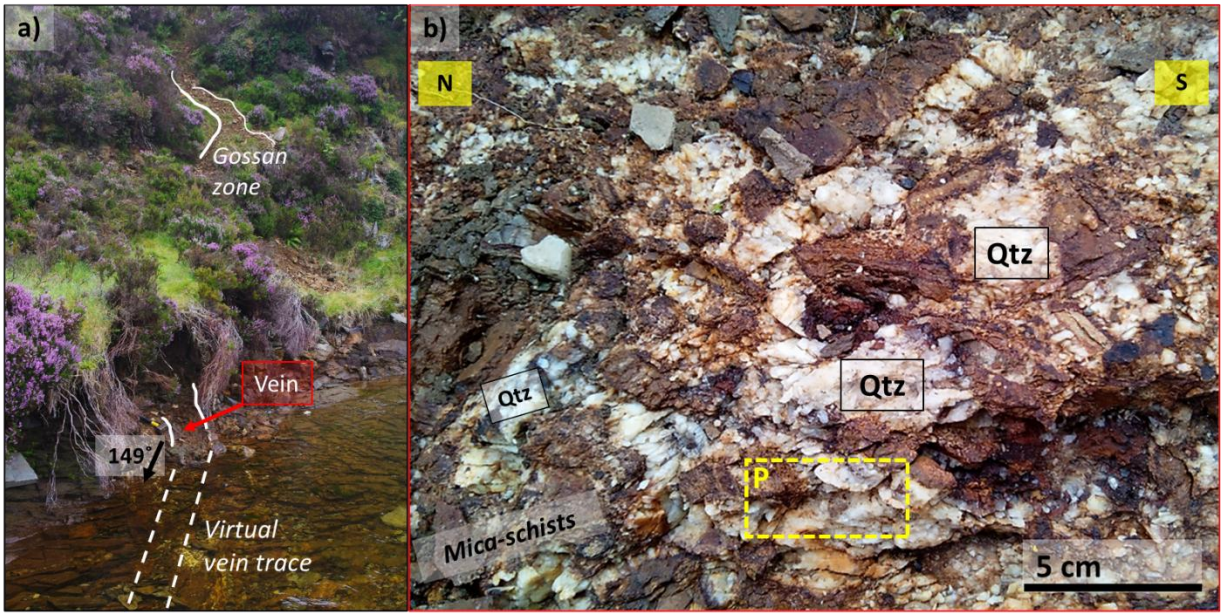

Figure 4.5 'Discovery Vein' field outcrop. a) Contextualization across the stream; b) Detail on the actual vein surface.

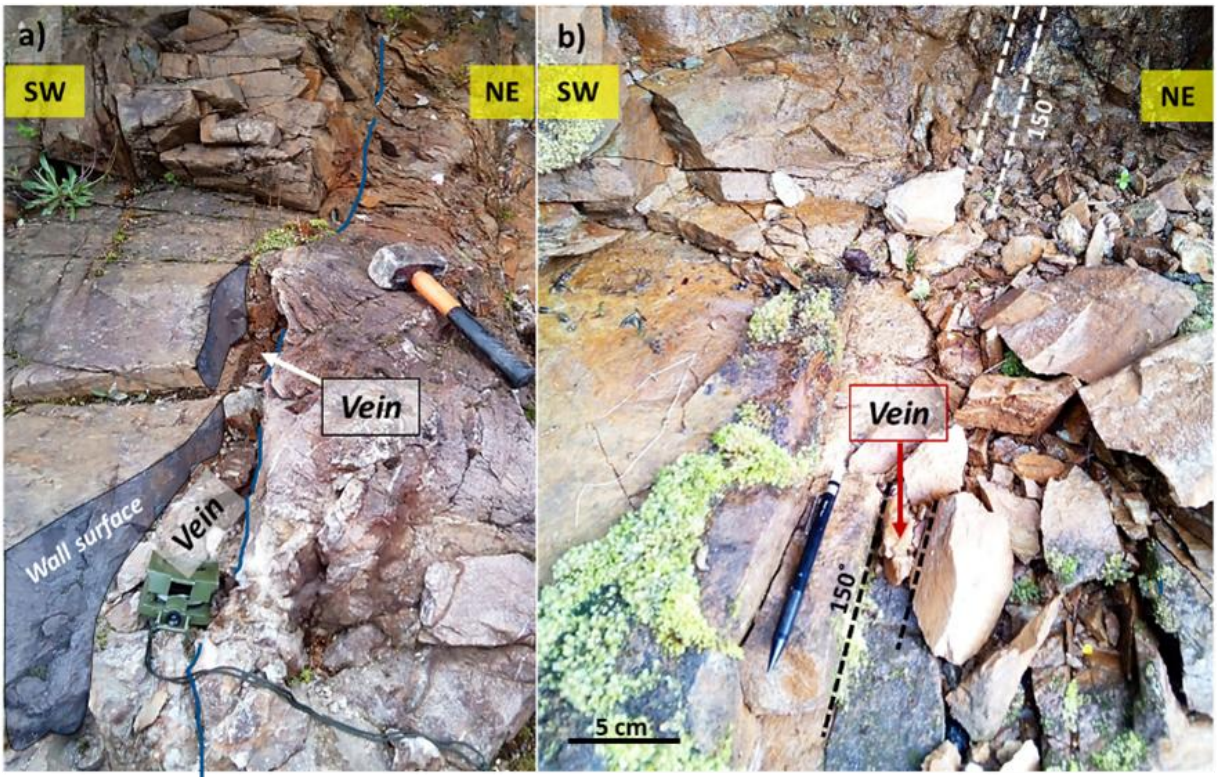

Figure 4.6 V9 Vein outcrop. a) Main vein; b) parallel ~3cm thick vein.

<u>The V9 Vein</u> outcrops at NN 84108 45353 in an area showing intense weathering (fig. 4.6a). The main vein strikes 150˚and dips 84˚to the SW (Figure 4.2); same strike value is recorded on a

narrower (~3 cm thick) vein nearby (fig. 4.6b). Upon centimetre-scale observation, the vein shows brecciation of an open-space quartz texture with dominant blocky crystals (Figure 4.7b). No sulphide mineralisation was observed at outcrop.

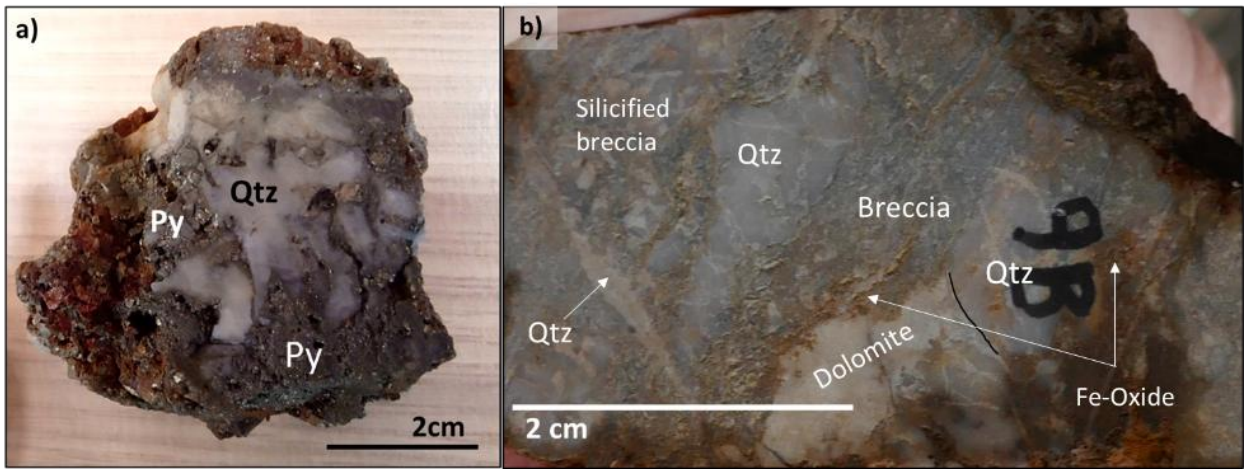

Figure 4.7 G Vein (a) and V9 Vein (b) hand specimens.

Figure 4.7 shows two different specimens that were extracted (at outcrop) from gossan material at the G Vein (fig. 4.7a) and from the V9 Vein (fig. 4.7b). The **G Vein** is very poorly exposed at outcrop; the relevant textural features at the macro-scale can be appreciated by optical inspection of the available hand specimen (Figure 4.7a). Coarse pyrite mineralisation appears enclosed in between quartz crystals showing a homogeneous white colouration and additionally fills later micro-cracks.

V3 Vein. The vein is located ~150 metres downstream from the V9 outcrop (Figure 4.9d). A strike orientation of 30˚ was measured on a locally exposed portion, dipping ~40˚to SE (Figure 4.8a; this also displays a sigmoidal shape, possibly indicating an opening direction to the left); however, the overall strike and dip direction have appeared to be 140/86S (as indicated on the map in Figure 4.2). Vuggy, rust-stained quartz represents the gangue mineral; abundant coarse galena and minor chalcopyrite have been identified as sulphide species in hand specimen (Figures 4.8b and c). The hosting bedrock lithology (shists) shows intense clay alteration, with gossan mineralisation laying on top of the vein surface (Figure 4.9c); measurements of local foliation planes range from 146˚to 165˚ for the dip direction, and record a stable 28-29˚of dip.

LS Vein. This represents the northernmost (and consequently the most downstream) vein being treated in this section. It is very steep (70˚- 80˚) and strikes ~340˚across altered shists (Figure 4.9b), measuring 70˚ of dip direction. Following from the outcrop analysis, glassy quartz made of elongate-blocky crystals is the main mineral forming this vein, shallowly pervaded by iron-

oxide alteration (Figure 4.9a) and rust staining. Small pyrite crystals (< 1mm size) were locally observed. Minor veinlets of vuggy quartz with a generally sigmoidal shape were observed nearby (Figure 4.9e, f), on surfaces that are cut by 160˚striking joints.

Figure 4.8. a) V3 Vein outcrop, where a possible sigmoidal geometry is also visible. b), c), d) Main textural and mineralogical features of the V3 Vein, highlighting the abundance of galena mineralisation.

Urlar Veins. Field observations focused on the few locations in the Urlar Burn section where quartz/sulphide-bearing veins were noted and sampled (Figure 4.4). An in-situ vein has been recorded (LS4 Vein), striking 310˚ and dipping 50˚to the NE (Figure 4.2). Two rock samples were retrieved from/close to the vein (namely LSAH and LS4B), whereas a float sample was retrieved from a restricted spoil heap nearby (LSCL3). Quartz is dominant in all of these, appearing glassy to milky and showing a blocky texture (Figure 4.10); traces of rust staining are also frequently noted, especially in the proximity of vugs. Coarse galena (mostly) and chalcopyrite are the main sulphides observed in LS4B (especially, Figure 4.10b) and LS4H; sporadic pyrite and malachite mineralisation have additionally been identified in LSCL3 (Figure 4.10a).

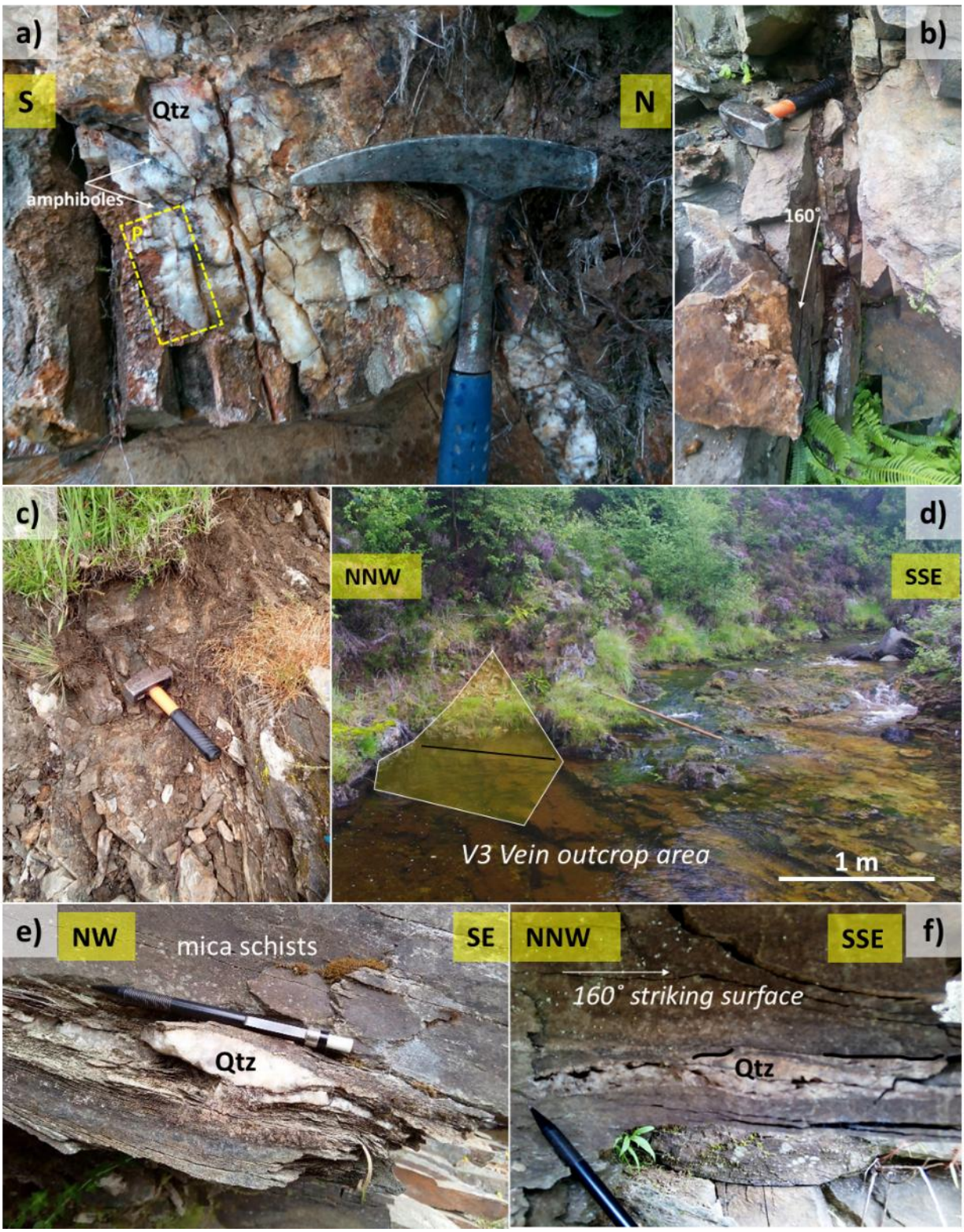

Figure 4.9 General and in-detail features around the V3 and LS veins. a) and b) LS Vein; c) and d) V3 Vein; e) and f) LS vein structural markers.

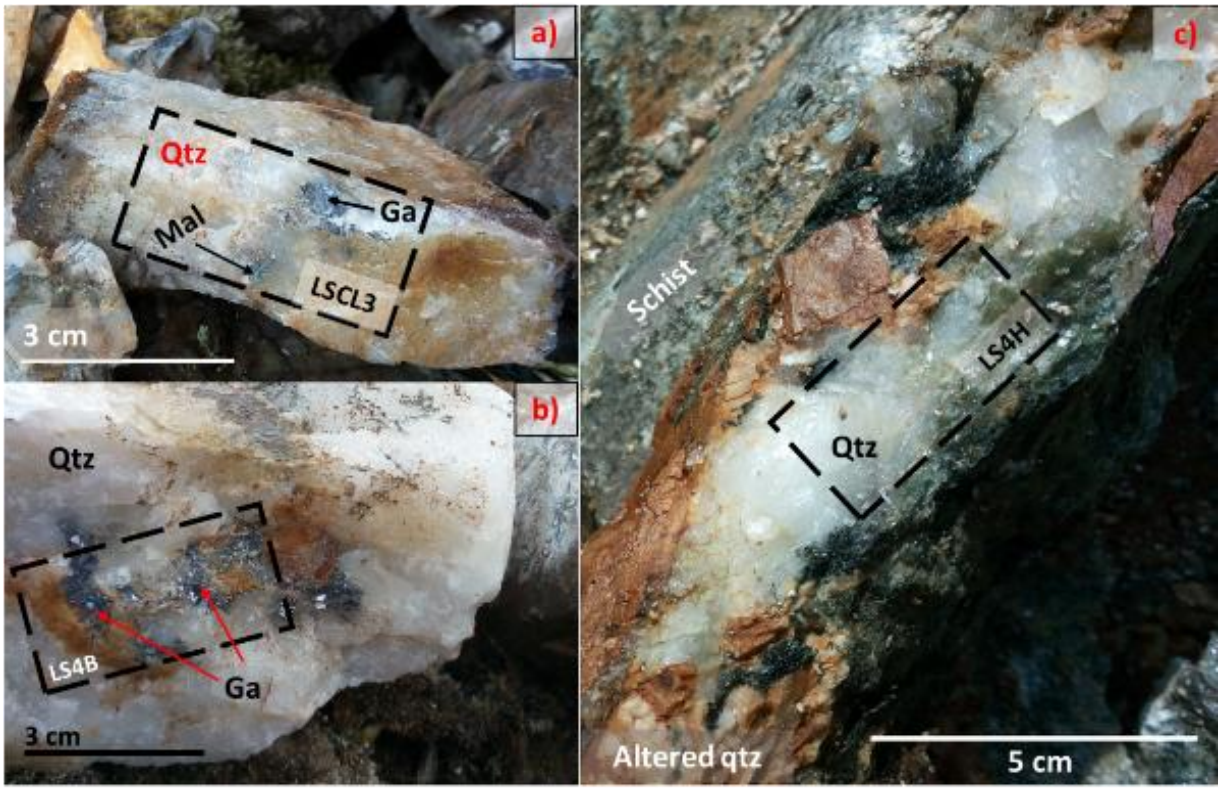

Figure 4.10 Float (a) and b)) and in situ (c)) quartz-bearing specimens from Urlar Burn that have also been used for SEM-CL investigations.

4.2.2 River Almond

Field investigations at this locality have recorded the dominance of mica schists as lithology, generally showing brown-reddish colouration and abundant iron-oxide alteration. The mica schists host several quartz-bearing veins and veinlets (typically a few millimetres wide) and are sporadically cut by dolerite dikes. Pelites are subordinate and have been sometimes found hosting quartz as blebs.

4.2.2.1 Structures and veins

In spite of the thick overburden present in the area (Figure 4.11), several faults have been inferred by coupling lithological with morphological data sources; additional effective measurements were made available by Erris Resources following their on-site investigations. The orientations of these faults are comprehensively reported on the map in Figure 4.12; no preferential trend could be deducted. The map additionally displays an array of (hydrothermal) veins, striking 105° to 170°, which were recorded across the Upper Almond catchment (W side) both by Erris Resources and during one of this PhD's project field campaigns. Data from these different sources (studies) have overall appeared to be mutually consistent.

The local, major hydrothermal vein ("Glen Almond Vein" e.g., Webb et al. 2024, Figures 4.12 and 4.13a) strikes 124°and dips ~75°to the SW. Extremely tiny (a few mm wide) sub-vertical veins occur in its proximity and strike from 114°to 140°. The schistosity of the host rock shallowly dips (~24°) to 124°(dip direction). The Glen Almond Vein can be traced for over 10 metres along the strike and reaches a thickness of 20 cm (Webb et. al, 2024). Slickenlines have been identified on a surface striking 124°(at NN 72981 32822) and suggest a dextral sense of motion.

Figure 4.11 Panoramic photograph of the Glen Almond catchment, taken during fieldwork activity.

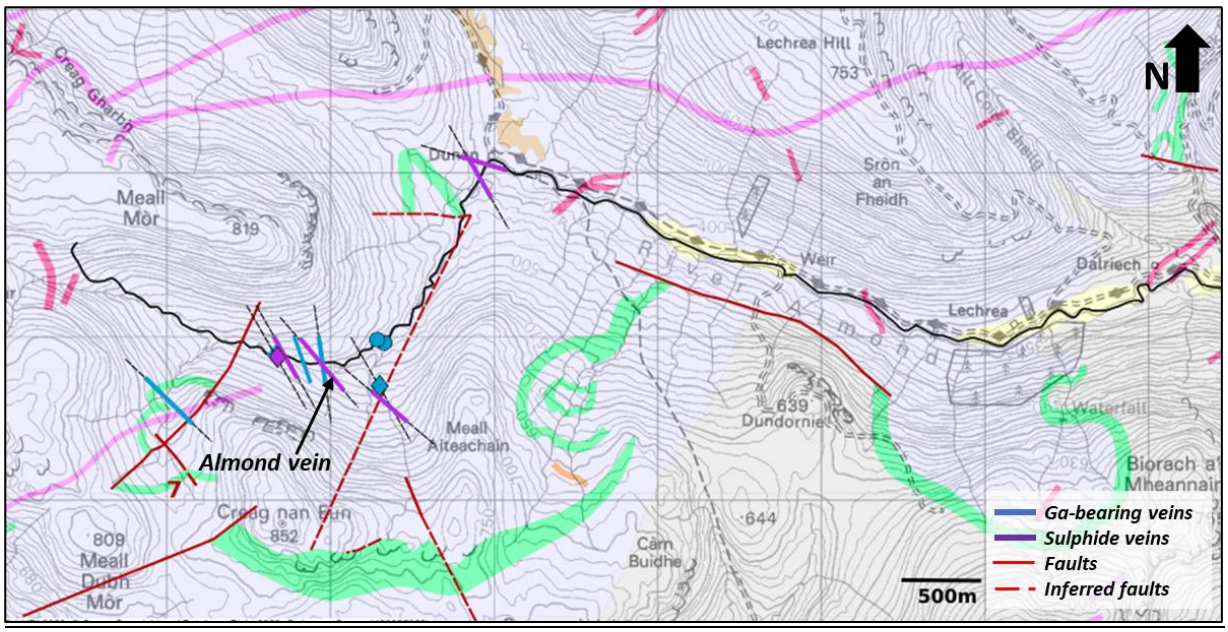

Figure 4.12 Map displaying (deducted) fault and vein occurrences across River Almond (modified after the BGS geological map from https://digimap.edina.ac.uk/).

Sulphides have been observed and reported (i.e., Erris Resources, 2020) within the vein array to variable extents - these include galena, chalcopyrite, sphalerite, and pyrite (Figure 4.13b and c), which also separately occurs as disseminated bits in wall rock. Limonite is frequently observed in quartz, as well as sericite alteration. Quartz textures generally appear glassy and vuggy, possibly indicating mechanical sulphide removal; the crystals tend to grow perpendicularly to

the vein strikes (Figure 4.13a). Veining occasionally develops into 'stockwork' patterns. Across the riverbed, the Almond Vein comprises altered (sericite) quartz with dark sphalerite, chalcopyrite, and subordinate galena. These sulphides have repeatedly been found associated with iron-oxides, which also abundantly infill separate stringers of the same vein (Figures 4.13a and b).

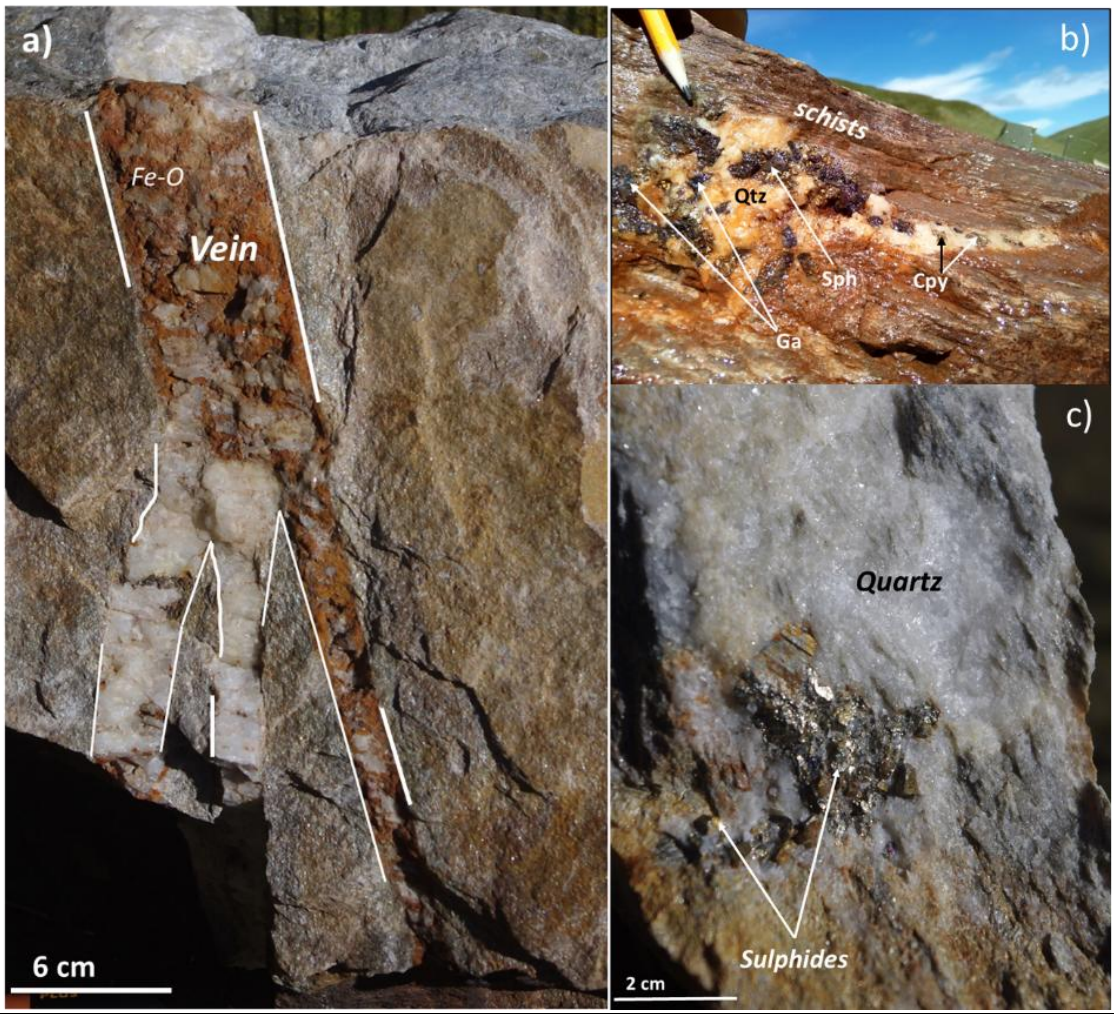

Figure 4.13. a) The Glen Almond Vein in its host-rock; b) in-situ mineral evidence on one the Almond vein(s) surfaces; c) Detail on quartz texture and sulphide mineralisation in the Glen Almond Vein. Photographs in a) and c) were taken by Rob Chapman.

4.2.3 Lead Trial

Outcrops have been found across an area of >1.5 km extension (Figure 4.14), mostly consisting of stockworks of mineralised veins and quartz breccias in rhyolite. Trains of ore-bearing boulders increase the zone length of >3 km, following a general N-S trend (Erris Resources, 2020) and consistently with the orientation of the main morphological lineaments. Schists and rhyolites represent the dominant lithological bodies, with faults and veins sometimes marking the boundaries between each other as well as localised silicification (e.g., Figures 4.15b and c); both schists and rhyolites are generally gentle-dipping. Rhyolite breccias have appeared to be more densely distributed at higher elevations. The schists are in general poorly altered and show scarcer vein occurrence; stockworks of quartz veins and breccias (Figure 4.17) mostly pervade the rhyolites, where sericitic alteration can consistently be observed in the wall rock.

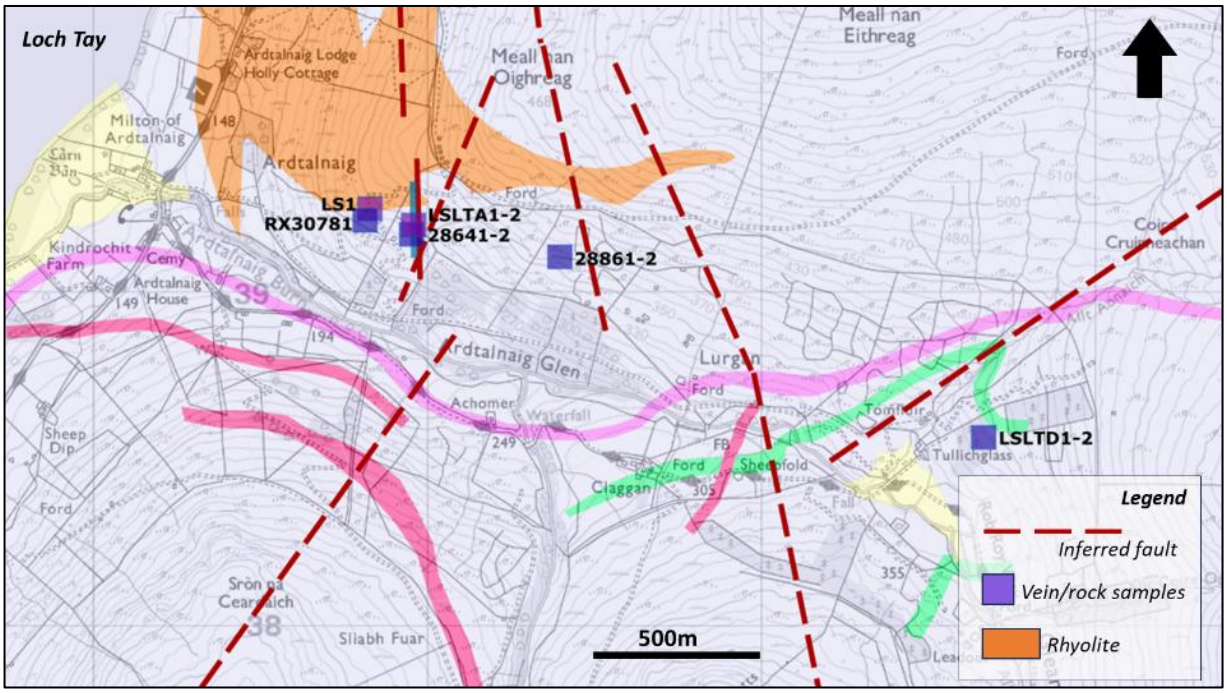

Figure 4.14 Geological map of the Lead Trial area, inclusive of sample locations (modified after the BGS geological map from https://digimap.edina.ac.uk/).

4.2.3.1 Structures

Hydrothermal veining has been observed across several boulders, with some veins up to 1 m wide – these are typically the sulphide-rich (galena±sphalerite) ones. The major veins are hosted in faults, and slickenlines are often visible on marginal sides of boulder surfaces. A gold-bearing quartz vein (LSLTA, Figure 4.14), exhibiting the local, characteristic sulphide mineral assemblage, was identified at the main Lead Trial location (first by Erris Resources, 2019) and is shown in

Figure 4.15a. The vein is roughly W-dipping at 70°; measurement of an adjacent, subvertical fault has consistently recorded 270°dip direction. A few other narrower veinlets (Figure 4.16b) have been identified in nearby rhyolites and generally strike NS.

At higher elevations and towards NE, further measurements were collected on schists (Figure 4.16a), scarcely exposed at NN 70908 39284, and on rhyolites (NN 70819 39331). The stretching lineation, visible on some of the schists surface, strikes from 56°to 64°; rhyolite breccia-packs strike ~62°, and minor quartz veinlets that show syntaxial crystal growth crosscut them (Figure 4.16c).

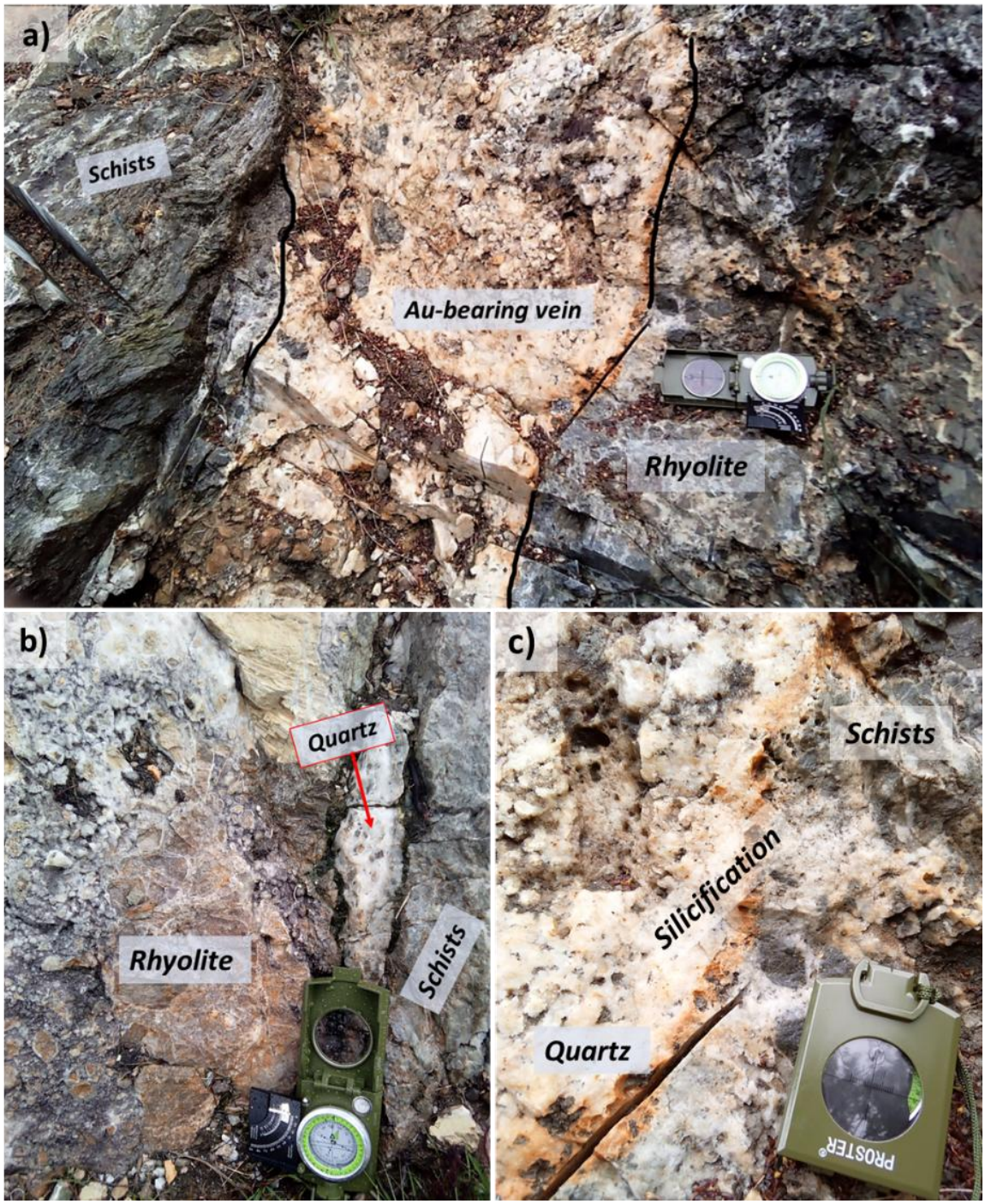

Figure 4.15 Lead Trial outcrops at the main site. a) and b) In situ gold-bearing main veining; physical relationships between the main local lithologies (rhyolite and schists); c) detail on silification evidence at the contact between quartz and schist.

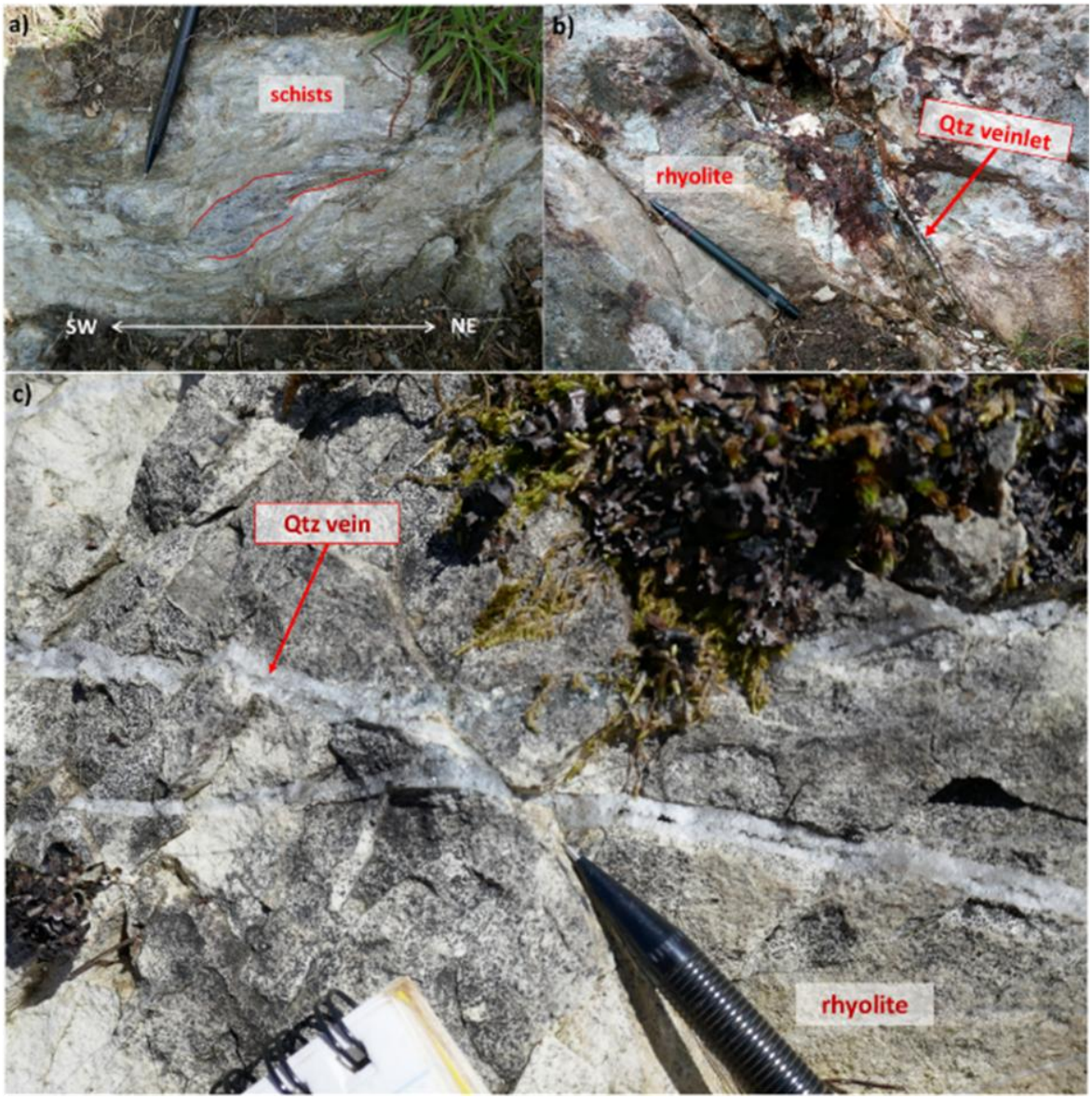

Figure 4.16 Additional outcrop features at the Lead Trial. a) in situ schist reporting evidence of schistosity planes; b) quartz veinlet in rhyolites; c) minor vein in rhyolite, for which internal (syntaxial) crystal growth has been observed.

4.2.3.2. Vein textures and mineralisation

The vein textures and their modes of occurrence in the respective host-rock have appeared complex and extremely variable at outcrop, ranging from mm-scale veinlets to up to metre-wide stockworks and veins; these include from quartz breccia to almost massive textures (Figure 4.17). Quartz systematically forms the main gangue mineral, showing from white to translucent coloration and generally open-space textures. These consist of quartz breccia (Figure 4.17b), microcrystalline-sugary, comb, cockade and plumose crystals, all frequently disconnected by vugs (Figures 4.17c, d). Additionally, polymictic breccias of mica schist and/or rhyolite clasts (Figure 4.17a) can often be found in association with the veins. Surface weathering has

systematically been observed, mostly indicated by orange stains and vugs on/in quartz (Figure 4.17d). The main sulphides observed at outcrop are coarse sphalerite, ranging in coloration from pale yellow/green to brownish, and generally coarse, silverish galena (Figures 4.17c, d), sometimes accompanied by subordinate pyrite and (rarely observed) chalcopyrite. Calcium-rich veins (Figure 4.17a) of pinkish coloration sometimes crosscut quartz and fill up open vugs. These occur in silicified zones that show traces of (possibly chloritic) alteration. Hydrothermal quartz breccia (Erris Resources, 2020) is commonly observed at the contact with silicified schists and rhyolites (Figure 4.17b), with minor calcite and barite that sporadically fill up the spaces in/between breccia clasts. Relatively abundant bladed barite can additionally be observed on some of the boulder surfaces, and often in association with the polymictic breccia (Figure 4.17b).

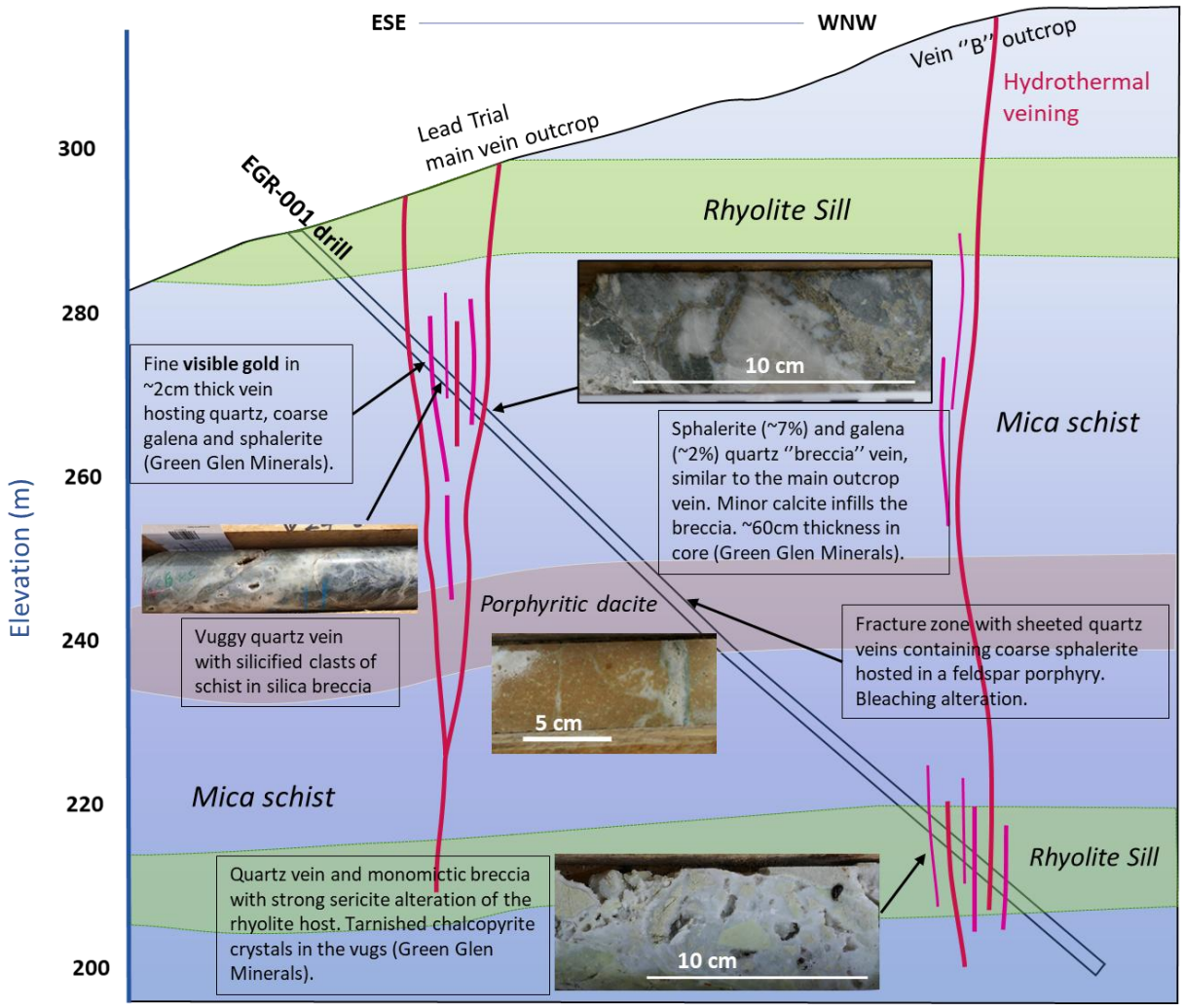

Figure. 4.17a. Sketch section across the Lead Trial main vein outcrop, inclusive of the EGR-001 drill projection. Built upon sketches and data provided by Erris Gold Resources (Lavelle, 2020b).

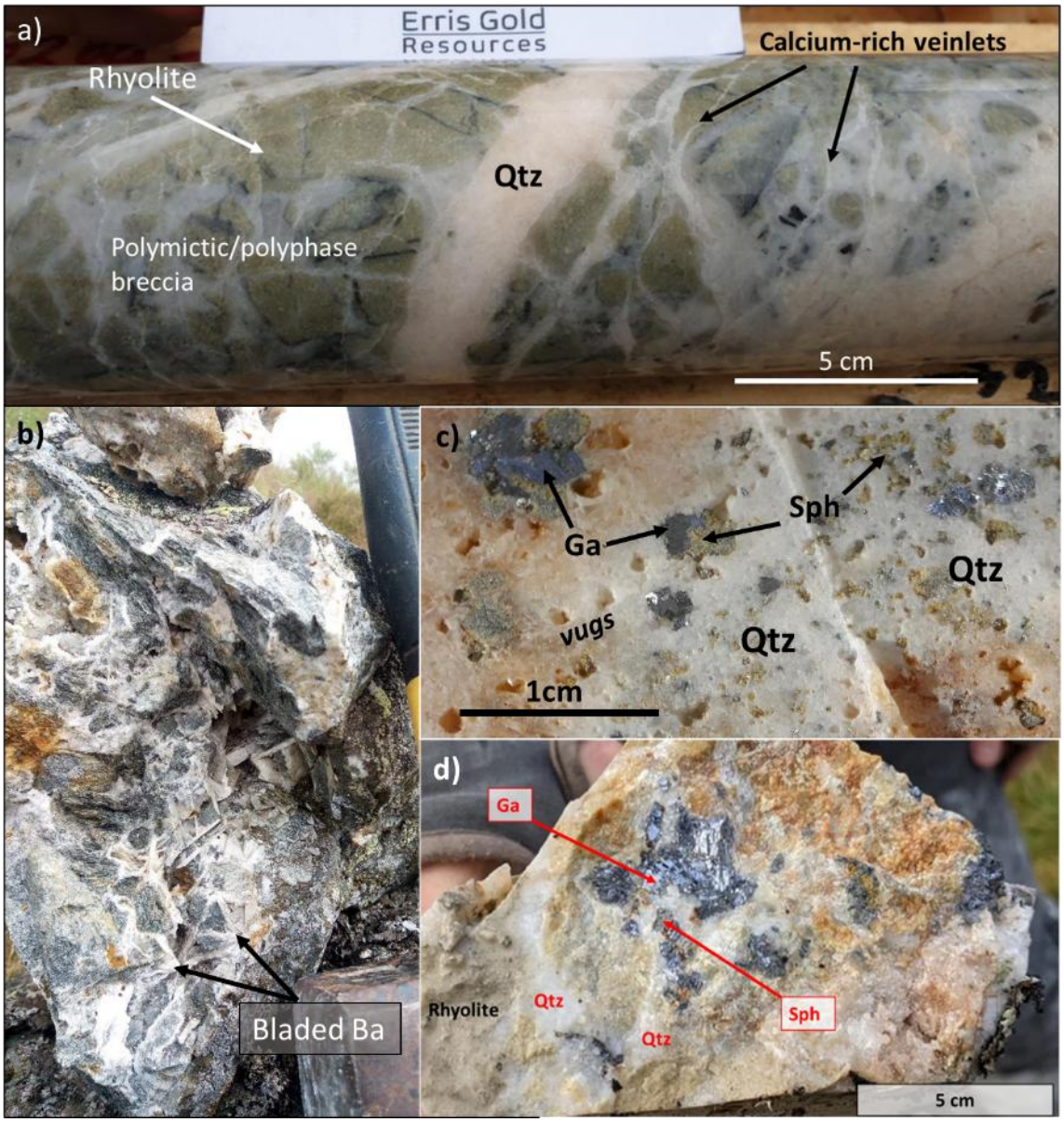

Figure 4.17b Lead Trial main textures. a) Polymictic/polyphase breccia (photo source: Erris Gold Resources, 2021); b) Hydrothermal breccia with bladed barite (Ba); c) microcrystalline, white quartz and sulphides; d) weathered quartz with sulphides and rhyolite.

.

4.2.4 Coire Buidhe

The Coire Buidhe mine sites are located approximately 5 km south of the Lead Trial sites (Figure 4.18). Mineralisation is hosted in a series of north and east quartz–carbonate veins, which cut nearly horizontal meta-limestones and calc-schists (hornblende schists and the quartz-rich 'Pitlochry' mica schists); the veins outcrop in a subcircular pattern on top of Meall nan Oighreag. Further to this location, sampling activities also took place about ~1.5 km WNW of the historic mine sites (e.g., Pattrik 1984; Figure 4.18), where Erris Gold Resources identified a spoil heap of white quartz-bearing veins in 2021.

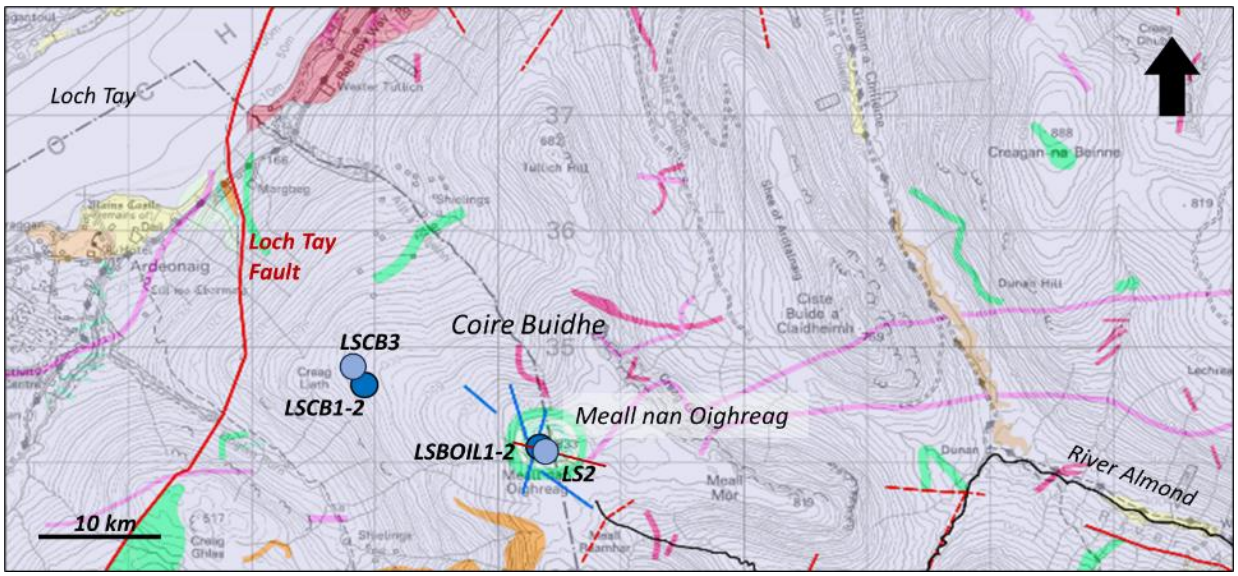

Figure 4.18 Geological map highlighting the Corrie Buidhe site locations (modified after the BGS geological map from https://digimap.edina.ac.uk/).

4.2.4.1 Structure and textures at outcrop

Limited in-situ evidence of the mineralisation has been observed, mostly in the form of prismatic/glassy quartz veins (NN 700 347; Figure 4.19a and b). Most of the material has been found accumulated in the mine dumps, where local identification of some characteristic mineral assemblages has taken place.

Table 4.1. Vein and faults measured across the Coire Buidhe outcrops.

Meas. Type/no	Strike	Dip direction	Dip	Grid Reference
1) Vein	180	270		NN 7059 3397
2) Vein	130	50	50	NN 7059 3397
3) Vein	70	340		NN 7059 3397
4) Fault	20			NN 7059 3397
5) Fault	100	10	45	NN 7059 3397
6) Vein	170	80	75	NN 6999 3472
7) Vein	150	60	60	NN 6999 3472

Structural measurements of veins and faults were collected at three different sites, distributed less than 200 metres away from each other and along the E-W direction (Figure 4.18; Table 4.1). The veins range in width from less than 5cm to more than 20 cm. The quartz textures identified macroscopically, at the main Coire Buidhe dump (NN 70452 34031), vary from coarsely

crystalline to microcrystalline, showing an overall 'sugary' appearance (LSBOIL sample, Figures 4.19c and b) and coloration ranging from translucent to white. The shape of crystals is generally blocky, with a smaller percentage of elongated ones. Galena occurs as blue, metallic, coarse crystals (Figures 4.19c, b) which extensively fill up vugs in and between quartz and (where present) calcium carbonate; malachite has also been sporadically observed.

Figure 4.19 a) In-situ quartz and galena vein exposure at the Coire Buidhe mine sites; b) Zoomed in detail of 4.19a; c) and d) Quartz textures at one of the Coire Buidhe sites (NN 70452 34031); areas selected for petrographic thin sections are also indicated.

Only loose specimens could be observed at the 'second' Coire Buidhe mine dump (LSCB-LScb, Figure 4.18). Their textural and mineralogical characteristics have appeared substantially different from the ones noted for the former site. Quartz still represents the volumetrically dominant mineral, overall showing a more massive and compact texture as well as consistently white colouration (Figure 4.20a). The sulphide species identified at outcrop mostly entail disseminated pyrite, pyrrhotite and chalcopyrite (Figures 4.20a and b), accompanied by very sporadic arsenopyrite (Figure 4.20b). Orange stains (due to Fe-oxidation) and weathered textures are also recurrent.

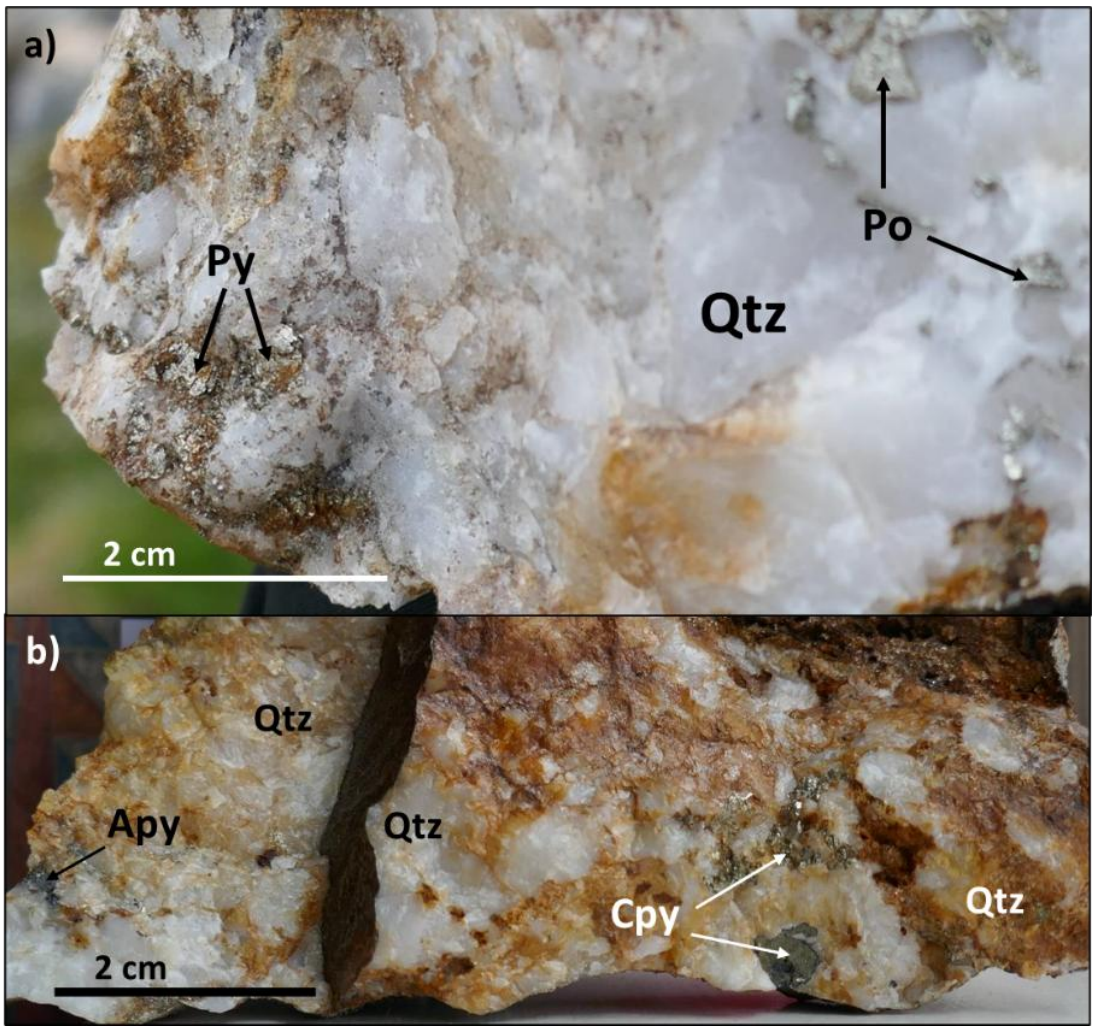

Figure 4.20 Photographs of rock specimens from the WNW Coire Buidhe mine site, indicating the typical mineral associations. a) LSCB; b) LScb.

4.2.5 Loch Tay area South

This area covers approximately 15 Km² south of the Almond River. Igneous bodies outcrop at Invergeldie and Glen Lednock, specifically the Early Devonian granitic suite, and near Keltie Burn (Devonian andesite/basalts). Due to the nature of the landscape, collection of structural data in this region has been somewhat challenging – however, a few faults have been deducted by interpolating local lithologies and topography, in addition to the ones reported on historical maps (Figure 4.21). The area was targeted mostly for the purpose of gold sampling campaigns, due to some reported gold occurrences; sampling locations entail Keltie Burn, Glen Lednock, Invergeldie and Monzie (Figure 4.21).

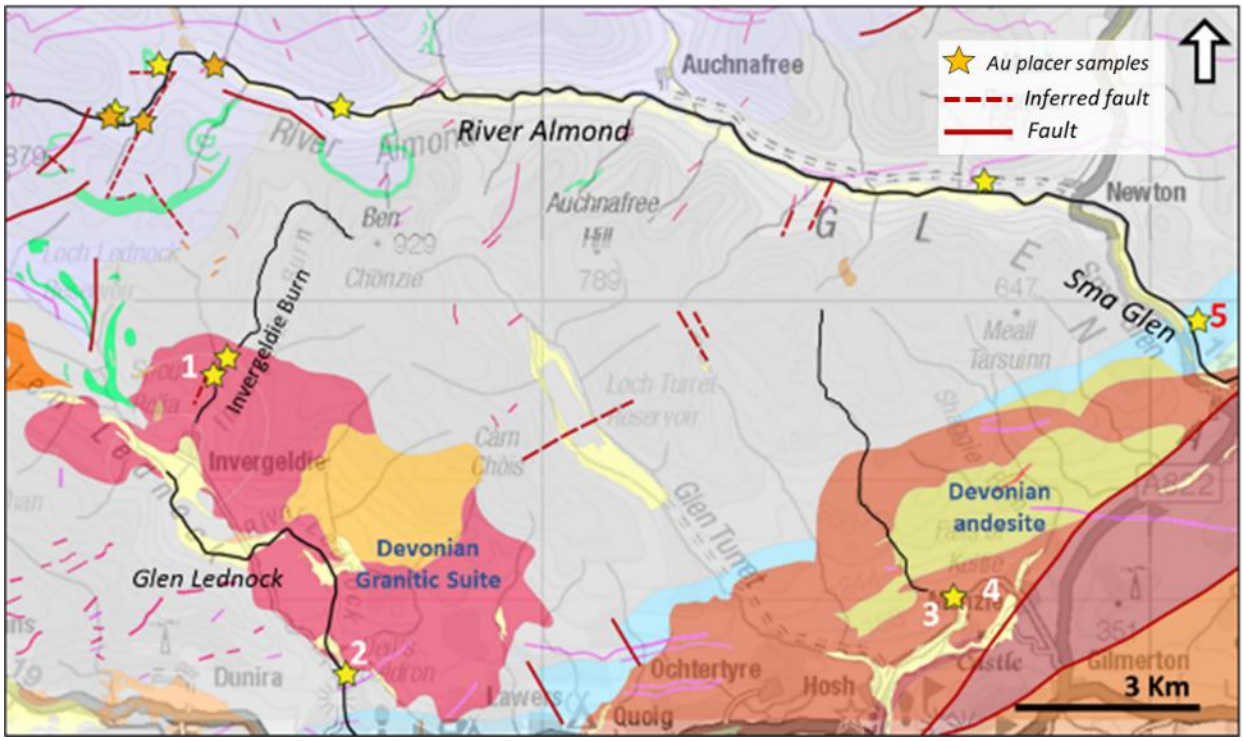

Figure 4.21 Geological map showing the distribution of the placer gold samples from the Southern Loch Tay area (modified after the BGS geological map from https://digimap.edina.ac.uk/.

4.3 Interpretation of the structural data

4.3.1 Possible localisation of the veins in dilational or Riedel shear zones

The orientations of the main sulphide-bearing quartz veins in the Calliachar-Urlar area have systematically been recorded around the strike value of 330°. This NW-SE trend is overall maintained by the barren quartz veins and the vertical joints that extensively crosscut the area, although displaying some slight variability (Figures 4.2 and 4.3 in section 4.2.1.1) Major and minor fault planes around Loch Tay (e.g., relating to the Loch Tay Fault, Urlar Fault and some local-scale faults recorded towards NE) consistently developed along a NE-SW strike and typically display a sinistral component of shear. First-order faults or shear zones are generally regarded as the primary channels for regional fluid flow, enabling a subsequent localisation of the ore-fluid fluxes in lower-order faults, shear zones and/or folds (e.g., Groves et al., 2020). For this reason, the NW-SE pattern of vein arrays at Calliachar and Urlar Burn might suggest their occurrence either in localised dilational jogs or as Riedel-shears planes (e.g., Tanner, 2014), or both.

4.3.1.1 Occurrence in dilational jogs

Groves et al. (2000, 2018) exemplify real geological cases to support a model where mineralisation occurs along fault arrays that are oblique to the belt-parallel structural trends. These features tend to localise around flexures or jogs on the first-order faults; moreover, the 'accommodation' fault arrays are often oriented at ~70˚to the local first-order structure strike or trend (Groves et al., 2018). In the Loch Tay area, zones of increased porosity, favourable to the development of faults, fractures and shears zones to different degrees, can especially be located across the Calliachar Burn catchment. Several hydrothermal veins were identified downstream (towards N) and a number of local, minor faults were measured mid-upstream (> 1Km towards S), together with less frequent veining (Figure 4.2, section 4.2.1.1). Joint arrays are distributed throughout the catchment, with the joints being more or less spaced between themselves depending on the variability in the rheological response of the lithology. There does not appear to be a direct correlation between the density of the joint distribution and sulphide-bearing vein distribution, although both joints and veins share consistent NW-SE orientations. Importantly, some of the vein and fault strikes form angles of 60˚-70˚with the Urlar Fault, if prolonged towards NW. The location and orientations of these hypothetic dilation zones would coincide with those of tensile failure zones along strike-slip faults (Zhang et al. 2008). Bringing these observations ~10 Km towards the SW of the area, similar spatial relationships could be interpreted to take place between the regional-scale Loch Tay fault and other gold-bearing veins located further south (i.e., the Almond Vein and some of the Coire Buidhe Veins; Figure 4.1). However, more investigation is required to validate these hypotheses, in light of the relationships between the hydrothermal fluids responsible for the veining and their associated structural and lithological framework. In general, the dynamic of concentration of supra-lithostatic ore fluid into dilatant zones takes place over the later evolutionary stages of an orogeny history (Groves et al., 2020) which would be consistent with early Devonian ages (post-Scandian orogeny), generally accepted for gold-bearing mineralisation in the area. Additional structural and quantitative lithological data would ideally clarify local feedback mechanisms between pore (fluid) pressure and lithostatic load (e.g., to model fluid flow; Cox et al., 2001, Sibson., 2001), but excessive vegetation and overburden that characterise the field localities make the procedure of data-recovery challenging.

4.3.1.2 Occurrence as Riedel shears

It is now widely accepted that whilst major shear zones can be exploited by fluids to reach the upper crust, the deposition of minerals largely takes place in networks of second-order Riedel fractures that accompany them (e.g., Mueller et al., 1988; Vearncombe, 1998; Neumayr, Hagemann & Couture, 2000, Tanner, 2014). In the Loch Tay area – and especially its

northernmost region - the observed general configuration and localised patterns of major and minor faults would allow their contextualisation in a multi-scale transcurrent system with associated subsidiary structures (i.e., Riedel Shear planes, Figure 4.22 c, d). Tanner (2014) exported a similar concept to the entire metallogenic framework of the Grampian Terrane, incorporating evidence from the Tyndrum/Cononish, Curraghinalt, Cavanacaw and Loch Tay mineralisation. In the latter case, they inferred that faults and fractures at Calliachar/Urlar Burn form a conjugate pair of Riedel Shears with the Loch Tay Fault and that local mineralisation accumulates in a secondary stress field produced by the Loch Tay Fault left-lateral movement (giving σ1 = 351°). Taking this theory a step further - and assuming the maximum principal stress tensor (σ1) to be roughly N-NNW oriented - the principal shear plane could also be represented by the Urlar Fault and the Riedel shear fractures by the several discontinuities that host the mineralised veins along some of their 330˚strikes. This model would be perfectly consistent with the 'Sibson-Coulomb' model (Tanner, 2014) which also accounts for the effect of pore fluid. Such model advances that a pair of Riedel fractures (synthetic and antithetic) initially form at an angle of 27–30° to either side of σ1 (that is to say at ~330˚ for a NS-oriented σ1). Additional supporting evidence to the Calliachar-Urlar system would be provided by centimetre-scale strain markers observed in the field, involving local veinlets (Figure 4.22 a, b); these critically suggest a dextral sense of motion, in line with the presumed shear sense of antithetic Riedel planes in sinistral transcurrent faults, as illustrated by the 'Sibson-Coulomb' model. According to some examples from literature (e.g., Katz, Weinberger & Aydin, 2004; Davis et al., 1999; Tanner, 2014), the mineralized quartz veins that occupy these Riedel shears frequently appear unusually long compared to their width. A similar style can be noted for the Calliachar Burn Veins.

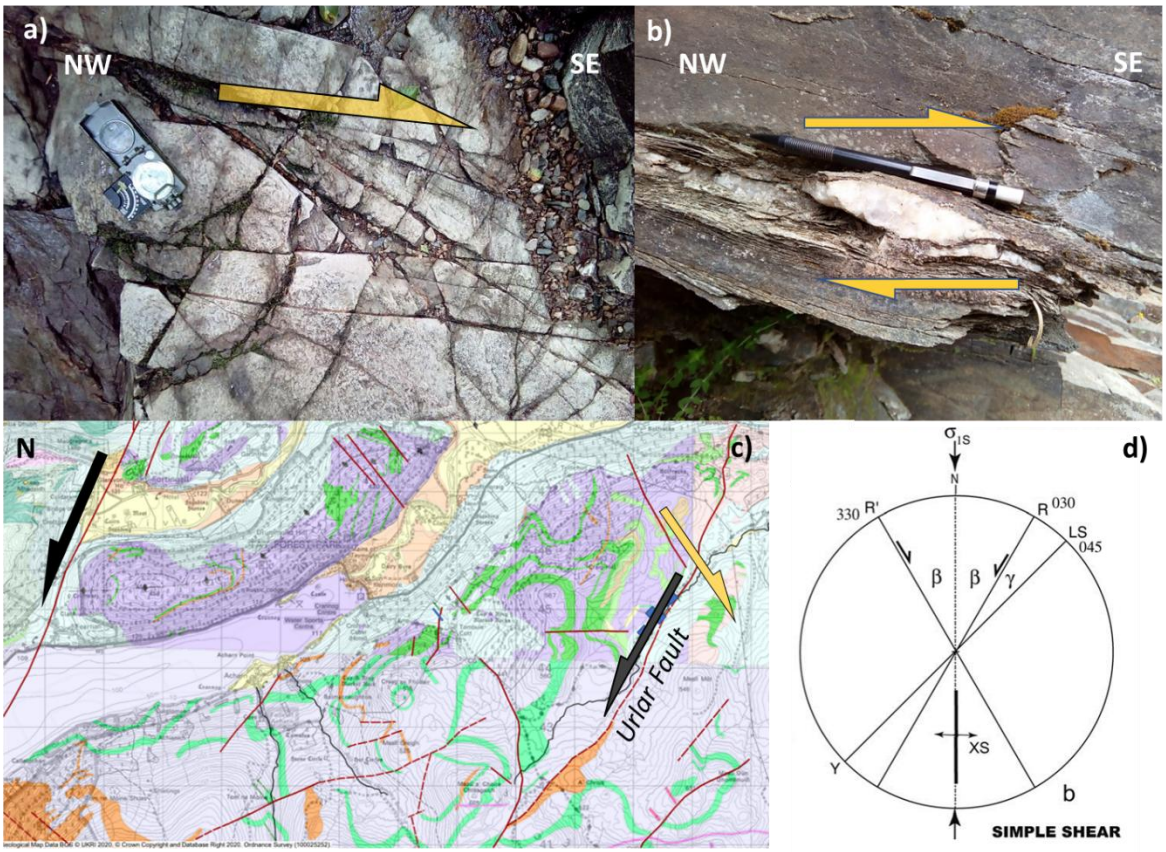

Figure 4.22 a), b). Structural markers in Calliachar Burn (a) horse-tail structures; b) qtz vein passive marker. c), d). Riedel-shear model accounting for both the Urlar and the Loch Tay Fault. The yellow arrows represent the dextral sense of motion of both the structural markers and the Riedel Shear planes.

Chapter 5.

Paragenesis of the hydrothermal veins near Loch Tay

5.1 Introduction

This Chapter is formed of three main sections. The first two focus on the paragenetic analysis of hydrothermal veins sampled at specific localities in the Loch Tay area (Calliachar-Urlar Burn, Glen Almond, Lead Trial and Coire Buidhe). Specifically, section 5.2 provides detailed descriptions of mineralogical and textural components of the vein samples via SEM-CL observations and EDS elemental analysis, while the following one (5.3) deals with sequential interpretations of the vein paragenetic histories, accounting for possible intrinsic factors which influenced their evolution. Since the SEM-cathodoluminescence analysis of quartz and sulphide bearing veins is crucial part of this Chapter, it is important to note that the luminescent response produced by the sulphide minerals, described in the following sections, is an artefact resulting from the SEM instrument used during this study. This derives from the blending of the CL with the BSE signal (i.e., the electrons backscattered from the sulphides by the Al-coated BSE detector generate "artificial" CL signals, also displayed by the captured images). Sulphides (and gold) do not normally luminesce since they have metallic lustre; consequently, they could not support the required band range.

The final section (5.4) complements the chapter by presenting and evaluating the Pb dataset available from a few galena-bearing samples in the study area.

5.2 Quartz-bearing veins, BSE and CL characteristics

5.2.1 Calliachar and Urlar Burn

SEM-CL analyses have been conducted on five quartz- and sulphide-bearing (vein) samples from Calliachar Burn. These were extracted from the main veins exposed downstream (Table 5.1; Figure 4.2); the relevant outcrop features have been treated over the previous paragraphs. Optical and compositional characteristics of the veins, obtained in both BSE-EDS and CL modes, are reported in the next sub-paragraphs and refer to 1 or 2 perpendicular thin sections (or occasionally a block) from each rock sample. Label specifications are indicated in Table 5.1, basing on a 'downstream to upstream' sequence of the corresponding hydrothermal veins. Three quartz- and sulphide-bearing vein samples, collected about midstream of the Urlar catchment, were additionally used for SEM-CL analyses, and equally reported in Table 5.1. The LSCL3 and LS4B samples were retrieved as float (loose) ones, while LS4H was directly obtained from the in-situ vein (LS4) also associated with LS4B. Since the latter has provided more complete information, a description of LS4H has not been included in the following paragraphs;

however, the data derived from its investigation has been considered to constrain mineralogy and cross-cutting relationships in LS4B.

Table 5.1. Polished thin sections from the Calliachar and Urlar Burn veins that have been used for SEM-CL characterisation.

Thin section(s) ID	Corresponding vein ID	Grid reference
LSCG	G (''gossan'') Vein	NN 83921 45645
LSCL2	LS Vein	NN 84144 45466
LSCV3	V3 Vein	NN 84153 45413
LSCV9	V9 Vein	NN 84146 45436
LSCDV	Discovery Vein	NN 83999 45177
LSCL3	LS3	NN 82535 44956
LS4H	LS4 Vein	NN 82315 44927
LS4B	LS4 Vein	NN 82315 44927

LSCG. A BSE montage map of the LSCG block is provided in Figure 5.1a; quartz and pyrite are the dominant mineral species. A primary quartz texture, which results in medium grey, euhedrally zoned patterns, has been identified in CL Blue mode (Figures 5.1c, 5.1b) and here named QA_gv. Zonation grows inwards from crystal boundaries – these are not to be confused with sets of cracks belonging to a later stage, often infilling and parting crystal surfaces (fig 5.2e). Darker quartz bands (QB_gv) cut the former zonation, and visually align with the boundaries of the main pyrite crystals (Figures 5.1c, 5.2b and e). A third quartz generation (QC_gv) fractures QA_gv and QB_gv through very bright and fluorescent CL bands; these range in thickness from 10 to 200 microns and inward crystal growth can be recognized in the wider zones (e.g., Figures 5.1c, 5.2b). Adjacent cracks are directly visible on the section surface. This event is in turn crosscut by a minor set of injections, at 45˚orientations to the QC_gv ones (fig. 5.1c).

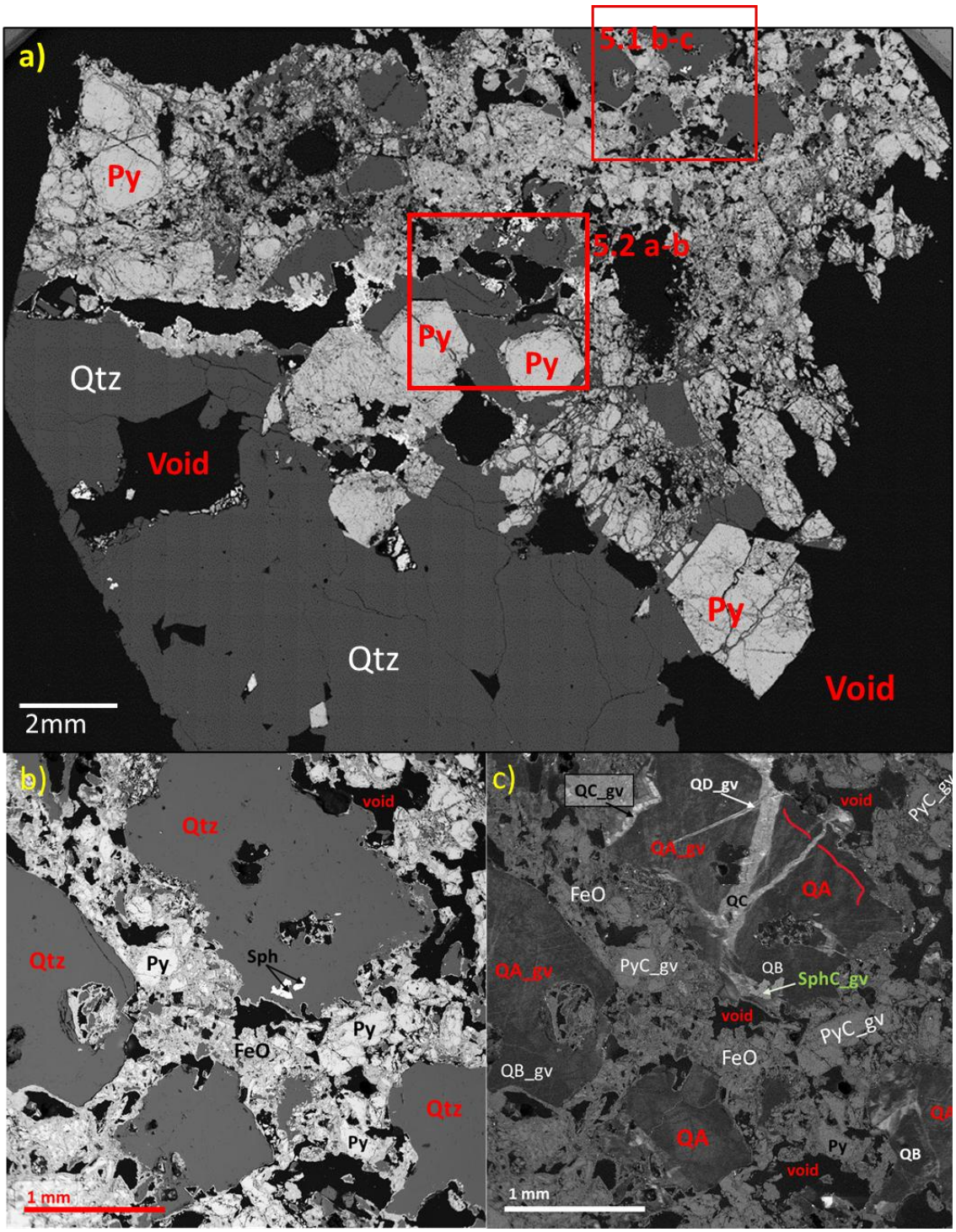

Figure 5.1 SEM-CL images of the LSCG block. a) BSE-mode montage map, where specific sub-areas in Figures 5.1 and 5.2 are also located (5.1b-c and 5.2a); b) and c) BSE and CL Blue modes of the same section area. Quartz (Qtz), pyrite (Py) and sphalerite (Sph) are displayed as mineralogical components. Multiple quartz generations are visible in CL Blue mode (c).

Pyrite is the most abundant sulphide specie in the sample. It has been observed in two main forms: as millimetre-scale euhedral crystals which appear physically incorporated in QA_gv (i.e., PyA_gv, Figure 5.2b and e), where they are sometimes countered by QB_gv; and as cataclastic

agglomerates of smaller crystals (i.e., PyC_gv) that are accompanied by associated Fe-oxidation products (Figure 5.1b and c) and, often, by the QC_gv quartz phase (Figures 5.2e, f and 5.4b). Minor sulphides are arsenopyrite and sphalerite (namely ApyC_gv and SphC_gv), which were found either enclosed in or in contact with QC fractures (e.g., Figures 5.1c, 5.2a-b and 5.4a). Figure 5.4b also indicates the prominent presence of a rhomb-shaped void, suggesting weathered-out dolomite (or ankerite).

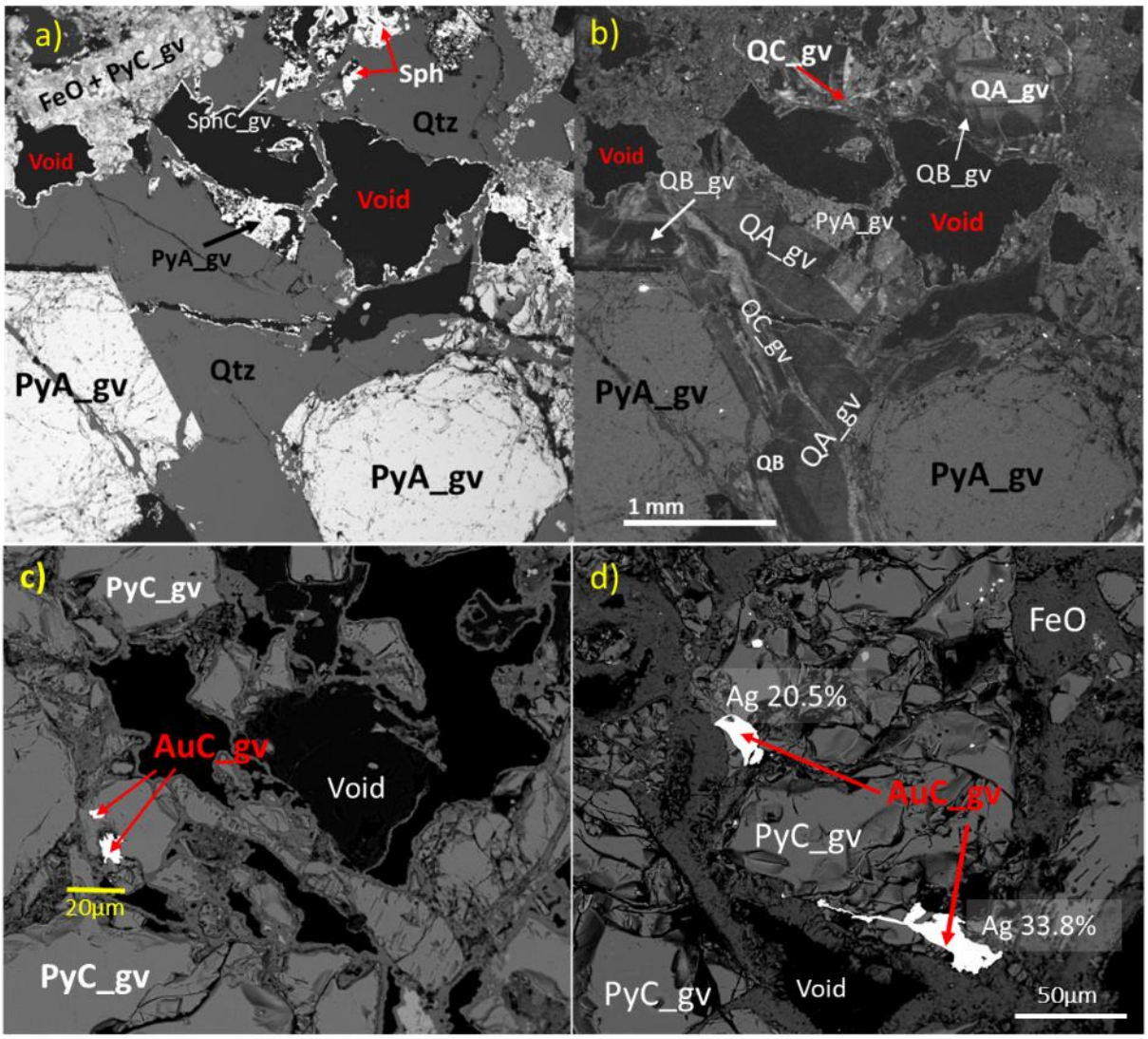

Figure 5.2 SEM-CL images of the LSGC block. a) and b) BSE and CL Blue modes of the same section area; c) and d) BSE mode pictures that highlight the presence of gold grains in specific sections of the block (pictures taken by Rob Chapman).

Around 20 gold particles were observed in pyrite, ranging in size from 10 to nearly 50 microns and showing mostly flat and jagged morphology (e.g., Figures 5.2c and d). The particles occur in two main forms: dominantly as crack-fills, where they are represented by overall coarser grains - mostly in PyC (AuC_gv, Figures 5.2c, d) but also in PyA (AuA2_gv, Figure 5.3a); and as a few

small (~10 µm) inclusions in PyA (AuA_gv; Figure 24b). The coarser and fracture-hosted gold (AuA2_gv, AuC_gv) has appeared to be generally more silver-rich than AuA_gv (Figures 5.2d and 5.3b). A couple of low-silver, micron-scale particles were additionally identified in PyC, largely surrounded by iron oxidation; it hasn't been possible to classify these as either inclusion or crack-hosted gold, due to the blurred appearance in SEM of the grain boundaries. Quantitative compositional information on all these in-situ gold occurrences will be provided in section 6.2.1.

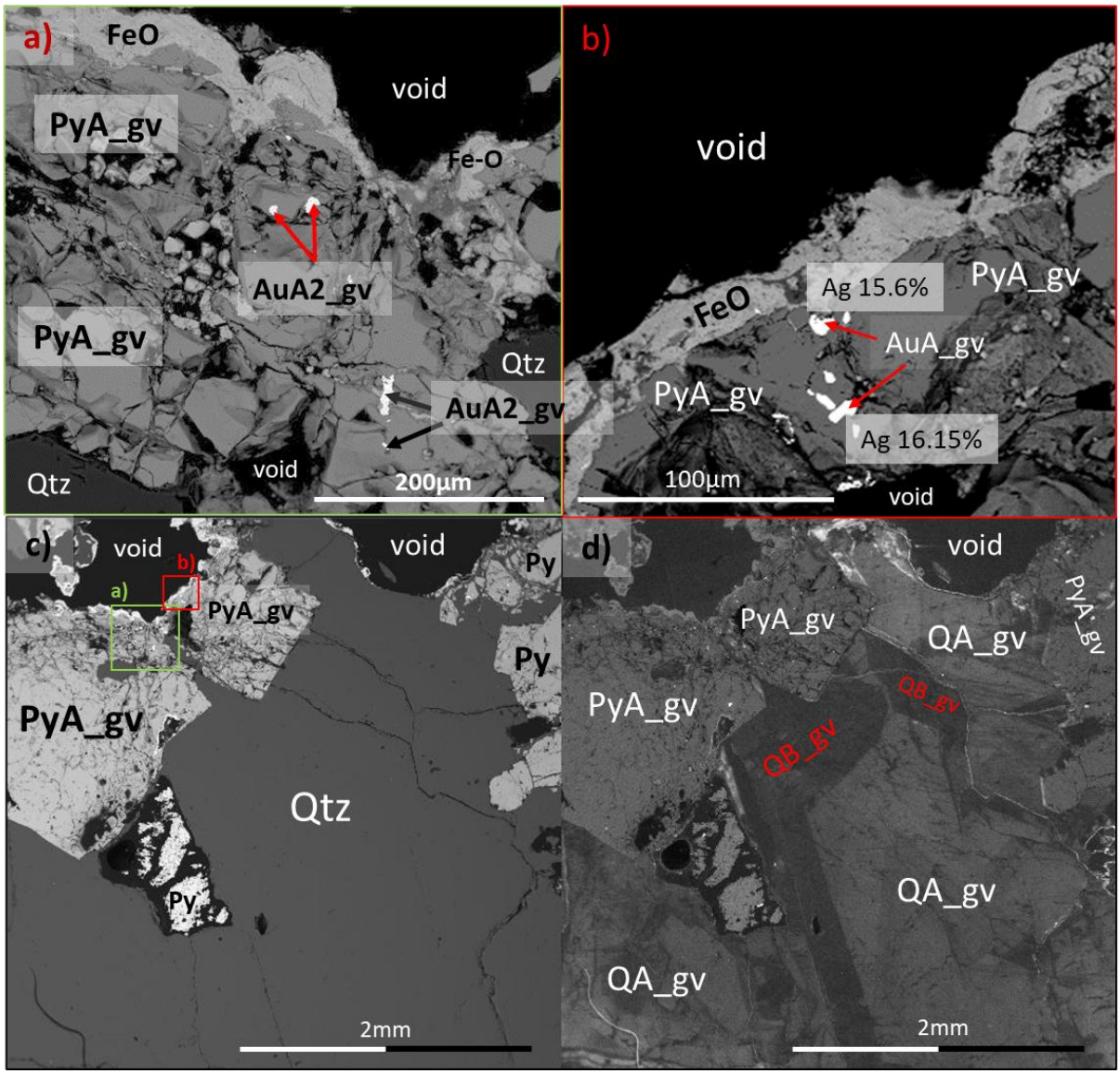

Figure 5.3 BSE-mode (a, b, c) and CL-blue mode (d) images of the LSGV (the image in a) was taken by Rob Chapman). The context of a) and b) is given by figure c), where relevant areas are highlighted; gold (Ag content also displayed) is visible alongside the other mineral components in figures a) and b). Images c) and d) were taken on the same area of the section using two different detectors (BSE and CL) – multiple quartz generations are visible in d).

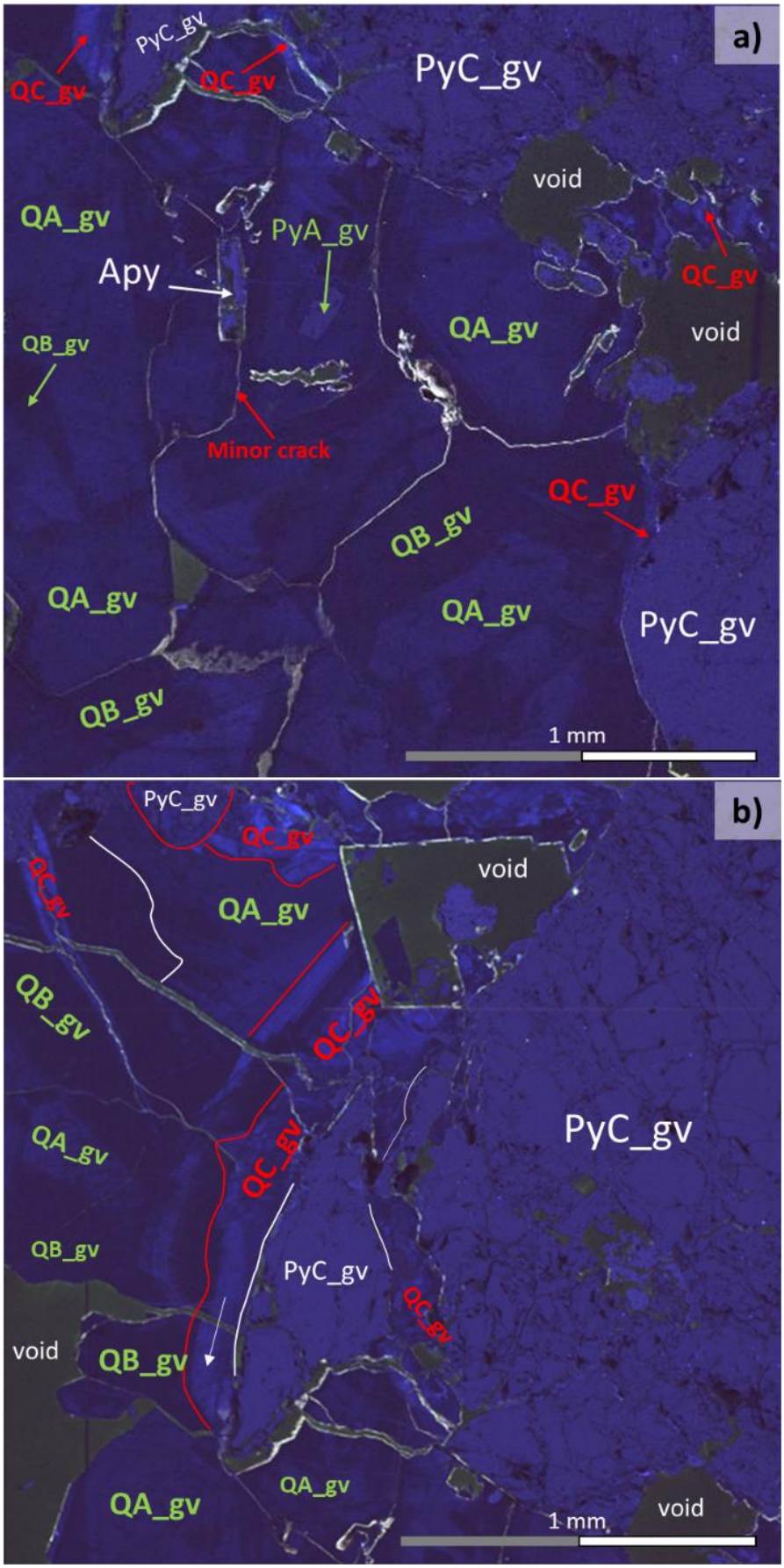
a)
PyC_gv
QC_gv
QC_gv
PyC_gv
void
QA_gv
PyA_gv
Apy
QC_gv
QA_gv
void
QB_gv
Minor crack
QC_gv
QB_gv
QA_gv
QA_gv
PyC_gv
QB_gv
1 mm
b)
PyC_gv
QC_gv
void
QC_gv
QA_gv
QB_gv
QC_gv
QA_gv
QC_gv
PyC_gv
QB_gv
PyC_gv
QC_gv
void
QB_gv
QA_gv
QA_gv
1 mm
void

Figure 5.4 CL-color mode images of LSGV (section sub-areas). Multiple quartz generations (QA_gv, QB_gv, QC_gv) are visible, as well as minor intra-crystal fractures and crystal boundaries. Pyrite and arsenopyrite are the two sulphides identified in these sample areas. Figure b) displays clearly the relationship between quartz and pyrite, which occurs together with QC; the prominent rhomb-shaped void may suggest weathered-out dolomite.

LSCL2

The analysis of quartz in this sample has reported some main repeating features with respect to what has been previously observed. An initial phase, here named QA_ls, consists of medium to light grey quartz (in the 'CL blue' mode), showing a weak, euhedral zonation, with slight tone variations and sharp boundaries between the different zones (Figure 5.5). QB_ls has been identified as following quartz event, overprinting the first one with medium to dark grey, homogeneous bands at very low CL intensity (Figures 5.5a, b, c, and e). Dolomite (DolE_ls; producing high fluorescence in CL-Blue mode) and minor ankerite fill-up fractures and cavities that intersect QA_ls and QB_ls (Figure 5.5b). Some of these fractures also host a third (QC_ls) and some others a fourth and thin (QD_ls) quartz generation (Figures 5.5a, c and e). Specially QC can be distinguished through brighter, euhedrally crystallised injections evolving into indented patterns within the section area (fig. 5.5c).

Pyrite and arsenopyrite are the only sulphide species (sporadically) observed in thin section. Pyrite (PyD_ls or PyE_ls) occurs as isolated fragments (up to 100µm size), sometimes closely associated with dolomite and ankerite (e.g., Figure 5.5b; DolE_ls and AnkE_ls) across the QD_ls fracturing event. Arsenopyrite (ApyC_ls) occurs as localised, chaotic agglomerates (individual fragments smaller than 100µm, fig. 5.5d and e) whose boundaries are in contact with either/both QB and QC - although to a greater extent to the latter; in addition, the sulphide partially fills vacant QC_ls cracks (fig. 5.5e).

LSCV3

Fractured, vuggy quartz is the dominant mineral in this vein, followed (in abundance) by coarse galena (Figure 5.6a). A primary texture, identified as QA_v3, takes place in the form of medium to light grey quartz, weakly zoned, with slight tone variations and sharp boundaries between different zones. A different quartz generation (QB_v3), cutting across the first one, is represented by dark grey to black, featureless bands, with no luminescence (Figures 5.6d and e). A third stage (QC_v3) fractures QA_v3 and QB_v3, hosting sporadic but extended, bright quartz injections (Figure 5.6e) with galena coming across, inter/overgrowing quartz.

Galena (GaC_v3) appears to be the most abundant sulphide species in LSCV3, characterised by the typical cleavage pits (e.g., fig. 5.6e). Chalcopyrite (CpyC_v3) mineralisation has only been

observed in the rock chip processed to produce the LSCV3 thin section, where the crystal margins appear to be in contact with galena mineralisation (Figure 4.8c). Later fracturing pervades all the former phases; these cracks sometimes accommodate the original quartz crystal boundaries and can occasionally be filled in Pb-rich fluids (fig. 5.6e). Fe-oxides infill galena and quartz, and Pb-derived alteration products (cerussite, S1 in Figure 5.6b, and anglesite) track further fractures occurring in galena.

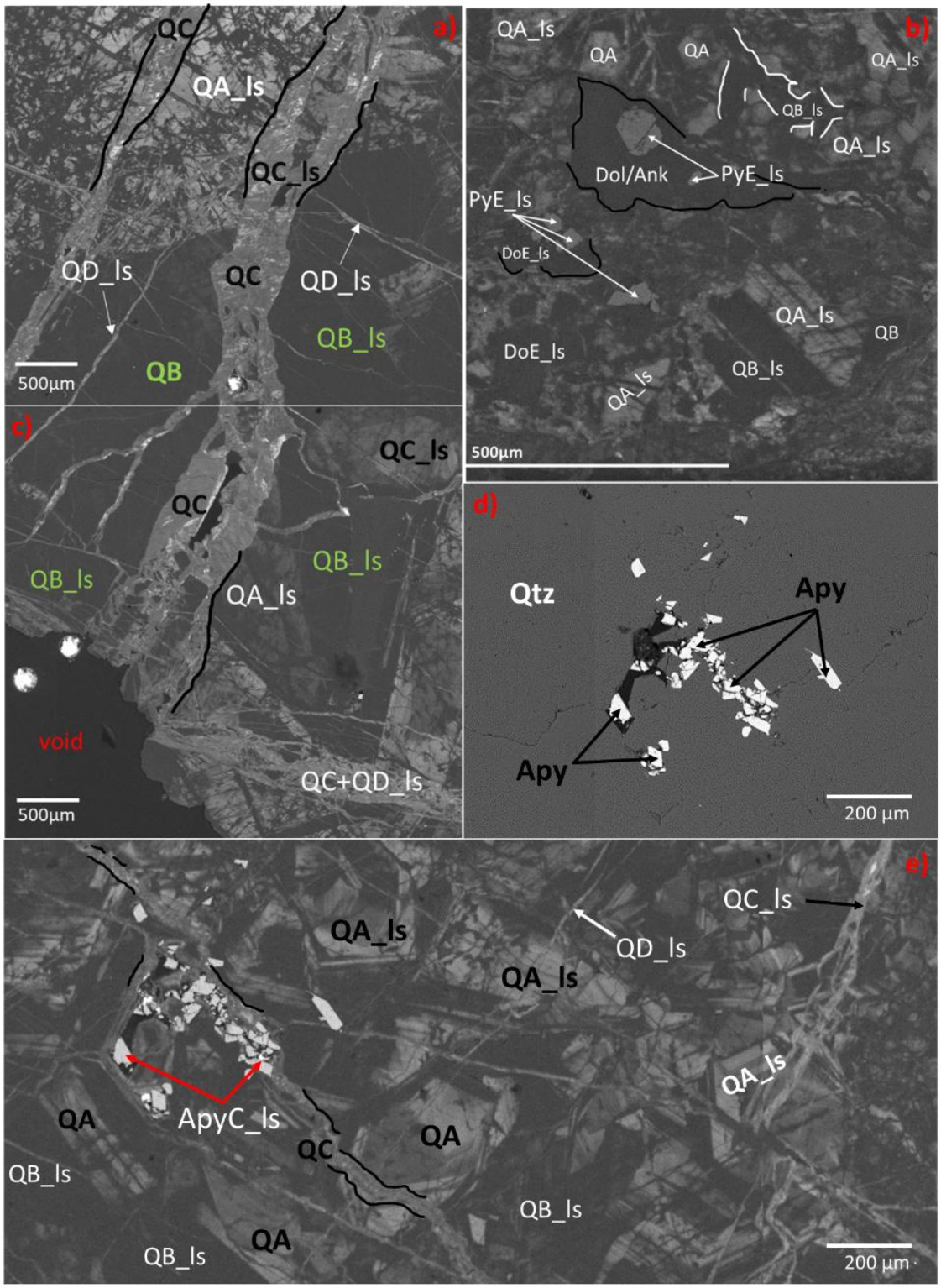

Figure 5.5 SEM-CL analysis of LSCL2. a), b), c), and e) CL Blue mode photographs of different sub-areas of the thin sections, that indicate the different quartz stages, their inter-relationships and their relationships with the two identified sulphides; in particular, arsenopyrite (ApyC_ls) occurs aslongside QC and pyrite (PyE_ls) and dolomite (DoE_ls) occur as later phases (figures b and e); d) BSE mode photograph that zooms into arsenopyrite mineralisation in quartz. Full montage maps of LSCL2 are available in both BSE and CL Blue modes in Appendix 2.

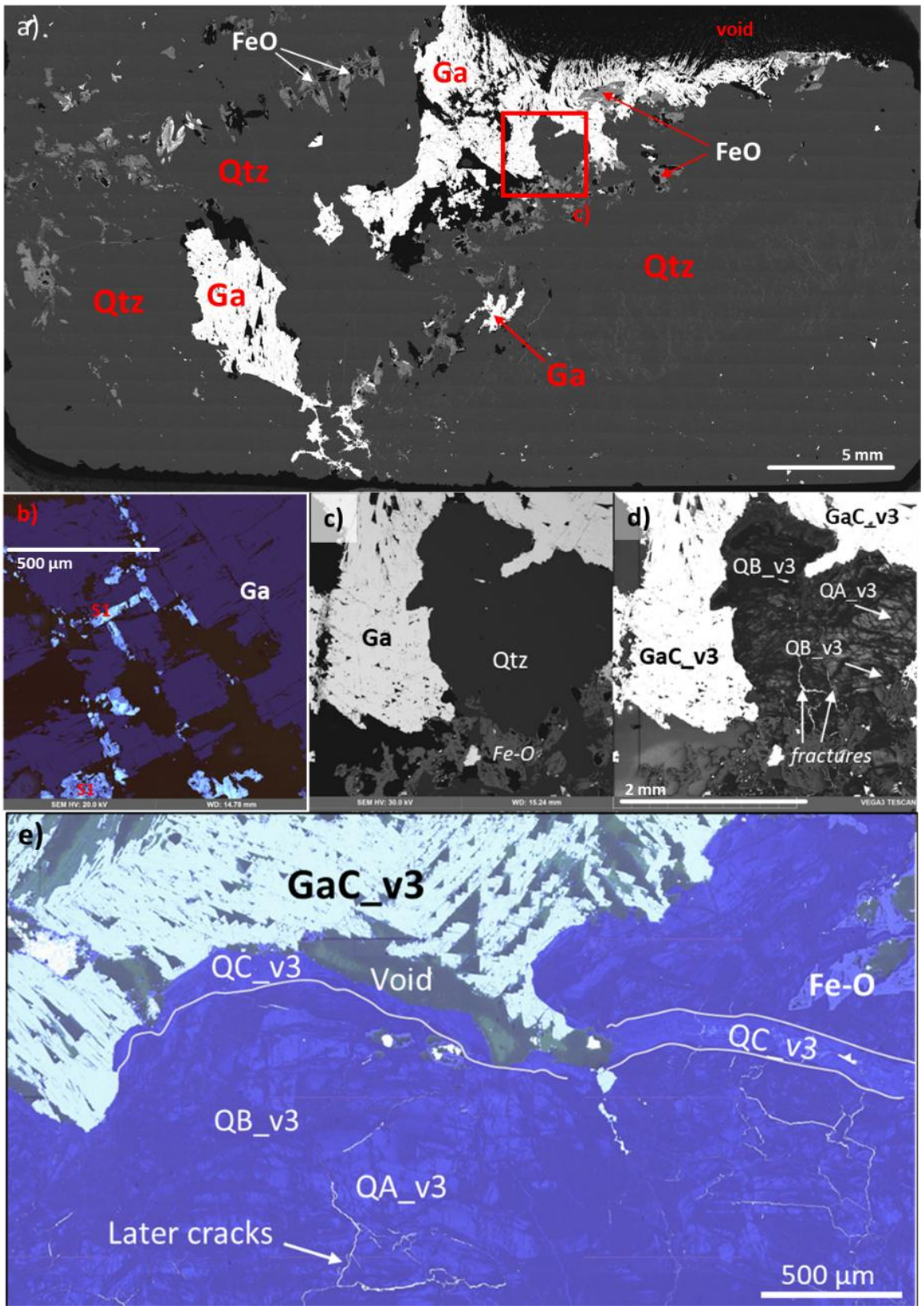

Figure 5.6 SEM-CL analysis of LSCV3. a) full montage map in the BSE mode, where the main mineral phases are visible; b) detail of galena mineralisation in void – secondary products (s1= cerussite) fill cracks in galena; c) and d) BSE and CL Blue modes pf the same sub-area in the thin section (also indicated in 27a); e) partial CL-Color mode montage (the full one is available), that highlights the three quartz stages identified and their relationship with the galena mineralisation.

LSCV9

Three main quartz stages have been recognized within this sample, mostly in the CL-Blue mode (Figure 5.7b). The first one has been labelled as QA_v9 and can be distinguished through pale grey colouration and patches of sharp euhedral zonation. The second one (QB_v9) appears darker, featureless and overprints QA_v9. The third quartz generation (QC_v9) is represented by light grey, thin injections (max 500µm thick) that are hosted in fractures across QA and QB – these are sometimes additionally infilled with calcium carbonate (Figure 5.7b). A fourth quartz generation (QD_v9) has sporadically been observed as thin infills that crosscut QC_v9. Dolomite is the volumetrically dominant phase after quartz, overgrowing all the previous stages (DoE_V9; fig. 5.7a).

Disseminated pyrite has been identified in the SEM-BSE mode (grain size up to 400µm) in the form of shattered agglomerates, frequently alongside patched dolomite mineralisation and chaotic quartz (Figure 5.7a). Because these latter mineral assemblages have appeared to overgrow (Figures 5.7e and f) all the other mineral phases (described earlier), they have been related to a separate, later stage accompanied by 'QE_v9' quartz. A few pyrite (PyE_v9) grains host themselves rare micron-size galena and chalcopyrite inclusions (GaE_v9 and CpyE_v9; Figures 5.7c and d).

LSCDV

LSCDV represents the most upstream vein sample analysed for Calliachar Burn. SEM-CL analyses have revealed two former quartz generations (QA_dv and QB_dv), consistently with what has been observed in the previous samples. In CL-blue mode (fig. 5.8), QA_dv displays pale to medium grey tones which weakly progress into zoning; QB_dv appears darker and dull in thick/thin grill-shaped bands. Marginally in the section, a third, brighter and luminescent quartz phase (QC_dv), crosscuts QA_dv and QB_dv (fig. 5.8c). Patched mica overgrows quartz and often incorporates rutile (Figure 5.8a) and different species of iron oxide. Later sets of cracks infill all the previous paragenetic stages, producing Fe-rich injections and local alteration halos. No sulphides have been observed upon thin section analysis.

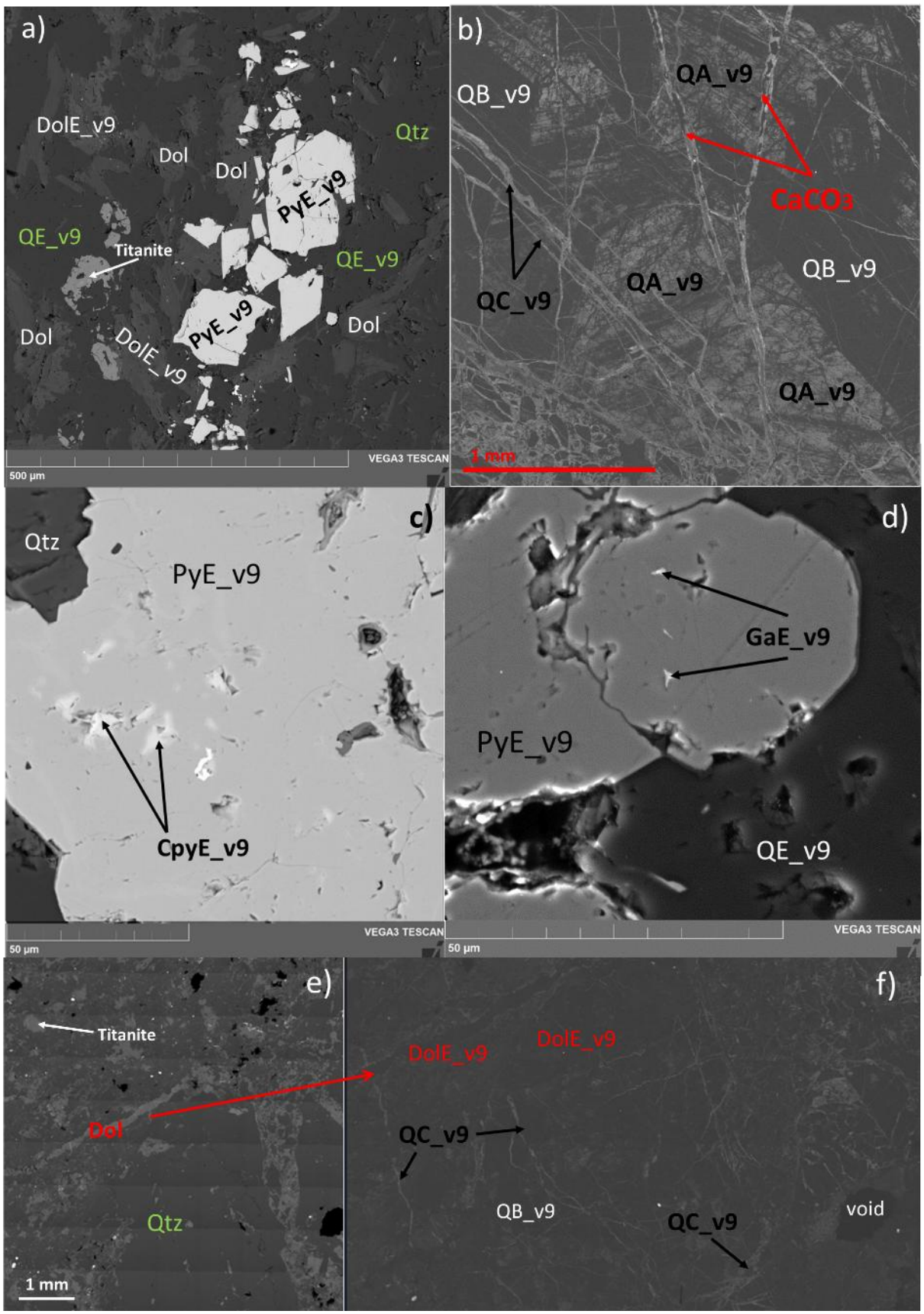

Figure 5.7 SEM-CL analysis of LSCV9. a) and e) BSE mode photographs of different sub-areas of the thin section; c), d) SE mode photographs highlighting specific mineral phases; b) and f) CL-Blue mode photographs highlighting the different quartz generations. Full montage maps of LSCV9 are available in both BSE and CL Blue modes.

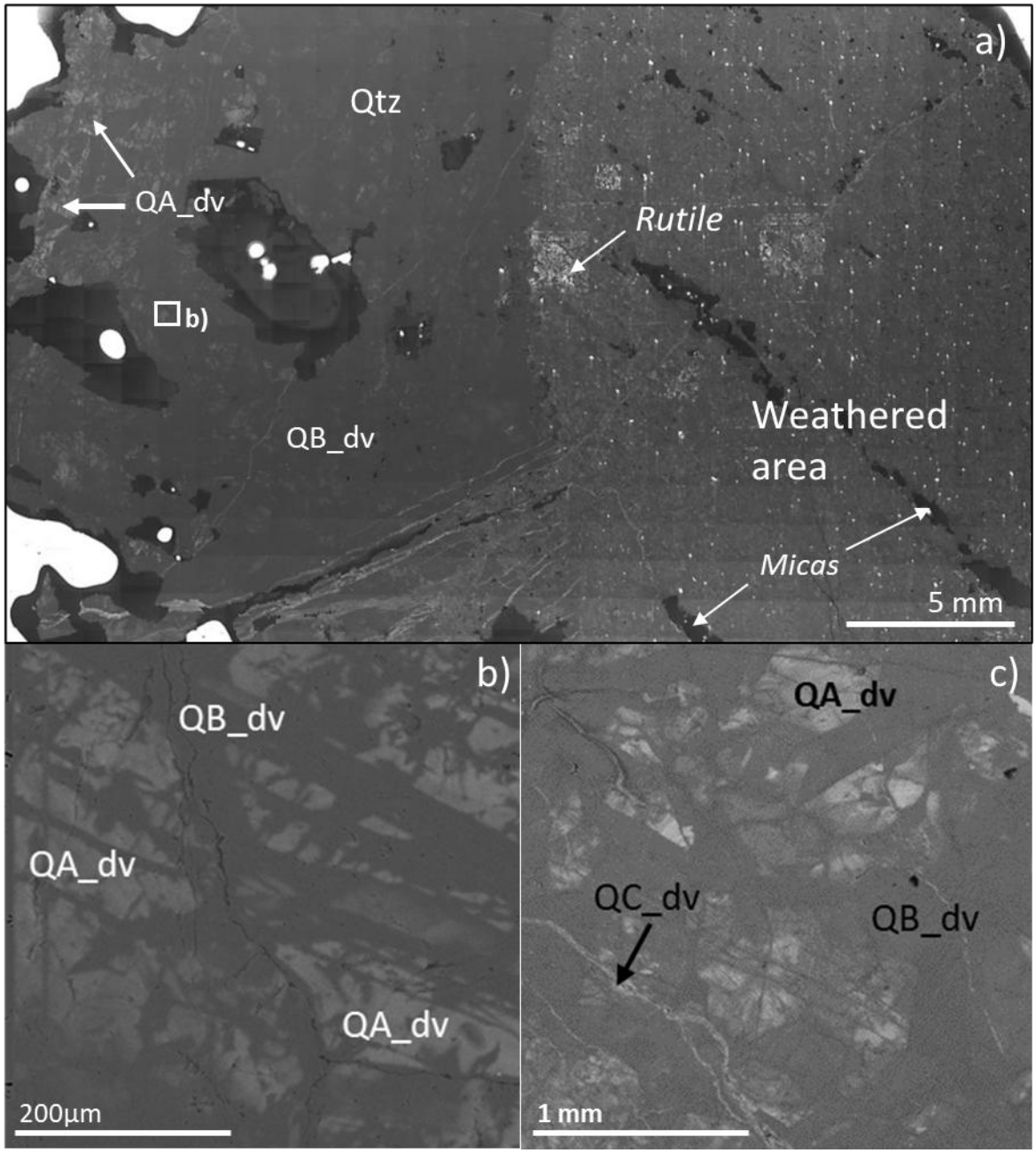

Figure 5.8 Analysis of LSCDV in sole Cl Blue mode. a) Overview-montage map, that indicates the occurrence of quartz and its physical interaction with the wall-rock (weathered area); b) sub-area of the overview map (as labelled in 29a) where QA and QB are well visible; c) sub-area of the section where QA, QB and QC are visible.

LSCL3

Two main CL quartz textures have been here identified: the first one is labelled as QA_l3 and features medium to light grey tones, with poorly visible traces of zonation; the second one, labelled as QB_l3, overprints QA_l3 with dark grey, featureless dark bands of variable thicknesses (Figures 5.9a-c). These two generations appear crosscut by two minor fracturing events, as well associated with quartz precipitation. Namely, QC_l3 consists of thicker fractures that are occupied by quartz, sulphides (details in the following) plus derived secondary minerals; QD_l3 is recognisable from sets of extremely thin infills which cut QC_l3 and the sulphide mineralisation (Figure 5.9b).

Among the sulphides that have been identified, galena (GaC_l3) is immediately visible because of the very bright coloration in both BSE and CL-Blue mode, and the typical cleavage pits (Figures 5.9c and e); it also appears to be in connection with/contoured by QC_l3. Chalcopyrite has been found connected and infilled with galena (CpyC_l3; Figures 5.9d, e). Pyrite (PyC_l3) has been observed in the form of isolated crystals, which do not appear directly in contact with any of the other two sulphides, nor with quartz (Figure 5.9d). These are however surrounded by intense Fe-oxidation, which has in turn resulted in contact with the galena and chalcopyrite mineralisation (Figure 5.9d).

LS4B

Following on from the investigations on LSCL3, the analysis of LS4B has turned out somewhat straightforward. Again, two main quartz stages have been observed within this section (QA_ub and QB_ub) and their characteristics have been inspected mostly in CL-Colour mode (Figure 5.10). Between these two, QA_ub represents the paler phase, despite displaying relatively low luminescence; its texture looks slightly mottled and systematically pervaded by a different, darker quartz stage (QB_ub). The latter is essentially featureless. A set of irregular fractures displaces the two main quartz textures, carrying abundant galena and minor chalcopyrite (GaC_ub and CpyC_ub), along with sporadic quartz (QC_ub). A further stage of very thin fractures only occurs internally to the galena and is infilled with secondary Lead-derived mineralisation (i.e., cerussite). These fractures show no continuity with the previous ones, indicating that they are part of a separate event (i.e., QD_ub).

Table 5.2 has been included to synthesize all the main textural and mineralogical features with the mutual crosscutting relationships in the Calliachar and Urlar samples, as they have been illustrated in this (5.2.1) section.

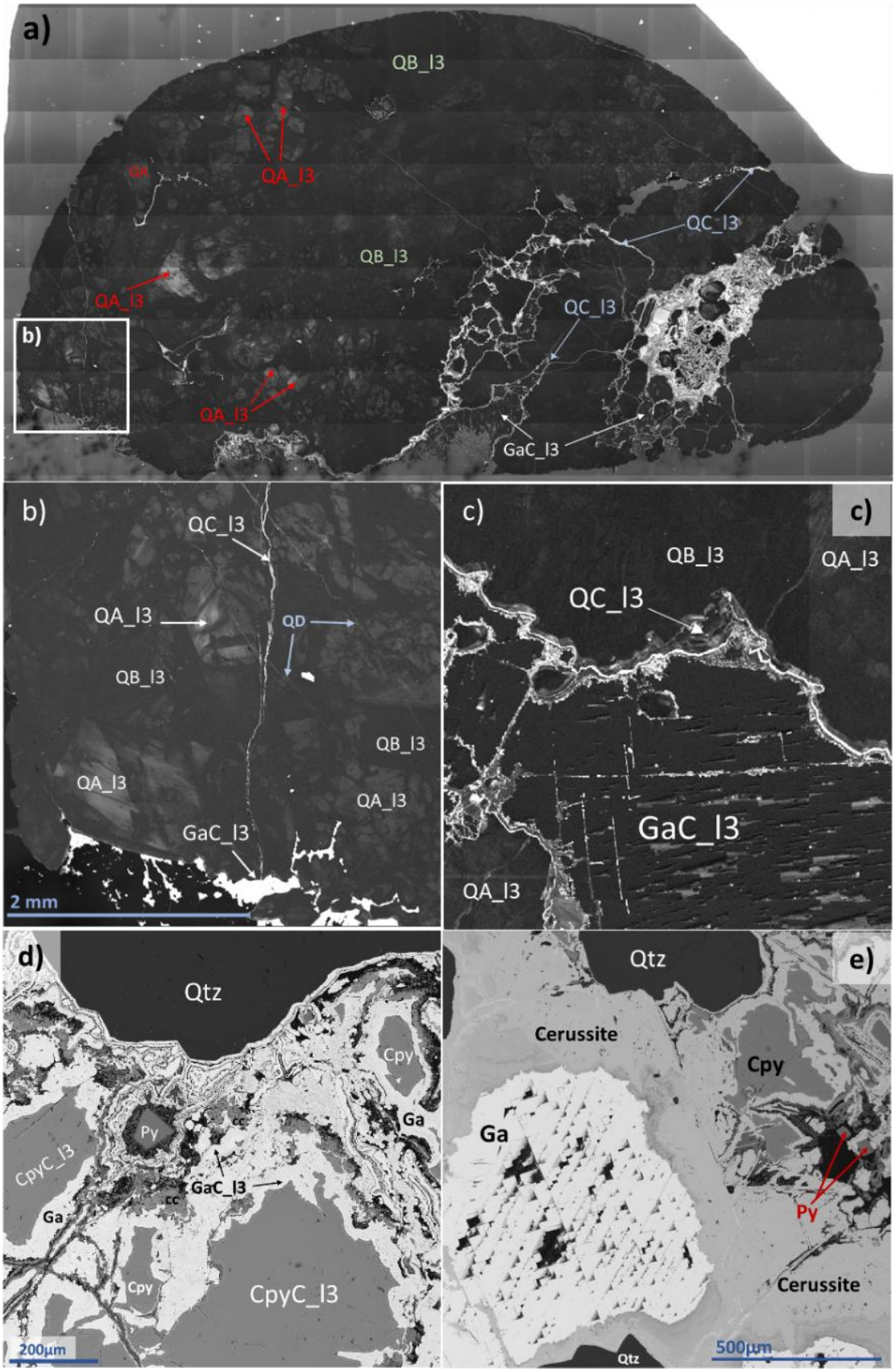

Figure 5.9 SEM-CL analysis of LSCL3. a) full montage map in CL Blue mode. A sub-area (b) which is also presented in further detail in Figure 5.9, is marked; b) and c) CL Blue mode pictures of sub-areas of the full montage, highlighting

the spatial relationships between quartz and galena; d) and e) BSE mode of two other sub-areas of the same thin section, where sulphides and secondary products (i.e., cerussite) are visible.

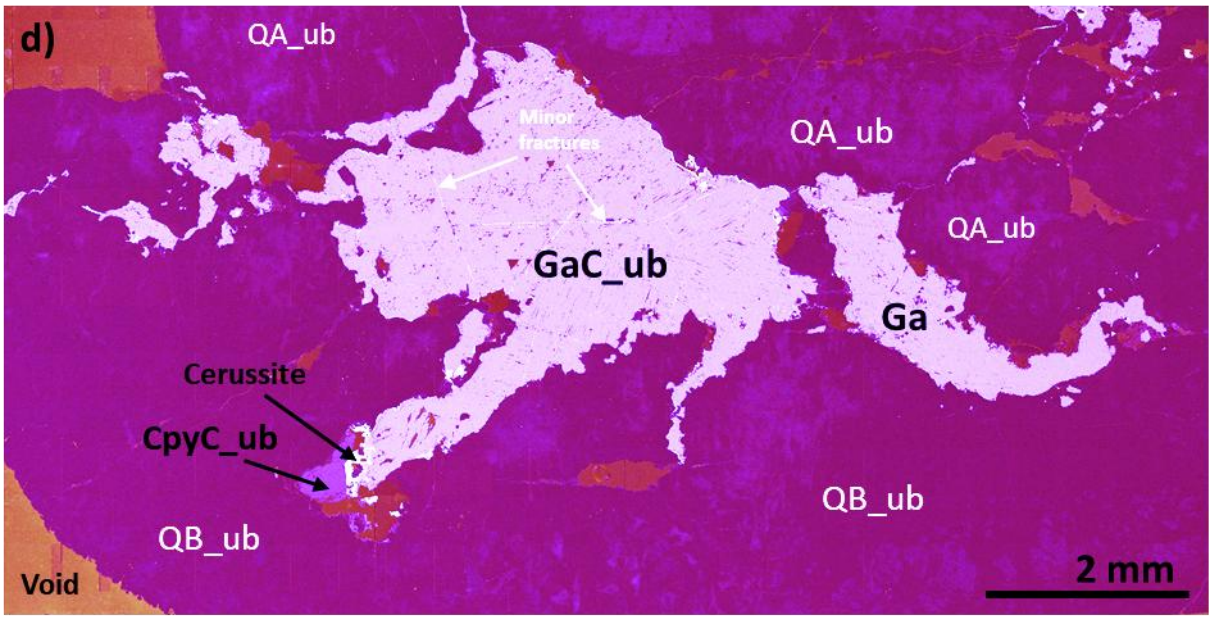

Figure 5.10 CL Color mode overview map of LS4B thin section, displaying the relationships between galena (GaC_ub), chalcopyrite (CpyC_ub), CL lighter quartz (QA_ub), and CL darker quartz (QB_uc). The two sulphides fill fractures across QA_ub and QB_ub; galena is, in turn, crosscut by minor fractures.

Table 5.2. Summary of the textural features and crosscutting relationships in and between the Calliachar-Urlar vein samples.

Mineral	***Thin section(s) ID***	**A**	**B**	**C**	**D**	**E**
Quartz	*LSCG, LSCL2, LSCV3, LSCV9, LSCDV, LSCL3, LS4B*	Relatively high-luminescent, weakly euhedrally zoned and mottled. Crosscut by all the other stages.	Featureless, CL-dark bands. Overprinting/fracturing A.	CL-bright fractures and infills. In all samples except LSCDV and LS4B, internal euhedral microcrystals are visible. Fracturing A and B.	CL-bright thin fractures and infills. Fracturing A, B and C.	Re-cemented, chaotic agglomerates - only observed in LSCV9, in association with PyE and DolE.
Carbonate	*LSCL2, LSCV9*				Ankerite/calcium carbonate injections in C-D fractures.	Dolomite (DolE) and Ankerite (AnkE) overgrowing all the previous stages.
Pyrite	*LSCG*	mm-scale euhedral crystals, internal fracturing observed. Embedded in QA_gv. Hosting Au		Shattered, cataclastic pyrite, associated with QC_gv. Hosting Au		
	LSCL2, LSCV9					Shattered, cataclastic pyrite. PyE_v9 hosts Ga and Cpy inclusions (GaE_v9; CpyE_v9)
	LSCL3			Micron-scale isolated crystals, surrounded by Fe-O, GaC_lc and CpyC_lc.		
Arsenopyrite	*LSCG, LSCL2*			Micron-scale fragments occurring with QC.		
Galena	*LSCV3, LSCL3, LS4B*			CL-bright, relatively abundant in thin section. Occurs within fractures and precipitates with QC and CpyC.		
	LSCV9					Micron-scale inclusions in cataclastic pyrite (PyE)
Chalcopyrite	*LSCV9*					Micron-scale blemishes in cataclastic pyrite (PyE)
	LSCL3, LS4B			Partially dissolved, occurs within fractures and precipitates with QC and GaC.		
	LSCV3			Only observed in hand-specimen. Appears to co-precipitate with Ga (GaC_v3)		
Sphalerite	*LSGV*			Rare micron-scale crystals in contact with QC_gv		
Gold	*LSGV*	AuA_gv. Occurs as (10µm-scale) inclusions and within micro-fractures in PyA_gv.		AuC_gv. Coarser (up to 50µm), more silver-rich gold. Occurs within micro-fractures in PyC_gv.		

5.2.2 (Glen) Almond Vein

5.2.2.1 Hand specimen observations

A closer inspection of the Almond Vein specimens (Figure 5.11), used to produce polished thin sections, has illuminated higher-resolution crystallographic details that were not possible to appreciate during the preliminary field investigations - the samples were obtained by breaking the portions of the veins ≤ 2.5 cm wide. Quartz crystals range in size from 500µm to 5 mm, and generally present elongated, comb morphologies (Figure 5.11b). Sulphides appear coarse on the surface, with irregular individual habits and traces of weathering (Figures 5.11a and 5.11a). Sphalerite is the most evident one, showing a nearly black colouration and compact texture; it occurs with chalcopyrite and/or quartz, showing an iridescent appearance that ranges from yellowish to pale green.

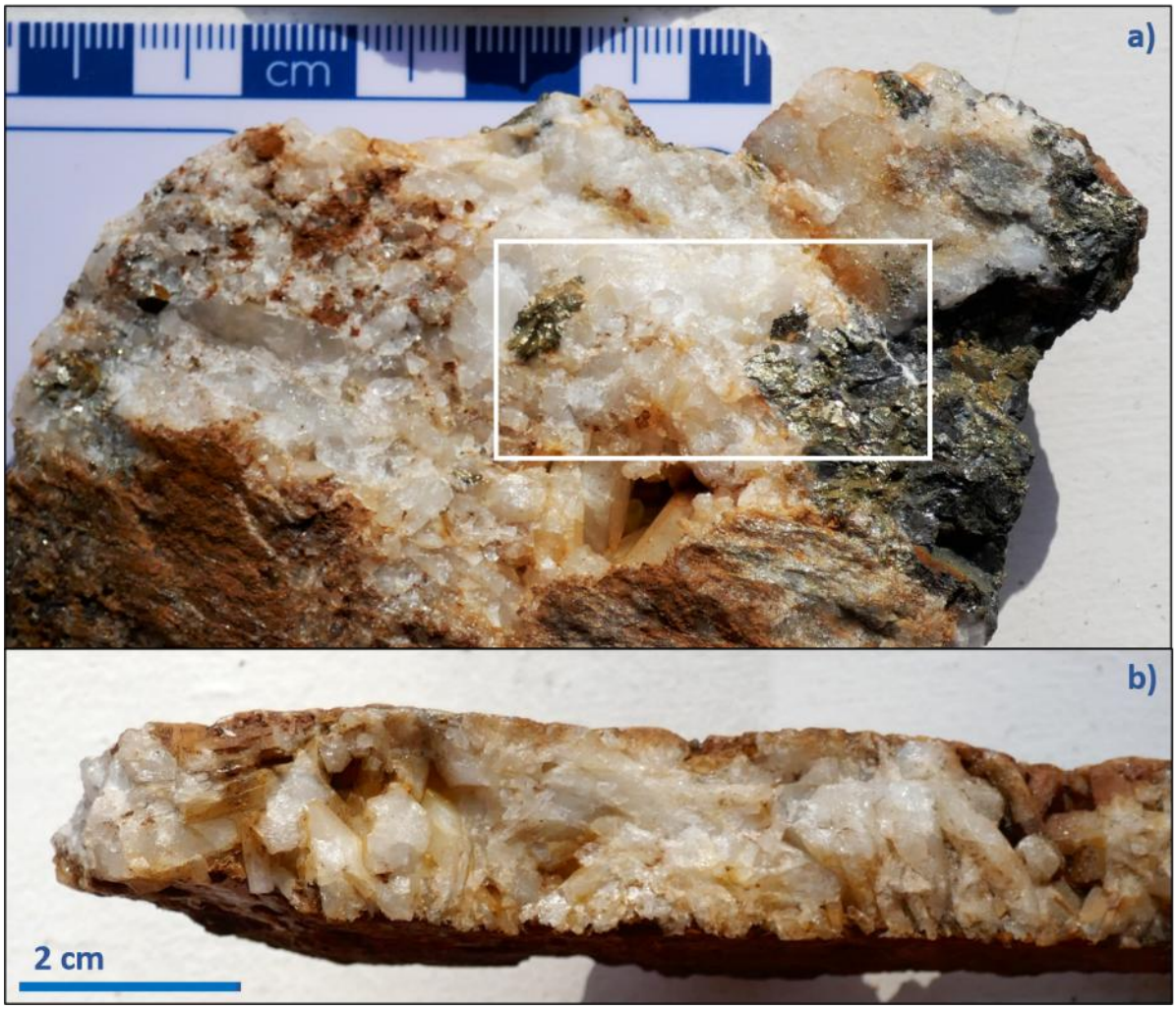

Figure 5.11 Rock specimens used for the extraction of the Almond Vein sections/blocks, before being processed. One of the two thin section traces is indicated in Figure 5.11a, where sulphide mineralisation is visible. 11b shows a section of the vein thickness, where the elongated (comb) morphology of the quartz crystals can be observed.

5.2.2.2 SEM-CL investigations

SEM-EDS analysis of the Almond vein samples, in BSE and CL mode, has allowed clarification of the relationships between the observed sulphides, and between these and the hosting gangue. Investigations have been conducted on 4 different polished blocks and 2 polished thin sections (e.g., Webb et al., 2024). The results are reported in the following sub-paragraphs.

SEM-BSE overview: Figures 5.12 and 5.13 show that galena, chalcopyrite, and sphalerite are all spatially contiguous; in addition, galena extensively fills-up discontinuities and fractures in and between sulphides, quartz, and dolomite - this is represented in closer detail in Figure 5.12b and 5.13. Pyrite has been observed in direct contact with quartz and sphalerite (Figure 5.16); galena, sphalerite, and chalcopyrite have additionally been found as blebs in pyrite (e.g., Figures 5.14d, 5.16e).

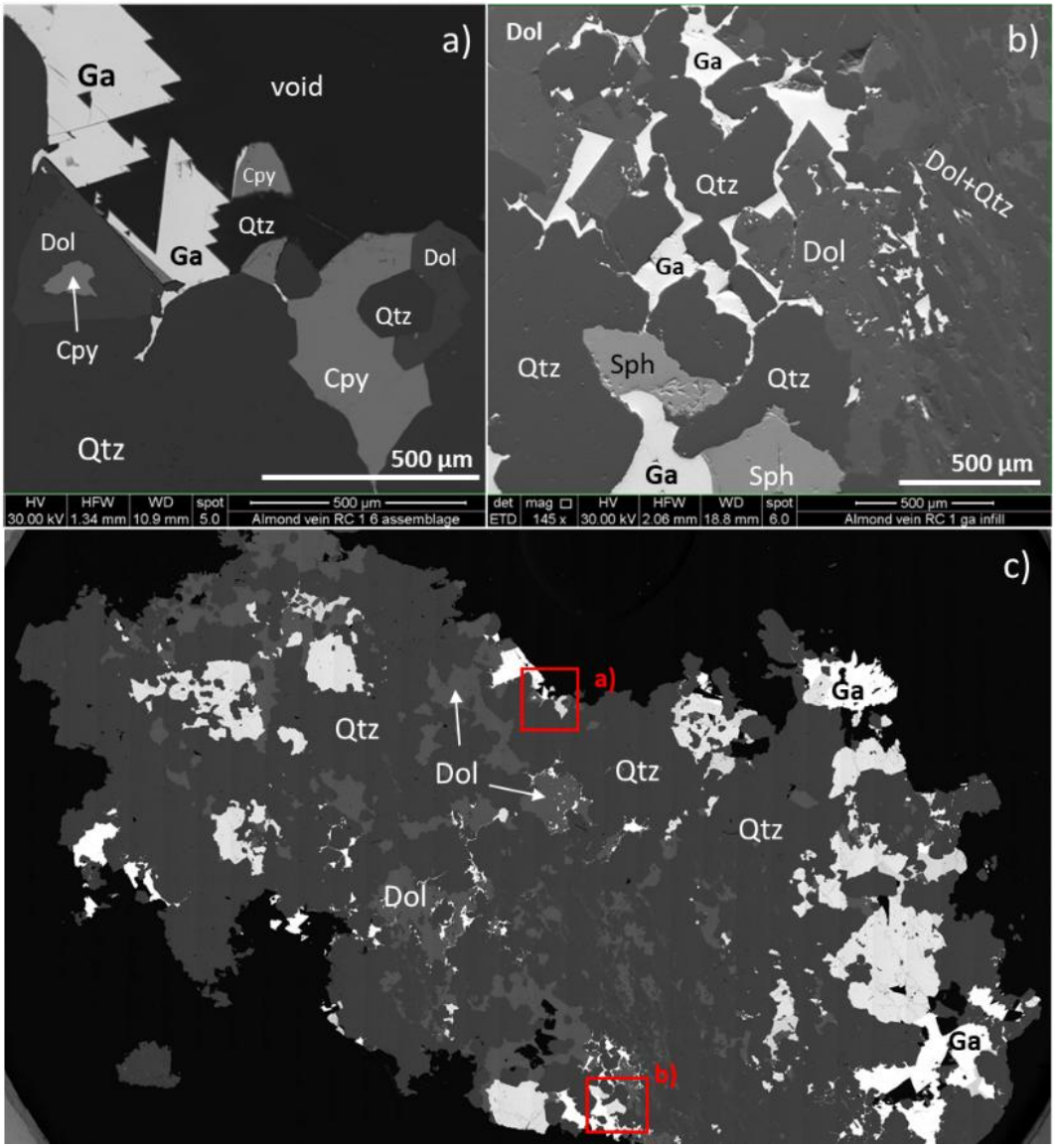

Figure 5.12 BSE mode images of one of the polished blocks used for the optical characterisation of the Almond Vein. 5.12a and 5.12b represent two sub-areas of the overview montage map (SEM images taken by Rob Chapman), represented in 5.12c. The images provide a preliminary overview of the mineral composition (Qtz, Dol, Ga, Sph and Cpy) of the analysed block.

Dolomite appears interconnected with quartz, galena and sphalerite (Figures 5.12b and 5.13). Importantly, gold has been observed in all the sulphide species except galena, showing a bimodal occurrence (as inclusions and fracture-fills). Textural details on each of these mineral phases and their mutual crosscutting relationships are illustrated as follows, often in line with the paragenetic descriptions in Webb et al 2024.

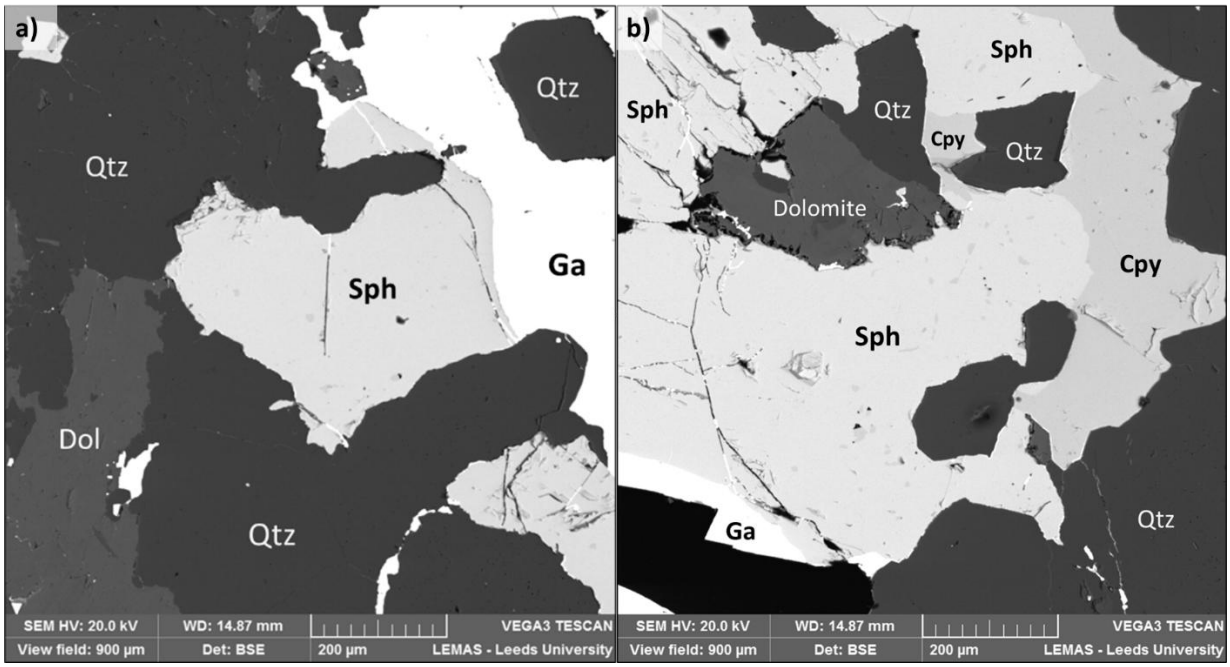

Figure 5.13 BSE mode image that shows the spatial relationships between sphalerite, galena, chalcopyrite, quartz and dolomite in the Almond Vein.

Quartz: Three different quartz stages have been identified in this vein, with two of them (namely QA_av and QB_av) being volumetrically dominant (Figure 5.15a, c, d, f). QA_av is represented by weakly euhedral to mottled textures and appears light grey in the CL-Blue mode. QB_av has been associated with the overprinting, CL-dark quartz bands that crosscut QA_av and are observed in contact with all the sulphide species, except chalcopyrite. A third quartz generation (QC_av) has been identified in sporadic, CL-bright fractures apparently carrying no sulphide mineralisation (Figure 5.15f).

Pyrite occurs along with QB_av (and is consequently labelled 'PyB_av') and sphalerite (SphB_av) and chalcopyrite (CpyB_av) as displayed in Figure 5.16. The PyB_av crystals can reach fairly large sizes (mm-scale) and often show an internal phase zonation (Webb et al. 2024), noted from the presence of arsenic in the PyB_av rims, which is absent in the PyB_av cores (Figure 5.14b). Additionally, PyB_av hosts inclusions of galena, sphalerite, chalcopyrite (namely GaB_av, SphB_av and CpyB_av) and gold (AuB_av), as shown in fig. 5.14a, d; 5.16b-e.

Sphalerite is likely the second most abundant sulphide species observed in thin section after PyB_av, which is in direct contact with (SphB_av) and, sometimes, incorporated-in as inclusions (e.g., fig. 5.14d). It is generally coarse (up to mm-size) and additionally occurs with QB_av, GaB_av and CpyB_av.

Chalcopyrite has been observed in direct contact with ShpB_av and in the form of inclusions in PyB_av (CpyB_av). CpyB_av hosts itself gold as micron-scale inclusions and fracture-fill (AuB_av1; Figure 5.14c).

Galena appears optically very bright and often in direct connection with SphB_av, CpyB_av and QB_av (GaB_av, Figures 5.15a, b, e); it has additionally been observed as micron-scale inclusions in PyB_av and SphB_av. A later galena stage (GaD_av) appears to occur within a set of fractures crosscutting all the other sulphide species and the three quartz generations (Figures 5.14e and 5.15e).

Dolomite has been found within fractures that crosscut QA_av, QB_av and the associated sulphide mineralisation (DolC_av; Figure 5.14e). Some of these fractures can be linked to the QC_av quartz stage; however, DolC_av and QC_av don't appear to come across the same ones.

Gold (~16 particles) has been observed as micron-scale inclusions in pyrite and chalcopyrite (AuB_av1, e.g., Figures 5.14c and 5.16d) and filling cracks that fracture coeval pyrite, chalcopyrite and sphalerite (AuB_av2; e.g., Figures 5.14d; 5.16d, e). The crack-hosted gold is characterised by a higher silver content in the alloy and appears overall coarser (up to ~80µm size) than the gold as inclusions. Quantitative compositional data on the alloy of these particles will be illustrated in section 6.2.2.

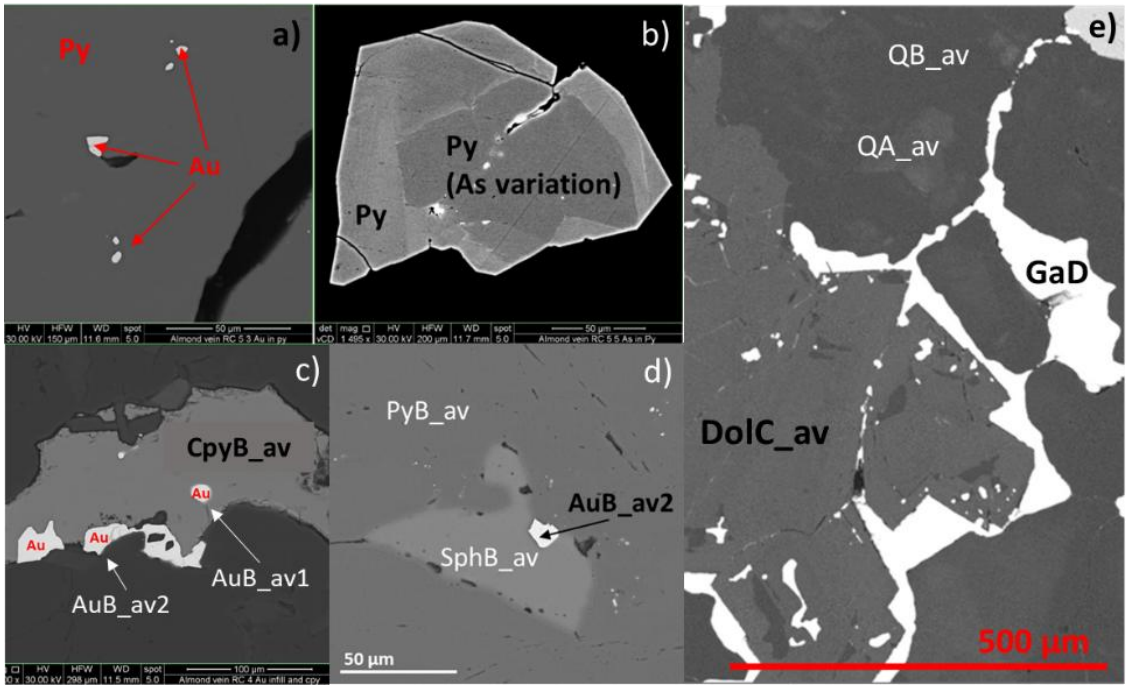

Figure 5.14 a), c), d) and e) BSE mode images of specific sub-sections of the Almond Vein samples that highlight the physical features of gold in sulphides; b) SE mode image that shows internal compositional variations in a pyrite grain; e) CL Blue mode image that highlights the physical relationships between galena, two quartz phases (qA and qB) and the Dolomite. SEM images in a) to d) taken by Rob Chapman.

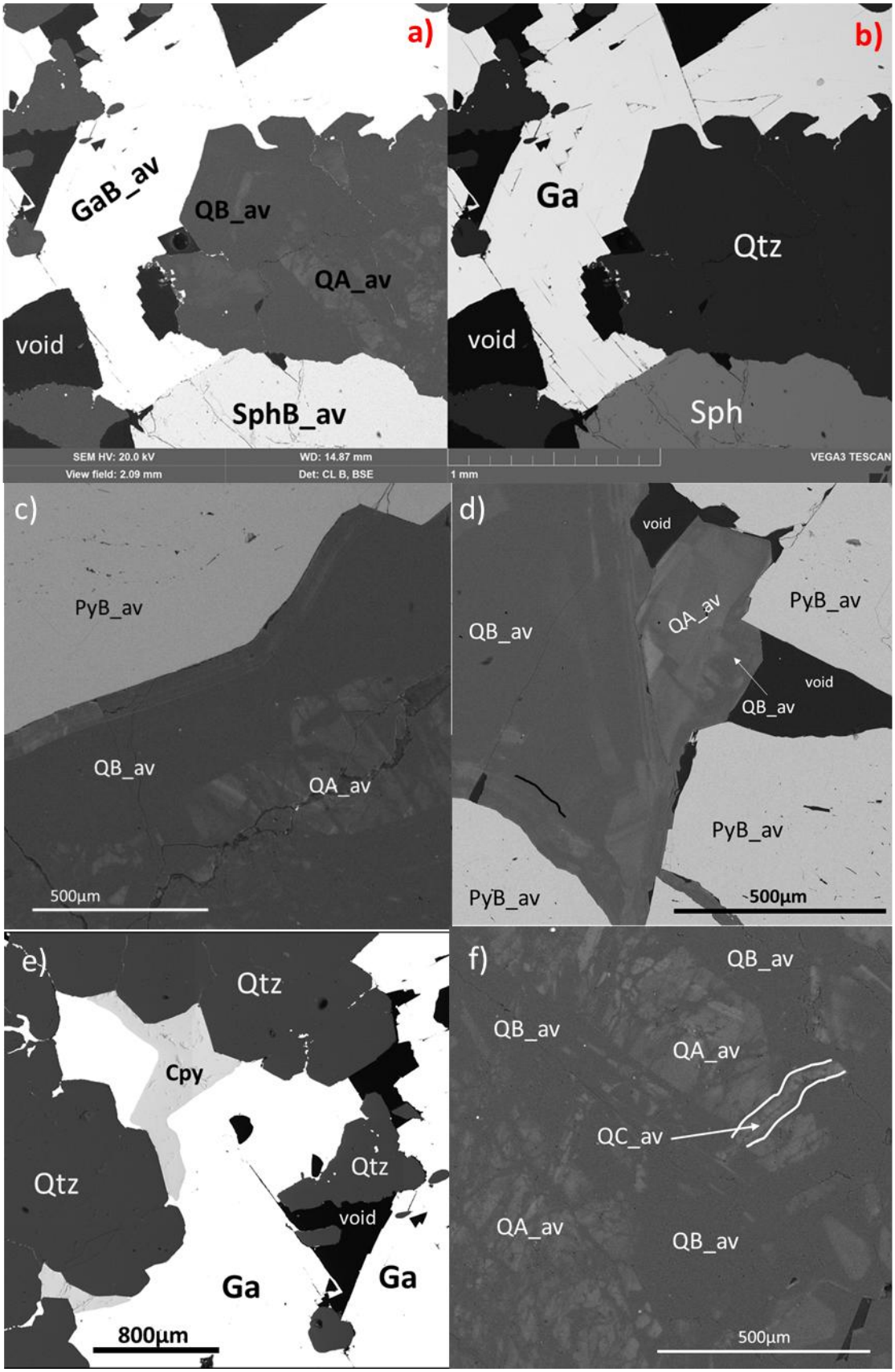

Figure 5.15 CL Blue mode images (Figures a, c, and f) and BSE mode images (Figures b, d, e) three different sub-sections s in the Almond Vein, to highlight the relationships between quartz and sulphides.

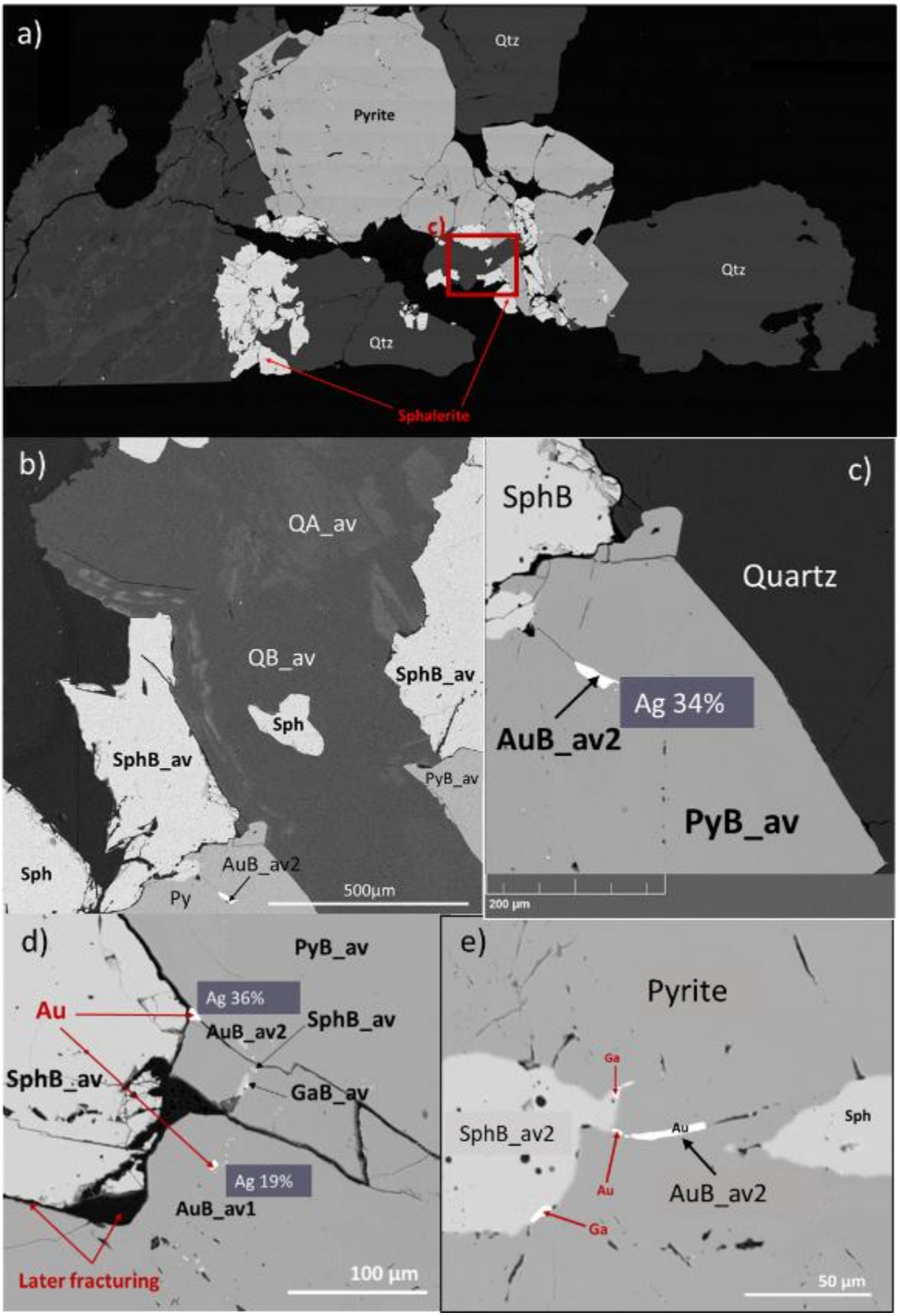

Figure 5.16 a) Full montage BSE map of one of the 'Almond' polished blocks; b) and c) CL Blue and BSE modes, respectively, of two sub-areas in one of the Almond blocks; d) and e) BSE mode images of two close sub-areas in one of the Almond blocks, which emphasizes the spatial relationships between gold, sulphides and fracturing.

5.2.2.3 Analysis of vein-crushed material

SEM-EDS analyses were additionally conducted on pan-concentrate minerals, obtained by mechanically crushing some parts of the Glen Almond Vein. Overall, the optical and compositional characteristics of the mineral particulate are consistent with the information deducted from investigation of the cohesive vein material, as described in the previous paragraphs. A few specific observations are outlined in Figures 5.17 a) and b) and as follows.

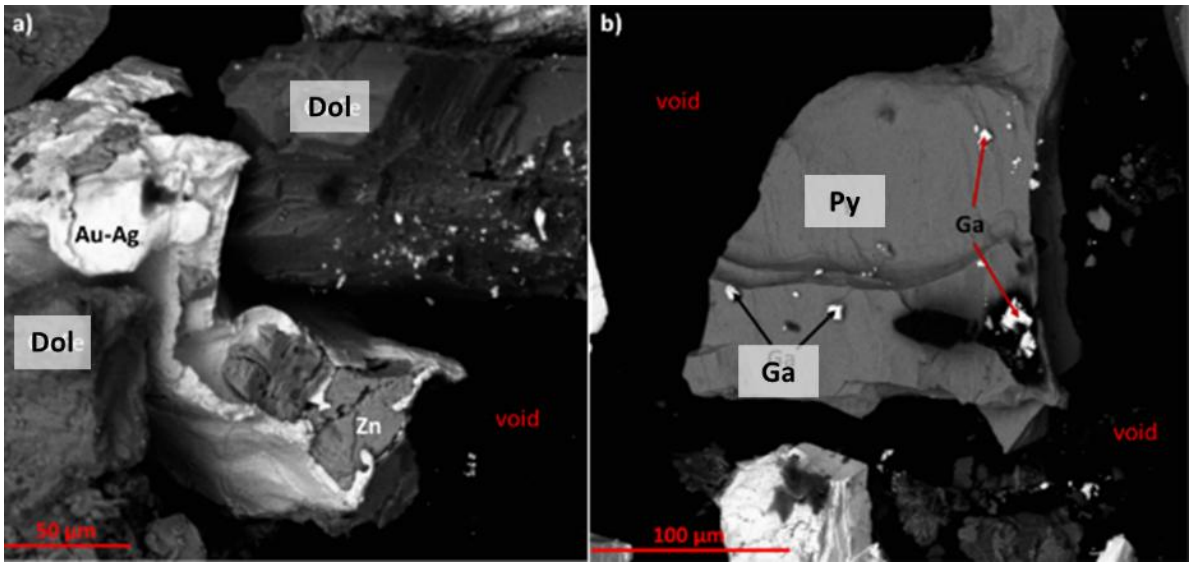

Figure 5.17 BSE mode images that represent specific minerals from the pan-concentrate and their physical interactions (SEM images taken by Georgian Manuc); a silver-rich gold particle can be observed in 5.17a. The sample was prepared by simply fixing the material on a stub, prior to SEM analysis.

A gold particle (of >150µm size) has been found in contact with dolomite mineral and shown unusually high Ag content (wt. ~42.5% by EDX analysis) in the alloy. A large zinc-bearing inclusion has also been detected internally in the grain (Figure 5.17a)). Figure b) highlights, instead, the occurrence of micron-scale galena inclusions in a pyrite grain.

5.2.3 Lead Trial

Samples to perform SEM-CL analyses were selected through different field campaigns (2019 to 2021, including a couple conducted by Erris Gold Resources) to underpin the occurrence of multiple generations of quartz, their inter-relationships, and their connection to the main sulphide assemblage and gold mineralisation. Samples have been approached depending on their location (map in Figure 4.14), specimen type and main mineralogical/textural features, as indicated in Table 5.3; sample descriptions partially rely on data made available by Erris Gold Resources. Examples of typical textures are also reported in Figure 5.18, in line with the features that have been described in the Table 5.3 and in section 5.2.3.

Table 5.3 Thin section IDs and textural, mineralogical features of the Lead Trial rock samples.'' indicates the samples provided by Erris Gold Resources.*

Thin section IDs	***Rock sample ID***	***Hand specimen texture***	***Hand specimen mineralogy***	***Sample type***	***Grid reference***
LSLTA1, 2	***LSTA***	Microcrystalline, milky Qtz with vugs (figure 38a). Weathered.	Sphalerite, galena and baryte. Au-bearing.	In-situ vein	NN 70840 39260
LS1a, b	***LS1***	Microcrystalline, milky Qtz with vugs. Weathered.	Galena, subordinate sphalerite and baryte	Mine dump - float	NN 70833 39253
28641 - 28642	***RX2864****	White, microcrystalline Qtz with minor vugs (figure 38b).	Coarse galena and sphalerite (figure 38b). 8.87 ppm Au.	Float	NN 70999 39135
28861 - 28862 *(channel)*	***RX2886****	Vuggy and banded Qtz (figure 38c).	6% galena and vugged-out sphalerite. >10 ppm Au.	Float, channel repeat	NN 71384 39068
RX30781-2	***RX3078****	Quartz stock breccia with rounded litho-clasts (figure 38d).	5-6% sulphides, mica schists and rhyolite clasts. >10 ppm Au.	Float	NN 70778 39216
LSLTD1, 2 *(Dunan)*	***LSLTD****	Creamy, vuggy Qtz with minor mica schist clasts	Galena, micas.	Float	NN 72669 38539

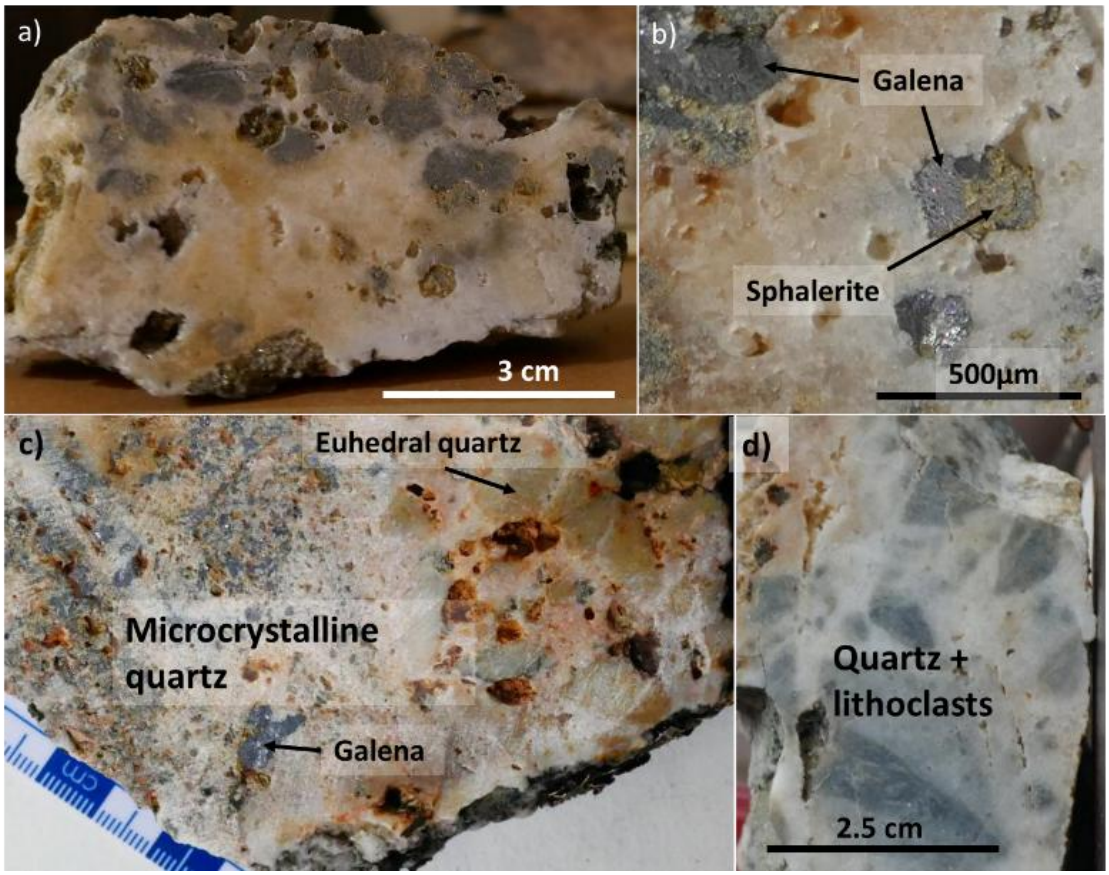

Figure 5.18 Typical quartz textures and mineral assemblages observed in the Lead Trial samples. a) LSLTA; b) 28641-2; c) 28861-2; d) RX30781. See also Table 5.3. The sample cuts highlight the distinctive quartz textures – vuggy, microcrystalline – the morphology of some of the crystals, and the physical relationships between quartz and sulphides. In figure 5.18c a physical scale is placed beneath the sample.

5.2.3.1 SEM-CL investigations

The SEM-CL analysis of vein samples collected at this location has revealed relatively complex textural features and a distinctive mineral assemblage. The next sub-paragraphs report optical and compositional features deduced by the analysis of 1 or 2 perpendicular thin sections extracted from each of the vein/float samples investigated (i.e., Table 5.3). Sampling locations are also indicated in Figure 5.14 (section 5.2.3).

LSLTA1-2

Quartz: Four different quartz textures have been identified in thin section and labelled QA_lt1, QA_lt2, QB_lt and QC_lt (Figure 5.19b to e). QA_lt1 is the dominant one and can be distinguished through euhedral to sub-euhedral crystals, showing internal (both symmetric and asymmetric) facets, sector zoning and euhedral zones of growth (Figures 5.19c and 5.20e); the crystals emit relatively high luminescence in CL-Color and CL-Blue modes. QA_lt2 is found

adjacent to the QA_lt1 crystals and consists of a fine-grained quartz texture that emits weaker CL response (slightly darker colouration in CL-Color and CL-Blue mode (Figures 5.19b, c and e). QA_lt1 and QA_lt2 can be considered together as a composite QA_lt texture. QB_lt brecciates the QA_lt quartz and emits the lowest CL response, appearing dark grey and featureless in the CL-blue mode (Figure 5.19b, Figure 5.20e). QC_lt has been recognised from micron-scale, sporadic sharp-edged veinlets which crosscut QA_lt and QB_lt (Figure 5.19e); their CL response (e.g., in CL-Color mode) appears as the brightest among the ones generated by quartz in these two thin sections.

Sulphides: Galena and sphalerite are the two sulphide species identified in the LSLTA thin sections. These occur either separately (Figure 5.19a, b, d) or as interconnected agglomerates (Figure 5.19e); in all cases, they overgrow QA_lt and are sometimes contoured by thin QB_lt films (Figure 5.19d). The two minerals have overall appeared to occupy similar volumetric proportions (ranging from µm to mm scale), with galena dominating in LSLTA1 and sphalerite in LSLTA2. Through all the SEM-CL channels that have been used, galena and sphalerite mineralisation generally show brighter colouration than the surrounding quartz (i.e colour in CL Blue). They have also consistently shown indented morphology and weathered surfaces, particularly galena (Figures in Appendix 2). Both the sulphides are crosscut by fractures filled with lead- and zinc-rich secondary products, respectively (e.g., Figure 5.19e and Appendix 2).

Baryte mineralisation sporadically fills up minor morphological discontinuities and cracks in QA_lt, QA_lt2 and QB_lt (Figures 5.19a, b). Alteration minerals (e.g., *chlorite* and *sericite*) shallowly overgrow the quartz and appear completely obscured in the CL Blue mode (Figures 5.19b, e).

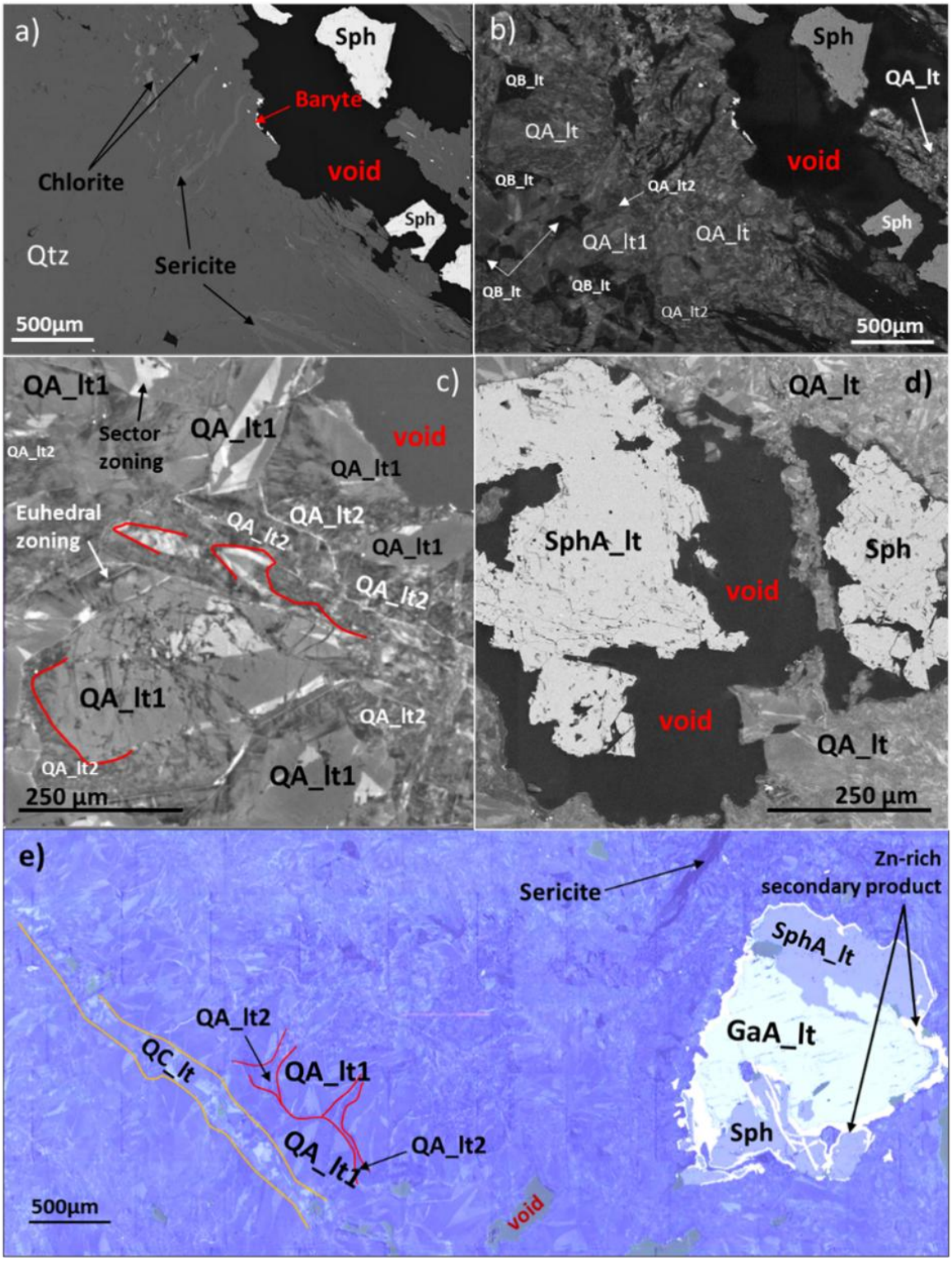

Figure 5.19 LSLTA. a) BSE-mode; b)-d) CL-Blue mode; e) CL-Color mode. A) and b) are images acquired on the same section area. Quartz, sulphides (i.e., galena and sphalerite), baryte and micas (chlorite and sericite) are visible as mineralogical components, alongside zinc secondary products. Pictures 5.19b to 5.19d are especially useful in distinguishing zonation and the first two quartz generations (QA_lt and QB_lt); the larger scale of 5.19e enables view on QC_lt as well. The red lines in c) and e) help distinguishing two quartz pluses in QA_lt (namely, QA_lt1 and QA_lt2).

Gold has been observed in LSTA1 and LSTA2 (Figure 5.20) in the form of rare particles with <10µm diameter, occurring marginally and/or in isolation across the QA_lt phase (Figures 5.20b and e).

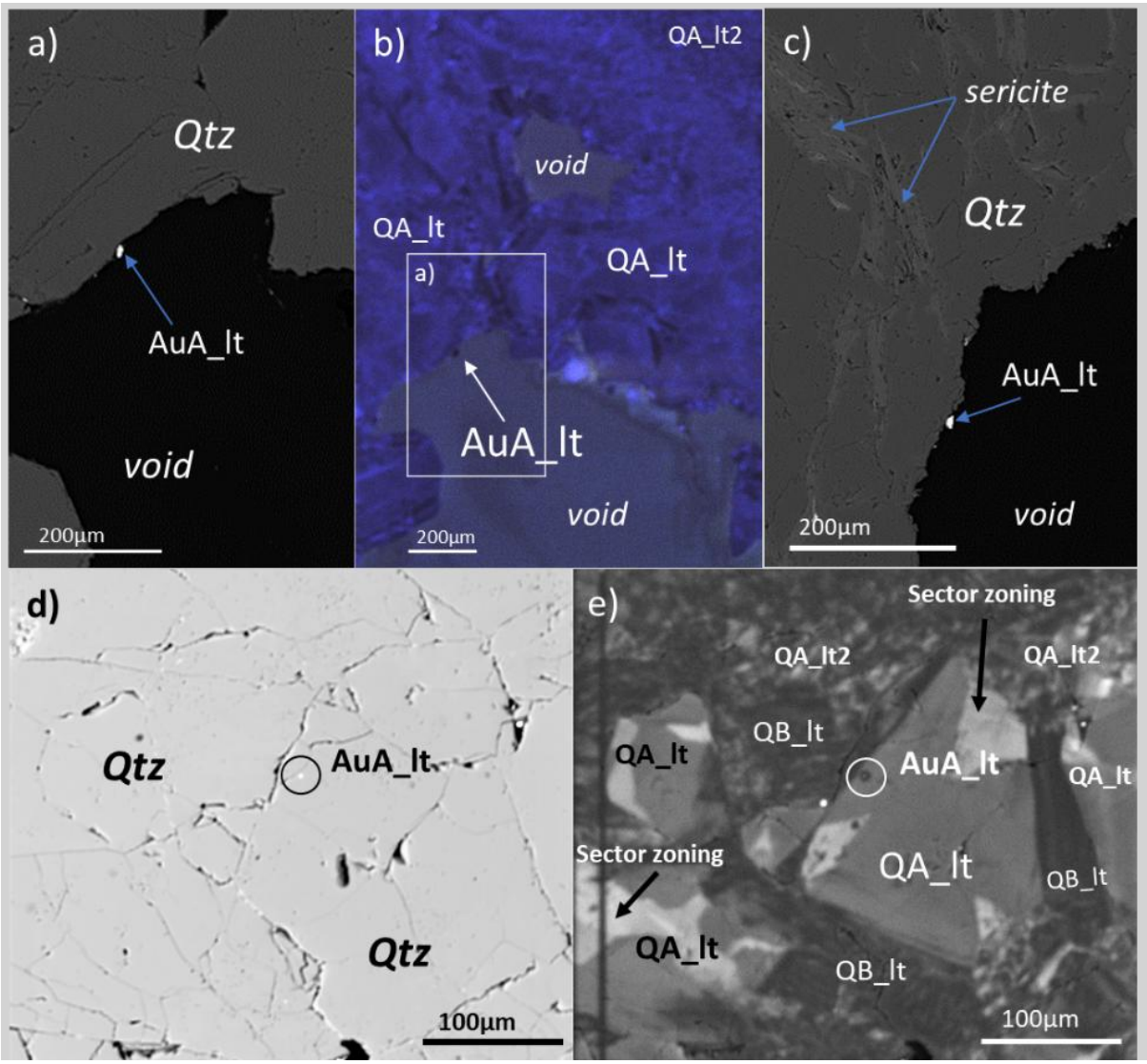

Figure 5.20. Gold in LSLTA. a), c) and d) BSE mode; b) and e) CL Blue mode. d) and e) are images acquired on the same section area.

LS1a-b

Quartz: The quartz generations identified in these sections show some textural and morphological features comparable to those identified in LSLTA1 and LSLTA2. The previous labelling code has been retained in lowercase and adjusted accordingly. Qa_lt1 represents the dominant texture, corresponding to CL-bright sub-euhedral to euhedral quartz crystals (Figures

5.21; 5.22a and c). Patches of qa_lt2 appear to be embedded in qa_lt1 and have been classified as concentric, hexagonal to plumose (e.g., 'feather-like') textures (Figures 5.21, 5.22a). These are often surrounded by a CL-darker (qb_lt) quartz (Figures 5.21, 5.22a), which is similarly and often found adjacently to galena and sphalerite agglomerates (Figure 5.22c; as observed in the previous two sections). In LS1b, qc_lt has additionally been recognised from sporadic sharp-edged veinlets which crosscut qa_lt1, qa_lt2, and qb_lt (Figure 5.22a).

Sulphides: The association of galena and sphalerite is confirmed in LS1a and LS1b, where no further sulphide mineralisation has been observed. In general, their characteristics are in line with those observed in LSLTA1-2. The two mineral species appear to occur either separately or as interconnected agglomerates (Figures 5.21 and 5.22), in similar volumetric proportions. They overgrow both qa_lt1 and qa_lt2 (fig. 5.21) and are sometimes contoured by qb_lt (Figure 5.22c). Fractures internal to the sulphides are present and consistently filled with lead- and zinc-rich secondary products (e.g., Figure 5.22b, c and 5.23). More specific optical and morphological features of galena and sphalerite can be referred to as those observed in LSLTA1 and LSLTA2 (see previous paragraph).

Barite (BaD_lt) is observed to occur sporadically in micro-cavities and fractures in quartz and sulphides (fig. 5.22a).

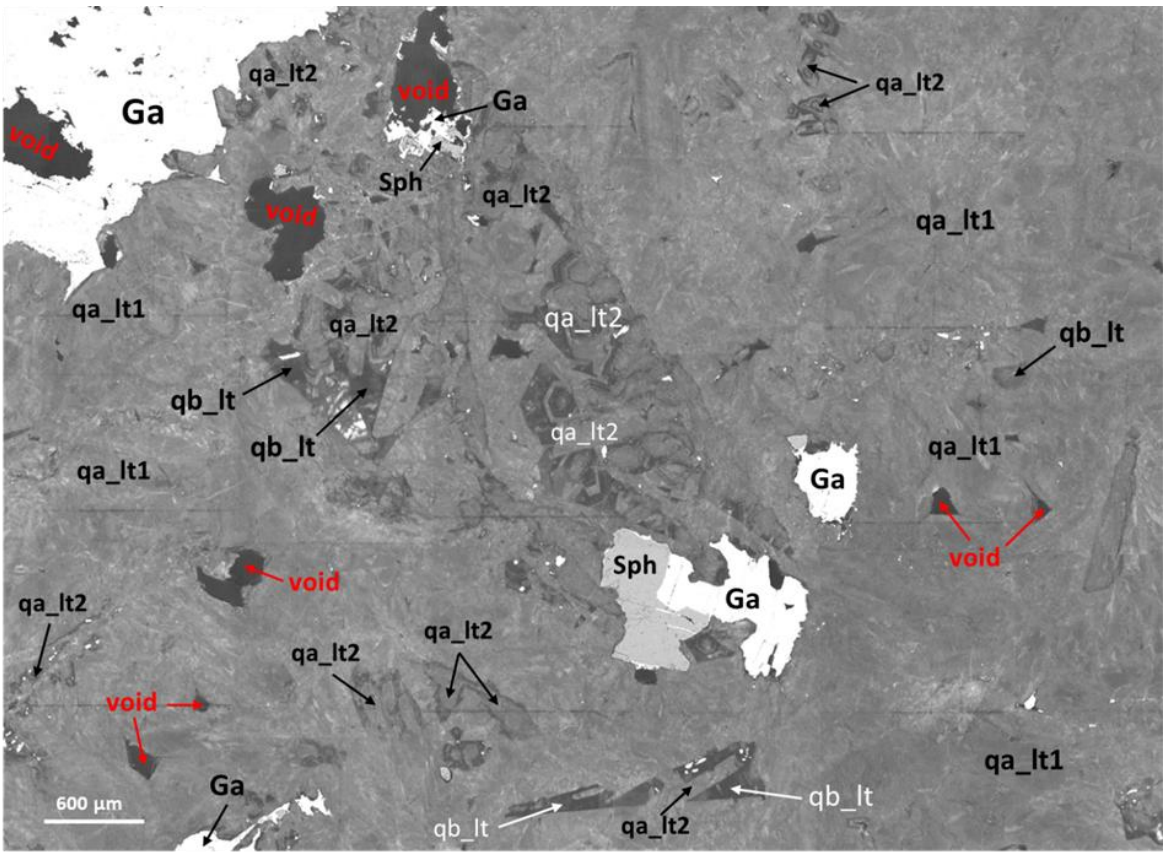

Figure 5.21 CL Blue mode image from the LS1b thin section. Three quartz textures are evident (qa_lt1 ; qa_lt2 ; qb_lt) alongside galena and sphalerite.

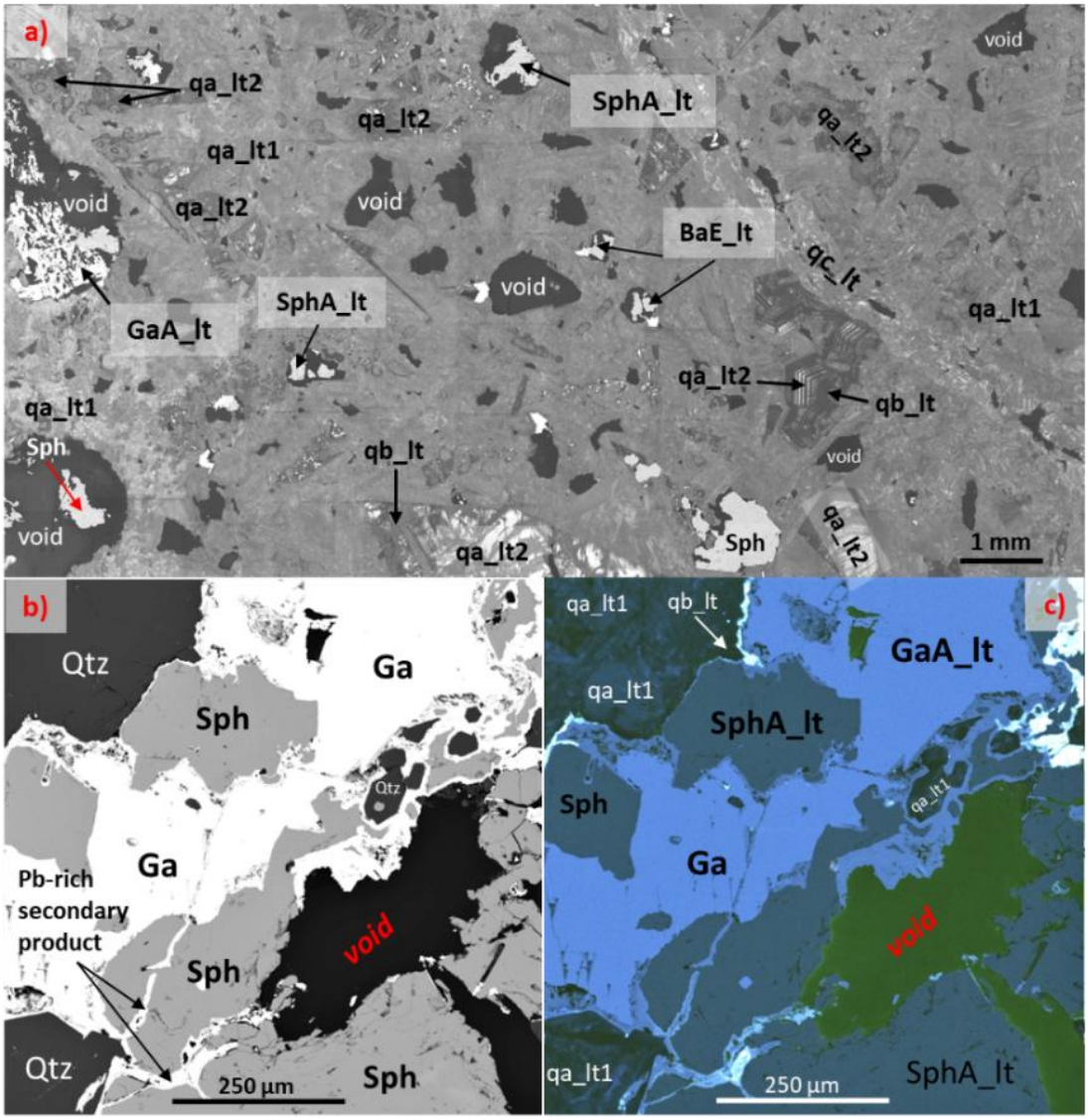

Figure 5.22 LS1b thin section. a) CL Blue mode, with emphases on the quartz phases, their mutual relationships and their relationships with the sulphides; b) BSE mode; c) Color CL mode, highlighting the galena and sphalerite intra-relationships.

28641-2

Quartz: The main quartz texture observed is represented by sub-euhedral to euhedral crystals (qa_at1), overall showing homogenous sizes and medium grey colouration in the CL-Blue mode (e.g., Figure 5.24). Qa_at2 constitutes a subordinate texture, appearing physically connected to qa_at1. This is formed of patterns of concentric, sub-spheric and *plumose* crystals (e.g., Figures 5.24 and 5.26a, b, c), frequently embedded in a contiguous CL-darker quartz matrix (qb_at); the texture as a whole display a turbid, moss-like appearance. The sub-spheric crystals generally present internal oscillatory zoning (fig. 5.24a). Qb_at can additionally be recognised from thin films, contouring galena and sphalerite (e.g., fig. 5.26e).

Sulphides: Galena and sphalerite remain the only two sulphide species observed, frequently forming agglomerates. They show characteristics analogous to the ones reported previously, although the internal fractures appear overall scarcer. The sulphides overgrow both qa_at1 and qa_at2, becoming more densely distributed and smaller (up to the µm scale) in proximity to the qa_at2 patterns (Figures 5.24 and 5.26b, d).

Baryte mineralisation occurs more abundantly in this set of thin sections and can almost entirely be located within the qa_at2 cavities and/or on top of the qb_at texture, where it forms micron-scale agglomerates (Figure 5.26a).

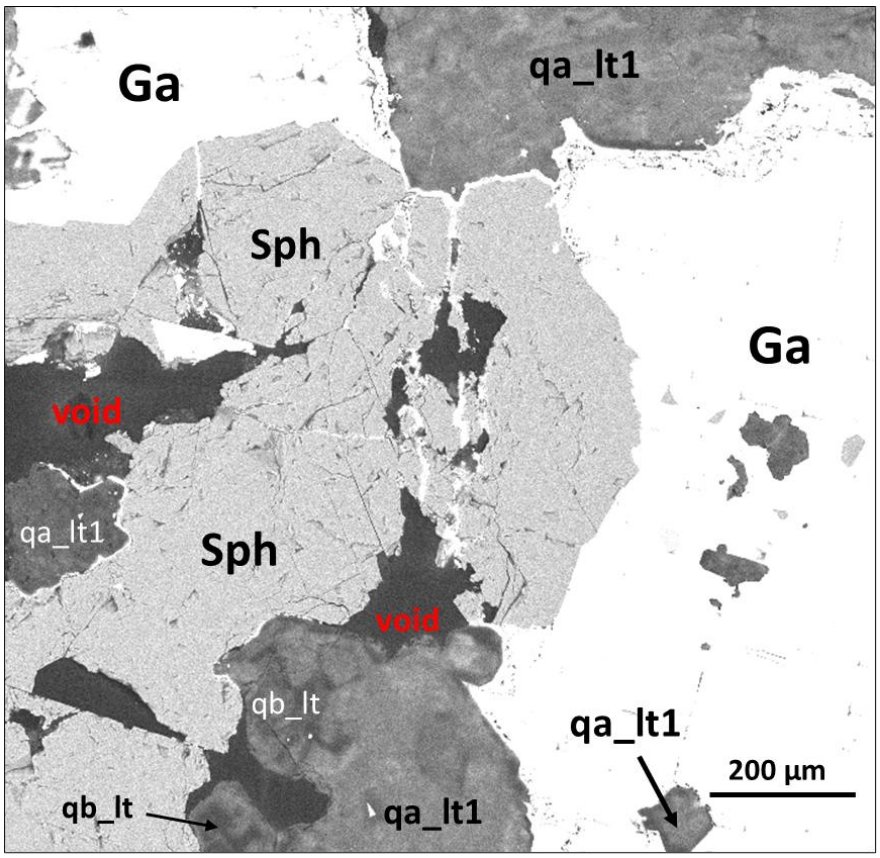

Figure 5.23 CL Blue mode image extracted from the LS1b thin section analysis, especially showing the relationships between galena and sphalerite. Galena also occurs in sphalerite fractures.

28861-2

Quartz: Euhedral to sub-euhedral quartz crystals (QA_ch1; e.g., Figures 5.25a, b, c) represent the dominant and almost exclusive texture identified in thin section; the crystals show variable sizes (~50µm to ~800 µm of diameter) and medium grey colouration in the CL-Blue mode (Figure 5.25a, b). The texture labelled as QA_ch2 corresponds to the finer-grained quartz found adjacent to QA_ch1, emitting a slightly weaker response in SEM-CL (Figures 5.25a, c, f). The CL-Color mode additionally revealed a darker quartz texture (QB_ch), occurring only sporadically in the two thin sections (Figure 5.25d). Fractures that accommodate the original crystal boundaries and visually connect to galena mineralisation can also be observed (Figure 5.25c, e).

Sulphides: Galena is by far the dominant sulphide species observed in thin section; this shows somewhat worn texture with micron-scale vugs/fractures and an indented, extremely jagged morphology (Figures e.g., 5.25a, b). Sphalerite mineralisation has rarely been identified in physical connection to galena (Figure 5.25e), as most of it appears to have been vugged out. Both species overgrow QA_ch, where their secondary products fill inter and intra-crystal fractures.

Baryte is observed to occur sporadically and especially replenishing micro-vugs and cavities in galena.

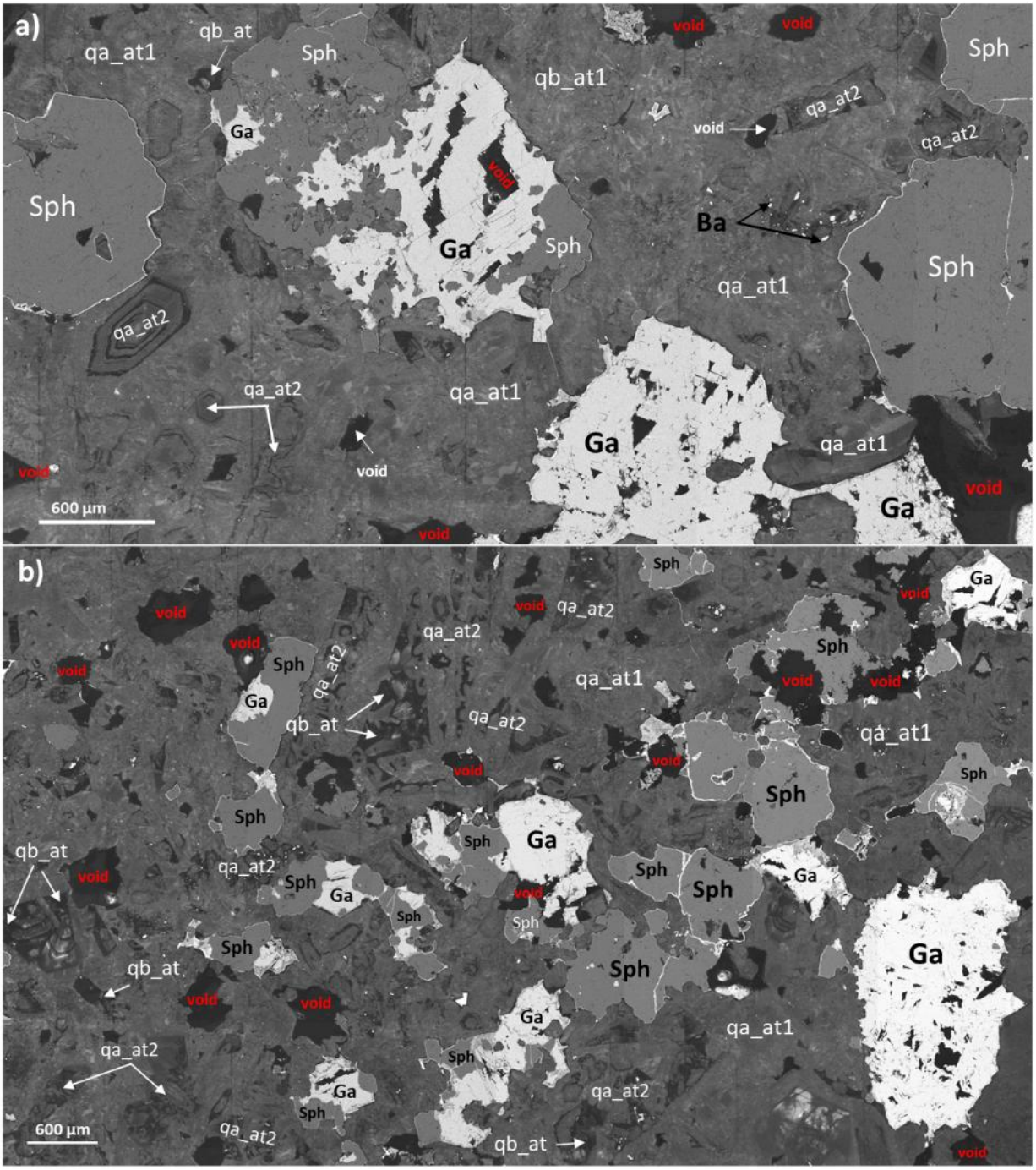

Figure 5.24 Relationships between quartz textures (qa_at1; qa_at2; qb_at) and sulphides (Ga and Sph) in the 28641 thin section. CL Blue mode.

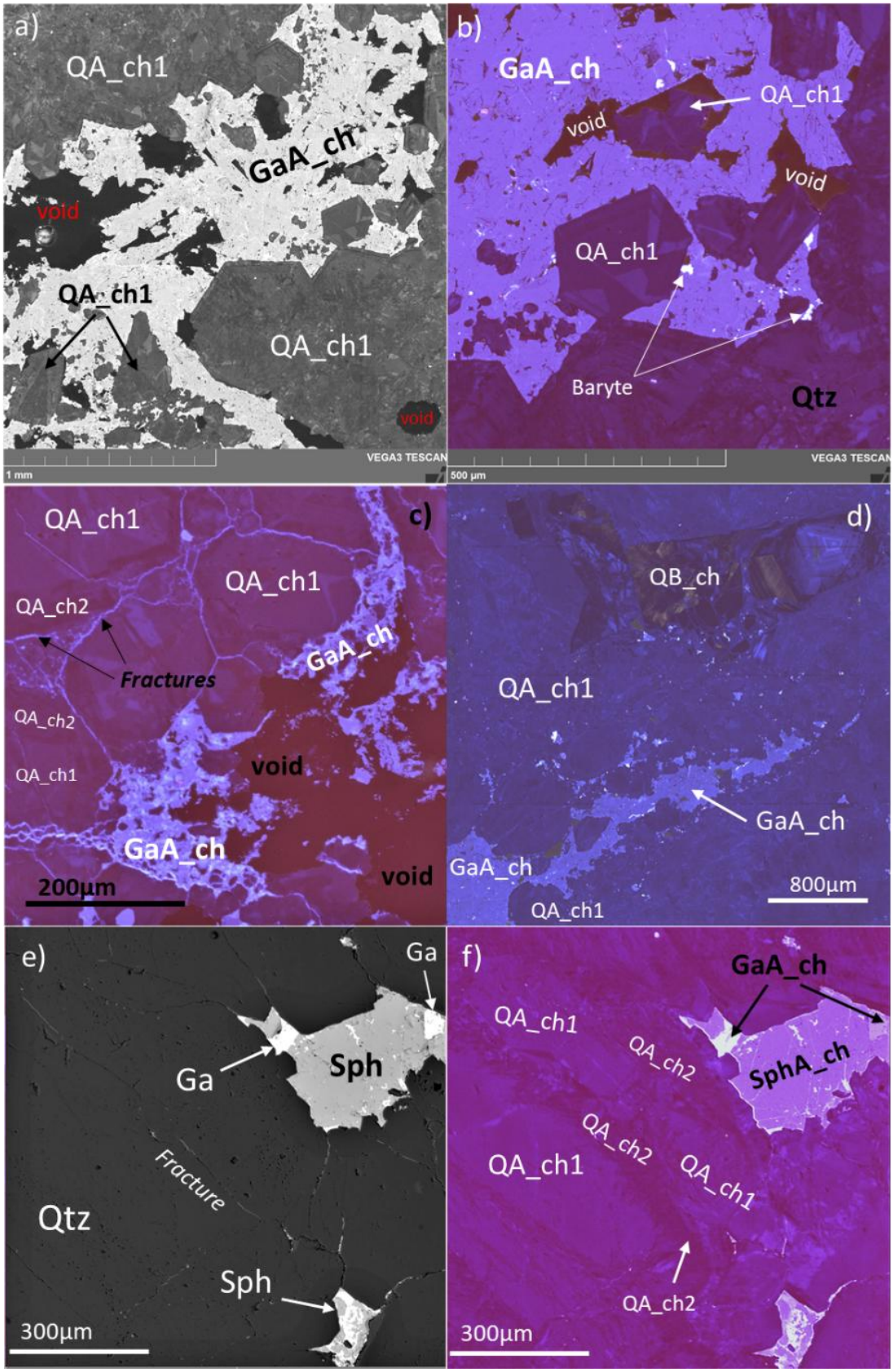

Figure 5.25 Textural and mineralogical characteristics in the 28861-2 thin sections. a) CL-Blue mode; b), c), d) f) CL-Color mode; e) BSE mode. Figure 5.25b shows a zoomed-in area of 5.25a, where the euhedral morphology of the QA_ch1 (quartz) crystals is clearly visible. In 5.25c, fractures tend to accommodate the original crystal boundaries; QA_ch1 and QA_ch2 can be distinguished within the crystals. Sphalerite (dominantly) and galena are the two sulphides visible in these sections.

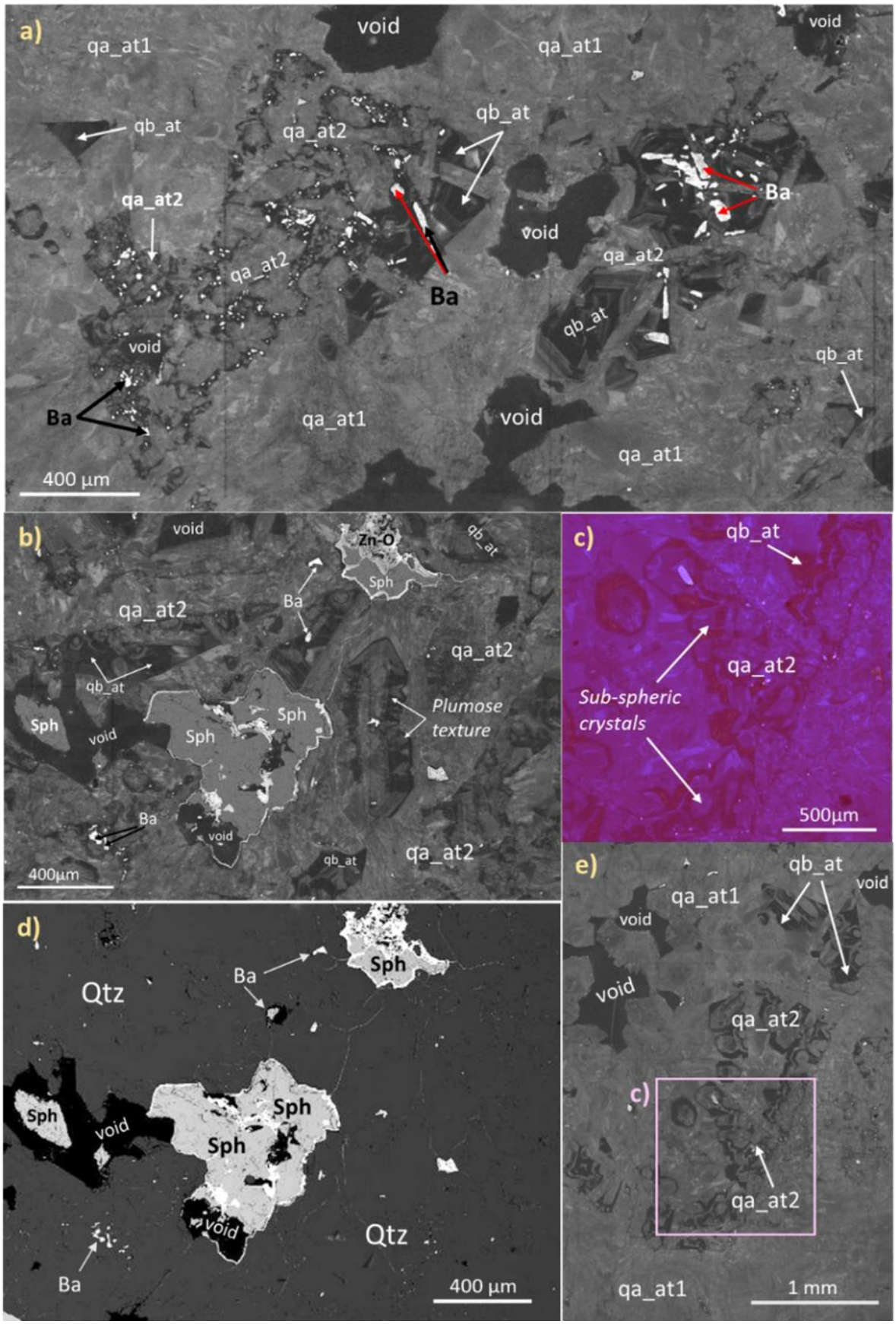

Figure 5.26 28641. Textural and mineralogical details in sections 28641-2. The observed mineralogical species are quartz, sphalerite, galena and baryte. Images a), b) and e) were captured using the CL blue channel, to highlight

characteristic quartz textural features (e.g., plumose texture) and distinguish between mineralisation events; some of these features are also displayed in 5.26c, obtained using the CL color channel.

RX30781-2

Quartz: SEM-CL investigations on this pair of thin sections have revealed a slightly greater variety of quartz textures and distinctive features. Fine-grained quartz interspersed with micas and mica-schist fragments has been identified from an overall chaotic, patchy appearance and a discrete CL-response, and indicated as QS_rx (Figures 5.27a and 5.29b, d). This texture occurs in physical continuity (e.g., Figures 5.27a and 5.29a) with larger (up to >1mm in length), elongated *comb* quartz crystals (QA_rx1), extending perpendicularly to the fine-grained quartz layer (Figures 5.27a and 5.29a, c). Frequent euhedral to sub-euhedral crystals, ranging in diameter size from 50µm up to 1mm and displaying consistent sector zoning, have been classified as the 'QA_rx2' texture. This appears to be continuous with QA_rx1, with a CL-brighter, microcrystalline texture (QA_rx3) and with a dark grey to black, almost featureless quartz texture (QB_rx; Figures 5.27s and 5.29a). A further, high-luminescence quartz stage (QC_rx) has been distinguished through sharp-edged veinlets formed of microcrystals that crosscut the previously described textures (e.g., Figure 5.27c).

Sulphides: A few pyrite crystals (up to) have been identified within the QS_rx stage and represent the only sulphide species observed in thin section (Figures 5.a29, b). They show shattered morphology and appear as re-cemented with the chaotic quartz gangue.

Baryte mineralisation occurs frequently in micro-fractures and cavities, particularly the ones located at the interface between QS_rx and QA_rx1 (Figures 5.28b, c and 5.29c). REE have also been very sporadically identified in quartz (Figure 5.29f). Only an extremely tiny *gold* particle (Figure 5.29e) has been detected in thin section; it has not been possible to relate it to any specific quartz stage.

LSLTD *(Dunan)*

The textural and mineralogical SEM-CL features exhibited by this sample are analogous to the ones reported for RX30781-2 (e.g., ''QS_dn'' quartz with embedded PyS_dn and euhedral QA_dn2; Figure 27d and f; Table 5.4), therefore they won't be repeated here. However, molybdenite has been identified in thin section as additional mineral species, sporadically occurring in micro-fractures that crosscut all the previous quartz generations (Table 5.4; Figure 27e). Furthermore, gold has here been detected as (a couple of) micron-scale particles located

on the surface of QA_dn2 - corresponding to the euhedral quartz crystals 'QA_rx2' in RX30781 (Figure 27f).

Figure 5.27. Thin sections RX30781 (a, b, c) and LSLTD (d, e, f). b), d), e) are in BSE mode.; a), c), f) are in CL Blue mode. SEM-CL imaging of these samples has illuminated the morphology of quartz crystals (5.27a and 5.27c), helped underpin the relationships between quartz and baryte (5.27a), and detected the presence of molybdenite and gold (5.27e and 5.27f, respectively).

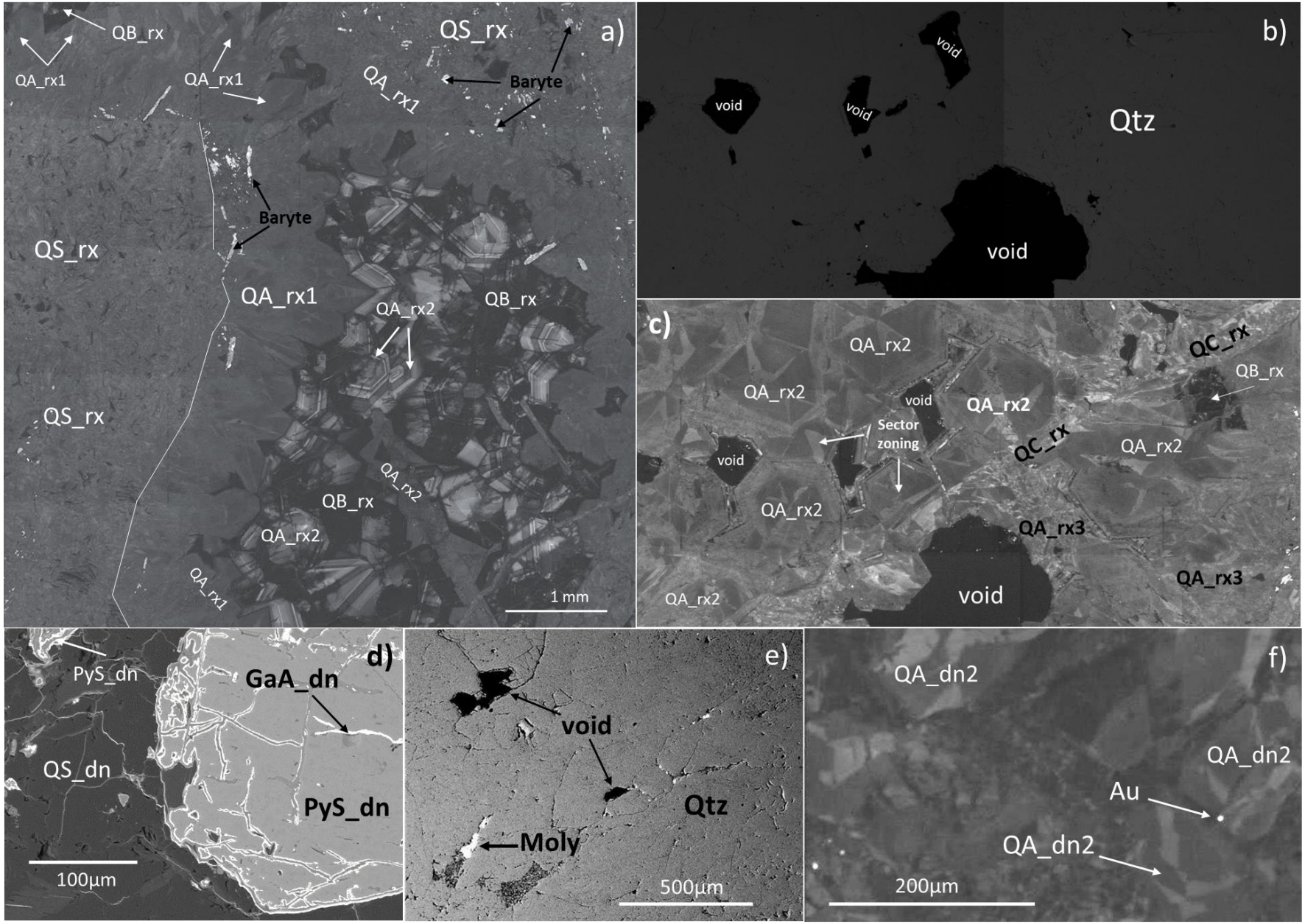
a)
QB_rx
QA_rx1
QA_rx1
QS_rx
QA_rx1
Baryte
Baryte
QS_rx
QA_rx1
QA_rx2
QB_rx
QS_rx
QA_rx2
QB_rx
QA_rx2
QA_rx1
1 mm
b)
void
void
void
Qtz
void
c)
QA_rx2
QC_rx
QB_rx
QA_rx2
void
QA_rx2
Sector zoning
QC_rx
QA_rx2
void
QA_rx2
QA_rx3
QA_rx3
QA_rx2
void
d)
PyS_dn
GaA_dn
QS_dn
PyS_dn
100µm
e)
void
Qtz
Moly
500µm
f)
QA_dn2
QA_dn2
Au
QA_dn2
200µm

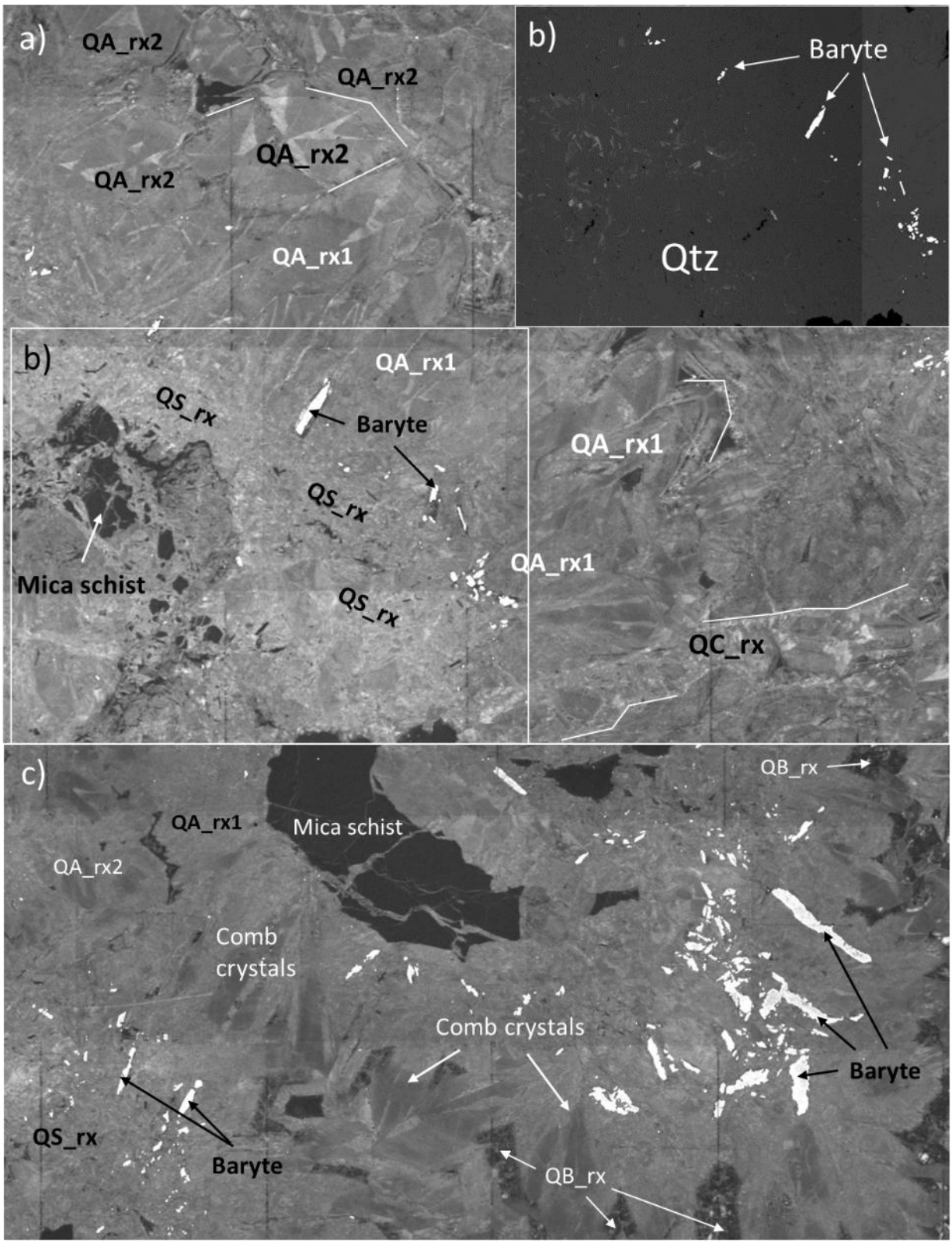

Figure 5.28 RX30781. All images are in the CL Blue mode, except 5.28b, which is in the BSE mode. Besides quartz, mica schist fragments appear in figures b) and c), while baryte, filling quartz intercristal spaces, can be distinguished from the bright coloration in c). The characteristic "comb" shape of the crystals can be distinguished in 5.28c. QS_rx indicates the fine-grained quartz interspersed with mica-schist fragments.

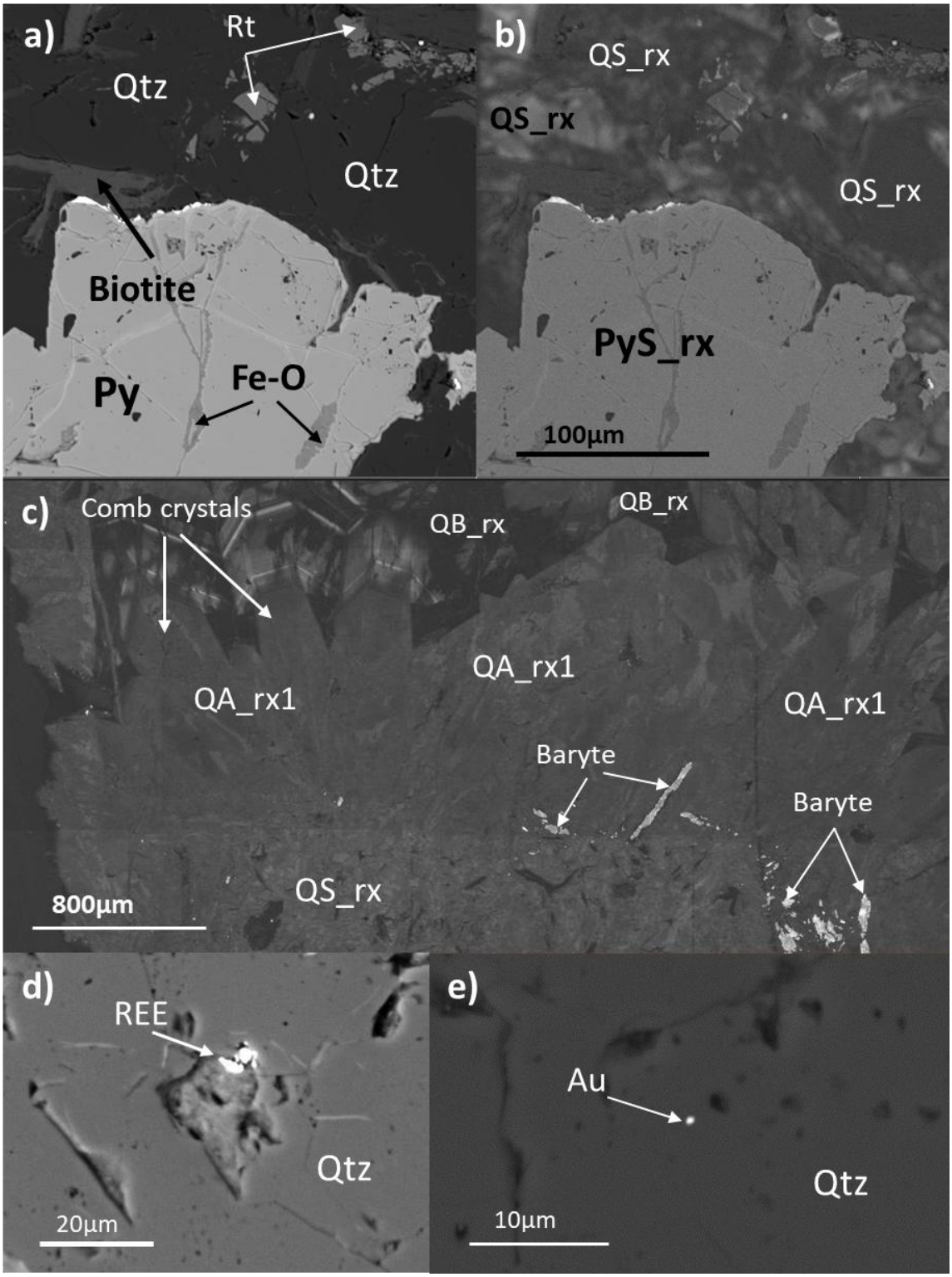

Figure 5.29 RX30781-2 thin sections. A), d), e) SEM-BSE mode; b) and c) CL Blue mode. Comb morphologies are visible in c).

Table 5.4 synthetizes all the main textural and mineralogical features with their mutual crosscutting relationships in the Lead Trial vein samples, as these have been observed and illustrated in the present (5.2.3.1) section.

Mineral	*Thin section(s) ID*	S	A1	A2	B	C	D
Quartz	*LSLTA*		CL-bright euhedral to sub-euhedral crystals, internally showing both sector and euhedral zoning. In contact with A2 and brecciated by B and C. Overgrown by GaA and SphA.	Fine-grained quartz adjacent to A1, emitting slightly weaker response in SEM-CL. Overgrown by GaA and SphA. **Au** particles on the surface.	Dark grey and featureless, emits the weakest CL response. Brecciates A, sometimes contoures GaA and ShpA.	Highly luminescent, sporadic sharp-edged veinlets. Crossuct A and B.	
	LS1, 2864		CL-bright sub-euhedral to euhedral crystals. In contact with A2 and B. Overgrown by GaA and SphA and crosscut by C in LS1.	Medium-grey, concentric, hexagonal to feather-like textures. Overgrown by GaA and SphA, embedded in A1 and often surronded by B.	CL-dark, featureless texture. In contact with A1, surrounds A2 and sometimes GaA and SphA.	Highly luminescent, sporadic sharp-edged veinlets (observed in LS1). Crossuct A and B.	
	2886		CL-bright euhedral to sub-euhedral crystals with internal sector zoning. In contact with A2 and overgrown by GaA and Sph.	Fine-grained quartz adjacent to A1, emitting slightly weaker response in SEM-CL. Overgrown by GaA and SphA.	Sporadic, CL-dark texture. In contact with A.		
	RX3078, LSLTD	QS_rx (A0) and QS_dn texture; patchy, fine-grained quartz interspersed with micas. In contact with A1 and hosting PyS.	**A1**: QA_rx1 (and QA_dn1) texture; quartz crystals elongated perpendicularly to the QS_rx layer. In physical continuity with A2.	**A2**: QA_rx2 (and QA_dn2) texture; CL-bright euhedral to sub-euhedral crystals with internal sector zoning. In contact with A1, A3 and B. **A3**: A3 texture; CL-bright microcrystalline quartz. In contact with A2 (QA_rx2).	CL-dark, featureless texture. Found in contact with all the other quartz phases.	Highly luminescent, sporadic sharp-edged veinlets. Crossuct A and B.	
		S	**A1**	**A2**	**B**	**C**	**D**
Baryte	*LSLTA, LS1, 2886, LSLTD*						Sporadic, generally fills up micro-discontinuities in any of the quartz textures and sulphides.
	2864					Relatively abundant micron-scale agglomerates, occur almost entirely in QA2 cavities and/or on top of QB.	
	RX3078		Frequent, particularly occurs in micro-fractures and cavities at the interface between QAS and QA1.				
Galena	*LSLTA, LS1, 2886*			CL-bright, generally shows indented boundaries and internal fractures. Overgrows QA1 and QA2 and coprecipitates with SphA.			
	2864			Overgrows qa_at1 and qa_at2, becoming more densely distributed and smaller (up to the µm scale) in proximity to the qa_at2 patterns. Coprecipitates with Sph.			
	LSLTD		Ga1_dn. Fills up micro-fractures in PyS_dn.	Pb-rich fluids. Infill spaces in between			
Sphalerite	*LSLTA, LS1, 2886*			Homogeneous coloration. Often shows indented boundaries, internal fractures and intense weathering. Overgrows QA1 and QA2 and coprecipitates with GaA.			
	2864			Overgrows qa_at1 and qa_at2, becoming more densely distributed and smaller (up to the µm scale) in proximity to the qa_at2 patterns. Coprecipitates with Ga.			
Pyrite	*RX3078, LSLTD*	Shattered crystals embedded in QS_rx and QS_dn.					
Gold	*LSTA, RX3078, LSLTD*			Micron-scale particles on the surface of QA			
Molybdenite	*LSTD*						Sporadic, occurs in micro-fractures across previous stages.

Table 5.4. Summary of the textural features and crosscutting relationships in and between the Lead Trial vein samples.

5.2.4 Coire Buidhe

Information on the rock samples selected from this locality for the purpose of SEM-CL analyses is summarised in Table 5.5, in line with the field observations described in Section 5.2.4. The specimens were first approached based on their sampling location and macrotextures (Figure 5.30).

Table 5.5 Thin section IDs and textural, mineralogical features of the Coire Buidhe rock samples.'' indicates that the sample was provided by Erris Gold Resources.*

Thin section IDs	***Rock sample ID***	***Hand specimen characteristics***	***Sample type***	***Grid reference***
LSBOIL1, 2	***LSBOIL***	Translucent/white, crystalline to microcrystalline (figure 1a). Visible coarse galena (figures 19c, d - section 3.1.4.).	Mine dump - Float	NN 7045 3403
LS2	***LS2***	White, crystalline quartz. Visible coarse, metallic galena (figures 1c, d).	In-situ vein	NN 6999 3472
LSCB1-2	***LSCB****	White to glassy quartz and a few visible pyrite and pyrrhotite (figures 1b).	Mine dump - Float	NN 6892 7345
	LScb	Quartz texture and mineral assemblage analogous to LSCB.	Mine dump - Float	NN 6892 7345

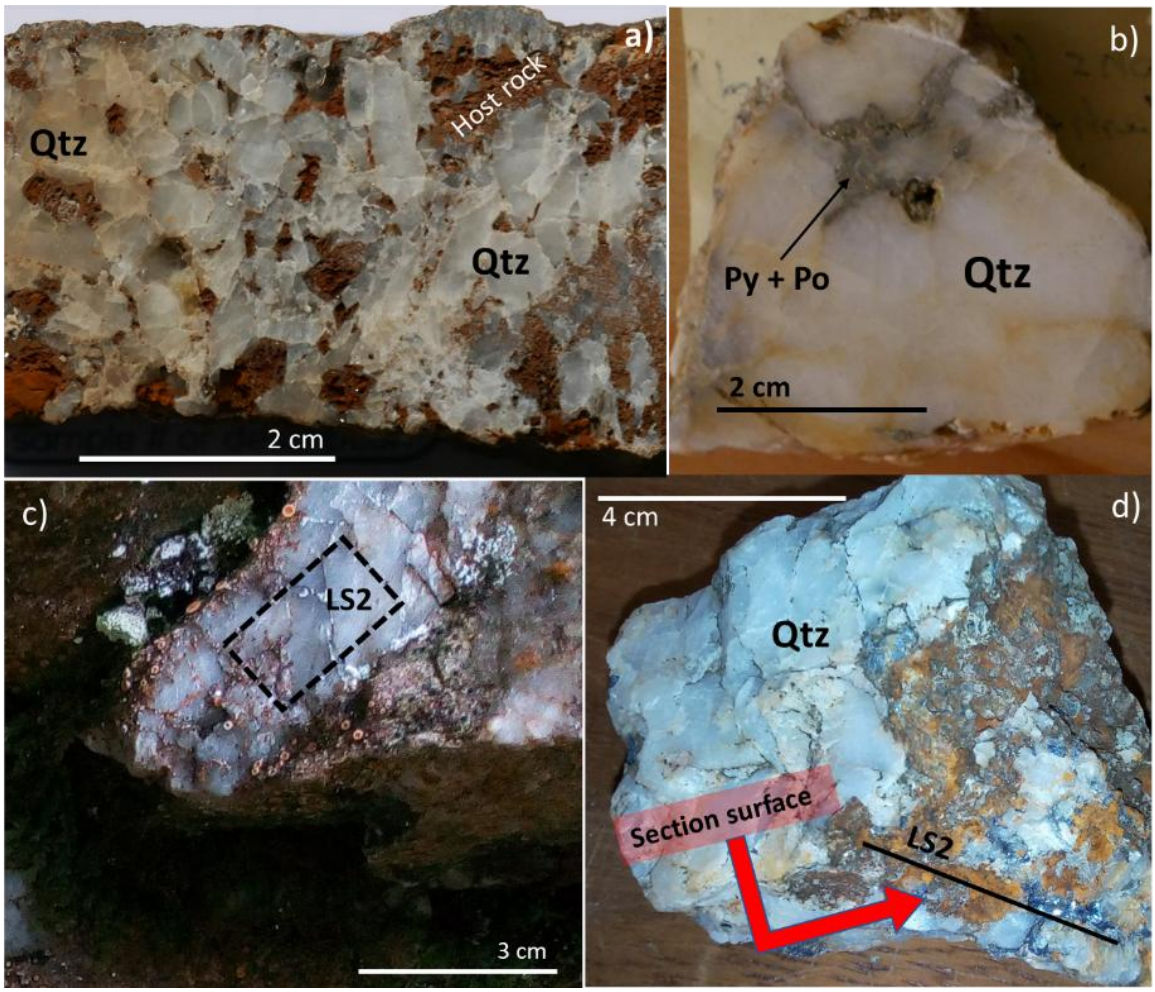

Figure 5.30. a) and b) ''fresh-cut'' quartz surfaces across the LSBOIL and LSCB rock samples to extract the respective thin sections; c) and d) LS1 in-situ vein and derived rock sample.

5.2.4.1 SEM-CL investigations

'LSBOIL' set

Figure 5.31 provides BSE and CL overviews (5.31a and b, respectively) and in detail (5.31d and c) of LSBOIL2. Two main quartz stages have been distinguished – QA_bl is light grey, slightly mottled, and shows traces of euhedral zonation; QB_bl is much darker, homogeneous, and overprints QA with non-luminescent bands of variable thickness (fig. 5.31c). Galena is the dominant sulphide mineral in LSBOIL1, appearing somewhat weathered and crosscut by micro-fractures; it is enclosed in QB (Figures 5.32c and d). A more detailed BSE-mode investigation of both LSBOIL2 (Figure 5.32a) and LSBOIL1 (Figure 5.32c) has revealed the presence of very sporadic pyrite (one ~250µm crystal) within the quartz gangue, and overgrowing ankerite. The latter massively comes across fractures (QC? fig. 5.32b) that cut QA and QB, forming angularly shaped agglomerates infilled with Fe-oxide.

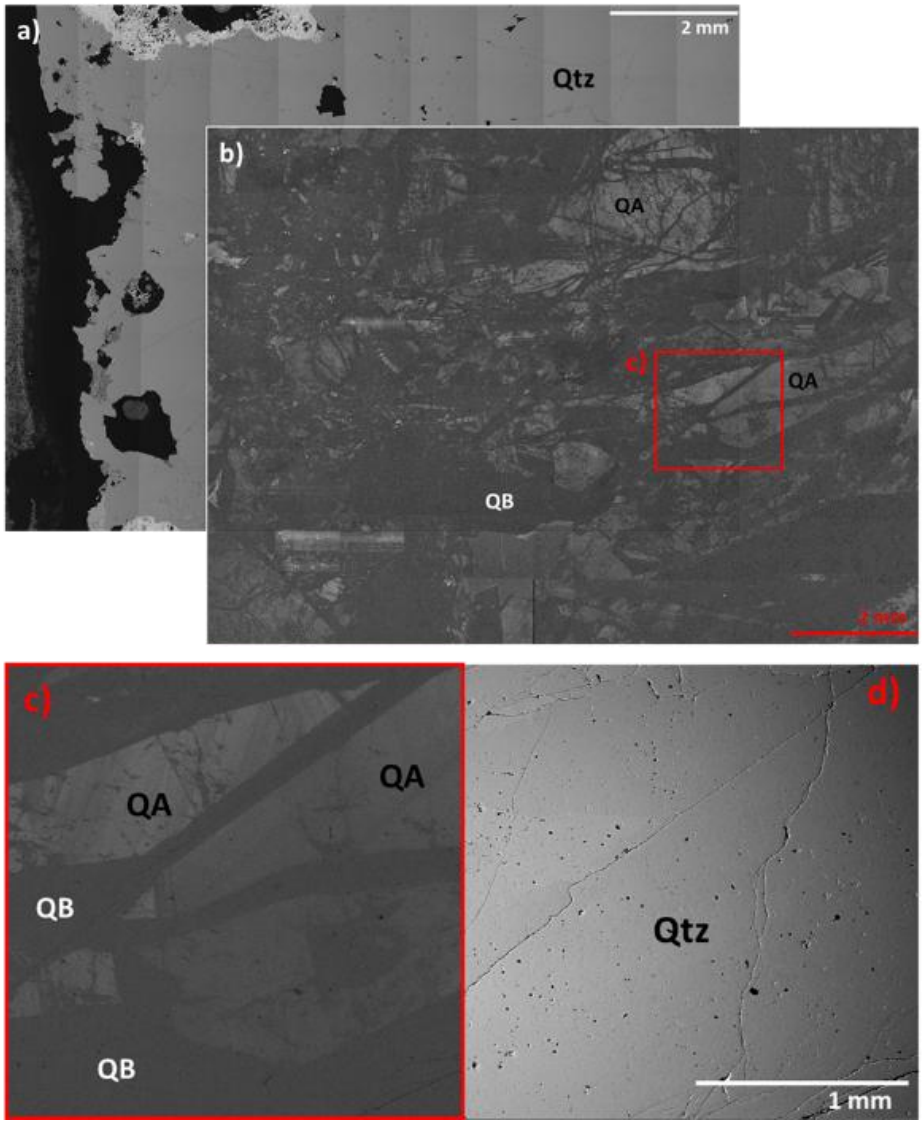

Figure 5.31 investigation of the LSBOIL2 thin section. 5.31a and b are BSE and CL Blue overviews (respectively) of two section areas and of the same section area, where the two images overlap (the underlaying area of the BSE map is visually mostly homogeneous due to the dominant presence of quartz; full view available in the Appendix; c) is a detail of 5.31b (still CL Blue mode), and d) is the BSE equivalent of the same section area.

LS2

This thin section is derived from one of the few in-situ veins found exposed at Coire Buidhe (Figures 5.19a and b). Quartz and galena are the two main minerals identified in SEM-BSE mode (Figure 5.32f), accompanied by a few alteration species (e.g. Fe-oxides and Pb-derived products/cerussite). In CL Blue mode galena appears enclosed in/infills a grey, uniform, non-luminescent quartz stage (QB). This quartz texture dominates the thin section thoroughly, although it is occasionally found fractured by very thin and brighter quartz injections (QC, Figure 5.32e). The 'LS2' galena mineralisation has resulted in an overall more cohesive and less weathered texture than the one observed in the LSBOIL thin sections; micron-scale crystals of (presumably) lilianite marginally overgrow the galena (relevant image included in Appendix 2).

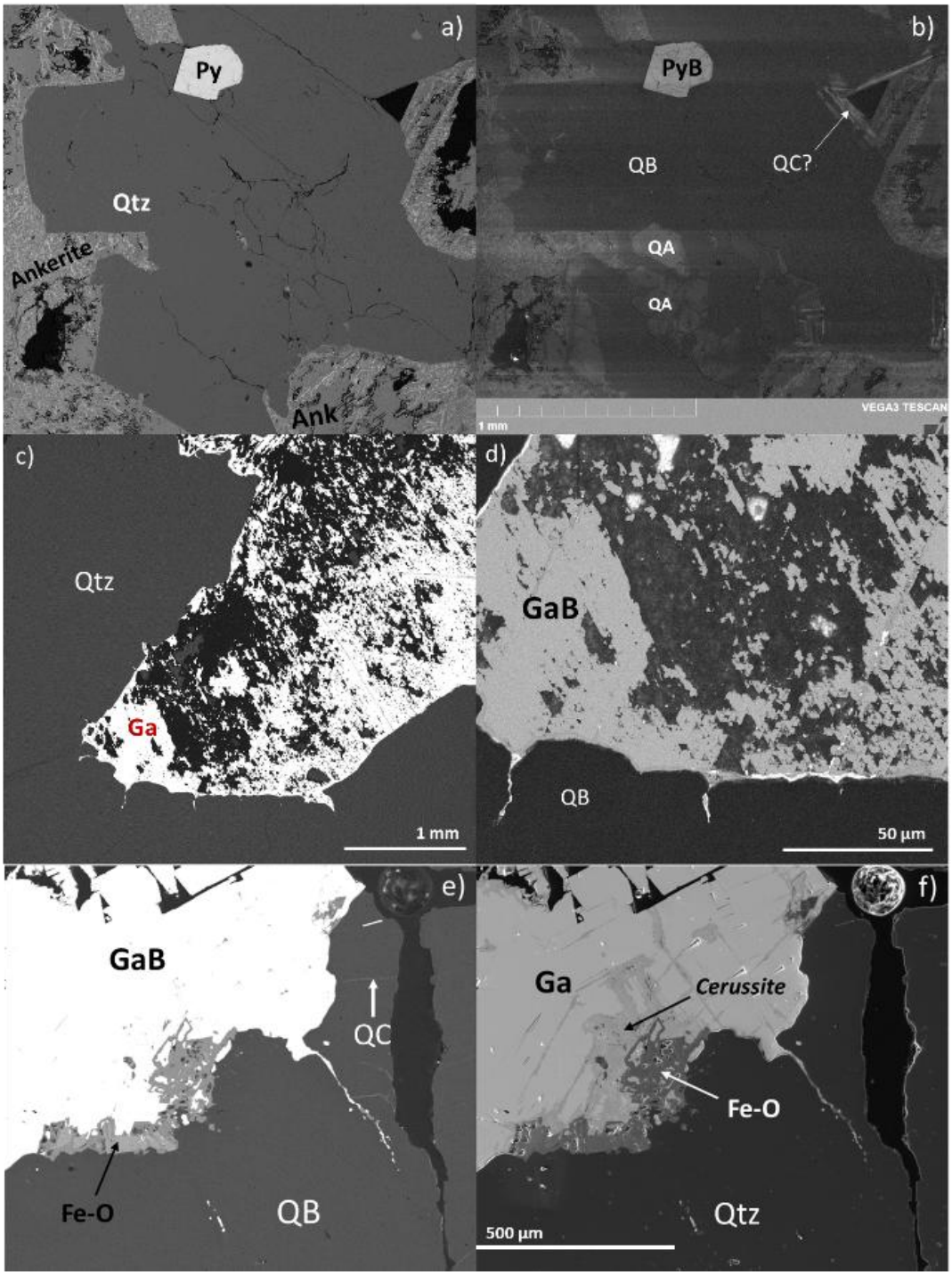

Figure 5.32 a) and b) BSE and CL Blue mode images, respectively, of the same section area in LSBOIL2; c) and d) are BSE and CL Panchro mode images, respectively, of two different areas of LSBOIL1; e) and f) are, respectively, CL Blue and SE mode images of the section area in LS1, where galena and quartz relationships can best be appreciated.

LSCB1-2

The rock sample was retrieved as *float* in a spoil heap and made available by Erris Gold Resources (2020). It has appeared mostly composed of white to glassy quartz and a few visible pyrite and pyrrhotite (LSCB, Table 5.5).

Quartz: Two major quartz textures have been identified and labelled as 'QA_cb' and 'QB_cb' (e.g., Figures 5.33c, 5.34f and 5.35c). QA_cb is pale, luminescent and shows patchy traces of internal zonation; QB_cb appears darker, featureless, and overprints QA_cb. A third quartz phase (QC_cb) might be associated with the bright contours (optically similar to QA_cb) that surround a few pyrrhotite crystals in both thin sections (Figure 5.35b); this would be the most luminescent phase, however, it is unclear whether it represents a separate quartz stage or a simple optical feature related to a mechanical process in QB_cb. QD_cb consists of bright, thin fractures crosscutting the previous quartz phases (Figure 5.35d).

Biotite appears to overgrow both quartz generations and sulphide mineralisation; in particular, it extensively brecciates the chalcopyrite (CpyB_ch) mineralisation (Figure 5.33).

Sulphides: Chalcopyrite, pyrrhotite and pyrite are the three main sulphide minerals identified in LSCB1 and have all been found in contact with quartz. Pyrrhotite and pyrite are in direct contact with each other and are often difficult to distinguish without EDS analysis (e.g., Figure 5.34c); it has not been possible to observe chalcopyrite in physical contact with the other two sulphides, because of the intense brecciation especially occurring within and around the former. Pyrite appears subhedral to anhedral and is generally embedded in the dark quartz overprint (QB_cb) (e.g., Figure 5.34f). Chalcopyrite shows extremely irregular boundaries and, when unaffected by brecciation (Figure 5.33c), is also surrounded by QB_ch. In LSCB1, pyrrhotite has been observed in the form of irregularly-shaped crystals, in an overall physical continuity with each other and no surrounding gangue (e.g., fig 5.34c). In LSCB2, pyrrhotite is the only sulphide species detected and overall shows well-defined boundaries; it is overall enclosed in QB_cb (Figure_5.35a, b, e), although a couple of crystals have been found in direct contact with the uncertain, brightest quartz phase, QC_cb (Figure 5.35b). Sphalerite and galena have only been identified as blemishes/inclusions in a couple of pyrite crystals (LSCB1, SphB_cb, GaB_cb; Figures 5.34a, d). Arsenopyrite has been identified as micron-scale fragments embedded in QB_cb (LSCB2, Figures 5.36a, b), likely within micro-fractures.

Gold has only been observed in the form of extremely small particles (up to 25µm), almost always on the surface of QB_cb, often within local micro-cracks (AuB_cb and AuC_cb, Figures

5.36d-g). One gold particle has additionally been found right on the edge of a pyrite crystal (Figure 5.34b), in turn, connected to QB_cb.

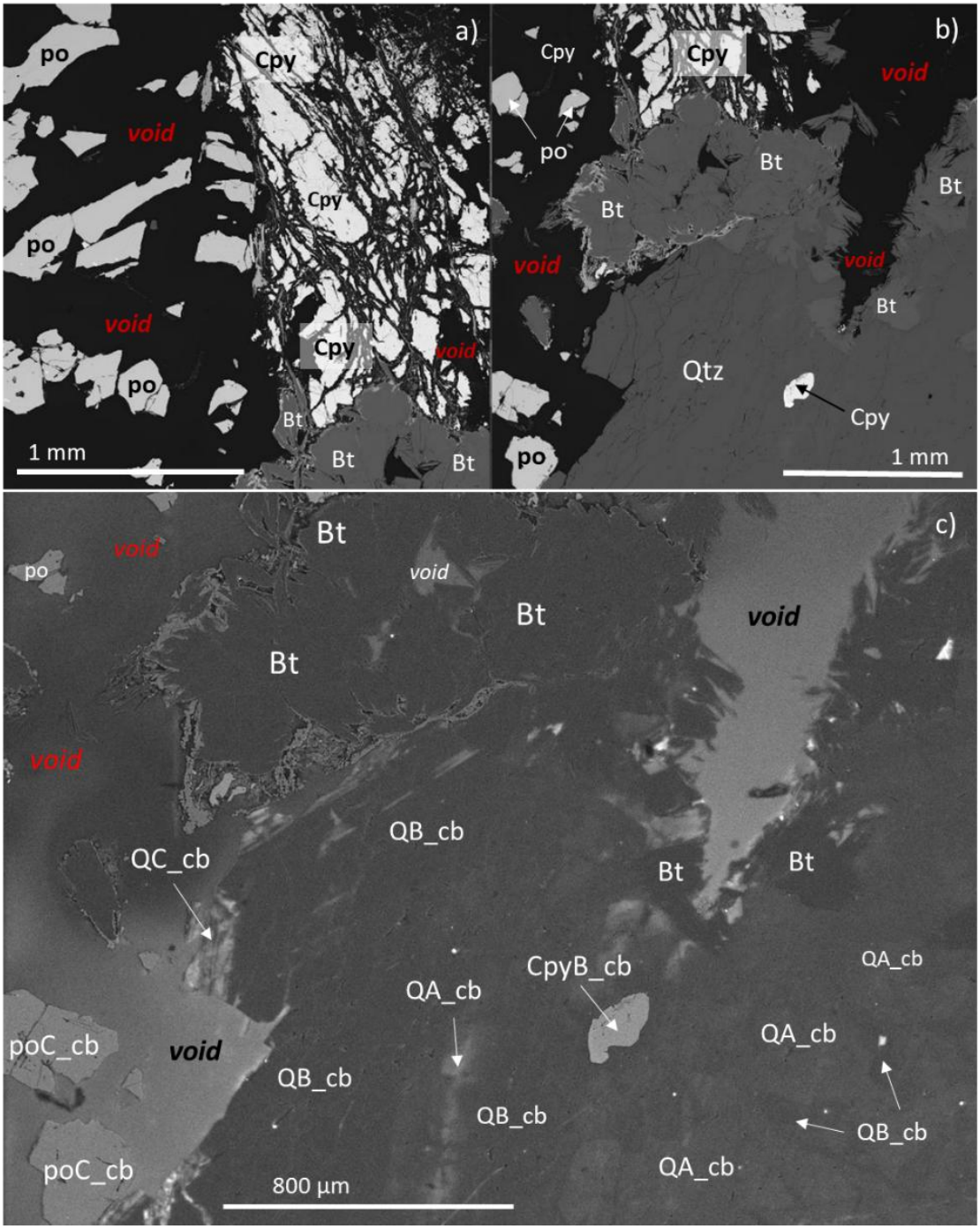

Figure 5.33 LSCB1. a) and b) BSE mode; c) CL Blue mode. Fragmented pyrrhotite (Po) and brecciated chalcopyrite (Cpy) are well visible as sulphides in LSCB1a and LSCB1b; Biotite (Bt) is also visible in all three figures, appearing in physical contact with chalcopyrite and quartz.

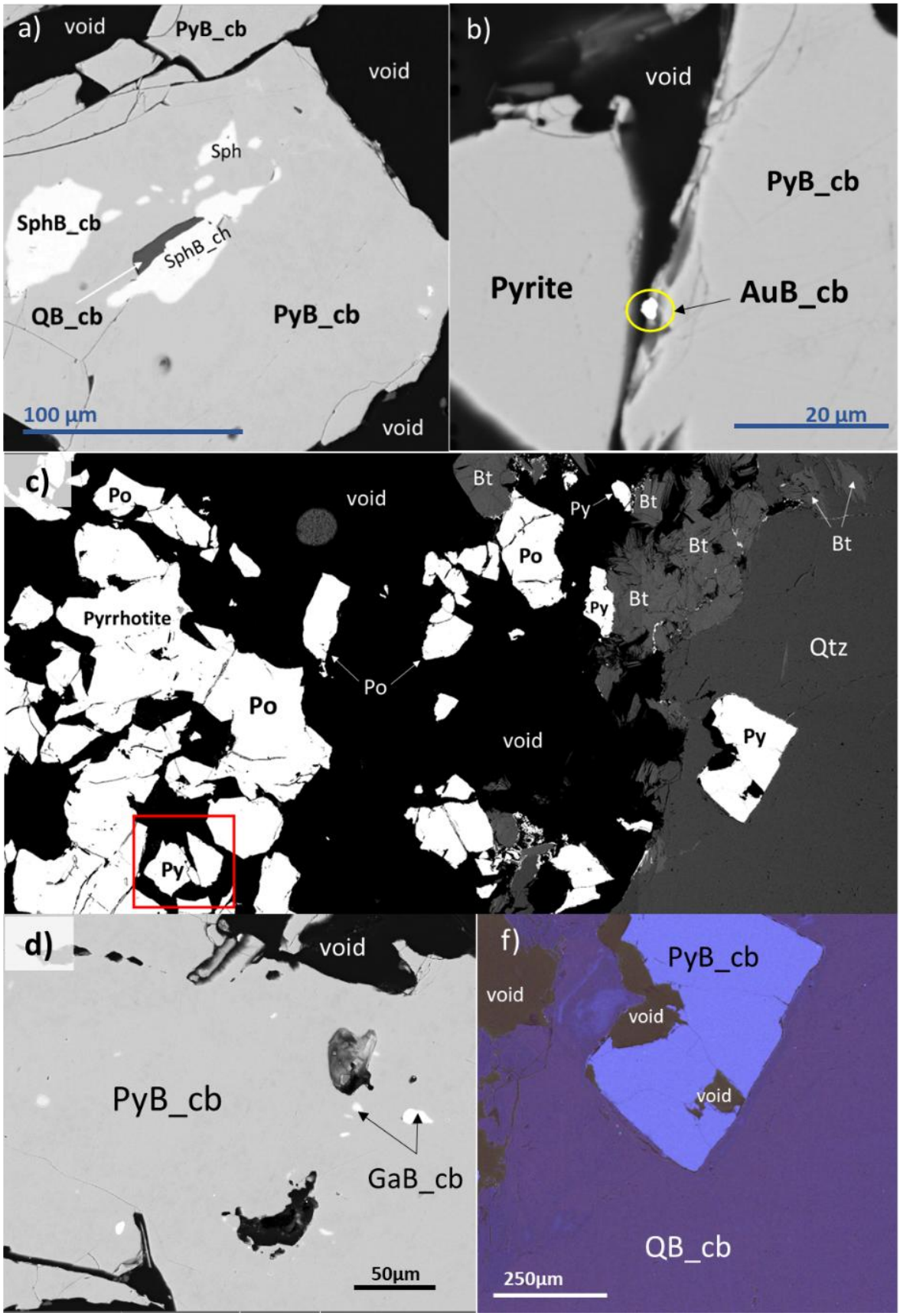

Figure 5.34 Mineralogical components in LSCB1 & LSCB2. a) to d) BSE mode; f) Color CL mode. 5.34a and 5.35b respectively display sphalerite blemishes and galena inclusions in pyrite; gold in a pyrite fracture is shown in 5.34b. The sample contest (in BSE) of 5.34b is provided in 5.34c.

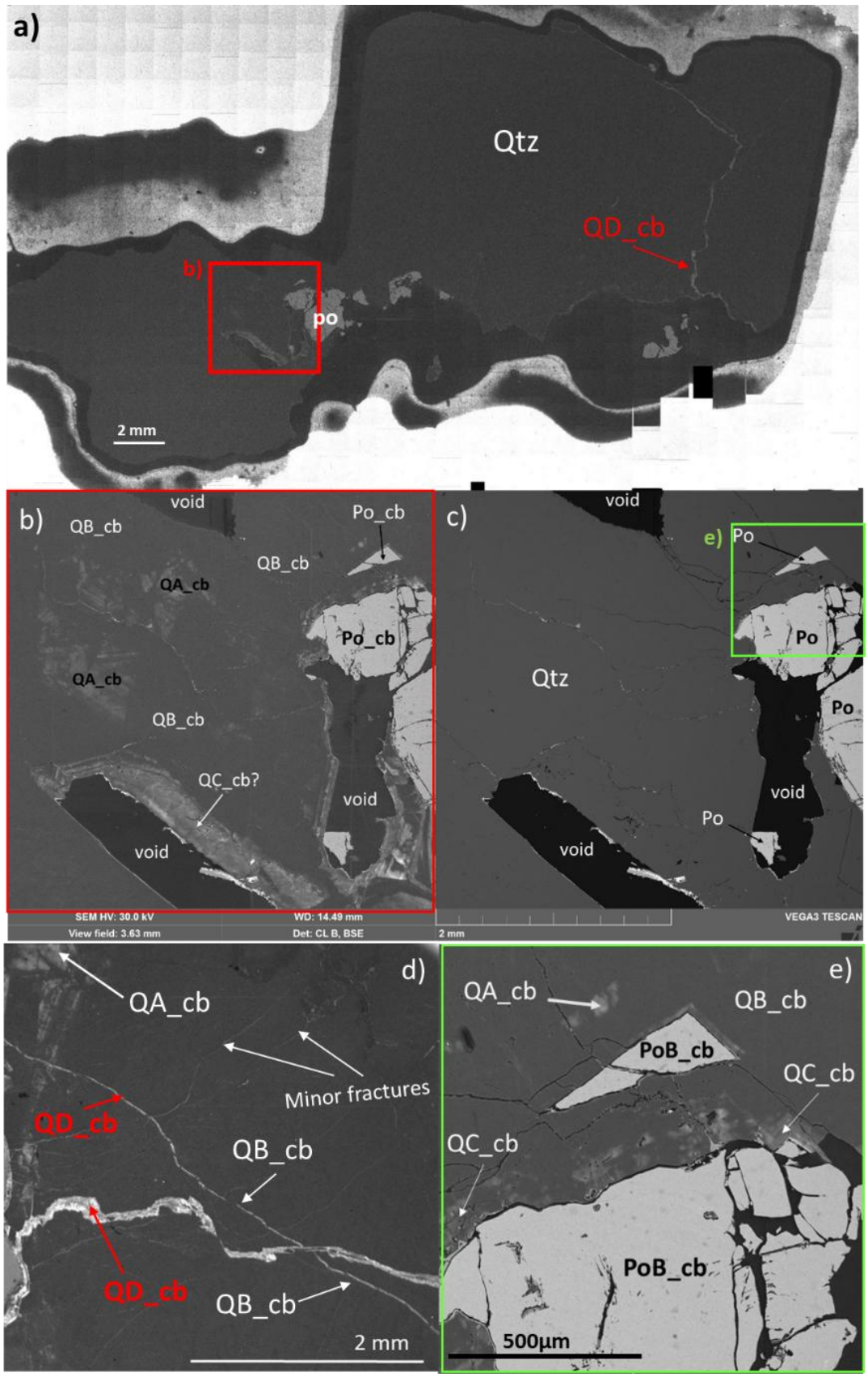

Figure 5.35 LSCB2 thin section. a), b), d) and e) CL Blue mode; c) BSE mode. a) shows an almost full thin section scan in CL. The relationships between quartz and pyrrhotite (Po) are clarified in b) and e), where the "uncertain" QC_cb phase is also evident. Minor veinlets and fractures are visible in d).

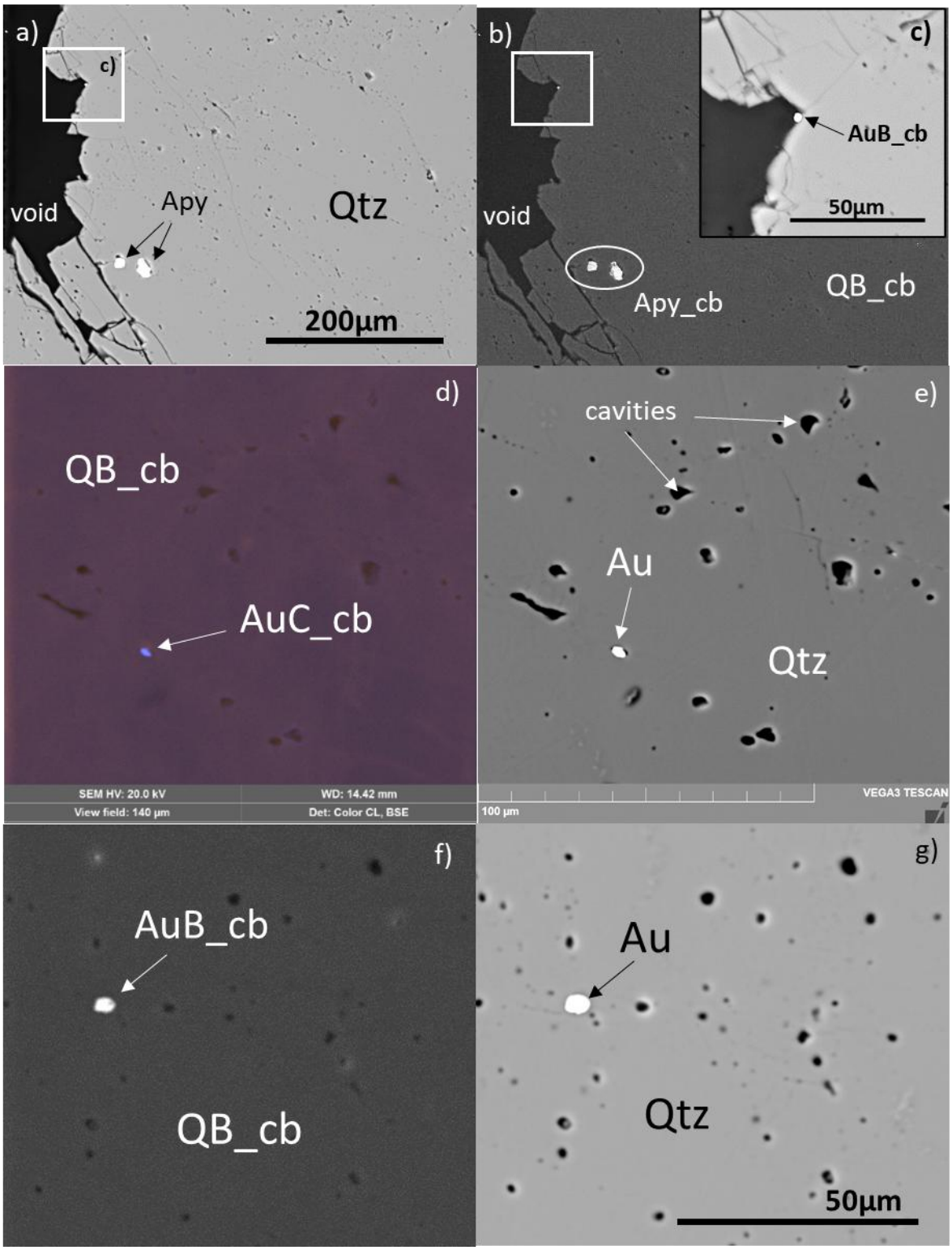

Figure 5.36. LSCB1 & LSCB2. a), c), e), g) BSE mode; d) CL Color mode; f) CL Blue mode - the bright Au response is a BSE artifact, not a true CL response. Au appears to fill cavities in most of these cases displayed in this figure. The context of c), where the gold particle is located on a QB_cb margin, is indicated in b).

Table 5.6 reports the main textural and mineralogical features in the Coire Buidhe vein samples according to their relative occurrence stages, as these have been illustrated in the present (5.2.4.1) section.

Table 5.6. Summary of the textural features and crosscutting relationships in the Coire Buidhe vein samples (Figures refs relative to each description to be added).

Mineral	***Thin section(s) ID***	**A**	**B**	**C**	**D**
Quartz	*LSBOIL*	Light grey, slightly mottled, showing weak euhedral zonation.	Dark grey, homogeneous, overprints QA_bl and incorporates GaB and PyB.	QC? Fracturing event associated with Ankerite.	
	LS2		Dark grey, homogeneous, incoroporating GaB and fractured by QC.	Hairline infills (QC) in QB.	
	LSCB	Pale, luminescent, with patchy internal zonation.	Dark grey, featureless, overprints QA_cb. Hosting the sulphide mineralisation (at least PyB and CpyB).	Uncertain whether this constitutes a separate, later quartz stage or simply mechanical overprint - bright contours around vugs and sulphides.	Bright, thin fractures crosscutting the previous quartz phases (If QC is not to be considered as actual quartz stage, then QD becomes QC).
Ankerite (?)	*LSBOIL*			Fairly massive, comes across fractures cutting QA_bl and QB_bl.	
Pyrite	*LSBOIL*		Micron-scale grains incorporated in QB; internal fracturing observed.		
	LSCB		Subhedral to anhedral, embedded in QB. Sometimes in contact with Po or with Bt.		
Pyrrotite	*LSCB*		Irregularly-shaped crystals, embedded in QB. Sometimes in contact with Py or with Bt.		
Chalcopyrite	*LSCB*		Often brecciated and with irregular morphology. Primarily found in contact with Bt, but also surrounded by QB.		
Arsenopyrite	*LSCB*		Micron-scale fragments embedded in QB_cb.		
Galena	*LSBOIL*		GaB_bl'. Somewhat weathered, enclosed in QB. Crosscut by minor fractures.	Partially infills extremely thin fractures that cut QA_bl and QB_bl.	
	LS2		GaB_ls2'. Less weathered and more homogeneous than GaB_bl, enclosed in QB. Crosscut by minor fractures.	Partially infills extremely thin fractures that cut QA and QB.	
	LSCB		Small inclusions (<20µm) in PyB_cb.		
Sphalerite	*LSCB*		Blemishes (up to 90µm) in PyB_cb.		
Gold	*LSCB*		Micron-scale particles on the surface of QB_cb and on the surface of PyB_cb.	Micron-scale particles in micro-cavities within QB.	

5.3 Vein paragenetic interpretations

An interpretation of the paragenetic histories of the main hydrothermal veins in the Loch Tay area has relied upon the characterisation of individual mineral components and textures (see section 5.2), and the understanding of their mutual spatial (crosscutting) and genetic relationships. Hydrothermal quartz textures, particularly, have represented an effective tool for the depiction of different paragenetic stages and, to an extent, their association with potential genetic environments. Mineral species/assemblages coeval to each other and to a given quartz event have subsequently been placed at a specific paragenetic stage; the possible overlap of multiple mineralising stages constitutes the paragenetic history of a certain system.

5.3.1 Calliachar - Urlar Veins

Hydrothermal quartz-bearing veins from these localities (Calliachar and Urlar Burn), whose mineralogy and textures have been investigated in detail for the purposes of this study, correlate to the ones that Ixer et al. (1997) classified as high-grade gold-bearing veins (with exception of V9 Vein) across Calliachar Burn, and as gold and sulphide-bearing veins across Urlar Burn.

5.3.1.1 Interpretation of the different quartz textures

Q1-Q2

Two volumetrically dominant quartz textures have been identified in all the hydrothermal vein samples selected for investigation and can be reconciled to nearly (details will follow) all the QA and QB texture types in the individual veins. Due to the strong recurrence of these two textures between veins, their paragenetic interpretation relies on an overarching approach and will be illustrated in the following paragraphs. The respective quartz stages are (comprehensively) indicated as Q1 and Q2, in line with their mutual chronology.

Q1 (QA_v3, QA_v9, QA_gv, QA_dv, QA_ls, QA_l3 in Section 5.2) is here assumed to be the first quartz event occurring in local veins. It has been recognised from the weak zoning of large euhedral crystals tending to nearly homogeneous texture, and has been interpreted as a 'mottled' euhedral quartz texture. Mottled textures may constitute primary precipitation features in cases where quartz grains grow at stable high temperatures and pressure, producing little internal lattice variation (Götze et al. 2005); however, they are typically associated with metamorphic quartz (Rusk, 2012) where original CL textures can be entirely or partially annealed, due to redistribution of lattice defects (e.g., Sprunt et al. 1978). It might sometimes be difficult to establish whether the quartz initially precipitated with little or no CL texture or whether a previously existing one was suppressed by annealing. Because evidence of original

textural features (i.e., internal zonation) is distinguishable to different degrees in the QA stage of all the hydrothermal veins at Calliachar/Urlar, QA is here interpreted as originally euhedral quartz, which precipitated in evolving fractures and developed zoning, and therefore corresponds to Q1.

Q2 (QB_v3, QB_v9, QB_gv, QB_dv, QB_ls, QB_l3 in Section 5.2) is represented by dark CL bands that overprint and sometimes fracture the mottled/euhedral quartz. Dark bands/infills are a common type of secondary texture in hydrothermal quartz and are typically related to healing processes (Rusk et al. 2012). Due to the lack of additional diagnostic features, this quartz generation has been similarly interpreted here and allocated to the second paragenetic stage. In one of the samples (G Vein), localised CL-dark bands (QB_gv; e.g., Figures 5.3 and 5.4) have additionally been found contouring the brighter, euhedral QA; they have been classified as a local Q2 sub-event (Q2gv), although this probably does not extend as a sub-category of Q2 in other veins.

Quartz stages after Q2

Later fracturing events have consistently been observed in all the hydrothermal veins at Calliachar/Urlar Burn. The quartz generations labelled 'QC_v3, QC_v9, QC_gv, QC_dv, QC_ls' in section 5.2 refer to the main CL-bright quartz event recognised in each Calliachar, which fractures the QB textures. Despite the shared optical and morphological similarities of such 'QC' textures between veins, it is however not possible to deduct from sole SEM-CL analysis whether the QC stage of a certain vein exactly corresponds to that of others. The individual Q3 stages are thus labelled by adding the respective vein label abbreviation (e.g., Q3_v3, Q3_gv). An overarching Q3 stage, at Calliachar-Urlar Burn, could be referred to by using the QC_ls (LS Vein, Calliachar Burn) texture as the most evident example. Diagnostic features are the inward-growing euhedral crystals which may suggest precipitation in open space during brittle deformation (Baele et al., 2019).

Similar reasoning applies to the later quartz events identified in individual veins on the basis of cross-cutting relationships (i.e., the QD type in section 5.2). The main shared feature is provided by their occurrence as tiny fracture infills, which is not in itself diagnostic. However, for the purpose of an overarching framework, these minor quartz pulses have been grouped as the Q4 event.

5.3.1.2 Constraints from the sulphide mineralisation

Sulphide minerals have been identified and located via SEM-EDS and SEM-CL in all the analysed veins from Calliachar/Urlar Burn, except the Discovery Vein (sulphides were reported in the latter by Ixer et al., 1997).

Pyrite

Pyrite mineralisation has been interpreted as occurring across at least two separate stages. The former pyrite comprises larger euhedral crystals that were only located in the G Vein, where they appear partially enveloped by both Q1 and Q2g. As mentioned earlier in the text, Q2g is interpreted to represent a restricted quartz event that locally overprints Q1, where the pyrite crystals are assumed to be already enclosed. Therefore, the euhedral (former) pyrite has been associated with the Q1 event and labelled 'Py1'. These pyrite crystals also appear to be crosscut by arrays of minor fractures, which can be visually prolonged into the surrounding quartz and dissect the pre-existing mineralisation. The earlier pyrite is likely to have been shattered, physically transported and cemented by 'new' quartz in a later stage (as supported by the visual juxtaposition of cataclastic, fragmented, pyrite that 'flows' above the former quartz and pyrite mineralisation), visible in the same sample. This subsequent pyrite (py3_gv, Figure 5.37a) event has been associated with a third, brighter quartz pulse (Q3_gv, Figure 5.37a) in the G Vein, where it appears accompanied by extensive iron oxidation and (sporadically) by shattered arsenopyrite (Apy3_gv) and sphalerite (Sph3_gv). A possibly coeval mineralising event is interpreted to occur in one of the Urlar Veins (py3_l3 in LSCL3), where it can be recognised from tiny pyrite crystals that are similarly surrounded by iron oxidation and come with the local third quartz event (Q3_l3, fig. 5.37a). In LSCL3, galena and chalcopyrite co-precipitate during such third stage (ga3_l3 and cpy3_l3, respectively; Figure 5.9d).

Shattered pyrite mineralisation has also consistently been observed in the LS and V9 Veins (py5), where it appears to be transported/recemented by chaotic quartz (Q5_v9) dolomite (dol5), and ankerite (ank5) agglomerates. The form in which these two gangue minerals have been noted across the sample suggests that they are part of a later paragenetic stage (S5) which incorporated pyrite clasts (Figure 5.7). Therefore, pyrite mineralisation could have been either coeval to Q5, or constitute an earlier phase that was re-cemented during S5. In the V9 Vein, such cataclastic pyrite sometimes hosts inclusions of galena and chalcopyrite, supporting the hypothesis of their coeval or potentially earlier stage in the paragenesis.

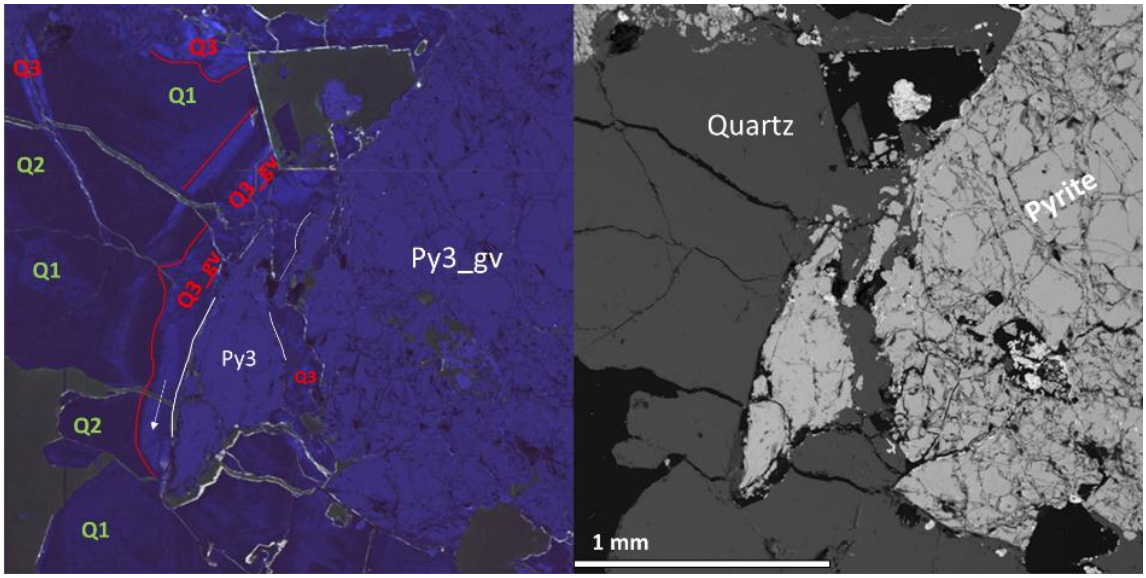

Figure 5.37 SEM-CL (a) and BSE (b) images of a section area from the G Vein, where the relationships between the Py3 cataclastic pyrite and the quartz stages (Q3_v3, Q2 and Q1) are visible. The rhombic void indicates the original presence of a carbonate (dolomite or ankerite) crystal.

Arsenopyrite

Arsenopyrite (apy3, fig. 5.38 b, c) has been identified in two of the Calliachar Veins (G Vein and LS Vein), where it consistently occurs with Q3_gv and as fragments and regular crystals. This modality might favour the hypotheses of either a possible arsenopyrite stage earlier in the paragenesis or of arsenopyrite coeval to Q3_gv in the relevant vein that has been physically shattered and recemented.

Galena

Galena mineralisation can be observed at a relatively high abundance in the V3 Vein (Calliachar) and LSCL3 (Urlar) samples, where it appears in contact with QC quartz textures. It has then been interpreted to precipitate with the Q3 quartz events (ga3, fig. 5.38 a, d). In LS4B (Urlar Burn), galena overall fills fractures that cut Q1 and Q2 and can consistently be linked to a later paragenetic stage; as supporting evidence, later fracturing in turn cuts galena mineralisation and shows no spatial continuity with earlier fracturing. The sulphide can additionally be observed in the form of small inclusions in cataclastic pyrite of both the G Vein and the V9 Vein; it can thus indirectly be linked to the respective third and fifth mineralising stages (ga3_gv and ga5_v9). Since inclusions are found in shattered pyrite (V9 vein, py5), they might however indicate the occurrence of an earlier galena mineralising stage before Q3.

Chalcopyrite

Chalcopyrite mineralisation, as it is observed in the Calliachar and Urlar veins, has been related to paragenetic stages interpreted to be equivalent to those of the galena mineralisation, because it co-precipitates with galena in both the rock samples from Urlar Burn and in the V3 Vein from Calliachar Burn (along with the Q3 stage). It additionally occurs as small inclusions within the cataclastic pyrite in the V9 Vein (py5). Chalcopyrite is consequently assumed to occur at least across S3 (cpy3) and S5.

Sphalerite

Sphalerite mineralisation has only been identified in the form of small crystals across the QC event of the G Vein. It is thence interpreted to precipitate during the S3 stage of the same vein.

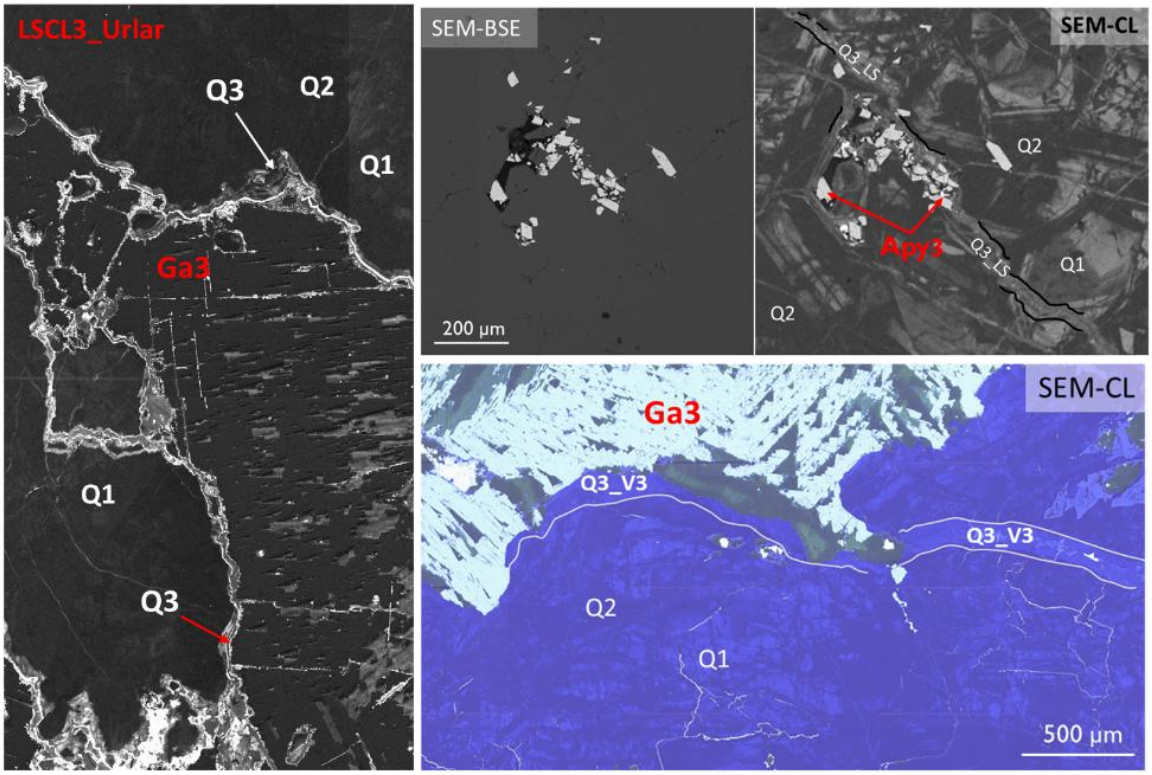

Figure 5.38 Some specific paragenetic relationships (i.e., between quartz and sulphides) in the Calliachar and Urlar Burn veins.

5.3.1.3 In situ gold

Gold has been located in a single rock sample from the Calliachar and Urlar Burn vein suite and, specifically, the G Vein ('gossan' vein). The observed heterogeneity in size and the 'bimodal' occurrence (i.e., as inclusions and in cracks) of particles indicate the possible overlap of two separate gold mineralising events, which is validated by the variations in silver content in the

alloy (Table 5.2, section 5.2). The smallest gold particles are inclusions and exhibit internal silver contents in the range of ~16%-18%, whereas larger grains are hosted in micro-fractures and record silver contents in the main range of ~19% to 36%. Because a few, tiny gold inclusions were found within the 'former' euhedral pyrite (Py1), these are considered coeval to that (Au1). Some fracture-hosted gold particles were observed in Py1 (AuA2_gv) whereas most of them (AuC_gv) come across the later, shattered pyrite (Py3_gv) (Figures 5.2 and 5.3. Because AuA2_gv and AuC_gv share similar physical and chemical characteristics, they have been interpreted to be part of the same "Au3'' event, slightly postdating Py3_gv (during S3) and later than S1 and S2. While it has been relatively straightforward to associate the fracture-hosted gold with the S3 stage of the vein, the origin of the rare gold inclusions (presumed to be) in Py3_gv is ambiguous. In fact, these might either be related to the respective S3_gv event or - equally to gold inclusions in Py1 – related to Py1 and the associated S1 stage, assuming that (at least part of) Py3_gv represents reworked Py1 that has been transported and recemented with later quartz (Q3_gv). This is a difficult point to address: the silver content (~18%) of the two gold particles observed as 'S3' (presumed) inclusions in Py3 does not hint at any particular affiliation to either the Au1 or Au3 category, because it places right at the value transitional interface (Table 5.2, section 5.2). The few mercury-rich (wt 1.4% to 5%) particles represent a sub-class of the fracture-hosted gold, showing narrower values of the respective silver component (Table 5.2, section 5.2); however, there doesn't appear to be any further constraint related to their hosting sites, which are micro-fractures coming across both Py1 and Py3_gv. This sub-population is therefore considered part of the later gold event. In light of all these considerations, the two main gold precipitation stages have been respectively labelled Au1 and Au3.

Pyrite tends to precipitate earlier than many other phases from solution but might easily deform over a wide range of P-T conditions (e.g., Webb et al., 2024); for instance, it can fracture due to thermal expansion during prolonged depressurisation (Cox et al., 1981; Liu et al., 2010) and can thence fracture during the ongoing event with possible deposition of other phases (e.g., gold) in microfractures (Huston et al. 1992; Cook et al., 2013; Sahoo and Venkatesh, 2015; Yang et al. 2016; Li et al., 2020, 2022; Fougerouse et al., 2021). Further to these processes, it can be possible that gold was remobilised from the crystal lattice of pyrite precipitated in an earlier event, and redeposited in the pyrite fractures (Mills et al., 2015; Fougerouse et al., 2016; Lebrun et al., 2016; Hastie et al., 2020). In a scenario of gold remobilisation, or an alternative scenario where gold has been introduced in fractures by a later fluid, two separate fluid events would be needed. Hastie et al. (2020) proposed remobilization and local reprecipitation of gold as a mechanism to coarsen gold mineralisation in hydrothermal veins.

5.3.1.4 Overarching paragenesis

Detailed paragenetic investigations of the hydrothermal veins from Calliachar and Urlar Burn have provided a robust platform to assess the degree of co-existence and reproducibility of mineralogical components/assemblages over multiple hydrothermal events. The first mineralising stage (S1) has been associated with euhedral/mottled quartz textures (Q1) enveloping sporadic euhedral pyrite (Py1) which, in turn, hosts a relatively low amount of visible gold (Au1) as tiny inclusions. No sulphide mineralisation has been allocated to the second paragenetic stage (S2) that is mainly represented by overprinting, dark CL bands (Q2). The third paragenetic stage (S3) is initiated by fractures in which quartz precipitates to form open-space textures (Q3). Albeit it seems plausible that each of the analysed veins hosts their own third hydrothermal event with localised features, certain mineralogical and textural elements that repeat over different veins have helped reconstruct a 'global' paragenetic stage (Figure 5.39) in the overarching hydrothermal history at these locations; this stage (S3) is characterised by the greatest variety in sulphide mineralogy. Galena and chalcopyrite dominantly coprecipitate over S3 in both the V3 Vein (Calliachar) and the LSCL3 Vein (Urlar); in the latter, pyrite can be identified as a subordinate component of the same hydrothermal pulse. Petrographic investigations reported in a previous work by Mason (1990) on the V3 Vein (Calliachar Burn) highlight the occurrence of local cataclastic pyrite overgrown by synchronous galena. The corresponding S3 paragenetic stage in the G Vein, at Calliachar Burn, hosts shattered pyrite along with minor arsenopyrite and sphalerite, suggesting local physical transport and re-cementation. Pyrite here incorporates gold mineralisation in two forms (in cracks and as inclusions); gold in cracks, which is the dominant form, is equally reported in the cataclastic pyrite of the V3 Vein (Mason 1990). The G Vein sampling location critically lies on the strike of the V3 Vein, if prolonged towards NW, supporting the hypothesis of genetic relationships between the two samples and subsequent correlation of the respective paragenetic assemblages/histories. Furthermore, the assemblage of galena plus pyrite consistently appears within the S3 stage of the LSCL3 at Urlar Burn (as mentioned earlier in the text), raising the possibility of a correlation between the Calliachar and Urlar vein systems. This match of information from separate sources is crucial because it helps place the later gold event (Au3) at a specific, yet overarching paragenetic stage (S3), as it is here interpreted (Figure 5.39). The fourth stage has been associated with minor brittle events bringing tiny quartz injections and ankerite mineralisation, with no sulphides. The fifth paragenetic stage (S5) can be explained as a consequence of a minor, later fluid pulse, resulting from vein reactivation-reopening and injection of calcium-rich fluids (as exemplified by the presence of dolomite in two of the

analysed samples) and minor silica. These fluids are regarded as responsible for the physical transportation and re-cementation of pre-existing pyrite mineralisation that re-occurs at this stage in the form of sporadic, shattered grains hosting galena and chalcopyrite inclusions.

	Stage 1	**Stage 2**	**Stage 3**	**Stage 4**	**Stage 5**
Gangue	***Q1 (mottled, zoned)***	***Q2 (overprint)***	***Q3 (fractures)***	***Q4 (fractures)***	***Dolomite/Calcite***
Pyrite			**cataclastic**		**cataclastic**
Arsenopyrite			**cataclastic**		
Chalcopyrite					**inclusions**
Galena					**inclusions**
Sphalerite					
Gold	**inclusions**		**in-cracks**		

Figure 5.39 Calliachar and Urlar Burn overarching, schematic paragenetic table.

The overarching paragenetic history of the Calliachar Veins, as it is here proposed (Figure 5.39), can only be deemed valid if it is assumed that the fluids responsible for the precipitation of the different mineralising stages in multiple veins derive from the same hydrothermal system, which might show ramifications at different degrees. For instance, the vein-hosting fractures might have experienced parallel re-opening episodes with some margins of variability between themselves, depending on their relative localisation in the system. This would determine sectorial fluid transport and localised deposition of certain mineral assemblages; additionally (or alternatively) vein discontinuity and sample biases can be accounted for as supporting evidence that the hydrothermal veins at Calliachar and Urlar Burn do not share 'universal' mineralogical features to systematically occur in each of them.

5.3.2 Almond Vein

5.3.2.1 Interpretation of the quartz textures and role of dolomite

At least three different quartz events have been recognised within the hydrothermal vein sample available from River Almond. Two of these are volumetrically dominant, similarly to what has been found for the veins at the previous localities (Calliachar & Urlar Burn). The former quartz event (Q1_av) has been associated with the QA_av quartz phase in the vein description (section 5.2.2.2), represented by weakly euhedral to mottled textures. The subsequent Q2 (Q2_av) event has been associated with the overprinting, dark quartz CL bands that crosscut the former generation (Qb_av; section 5.2.2.2). Both the quartz stages show features that are consistent with the interpretation that has been formulated for the former quartz events at Calliachar-Urlar Burn, which would also be compatible with precipitation in an orogenic hydrothermal environment. The 'Q1 and Q2' nomenclature has consequently been retained. A third quartz event is associated with QC_av in section 5.2.2.2, which is reflective of sporadic, brighter CL fractures carrying no sulphide mineralisation. This latter quartz event is probably to be related to internal little fracturing occurring after the main sulphide-bearing event. It is unclear whether the dolomite mineralisation occurs with Q3_av or is part of a separate stage; it is certainly hosted in fractures that cut the S2 mineral phases and it is, in turn, crosscut by later fractures that carry galena mineralisation (ga4_av; S4).

5.3.2.2 Constraints from the sulphide mineralisation

Pyrite, galena and sphalerite mineralisation all occur alongside the second quartz pulse (Q2_av), and are therefore assumed to be coeval with it (Py2_av; Ga2_av; Sph2_av). It has not been possible to identify the quartz phase to which chalcopyrite is directly connected, but since the latter appears to coprecipitate with all the other sulphides present in the vein (and aforementioned), it is here interpreted to be part of the same mineralising event and thus coeval to Q2_av (Cpy2_av). It is common that quartz adjacent to sulphides has elevated content in Fe, which could account for a dark CL response (Penniston-Dorland, 2001; Müller et al., 2010; Baele et al., 2019). Inclusions of chalcopyrite, galena and sphalerite were additionally identified in Py2_av; as such, they might either be considered coeval to the second paragenetic stage (S2) or predating it. Later galena mineralisation fills a set of fractures that cut all the previous mineral phases and are linked to the fourth paragenetic stage (S4). This latter does not appear to be related to quartz precipitation and post-dates the dolomite mineralisation overgrowing the S2 mineral associations (S3). Gold mineralisation takes place over S2 in the form of both inclusions

and cracks in sulphide mineralisation (see section 5.2.2.2); the relevant paragenetic interpretation is illustrated in the following paragraph.

5.3.2.3 In-situ gold paragenesis

Gold has been found in the form of inclusions in pyrite and chalcopyrite (Py2_av, Cpy2_av, Au2_av1) and filling cracks that fracture coeval pyrite, chalcopyrite and sphalerite (Au2_av2). The fracture-hosted gold is more silver-rich and overall coarser than the gold inclusions (section 5.2.2.2), which are here interpreted to have been introduced earlier in the system (e.g., Webb et al, 2024). In view of the observed gold compositions (alloy variations between Au2_av1 and Au2_av2) and textures (Au2_av2 coarser than Au2_av1), the two gold inputs might likely be related to separate fluid events (e.g., Webb et al., 2024). To support this hypothesis, Webb et al. (2024) also considered the textural and volumetric differences that were observed in part of the sulphide assemblage coeval with the two gold mineralising inputs (e.g., chalcopyrite and sphalerite associated with the fracture-hosted gold mineralisation appeared more voluminous than the ones associated with the gold inclusion stage) as well as the internal compositional variation of the respective pyrite hosts (the As-rich pyrite is coeval with the silver-rich gold event; Webb et al., 2024).

Furthermore, the pyrite hosts show zonal variations dependent on As content increase as a consequence of local fluid modification - similar to what Hastie et al. (2020) observed in their pyrite samples. Nevertheless, it has not been possible to link the bimodal occurrence of gold in the (Glen) Almond vein to CDR processes because, as Webb et al. 2024 point out, further investigations (e.g., at the trace-element level, by LA-ICP-MS) would be necessary to underpin any proxies for re-mobilisation in this sample.

5.3.2.4 Almond Vein paragenesis

A schematic paragenetic table for the (Glen) Almond Vein is provided in Figure 5.40, to summarise the information provided in the previous paragraphs.

	Stage 1	**Stage 2**	**Stage 3**	**Stage 4**
	Q1 (euhedral)	***Q2 (overprint)***	***Dolomite***	***fractures***
Pyrite				
Chalcopyrite				
Galena				
Sphalerite				
Gold		**in-cracks**		

Figure 5.40. Schematic paragenetic table for the (Glen) Almond Vein.

5.3.3. Lead Trial Veins

5.3.3.1 Interpretation of the different quartz textures

Detailed optical analyses of the hydrothermal quartz-bearing veins from this locality revealed a variety of internal textural features to different degrees of complexity, making the formulation of a univocal interpretation somewhat challenging. The textures have been classified according to a hypothetic cooling sequence that spans from the vein margins to the inner zones of the system, and are presented as follows.

1) Bands of fine-grained crystals (Q0_LT; QS_rx in section 5.2.3, table 5.4) that are found partially adhering to the lithoclasts constitute a "reaction front" texture and are the first to crystallise. The relatively small size of the crystals suggests instantaneous depressurisation of the system, contact of the hot fluid with the fracture walls (host rock), then a fast temperature drop and cooling. The texture is associated with a high degree of silica supersaturation, resulting in rapid nucleation and precipitation of the crystals (Fournier, 1985; Shimizu, 2014)
2) The volumetrically dominant quartz texture (in the set of samples analysed) is represented by bright, euhedral quartz crystals (Q1_LT1, fig. 5.41b; 'QA' textures in section 5.2.3) that at first precipitated in an open space and at low-temperature conditions (Götze et al. 1999; Lehmann et al. 2009, Rusk 2012, Shah et al., 2022). In specific samples (e.g. RX3078, LSLTD) these morphologies can be in large part reconciled to comb crystals (Q1_LTa; 'QA_rx1' in section 5.2.3), a type of primary texture indicating parallel or subparallel quartz crystals that are elongated perpendicular to vein walls and projecting into free space (section 2.2.2.3). It typically originates from fluid slightly supersaturated with quartz (Shimizu, 2014), suggesting mildly fluctuating conditions of the physicochemical parameters of the solution (i.e., temperature, pressure, and pH) during growth (Fournier, 1985). In most portions of the samples (e.g., Figure 5.27c), the internal crystal faces are clearly visible and give rise to regular patterns; however, in more evolved euhedral crystals (Q1_LT1) these often display variable CL responses at different angles. Such an effect can be attributed to sector zoning, indicating trace element compositional variations at different faces as a function of their crystallographic orientation (Rottier and Casanova 2021). Sector zoning is mostly experienced by quartz that precipitated at low temperatures (< 300 °C; Jourdan et al. 2009); as such, euhedral sector-zoned crystals are characteristic of quartz from epithermal systems (Frelinger et al., 2015).

3) Patterns of concentric, *moss* and *plumose* crystals ('Q1_LT2' texture, fig. 5.41a; 'qa_at2' and 'qa_lt2' in section 5.2.3) have been observed in samples 2864 and LS1, in physical continuity with Q1_LT1, and interpreted to have derived from a silica gel precursor. Silica gel forms in response to fluid supersaturation with respect to amorphous silica (Fournier, 1985). According to Dong et al. (1995), *moss* patterns specifically originate from an initial nuclei suspension in silica gel during the fast ascent of the hydrothermal fluid, whereas *plumose* crystals derive from recrystallisation of smaller crystals in approximate crystallographic continuity with a larger host crystal. Because Q1_LT2 incorporates both morphologies, it is here classified as a primary texture with localised secondary features. Sub-spherical textures are systematically reported to be related to epithermal settings, and they are often found filling vugs (e.g., Rusk et al 2012; Shah et al., 2022). The oscillatory zoning that is frequently observed within the Q1_LT2 concentric crystals may have been dictated by a diffusion-controlled mechanism intrinsic to crystal growth (Shore and Fowler, 1996) and can additionally indicate depressurisation of the fluid at higher temperatures (e.g., 250° to 450°; Rottier and Casanova 2021). Since the Q1_LT2 patterns have been identified in spatial continuity with other well-established textural morphologies (i.e., Q1_LT1 euhedral crystals) in the same samples, they have ultimately been interpreted as the product of a possibly zonal depressurisation and cooling of the same hydrothermal fluid to a different degree. The process is here assumed to take place in the middle of the vein rather than at the edges, where the crystal nuclei could remain suspended in the silica gel for longer.

Sector zoning (dissolution feature) is identified thoroughly within the 'Q1_LT' primary textures, supporting the interpretation of quartz growth at disequilibrium and relatively low temperatures (Rottier and Casanova 2021, Shah et al., 2022).

4) Q2_LT is represented by a brecciated to fine-grained texture that typically shows a weaker CL response (slightly darker colouration) and pervasively infills inter-crystal channels within the Q1_LT quartz ('QB' textures in section 5.2.3). It can be recognised in all the samples and is interpreted as the result of dissolution mechanisms post-Q1_LT mineralisation, bringing to a fast "new" quartz recrystallisation in the available space. Possible causes for the dissolution of hydrothermal quartz are fluctuations in pressure, temperature, and fluid composition (Rusk and Reed 2002). Signs of dissolution and healed microfractures are often identified in quartz from porphyry systems (Rusk, 2012), which is generally characterised by well-preserved growth zones. Dissolution textures are more uncommon in quartz from epithermal systems (Frelinger et al. 2015).

5) Q3_LT is associated with the sharp-edged veinlets (fig. 5.41b; ''QC'' textures in section 5.2.3, Table 5.4) that were sporadically identified in almost all the studied samples (except 2886) and crosscut all the previous quartz generations. These are thus interpreted to be the latest quartz event, likely to have been associated with later fracturing of the veins. The fractures are filled with CL-bright sub-euhedral quartz that could have originated from re-precipitation of silica dissolved from the earlier quartz.

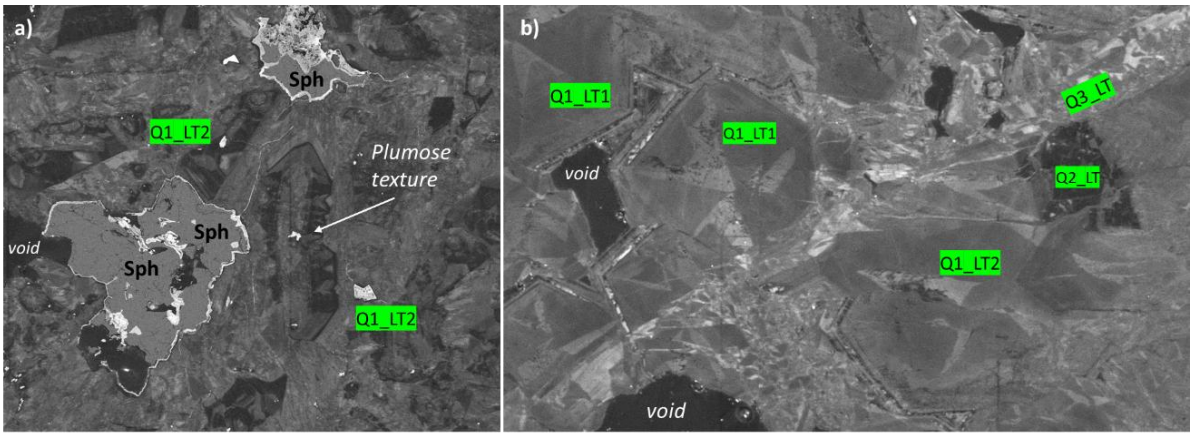

Figure 5.41. Characteristic textural features in Lead Trial vein samples. a) Plumose texture in quartz, partly overgrown by sphalerite; b) Q3_LT crosscuts Q1_LT(1and 2) and Q2_LT.

5.3.3.2. Constraints from sulphide mineralisation

Co-precipitation of galena and sphalerite forms the main sulphide event. These agglomerates systematically overgrow Q1_LT1 and partly Q1_LT2; as such, they are deemed to precipitate with Q1_LT1 and keep developing until (at least) Q1_LT2 nucleation. In some cases (e.g., LS1), the subsequent (Q2_LT) quartz event contours galena and sphalerite assemblages through CL-dark films, interpreted as the product of recrystallisation of the earlier Q1 textures.

Pyrite is only observed in the LSLTD2 and RX7081 thin sections (see Table 5.4) and, because it appears chaotically incorporated in an embedded lithoclast within the quartz vein matrix, it will not be strictly considered in the light of a potential overarching paragenetic history of the Lead Trial Veins.

5.3.3.3. Paragenesis of the veins (interpretation)

Although further investigations would be needed to determine the exact temperature ranges and pressure gradients involved in the evolution of textures and mineralisation of the Lead Trial veins, a preliminary paragenetic interpretation is proposed in accordance with the evidence

analysed for this study. However, it would be important to note that this is likely to be effective for just a portion of the entire vein system, due to the multigenerational nature of the quartz mineralisation observed at outcrop.

Overarching paragenesis

The initial phase to precipitate (Q0_LT) is represented by the microcrystalline bands that were discontinuously found adhering to the vein walls; timewise, this stage (S0) is interpreted to be extremely rapid, due to instantaneous de-pressurisation of the system and cooling. The 'effective' first stage (S1) is represented by patterns of comb crystals (Q1_LTa) which grow on top of the previous microcrystalline layer and develop mostly in length, perpendicularly to the vein walls and towards free space; these crystals were consequently subject to gradual cooling conditions, leading to the formation of euhedral morphologies that can be observed in thin section. The second stage (S2) corresponds to an evolution of the comb crystal precursors into well-developed euhedral crystals (Q1_LT1) showing normal zonation, indicating stable conditions of gradual cooling. Sulphide mineralisation in terms of sphalerite and galena precipitates at this point, as they have systematically been found overgrowing the euhedral quartz (Q1_LT1, S2); gold mineralisation (in hand specimen) is consistently found in association with this (dominant) sulphide assemblage and, when rarely observed in thin section, right on the surface of CL-bright euhedral crystals. Therefore, it is assumed to have been introduced in the system at this stage, which is consequently classified as the ore-bearing one. Later dissolution and recrystallisation of the quartz Q2_LT, represented by the pervasive CL-darker, microcrystalline bands that brecciate/surround the CL-bright euhedral cores (not to be confounded with the inter-crystal normal zoning), constitute a later paragenetic stage. It is uncertain whether the concentric/moss texture (Q1_LT2) crystallised before or (roughly) simultaneously with Q2_LT. The Q1_LT2 texture is interpreted to have crystallised in the inner portions of the veins, implying longer times of suspension/residence of the initial nuclei in the system. Evidence of extensive recrystallisation occurring around sub-spheric and in plumose crystals might either indicate an effect of the dissolution process related to the Q2_LT stage or the effect of sectorial instability after crystal precipitation or even an overlap of both. In thin section, the Q1_LT2 texture appears embedded in the Q1_LT1 texture and the galena-sphalerite agglomerates that overgrow the euhedral quartz (Q1_LT2) become more densely distributed in the proximity of (Q1_LT2) patterns. Furthermore, the euhedral quartz crystals (Q1_LT1) form a continuum with the sub-spheric and plumose crystals in the concentric/moss texture. Therefore, it is likely that Q1_LT2 formed slightly later than Q1_LT1 and similarly pre-dates the pervasive CL-darker brecciation (Q2_LT). As such, the Q1_LT2 concentric/moss texture has been

allocated to an S3 stage, also characterised by an increased abundance of galena and sphalerite and localised recrystallisation patterns. The Q2_LT infills/brecciations consequently form the S4 paragenetic stage.

Based on the hand-specimen evaluation, the frequency (i.e., abundance) of gold mineralisation appears to decrease from the margin (coarser quartz, vein breccia) towards the inner of the veins, in line with a hypothesis of either precipitation during earlier/intermediate stages of the paragenesis, or two gold mineralising pulses – a paragenetically earlier one, and a later one happening at shallower levels of the system which might justify an increase in gold abundancy in coarser/brecciated quartz. The physical features of gold mineralisation in relation to local quartz textures will be however further discussed in the next paragraph.

Baryte likely precipitates during two main stages (at least): just after the S0-S1 stage, since it occurs in micro-fractures at the interface between Q0_LT and Q1_LTa; and during an S6 stage, the latest in the entire vein paragenesis, whence it occupies cavities and micro-fractures in/throughout quartz and sulphide mineralisation (example in fig. 5.43a).

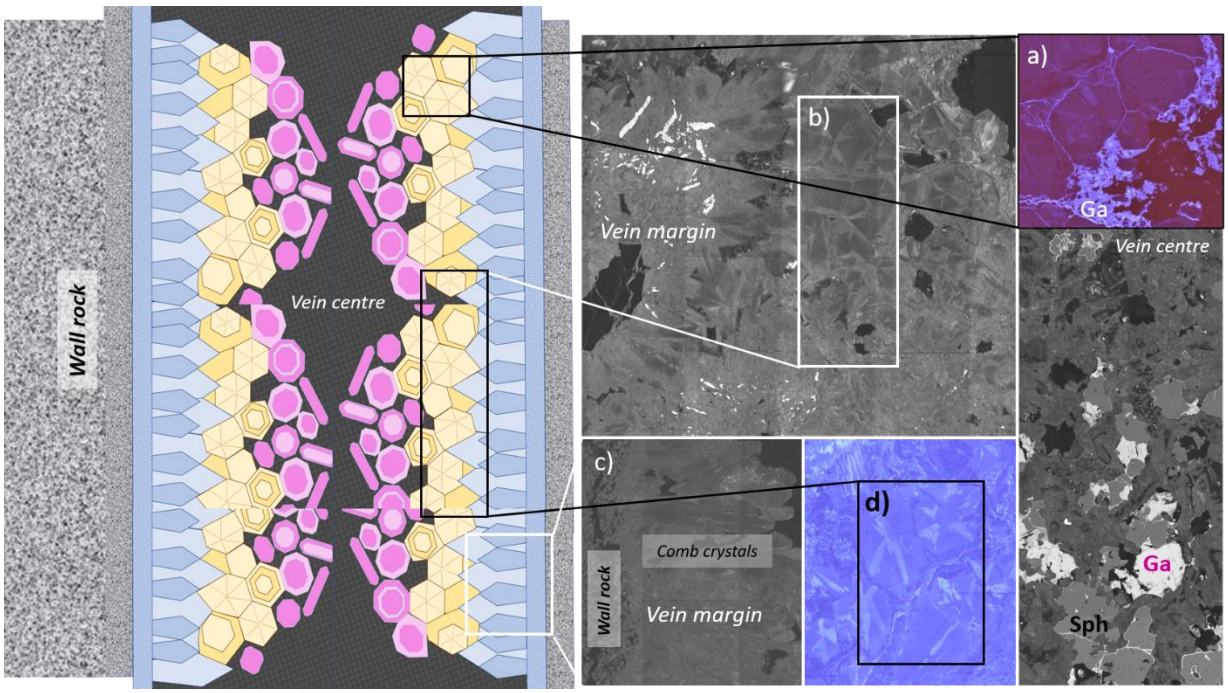

Figure 5.42. Model for interpretation of the quartz textures at the Lead Trial, in the ideal scenario of precipitation in a single vein/widening fracture. Ga = galena; Sph = sphalerite. a), b), d) quartz euhedral crystals; c) quartz comb crystals. Different quartz crystal morphologies (e.g., sub-spherical and plumose) can be observed in the vein centre, along with galena and sphalerite.

This preliminary paragenetic interpretation of the hydrothermal veining at the Lead Trial could refer to either an evolution of textures through an ideal cross-section from the vein wall to the

middle of the vein (Figure 5.42), or the evolution of textures across different branches of the hydrothermal system; in such second scenario, it would integrate portions of potentially different veins/transects. In both cases, the interpretation relies on a principle of sequential phase crystallisation from fluid(s).

5.3.3.4. Possible implications from sector zoning at the Lead Trial

There are two main forms in which sector zoning might occur (e.g., Northrup & Reeder, 1994; Watson et al., 1995) which are i) rounded or embayed bright cores with dark CL euhedral overgrowths (Fig. 5.43c; e.g., Onasch & Vennemann, 1995; Rusk et al.2012) and ii) crystal faces with a different arrangement of their outward-facing atoms due to sectorial trace element substitutions (Figure 5.43 a, b; Hollister, 1970; Chouinard et al., 2005; Hastie et al, 2020). In the vein sample suite from Ardtalnaig, sector zoning is observed to different degrees in both forms (Figure 5.43). The first mode has been particularly noted in relation to the 'inner' Q1_LT2 texture, whereas the second (sectorial) mode recurs over the Q1_LT1 texture, hence taking place towards more external regions of the vein(s). Either way, the mechanism accounts for the dissolution of early quartz by later hydrothermal fluid, resulting in fracture and pore-space filling by dark quartz that generates localised 'secondary' textures (Shah et al., 2022).

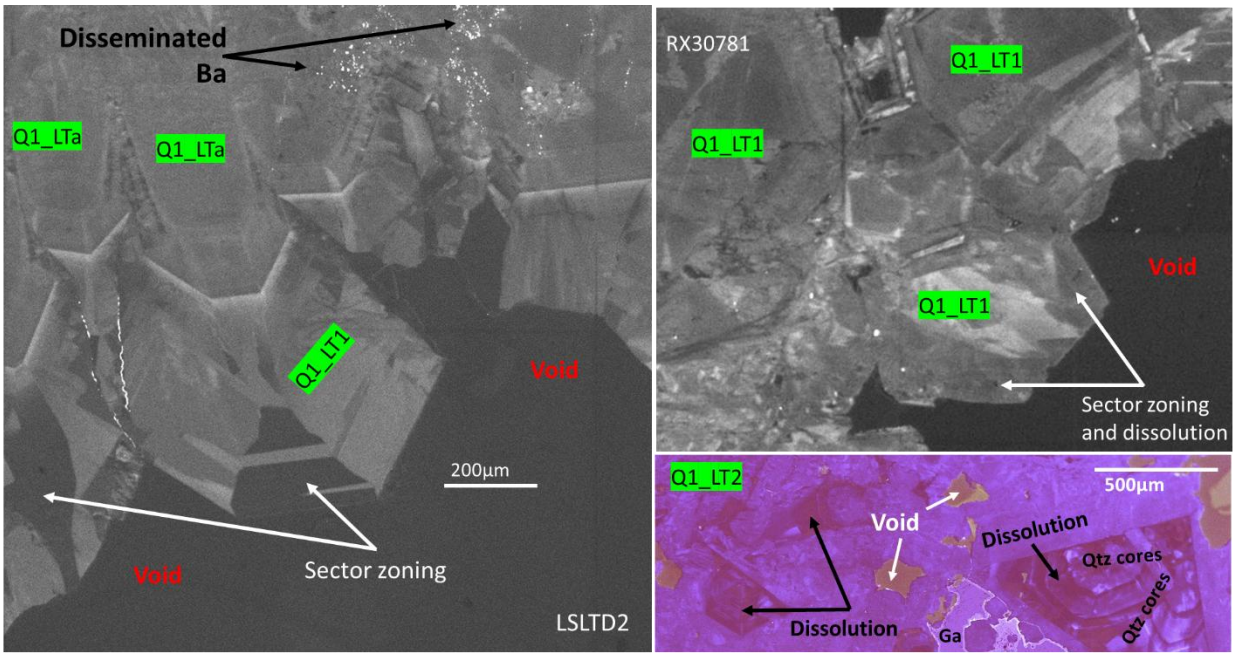

Figure 5.43. Quartz textures from some Lead Trial vein samples (LSLTD2, RX30781 and 2864) showing evidence of sector zoning.

Gold mineralisation abundance (e.g., Table 5.3) progressively increases towards the outer

portions of the hydrothermal veins, where the 'second' mode of sector zoning is observed. Evidence of sector zoning implies disequilibrium growth in quartz exterior zones at <250˚(Shah et al., 2022). The assumed conditions of disequilibrium would be consistent with a later alloy modification (Chapman et al. 2021) of the in-situ gold mineralisation, as supported by the observed enrichment in silver of the gold alloy at the Lead Trial (Figure 5.44). The particles used for optical and compositional analysis were, in fact, liberated from crushed ore and, where observed, the in-situ grains detected in thin sections from the vein samples are consistently located in the (Q1_LT1) quartz texture, directly linked to sectorial zoning (Q1 in Figure 5.44c). Such areas are also associated with intense quartz-brecciation and (later) baryte mineralisation (i.e., sample RX3078). These combined pieces of evidence would indicate new instability of the physicochemical conditions (e.g., temperature, fluid supersaturation) of precipitation, in this case intensifying towards the exterior portions of the veins and/or at shallower levels of the system. The gold alloy modification could have been dictated by evolving conditions of the same fluid and/or influence from an external fluid (e.g., baryte mineralisation), which might have also influenced a subsequent input of gold mineralisation.

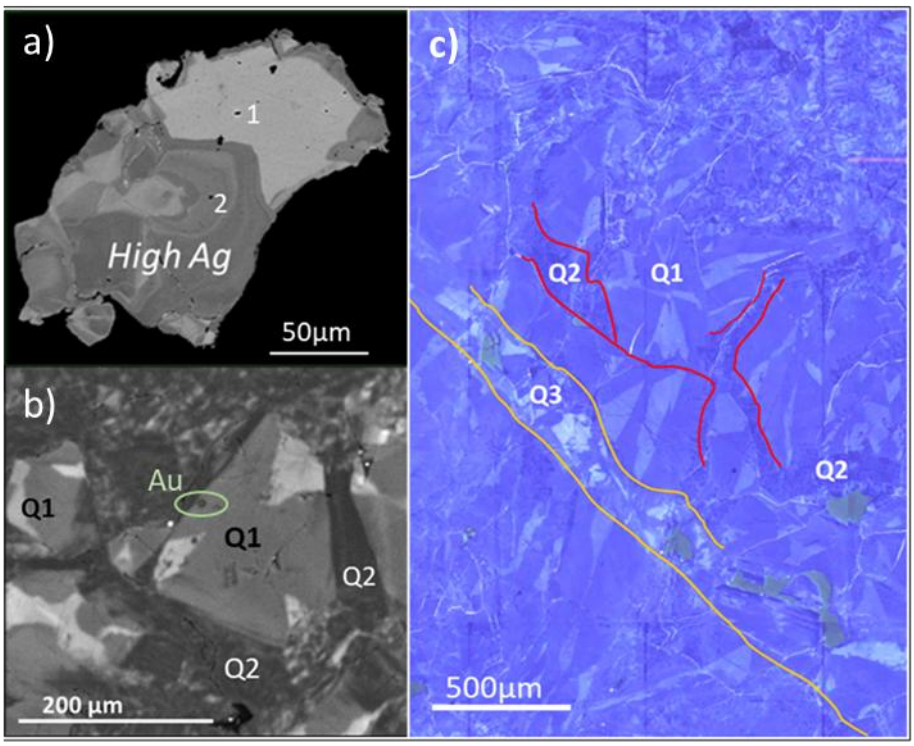

Figure 5.44. a) Gold particle from the Lead Trial crushed-ore (photo credit – Rob Chapman); b) tiny gold particle on euhedral quartz in one of the Lead Trial vein samples (LSLTA); c) three main CL quartz generations in one of the Lead Trial vein samples (LSLTA).

The baryte mineralisation (BaSO4) could have been produced by mixing of hydrothermal fluids with meteoric ones; meteoric waters are a common source of sulphate (SO_4^{2-}) which enables Ba^{2+} removal from fluids (e.g., Wind et al., 2023).

5.3.4 Coire Buidhe

The hydrothermal vein samples from Coire Buidhe have resulted in substantially different quartz textures and variability of their mineral assemblages, depending on the two main locations where they were collected (see section 5.2.4). Their paragenetic features have been reconciled into two main vein types, whose details are illustrated in the following sections.

5.3.4.1 Interpretation of the different quartz textures/mineral assemblages

LSBOIL and LS2 sets

These samples have been interpreted to derive from veins that were presumably part of the same hydrothermal system, due to strong textural and mineralogical similarities both at outcrop and by thin section analysis. The 'sugary' (to the naked eye) quartz texture may simply indicate evidence of intense weathering; the sulphide assemblage of dominant galena plus very subordinate pyrite is not in itself diagnostic, and compatible with the hypothesis of both orogenic and magmatic-related systems. The latter interpretation may be supported by the presence of local minor faults close to the sampling location (Figure 4.18 and Table 4.1, section 4.2.4).

LSCB set

The four thin sections that have been analysed from this different Coire Buidhe location (spoil heap) revealed a mineralogical assemblage that is consistent with the ones normally observed in veins from the Loch Tay area. It shows, however, generally different characteristics from the LSBOIL-LS2 samples and it is therefore not possible to assume a shared genetic environment for both types of mineralisation.

5.3.4.2 Paragenesis of the veins

LSBOIL and LS2 sets

Since the two samples have been assumed to be part of the same system, the interpretation of their paragenetic histories is here approached in conjunction, by adopting the univocal nomenclature of "QX_bl". Q1_bl, represented by the QA stage in (section 5.2.4.1), precipitated as the first quartz event with no synchronous sulphide mineralisation during S1. The S1 stage was later overprinted by the darker, homogeneous 'Q2_bl' quartz, carrying both galena and (subordinately) pyrite mineralisation (S2). These two main, former events were followed by a phase of minor fracturing (S3), suggested by the occurrence of hairline quartz infills in LS2 and fractures in LSBOIL (Q3); the latter were subsequently filled by extensive ankerite mineralisation.

Finally, the galena mineralisation (Ga2_bl) was possibly injected into the newly-formed Q3 thin fractures of both LS2 and LSBOIL, where it has been observed to occur scarcely.

LSCB set

The first mineralising event to take place (S1) in the LSCB veins (Table 5.6) is constituted by the relatively bright, zoned QA_cb quartz, with no associated sulphide mineralisation (Q1_cb). Q2_cb (QB_cb) precipitates along with the characteristic sulphide assemblage of PyB_cb + CpyB_cb + PoB_cb (S2) and overprints the previous 'Q1_cb' stage. Because of the presence of small galena and sphalerite (GaB_cb and SphB_cb) inclusions in pyrite, the S2 stage has been interpreted to be inclusive of these species as well, which would co-precipitate with the main sulphide assemblage; alternatively, GaB_cb and Sph_cb could have precipitated slightly earlier and been incorporated just after into PyB_cb. It has not been possible to allocate the few arsenopyrite fragments, found embedded in PyB_cb, to a specific paragenetic stage since these are presumably hosted in micro-cracks. Therefore, arsenopyrite is likely to have been introduced by a slightly later fluid than the one responsible for the S2 assemblage. A similar issue has been encountered for the paragenetic interpretation of the micron-scale gold particles observed. A few of them occur right on the surface of either Q2_cl or Py2_cl and could, consequently, be linked to the same S2 (ore-bearing) paragenetic stage; on the other hand, a few other particles were observed within micro-fractures across the same QB_cl (Q2) quartz, allowing the hypothesis of a gold precipitation episode taking place just after the S2 stage.

5.4 Pb Isotope data

Pb Isotope data were obtained by analysing galena samples from selected locations in the Loch Tay area (Figure 5.45), for which the respective in-situ vein mineralogy was also investigated. The raw data were corrected using the published values of standard SRM981 (Yuan et al. 2016) to increase the reliability of the model ages. The calculated model ages (Table 5.7 - credit to Dr. Steve Hollis and Dr. David Van Acken) for all the samples (~from 498 to 308 Ma) have been plotted on the geological map in Figure 5.45, where the locations of the corresponding rock samples are also indicated.

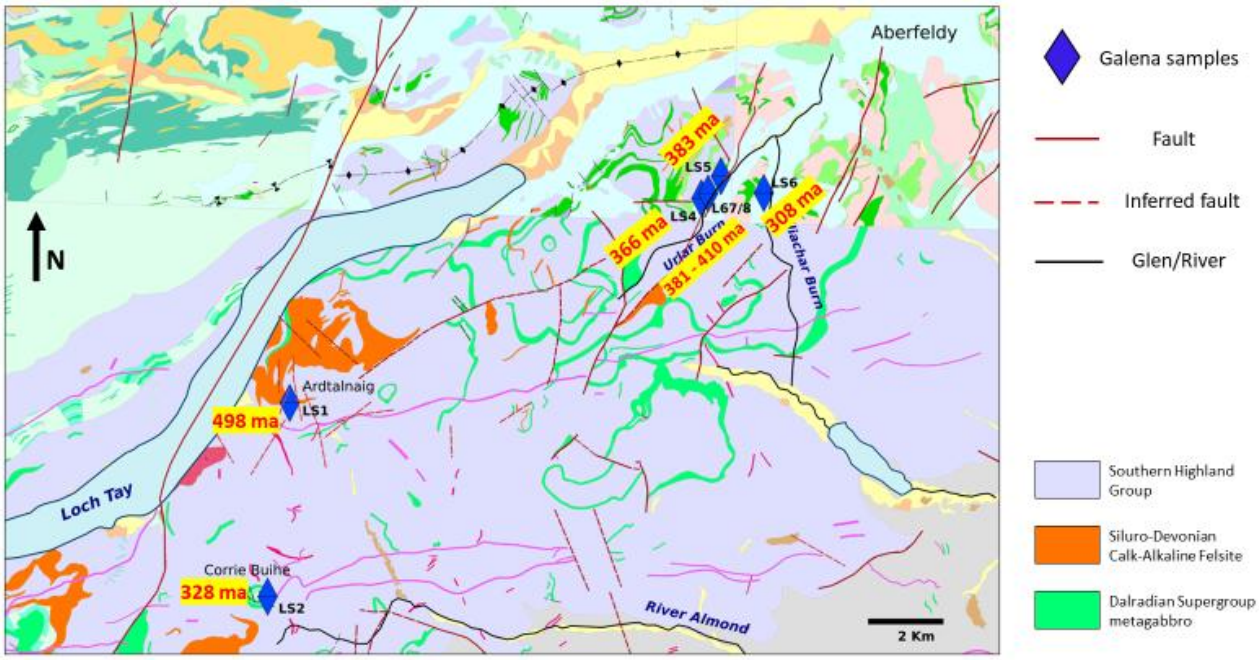

Figure 5.45 Geological map (modified after the BGS geological map from https://digimap.edina.ac.uk/) correlating the Pb model ages to the respective rock sample sites.

These ages overall cover the whole Caledonian temporal range (490 to 390 Ma); the youngest ages were obtained from the Calliachar Burn and Coire Buidhe samples (within the Upper Carboniferous range), whereas the oldest has been recorded for the Lead Trial (LS1) sample (Upper Cambrian). Mu values range from 9.0 to 9.3 (with 9.2 being the most common value), as indicated in Table 5.6. Mu is a parameter used to infer how juvenile or evolved the lead source reservoir was, since it is considered to be the primordial $^{238}Pb/^{204}Pb$ ratio; a value of 9.2 is typical of the Laurentian crust. In general, the ratio variations between samples are outside of error - the data points cluster away from each other (Figure 5.46) - particularly between LS1 (Mu value of 9.0) and the rest of the samples (Figure 5.46). Please refer to Appendix 4 for the full raw dataset. Implications from these results will also be discussed in 7.2.4 and 7.3.

Although Mu (model) ages are generally not accurate, they can be used to identify variations in the types of deposits located in a region. This dataset has been incorporated in the work of Webb et al. (2025), who complemented it with additional model age values obtained for other localities in the Loch Tay area (e.g., Glen Almond, Coire Buidhe). It was found that the ages vary considerably between sites but behave consistently at individual ones, with the oldest ones being confirmed for the Lead Trial samples (520–507 Ma, Webb et al., 2025).

Table 5.7 Table summarising Pb isotope sample IDs, corresponding rock samples in the Loch Tay area, and the calculated Model ages and Mu values. Raw data, inclusive of the absolute errors, are available in the Appendix.

Sample ID	Rock sample	Model age (Ma)	Mu value
LS1	LS1 - Lead Trial (not in situ)	498.1	**9.0**
LS2	LS2 - Coire Buidhe (in situ)	328.2	9.2
LS4a	LS4 - Urlar Burn (in situ)	366.0	9.2
LS4b	LS4 - Urlar Burn (in situ)	364.5	9.2
LS4c	LS4 - Urlar Burn (in situ)	364.2	9.2
LS4d	LS4 - Urlar Burn (in situ)	364.4	9.2
LS4x	LS4 - Urlar Burn (in situ)	367.7	9.2
LS4z	LS4 - Urlar Burn (in situ)	370.0	9.2
LS5	LS3 Vein - Urlar Burn	383.9	**9.3**
LS6	Calliachar Burn - not in situ, big galena clot	308.8	**9.3**
LS7	Urlar Burn - not in situ	381.0	9.2
LS8	Urlar Burn - not in situ	410.7	9.2

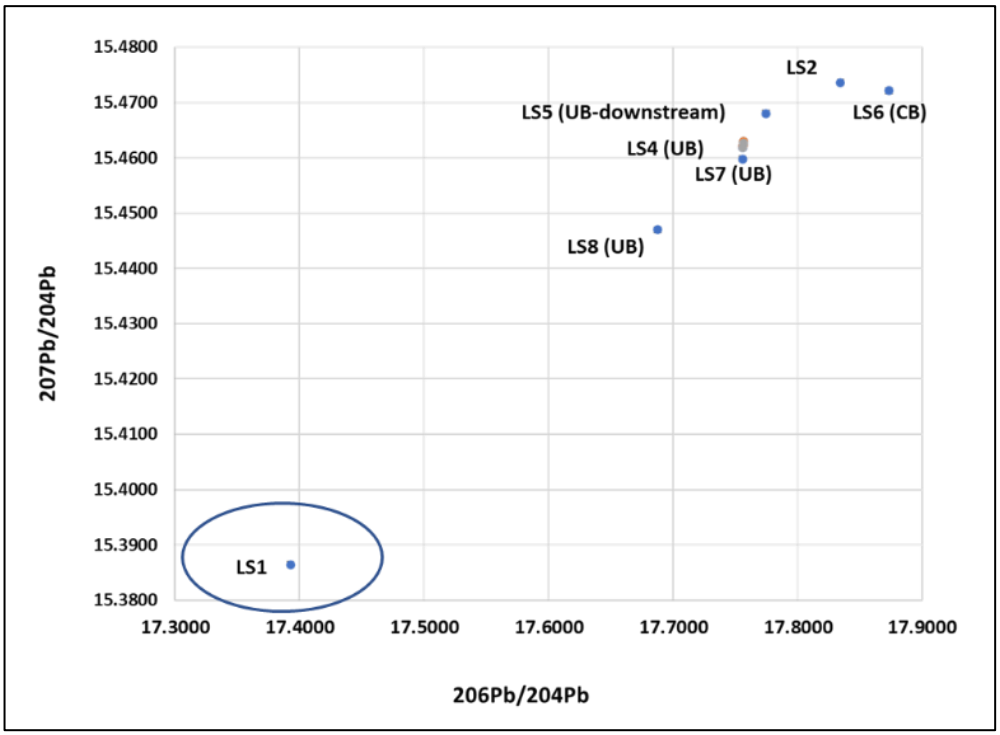

Figure 5.46 Plot of all the (corrected, Yuan et al. 2016) Pb Isotope data.

Chapter 6.

Gold compositional signatures in the Loch Tay area

6.1 Introduction

This Chapter is aimed at establishing gold compositional signatures across several localities in the Loch Tay area of Central Scotland, mainly to identify possible genetic environments of gold formation alongside the known vein systems. Results from the analysis of gold particles in terms of alloy and inclusion suites for in-situ, eluvial and placer gold samples are presented in the first part of the chapter, whilst the interpretation of the respective gold compositional signatures based on the same criteria and presentation order is proposed in the second part of the chapter. Additionally, both sections include (respectively) the preliminary analysis and subsequent evaluation of trace element data obtained on gold particles from some of these populations.

6.2 Gold (physical and) compositional characteristics

6.2.1 Calliachar Burn

A total of seven samples of gold particles are available from Calliachar Burn (Figure 6.1; Table 6.1). The first four listed, Calliachar_1, _2, _3 and _5, are placer gold samples, whilst the other three (Calliachar_6 to _8) are samples of gold particles from in-situ material (gossan or mineralised vein).

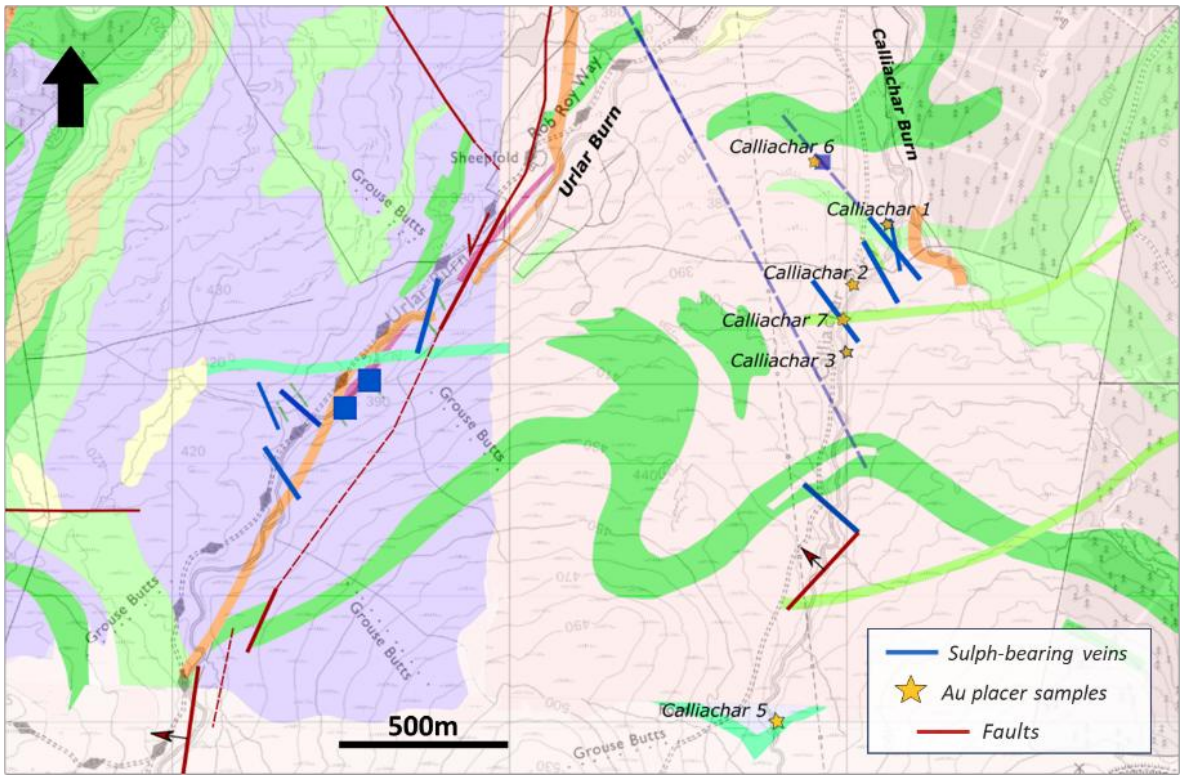

Figure 6.1 Map of Calliachar Burn showing the gold sample locations described in this section (modified after the BGS geological map from https://digimap.edina.ac.uk/).

Table 6.1 Gold particle samples from Calliachar Burn and respective details.

Locality	Sample type	Sample ID	No of particles	Summary of morphology and particle size	Grid reference		
Calliachar @veins	Placer	Calliacher _1	190	Often equant and with rough textures (Chapman et al. 2023c). Fine particles.	NN	84114	45471
Calliachar lower	Placer	Calliacher _2	139		NN	84009	45281
Calliachar mid	Placer	Calliacher _3	131		NN	84011	45090
Calliachar top	Placer	Calliacher _5	193	Similar to Calliachar_1 to _3, but generally more waterworn. Up to 10mm size.	NN	83800	44000
Calliachar Hilltop	Gossan-derived	Calliacher _6	77	Mostly flat and jagged. Fine particles.	NN	83921	45641
Calliachar @Discovery Vein	Gossan-derived	Calliacher _7	149	Mostly flat and jagged. Fine particles.	NN	83999	45177
Calliachar Hilltop	Vein-hosted	Calliacher _8	16	Flat and jagged, up to 50µm size.	NN	83921	45641

6.2.1.1 In situ and gossan gold (including both alloy and inclusion suite – where observed)

Figure 6.2 displays both 'wt.% Ag' and 'wt.% Hg' versus cumulative percentile plots relating to the Calliachar_6, Calliachar_7 and Calliachar_8 samples. The latter forms part of a sulphide-bearing quartz vein ('G Vein', see section) found at the same 'Calliachar_6' location: in Calliachar 8, gold is hosted in pyrite, in the form of both inclusions and fracture-fills (e.g., Figures 5.2 and 5.3; Table 6.2). The lowest silver contents (~16 to ~18 wt.%) have been observed for the few gold inclusions, which broadly correspond to the smallest (≥10µm) particles of the sample, as opposed to the more abundant, generally coarser (mostly ≥30 in diameter) fracture-fills, which tend to show higher silver contents (Table 6.2 and Figure 5.2). The Calliachar_6 and Calliachar_7 profiles indicate relatively narrow distributions of the silver content in the respective gold alloys (Figure 5.2a). The silver percentages in Calliachar_6 show a median value close to 30 (29.6), whereas two main classes can be observed Calliachar_7 - respectively around 25%, and in the interval between 31% and 34%. The Calliachar_8 plot overall reports lower silver values than the Calliachar_6 and Calliachar_7 ones. This evidence can possibly relate to the different gold particle sizes involved in these samples: when gold grains are liberated from gossan material by mechanical separation, the smallest ones (≤50 µm) can easily be lost during the process, yielding gold populations formed of overall larger particles. Instead, Calliachar_8 is formed of gold showing particle sizes between 10 and 50µm, which may explain their generally low silver content.

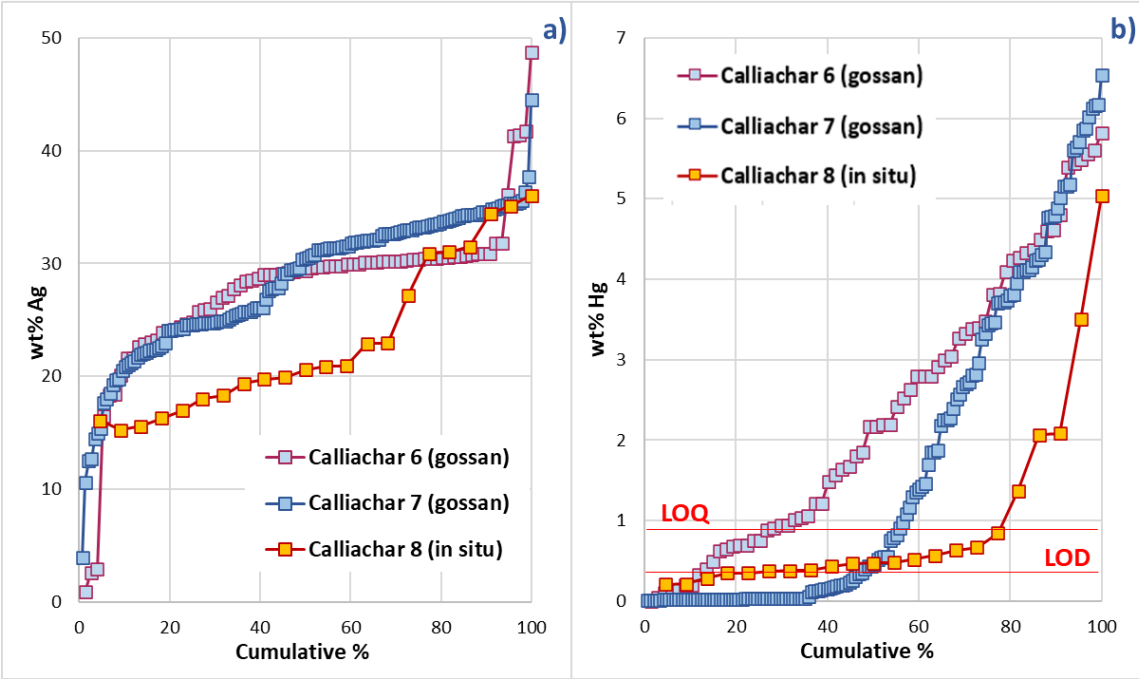

Figure 6.2 wt% vs cumulative% plots for Calliachar_6, Calliachar_7 and Calliachar_8. Silver (a) and mercury (b) contents in the gold alloy. LOD = Limit Of Detection; LOQ = Limit Of Quantification.

Table 6.2. Calliachar_8 gold: morphological, compositional and paragenetic characteristics.

Particle ID	Mode	Host	Approx. size (µm)	Ag (wt%)	Hg > LOQ (wt%)
G1	*inclusions (AuA_gv)*	*PyA_gv*	~10	~16	
G2			~10		
G3	*inclusions?*	*PyC_gv*	~10	~18	
G4			~10		
G5	*fracture-fills (AuA2_gv; AuC_gv)*	PyC_gv	≥ 30	19.35	
G6			≥ 30	19.75 to 22.91	1.4
G7			≥ 30		2.1
G8			≥ 30		2.1
G9			≥ 30		4.8
G10			≥ 30		5
G11			≤20	30.91	
G12		PyA_gv	≥ 30	31	
G13		PyC_gv	≥ 30	31.5	
G14			≥ 30	34.41	
G15		PyA_gv	≤20	35.08	
G16		PyC_gv	≤20	36	

Figure 6.2b highlights that 'Calliachar 6' and' 7' display overall higher mercury percentages, compared to the Hg plots of the placer populations (Figure 6.5b), with respectively ~76% and ~43% of their profiles falling above the LOQ. Additionally, the two curves overlap in the interval between wt% Hg 3.3 and 5.5. The mercury content in Calliachar_8 shows a dominant percentage

range between 0% and 1%, therefore below the LOQ. A subordinate portion of the population shows values from ~1.4% to ~5%. The data points recording the highest mercury contents correspond to larger, crack-hosted gold grains, although these particles do not coincide with the most silver-rich ones (Table 6.2). Binary plots have been used to illustrate Ag-Hg relationships in the same set of gold samples (Figure 6.3). The dominant silver percentage ranges (25%, 30% and 35%) broadly correlate with the full range of mercury percentages (> LOQ) observed in the gossan samples (Figure 6.3). A graphical display of the Ag-Hg relationships in in-situ gold (Calliachar_8) has additionally highlighted the concentration of higher (> LOQ) mercury amounts around a restricted silver range, as anticipated by Table 6.2. The relevant particles all show a diameter of ≥30 µm. Figure 6.4 indicates the distribution of inclusion species in the two gossan-derived gold samples (Calliachar_6 and Calliachar_7). The respective datasets have been merged in a radar plot ('Calliachar 6+7') due to the unavailability of a sufficient number of observed inclusion species (i.e., ≥ 15) for each of the samples. This has been possible due to their mutually compatible inclusion assemblages, individually depicted by spider plots (Figure 6.4a). The plots are built upon the abundance of these inclusion species in terms of their mineralogy, and highlight the dominance of pyrite species, followed by subordinate chalcopyrite and galena species; the same metallic signature can be observed in the elemental composition of these inclusions (Calliachar 6+7), reported in Figure 6.4b.

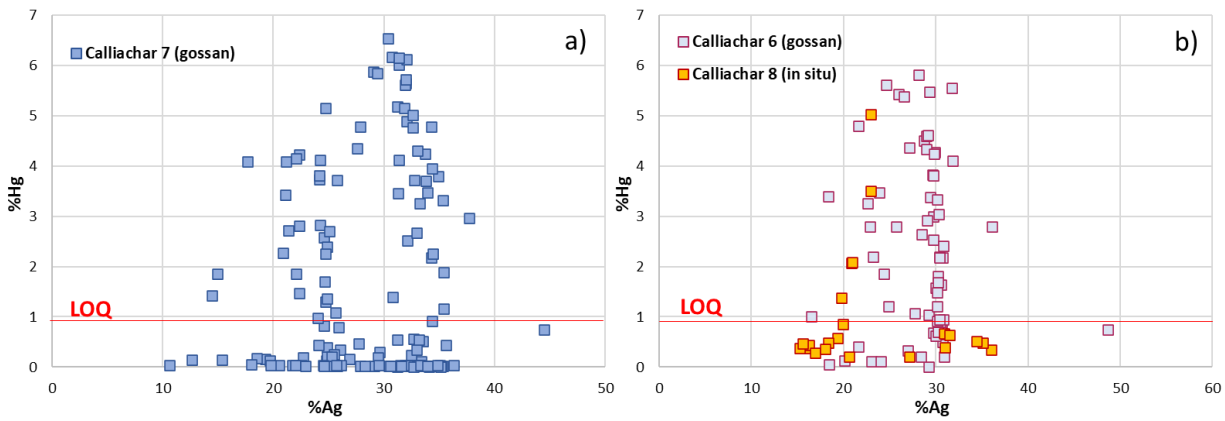

Figure 6.3 %Hg and %Ag bivariate plots that account for gold in gossan and in-situ samples from Calliachar Burn.

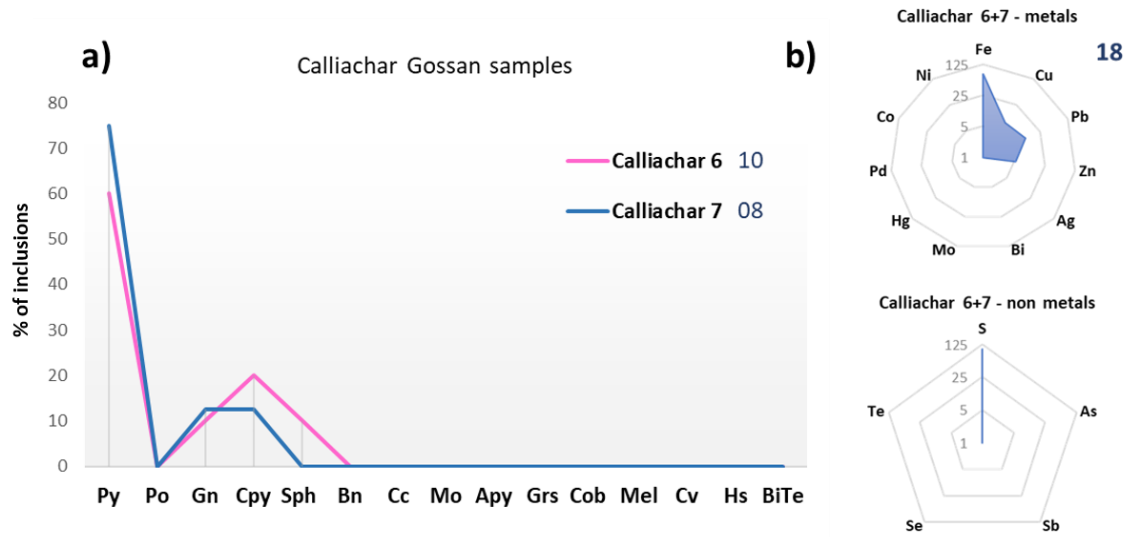

Figure 6.4 Inclusion suite observed for Calliachar 6 and 7. a) Mineralogical composition '10' and '08' indicates the total number of inclusions reported for each sample; b) Elemental composition. '18' indicates the total of inclusions reported for this sample.

6.2.1.2 Placer gold

Gold alloy analysis

Samples are numbered progressively from downstream to upstream in the drainage. Figure 6.5 indicates the relevant 'wt.% Ag' and 'wt.% Hg' versus cumulative percentile plots. Calliachar 1, 2, 3 and 5 display similar silver profiles that increase regularly (Figure 6.5a), as shown by the roughly constant gradients of individual curves and >75% of them falling above a wt. Ag% value of 20 (e.g., Chapman et al. 2023c). However, all four placer samples show a concentration of their mercury contents between 0.1% and 0.9% (below LOQ) - this is displayed by the relevant plots (Figure 6.5b), all hosting >62% of data points within such interval. The mercury values that are displayed above the LOQ reach wt.% ~6.3 and ~6.5 in Calliachar_5 and Calliachar_2, respectively, and a maximum of ~7.8 in Calliachar_1.

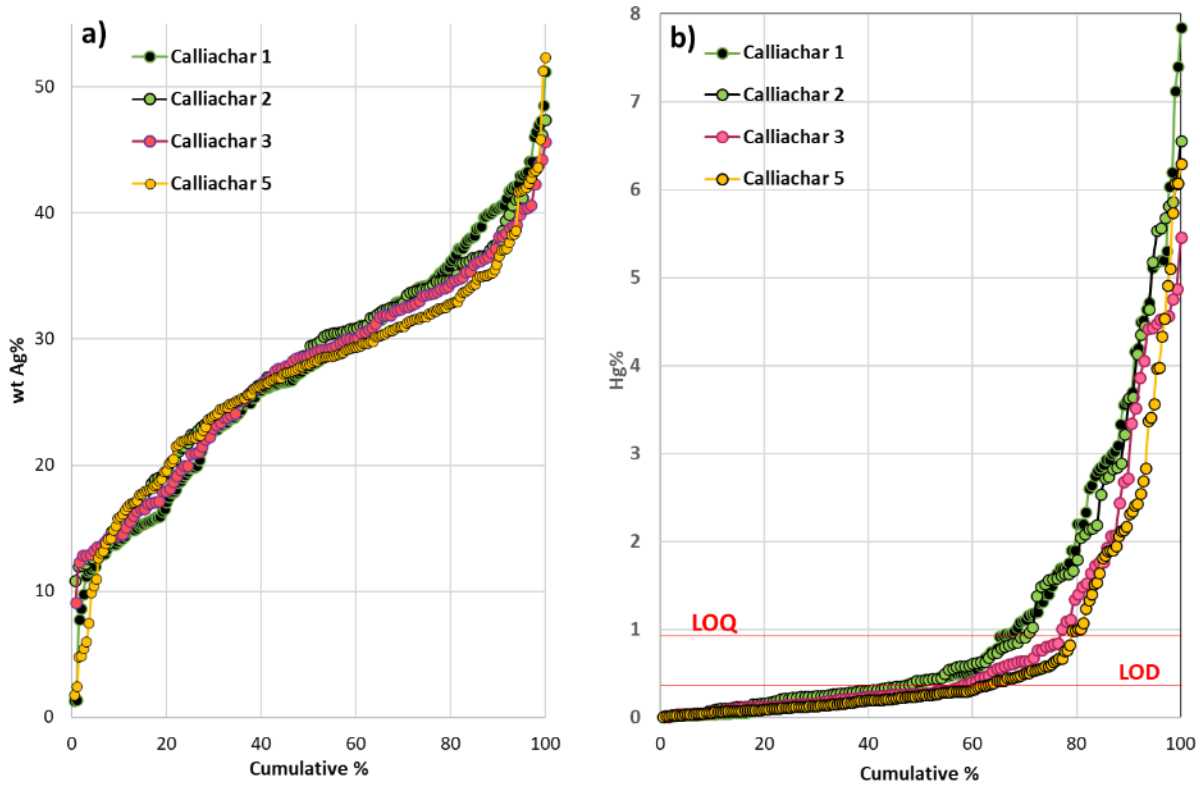

Figure 6.5 wt% vs cumulative% plots for Calliachar_1 to Calliachar_5. Silver (a) and mercury (b) contents in the gold alloy. LOD = Limit Of Detection. LOQ = Limit Of Quantification.

Analysis of the gold inclusions

The inclusion species recorded in the placer gold sample suite from Calliachar Burn have been investigated and accounted for in line with their relative amounts. These are here illustrated via radar (Figure 6.6) and spider (Figure 6.7) plots. Radar diagrams here indicate a general dominance of base metals (Fe, Cu, Pb, Zn) and of As and S, as non-metals. Pb specifically results in higher proportions across Calliachar 1 and - as previously observed (Figure 6.4b) – Calliachar 6+7, while Zn is relatively abundant in Calliachar 2. Arsenic occurs in very low proportion in Calliachar 3. Five spider profiles are presented in Figure 6.7 and reflect the inclusion suite of the five 'Calliachar' gold samples, in terms of mineral species. Beyond pyrite, the samples from downstream in the drainage (Calliachar 1, 2; 6 and 7 in Figure 6.4a) have recorded inclusions of galena, sphalerite, arsenopyrite and chalcopyrite in percentages ≥ 15. This indicates greater abundance and variety than in gold from the mid-upstream samples (Calliachar 3, 5), where these species have been scarcely recorded. Pyrite is also the dominant inclusion mineral in Calliachar 3 and 5 (reaching 65%-70% in relative abundance), followed by pyrrhotite.

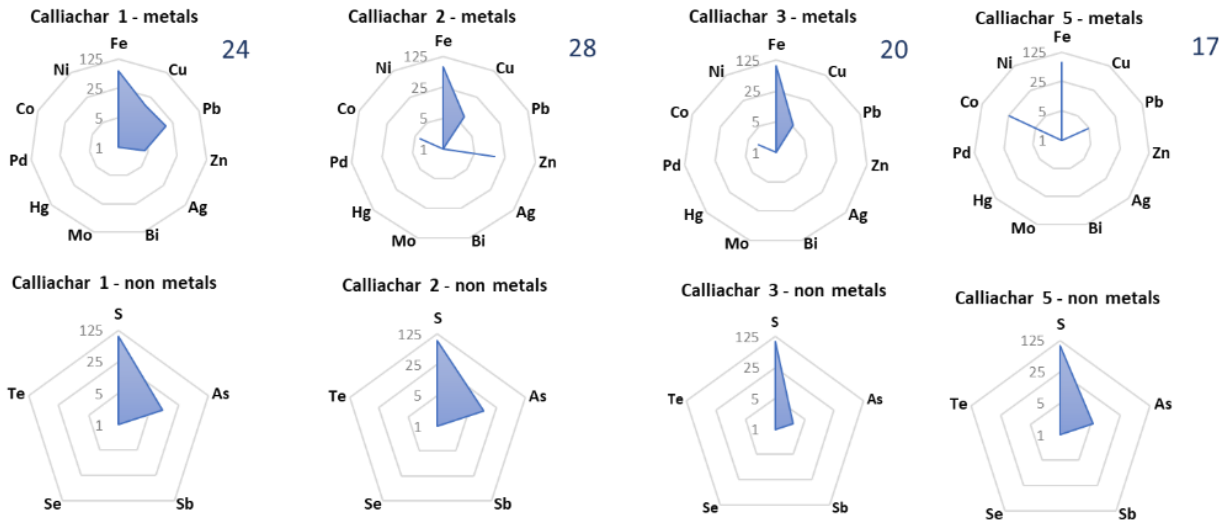

Figure 6.6 Radar diagrams indicative of the elemental inclusion components in gold samples from Calliachar Burn, downstream (Calliachar 1) to upstream (Calliachar 5). The numbers on top-RHS indicate the total of inclusions reported for each sample.

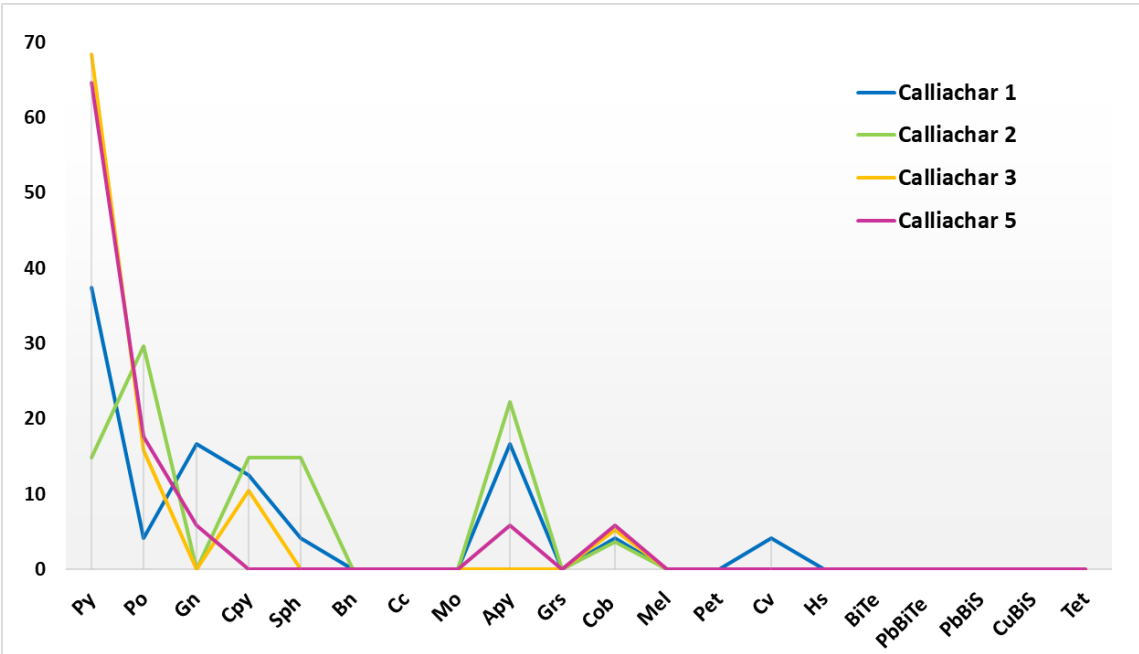

Figure 6.7 Spider diagrams indicative of the inclusion mineral species (respective amounts) in gold samples from Calliachar Burn, downstream (Calliachar 1) to upstream (Calliachar 5).

6.2.2 River Almond

A total of eight samples of gold particles are available from River Almond (Figure 6.8; Table 6.3). The first six listed (Almond_1 to Almond_5) are placer gold samples, whilst the remaining two are samples of gold particles liberated from (Almond_6a) or directly observed in (Almond_6b) mineralised vein material.

Table 6.3 Gold particle samples from River Almond and respective details.

Locality	Sample type	Sample ID	No of particles	Summary of morphology and particle size	Grid reference		
Sma Glen	Placer	Almond_1	334	Fine, waterwarn/flacky particles as well as rough particles.	NN	90561	29437
W Almond	Placer	Almond_2	115		NN	87326	31684
Almond Auchnafree	Placer	Almond_3	334	Often equant and with rough textures (Chapman et al. 2023c). Up to 10mm size.	NN	76553	33015
Almond near Au March	Placer	Almond_4a	230		NN	74534	33866
Almond upper	Placer	Almond_4b	227		NN	73798	33629
Almond top	Placer	Almond_5	145		NN	72983	32822
Almond from vein (hypogene)	Crushed-ore	Almond_6a	104	Overall fine particles, but never <50µm. Rough morphologies.	NN	72983	32822
Almond from vein	Vein-hosted	Almond_6b	18	Inlcusion and fracture-fill particles. From ~10µm to ~80µm.	NN	72983	32822

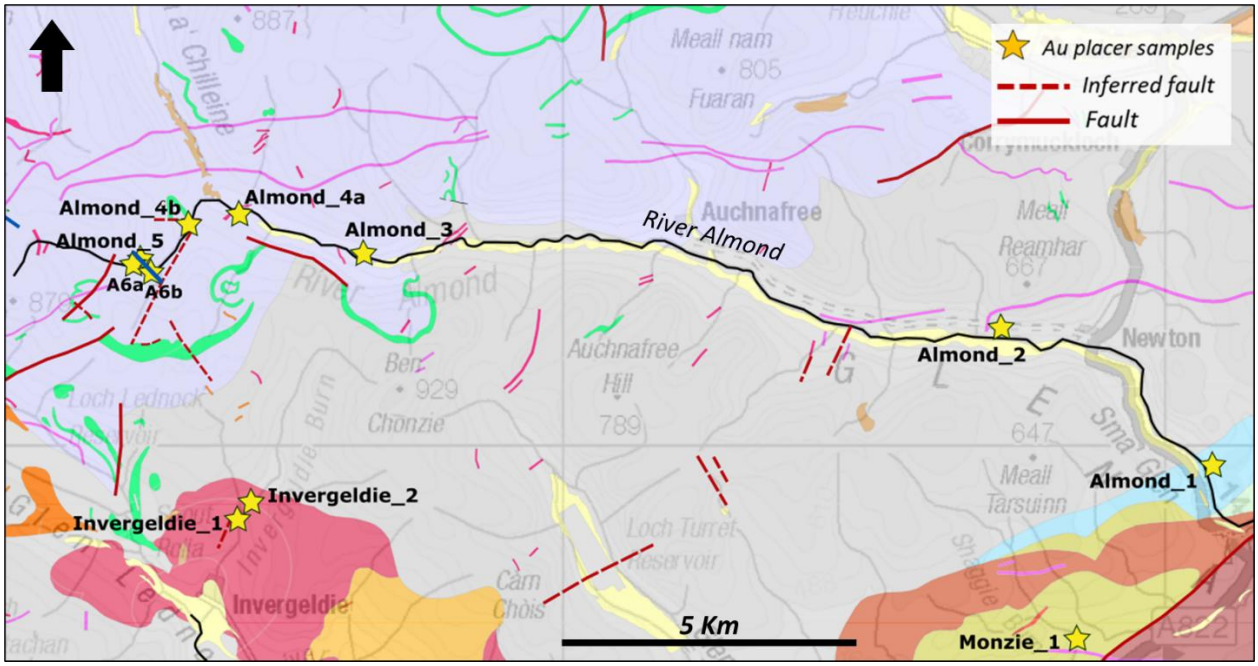

Figure 6.8 Map of River Almond showing the gold sample locations described in this section (modified after the BGS geological map from https://digimap.edina.ac.uk/).

6.2.2.1 In-situ gold

The compositional characteristics of the in-situ gold from River Almond are reported in Figure 6.9. Almond_6b is the sample which records the highest Ag content, with a median value of 34.64% - the respective curve is almost entirely flat; however, the sample size is very small (21

particles) . In general, the particles showing Ag content <25% correspond to the smallest ones, identified as inclusions in sulphides (Figure 6.9b; AuB_av1, section 5.2.2.2), whereas the remaining ones are fracture-fills (Figure 6.9b; AuB_av2, section 5.2.2.2). Almond_6a is a gold sample obtained by mechanically crushing pieces of the main local vein, also hosting Almond_6b (e.g., section 5.2.2.2). The distribution of silver in the respective alloy is described by i) two major plateaux below wt. % Ag = 20 and ii) a broader range of contents, from 20% to 38% Ag. The dominant silver-rich trend displayed by the Almond_6b profile is almost absent in Almond_6a. Almond_5 is descriptive of the Ag content in the alloy of placer gold from the same locality, which appears overall greater than the one in Almond 6a.

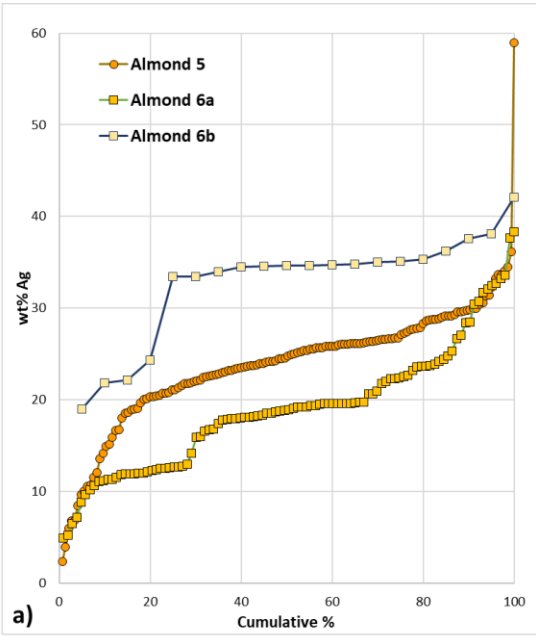

Particle ID	Mode	Host	Ag (wt%)
a1	inclusion	PyB_av	18.9
a2	in fracture	PyB_av (ga on the side)	~22
a3	inclusion	PyB_av	
a4	inclusion		26
a5	Inclusion		33.4
a6	fracture		
a7 to a9	in fracture		34 to 35
a10	in fracture		36.2
a11 to a13			37.56 to 42.1
a14	in fracture	CpyB_av	34.6
a15	inclusion		
a16 - a17	in fracture	CpyB_av and ?	34.7
a18	semi-fracture	SphB_av (PyB on the edge)	24.3
a19 to a21	in fracture	SphB_av	34.65 to 35.3

b)

Figure 6.9 Compositional characteristics of the in-situ gold from River Almond. a) wt% Ag vs cumulative% plots; b) Almond_6b complementary paragenetic information.

6.2.2.2 Placer gold

Gold alloy analysis

The investigated sample populations are all relatively large-sized (i.e., each containing more than 100 particles), particularly Almond_1 and Almond_3 (Table 6.3) and numbered progressively from downstream to upstream; the Almond _3 placer sample is a combined sample derived from multiple placer sub-samples obtained from very close sites. The plots of the silver contents in Almond_3 and _1 (Figure_6.10) show a steep increase in their gradients at wtAg ≥ 32% which corresponds to ~10% of the relevant populations. Profiles of the silver contents in gold from the Upper Almond catchment (Almond_4b and _5) have very similar

shapes, which show sharp gradient changes towards their edges, defining a dominant class (>75% of particles) with silver content between 20% and 30%-32%, and two subordinate ones, with silver content respectively below and above these thresholds (Figure 6.10). The shape of Almond_2 differs from the others mainly because of the lower number of grains involved in the analysis; the silver content distribution displays a stepped but constant profile (Figure 6.10).

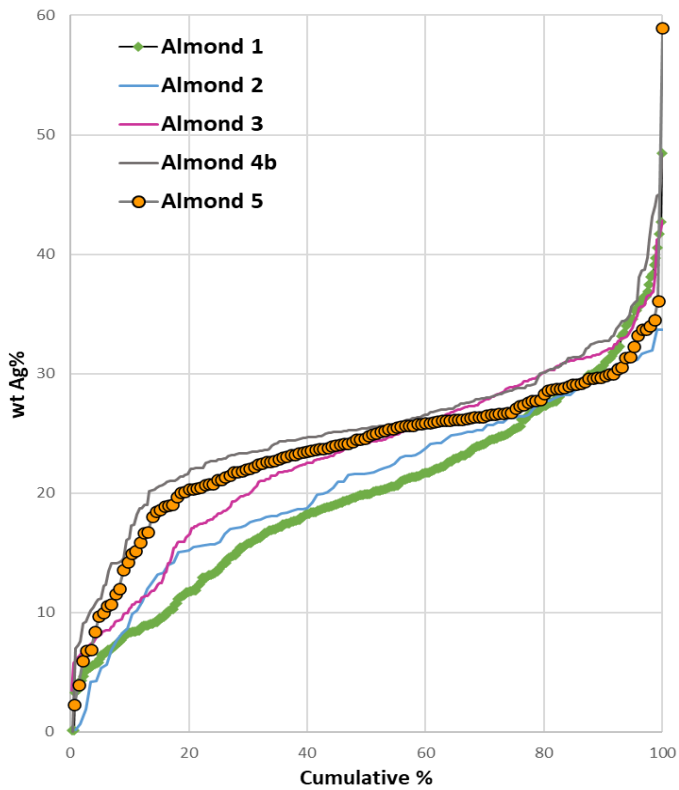

Figure 6.10 wt% Ag vs cumulative% plots relating to the placer gold samples from River Almond.

Analysis of the gold inclusions

The inclusion species recorded in the placer gold sample suite from River Almond are illustrated via radar (Figure 6.11) and spider (Figure 6.12) plots.

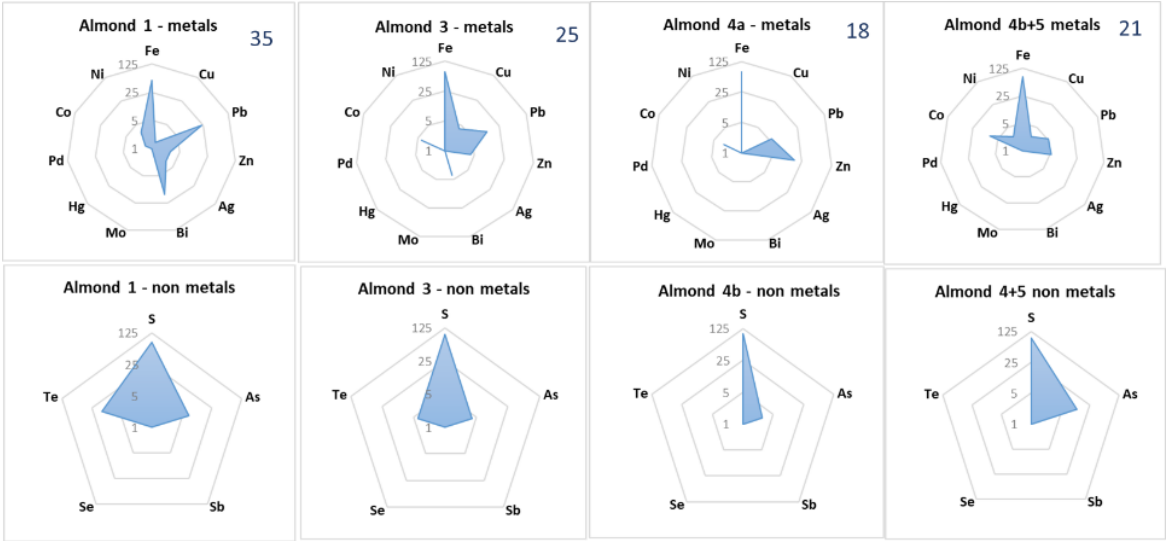

Figure 6.11 Radar diagrams indicative of the elemental inclusion components in gold samples from River Almond, downstream (Almond_1) to upstream (Almond_5). The numbers on top-RHS indicate the total of inclusions reported for each sample.

The Almond_4b and _5 samples have been merged due to the insufficient quantity of inclusion species recorded for each of them; this has been possible because the samples are both from Upper Almond sites - as well as Almond_4a where, instead, enough inclusions (≥ 15) have been identified. In general, samples from the lower portion of the river (e.g., Almond_1) have resulted in more complex mineralogical assemblages. The inclusions in Almond 1, corresponding to the Sma Glen location contain bismuth as metal and tellurium as non-metal. The presence of these elements, along with silver, can also be identified in Almond_2 (W Almond) and Almond_3 (Auchnafree) according to different proportions – namely higher silver and lower bismuth and tellurium amounts. Lead appears proportionally lower in the upstream samples (Almond_4a, Almond_4b+5). Zinc and arsenic generally keep in constant percentages among various populations, albeit different behaviours that can be noticed in the Almond_4a plots - these indicate higher zinc content in the metals, and significantly lower arsenic content in the non-metals.

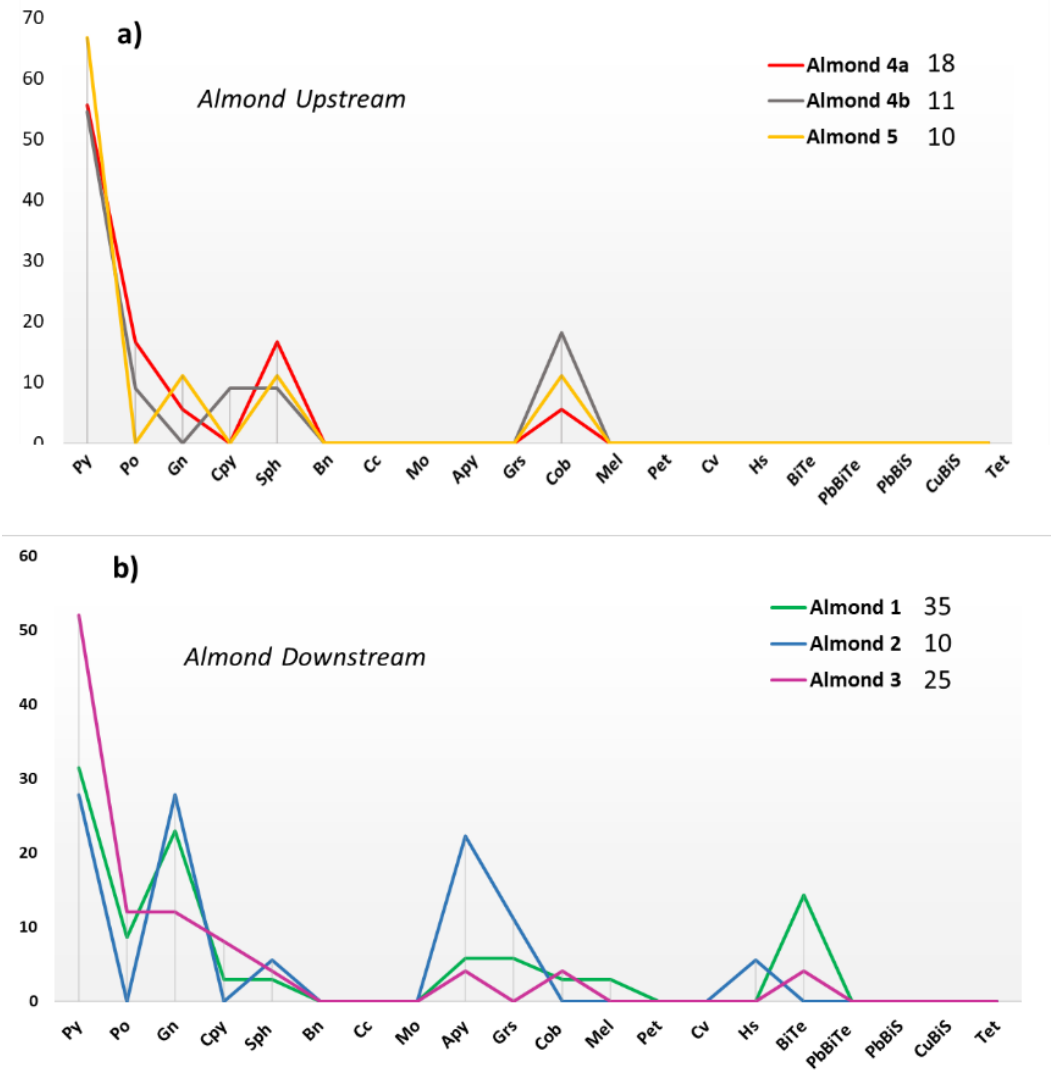

Figure 6.12 Spider diagrams indicative of the inclusion mineral species (respective amounts) in gold samples from Glen Almond, downstream (a) to upstream (b). The numbers to the right of the legend elements in b) indicate the total of inclusions reported for each sample.

The inclusion mineralogy in gold samples from Glen Almond (Figure 6.12) is not limited to Py, Gn, Cpy, Apy, but is sometimes inclusive of gersdorffite, cobaltite, hessite and BiTe. Placer samples from upper and lower reaches differ substantially in terms of both element and mineral compositions. Pyrite, sphalerite and cobaltite are relatively abundant in the mineral inclusion suites of Almond 4a, 4b and 5. On the other hand, Almond_1 and Almond_2 are the two gold populations that present the greater inclusion variety; the Almond_1 ('Sma Glen' locality) gold specifically includes bismuth-tellurides, whilst Almond_2 contains inclusions of arsenopyrite, which was not found in gold from the upstream sampling sites. Galena inclusions are relatively abundant in both populations.

6.2.3 Lead Trial and Ardtalnaig

Analyses were conducted on gold particles from crushed ore and placer samples, whose details are reported in Table 6.4. Their respective silver profiles are indicated in Figure 6.13c; Figures 6.13a and b have exceptionally been placed on the side to highlight specific SEM characteristics reflected in the gold alloy composition.

Table 6.4. Gold particle samples from the Lead Trial and Ardtalnaig, with respective details.

Locality	Sample type	Sample ID	No of particles	Summary of morphology and particle size	Grid reference		
Lead Trial	Crushed-ore	Tip_1	77	Typically in the scale of hundreds of microns, the largest ~700µm in length. Rough morphologies.	NN	70838	39250
Lead Trial	Crushed-ore	Tip_2	126		NN	70838	39250
Ardtalnaig Dike (2021)	Placer	Ardtalnaig_1	39	Variably sized and waterworn.	NN	72455	38466
Ardtalnaig Mid (2021)	Placer	Ardtalnaig_4	18		NN	71192	38773

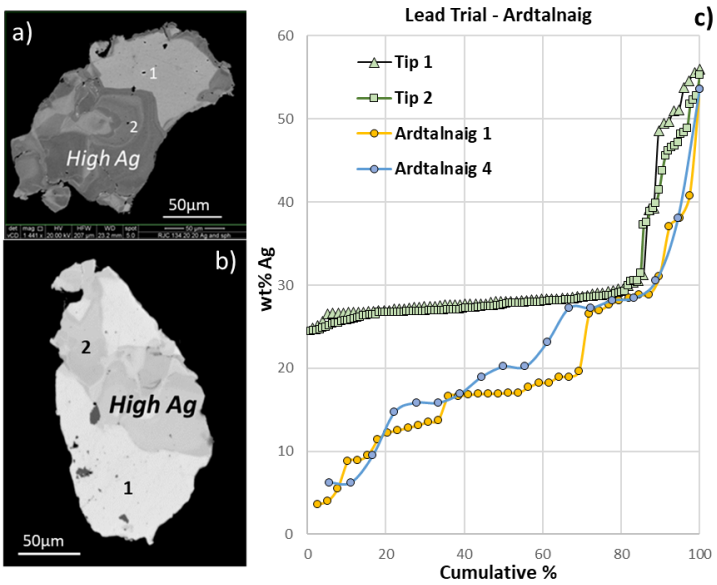

Figure 6.13 a) and b) SEM pictures of gold particles from the Lead Trial (a) was taken by Rob Chapman; c) Ag vs cumulative% plots relating to the gold samples from Lead Trial/Ardtalnaig.

Gold alloy analysis

The silver contents of the 'Tip_1' and 'Tip_2' gold populations have consistently resulted in two main classes (Figure 6.13c), which both show steady (median of ~27 wt.%) and steeply increasing (from ~29 to ~57 wt.%) trends; consequently, the data from these two populations can be later amalgamated in a single plot. These are confirmed by SEM-BSE imaging of the same gold samples, pointing at the co-existence of two major alloy phases (in the form of Ag-rich

patches and tracks) within many of the particles (Figures 6.13a, b). The silver profiles of Ardtalnaig_1 and Ardtalnaig_4 display substantially different trends, overall showing lower silver contents and more constant gradients.

Analysis of the gold inclusions

Pie charts (Figures 6.14a and b) have been used to depict the relative abundances of the mineral inclusion species observed in gold from Tip_1 and Tip_2. The 'Tip_2' gold has appeared to host a much larger number and a slightly greater variety of inclusions (e.g., inclusive of Molybdenite); sphalerite is by far the local dominant species, whereas galena dominates the 'Tip_2' mineral assemblage. Sphalerite, galena and chalcopyrite inclusions are present in both samples and, because of the strong similarity between the 'Tip_1' and 'Tip_2' silver profiles, all the inclusion species observed in the two gold populations have ultimately been treated in conjunction (Figures 6.14c and d). Both radar (Fig. 6.14c) and spider diagrams (Fig. 6.14d) emphasize the dominance of a Pb+Zn (Ga+Sph) assemblage and subordinate Mo (Molybdenite).

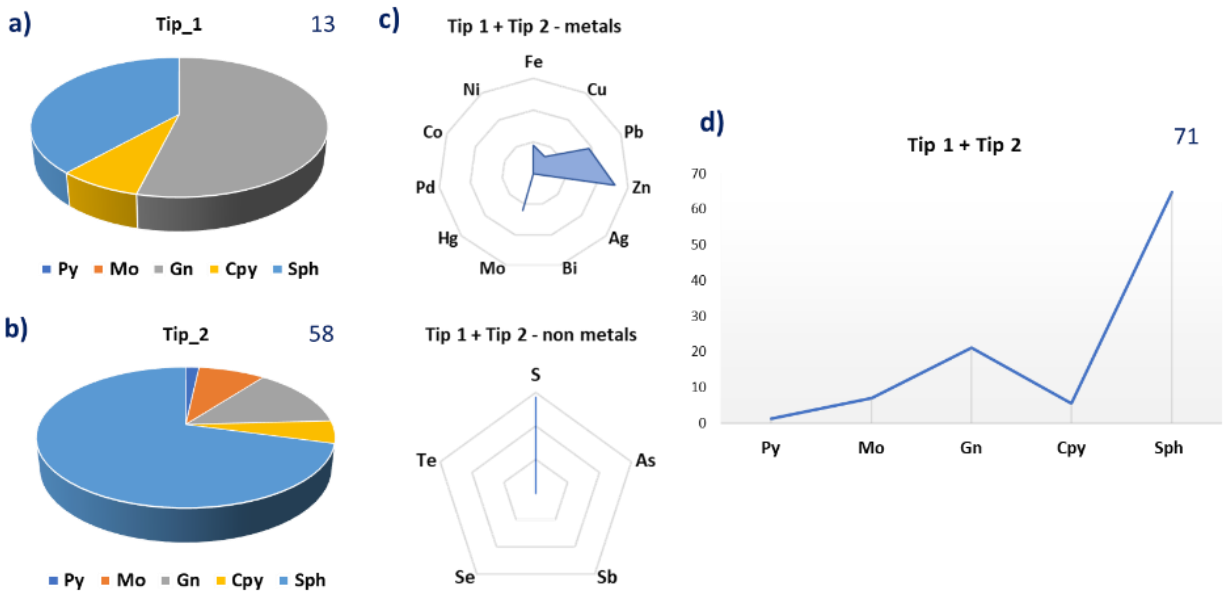

Figure 6.14 Inclusion assemblages in the Lead Trial gold samples. The numbers on the Top-right of each diagram indicate the total of inclusions reported for each sample.

The inclusion species observed in the proximal Ardtalnaig (placer) have generally recorded higher Mo and Cu and lower Zn and Pb relative abundances (e.g., Webb, 2024).

6.2.4 Loch Tay South

Investigations have focused on a total of six placer gold populations from the southernmost part of the Loch Tay area (Table 6.5). Some of them have been merged to generate composite samples (i.e., Invergeldie_1 + Invergeldie_2 and Keltie_1 + Keltie_2), due to their close geographical proximity (Figure 6.15), in the first place, and subsequent nearly equivalent silver profiles.

Table 6.5 Gold particle samples from the South of the Loch Tay area with respective details.

Locality	Sample type	Sample ID	No of particles	Summary of morphology and particle size	Grid reference		
Invergeldie Burn	Placer	Invergeldie_1	144	A range of particle morphologies and generally small particle sizes (up to 2-3 mm; Chapman et al. 2023c).	NN	74617	28676
	Placer	Invergeldie_2	126		NN	74769	29013
Glen Lednock	Placer	Lednock_1	192		NN	76808	23704
Keltie Burn	Placer	Keltie_1	103		NN	86808	25013
	Placer	Keltie_2	91		NN	86365	25142
Monzie	Placer	Monzie_1	90		NN	8858	2671

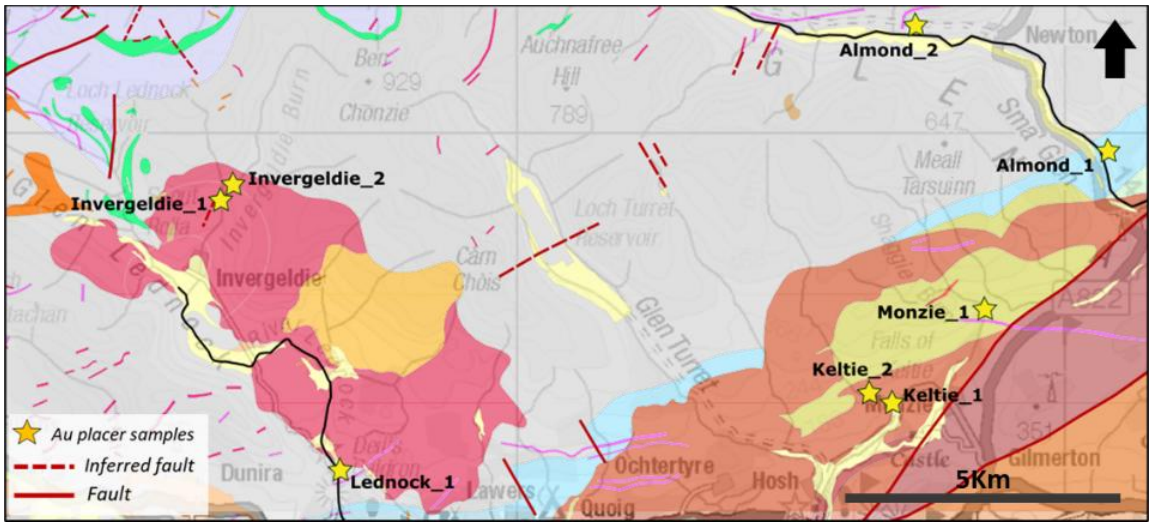

Figure 6.15 Geological map of the South of the Loch Tay area with gold sampling locations (modified after the BGS geological map from https://digimap.edina.ac.uk/).

Gold alloy analysis

The silver contents recorded in the gold alloys of these samples are illustrated by cumulative plots in Figure 6.16a. The 'Lednock 1' and 'Keltie 1+2' curves display roughly concave-up shapes, determined by ~70% of the particles containing <20% of silver in the alloy (Chapman et al., 2023c). The 'Invergeldie 1+2' (especially) and 'Monzie 1' curves overall indicate slightly higher silver contents in the respective populations (from ~48% to ~58% of particles with wt%Ag <20). The copper percentages detected in the alloys of the same gold samples are reported in Figure

6.16b. All the populations are characterised by detectable Cu contents, generally above the average values recorded by the Loch Tay gold samples; Keltie 1+2 and Monzie 1 are the ones showing, in proportion, the largest number of particles with quantifiable (> LOQ) Cu values, within the "Loch Tay South" sample suite.

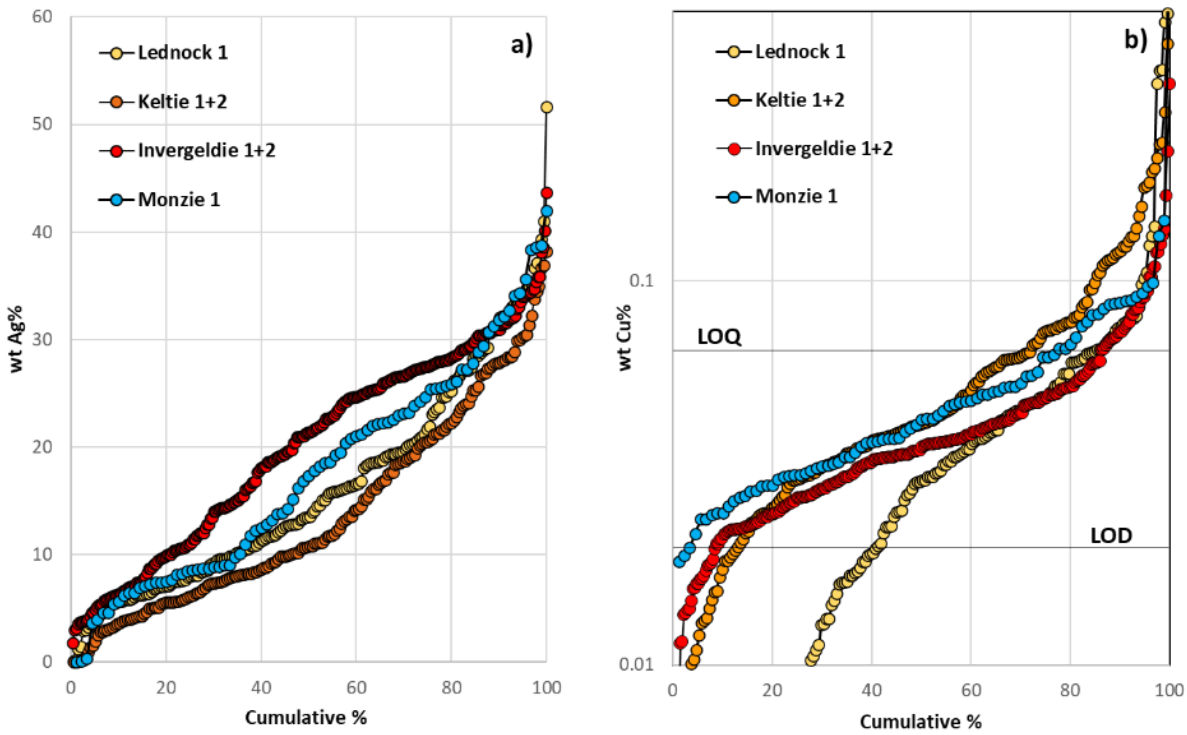

Figure 6.16 %Ag versus cumulative% plots accounting for gold samples from the Southern Loch Tay area. Figure 6.16b – Logarithmic scale

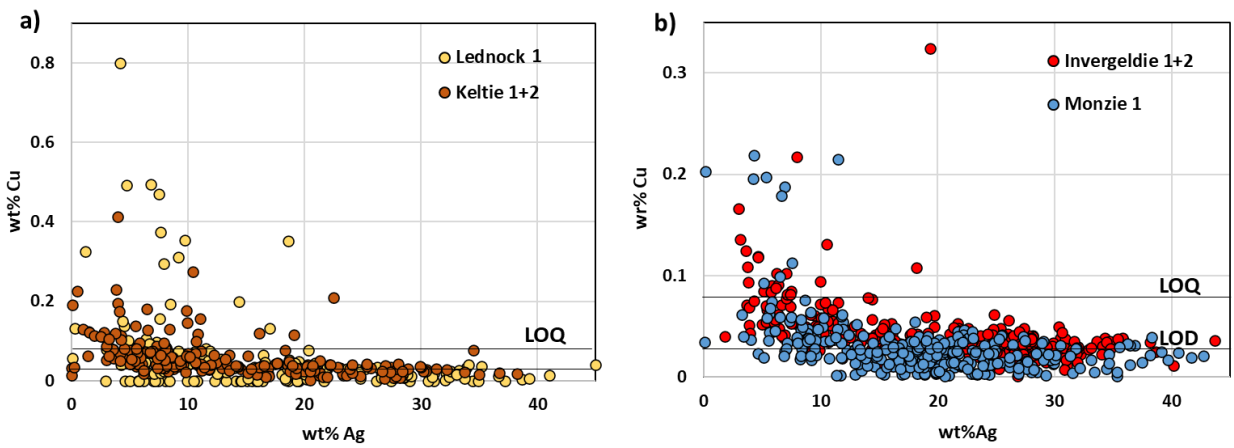

Figure 6.17 Cu-Ag binary plots for gold samples from the Southern Loch Tay area. LOQ= Limit of quantification LOD= Limit of detection.

The bivariate distributions of silver and copper are displayed in Figure 6.17a for the samples from Glen Lednock and Keltie Burn, and in Figure 6.17b for the ones from Invergeldie Burn and

Monzie. An inverse relationship between the two gold alloy components is generally observed (Chapman et al. 2023c); the highest Cu values correspond to particles from Glen Lednock and Keltie Burn. In addition, the Lednock 1 and Keltie 1+2 populations each contained two gold particles with Pd > 5 wt% (i.e., 6.4% and 5.6%, respectively), with the rest showing typical Loch Tay range values; Pd was unquantifiable in all the other Loch Tay populations.

Analysis of the gold inclusions

Graphical representations (radar and spider diagrams) of the inclusion content and relative abundances in gold samples from Glen Lednock, Keltie Burn and Invergeldie Burn are reported in Figures 6.18 and 6.19; only 8 inclusions were detected in the 'Monzie 1' gold population, therefore robust assessment of the inclusion suite of this sample has not been possible. A Bi-Te signature is ubiquitous in this set of samples (e.g, Chapman et al. 2023c), generally accompanied by lead, iron and cobalt, and notable amounts of copper and molybdenum specifically in the 'Lednock 1' metal suite (Figure 6.18).

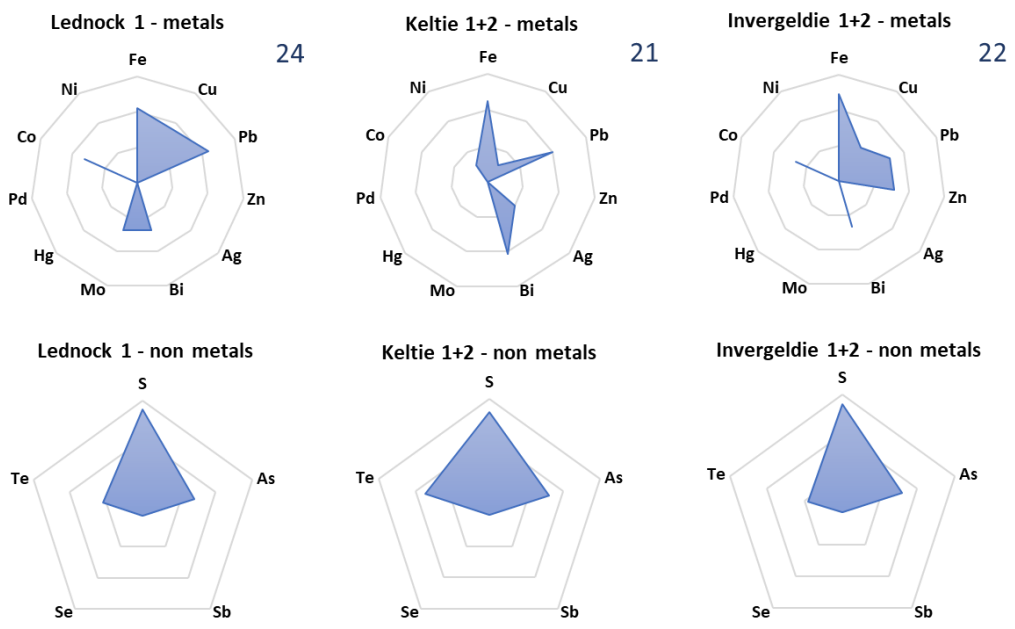

Figure 6.18 Radar diagrams indicative of the inclusion chemistry in gold samples from the Southern Loch Tay area. The numbers on the Top-right of each diagram indicate the total of inclusions reported for each sample.

Analysis of the mineral inclusion assemblage of these samples has highlighted a bornite-chalcocite-molybdenite signature in the 'Lednock 1' suite (Figure 6.19; Chapman et al., 2023c), confirmed by the elevated Cu content in the respective radar diagram (Figure 6.19). Additionally,

chalcopyrite is present in relatively high quantities in both gold from Glen Lednock and from Invergeldie (Figure 6.19). Galena, arsenopyrite and pyrite are common species in all three samples (Figure 6.19). A BiTe signature is only expressed by the 'Keltie' and 'Invergeldie diagrams (Figure 6.18); molybdenite is only present in the Lednock inclusion assemblage.

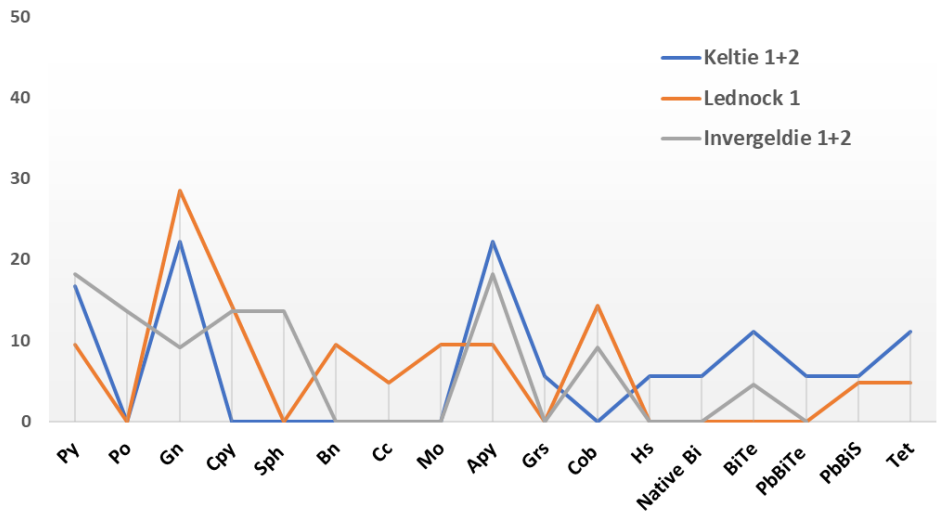

Figure 6.19 Spider diagrams indicative of the inclusion mineral species (respective amounts) in gold samples from the Southern Loch Tay area.

6.2.5 Glen Quaich

Analyses were conducted on gold particles from a placer sample, whose details are reported in Table 6.6. For the exact location of the sample, please refer (besides the grid reference coordinates in table 6.6) to figures 7.7 or 1.1.

Table 6.6. Gold particle sample from Glen Quaich; relevant details and grid reference.

Locality	Sample type	Sample ID	No of particles	Summary of morphology and particle size	Grid reference		
Glen Quaich	Placer	Glen Quaich	378	Flaky, flat morphology. Size in the range of 0.1 to 3 mm (Chapman et al., 2023)	NN	81863	40280

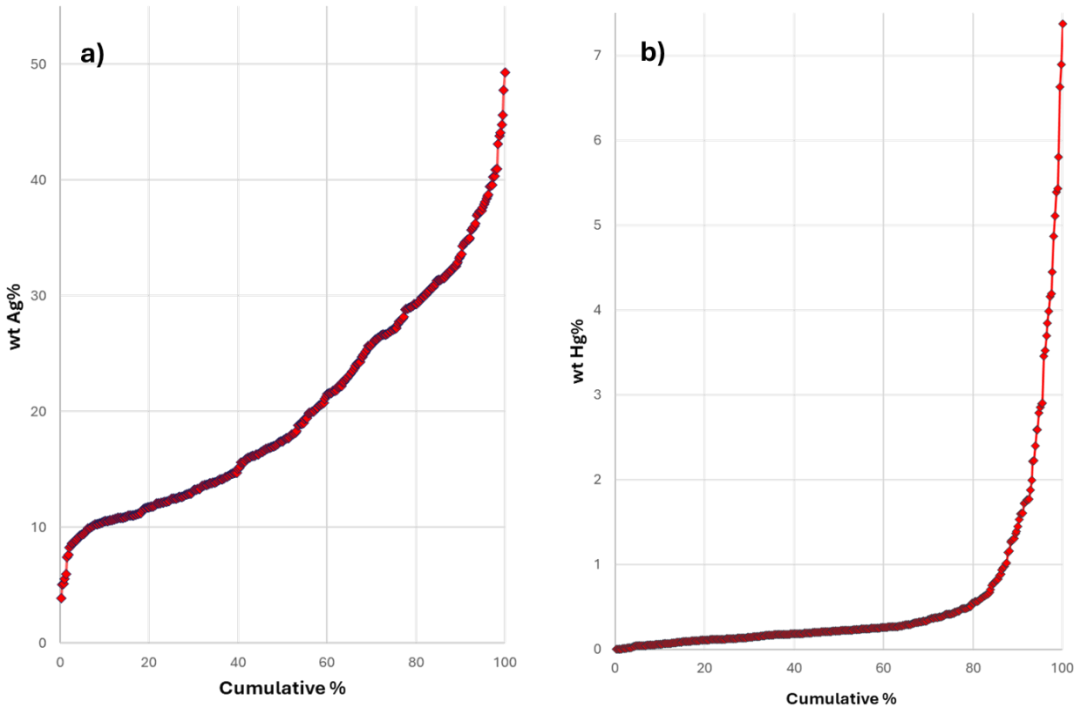

Figure 6.20. Wt.% vs cumulative% plots for the Glen Quaich placer gold sample. Silver (a) and mercury (b) contents in the gold alloy.

The silver and mercury profiles for the Glen Quaich population are indicated in Figure 6.20 (a, b). There is only one population from this locality, formed by a large number of particles (i.e., 378), whose gold compositional features have mostly been employed for comparative purposes with other placer populations (e.g., from Calliachar Burn and River Almond; Chapman et al., 2023c). These will be discussed in section 7.2.3.1, where more insights on the Glen Quaich placer sample (i.e., alloy and inclusion suite) will be provided. Figures 6.20 and 6.21 have been

included in this section for illustrative purposes of the composition and inclusion assemblage of the sample. It is noted that most of the particles show an Hg content below the limit of quantification (to be considered around 0.85, Figure 6.20b; Chapman et al., 2023c).

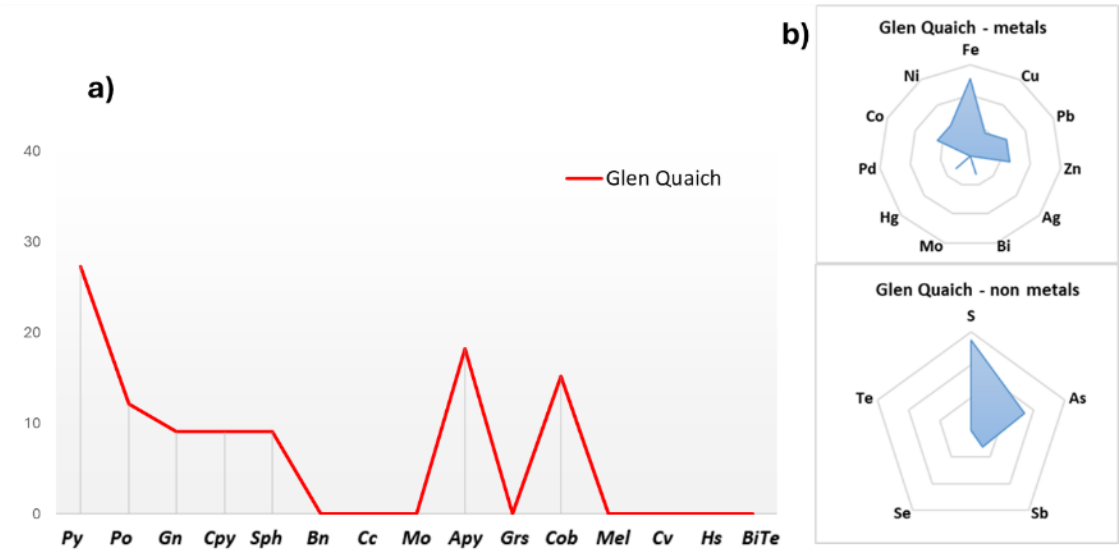

Figure 6.21. Inclusion suite in the Glen Quaich placer gold sample. a) mineral inclusions; b) inclusion chemistry. Inclusion count in the Glen Quaich sample: 37.

Among the base metal sulphides, the mineral inclusion composition of the Glen Quaich sample (Figure 6.21) indicates the presence of cobaltite. Molybdenum and bismuth additionally appear – albeit in low proportions - in the (metal) elemental suite of the inclusions, while antimony and sulphur in the (non-metal) one.

6.2.6 Composition of gold at the trace element level

Single-spot LA-ICP-MS analyses were conducted on gold particles from restricted sample sets (i.e., 10 to 30 particles each) from individual locations distributed across four sub-regions in the Loch Tay area - namely Calliachar Burn, River Almond, Lead Trial-Ardtalnaig and Invergeldie. Both SEM and EPMA investigations on the inclusion suite and gold alloy, respectively, were conducted ahead of performing LA-ICP-MS analysis. Au, Ag, Hg and Cu are ubiquitous in the gold alloy of the samples investigated. Their relative contents (expressed as percentages) were already obtained by EPMA analysis, and their comparison with LA-ICP-MS data has overall confirmed the same value ranges or, in specific cases, trends (Figure 6.22). Figure 6.22 reports examples of the silver and gold content comparisons, using EPMA and LA-ICP-MS data obtained on the same gold particles (30 in total) from the Calliachar Lower (Calliachar_02) placer and Lead Trial (crushed ore) gold populations. The EPMA data, originally expressed in weighted percentages, were converted into ppm to facilitate graphical display against the LA-ICP-MS data using the same types of plots (Ag ppm/Au ppm vs cumulative percentages).

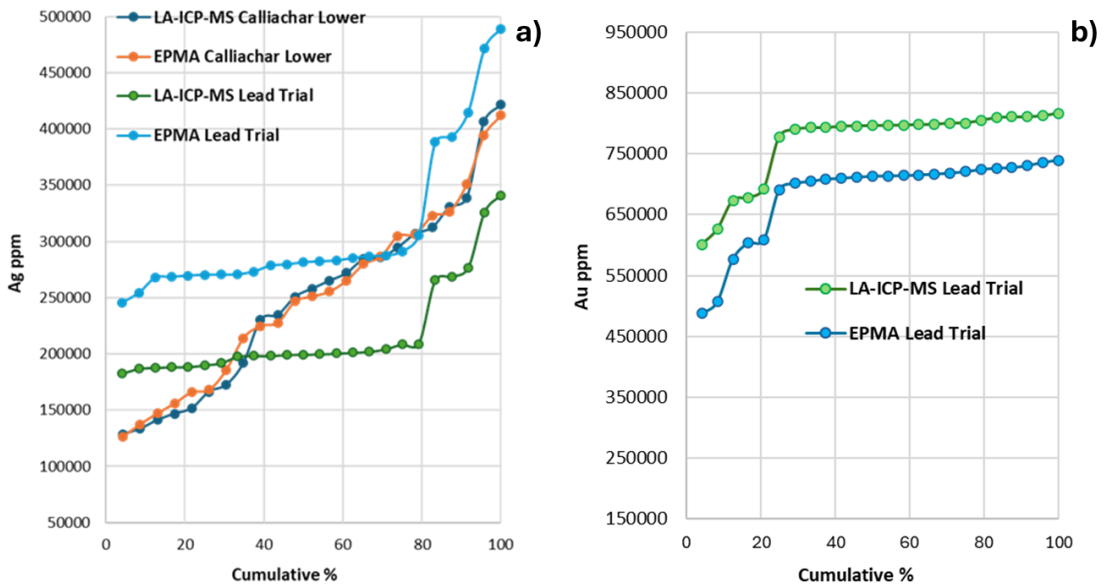

Figure 6.22. Ag (ppm; a) and Au (ppm; b) vs cumulative percentages plots of LA-ICP-MS and EPMA data obtained for the Calliachar 02 and Lead Trial gold populations (30 particles were used for each of the datasets). EPMA (wt%) values were converted into ppm units to facilitate graphical comparison with LA-ICP-MS values.

The distribution of the Ag contents in the Calliachar Lower gold particles is expressed by very similar profiles and value ranges for both the LA-ICP-MS and EPMA (Figure 6.22a); in the case of the Lead Trial sample, although the two (LA-ICP-MS and EPMA) datasets display very similar graphical trends, their overall Ag value ranges is different, with the LA-ICP-MS data showing

lower Ag abundances (in the order of ~50000 ppm). In light of this observation, a comparison of the results from both analytical techniques has been conducted on the same set of particles to evaluate the Au content distribution in the Lead Trial sample (Figure 6.22b). Even in this case, both gold profiles exhibit a very similar trend, with a gap of ~50000ppm between the value ranges of each of the two datasets (LA-ICP-MS and EPMA). However, in the case of Au distribution, the range of higher gold contents in the particles appeared to have been detected by the LA-ICP-MS analysis.

The opposite results from LA-ICP-MS and EPMA analyses and the consistency of the offset between the datasets suggest that the discrepancy is unlikely to be linked to the compositional heterogeneity observed within the gold particles at the Lead Trial (see section 6.2.3), as this would not be expected to affect all analyses to a similar degree. Instead, these results point towards a methodological or data-reduction effect associated with one or both analytical techniques. Potential explanations may include different correction procedures, calibration strategies, or conversion and normalisation approaches adopted during data processing and reduction. A check of the procedures followed and of the analytical totals did not identify any obvious error; however, in the Lead Trial sample, mercury concentrations determined by LA-ICP-MS have appeared to be generally higher than those measured by EPMA, indicating that the apparent Au–Ag discrepancy may partly reflect the greater sensitivity of LA-ICP-MS to minor Hg present in the alloy. Nevertheless, the magnitude of the observed offset is unlikely to be justified by the behaviour of mercury alone, and other possible causes need to be explored. Critically, because both analytical methods ultimately define the same compositional trends, the LA-ICP-MS datasets can still be used to formulate interpretations relating to the compositional evolution of the relevant gold populations.

The subsequent representation of the rest of the LA-ICP-MS data obtained for the Loch Tay gold samples has followed a dual approach, consisting of i) radar plots of the individual abundances (ppm) of multiple trace elements by average in each sample set, to provide preliminary distribution overviews (Figure 6.24); ii) bivariate plots of a certain trace element abundance against one (or more) other(s) in gold from specific locations (see section 6.3.5). Au, Ag and Hg data were excluded from the calculations for display in radar diagrams due to their respective contents (ppm) in each sample, generally several orders of magnitude greater than those measured for the rest of the elements (see section 3.5.2.3; Figure 6.23a and b.). Nevertheless, box and whisker plots have been constructed to illustrate the respective distributions in the abundances (ppm) of Au, Ag, Hg, and Cu for Calliachar Lower, Upper Almond, Invergeldie, Lead Trial, and Ardtalnaig, as measured by LA-ICP-MS (please also refer to the Appendix to view the

full dataset). The results are overall consistent with the ones measured by EPMA; however, because of the lower limit of detection of the LA-ICP-MS for Cu, the measured abundances can be assessed more quantitatively (Figure 6.23d).

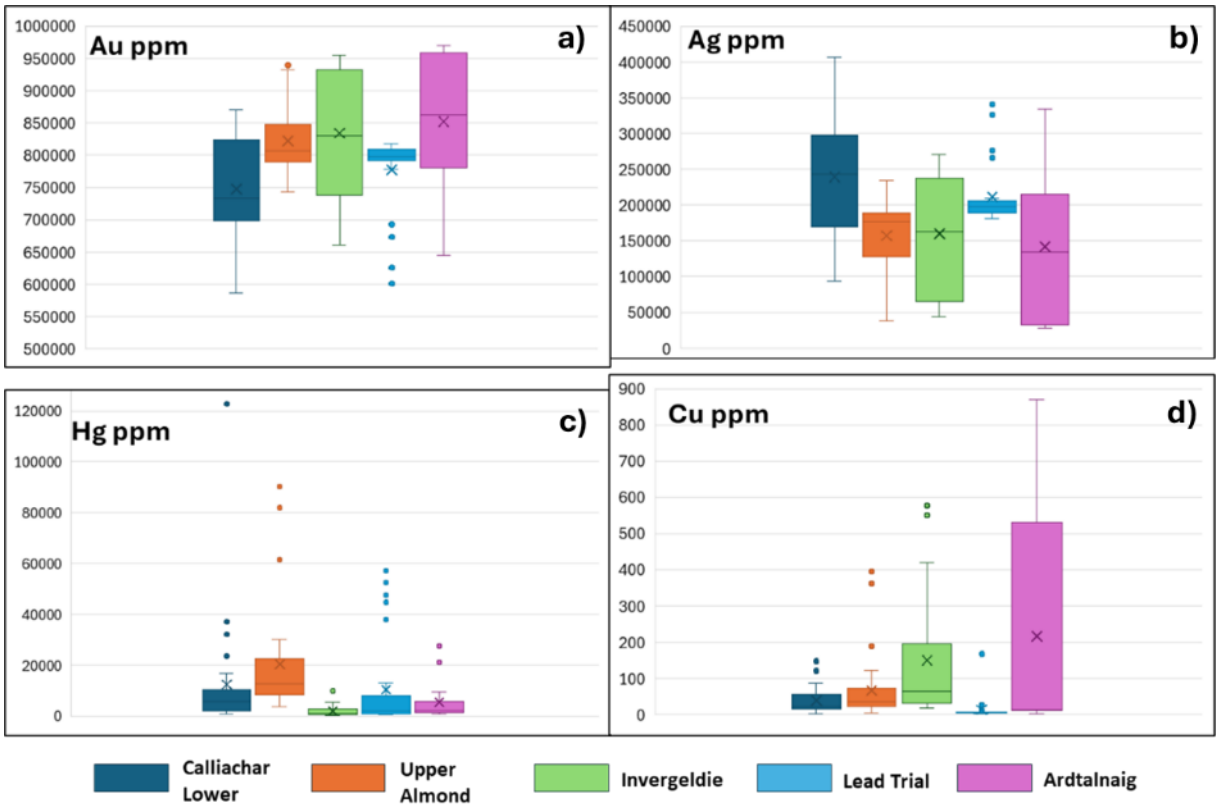

Figure 6.23 Box and whisker plots indicating the distribution in the abundances (ppm) of Au, Ag, Hg, and Cu for Calliachar Lower, Upper Almond, Invergeldie, Lead Trial, and Ardtalnaig, measured by LA-ICP-MS. The diagrams were built upon the analyses (Au197, Ag107, Hg202 and Cu63) from the same set of particles (30 in total) for each location, except Ardtalnaig (for which only 18 analysed particles were available).

As for the Cu analyses, due to the Cu LOD being set around 0.013 – 0.014 % for the probe, Cu values in ppm (as obtained by LA-ICP-MS analysis; Figure 6.23d) can often be more sensitive, therefore the element has also been included in the radar templates. The results are displayed in Figure 6.24.

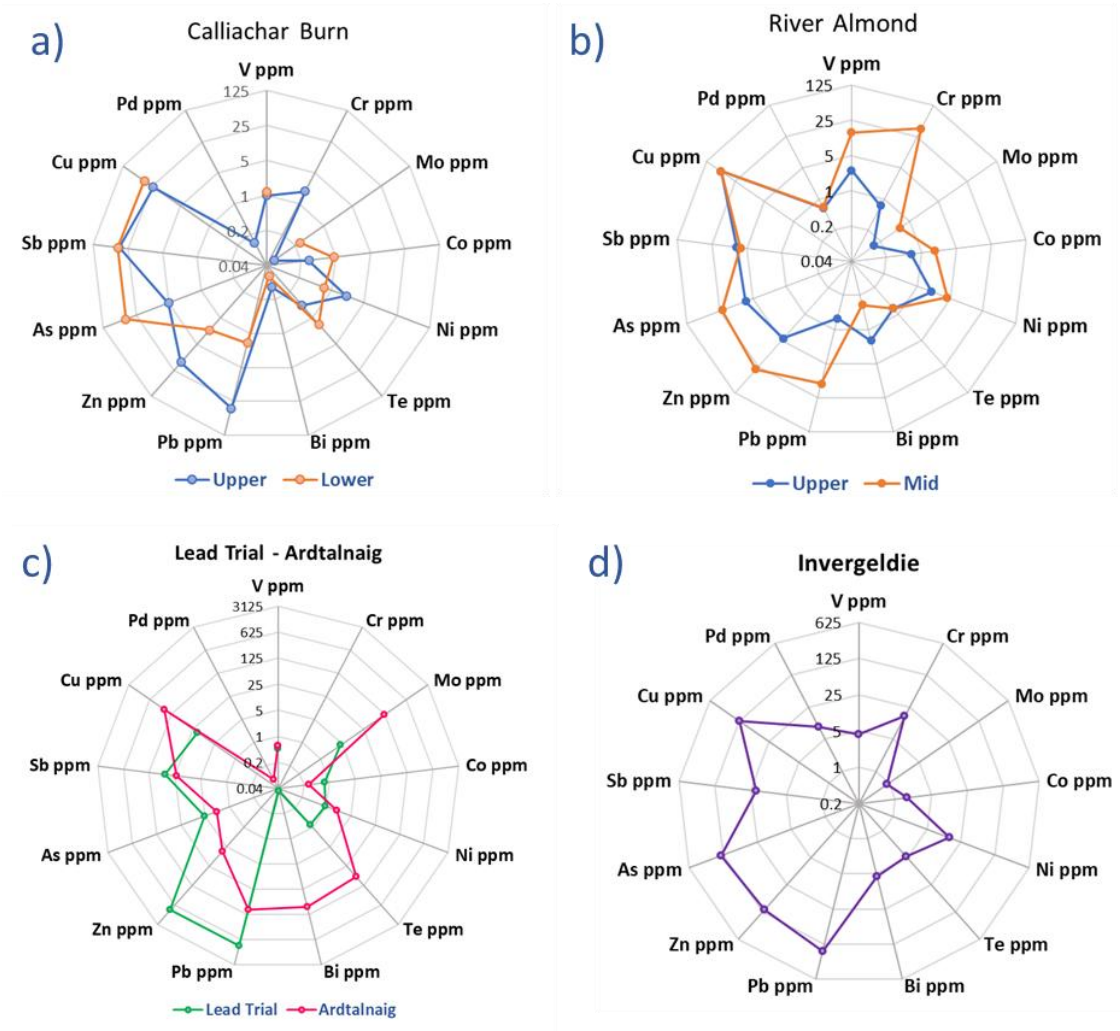

Figure 6.24 Radar displays of the trace element abundances (ppm) by average in the investigated sample sets.

The average abundances of Sb are similar in gold from the Calliachar Burn, the Lead Trial and Invergeldie; the element has been found in slightly lower amounts in the two samples from River Almond. Gold from Calliachar Burn and River Almond (Figures 6.24a and b) has also shown similar abundances of Cu, As, Zn, Co, Ni and Te. Cr and V are on average higher in the Mid Almond ('Almond 10 + 12') sample. The highest As and Pd average values have been recorded in the Invergeldie gold, also showing higher Cu quantities than the Calliachar and Almond gold. The greatest abundances of Bi and Te have been found in the Ardtalnaig placer sample (Figure 6.24c; dataset in Appendix 3) which, similarly to Invergeldie, shows relatively high Cu amounts. The Lead Trial gold sample (Figure 6.24c) is the one recording the highest average abundances of Zn and Pb; Mo, on the other hand, occur in higher amounts in the proximal placer (Ardtalnaig) sample. To note that differences in the overall elemental concentrations can also be observed between sub-samples sets collected from the same drainages (i.e., Calliachar Upper and Lower; Almond Upper and Mid; see full dataset in Appendix 3).

6.3 Gold compositional signatures

The following paragraphs deal with an interpretation of the gold compositional characteristics in relation to each main sampling locality, as described in section 6.2, and subsequently. Combining information from the alloy and inclusion suite of the gold particles has allowed the formulation of distinct gold compositional signatures (e.g., Chapman et al. 2000a, b) for both in-situ and placer samples, which ultimately serve to ascribe gold to specific environments of precipitation.

6.3.1 Calliachar Burn

6.3.1.1 In situ and gossan gold

Gold alloy composition

The 'Calliachar_8' gold sample is hosted in pyrite, in the form of inclusions and/or fracture fills (e.g., see section 6.2). The lowest silver contents have been observed for the few gold inclusions, which correspond to the smallest (~10µm) particles of the sample, whereas the more abundant, broadly coarser, fracture-hosted gold has appeared to be richer in silver. These combined pieces of evidence (particle size, mode of occurrence in pyrite and silver content) suggest that the 'Calliachar 8' in-situ gold might derive from two separate mineralising events, with the fracture-hosted grains belonging to a later, cooler one (e.g., Gammons and Williams-Jones, 1995).

The silver profiles relating to the gossan-derived gold are mostly described by plateaux along certain silver values, as a consequence of the particles being liberated from a restricted volume of mineralised material (Leake et al. 1998, Chapman et al. 2000a). They specifically suggest i) mainly stationary physicochemical conditions of the hydrothermal fluid responsible for the precipitation of 'Calliachar 6' gold; ii) two main sources of the fluid responsible for the precipitation of 'Calliachar 7' gold (with Ag median values of ~25 and ~33, respectively). Preliminary evaluation of the silver distribution in the vein-hosted (Calliachar_8) has driven some additional considerations. The relevant silver profile doesn't appear to be coincident with the 'Calliachar 6' profile, despite the sample being extracted from the same gossanous material (Figure 6.2a in 6.2.1.1). Justifications for this evidence might be provided by the restricted size of the in-situ gold sample (i.e., lower availability of data points for comparison), and by the individual sizes of the particles themselves involved in both samples. When gold grains are liberated by mechanically crushing gossan material, the smallest ones (<50 µm) can easily be lost during the separation process, thus the resulting gold populations are formed by overall larger grains; the in-situ gold sample that is here taken into account is, on the contrary,

constituted of ~20 grains with size variable between 10 and 50µm. Such an assumption would support the trend observed in the 'Calliachar 8 profile', which shows much fewer silver-rich particles (60% of them with %Ag < 22%) than Calliachar 6. The lower silver content might also be explained, in this case, as an analytical artifact produced by the "background" response of the material (pyrite) in which those gold particles were enclosed, interfering with Ag detection.

The mercury content of the vein-hosted and gossan-derived gold samples has also been investigated. Despite the limited number of values that can be used for quantitative analysis (Hg >LOQ), the Ag-Hg 'Calliachar_8' binary plot (Figure 6.3b in 6.2.1.1) highlights that an increasing mercury content (up to 5%) is recorded for particles with silver content in the range of ~20% to ~23%. Interestingly, such gold grains occur in cracks that postdate the host (Py) mineralisation (Table 6.2, section 6.2.1.1).

Gold from Calliachar Burn overall contains relatively high mercury amounts in the alloy, which are themselves up to three times higher in gossan-derived samples than in placer samples. The Ag-Hg bivariate plots relating to Calliachar_6 and Calliachar_7 (Figure 6.3 in 6.2.1.1) indicate that Ag-Hg do not co-vary. This evidence could be interpreted as mercury forming the alloy of the particles at the expense of gold or – in other words - mercury substituting gold while the silver content remains stable. Combining information on the mercury content behaviour from the in-situ and the two gossan-derived gold sample analyses suggests that an alloy variation, showing an enrichment in mercury, might have taken place for the later stage in-situ gold from Calliachar Burn downstream.

Inclusion suite

The mineral inclusion assemblage of the 'Calliachar 6' (Py-dominated; Figure 6.4a, section 6.2.1.1) gossan-derived gold is consistent with the sulphide mineralogy associated with the two gold-bearing stages in the G Vein, from which the sample was obtained. Additionally, the G Vein sampling site lies just on the projection of the V3 Vein strike (Figure 6.21) whose observed and reported mineralogy (Ixer et al., 1997) is strongly similar, although inclusive of galena and chalcopyrite. A possible genetic linkage between these two veins would, therefore, further support an association between the Py+Ga+Cpy+Sph inclusion signature of Calliachar 6 and the associated hydrothermal vein mineralogy. The inclusion assemblage (Py+Ga+Cpy; Figure 6.4a, section 6.2.1.1) of Calliachar_7 is perfectly consistent with the sulphide mineralogy reported for the associated Discovery Vein (Ixer et al, 1997).

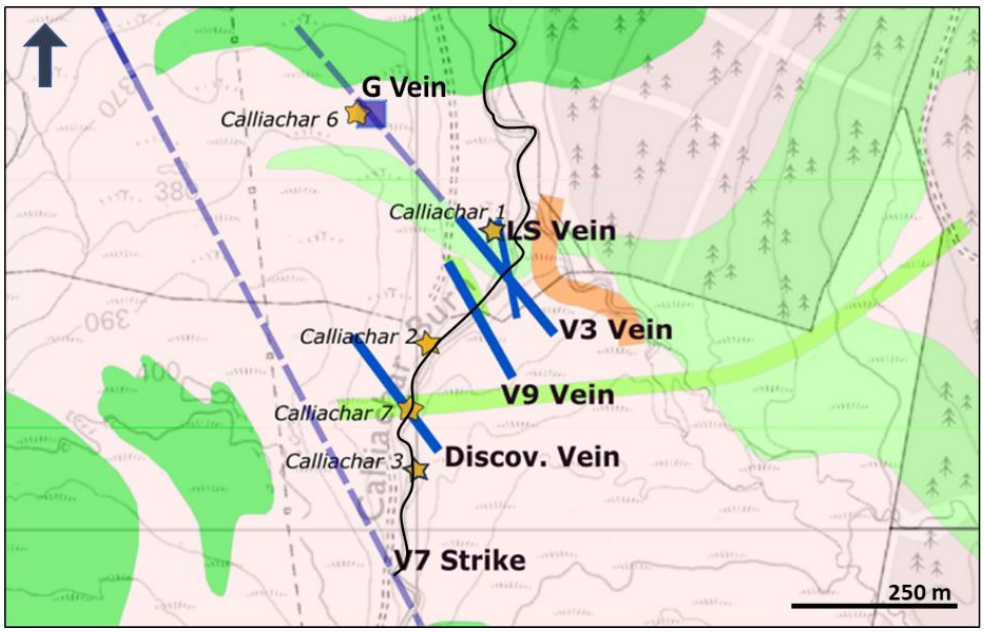

Figure 6.25 Schematic representation of the hydrothermal veins and gold sample localities in Calliachar Burn downstream; the projection of the V3 strike towards the G Vein outcrop is also indicated.

6.3.1.2 Placer gold

Gold alloy composition

The plots of silver percentages in the placer gold samples from Calliachar Burn (Calliachar 1-3 and 5; Figure 6.5a in 6.2.1.2) don't show flat horizons as part of their gradients. This has been interpreted as a consequence of multiple gold sources contributing to the samples, and their particles deriving from different conditions of precipitation (Chapman et al 2000a). A gradual increase in mercury has been observed by moving from the upstream samples towards the downstream ones, for which ~36% of the population shows values above LOD (Figure 6.5b in 6.2.1.2).

Inclusion suite

The detrital gold samples from Calliachar Burn have been divided into two main groups based on their inclusion mineralogy (ref to Section 6.2.1.2). Samples from downstream in the drainage (Calliachar 1, 2) show a greater variety of inclusion abundances and species than samples from mid and upstream (Calliachar 3, 5). The relative abundance of galena, chalcopyrite, pyrite and arsenopyrite inclusions in the 'Calliachar 1' placer gold is perfectly consistent with equivalent sulphide mineralisation that has been reported (Ixer et al., 1997) and partially observed in the adjacent V3 and LS veins; pyrite and arsenopyrite have additionally been observed in the V9

vein, lying ~100 metres upstream of the placer sampling spot. The 'Calliachar 2' placer gold has shown an inclusion assemblage consistent with that in 'Calliachar 1' plus a significant sphalerite component. This still appears neatly compatible with the sulphide mineralogy reported and observed in the nearby veins, including the Discovery Vein (Ixer et al., 1997) further upstream (Figure 6.21). Because vein erosion products would logically be conveyed to drainages from upstream to downstream, the locations of the Calliachar 1 and 2 sampling sites support the hypothesis of genetic correlation between gold inclusion assemblages and vein sulphide-bearing mineralogy. Pyrite and pyrrhotite inclusions are ubiquitous in the mid and upstream placer samples (Calliachar 3 and 5) but are themselves not particularly diagnostic; critically, these particles only very sporadically host other inclusion species, consistently with their sampling locations upstream of the mineralised veins.

Radar diagrams (Figure 6.6 in section 6.2.1.2) indicate the dominance of base metals (Fe, Cu, Pb) and of As and S as non-metals in gold inclusions from Calliachar Burn. These species are classically associated with (although not diagnostic of) Phanerozoic orogenic environments of Au deposition (e.g. Chapman et al. 2023b).

6.3.1.3 Preliminary conclusions

The main conclusion that can be drawn upon the evaluation of silver and mercury distributions, in gold samples from Calliachar Burn, is that their amounts are highly dependent on where such samples are collected and on the form in which they are found (i.e., whether they are placer or gossan-related), suggesting a zonation of the responsible hydrothermal conditions of precipitation. Even the two gossan samples show differences between themselves, despite being of a much smaller size. These zonal variations in the system would support the hypothesis of the potential differences in mineralisation between Calliachar and Urlar, where placer gold is scarce. Considerations of gold compositional variations across the Calliachar Burn stream section (i.e., upstream and downstream) will be discussed in 7.2.3.

6.3.2 River Almond

6.3.2.1 In situ & from crushed ore gold

Gold alloy composition

The 'Almond_6b' (vein-hosted) gold sample (e.g., sections 5.2.2.1 and 5.3.2.1) holds gold in the form of inclusions (Au2_av1), occurring in pyrite and chalcopyrite, and of coarser particles

(Au2_av2) filling fractures in pyrite, chalcopyrite and sphalerite, which record the highest silver contents (~34 to ~42 wt.%) in the alloy (e.g., Figure 6.9, section 6.2.2.2). Due to both physical (mode of occurrence) and compositional evidence, the generally coarser, silver-rich gold can be attributed to a separate, later mineralising event than the gold observed as inclusions in sulphides. The Ag content of gold particles increases as a result of lower temperatures and/or the lower Au/Ag ratio of the mineralising fluids (Gammons and Williams-Jones 1995). Therefore, the Ag-rich gold alloys are assumed to have formed later in the paragenesis, consistently with their mode of occurrence in cracks that postdate the host mineralisation.

The 'Almond_6b' gold alloy composition has overall appeared nearly twice as rich in silver as the one of 'Almond_6a' (gold obtained by crushing ore material from the same vein; section 6.2.2.1), as displayed by the silver profiles in Figure 6.9 (section 6.2.2.1). Evidence that the dominant, silver-rich trend in the 'Almond_6b' plot is hardly reflected in the 'Almond_6a' plot might point towards notable variations in the Ag content distribution across particles from the same hypogene environment (further discussed in 7.2.2.2).

6.3.2.2 Placer gold

Gold alloy composition

Influxes of auriferous fluids of diverse composition and/or physicochemical conditions are reflected in silver profiles of the gold populations from Upper River Almond (Figure 6.10, section 6.2.2.2). The profiles can be visually separated into three main classes – a dominant one (>75% of particles) with silver content between 20% and 30%-32%, and two subordinate ones, with silver content respectively below and above these thresholds.

In general, the profiles of the placer gold from the upper sites indicate greater silver contents than the others (i.e., Almond 3, 2 and especially Almond 1) and do show more 'flattened' gradients, probably due to the influence of local hypogene (from vein) gold. The silver plots that are representative of Almond 3 and 1 show an increase in their gradients at Ag ≥ 30%, corresponding to ~10% of the relevant populations. This partial commonality in the behaviour of the plots can be interpreted as local similarity in the gold origin (Chapman et al. 2000a), since the remaining and dominant portions of the curves do not overlap (Figure 6.10). The 'Almond 2' profile results from a lower number of grain analyses than the others and still indicates a stepped distribution of the silver content (e.g., Chapman et al. 2000a, Chapman et al. 2016).

Inclusion suite

The inclusion suite in detrital gold from River Almond (section 6.2.2.2) has similarly been evaluated in conjunction with potential geological constraints at the sampling site. Placer samples from upper and lower reaches differ substantially in terms of both element and mineral compositions (Figures 6.11 and 6.12 in section 6.2.2.2). In general, samples which are represented by a wider variety of inclusion species are the ones located downstream in the catchment (particularly Almond 1) although there doesn't appear (due to poor exposure) to be field evidence of bedrock sources to which they could directly be related. On the other hand, gold from Almond 4a, 4b and 5 ('upstream' samples) hosts inclusion assemblages that reflect the sulphide-bearing stage of a local hydrothermal vein.

The occurrence in the most downstream sample (Almond 1) of a greater variety of species, might be related in the first instance to the gold sampling location, allowing multiple potential contributions from the upstream gold. Some mineralogical traits (i.e., inclusions), typical of the gold from the upper Almond catchment, might however not have been retained by the 'Almond 1' gold due prolonged transport in the watercourse as supported by some of the particle morphology (Chapman et al. 2023). Additionally, the mineral inclusion suite includes a large component of bismuth and telluride species which are interpreted to be indicators of a possible magmatic-related source. Particularly the high tellurium contribution that emerges from the inclusion elemental composition suggests a linkage with a 'deep seated' epithermal system (Chapman et al., 2023).

Pyrite, sphalerite and cobaltite are relatively abundant in the mineral inclusion suites of the Upper Almond gold populations and the first two are consistent with the mineralogy observed in the Almond Vein, which outcrops upstream, at the same location of Almond 5. The vein hosts pyrite, sphalerite, galena and chalcopyrite mineralisation (section 5.2.2). The two latter species particularly occur as inclusions in Almond 3 (Auchnafree), although the relevant gold sampling location is nearly 4 Km downstream, and potentially receiving gold from upper tributaries. Base metals are recurrent in the elemental composition of the inclusions in the Almond Upper gold (Figure 6.11, section 6.2.2.2), and are often indicative of orogenic genetic environments (Chapman et al., 2023b). Also important to note is that the Almond 5 and Almond 4 gold samples contain minor amounts of specific inclusion species (FeCoNiAsS) which don't reflect the mineralogical assemblage of the sole hydrothermal vein analysed.

6.3.3 Lead Trial and Ardtalnaig

6.3.3.1 In situ gold (Lead Trial)

The silver content analysis of the gold from crushed ore material at the Lead Trial (Tip 1+2; section 6.2.3) has allowed the partitioning of the population into two main classes, respectively showing steady and increasing silver values in their particle alloys. The co-existence of two different alloy phases (in the form of Ag-rich patches or tracks, within the gold grains) has been deduced by combining the compositional data with SEM images of the same set of particles (Figure 6.13, section 6.2.3). Modified conditions of the fluid(s) responsible for gold precipitation have been assumed to explain this evidence (e.g., Chapman et al. 2021). The internal compositional heterogeneity of the particles can be attributed to evolving/cooling (>Ag) conditions of the same hydrothermal fluid (Gammons and Williams-Jones, 1995). Chapman et al. (2021) discussed the processes of replacement of original gold alloys by more silver-rich phases in the (post-deposition) hypogene environment; in such cases, the modification of the primary alloy can be reconciled to interaction with later fluids that are no longer in equilibrium with it. Hancock and Thorne (2011) previously pointed out that a spatial association of Au- and Ag-rich tracks can be explained as a product of different/evolving fluids exploiting the same conduit at different times.

Galena, sphalerite and molybdenite inclusions were detected in both the gold alloy classes (Figure 6.26; wt.% Ag <29.5 and >29.5) determined for the Lead Trial (Tip1+Tip2) gold. Consequently, they have been interpreted to be coeval with the earlier (< 29.5%) gold paragenetic stage. In addition, these mineralogical associations and parallel silver content of the alloy, alongside the quartz textures at this locality (described in 5.3.3), support a hypothesis of gold precipitation from magmatic-related hydrothermal fluids (i.e., LS epithermal, sections 1.1, 2.2.3 and 2.3.3).

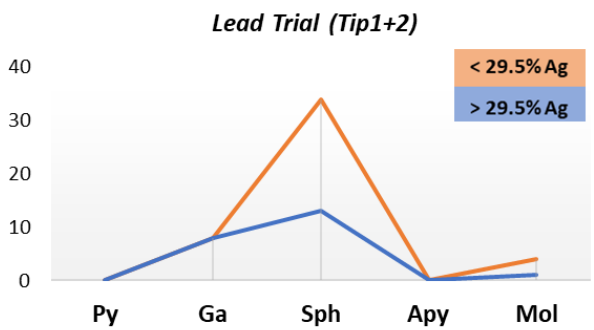

Figure 6.26 Partition of the inclusion suite in the gold from the Lead Trial based on silver content classes (<29.5% and > 29.5% Ag).

6.3.3.2 Placer gold (Ardtalnaig Burn)

The silver profiles relating to the Ardtalnaig 1 and Ardtalnaig 4 gold samples (Figure 6.13, section 6.2.3) indicate the contribution of gold particles with variable silver contents, typical of placer sample expressions – therefore, derivation from multiple locations. The inclusion species recorded in these populations - higher Mo and Cu and lower Zn and Pb relative abundances, compared to the ones in the Lead Trial gold (section 6.2.3; Webb, 2024) - are in line with the hypothesis of a linkage with different mineralisation stage(s), as reflected in the gold alloy (silver content) variations.

6.3.4 Loch Tay South

6.3.4.1 Gold alloy composition

The placer populations from the South of the Loch Tay area (Lednock 1, Keltie 1+2 and Monzie 1, but not Invergeldie) are all characterised by gold alloy compositions showing relatively low silver content ranges (Figure 6.16a in section 6.2.4) and relatively higher copper content ranges (i.e., >LOQ; Figure 6.16b in section 6.2.4), compared to the populations from other locations in the Loch Tay area described so far. Beyond suggesting the contribution of gold from multiple sources (e.g., also erosion of multiple sections of a deposit), the observed trends are common for gold associated with intrusion-related genetic environments and would be specifically compatible with a porphyry-epithermal source (e.g, Chapman et al., 2017; Chapman et al. 2023b; Chapman et al. 2023c). Their Hg content is also lower than that observed in other populations from the northern part of the area (e.g., Calliachar Burn gold; Chapman et al., 2023)

6.3.4.2 Inclusion suite

The inclusion mineralogy of the placer gold from Glen Lednock entails chalcopyrite, bornite and chalcocite plus molybdenum and bismuth as elemental components (e.g., Figures 6.18 and 6.19, section 6.2.4; Chapman et al., 2023c), assemblages that are conventionally associated with alkalic-porphyry genetic environment (e.g., Chapman et al., 2017, 2023c). Bismuth, tellurium, and silver elemental components feature in the Keltie Burn gold signature (Figure 6.18, section 6.2.4), where chalcopyrite inclusion species are absent; this association is suggestive of low-sulfidation epithermal environments of gold deposition (e.g., Chapman et al. 2005; Chapman and Mortensen 2016, Chapman et al. 2023c). The 'Invergeldie 1+2' mineral inclusion signature only partially incorporates elements of similarity with the 'Lednock 1' and 'Keltie 1+2' signatures

(Figures 6.18 and 6.19, section 6.2.4); this will be discussed in section 7.2.3.2. Intrusive bodies outcrop in the Loch Tay South area, specifically an Early Devonian granitic suite near Invergeldie and Glen Lednock and Devonian volcanic/mafic lithologies close to the Keltie Burn sampling location (e.g., Chapman et al, 2023c). The presence of these intrusives is likely to have played a role in the composition of the fluids associated with the local gold genesis (see section 7.2.3 for details).

Important compositional similarities were found in the inclusion suites of Almond 1 (Sma Glen) and Keltie 1+2, with respect to certain element abundances. These are, specifically, similar proportions of bismuth, lead and silver in the metal components, and almost equal tellurium proportions, in the non-metal ones. Extensive discussions on the implications of these relationships will be dealt with in Chapter 7 (Discussions; section 7.2.3.2).

6.3.5 Critical evaluation of the trace element data

This section seeks to elucidate the controls of hydrothermal fluids on gold mineralisation as reflected in gold alloy at the trace element level. A full, preliminary appraisal of the compositional investigations on gold alloy and inclusions from various particle populations, as described in earlier sections, was thus essential. The following paragraphs will provide an integration of compositional insights based on the relative abundances of certain trace elements in/between the samples, for which data were available.

6.3.5.1 Data reproducibility and quality-checks

EPMA and LA-ICP-MS analyses of both silver and mercury in the particle alloys were compared to validate the expected increase in data precision and sensitivity from LA-ICP-MS investigations. Such comparison confirmed that the laser-data precision of some major discriminants, such as Hg and Cu, is far greater than the respective probe data (Banks et al., 2018). Therefore, the LOD is far lower, and the data can be treated quantitatively even in minor concentrations. In specific populations, the gold alloy has also appeared somewhat heterogeneous at the trace element level. For example, the (trace) elemental content of the Upper Calliachar (Calliachar 5) placer suite overall resulted in a richer range than the Lower Calliachar suite (e.g. Cr, V., refer to Figure 6.20); also, the overall elemental content of Almond "mid-stream" (Almond 10) has appeared more variable than that of the respective up-stream gold population (Almond 5). This type of behaviour informs on the existence of another independent line of evidence, represented by LA-ICP-MS investigations, which further demonstrates that placer gold populations from the

same catchment can show different characteristics depending on where they are sampled. It is, however necessary to take into account that gold particle populations from upper reaches can be, at least partially, conveyed to lower reaches.

6.3.5.2 Implications of LA-ICP-MS results for the interpretation of gold signatures

Lead Trial – Ardtalnaig

Certain elements, such as tellurium and bismuth, are regarded as possible indicators of magmatic-related genetic environments of gold formation (Chapman et al., 2018; Spence-Jones, 2021). As such, their concentrations at the trace level (ppm) in the Lead Trial gold sample (section 6.2.6) has been assessed alongside the one(s) detected for other elements. The plot in Figure 6.27a indicates that tellurium, especially when reported in relatively low concentrations (<1 ppm), most frequently occurs in the gold particle alloys alongside silver content values ranging from ~18 to ~21 *wt.%* (converted from equivalent *ppm* concentrations). It should be noted that the lowest Ag content recorded (from LA-ICP-MS analyses) in the examined set of particles is 17.9 wt.%. Since it was previously deduced - from optical and EPMA analyses of gold from the same sample (e.g., sections 5.3.3 and 6.3.3) - that lower silver contents in particle alloys can be linked to earlier paragenetic stages, the trend observed in Figure 6.27a may suggest that tellurium at the trace level started to concentrate in the gold alloy during the earlier stages of mineralisation.

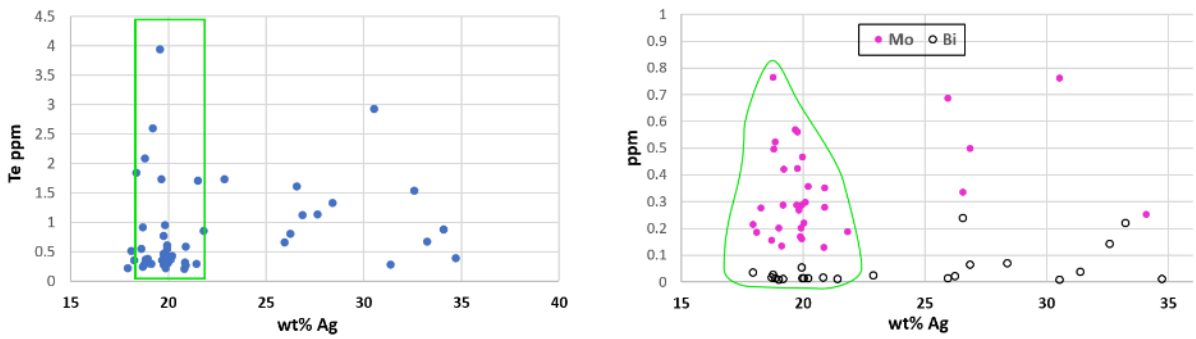

Figure 6.27 a) Te-Ag binary plot for the Lead Trial gold sample (introduced in 6.2.6); b) Mo-Bi vs Ag plot for the Lead Trial gold sample within a specific range of values (full Mo range in ppm is available in Appendix 3). The original Ag content values in ppm have been converted into wt.% to facilitate data visualization on these graphs.

The content of molybdenum at the trace level in the gold alloy was investigated to possibly explore the significance of molybdenite inclusions detected by SEM inspection (section 6.2.3) in some gold particles from the Lead Trial sample, also suggesting derivation from a magmatic-hydrothermal system (as mentioned in 6.3.3.1). Mo and Te do not co-vary overall (Figure 6.28a,

b), suggesting that the assimilation of such elements into gold is probably connected to different hydrothermal controls. No particular trend has been observed between Bi and Ag concentrations (Figure 6.27b), although there appears to be a more pronounced concentration of Mo around lower (16-21 wt.%) Ag values.

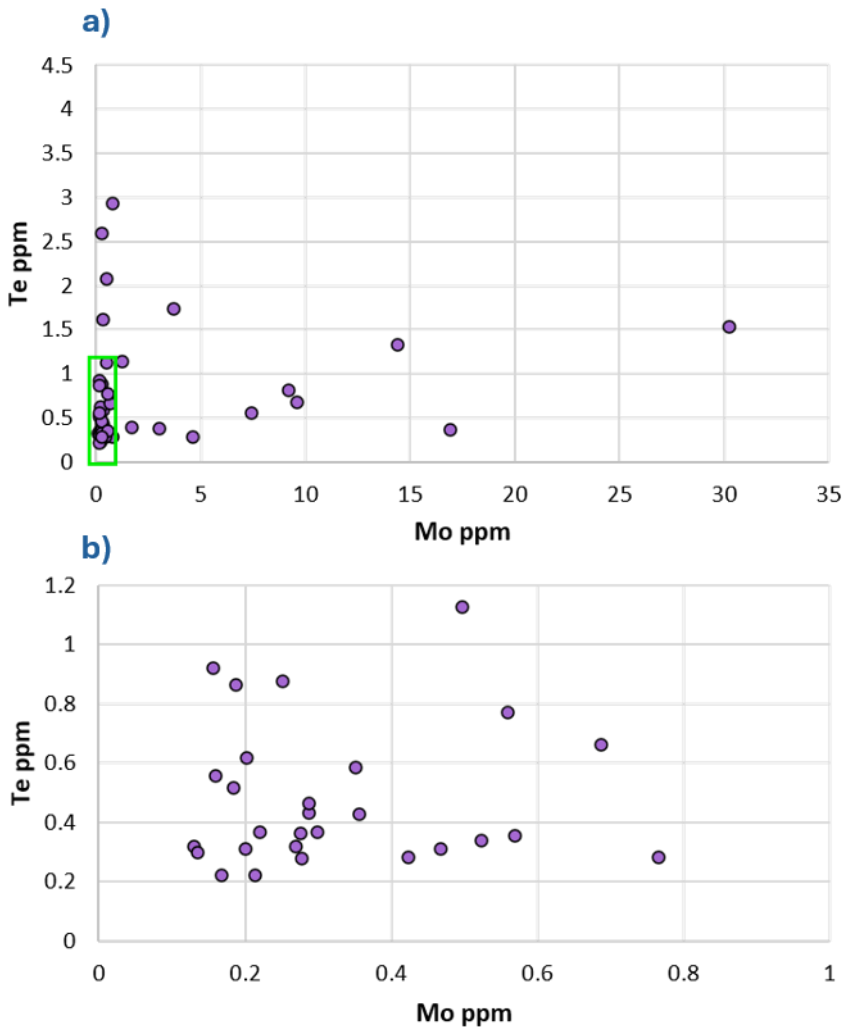

Figure 6.28 Te-Mo Binary plots for the Lead Trial gold sample; data in b) are a sub-set of the range displayed in a) - i.e., highlighted by the green rectangle in a).

Mo, Te and Bi (Fig. 6.27) are generally not covariant with silver and have been recorded (at the trace level) in gold throughout the alloy history at this locality (i.e., both in the lower and the higher silver particles). Relatively lower Mo and Te abundances, with respect to the sample considered, have mostly been reported alongside lower silver contents (≤21 wt.%). It should also be noted that molybdenite mineral inclusions were observed in gold particles coming from the same sample of crushed ore ('Tip_2' gold, section 6.2.3). Higher Mo values detected in gold at this locality (i.e., Figure 6.29) might be associated with the presence of micro-inclusions,

rather than being read as alloy constituents (see section 3.4.3). The plots in Figure 6.29 indicate the distribution of Mo and Te concentrations (ppm), respectively, across the sample of Lead Trial gold particles analysed by LA-ICP-MS. Especially in the case of Mo, the outlier values (i.e., represented by dots in 6.29) are the ones that could most likely reflect the presence of mineral inclusions, due to differences in relative abundances with the measured interquartile ranges, represented by the boxes (e.g., thick line at the bottom of 6.29a), and with the "whisker" values (thinner lines above and below the boxes in 6.29).

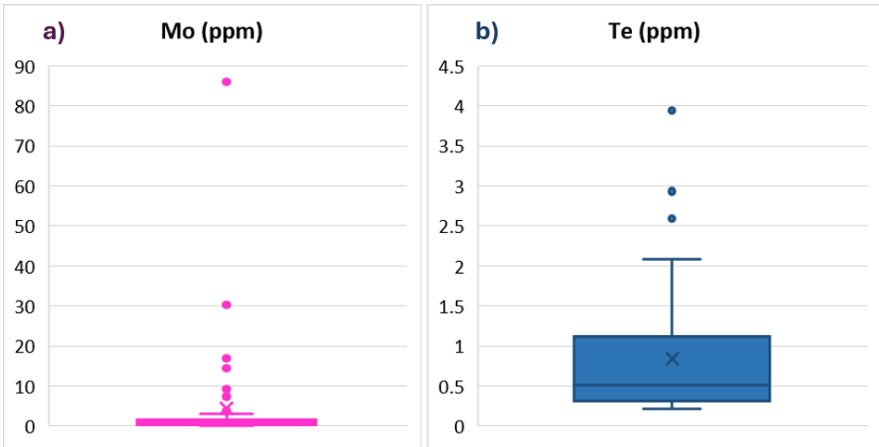

Figure 6.29. Box and whisker plots indicating the distribution in the abundances (ppm) of Mo (a) and Te (b) across the Lead Trial gold sample (data available in Appendix 3), measured by LA-ICP-MS.

During the process of ablation of the selected gold particles, only regions that appeared visually free from inclusion and/or impurities were chosen. However, small mineral inclusions could still have been present within the particles, either underneath their exposed surface or within a size range below that identifiable by optical resolution. As a result, the elemental concentrations measured by LA-ICP-MS could reflect the influence of microscopic inclusions intercepted during laser ablation, rather than unequivocally record elements dissolved within the Au-Ag alloy. As anticipated in section 3.4.3, this scenario could be especially plausible for certain elements, including Te and Mo, which do not normally occur in native gold solid solutions (e.g., Banks et al., 2018; Chapman et al., 2021). To provide potential complementary evidence in support of this hypothesis, LA-ICP-MS data (exceptionally) obtained from two different locations within the same gold grain were compared (Table 6.7).

Table 6.7. LA-ICP-MS elemental (Ag, Au, Pb, Mo) concentrations from two ablation spots in the same gold particle (RJC-134-21-19).

Particle lable	**Ag**	**Au**	**Pb**	**Mo**
	(ppm)			
RJC-134-21-19a	313833.4	551469.8	25151.9	4.6
RJC-134-21-19b	332524.2	565078.3	5457.5	9.6

Considering the Mo value ranges (ppm) displayed by the plot in 6.29a, the values reported in the table do not appear to form a narrow compositional range themselves; this may indicate Mo compositional heterogeneity within the same gold particle, possibly connected to the presence of one or more microscopic molybdenite inclusions. Similar behavior has been observed for the reported Pb concentrations – i.e., notably divergent - and will be discussed in the following paragraphs.

Exceptionally high (e.g., outlier) concentrations of Mo and Te (ppm) could ultimately affect the values of measured Au and Ag (ppm) concentrations within the same particle (Banks et al., 2018); however, there doesn't appear to be any systematic relationship between the recorded "higher" Mo and Te contents (ppm) and the corresponding Ag (ppm) content on a particle basis (Figure 6.30a), which can be, at least in part, due to the heterogeneous nature of the Au-Ag alloy in the examined sample.

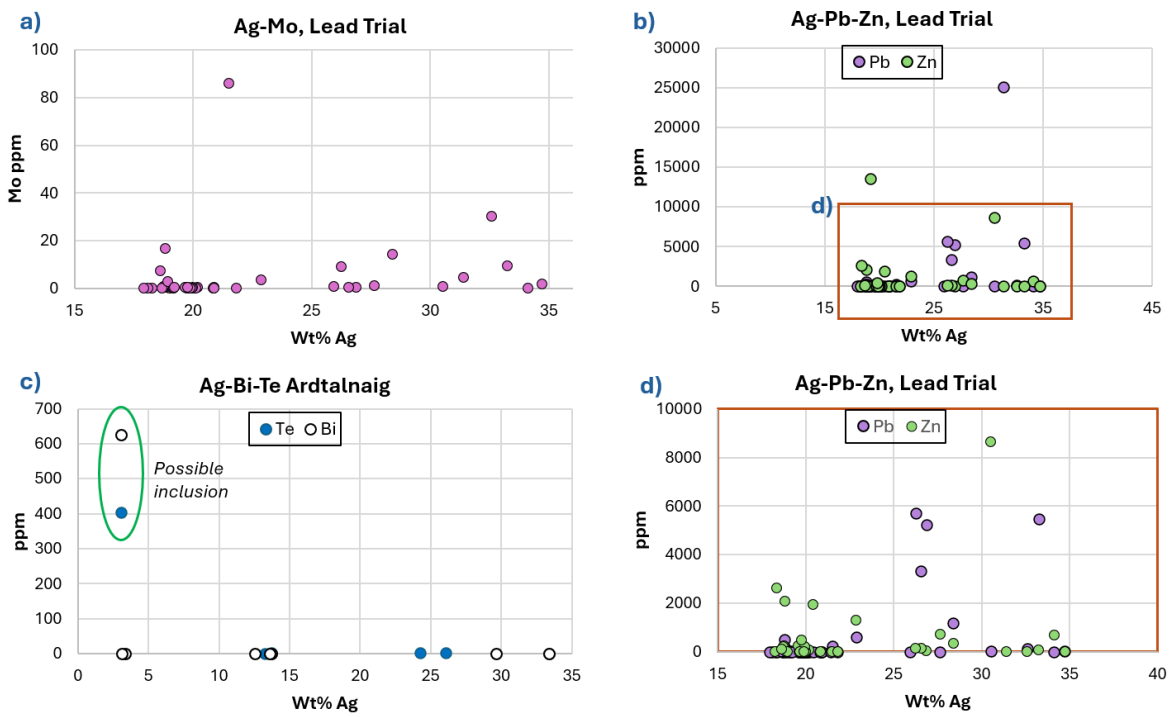

Figure 6.30. Multivariate plots of trace elemental concentrations for a) Ag-Mo in the Lead Trial sample; b) and d) Ag-Pb-Zn in the Lead Trial sample ("d" represents a sub-set of the range shown in "b"); c) Ag-Bi-Te from Ardtalnaig.

The mineral inclusion assemblage identified (by SEM) in the Lead Trial gold (Ga+Sph, section 6.2.3) is also reflected in the elemental composition of the gold alloy at the trace level (Figure 6.24c, section 6.2.6). The Pb and Zn measured concentrations in ppm have been plotted against the Ag contents (wt.%) of the same set of particles to assess whether any consistent pattern could be identified (Figures 6.30b and d); however, there doesn't appear to be any steady covariance between lead or zinc elemental concentrations and the respective silver concentrations.

LA-ICP-MS analyses conducted on the proximal Ardtalnaig placer sample revealed higher Cu and Mo and lower Zn and Pb average concentrations (Figure 6.24c, section 6.2.6), which would also be consistent with the mineral inclusion assemblage that has been locally identified (e.g., Webb, 2024). Additionally, exceptionally high concentrations of Te and Bi (ppm) have been simultaneously reported for one of the particles analysed from this locality (Figure 6.30c) alongside a relatively low Ag (ppm) concentration. This combined evidence would validate the interpretation of a localised influence of a mineral inclusion - Bi-Telluride species and relatively big, in this case - which could have been present in the cylinder of the ablated material.

River Almond

The River Almond gold composition at the trace element level (Figure 24b, section 6.2.6) is substantially consistent with the mineralogical composition of the gold from the hydrothermal-bearing vein at the Upper site, especially in the Mid-Almond sample (section 6.2.2; Figure 6.9b). The calculated averages may account for (partial) contributions of micro-inclusions to these elemental abundances.

Invergeldie

The Pb-Zn-As (trace) elemental association observed for the Invergeldie gold sample (Figure 6.24d, section 6.2.6) appears to be in line with the metallic signature of the inclusions in gold particles from the same locality (Invergeldie 1+2, Figure 6.19 in section 6.2.4). The presence of notable Cu and Cr amounts (ppm) is also compatible with the interpretation of a possible gold derivation from a magmatic (porphyry) related environment, as previously described in paragraph 6.3.4. However, the shape of the Invergeldie radar plot (Figure 6.24d) is similar to that of Almond Mid (Figure 6.24b). This point will be explored in 7.2.3.2.

LA-ICP-MS investigations on gold from the above localities constrained the partitioning of specific trace elements in gold particles associated with mineral inclusions. This approach – inclusive of relevant comparisons with datasets obtained from EPMA and SEM analyses - may facilitate the allocation of individual gold grains to a mineralising stage in the gold evolutionary history, with respect to a specific source style (will be discussed further in 7.2.2.3).

The arguments presented in this section are mostly based on the reduced (i.e., after processing via Sills) LA-ICP-MS dataset. Time-resolved ablation signals (raw data - available in the archive) could only be partially re-examined, therefore it is not possible to claim an unequivocal distinction between trace elements present in solid solution (within the Au-Ag alloy) and those forming sub-microscopic inclusions (in this case, e.g., Mo, Bi, Te, Pb and Zn). A thorough analysis of the full LA-ICP-MS dataset (both unprocessed and processed) for gold from these localities would be required to further constrain the above interpretations.

Chapter 7.

Discussion & Synthesis

7.1 Introduction

This chapter aims to holistically contextualise the information provided in Chapters 4, 5 and 6 and generate an overarching, effective picture of what we have learned through interpretation of the datasets involved in this study. The main lines of research that were followed required investigations of hydrothermal vein parageneses, gold compositional signatures and the local structural/tectonic context, with the ultimate objective of generating a metallogenic framework for the Loch Tay area of Central Scotland.

The first section of the chapter deals with local and regional-scale critical comparisons of the available datasets and, where applicable, places these into the context of pre-existing literature and work conducted either in the same/close locations or in different locations, based on the same or analogous theoretical principles. This type of approach has especially served the gold composition research segment involved in this work, for which more targeted literature data are currently available. The aim is to add a layer of consistency to the analyses and interpretations developed in the previous chapters to set up the foundations for an effective metallogenic model and define possible exploration targets.

The final section of the chapter deals with a reflective synthesis where the discussions that took place in the former part of the chapter are constructively conveyed to propose a model for the metallogeny of the Loch Tay area. This synthesis also provides ground for addressing subsequent (research) questions and tailoring future work objectives.

7.2 Discussion

7.2.1 Comparisons between vein systems across the Loch Tay area

The paragenetic interpretations of the Calliachar-Urlar, Lead Trial, River Almond and Coire Buidhe vein systems proposed and described in Chapter 5 are cross-compared in this section to identify and quantify mineralogical, textural and structural similarities and differences, and speculate on potential genetic links between vein arrays, which would help associate these to either separate or continuous, interconnected hydrothermal systems.

7.2.1.1 Shared mineralogy

The mineralogy of the veins has been chosen as the first parameter to consider for comparison since it may constitute a useful discriminant for vein genetic relationships in ore-bearing hydrothermal systems. The main assemblages observed for each vein system in the Loch Tay area are reported in Table 7.1.

Table.7.1. Comparative paragenetic Table for the Loch Tay vein systems investigated in this study. The Almond Vein paragenesis partially incorporates the interpretation by Webb et al. 2024; the darker boxes in the 'Quartz' row correspond to the darker CL, overprinting paragenetic stages.

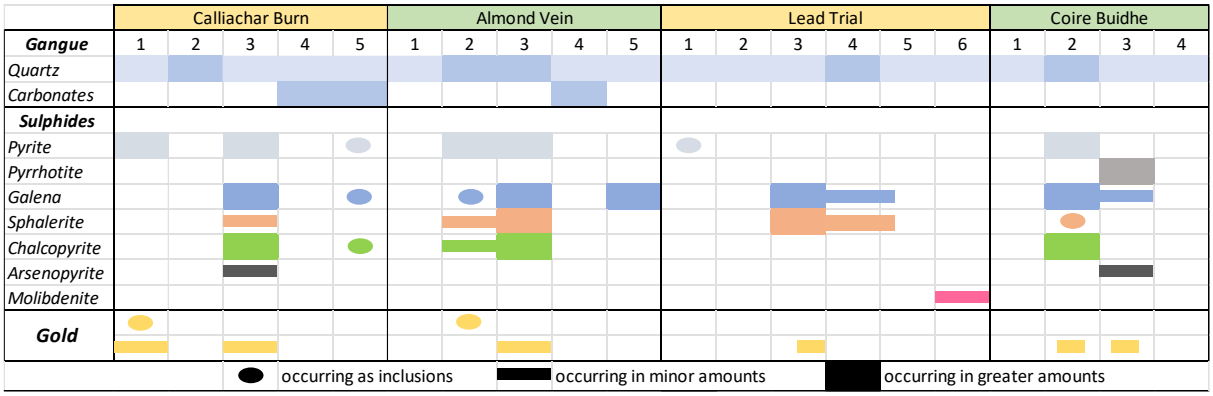

Strong mineralogical similarities have been observed between the paragenetic stages of the Calliachar-Urlar, Glen Almond and Coire Buidhe vein occurrences. However, because of the greater availability of in-situ vein samples and better-defined mineralogy at the respective outcrops, the Calliachar-Urlar and Glen Almond vein parageneses rely on a greater degree of sample representativeness in comparison to the Coire Buidhe overarching vein paragenesis; additionally, the latter may be derived from two potentially separate systems (as discussed in Chapter 5.3). Consequently, the intrinsic mineralogical similarities observed between the vein systems from the first two localities (Calliachar Burn and Glen Almond) have a higher chance of being correctly assessed and compared. The Calliachar-Urlar Burn and Glen Almond vein system

parageneses are overall very close in terms of their mineral associations, with two main differences identified: the first is linked to the presence of arsenopyrite, occurring alongside the third paragenetic stage in a couple of Calliachar Burn veins and not observed in the Glen Almond vein; the second, to the absence of apparent sulphide mineralisation alongside the second paragenetic stage at Calliachar-Urlar Burn (Table 7.1). In this latter case, the main ore-bearing stage has appeared to cut across the third, brighter-quartz pulse, interpreted to be initiated by a fracturing event (see Chapter 4). In contrast, in the Glen Almond vein, the ore-forming minerals all appeared to relate to the featureless, CL-darker, second-third quartz event(s) (e.g., Webb et al., 2024). These stages critically represent the main ones during which gold precipitated in the Calliachar-Urlar Burn and Glen Almond systems, respectively. On the other hand, one of the main points of commonality between the Coire Buidhe veins and the Glen Almond vein is represented by the relative synchronicity of their respective sulphide-bearing (main) episodes with the deposition of their own CL-dark/overprinting quartz episodes (Table 7.1). Pyrrhotite was only observed in one of the Coire Buidhe rock samples, and often in isolation from other mineral phases except quartz, evidence of which could be explained through the higher insolubility of this sulphide (different fS_2 ;see section 2.2.2) consequently deemed to precipitate earlier than other species in the associated paragenetic stage. The relative volumetric proportions in which the metallic assemblages are found across these three vein systems do not represent a major point of distinction, excluding the case of sphalerite which was observed far more abundantly in the Glen Almond Vein sulphide assemblages than in the others.

The dominant galena-sphalerite sulphide association recorded in the Lead Trial hydrothermal vein system and its mode of occurrence differ substantially from the ones observed in the other (investigated) Loch Tay hydrothermal veins; within this system, gold grains were directly observed only sporadically across the third paragenetic stage. Due to the nature of the related mineralogical assemblage, this group has not been included in the comparison preliminarily carried out above. The Lead Trial vein paragenetic implications will be discussed later in this section, more in relation to their textural context and possibly associated deposit type.

In light of the previous mineralogical considerations (i.e., Table 7.1, sections 5.3.1, 5.3.2 and 5.3.4), common fluid sources for the Calliachar-Urlar, Glen Almond and Coire Buidhe vein systems cannot be ruled out (e.g., Webb et al., 2024). The observed dissimilarities may be attributed to subtle variations in the local fluid conditions during sulphide and gold precipitation, which are entirely admissible for these types of systems (e.g., Robb, 2020; Reed and Palandri, 2006). The mineralogical variations may be due to slight change(s) in the physicochemical

parameters (temperature, pressure, pH, sulphur fugacity) of the hydrothermal fluids locally associated with the ore-bearing events, or be dictated by the contact of a shared fluid with diverse types of rocks (e.g., Chapman et al., 2023c). Another reason why some mineralogical (i.e., metallic) phases would only seem to occur in certain veins and/or are not visible within others can be found in a possible ''nugget effect'', which is observed when high-grade, gold-bearing hydrothermal veins just occupy a restricted portion of the entire system and the rest of it is formed of low-grade/unmineralized veins (e.g., Platten & Dominy 2001). This scenario may account for at least the Calliachar-Urlar and Glen Almond veins, in proximity of which large populations of gold particles were recovered in the form of placer deposits in fluvial drainages, thence implying their derivation from an associated, significant, in-situ auriferous mineralisation. Besides, it is normally very uncommon that all the mineralogical phases and/or associations occurring in a vein system are deducible by observation and analysis of a limited number of samples from limited portions or segments of the veins (e.g., Spence-Jones, 2021). The variations in the metallic (and gold-bearing) assemblages in relation to the textural event along which they precipitated, as mentioned earlier with respect to the Calliachar-Urlar and Glen Almond vein system, will be discussed in the next paragraph.

7.2.1.2 Constraints from textural similarities

The textural and morphological features of the Loch Tay veins have been re-examined in this section, to extract more information that could help understand whether the hydrothermal processes behind their genesis were individual to each vein or were part of a major, common system. It is essential to keep in mind that vein textures alone cannot provide determinant indications on the genetic environment of a vein array or system, for which they necessarily need to be assessed against the respective mineralogic or metallic assemblages (e.g., see sections 7.2.1.1 and 6.3). Nonetheless, the vein textural features have proved useful in establishing 'same or different' criteria when multiple samples from one or more veins (from a single or multiple localities) are available, and helping understand whether the veins formed under the same conditions or not. The Calliachar-Urlar, Glen Almond and Coire Buidhe veins are all characterised, in their respective parageneses, by the occurrence of initial, medium-luminescence, weakly-zoned euhedral quartz, systematically followed by a poorly luminescent, featureless quartz (Table 7.1, Figure 7.1, Chapter 5). These two volumetrically dominant textures are often fractured by minor, highly luminescent quartz pulses formed of euhedral to sub-euhedral crystals. The origination and development of hydrothermal veins is generally a complex process, which in all cases is achieved through an initial, rapid fracture propagation, associated with immediate fluid depressurization, subsequent crystal precipitation, and instant

cooling (e.g., Fournier, 1985; Sibson, 1994). Due to the textural likeness between veins, it might then appear realistic that the hydrothermal veins from these three localities (Calliachar-Urlar Burn, Glen Almond and Coire Buidhe) formed via analogous processes of cyclic fracturing and sealing, allowing the precipitation and overlap of different types of fluids (e.g., with different chemistry) and phases over time (e.g., Ramsay et al., 1980; Sibson, 1994). These mechanisms could have been triggered by regional-scale tectonic events having an impact on the local stress fields and would be in line with the slight mineralogical and morphological differences observed from one vein system to another and between the veins themselves. For instance, it is plausible that the opening of veins of particular orientations took place at a specific tectonic stage, during which certain mineral phases were simultaneously precipitated, and was followed by later reactivation of some of the veins, which allowed preferential deposition of slightly different assemblages. A similar mechanism was suggested by Webb et al. (2024) to account for the formation of the Glen Almond Vein as opposed to other (larger) Loch Tay veins, in response to the absence of certain mineral species in its mineralogy, and it has been here proposed with respect to the Calliachar-Urlar veins (Chapter 5) formation. Possible genetic relationships between these veins may also be inferred on the basis of their orientation and texture across the area. A general NNW-SSE strike has been recorded for the Calliachar-Urlar, Glen Almond and Coire Buidhe veins, although their width and strike-lengths are variable (Chapter 4; Chapman et al., 2023c; Webb et al. 2024). These veins are all dilation-dominated, as deducible from the frequent euhedral crystals interspersed with vugs.

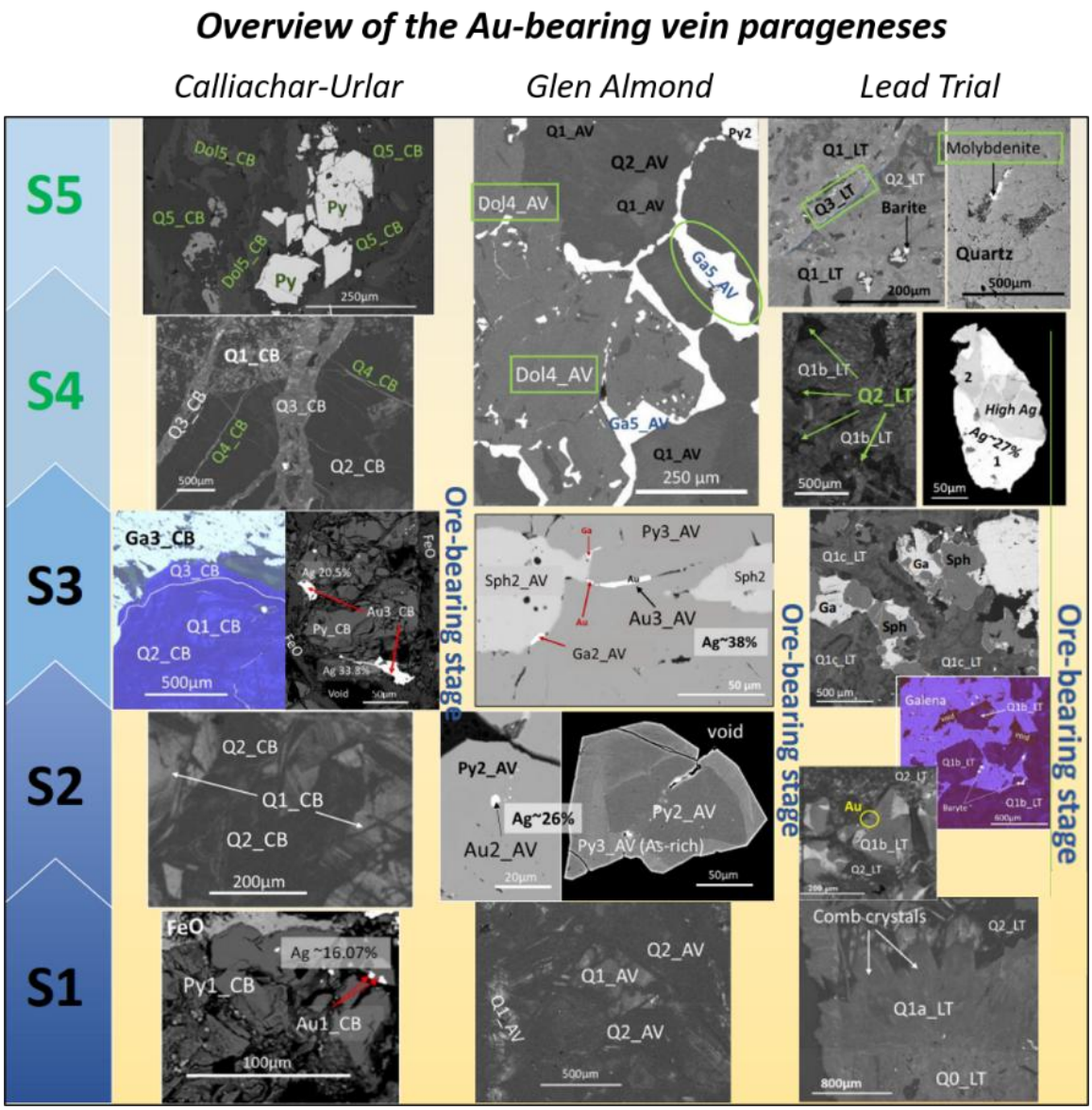

Figure.7.1. Schematic representation of the main textural and mineralogical associations in the Calliachar-Urlar, Glen Almond (e.g., Webb et al., 2024) and Lead Trial Vein systems. 'S1 to S5' are used to indicate the possible stages of the parageneses in an 'encompassing' sense. To be noted that the Lead Trial system has been interpreted in relation to separate genetic processes.

In conclusion, the hydrothermal fluids responsible for the metallic mineralisation were likely derived from a common source(s) as the general commonalities in the vein sulphide assemblages would support, but might have acted over slightly separate temporal pulses which may have determined the observed differences in the local gold and mineral associations.

The case of the Lead Trial hydrothermal veins deserves some appropriate differentiation with respect to the features and processes described above. This system comprises a number of multigenerational veins of variable width (e.g., up to a couple of metres wide, section 4.2.3) and

extension (i.e., arrays of up to a couple of kilometres in length) which are themselves characterised by an internal, widespread heterogeneity and localised textural anisotropies (e.g., Figure 7.1). This configuration, accompanied by the evidence of frequent and intense brecciation around the vein margins, was probably dictated by progressive changes in pressure and temperature gradients, as well as in fluid physiochemistry and supersaturation, during the vein(s) evolution (e.g., Shimizu, 2014; Jebrak, 1997) and had implications on the spatial distribution of the porosity and concentration of the precipitated phases (e.g., Micklethwaite, 2009; also see section 5.3.3). Details on the textural and mineralogical/metallic traits of the Lead Trial veins were provided in Chapter 5 (sections 5.2.3 and 5.3.3); these, together with other types of investigations - i.e., relatively high silver contents in the gold alloy and mineral inclusion suite dominated by lead and zinc (sections 6.3.3.1 and 6.3.5) - permitted the interpretation of the mineralised vein occurrences as the expression of a low-sulphidation epithermal setting (e.g., Chapman et al., 2018; Sillitoe, 2020). These features indicate that the Lead Trial hydrothermal system is substantially distinct from the others (i.e., Calliachar-Urlar, Glen Almond, and Coire Buidhe) previously discussed, and the fluid(s) involved in its genesis and evolution are probably unrelated to the ones involved in the genesis (and evolution) of other Loch Tay vein arrays.

The implications of the comparative analysis undertaken above will now be evaluated in the context of the existing literature. It is important to note that most of the previous studies (i.e., Pattrick, 1984; Mason, 1990; Ixer et al., 1997) exclusively relied on the application of traditional optical approaches (i.e., transmitted and reflected light microscopy), whereas the present work relies on the outcomes of SEM-CL analysis performed on all the investigated vein samples. This methodology not only allowed discrimination of the type(s) of quartz textures forming the different paragenetic stages, but it was vital to the definition, distinction, and quantification of these (e.g., Chapter 5). In fact, without the application of the cathodoluminescence technique, it would not have been possible to solidly attempt any reconstruction of the paragenetic history for the analysed hydrothermal veins. In general, the findings from this work are consistent with what was previously reported by other authors for the same/similar veins, in terms of their mineralogical content. Ixer et al. (1997) describe the Calliachar Burn veins as mainly constituted by quartz, galena, pyrite, chalcopyrite mineralisation and electrum, and classify them as either high- or low-grade. Among other metallic species which were reported in the literature, but not identified in the course of this work, there are pyrrhotite, minor tetrahedrite-group minerals and hessite; pyrrhotite mineral inclusions have however been recorded in the placer gold suite from Upper and Lower Calliachar Burn analysed in Chapter 6. The mineralogical assemblage

proposed for the Urlar Burn veins by Ixer et al. (1997) comprised quartz, galena, chalcopyrite, pyrite, nickeliferous minerals (e.g., gersdorffite), sulpharsenides and (in comparison to the Calliachar Burn veins) minor amounts of gold. Except for the latter species (gersdorffite and sulpharsenides), this association has appeared consistent with the up-to-date paragenesis of the two Urlar Burn veins investigated for this study (e.g., Chapter 5). The Coire Buidhe paragenetic overview, as illustrated in Chapter 5, is in line with the petrographic outcomes of Pattrick (1984) on veins from the same locality, which identified dominant quartz and galena with minor chalcopyrite, pyrrhotite, sphalerite and electrum (galena-hosted) as main components. Only unpublished data exist, at present, about the Lead Trial ore-bearing veins (e.g., Green Glen Minerals 2023; Armstrong, 2021) whose descriptions and preliminary interpretations are compatible, to an extent, with the new model proposed here. For example, it was previously reported by Armstrong (2021) that gold, in the form of electrum, precipitates immediately after the galena and sphalerite co-mineralisation, during the main ore-forming event; however, the author ultimately interprets the Lead Trial deposit as intermediate-sulphidation (IS) epithermal, in response to the mineral assemblages (galena, sphalerite, chalcopyrite and electrum), sericitic type of alteration, and textures (e.g., cockade, breccias) they observed. As anticipated and partly discussed in Chapter 5, a paragenetic study of the Glen Almond Vein was conducted by Webb et al. (2024) by the additional means of SEM-CL techniques; therefore their main findings have already been accounted for in the process of developing the paragenetic history of the Glen Almond Vein for this study (see Chapter 5 for more details).

7.2.1.3 Genetic relationships between the Calliachar and Urlar Veins

The first attempts to establish gold paragenetic relationships and the nature of the fluids sourcing the mineralisation at Calliachar and Urlar Burn were made by Mason (1990) and Ixer (1997), respectively. Their investigations provided a robust platform to assess the occurrence of multiple mineralising episodes and to place gold precipitation events in a comprehensive petrological and genetic (e.g., fluid inclusion studies; gossan investigations) framework. However, the exact relationships between the auriferous stages of the mineralisation as well as the degree of genetic linkages between the mineralisation at Calliachar and Urlar Burn still needed to be clarified. Ixer et al. (1997) proposed that despite their evident proximity, these two branches of the same system would have experienced different controls on their primary sulphide-bearing occurrences, which would have been dictated by gradational variation – as testified by the shared mineralogical assemblages (e.g., galena, sphalerite and chalcopyrite) identified in the south-westernmost Calliachar veins “6 and 7”, closer to the Urlar ones - rather

than episodic incongruency of the hydrothermal fluids. The present work shows that a spatial continuity of the hydrothermal veining is plausible, as testified by the mineralogical and structural similarity between the V3 vein and the LSCL3 vein (see Chapter 5, section 5.2.1), and the mineralisation is plausibly genetically less variable than what was argued by Ixer et al. (1997), as demonstrated by new cathodoluminescence constraints. Compositional analysis of placer, gossan-related and in-situ gold from Calliachar also revealed mercury percentages up to 5% in the alloy, quantities that Ixer et al. (1997) almost entirely ascribed to the Urlar Burn gold.

This study has confirmed (e.g., sections 5.2.1 and 5.3.1, via a SEM-CL approach) that high-grade gold mineralisation is unlikely to have precipitated in the Urlar Burn veins, as opposed to the Calliachar Burn ones. Placer gold samples could hardly be retrieved in the Urlar Burn, and the local absence of abundant cataclastic pyrite - which has been repeatedly observed (beyond being reported) at Calliachar Burn - constitutes another element of distinction between the two catchments. Critically, this type of pyrite mineralisation is the one with which the main gold-bearing stage at Calliachar Burn was found in association (see Chapters 5-6).

7.2.2 (Vein-hosted) gold mineralising history

This section is aimed at exploring and constraining possible genetic linkages between the in-situ gold mineralisation, with respect to the paragenetic position(s) at which this has been observed in some of the Loch Tay hydrothermal veins, and the eluvial and placer gold deposits recovered in nearby drainages by looking into the compositional variations of gold between paragenetic stages. Quantification of the gold alloy composition was already adopted as a tool by several authors (e.g., Parnell et al., 2000; Arif and Baker., 2004; Spence-Jones et al., 2018) to firm up detailed paragenetic sequences in various hydrothermal systems. In addition, the mineral inclusion assemblages of placer gold populations can illuminate the nature and proximity of the in-situ mineralisation, if similar species and associations are found in the hypogene environment (e.g., Chapman and Mortensen, 2016; Chapman et al., 2010b).

7.2.2.1 Gold paragenetic history and signatures at Lower Calliachar Burn

In the paragenetic evolution of the Calliachar-Urlar Burn veins, gold mineralisation has been demonstrated to take place during the first (as inclusions) and the third (mostly as fracture-fills) stage. An association of gold with specific mineral species during the precipitation stage, as these would occur in the hypothesized hydrothermal system, might be extrapolated from the paragenetic history of the G Vein (gold host, Chapter 5) and the overarching paragenesis of the Calliachar-Urlar Veins, as described in section 5.3.1. Further constraints might be provided by the inclusion mineralogy of eluvial/placer gold samples from adjacent/close sites (e.g., Calliachar_6 and Calliachar_1), having first considered the intrinsic compositional features of the vein-hosted sample. The genetic similarities between the Calliachar Veins and the inclusion mineralogy of nearby populations of placer gold were anticipated in section 6.3.1, when discussing the role of certain inclusion assemblages as proxies in the investigated gold sample suite. In the following paragraphs, the variations between silver contents from individual gold particles will be accounted for as the first potential indicator of multiple gold precipitation stages.

Table 7.2 has been constructed to correlate the compositional features of vein-hosted gold at Calliachar Burn with i) the mineral assemblages directly connected to it, in the vein where it has been located; ii) the mineral assemblages in a paragenetic framework that accounts for the inter-vein relationships; iii) the mineral assemblages in both the gossan-derived and placer gold samples (e.g., section 6.3.1). With respect to the gossan-related and placer gold samples used for comparison, the total number of particles hosting inclusions (regardless of their species) is

specified (bottom-right of Table 7.2) in order to provide an appreciation of the degree of data representativeness.

Table 7.2. Comparative assessment of the compositional signatures relating to the vein-hosted, gossan and placer gold from Calliachar Burn. The total number of particles hosting inclusions is specified bottom-right.

Particle ID	Mode	Host	Ag (wt%)	Paragenetic sulphide assemblage in veins	Gossan Au particles with compatible Ag and incl. content	Placer Au particles with compatible Ag and incl. content
G1 to G4	***inclusions (Au1_gv)***	***Py1***	~16	**pyrite**		1
	inclusions	***Py3***	~18	**pyrite + galena (main)**; chalcopyrite, sphalerite, arsenopyrite	1	
G5 to G16	***fracture fills (Au3_gv)***	***Py3***	~ 19.35 to 23		2	
			~31 to 36		7	7
					SUM = 10	SUM = 8
					10 = tot. particles with incl.	**21 = tot. particles with incl.**

This schematic representation outlines a high degree of compatibility (from 10 out of 10 particles available) between the compositional features of the in-situ gold, accounting for the parallel sulphide assemblage of the vein(s), and the gossan-related gold. In this context (Calliachar Burn), information from the inclusion suite of the gossan-related gold can therefore be used to pin down the sulphide mineralogy coeval with the auriferous stage of mineralisation as it would be reflected in the respective hydrothermal vein(s). The gold populations show increased abundances of Ag-rich particles in the vein material associated with the placer. (Figure 7.2). The distinctive compositional signature (i.e., Ag content in the alloy and associated sulphide assemblage in vein) of the Au3_gv sample (Chapter 6) has therefore appeared consistent with the signature of the Calliachar_6G sample (Figure 7.2, Table 7.2).

The relationships between the in-situ and the placer gold (Calliachar 1) appear to be much less tight, in that only eight particles out of the 21 with inclusions could be related to vein-hosted and gossan-related particles with close silver contents and sulphide assemblages. Furthermore, four of the seven placer particles with Ag ~31 to 36 derive from a pre-existent BGS (British Geological Survey) gold sample, whose analyses might have been undertaken following a slightly different protocol (e.g., Leake et al., 1997a). However, due to the relatively low amount of in-situ and gossan-related gold data available to possibly infer these types of constraints, it is currently inappropriate to regard the relevant dataset as a definitive template against which the placer gold data can be assessed. In fact, the broader range of composition exhibited by the placer populations would suggest possible contributions from additional in-situ gold

occurrences, which does not preclude any relationship of compatibility between the Calliachar_1 gold and the in-situ gold samples that have been here compared. Their mutual relationship additionally suggests the occurrence of at least a couple of gold generations showing different mineral signatures – i.e., a first one dominated by pyrite, and a later one associated with a richer sulphide assemblage (see Table 7.2). No firm relationship between inclusion assemblage and mercury content increase in the gossan-related gold sample could be established; therefore, mercury has not been considered in this ultimate gold paragenetic analysis.

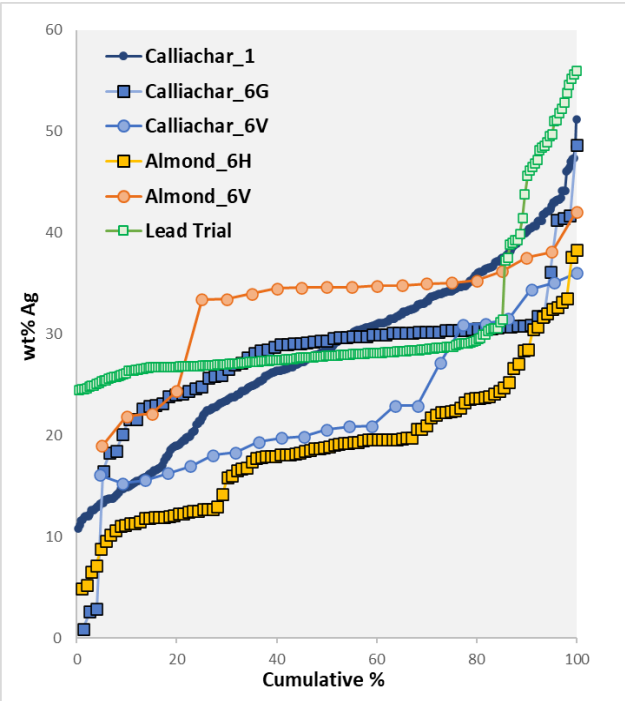

Figure 7.2 Cumulative percentile of the number of particles vs increasing wt.% Ag plots, for the examined gold samples. V=VEIN HOSTED. Calliachar_6G = Calliachar 6 in previous sections (also "gossan-derived"); Almond 6H = Almond 6a in previous sections.

Due to the better paragenetic constraints that can be obtained from the gossan-derived gold in spite of the placer gold, further investigations have helped depict the relative proportions of inclusion species according to two main classes of silver content (Ag 1 and Ag 2) in the alloy of the gossan-related gold (Figure 7.3). The relative abundance of pyrite, as it can be observed across these two silver categories, would be compatible with the paragenetic relationships that were established between the gossan-related gold and the in-situ gold from the respective sulphide-bearing vein (occurring as both inclusions and fracture-fills in pyrite). The relative abundance of galena and chalcopyrite inclusions in the Ag (2) gold category would also conform to the comprehensive paragenetic interpretation. Nevertheless, it is essential to keep in mind

the restricted number of gold particles available for this type of assessment and the consequent limitations to the robustness of the conclusions drawn above.

Inclusion species abundance by gold particle Ag% classes (Calliachar_6G)			
wt% Ag			
21.5 to 23	**28.5 to 32**		
Py	***Ga***	***Cpy***	***Py***

Figure 7.3. Distribution of the inclusion species (relative abundance) by gold particle (wt.% Ag) classes in the Calliachar_6 (gossan-derived) sample.

Ixer et al. (1997) first performed compositional analysis on electrum grains in pyrite. Their results appear to be consistent with the silver values here obtained for in-situ (mostly fracture-hosted) gold; however, their observations, as well as those of Mason (1990), repeatedly locate electrum grains also in galena mineralisation. Albeit this association couldn't directly be deduced from the SEM analyses performed in the course of this study, it may be extrapolated from the overall paragenetic history of gold at Calliachar Burn as it has been here proposed (e.g., Chapter 5), suggesting that previous work likely focused on the analysis of a different set of vein specimens and gold particles from the same locality.

7.2.2.2 Gold paragenetic history and signatures at River Almond

The relationships between gold mineralising history and respective paragenetic stages at River Almond can be deduced more easily than those at Calliachar-Urlar Burn, due to a slightly larger availability of quantitative alloy data from the in-situ gold and better-constrained linkages with the in-situ sulphide mineralisation (see Chapter 5; e.g., Webb et al., 2024). Three placer gold samples from the Upper Almond catchment are considered for comparison – two were recovered very close to the gold-bearing vein sampling site (Almond 5 and 4b, respectively) and one about 1.5 Km downstream (Almond 4b). The comparative gold paragenetic analysis is indicated in Table 7.3. The relationships between gold mineralisation and the established sulphide assemblage (from detailed in-situ paragenesis) are broadly reflected in all the placer gold particles utilised, but relatively robust linkages can only be appreciated for gold with silver values in the range of ~19 to ~33 (Table 7.3; Figure 7.2 – Almond_6V = vein-hosted gold; Almond_6H = gold from hypogene) and with respect to in-situ particles (almost always) hosted in pyrite (Table 7.3). The inclusion mineralogy of the Almond 5 placer sample, recovered right at the sampling location of the studied auriferous vein, is additionally highlighted in Figure 7.4. The in-situ metallic associations (Py, Ga and Sph) are more effectively reproduced in the first

alloy class (up to ~27 wt.% Ag). Silver-rich alloys are interpreted to have formed later in the overall gold paragenetic history, consistently with their mode of in-situ occurrence (i.e., in fractures that postdate the hosting mineral), but possibly precipitated from a common fluid source (e.g., Webb et al., 2024). Placer gold particles characterised by higher silver contents (i.e., from 34 to 42) tend to show a weaker association between their inclusion suite and the sulphide assemblage coeval with (or slightly pre-dating) the in-situ gold mineralisation (Table 7.3).

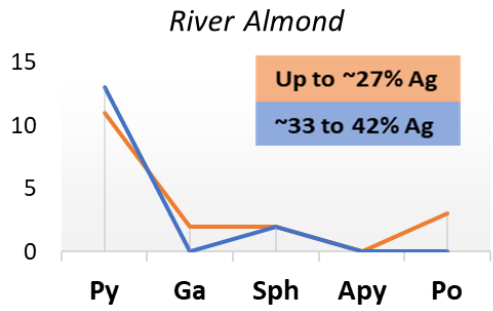

Figure *7.4*. *Distributi*on of the inclusion suite in the gold from River Almond based on silver content classes (up to ~27% and between ~33 and 42% Ag).

The high-silver, dominant trend of the Almond_6V plot (vein-hosted gold, Figure 7.2) is only partly reflected in the Almond_6H plot (gold from relevant crushed ore, Figure 7.2), hinting at considerable variations in the silver content distribution across gold from the same hypogene environment (e.g., Savastano et al., SGA 2023). The first implication from this result is that recovering gold particles from small volumes of material typically generates samples showing relatively narrow, and possibly distinct, silver content ranges. Therefore, it is not possible to assume an equivalent composition for vein-hosted gold and close hypogene-derived populations, because of the possible (and likely) variations in the physicochemical parameters that governed the precipitation of the various groups of gold particles considered for analysis (Spence-Jones, 2021). Furthermore, the placer samples (e.g., Almond 5) represent averages derived from a substantially larger volume of material and thus tend to exhibit a more homogeneous distribution of the alloy composition (e.g., Chapman et al. 2000a). This reflects the input of numerous localised sources, each characterised by a distinct Ag signature – for example, Almond 6V represents a single source, Almond 6H incorporates material from at least two such sources, and Almond 5 reflects an average composition across the broader population.

Table 7.3. Comparative assessment of the compositional signatures relating to the in-situ and placer gold samples from River Almond.

Particle ID	Mode	Host	Ag (wt%)	Paragenetic sulphide assemblage in veins	Placer (Alm 4 &5) Au particles with compatible Ag and incl. content	Placer (Alm 9) Au particles with compatible Ag and incl. content
A1	inclusion	**pyrite**	18.9	**pyrite,** sphalerite, galena and chalcopyrite		1
A2	in fracture	**pyrite** (ga on the side)	21.8		2	2
A3	inclusion	**pyrite**	22.1		4	2
A4	inclusion		26		4	1
A5	Inclusion		33.4		2	2
A6	fracture					
A7 to A9	in fracture		34 to 35			
A10	in fracture		36.2		1	
A11 to A13			37.56 to 42.1			
A14	in fracture	**chalco and ?**	34.6			
A15	inclusion	**chalcopyrite**	34.6			
A16 - A17	in fracture	**chalco and ?**	34.7			
A18	semi-crack	**sph (py on the edge)**	24.3		1	3
A19 to A21	in fracture	**sphalerite**	34.65 to 35.3			
					SUM = 14	**SUM = 11**
					21 = tot part with incl.	18 = tot part with incl.

7.2.2.3 Possible genetic relationships between gold from the Lead Trial and Ardtalnaig Burn

The silver content distribution in the gold populations (Tips 1 & 2) from the Lead Trial crushed-ore material concentrate around two main trends (respectively wt. % Ag <29.5 and >29.5; see section 6.2.3), which can also be identified in the silver content distribution of the populations from Ardtalnaig Burn (e.g., section 6.3.3.2; Webb et al., SGA 2023). The presence of galena and sphalerite inclusions in both the Lead Trial gold alloy classes suggests that they are coeval with the earlier gold paragenetic stage, as also the physical evidence of "reaction fronts" at the interface between inclusions and silver-rich phase would confirm (i.e., Figure 6.13). Likewise, the few molybdenite inclusions detected in particle alloys with silver contents from ~26% to 37%, suggest no specific affiliation to either of the two main gold paragenetic stages. Higher Mo and Cu and lower Zn and Pb relative abundances were observed in the inclusion suite (by SEM inspection) from the Ardtalnaig placer samples (see section 6.2.3; e.g., Webb et al., SGA 2023).

The distribution of molybdenum at trace levels (ppm) in gold from the Lead Trial would suggest incorporation of this element in the alloy during the early mineralising stages - i.e., particles belonging to the wt. %Ag ~18 to 20 compositional range; see section 6.3.5.2 and Figure 6.27b - of the associated (interpreted) hydrothermal system. Mo occurrences also reach higher, clustered concentrations (i.e., Figure 6.29a), irrespective of Ag content variations, which have been interpreted to represent the effect of micro/sub-micro molybdenite inclusions present in the gold population. Similar investigations conducted on gold particles from the proximal Ardtalnaig locality revealed higher Mo and Cu and lower Zn and Pb relative elemental abundances, as well as a higher concentration of Bi and Te (ppm).

These results, beyond being consistent with the inclusion assemblage that has been observed for this population (e.g., Webb et al., SGA 2023), would also favour the hypothesis of a different evolutionary stage of a genetically related magmatic-hydrothermal system. The trends extrapolated from gold alloy, mineral inclusion, and elemental composition analyses have additional implications for the understanding of the mineralisation styles which may be associated with these deposits. These will be explored in section 7.3.

7.2.3 Genetic comparison of placer gold signatures in the Loch Tay area (and potential for undiscovered mineralisation)

The compositional signatures obtained by analysing placer gold from multiple locations in the Loch Tay area, for which preliminary interpretation has been provided in Chapter 6, will now form the basis of a more in-depth discussion, not simply concerning the geological factors which most likely contributed to the style(s) of gold mineralisation, but also their deeper interplay with the hydrothermal fluids potentially involved and possible implications at different scales. All the relevant considerations are aimed at defining the potential for undiscovered, gold-bearing mineralisation in the area and establishing the effectiveness of this approach for exploration targets.

Extensive comparative investigations between gold signatures in the Loch Tay area were previously conducted by Chapman et al. (2023c), who relied on a highly representative sample set to define two main compositional groups locally. These two main compositional groups were carefully analysed in the context of the local geology. Further details will be here provided with regards to the sub-populations of gold particles constituting the main sample populations used for analysis by Chapman et al. (2023c), and additional gold populations aimed at complementing the regional metallogenic picture (e.g., Lead Trial/Ardtalnaig gold sample; Invergeldie gold sample). As also partly described in Chapter 6, some fundamental compositional differences have been noted between gold populations from Calliachar Burn, Glen Quaich, River Almond ("Group 1") and specific gold populations from drainages in the south of the Loch Tay area, namely Glen Lednock, Keltie Burn, and Sma Glen ("Group 2") to an extent (respectively classed as Group 1 and Group 2; Chapman et al. 2023c). More subtle compositional distinctions and/or further peculiar signatures can be conceived for the rest of the Loch Tay samples and will be illustrated and discussed in the following paragraphs.

Rock lithologies and catchment areas

All the sampling sites used for this study are located within the Grampian Terrane of central Scotland, substantially constituted of Neoproterozoic to Ordovician metasedimentary and igneous units; the Terrane is bounded by two regional scale faults (i.e., Great Glen and Highland Boundary Faults) and extensively crosscut by a number of minor, local faults whose total displacement and geometries are often poorly visible. The observed variations in gold compositional signatures, as preliminarily argued in Chapter 6, have appeared to be sympathetic to local geological constraints/rock types. Calliachar-Urlar Burn and Glen Quaich (details provided in the next paragraphs) flow through the metapelites and psammites (Pitlochry

Formation) of the Southern Highland Group (SHG). The River Almond's catchment (e.g., Figure 6.8) extends E-W for several kilometres and therefore, while the upper part of the stream roughly crosses the same lithologies as above, the rest of it flows through the metapsammites of the Ben Ledi Formation of the SHG (Chapman et al. 2023c). Glen Lednock is still within the Ben Ledi Formation, although the associated gold sampling site is adjacent to an Early Devonian Granitic Suite (Comrie Pluton; Chapman et al. 2023c); similarly, the Invergeldie Burn flows across both the Ben Ledi Formation and the Early Devonian Granitic Suite, with the respective sampling location lying just on top of the latter. The Keltie Burn sampling location is sited southwards of an unconformity created by the Devonian sedimentary and igneous rocks sitting on top of the Southern Highland Group (Chapman et al. 2023c); a few kilometres to the NE, the Monzie location lies on top of Early Devonian basalts and andesites, to the south of the same unconformity. Later paragraphs will treat the geological features associated with the Lead Trial and Ardtalnaig sampling localities separately, due to the slightly different approach adopted for their investigation.

Keeping in mind the geological context provided above, some first-order, regional-scale distinctions can be made based on the presence/absence of exposed igneous bodies proximal to the gold sampling localities, which would align with the variations in the inclusion assemblages observed in the Loch Tay gold samples; although the inclusion contents of these populations are generally not elevated - with respect to the number of gold particles available for each population, which could thus affect sample representativeness – a large regional gold sample set is available to allow robust comparison (e.g., Chapter 6; Chapman et al. 2023c). The first compositional group examined comprises placer gold samples from Calliachar Burn, River Almond and Glen Quaich ('Group 1', Chapman et al. 2023c).

7.2.3.1 Calliachar Burn, River Almond, Glen Quaich – Group 1

Comparison among inclusion assemblages

The metallic signature of the Glen Quaich inclusion suite gathers elemental components that are found to variable extents in the assemblages from both Calliachar Burn and River Almond (Figure 7.5). Specifically, a lead and zinc association has appeared common in inclusion suites from Glen Quaich, Calliachar downstream and Almond up-midstream; the combination of these two elements with cobalt is however prominent in samples from Glen Quaich and from both River Almond and Calliachar Burn upstream. Nickel is relatively abundant in the elemental composition of the Glen Quaich inclusions, but occurs in tiny amounts in the ones from the other two localities (see Figure 7.5). The non-metallic inclusion assemblages of Glen Quaich,

Calliachar downstream and Almond Upstream are overall similar, although minimal abundances of antimony can only be observed in the Glen Quaich and Calliachar 3 (mid-stream) suites (see "non-metal" radar plots in 7.5).

A strong arsenopyrite component can be distinguished in the Calliachar Burn Downstream and Glen Quaich samples. In general, the gold populations from River Almond show a greater variety of species (e.g., Chapman et al. 2023c), but the assemblages that are consistently observed in all three population sets used for comparison (Calliachar Burn, River Almond and Glen Quaich) are the base-metal bearing ones (e.g., Py, Cpy, Ga, Sph).

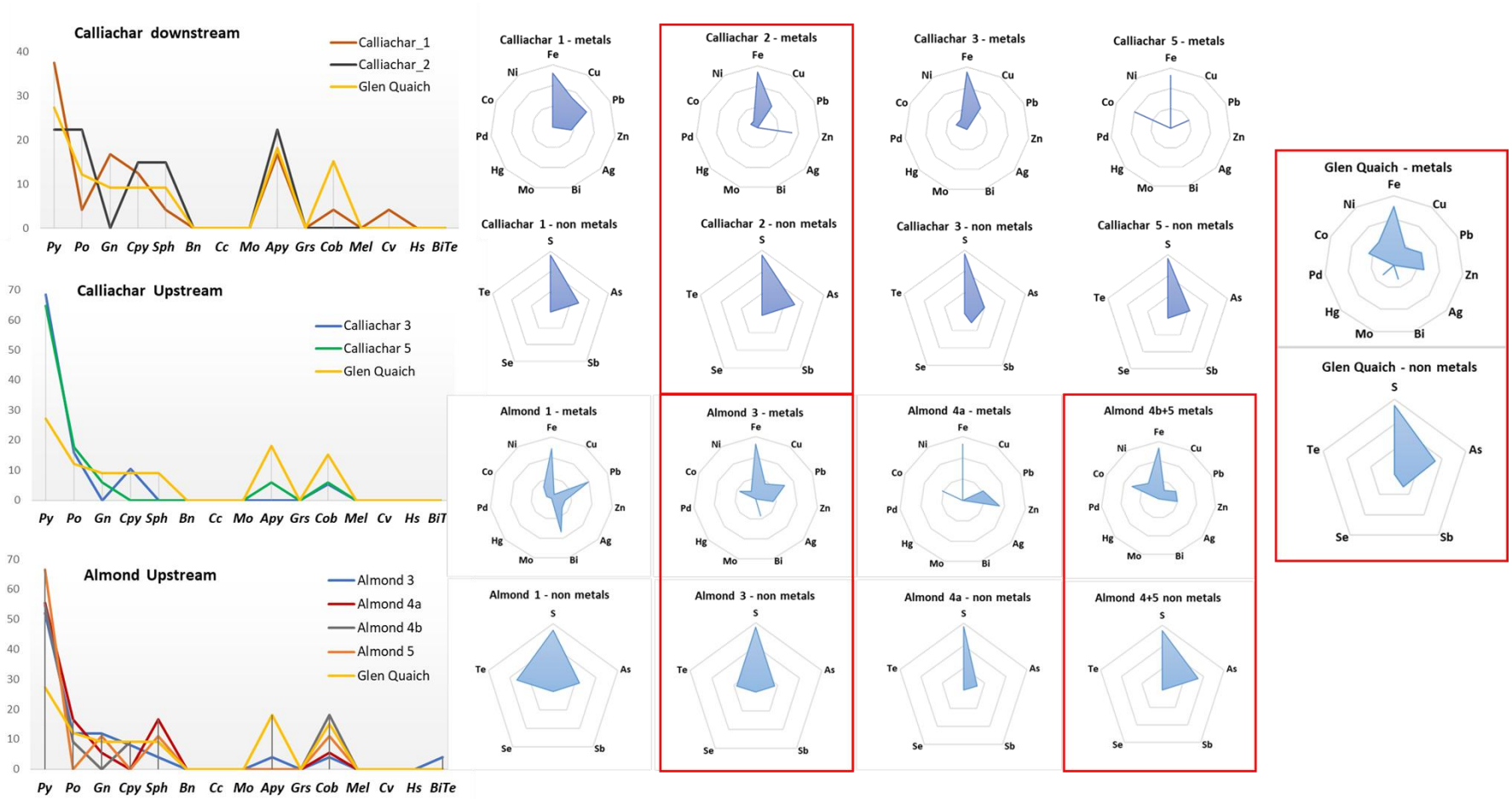

Figure 7.5 Graphical comparison of the mineral (spider plots) and elemental (radar plots) inclusion suites of the placer gold samples from Calliachar Burn (Upstream and Downstream), River Almond (Upstream) and Glen Quaich (tot. inclusion number forming the Glen Quaich sample: 37). Chapman et al. (2023c) employs the same datasets presented here; however, the sub-sets relevant to some of the localities (e.g., Calliachar 1, 3, 5 and Almond 4, 5) have been merged in the paper (e.g., "Calliachar Burn", "Glen Almond"), and Almond 1 is regarded as "Sma Glen".

Comparison among gold alloy compositions (Ag and Hg)

Mercury and silver contents in placer gold from these localities have also been compared. The mercury profile of the Glen Quaich gold lies in between the profiles of Upper Calliachar and Lower Almond gold, suggesting that there might be a spatial decrease in alloying mercury from north to south in the area (Chapman et al., 2023c). Interestingly, a decrease in mercury from downstream to upstream can also be appreciated in gold from both the Calliachar and Almond catchments (Figure 7.6a).

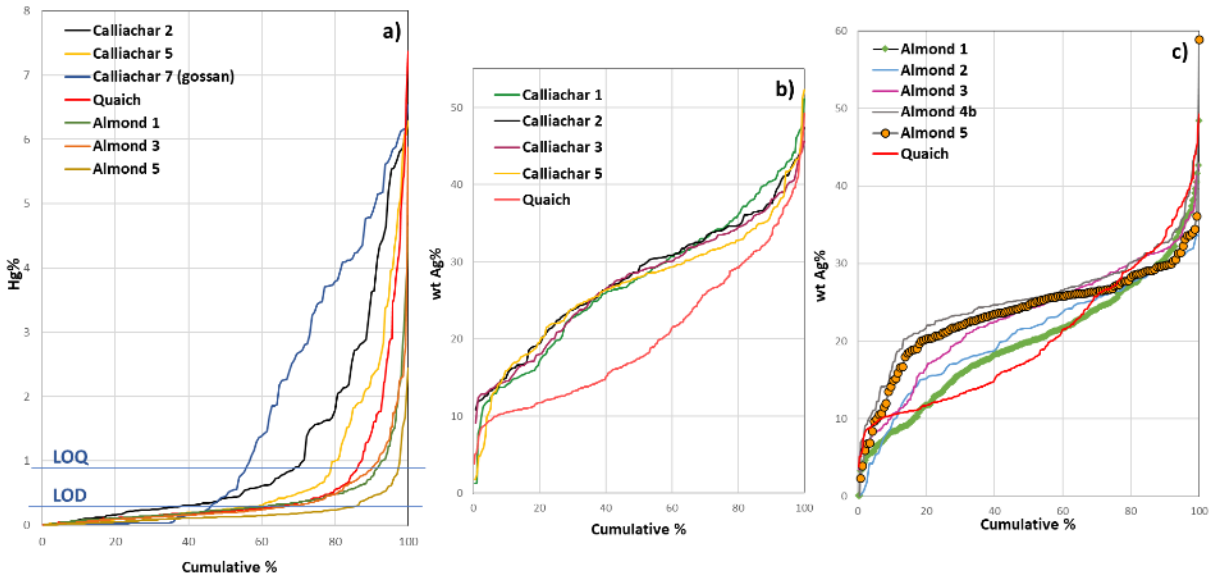

Figure 7.6. Graphical comparison of the gold alloys (Hg and Ag Cumulative%) from the Calliachar Burn, River Almond and Glen Quaich placer samples.

Evaluation of the relative silver contents in gold from the three localities does not suggest a particular linkage between the Glen Quaich placer population and either Calliachar or the Almond populations (Figure 7.6b and c), although the Glen Quaich sample shows overall lower silver contents (Chapman et al., 2023c). In general, the silver profiles descriptive of the gold from these localities display broad variability in their ranges; these would be compatible with variations in the physicochemical parameters which dictated gold precipitation during a large, evolving hydrothermal event, but also with variations connected to multiple, genetically unrelated hydrothermal pulses (e.g., Chapman et al., 2023c).

The Glen Quaich placer population, used for such comparative investigations, was sampled along the watercourse in two locations that lie approximately 5 km to the SW of Calliachar Burn and 8 km to the NE of River Almond (Figure 7.7). Although signature commonalities have been observed between the Glen Quaich placer gold and both the Calliachar and Almond placer gold,

a linkage with the upper Almond gold composition might appear easier to constrain because of the mutual occurrence in similar proportions of more than three inclusion species (e.g., galena, sphalerite and cobaltite) and slightly closer similarity in the alloy composition (Figure 7.6). Nevertheless, possible geological evidence that could support this case is potentially less than that which would support an association with the gold from Calliachar Burn. A NE-SW-trending fault directly crosscuts segments of both Glen Quaich and Calliachar Burn, while there doesn't appear to be any similar feature to immediately connect Glen Quaich and River Almond (Figure 7.7); on the other hand, a number of local faults have been directly observed or extrapolated across the area in between (Figure 7.7). Faults are, in this context, assumed to act as potential conduits for mineralising fluids, and that could explain the commonalities in placer signatures.

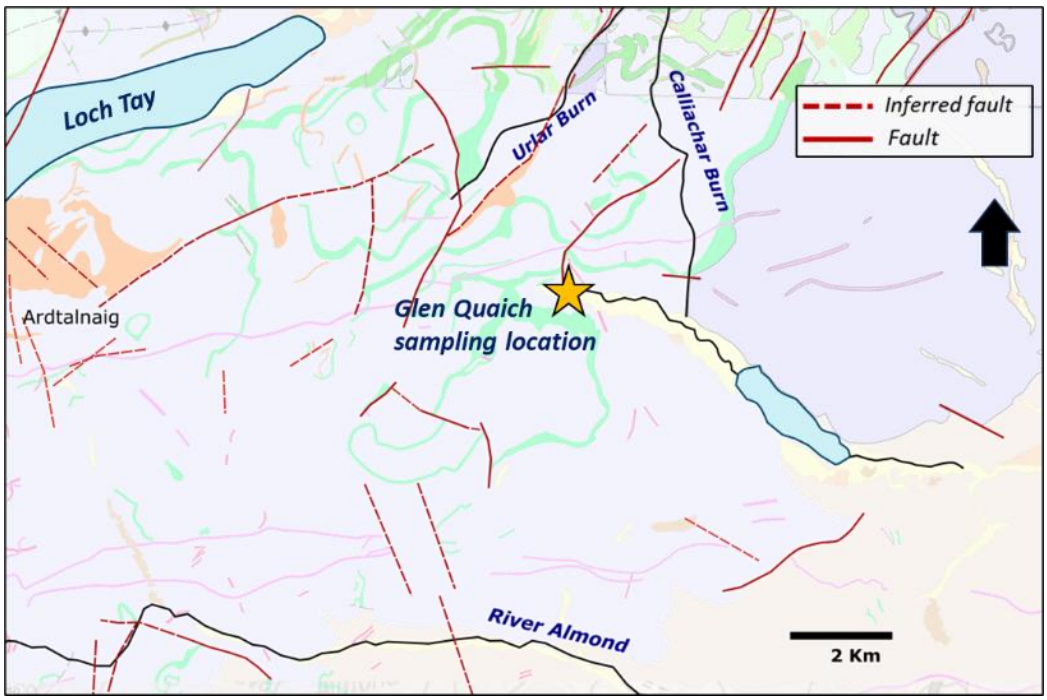

Figure 7.7 Simplified geological map of the Calliachar-Urlar Burn, Glen Quaich and Glen Almond area, highlighting the local presence of reported and interpreted (inferred) faults (modified after the BGS geological map from https://digimap.edina.ac.uk/).

The gold particles from Glen Quaich are characterised by a flat and flaky morphology and never reach very large individual sizes, suggesting they were subject to prolonged stream transport. On the other hand, the particles sampled in the Upper Calliachar Burn reach sizes up to 10 mm and are often characterized by rough textures (e.g., Chapman et al., 2023c).

Some further considerations can be made by accounting for the morphological and compositional characteristics (see section 6.2) of placer gold from upstream and downstream in drainages, for the populations (within Group 1, Chapman et al., 2023c) examined. The same

model for placer gold mineralisation, in relation to hydrothermal vein arrays, is proposed for both the Calliachar Burn and River Almond systems.

Upper and Lower Calliachar Burn

The placer gold samples from Calliachar Burn show features that vary depending on the point of the catchment where that specific sample was collected (section 6.2.1.2). To begin with, the gold populations from Calliachar Burn downstream have appeared to host generally higher numbers of inclusions with more complex mineralogy; additionally, these populations are characterised by higher Hg contents in the alloy than the one from upstream, backed by even greater Hg contents in the gossan-derived gold samples (Calliachar Burn downstream). These features have been linked to the presence of a vein array downstream, whose mineralogy and paragenetic position of the in-situ gold (where observed) are consistent with the inclusion suites and alloy composition ranges of the placer gold sampled in its proximity (see Sections 6.3.1 and 7.2.2). Further point of contrast between the populations from Lower and Upper Calliachar Burn is provided by some of the individual gold particle sizes, much greater in the Calliachar_5 placer sample than in all the rest of the samples from the same drainage, suggesting the likely proximity of an in-situ mineralised source; in fact, it would be difficult for particles reaching several millimetres of diameter to travel too long distances (e.g., greater than hundreds of metres), even when the energy of the stream is elevated. Relatively rough morphologies additionally feature in some of the gold particles from the Upper Calliachar Burn. Some of the smaller particles from the upper reaches could have however been transported downstream, as testified by the mostly rounded/smoothed morphology of part of the grains in Lower Calliachar Burn. The inclusion signature of the Calliachar_5 placer sample can, to an extent, be recognised in the compositional features of the gold populations from Calliachar downstream, implying the partial inheritance of the mineralogical traits of the upstream gold (i.e., Py, Po, Cob – Figure 7.5). The silver profiles descriptive of both these (placer) compositional groups show very similar gradients and, although the silver content of the (downstream) gossan-related gold is perfectly compatible with the range of silver contents recorded in the placer gold populations from lower Calliachar Burn, the fact that the relevant silver profiles only marginally overlap may also be interpreted as local evidence of gold influxes from upstream. The extensive variability in silver contents is normally expected within individual placer samples and may be explained as a result of the contribution of gold particles deriving from separate mineralising episodes (narrower Ag ranges each) from either univocal or multiple sources throughout the catchment area (e.g., Chapman et al. 2023c).

The hypothesis of the presence of an additional and possibly distinctive in-situ source for the Upper Calliachar Burn gold would be supported by the composition of the respective sample at the trace element level, which differs substantially from the one recorded for the Lower Calliachar Burn gold. Chromium (see section 6.2.6) was only detected (even though in reduced ppm amounts) in the former, suggesting a possible influence of Cr-bearing (mafic) lithologies on the hydrothermal fluid associated with local gold precipitation. While these types of lithologies have not directly been observed to outcrop in the area, an extended layer of meta- and micro-gabbro is mapped and reported within the local geological stratigraphy (e.g., section 2.4). Nickel is another element generally associated with mafic and ultramafic lithologies (Spence-Jones 2021; Chapman et al., 2023d), and its occurrence is also more pronounced in the trace element signature of the Upper Calliachar than of the Lower Calliachar Burn gold (see Chapter 6 – 6.2.1). Ni-bearing inclusion species in minimal amounts were detected in both the Calliachar 3 and Calliachar 2 placer gold samples (see radar plots in Figure 7.5), where particles from upstream could have been conveyed. A simplified conceptual model is shown in Figure 7.8 to illustrate this theory. Worthy of notice is that no Ni-bearing minerals were identified as inclusions in the two gossan-derived gold samples from Calliachar Burn downstream, providing a supporting point to the hypothesis of mafic (or ultramafic) lithologies being located around the upper portion of the Calliachar Burn catchment.

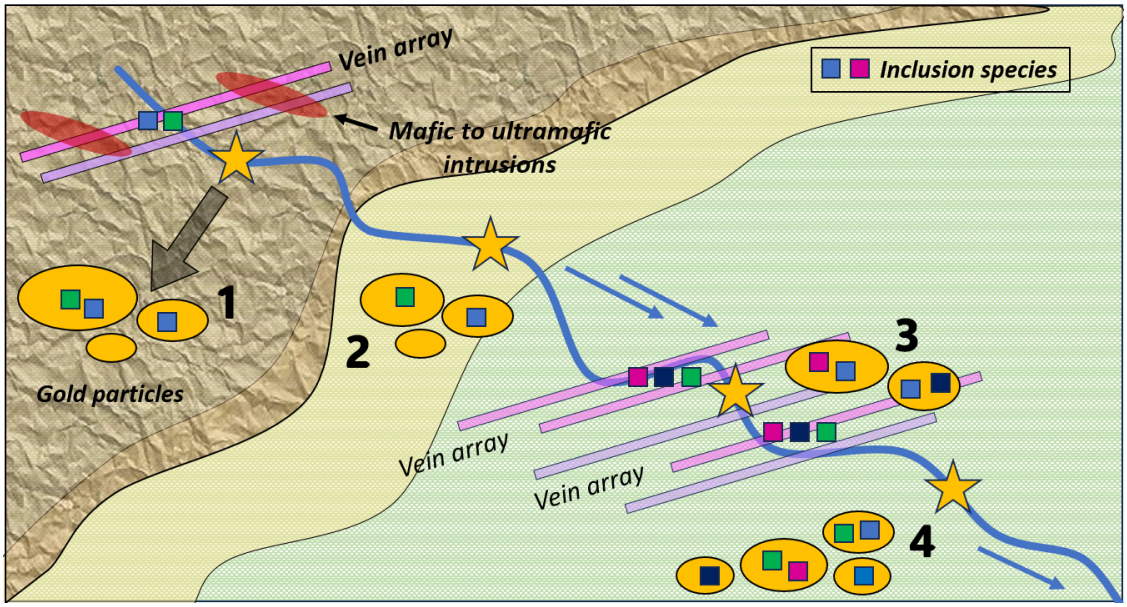

Figure 7.8 Conceptual model illustrating how the inclusion signature of the placer gold populations may vary across a stream section (i.e., from upstream to downstream) receiving contributions from the 'upper' gold occurrences.

If zooming out of this location slightly, it can be noted that nickel is relatively abundant in the

elemental inclusion suite of Glen Quaich. With reference to possibly similar cases at the global scale, Chapman et al. 2023d reported an association of Ni-Co with mixed S–As–Te ± Sb in gold occurrences from an area (i.e., Atlin area, British Columbia) dominated by mafic-ultramafic host lithologies.

Upper and Lower River Almond

The placer gold populations from River Almond have also shown some considerable mineralogical variations within their inclusion assemblages conditional to where the samples were collected along the stream (see Section 6.3.2). The observed differences were partly discussed in Chapter 6, where separate genetic contexts have been accounted for to justify the compositional signature of the gold samples from Upper River Almond against the distinctive signature of the gold samples from Lower River Almond (i.e., Sma Glen locality; Chapman et al., 2023c). Further points of discussion can be raised upon consideration of the specific composition of individual placer samples. Although the inclusion mineralogy of the gold populations from the upper sites of the catchment conforms with the sulphide mineralogy established for the Almond Vein (e.g., Webb et. al 2024), a couple of species were additionally identified as part of these assemblages. Sulfarsenides (FeCoNiAsS) inclusions recur in placer gold from the Almond 4a, Almond 4b and Almond 5 (inclusive of a small sample from a local tributary; Figure 6.8) samples; pyrrhotite inclusions were notable in the gold from Almond_3 and Almond_4a and, subordinately, in gold from Almond 4b; a single arsenopyrite inclusion was additionally found in the Almond_3 sample. To this end, some slight inter-sample variations have also been deduced by examining the respective silver profiles, which indicate generally higher silver contents in the placer gold from Almond 4a, 4b and Almond 5 in comparison to Almond 3 and 2 and especially Almond 1 (i.e., Sma Glen locality, as discussed in section 6.3). As anticipated in Chapter 6, Chapman et al. (2023c) formulated the hypothesis of a local influx of gold, being derived from an undiscovered magmatic-hydrothermal source near Sma Glen, to possibly explain the distinctive Au-Bi-Te signature of the Almond_1 placer sample. This conclusion, however, doesn't extend to the slight dissimilarities in inclusion suites and gold alloy (reported above) observed between the Almond_5, Almond_4b, Almond_4a and Almond_3 populations, obtained from sites distributed more than >12 Km upstream of the Almond_1 (Sma Glen) one (see map in Figure 6.8). Taking into consideration a wider-scale compositional picture, the Co-Ni assemblage - plus the Po component, although this is not in itself diagnostic - of the Upper River Almond gold inclusion suite can be mapped onto the Glen Quaich gold inclusion signature, where such elements are present in similar proportions. This linkage would allow speculation of a possible shared nature of the fluid(s) precipitating gold at these two localities

(Upper River Almond and Glen Quaich), which might have interacted with potential ultramafic or mafic lithologies providing the source for nickel (e.g., Spence-Jones, 2021) and chromium, again detected (ppm) in the trace element composition of the some placer gold particles from River Almond, near Auchnafree. The aforementioned arsenopyrite inclusion identified in the Almond_3 (Auchnafree) placer sample adds support the hypothesis of a local influx of gold, whose fluid sources may have been shared with the fluids that precipitated gold mineralisation near Glen Quaich.

Nevertheless, sulfarsenide inclusions (FeCoNiAsS) were particularly observed in placer gold from a tributary of the upper River Almond (later incorporated into the Almond 5 sample), which could be evidence of an undiscovered vein system in proximity to the known Almond Vein. It is currently not possible to deduce the mineralogy of this hypothetical vein system (or individual vein), whose characteristics would be expected to match the Glen Almond Vein ones at least partially. Regardless, the hydrothermal fluids involved in the genesis of the gold-bearing mineralisation would have likely been affected by interaction with mafic/ultramafic lithologies.

The model proposed to decipher the distribution of the placer gold composition across the Upper and Mid Almond catchment is comparable to that proposed for the Calliachar Burn gold/vein system in the previous section, where the inclusion species recorded in particles from upstream are, to an extent, reproduced in the inclusion signature of the gold particles sampled downstream due to their partial and prolonged transportation by the water flow (Figure 7.8). The assumption that contributions from localised influxes of gold, possibly deriving from different vein systems, enter the stream at specific points is therefore key. Furthermore, the influence of mafic and possibly ultramafic lithologies on the hydrothermal fluids, prior to gold deposition, has been suggested for both systems to explain the Ni-Co (and, where observed, Cr) gold signatures. Possibly, the presence of hydrothermal vein systems deemed to be the result of the ore-bearing fluid interaction with these lithologies, would not be limited to the Calliachar Burn and River Almond headwaters, but also extend to some (presently unknown) location(s) in the area in between Almond Auchnafree and Glen Quaich.

7.2.3.2 Loch Tay South localities – Group 2

The second compositional group (after Group 2 in Chapman et al. 2023c) comprises placer gold samples from the south of the Loch Tay area and principally from Glen Lednock, Invergeldie Burn, Keltie Burn and Monzie Burn. The compositional signatures and genetic environments relating to the gold from Glen Lednock and Keltie Burn were discussed extensively by Chapman

et al. (2023c) along with a genetic contextualisation of the placer gold sample from Sma Glen (equivalent to Almond_1, Chapter 6).

After consideration of the occurrence of Early Devonian igneous lithologies in the area, the work argued for the derivation of these gold occurrences from a multistage magmatic-related hydrothermal system, mostly in response to some distinctive inclusion species recorded in the Glen Lednock and Keltie Burn sample populations, along with relatively Cu-rich alloy composition. As described in Chapter 6, a mineral inclusion association of chalcocite, molybdenite and bornite in the gold from Glen Lednock has been regarded as an indicator of porphyry mineralisation style, while the combination of silver and bismuth tellurides in the Keltie Burn gold points towards a low-sulphidation epithermal style (Chapman et al., 2023c). To further support such associations, the silver contents of the gold from these localities are comparable to those generally attributed to porphyry-epithermal settings (e.g., Chapman et al., 2023b; Morrison et al., 1991; Chapman et al., 2005; Chapman et al., 2014).

The compositional signatures deduced for the Glen Lednock and Keltie Burn gold populations were assessed against some pre-existing gold compositional datasets relating to magmatic-hydrothermal systems in the Canadian Cordillera and in the Ochil Hills igneous rocks of Scotland (Chapman et al., 2005, 2022 and 2023c). Comparison of the inclusion suites of the Glen Lednock and Keltie Burn gold with those of the calc-alkaline porphyry – low-sulphidation epithermal systems in Yukon (Chapman et al., 2018) and British Columbia and of alluvial gold from Ochil Hills (Chapman et al., 2022) facilitated the allocation of these samples to the deposit types indicated above.

The Almond_1 (Sma Glen) gold signature is described by compositional elements from both the Group 1 and Group 2 sample populations (Chapman et al., 2023c). The 'Group 1' compositional characteristics (e.g., partial similarity in the alloy composition) have been interpreted to be due to the presence of some water-worn gold particles within the Almond_1 sample, being transported from upstream (i.e., Upper River Almond gold samples) to downstream in the catchment (see Chapter 6 for details); the 'Group 2' compositional characteristics (e.g., some distinctive inclusion species) of the Almond_1 gold sample were instead interpreted to be the results of a more local influx of gold (Chapman et al., 2023c). The placer gold from Sma Glen shows a clear Au-Bi-Te signature (Figure 6.11) which has been explained by accounting for limited compositional contributions from porphyry, epithermal and their related transitional environments (Chapman et al., 2023c), to which the gold signatures of the Glen Lednock and Keltie Burn samples were previously associated. This hypothesis is consistent with the presence

of Devonian igneous lithologies proximal to the Sma Glen (Almond 1) locality, currently absent at the sampling site due to past erosional processes. The gold sample from Sma Glen has conclusively been related to a 'deep-seated' epithermal mineralisation style (see Chapter 6; Chapman et al. 2023c), whose low-temperature expression would be linked to an Au-Ag-Te signature. This outcome has implications for the potential of a new, undiscovered, in-situ gold source near Sma Glen (e.g., Chapman et al. 2023c).

Invergeldie Burn and River Almond

The placer gold sample from the Invergeldie Burn was obtained from two sites sitting on top of the Early Devonian Granitic Suite (as anticipated in the early 7.2.3 section). Hence, consideration of the geological context of this gold occurrence would easily lead to the assumption that the environment of the associated mineralisation is not genetically far from that of gold from Glen Lednock, and even of some other populations from the south of the Loch Tay area. However, some evident compositional correlations can be drawn from a comparison of the Invergeldie gold sample with some of the 'Group 1' gold populations and, particularly, the Almond 3 (i.e., near Auchnafree) one.

To begin with, the elemental inclusion signature of the gold from Invergeldie (i.e, section 6.2.4) hosts some base metals (especially Fe, Pb and Zn) which, in this context, have been frequently observed as components of gold from the Group 1 localities. Nevertheless, a few elements (Bi, Co and As), which equally form the Invergeldie gold inclusion assemblage, have so far been reported in populations from both the (main) compositional groups (Group 1 and Group 2). The presence of tellurium is particularly intriguing, in that this element appears to be distributed across the Loch Tay placer gold samples according to some regional trend, that is increasing gradually from north to south – therefore, an (almost) absence of tellurium is recorded in the elemental composition of the inclusion suite from the Calliachar Burn, Glen Quaich and the uppermost River Almond gold populations; relatively low tellurium amounts are recorded in the inclusion signatures of the Almond 3 (midstream) and Invergeldie gold; and relatively high tellurium proportions are generally observed in the inclusion signature of the placer gold samples from the south of the Loch Tay area (e.g., Almond 1 and Keltie Burn). In terms of inclusion mineralogy, the Invergeldie and Almond 3 gold populations show notable resemblance due to the shared occurrence of certain species (e.g., pyrite, pyrrhotite, galena, chalcopyrite, – Figure 7.9a).

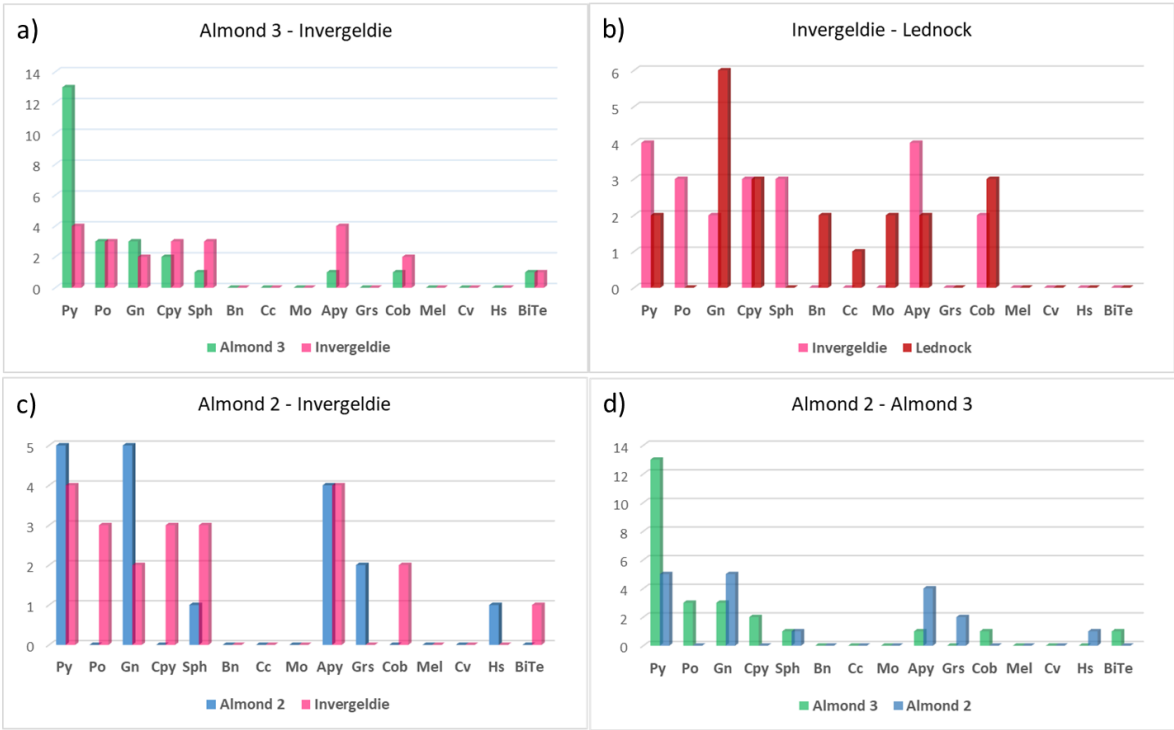

Figure 7.9 Histogram depictions and comparisons of the mineral components (actual quantities) of the inclusion assemblages in the Almond 3, Invergeldie, Glen Lednock and Almond 2 placer gold samples.

Mineralogical similarities to a lower degree can also be noted between the Invergeldie and Glen Lednock gold samples (Figure 7.9b), especially in relation to the occurrence of pyrite, chalcopyrite, arsenopyrite and cobaltite. Nonetheless, specific mineral species can only be found in the Glen Lednock inclusion assemblage, namely bornite, chalcocite and molybdenite (Figure 7.9b) – these were critically the ones that helped discriminate the Glen Lednock gold occurrence as a porphyry-derived one (see section 6.3). Worthy of notice is also that the non-metal inclusion assemblage of these two gold populations is almost coincident (e.g., section 6.2.4).

The alloy composition of the Invergeldie gold sample shows elements of commonality with that of both the Almond 3 and Glen Lednock gold samples. The gradient and overall Ag content exhibited by the Invergeldie silver profile appear to be closer to the Almond 1 - Almond 3 ones than the Glen Lednock and Keltie Burn ones (Figure 7.10a). The Monzie silver profile lies just in between these two categories, showing a gradient that is not too dissimilar from that of the Invergeldie profile. Unfortunately, the total abundance of inclusions detected in the relevant gold sample is below the minimum values to draw any signature-related conclusions, but the species identified would be compatible with both a 'Group 1' and 'Group 2' composition. However, the Cu profile of the Invergeldie placer gold (Figure 6.16 in section 6.2.4) indicates

relatively high Cu contents in the Invergeldie gold alloy - much closer to the ones recorded in the gold populations from the south of Loch Tay than the ones recorded in the Almond 1, Almond 2 and Almond 3 gold populations, which could suggest a higher temperature environment of gold formation (see section 2.3.1). The Ag content ranges in gold particles from the same sample, on the other hand, have also appeared higher than the ones detected in the Lednock, Keltie and Monzie gold alloys (Figure 7.10a).

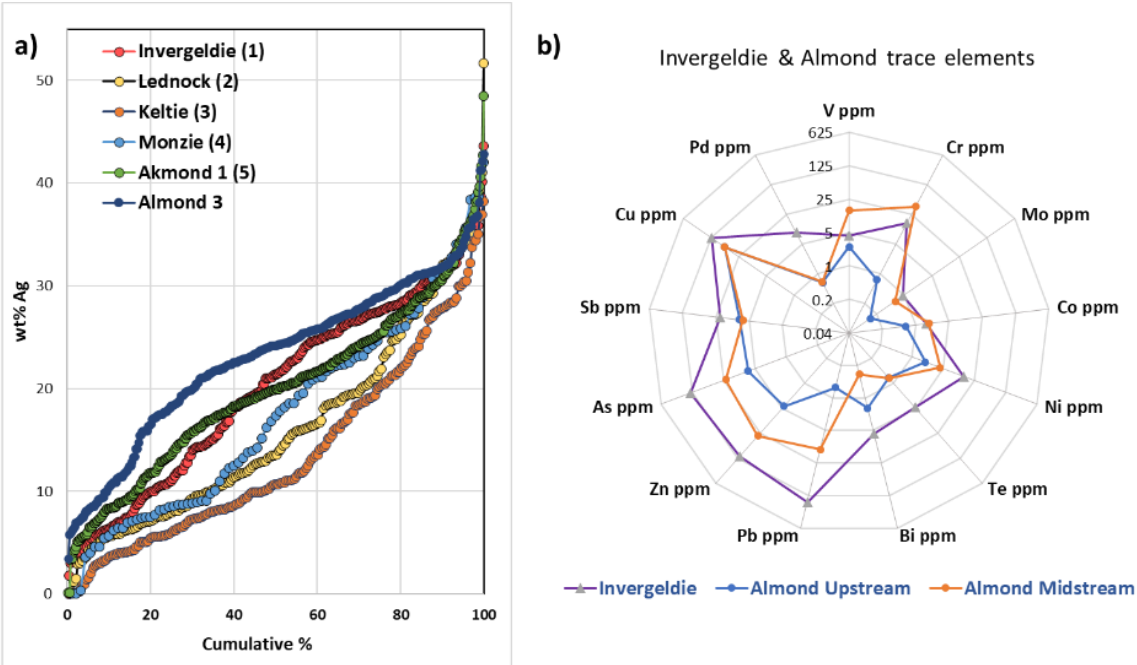

Figure 7.10 Graphical comparison of gold compositional data from the Invergeldie Burn and localities from both Group 1 and Group 2. a) Ag% vs cumulative plots; b) trace element (ppm) radar diagrams.

Figure 7.10a displays the Ag cumulative profiles for the gold populations from Loch Tay South, Almond 1 and Almond 3. In general, silver profiles are not considered first-order discriminants as they result from the combination of drainage geometry, erosion profile of the system and sampling spot (e.g., Chapman et al., 2023c; Figure 7.10a). Insightful information can be extracted by comparing the trace element composition (ppm) of the Invergeldie placer gold sample with that of placer gold samples from River Almond upstream and midstream (Figure 7.10b). It is important to keep in mind that the number of particles forming each of the samples (defined by locality) used for LA-ICP-MS investigations is, by far, lower than the number of particles effectively analysed with EPMA and SEM (analysis of the inclusions) for each population/locality. The trace element compositional profile of the Invergeldie gold has appeared almost congruent to the one descriptive of the elemental composition of the gold

from River Almond midstream, especially in relation to As, Zn, Cu, Ni and Cr relative abundances (ppm, Figure 7.10b).

The Invergeldie gold sample composition may be read as the product of an influx from a mineralised source not dissimilar to the one draining (i.e., influx) into the River Almond above the Almond 3 placer sample location – which, in addition, shows characteristics of the gold deriving from upstream in the drainage. The presence of chromium suggests, accordingly, the influence of mafic or possibly ultramafic lithological layers on the hydrothermal fluids precipitating the mineralisation. It is probable that the undiscovered sources are located somewhere between the two main watercourses (River Almond and Invergeldie Burn – see Figure 4.1), in locations suitable to feed the respective tributaries. The relatively high copper content in the Invergeldie gold alloy, however, along with some other (minor) compositional features would suggest another potential genetic source to be possibly located in a distal part of the porphyry hydrothermal system (transitional environment, LS epithermal not to be ruled out, e.g., Chapman et al. 2023b; Chapman et al., 2018) invoked to explain the origin of the Glen Lednock placer gold. Consequently, the Invergeldie placer population is interpreted to represent the contributions from these different types of sources. These may be either genetically unrelated or reflect multiple fluid stages during the evolution of a single mineralizing system (e.g., Chapman et al., 2023c). Since certain compositional features are not observed in the Almond 3 gold signature, it is likely that the influxes feeding into both drainages derived from two distinct systems.

7.2.4 Regional structural/tectonic context of the mineralisation

The previous sections of this chapter have laid out an overarching petrographic and compositional background to firmly investigate the nature and extent of gold mineralisation in the Loch Tay area. To undertake a satisfactory analysis of the relevant metallogenic processes, however, the outcomes and spatial implications from the above necessarily need to account for the potential role and effect of local fault geometries and scales (as well as lithologies) on the gold-bearing mineralisation. Faults and (more widely) shear zones are assumed to act as primary conduits for the transit of the hydrothermal fluids involved in the gold-bearing genetic processes, as anticipated in section 4.3. Consequently, when similarities are observed in the mineralogical (and, more importantly, metallic) assemblages of spatially distinct gold deposits, meaningful inferences can be drawn in relation to the potentially shared nature of the fluids associated with their formation and their subsequent transport by faults.

In this respect (and unluckily), the generally poor exposure of the outcrops in the Loch Tay area do not permit extensive data collection; the process turned out relatively easier in the Calliachar-Urlar Burn catchments and, consequently, the bulk of the structural data analysis of this work relied on the information gained around those localities (see Chapter 4). Nevertheless, the availability of some literature data pertaining to geologically and geographically close case studies (e.g., concerning metallogenic investigations within the Grampian Terrane of Scotland), as well as digital maps, has partly allowed new speculations to be made in the view of multi-scale tectonic features and their possible controls on the ore-bearing mineralisation.

The distribution of the gold mineralisation in the Loch Tay area tends to cluster around major and minor faults (see section 4.2); this could be, at least in part, an effect of the fact that such faults were mapped in origin, and subsequent exploration efforts focused on nearby, exposed areas. Therefore, there are not as many occurrences reported for areas with poor or no exposure. In some of these cases, parallel considerations of the possibly associated vein-hosted occurrences have been directly possible whereas, in other cases, a preliminary understanding of these could only be inferred by interpreting the gold compositional signatures locally (e.g., samples from the south of the Loch Tay area, see section 7.2.3). The Loch Tay and Highland Boundary Faults (LTF and HBF, respectively) represent the main tectonic features of the area (e.g., Chapters 3 and 4). Whie the HBF development and reactivations have been interpreted to span from Ordovician to Devonian times (e.g., Tanner, 2008), the formation of the LTF has been attributed to the transpressional phase of the Caledonian Orogeny; therefore, crosscutting the territory delimited by itself and the HBF. A preliminary model accounting for the genesis of the Calliachar-Urlar hydrothermal veins is suggested next, assuming that these are associated with areas of enhanced fluid circulation (either dilational jogs or, less likely, Riedel shears) generated by left-lateral movement along a major fault.

A potential model for the formation of the Calliachar-Urlar veins

Field investigations and previous literature (e.g., Ixer et al., 1997; Corkhill et al. 2010) consistently demonstrate that sulphide- and gold-bearing hydrothermal veins crosscut the Pitlochry Schists formation in the Southern Highland Group, and are typically hosted in extended fractures, consequently assumed to form part of a later, brittle event. This event is also here considered to be inclusive of all the joint/fracture arrays that show a similar orientation to that of the veins (~140˚) and are systematically distributed across the (Calliachar-Urlar) area to different degrees of intensity. Vein mineralisation partially occupies these discontinuities across specific sections of both catchments, not just in the form of sulphide/gold-bearing quartz as it

is particularly observed in lower Calliachar and upper Urlar Burn, but also in the more frequent form of barren quartz with no associated sulphide (nor gold) assemblages. These joints/fracture patterns can therefore realistically be interpreted to be long-lived and connected to the late stages of the main (Grampian) collisional event. The major tectonic feature is locally represented by the Urlar Fault, interpreted to be Devonian (420-390 Ma) by Ixer et al. (1997). Sulphide- and quartz-bearing veins were found outcropping across the Urlar Burn and, specifically, on the western side of the Urlar Fault.

Two possible scenarios have here been considered in light of the discussed paragenetic relationships between the local and Calliachar veins, regarding the V3 and the LSCL3 veins as continuous ramifications of the same hydrothermal event.

The first one sees the hydrothermal veining in the area (e.g., Figure 6.1) as occurring in dilational jogs or Riedel shears, coevally (or nearly) with the nucleation/development of the strike-slip Urlar Fault. Later sinistral re-activation of the Urlar Fault, along the NW direction, could have dissected some of the original vein segments/systems that would have in principle been continuous for >1.5 Km from W to E, displacing the Urlar veins (LS4, LSCL3) towards SW. Given that the Urlar Fault extends for less than 10 Km, a dislocation of the original vein segment - calculated by projecting the V3 vein strike to NW - nearly 1.5 Km towards SW, where LSCL3 was sampled, would seem to have required considerable fault displacement. However, the apparent separation of 1.5 km should not be interpreted as “true” displacement value. In dilational-jog and releasing-band settings, the visible offset is controlled by fault geometry and vein orientation, such that the true displacement may be significantly smaller than the apparent map separation (Woodcock and Fischer, 1986; Sibson, 1987). Worth noting is also that the latter sample was retrieved in the form of a float, and not as a bedrock-hosted vein; therefore, the actual outcrop host could be located at some distance (i.e., in the range of several tens of metres) from the sampling site.

The second scenario assumes that all sulphide-bearing hydrothermal veins in the area are either coeval or post-date (i.e., re-activation) the original movement along the Urlar Fault (occurring between 420-390 Ma) but, in this case, the V3 and the LSCL3 veins occur in localised dilational jogs/Riedel shears and are not assumed to be part of an original physical continuum.

A third scenario would consider the veining being pre-existent at the time of faulting and then dissected by activation of the Urlar Fault; in this case, it would be necessary to invoke the documented transpressional activity of the Loch Tay Fault (slightly older than the Urlar Fault – i.e. Scandian) as responsible for hydrothermal fluid channelling and the Calliachar-Urlar Veins

formation. This latter case would not be dissimilar to the hypothesis of Tanner (2014), who interpreted the Calliachar-Urlar vein mineralisation to have formed in a secondary stress field due to left-lateral movement on the Loch Tay Fault during Scandian times.

Based on analogous mechanisms, some of the other main Loch Tay veins (e.g., Glen Almond Vein; Coire Buidhe veins) can be interpreted to have formed in response to left-lateral slip of the Loch Tay Fault or localised minor NNE-SSW trending faults (i.e., section 4.3).

The internal quartz textures of the veins, as revealed by SEM-CL analysis, are compatible with the hypothesis of a long-lived system. The two earliest-formed and volumetrically dominant textures record features that may be suggestive of annealing processes during their evolution. Euhedral quartz crystals, which once formed at relatively steady pressures and temperatures, were subsequently texturally transformed into mottled, weakly zoned patterns outlining the original euhedral oscillatory zoning. The second quartz event is a result of fracturing and healing (Rusk, 2012) and could represent, at least partially, evidence of the barren quartz pulse(s). In fact, barren quartz typically appears weakly to non-luminescent when observed in SEM-CL (Baele et al., 2019); further to this, after microscopic and field observations, these textures consistently do not incorporate any obvious sulphide mineralisation.

If it is assumed that both the first and second quartz stages at Calliachar and Urlar Burn experienced post-formation textural modification (i.e., annealing, Rusk, 2012), one or more brittle event(s) would then be required to allow new in-fracture precipitation of the hydrothermal quartz (Q3 and Q4, in the paragenetic interpretation) associated with greater sulphide precipitation. This might be explained by accounting for a re-opening phase of the veins, synchronous to such hydrothermal fluid pulse(s); critically, this event would coincide with the ore-bearing stage, when sulphides (mostly pyrite, galena, chalcopyrite) and coarser gold mineralisation precipitated (i.e., see section 5.3.1). Although these considerations would potentially suit all three of the proposed scenarios of vein formation, enunciated earlier in this section, they appear to show greater consistency with the first two. In fact, the first two hypotheses assume that the Urlar Fault represents the main (local) conduit for hydrothermal fluid flow connected to the genesis of the Calliachar and Urlar Veins. These veins show mineralogical assemblages that differ slightly from those of the Coire Buidhe veins and that of the Almond Vein, both of which are more proximal to the regional-scale Loch Tay Fault. Moreover, lead isotope data have indicated model ages of 410 to 366 Ma in relation to the galena mineralisation hosted in the Calliachar and Urlar Veins; these ages appear to be closer to the presumed transtensional/brittle phase, taking place post-Scandian orogeny, rather than

to Scandian times with which the Loch Tay Fault transpressional phase (~420 Ma to 410 Ma; Strachan et al., 2002) is associated.

On a pure structural perspective, regardless of the mechanism(s) which determined the hydrothermal veining in the area, it is at present not possible to convincingly allocate the vein formation to either the N-S transpressional or E-W transtensional phase of the (Scandian) orogeny, or even to the transitional phase of into the other. In fact, while these two tectonic stages imply distinct configurations of the associated regional stress fields, the specific disposition of the stress tensors around the veins would be that of a localised extensional system in any case. The overall consistent (~NNW-SSE) strike orientations of the veins and the evidence that certain metallic assemblages are repeated in most of them (i.e., in the Calliachar-Urlar Burn, River Almond and Coire Buidhe) would however suggest a roughly simultaneous injection of genetically related fluids, dictated by regionally shared stress fields (e.g., section 7.2.1; Webb et al., 2024). This fluid event would have acted independently of the one responsible for the emplacement of the barren, roughly parallel, quartz veins observed to crosscut the area thoroughly (though especially within the Calliachar-Urlar Burn catchments). However - and as discussed in section 4.3.2 - both types of mineralisation (barren and metallic-bearing) were found within the same set(s) of 330˚-oriented joints; it is thence implied that the associated mineralising events were spread through a pre-existing, long-lived extensional (i.e., fractures; joints) system subject to intermittent activation and re-activation cycles. The veins likely developed in a tensile regime, being compatible with a regional N-NNW oriented σ1 and connected NE-ENE-striking sinistral sense of shear (e.g., Shaw et al. 2022), as well as with a vertical regional σ1.

With respect to the genetic commonalities exhibited by these mineralised systems, more considerations can be made by investigating the (previously discussed, see section 7.2.3.1) gold compositional variations between the Calliachar Burn, Glen Quaich and Glen Almond deposits. As anticipated, direct evidence of a minor NE-SW trending fault array would locally connect the Glen Quaich and Upper Calliachar Burn hydrothermal systems (Figure 7.11), and may justify the observed gold signature resemblance. This can be visually connected to a similarly oriented fault pattern across the northernmost part of the area. However, no direct evidence can be claimed to equally support a genetic linkage between the close Glen Quaich and Upper-Mid Glen Almond gold signatures.

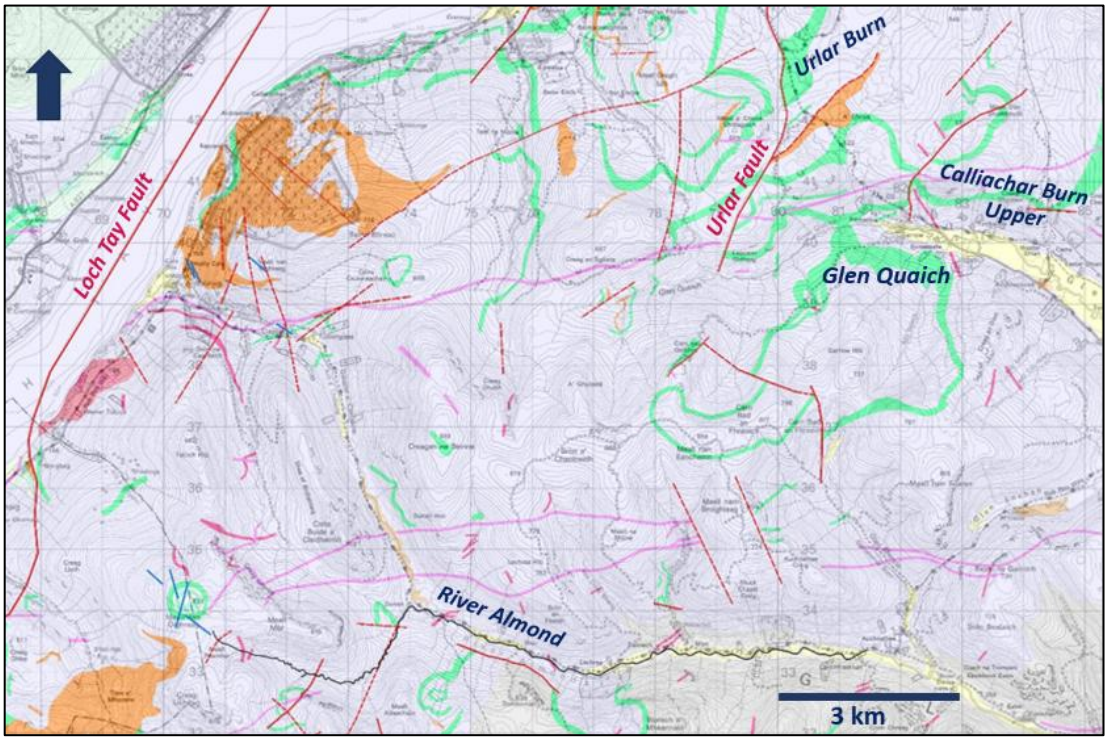

Figure 7.11. Faults (reported and interpreted) in the central region of the Loch Tay area. Modified from Digimap, Edina, 2021.

To complement the tectonic framework of the Loch Tay auriferous mineralisation, regional-scale comparisons should be made with the Cononish auriferous vein system, in the vicinity of the Tyndrum Fault (<50 Km W of the Loch Tay area). The structural mechanisms associated with the ore-bearing mineralisation were extensively investigated by Treagus (1999) who proposed a transtensional scenario to have induced the hydrothermal veining at Cononish. Their model particularly contemplated a WSW–ENE dilatant transtensional fault zone with components of left-lateral strike-slip and extension (e.g., in relation to the Eas Anie Vein and the Mother Vein formation), as opposed to Tanner's (2012 and 2014) view, favouring a roughly N-S-oriented transpressional scenario. Age data are available for the Cononish vein system as well as Rhynie in the Scottish Grampians (e.g., Treagus et al., 1999, Mark et al., 2011; Parry et al., 2011), which indicated a +/- 410 Ma age - and thus, at about the assumed Early Devonian transition from transpression to transtension - as time of their formation. These data are compatible with the hypotheses listed above with regards to the structurally-driven genesis of the Cononish mine system and, anyhow, imply that the respective vein formation took place more recently than the one proposed for the formation of the Cavanacaw (Shaw et al., 2022) and Curraghinalt (Tanner, 2014; Rice et al., 2016) deposits, respectively placed around Mid-Silurian and Mid-Late Ordovician times. The stress regime inferred to have determined the ore-bearing vein

development at Cavanacaw (in the Grampian Terrane; Shaw et al., 2022) does share some commonalities with the ones inferred for the veining processes at Cononish and in the Loch Tay area; for instance, sinistral transpressional shearing along ENE-striking structures was incorporated in the proposed model of progressive deformation.

Further to these considerations, the Cononish veins show certain mineralogical and geochemical features which are comparable to those of the Loch Tay veins, particularly an Au-Ag-Te association (e.g., Corkhill et al. 2010, Spence-Jones et al., 2018), and a Pb-Zn association specifically within the later paragenetic stages of the mineralisation (Spence-Jones et al, 2018). In the Loch Tay area, the latter components have been interpreted to take place late in the Glen Almond vein paragenetic history (Webb et al., 2024) and, to some extent, in the Calliachar-Urlar (e.g., Ixer et al., 1997) and the Lead Trial vein systems. Some authors (e.g., Treagus et al, 1999; Pattrick, 1984) attributed this specific Pb-Zn association to Carboniferous tectonic events. Additional implications of this evidence (late-stage galena) may be reflected in the regional contextualisation of the Pb-isotope data, which will be discussed in the following paragraph.

7.3 Regional synthesis

An effective metallogenic framework for the Loch Tay area is here presented to integrate the outcomes and implications of the gold compositional analysis, the vein paragenetic reconstructions and their tectonic and geological significance, in the view of defining potential genetically related and unrelated hydrothermal systems. This holistic discussion is undertaken on a "genetic type" rationale to distinguish and possibly characterise multiple gold deposit types/mineralisation styles being present in the region. The map in Figure 7.12 serves as support for this approach to highlight the spatial distribution (and possible relationships) of these deposits.

The northernmost and central portions of the Loch Tay area (e.g., Calliachar-Urlar Burn, Glen Quaich, Upper-Mid Almond River sampling localities) are characterised by the presence of both in-situ and allochthonous gold-bearing deposits with generally simple genetic signatures. A common Fe-Pb-Zn-Cu association (plus Co-Ni as subordinate components) has been deduced from the inclusion analysis of the placer gold particles sampled in all these drainages and, in large part, from the investigation of the mineral phases associated with the in-situ gold mineralisation (when hypogene-derived samples were available). This metallic association has appeared entirely compatible with the nature of the mineralogical assemblages in local

hydrothermal veins (i.e., Calliachar-Urlar veins, Glen Amond Vein), showing ubiquitous pyrite, chalcopyrite and galena as major components. The gold alloy of the populations from this sub-region features a large silver content range (10 to 40 wt%, e.g., Chapman et al., 2023c). Cu values almost always fall below the limit of quantification (e.g., Chapman et al., 2023) but, interestingly, unusually high Hg contents (up to 6-7 wt.%) were systematically detected in the gold alloy of some of these populations (e.g., particularly the Lower Calliachar Burn sites). The geological setting of all these auriferous occurrences does not feature any obvious evidence of potentially synchronous (Early-Devonian) intrusive bodies (e.g., Chapman et al., 2023c) and is essentially characterised by a metasedimentary substrate intersected by faults and dykes.

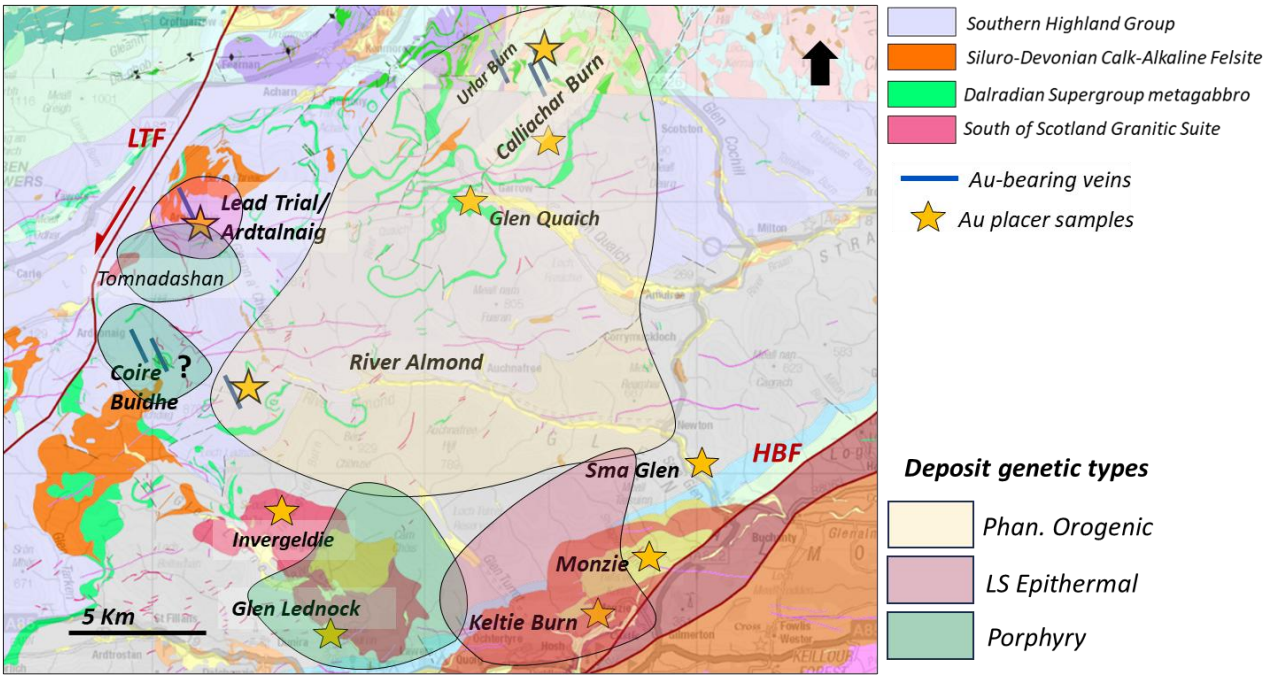

Figure 7.12. Schematic localisation and distribution of the genetic types of deposits identified in the Loch Tay area. The relative sizes of the polygons are indicative, and inclusive of the potential areas of ''influence'' of the relevant hydrothermal systems. Basemap from Digimap (BGS source), Edina (2022).

The compositional signatures of the samples and the entire context of the mineralisation indicate compatibility with genetic features typical of Phanerozoic orogenic gold deposits, which can be linked to both metamorphic and mantle-derived fluid sources (Goldfarb et al., 2015; Chapman et al., 2023b; Chapman et al., 2023c). The broadly similar composition of gold populations from Group 1 (Chapman et al., 2023c) can be attributed to congruous characteristics of the fluids responsible for gold precipitation. The generally subtle variations in the inclusion assemblages and alloy components between gold from different sampling sites

and even from different drainages can be a consequence of local lithological factors controlling the composition of the source fluid(s) and/or variability in the intrinsic fluid parameters (Gammons and Williams-Jones, 1995); the occasional Co-Ni association can be read as an effect of possibly mantle-derived fluid sources (Chapman et al. 2023c) and, in specific cases (e.g., Upper Calliachar), of local mafic/ultramafic lithologies. Furthermore, from the stable-isotope and fluid-inclusion work of previous authors (i.e., Smith, 1996) temperatures of c. 300-150° C and salinity ranges of 2-13 wt.% NaCl were estimated for the fluids circulating around Calliachar and Urlar Burn, suggesting both meteoric and magmatic inputs (e.g., Corkill et al., 2010).

The southernmost part of the Loch Tay area hosts gold mineralisation characterised by a diverse compositional signature. The placer populations from Glen Lednock and Keltie Burn have been interpreted as products of a porphyry-epithermal hydrothermal system (see 7.2.3.2 section for details; Chapman et al., 2023c) while the placer population from Sma Glen resulted from the combination of gold influxes from the Group 1 genetic environment (Phanerozoic-orogenic, see previous section) and an unknown, potential, in-situ source placed around the transitional domains of the Group 2 genetic environment (evolving porphyry-epithermal). Despite the lack of direct bedrock evidence, these deductions were strongly supported by the proximity of Early Devonian igneous bodies to the gold sampling localities and the validation of the proposed gold signatures against previously established templates (Chapman et al., 2018; Chapman et al., 2022). A high salinity (NaCl>35 wt.%) and high temperatures (>300ºC) were additionally inferred from fluid inclusion analyses conducted on rock samples from the Comrie pluton (Naden et al., 2010); these values are within the value ranges associated with porphyry mineralisation styles.

Consideration of the genetic signatures from these two main compositional groups had implications for the understanding of realistic hypogene mineralisation styles to be associated with the placer gold occurrences from nearby localities, such as Monzie Burn and Invergeldie Burn, whose compositional signatures would reflect elements from both orogenic and magmatic-related environments. Again, this result is entirely plausible due to the allochthonous nature of placer populations, not necessarily demanding immediate proximity of a related, univocal, in-situ source. However, the availability of a more robust dataset for the gold from Invergeldie (in terms of alloy and inclusion analyses) in comparison to the Monzie Burn one, has allowed more speculations to be made in relation to the location of possible hypogene sources (details in section 7.2.3.2). It is not unlikely that one of these sources sits on a distal zone of the porphyry hydrothermal system interpreted to have been present in the area (e.g., precipitating the Glen Lednock mineralisation). The lack of visible faults crosscutting the area, unfortunately, has impeded further hypotheses to be made.

The Lead Trial auriferous deposit is located within/around vein stockworks in the westernmost portion of the Loch Tay area, next to the homonymous major fault which defines the western boundary of the loch. Several hundreds of metres to the SE, the Ardtalnaig Burn crosses pelites and schists of the Pitlochry Formation. Gold from these locations exhibits a distinctive signature, showing notable variations depending on the nature of the samples and on whether these were recovered from the Lead Trial mine dump or in stream sediments from the Ardtalnaig Burn (see sections 7.2.2).

Beyond the gold compositional features and the ore-bearing vein petrography and paragenetic overview (Chapter 5), two other fundamental elements have been taken into sound consideration to interpret the nature of the hydrothermal system governing the ore-forming processes at this locality, namely the possible local action of brittle events (i.e., major and minor faults) and the potential proximity of a heat source to drive into the system. The rock samples extracted from the main auriferous vein incorporate fragments of the original host rock (schists and rhyolite) prior to the hydrothermal fluid injections, chaotically embedded in the hydrothermal quartz matrix. The absence of an observed spatial continuity between these lithoclasts and the parent host rock, in the quartz matrix, suggests that the fragments were transported and reworked during hydrothermal brecciation, after in-situ fracturing. Such textures are characteristic of hydrothermal breccia systems (e.g., Jebrak, 1997) and could indicate fluid ascent through a magmatic-related conduit or stockwork system (Sillitoe, 1985). Because widespread rhyolite fragments partially form these chaotic aggregates, it appears unlikely that such igneous lithologies represent the source of heat at the core of the hypothetic system; in fact, minor veins and veinlets - of presumably similar hydrothermal origin - are observed to extensively crosscut rhyolite host rock, more widely in the area. The main gold-bearing vein from which samples were derived is hosted in a ~170˚striking, sub-vertical local fault (and the whole vein system is close to the regional-scale Loch Tay Fault).

Further to all these features, evidence of intense faulting and fracturing processes at the Lead Trial could be deduced from direct field investigations (see Chapter 4) and company (i.e., Green Glen Minerals) reports. Most of these faults would have been very steep and roughly N-S (NNW-SSE to NNE-SSW) oriented, conforming to the potential effect of dilational mechanisms triggering fault breccia textures (e.g., Micklethwaite, 2009; Jebrak, 1997). The primary hydrothermal fluids could have been supplied by means of former movements along the major Loch Tay Fault and subsequently injected into these minor, sub-vertical and subsidiary faults. Pressure build-up from ascending, secondary (magmatic-related) fluids would have overcome the yield strength of the wall-rock and eventually fractured it in stockwork patterns and breccia

clasts. Ore-bearing fluids could have subsequently propagated along these fractures, precipitating quartz and metalliferous minerals at transient P–T conditions, in the manner of a hydrofracturing structural style (e.g., Frelinger et al., 2015). Hydrothermal breccia textures were observed throughout the vein outcrops and may be informative with regard to the driving structural and chemical mechanisms at different depths. However, their quantitative analysis was beyond the scope of this work.

Thin sections from samples 2864, LS1 and RX30781 host a range of quartz textures that, combined with the evidence of the bimodal (later stage Ag-rich) alloy distribution in the gold particles from crushed-ore material, would suggest derivation from a low-sulphidation epithermal system and subsequent cooling conditions at relatively shallow depths (< 1 Km). Other thin sections (e.g., from LSTD, 2886 samples) show less obvious features to allow reconciliation to the same exact mineralisation style, but which would however be compatible with it. It is here additionally argued that these samples incorporate physical and compositional proxies of a different evolutionary stage of the same hydrothermal system, possibly at deeper crustal levels, represented by sporadic molybdenite found in one of the samples and quartz dissolution textures in almost all of them. Quartz from epithermal systems generally displays colloform textures, euhedral sector-zoned crystals and more rarely dissolution textures (e.g., Frelinger et al. 2015; see Chapter 5); the latter, together with healed microfractures, are more typical of porphyry-related quartz (Rusk, 2012). The possible relationship with a porphyry-style (or high-T) mineralisation, not geographically far from the Lead Trial/Ardtalnaig localities, would be supported by the occurrence of molybdenite and chalcopyrite inclusions in the placer gold from Ardtalnaig, showing generally lower silver contents in the particle alloy (albeit comparable with the ones at the Lead Trial). A relatively small, Mo-bearing porphyry hydrothermal system hosted in granodiorites is reported at the Tomnadashan locality (Pattrick 1984; Corkhill et al., 2010), several kilometres from the Lead Trial outcrops. The gold composition at Tomnadashan was investigated by Webb (2024) and has appeared consistent with the hypothesis of gold derivation from a vertically zoned porphyry-epithermal system. It is inferred that the occurrences from the Lead Trial represent the most surficial, LS epithermal expression, and the occurrences from Tomnadashan represent the deepest expression of the evolving hydrothermal system. Fluid inclusion studies were also conducted on some Tomnadashan rock samples (Naden et al., 2010) and indicated high temperatures and salinities (>300ºC and NaCl>35 wt.%, respectively).

No actual diagnostic information has been obtained, in the course of this work, for the Coire Buidhe vein system, hosted in meta-limestone located c. 4 km SE to the Lead Trial deposit. Some

authors related the relevant auriferous mineralisation to felsic magmatism and a potential porphyry hydrothermal style (e.g., Pattrick, 1984), because of the observed Cu-Mo-As-Bi mineral association and the geographic location of the deposit (i.e., not distant from Tomnadashan). This explanation would not be in contrast with the petrographic and structural insights from this work (see Chapter 5); it would also critically align with the genetic position of this system in the whole Loch Tay context (Figure 7.12). However, an orogenic origin cannot be ruled out either.

The available Pb-isotope data were obtained by analysing samples of galena from several of the deposits discussed in this section (see 5.4), except River Almond and the Southern Loch Tay area localities (e.g., Glen Lednock, Keltie Burn, Invergeldie Burn). These results were mostly evaluated in light of previous work conducted around the investigation of Phanerozoic orogenic deposits (e.g., Mortensen et al., 2022; Godwin et al., 1988). The Pb isotope ratios can be used to discriminate multiple ore-bearing deposits in terms of composition and age, by exploiting the genetic information inherited from the relevant source of lead (e.g., Huston & Champion, 2023). The trend described by the $^{206}Pb/^{204}Pb$ against $^{207}Pb/^{204}Pb$ ratios calculated for the Loch Tay samples would fall within the "mantle" source field (e.g., Figure 7.13b; Torvela et al, 2022 and references therein). These values perfectly align with the $^{206}Pb/^{204}Pb$ and $^{207}Pb/^{204}Pb$ range ascribed to sulphide samples from the Grampian Terrane (Standish et. al, 2022) and with the range reported by Standish et al (2014) to define the less radiogenic NWT group (Figure 7.13a) based on a geographic origin of the crustal reservoirs of the Irish mineral deposits.

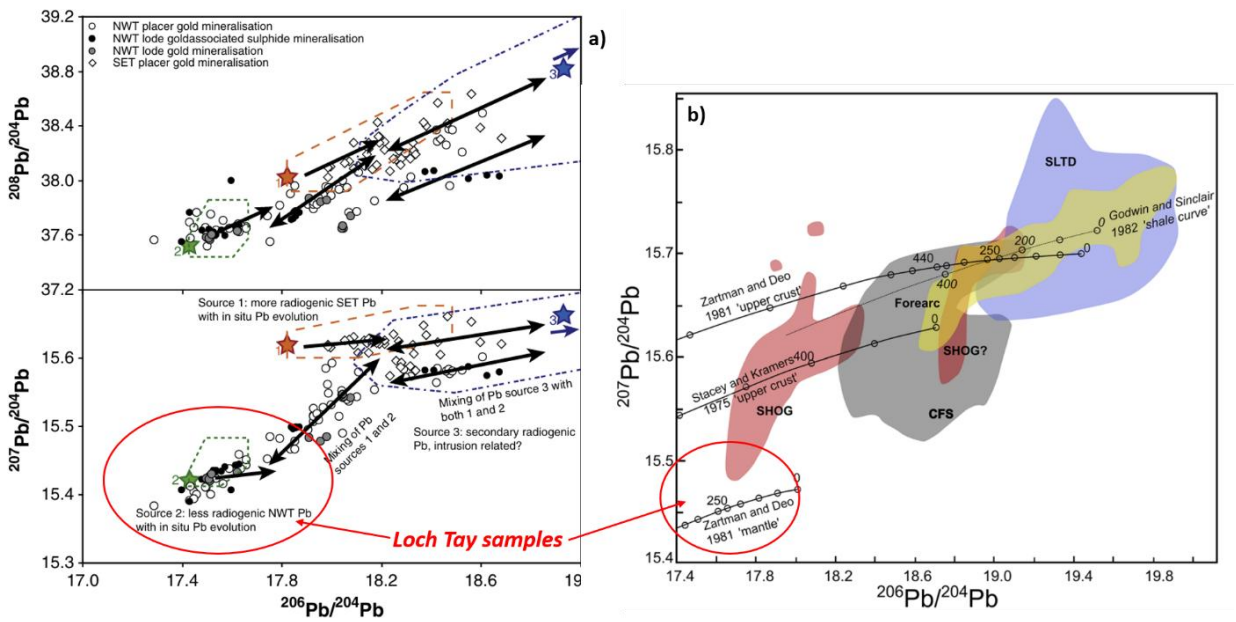

Figure 7.13 Projection of the $^{207}Pb/^{204}Pb$ and $^{206}Pb/^{204}Pb$ ratios calculated for the Loch Tay samples on graphical databases (modified after Standish et al., 2014 (a) and Torvela et al., 2022 (b; references therein), respectively.

The calculated model ages are always characterised by a minimum margin of uncertainty (Yuan et al., 2016). It is however apparent that the ~498 Ma age obtained for the Lead Trial galena mineralisation (see Table 5.7) diverges substantially from the ages obtained for the rest of the Loch Tay samples (ranging from ~328 to ~410). This result would fit the hypothesis that the Lead Trial ore-bearing mineralisation is sourced from genetically distinct hydrothermal fluids. Thence, if it is assumed that the Lead Trial deposit is the shallower expression of the porphyry-related hydrothermal system, interpreted to take place near Tomandashan, this system as a whole would be geologically older than the rest of the auriferous hydrothermal systems in the Loch Tay area (for which Pb data were available) attributed to a more likely orogenic origin. Alternatively, the relatively younger model ages calculated for the rest of the galena samples (i.e., from Calliachar-Urlar Burn and Coire Buidhe, see section 5.4) could be explained by invoking some genetic or tectonic processes bringing in later galena mineralisation (e.g., Carboniferous brines, Treagus, 1999 – see section 7.2.4), fluid mixing (Webb et al., 2025), and accounting for the possible uncertainty ranges of the ages. Calculated model ages for these types of deposits usually show a scattered behaviour, due to the mixing of lead from multiple sources and/or its contribution (variable isotopic ratios) from different host rocks during mineralisation (Mortensen et al., 2022).

Chapter 8.

Conclusions and Future work

To investigate the metallogenic controls on gold mineralisation in the Loch Tay area of Central Scotland, this study has primarily resolved compositional signatures for multiple gold-bearing occurrences alongside the textural and mineralogical analysis of paragenetic stages in nearby hydrothermal veins. An evaluation of their mutual similarities and variations enabled their allocation to distinct deposit types. To sum up:

- The vein paragenetic analysis revealed the occurrence of multiple fluid events and possibly shared fluid sources for up to three vein systems in the Loch Tay area. At least two separate gold mineralising stages have been identified in the vein paragenetic histories at Calliachar Burn and River Almond, which are only partially reflected in the placer gold alloy. An evolving hydrothermal fluid system, responsible for gold precipitation, internal compositional fluctuations, and textural variations has been interpreted to have taken place at the Lead Trial vein system.

- The later auriferous stages were evidenced by higher Ag contents in gold alloys which, in the case of the mineralisation at the Lead Trial, have been associated with fluid cooling in shallower portions of the hydrothermal system. In the Calliachar Burn and Glen Almond vein systems, the later (coarser) Ag-rich gold inputs occur within distinct fluid episodes with respect to the former gold inputs.

- The inclusion suites in detrital gold samples correlate with vein mineralogy and have helped refine the gold paragenetic stages. Placer gold can be used to underpin the associated mineralisation styles on a broader scale. A genetic mineralogical linkage may be drawn between the Calliachar Burn and River Almond gold-bearing systems, which have been linked to an orogenic mineralisation style having experienced a mantle input. The Lead Trial and Coire Buidhe deposits have been interpreted to form part of the same porphyry-epithermal system, where mineralisation at the Lead Trial represents the shallower, low-sulphidation expression and mineralisation at Coire Buidhe represents a deeper, higher-temperature portion of the system. Gold mineralisation in the southernmost part of the Loch Tay area has been associated with a multi-stage

magmatic-related environment of formation – porphyry-related at Glen Lednock and low-sulphidation epithermal at Keltie Burn; the composition of the gold from the Invergeldie Burn has shown features of both orogenic and magmatic-related environments (high-temperature, due to the relatively high Cu content in the respective alloy).

- Based on the gold compositional analysis and regional comparison, new potential undiscovered sources for gold mineralisation may occur (at least) near Upper Calliachar Burn and Sma Glen.
- At least part of the gold-bearing mineralisation across the Loch Tay area of Central Scotland (e.g., at Calliachar-Urlar Burn and River Amond) is hosted in a long-lived brittle system, which experienced cyclic fluid injections responsible for a (post-Scandian) hydrothermal vein emplacement. The vein-hosted mineralisation at the Lead Trial forms part of a tectonically distinct episode, probably related to earlier hydrothermal fluids sourcing through the Loch Tay Fault, as suggested by Pb isotope model ages. A possible association with older (pre-orogenic) magmatic intrusions has also been accounted for.

In light of these outcomes, opportunities to determine more quantitatively the genesis and nature of the mineralising systems in the Loch Tay area remain open.

Future work may include:

- LA-ICP-MS analyses on the pyrite mineralisation hosting gold in the form of inclusions (i.e., from Calliachar Burn and River Almond), to quantify the elemental composition of pyrite and possibly estimate whether coupled dissolution-reprecipitation processes (e.g., Hastie et al., 2020) occurred - e.g., As-rich pyrite, gold reprecipitation (and coarsening)?
- Fluid inclusion studies on hydrothermal quartz, to determine the ranges of temperature formation/stability of the hydrothermal fluids;
- Trace elements analysis by LA-ICP-MS on hydrothermal quartz, to determine elemental concentrations and distributions, and to be combined with the respective cathodoluminescence response(s), to possibly firm down the nature of the hydrothermal fluids.
- LA-ICP-MS analysis on gold particles from targeted populations in the Loch Tay area, to enhance the resolution of previous interpretations; specifically, on hypogene-derived

gold from some of the localities for which analyses were already performed on placer populations (e.g., Almond Vein; gossan-derived samples from Calliachar Burn).

References

Adams S. F. 1920. A microscopic study of vein quartz: Economic Geology, v. 15, p. 623–664.

Agee, C. B. and Walker, D. 1988. Mass balance and phase density constraints on early differentiation of chondritic mantle. Earth and Planetary Science Letters, 90(2), pp.144-156.

Aherne, S., Reynolds, N. A. & Burke, D. J. 1992. Gold mineralization in the Silurian and Ordovician of South Mayo. In The Irish Minerals Industry 1980–1990 (eds A. Bowden, G. Earls, P. G. O'Connor and J. F. Pyne), pp. 39–49. Irish Association for Economic Geology).

Ahmed, A., Arai, S. and Ikenne, M. 2009. Mineralogy and Paragenesis of the Co-Ni Arsenide Ores of Bou Azzer, Anti-Atlas, Morocco. Economic Geology, 104, 249–266, https://doi.org/10.2113/gsecongeo.104.2.249

Albarède, F., Desaulty, A.M. and Blichert-Toft, J. 2012. A geological perspective on the use of Pb isotopes in Archaeometry, 54(5), pp.853-867.

Allan, M., Meier, D. & Guillong, M. 2008. Sills (Version 1.1.0) [Computer software]. Zürich: Die Eidgenössische Technische Hochschule Zürich and University of Leeds. Available at: https://mineralsystems.ethz.ch/software/sills.html (Accessed: 30 November 2025).

Allan, M. M., Mortensen, J. K., Hart, C. J. R., Bailey, L., Sanchez, M. G., Ciolkiewicz, W. & Creaser, R. A. 2013. Magmatic and Metallogenic Framework of West-Central Yukon and Eastern Alaska. Society of Economic Geology Special Publication 111-168.

Allibone A., Blakemore H., Gane J., Moore J., MacKenzie D., Craw D. 2018; Contrasting Structural Styles of Orogenic Gold Deposits, Reefton Goldfield, New Zealand. *Economic Geology*; 113 (7): 1479–1497. doi: https://doi.org/10.5382/econgeo.2018.4599

Allmendinger, R.W., 2022. *Stereonet 11* [software]. Version 11. Available at: https://www.rickallmendinger.net/stereonet [Accessed 23 December 2025].

Andersen, M. B., Elliott, T., Freymuth, H., Sims, K.W. W., Niu, Y. and Kelley, K.A. 2015. The terrestrial uranium isotope cycle. Nature, 517(7534), pp.356-359.

Antweiler, J. & Sutton J., A. 1970. Spectrochemical analyses of native gold samples. US Geological Survey Report USGS-GD-70-003. Commerce National Technical Information Service. Springfield. Va.; US Geological Survey.; US Dept.

Antweiler, J. C. and Campbell, W. L., 1977. Application of gold compositional analyses to mineral exploration in the United States. In *Developments in Economic Geology* (Vol. 9, pp. 17-29). Elsevier.

Arif J, Baker T. 2004. Gold paragenesis and chemistry at Batu Hijau, Indonesia: implications for gold-rich porphyry copper deposits. Mineral Deposita 39:523–535

Armstrong K. 2021. Characterisation Of Gold Mineralisation In The Lead Trial Prospect. Unpublished MSc thesis, University of Exeter.

Atherton M. P., Ghani A. A. 2002. Slab breakoff: a model for Caledonian, Late Granite syn-collisional magmatism in the orthotectonic (metamorphic) zone of Scotland and Donegal, Ireland. *Lithos* 62:65–85

Badenszki, E., Daly, J.S., Flowerdew, M.J., & Whitehouse, M.J., 2019. Age and origin of deep crustal meta-igneous xenoliths from the Scottish Midland Valley: Vestiges of an Early Palaeozoic arc and 'Newer Granite' magmatism. Journal of Petrology, 60(8), pp.1543–1574. https://doi.org/10.1093/petrology/egz039

Baele, J. M., Decrée, S. and Rusk, B., 2019. Cathodoluminescence applied to ore geology and exploration. *Ore deposits: Origin, exploration, and exploitation*, pp.131-161. https://doi.org/10.1002/9781119290544.ch6

Baker T. 2002. Emplacement depth and CO2-rich fluid inclusions in intrusion-related gold deposits. Economic Geology , 97, 1109–1115, https://doi.org/10.2113/gsecongeo.97.5.1111

Banks, D. A.; Chapman, R.J.; Spence-Jones, C. 2018. Detrital Gold as a Deposit-Specific Indicator Mineral by LAICP-MS Analysis. Geoscience BC: Vancouver, BC, Canada; Report 2018-21. Bao, Z., Li, Q. and Wang, C.Y. 2017. Metal source of giant Huize Zn-Pb deposit in SW China: New constraints from in situ Pb isotopic compositions of galena. Ore Geology Reviews, 91, pp.824-836.

Barker, S. L. L., Cox, S.F., Eggins, S.M., Gagan, M.K., 2006. Microchemical evidence for episodic growth of antitaxial veins during fracture-controlled fluid flow. Earth and Planetary Science Letters 250, 331-344

Barrett, T. J. and Anderson, G.M. 1988. The solubility of sphalerite and galena in 1–5 m NaCl solutions to 300° C. Geochimica Cosmochimica Acta, 52, 813–820, https://doi.org/10.1016/0016-7037(88)90353-5

Bateman, R., Hagemann, S. 2004. Gold mineralisation throughout about 45 Ma of Archaean orogenesis: protracted flux of gold in the Golden Mile, Yilgarn craton, Western Australia. *Miner Deposita* 39, 536–559 (2004). https://doi.org/10.1007/s00126-004-0431-2

Benning, L. & Seward, T. 1994. Hydrosulphide complexes of gold (I) at high pressures and temperatures: equilibrium and kinetic problems. Mineral. Mag. A, 58, 75-76.

Berkley College of Natural Resources, 2023. [Online]. [Accessed 13 January 2014] Available from: https://nature.berkeley.edu/classes/eps2/wisc/gold.html

Bierlein F. P., Groves D. I., Cawood P. A. 2009. Metallogeny of accretionary orogens — The connection between lithospheric processes and metal endowment. Ore Geology Reviews Vol. 36, Issue 4, 2009, Pages 282-292

Blitchert-Toft, J., Delile, H., Lee, C.T., Stos-Gale, Z., Billström, K., Andersen, T., Hannu, H. and Albarède, F. 2016. Large-scale tectonic cycles in Europe revealed by distinct P b isotope provinces. Geochemistry, Geophysics, Geosystems, 17(10), pp.3854-3864.

Blake, S. and Jones, K. .2003. *Mountain building in Scotland*. Milton Keynes: Open University.

Bluck B. J. 1984 Pre-Carboniferous history of the Midland Valley of Scotland. *Transactions of the Royal Society of Edinburgh: Earth Sciences*. 1984;75(2):275-295. doi:10.1017/S0263593300013900

Bons, P. D., 2000. The formation of veins and their microstructures. In: Jessell, M.W., Urai, J.L. (Eds.), Stress, Strain and Structure, A Volume in Honour of W D Means. Journal of the Virtual Explorer (online).

Bons, P. D., 2001a. The formation of large quartz veins by rapid ascent of fluids in mobile hydrofractures. *Tectonophysics*, *336*(1-4), pp.1-17.

Bons, P. D., 2001b. Development of crystal morphology during unitaxial growth in a progressively widening vein: I. The numerical model. Journal of Structural Geology 23, 865-872.

Bons, P. D., Jessell, M.W., 1997. Experimental simulation of the formation of fibrous veins by localised dissolution e precipitation creep. Mineralogical Magazine 61, 53-63.

Bons, P. D., Montenari, M., Bakker, R. J. and Elburg, M. A., 2009. Potential evidence of fossilised Neoproterozoic deep life: SEM observations on calcite veins from Oppaminda Creek, Arkaroola, South Australia. *International Journal of Earth Sciences*, *98*(2), pp.327-343.

Bons, P. D., Elburg M.A., Gomez-Rivas E., 2012. A review of the formation of tectonic veins and their microstructures. Journal of Structural Geology 43, 33-62.

Boulter, C. A., Fotios, M.G., Phillips, G.N., 1987. The Golden Mile, Kalgoorlie: a giant gold deposit localized in ductile shear zones by structurally induced infiltration of auriferous metamorphic fluids. Economic Geology 82, 1661e1678.

Boyle, R. W. 1979. The geochemistry of gold and its deposits: together with a chapter on geochemical prospecting for the element, Geological Survey of Canada Ottawa.

Bozkaya G., Banks D., 2015. The importance of supersaturated silica deposition for base-metal Au-Ag mineralisation in western Turkey. *Turkish Journal of Earth Sciences 24* (2): 99-110. https://doi.org/10.3906/yer-1405-10

Browning, P., Groves, D.I., Blockley, J.G. and Rosman, K.J.R. 1987. Lead isotope constraints on the age and source of gold mineralization in the Archean Yilgarn Block, Western Australia. Economic Geology, 82(4), pp.971-986.

Burke, M., Hart, C. J. R. & Lewis, L. L. 2005. Models for epigenetic gold exploration in the northern Cordilleran Orogen, Yukon, Canada. In: MAO, J. & BIERLEIN, F. P. (eds.) Mineral Deposit Research: Meeting the Global Challenge: Proceedings of the Eighth Biennial SGA Meeting Beijing, China, 18–21 August 2005. Berlin, Heidelberg: Springer Berlin Heidelberg.

Byerlee, J., 1978. Friction of Rocks. Pageoph, Vol. 116, Birkhauser Verlag.

Cannon, R.S., Pierce, A.P., Antweiler, J.C. and Buck, K.L. 1961. The data of lead isotope geology related to problems of ore genesis. Economic Geology, 56(1), pp.1-38.

Carr, G.R., Dean, J.A., Suppel, D.W. and Heithersay, P.S. 1995. Precise lead isotope fingerprinting of hydrothermal activity associated with Ordovician to Carboniferous metallogenic events in the Lachlan fold belt of New South Wales. Economic Geology, 90(6), pp.1467-1505.

Carranza, E. Geochemical characteristics of mineral deposits: implications for ore genesis. 2012. Geochemistry: Exploration, Environment, Analysis, 12(2), pp.89-92.

Cawood, P. A. & Hawkesworth, C. J. 2014. Earth's middle age. Geology, 42, 503-506.

Chapman, R. J., Leake, R. & Moles, N. 2000a. The use of microchemical analysis of alluvial gold grains in mineral exploration: experiences in Britain and Ireland. Journal of Geochemical Exploration, 71, 241-268.

Chapman, R. J., Leake, R. C., Moles, N. R., Earls, G., Cooper, C., Harrington, K. & Berzins, R. 2000b. The Application of Microchemical Analysis of Alluvial Gold Grains to the Understanding of Complex Local and Regional Gold Mineralization: A Case Study in the Irish and Scottish Caledonides. Economic Geology, 95, 1753-1773.

Chapman, R.J., Shaw, M.H., Leake, R.C. and Jackson, B., 2005. Gold mineralisation in the central Ochil Hills, Perthshire, UK. *Applied Earth Science*, *114*(1), pp.53-64.

Chapman, R.J. and Mortensen, J.K., 2006. Application of microchemical characterization of placer gold grains to exploration for epithermal gold mineralization in regions of poor exposure. *Journal of Geochemical Exploration*, *91*(1-3), pp.1-26

Chapman, R. J., Leake, R. C., Bond, D. P. G., Stedra, V. & Fairgrieve, B. 2009. Chemical and Mineralogical Signatures of Gold Formed in Oxidizing Chloride Hydrothermal Systems and their Significance within Populations of Placer Gold Grains Collected during Reconnaissance. Economic Geology, 104, 563-585.

Chapman, R. J., Mortensen, J. K., Crawford, E. C. & Lebarge, W. 2010a. Microchemical Studies of Placer and Lode Gold in the Klondike District, Yukon, Canada: 1. Evidence for a Small, Gold-Rich, Orogenic Hydrothermal System in the Bonanza and Eldorado Creek Area. Economic Geology, 105, 1369-1392.

Chapman, R. J., Mortensen, J. K., Crawford, E. C. & Lebarge, W. P. 2010b. Microchemical Studies of Placer and Lode Gold in the Klondike District, Yukon, Canada: 2. Constraints on the Nature and Location of Regional Lode Sources. Economic Geology, 105, 1393-1410.

Chapman, R. J., Mortensen, J. K. & Lebarge, W. P. 2011. Styles of lode gold mineralization contributing to the placers of the Indian River and Black Hills Creek, Yukon Territory, Canada as deduced from microchemical characterization of placer gold grains. Mineralium Deposita, 46, 881-903.

Chapman, R. J. & Mortensen, J. K. 2016. Characterization of Gold Mineralization in the Northern Cariboo Gold District, British Columbia, Canada, Through Integration of Compositional Studies of Lode and Detrital Gold with Historical Placer Production: A Template for Evaluation of Orogenic Gold Districts. Economic Geology, 111, 1321-1345.

Chapman, R. J., Cook, M., Grimshaw, M. & Myles, S. 2016. Placer-lode gold relationships in the Nansen placer district, Yukon. Yukon Exploration and Geology, 63-78.

Chapman, R. J., Mileham, T., Allan, M. & Mortensen, J. 2017. A distinctive Pd-Hg signature in detrital gold derived from alkalic Cu-Au porphyry systems. Ore Geology Reviews, 83, 84-102.

Chapman, R.J.; Allan, M.M.; Mortensen, J.K.; Wrighton, T.M.; Grimshaw, M.R., 2018. A new indicator mineral methodology based on a generic Bi-Pb-Te-S mineral inclusion signature in detrital gold from porphyry and low/intermediate sulfidation epithermal environments in Yukon Territory, Canada, *Mineralium Deposita*, 53, pp.815-834.

Chapman, R.J.; Banks, D.A.; Styles, M.T.; Walshaw, R.D.; Piazolo, S.; Morgan, D.J.; Grimshaw, M.R.; Spence-Jones, C.P.; Matthews, T.J.; Borovinskaya, O. 2021. Chemical and physical heterogeneity within native gold: implications for the design of gold particle studies. *Miner Deposita* 56, 1563–1588 https://doi.org/10.1007/s00126-020-01036-x

Chapman, R.J., Craw, D., Moles, N.R., Banks, D.A. and Grimshaw, M.R., 2023a. Evaluation of the contributions of gold derived from hypogene, supergene and surficial processes in the formation of placer gold deposits. Recent Advances in Understanding Gold Deposits: from Orogeny to Alluvium. Geological Society, London, Special Publications 516, https://doi.org/10.1144/SP516-2020-260

Chapman, R. J., Moles, N.R., Bluemel, B. and Walshaw, R.D., 2023b. Detrital gold as an indicator mineral. Recent Advances in Understanding Gold Deposits: from Orogeny to Alluvium. Geological Society, London, Special Publications, Volume 516, pp. 291–312. https://doi.org/10.1144/SP516-2021-47

Chapman R. J., Torvela T.M., Savastano L. 2023c. Insights into Regional Metallogeny from Detailed Compositional Studies of Alluvial Gold: An Example from the Loch Tay Area, Central Scotland. Minerals 2023, 13, 140. https://doi.org/10.3390/min13020140

Chapman, R. J., Mortensen, J.K., Murphy, R. 2023d. Compositional Signatures of Gold from Different Deposit Types in British Columbia, Canada. Minerals 2023, 13, 1072. https://doi.org/10.3390/min13081072

Chew, D. M., Flowerdew, M. J., Page, L. M., Crowley, Q. G., Daly, J. S., Cooper, M. and Whitehouse, M. J., 2008. The tectonothermal evolution and provenance of the Tyrone Central Inlier, Ireland: Grampian imbrication of an outboard Laurentian microcontinent?. *Journal of the Geological Society*, *165*(3), pp.675-685.

Chew, D. M. and Strachan, R.A. de2013. The Laurentian Caledonides of Scotland and Ireland. Geological Society, London, Special Publications, 390, 45–91, https://doi.org/ 10.1144/SP390.16

Chouinard, A., Paquette, J. and Williams-Jones, A.E., 2005. Crystallographic controls on trace-element incorporation in auriferous pyrite from the Pascua epithermal high-sulfidation deposit, Chile–Argentina. *The Canadian Mineralogist*, *43*(3), pp.951-963.

Clayburn, J., Harmon, R., Pankhurst, R. *et al.* 1983. Sr, O, and Pb isotope evidence for origin and evolution of Etive Igneous Complex, Scotland. *Nature* 303, 492–497 (1983). https://doi.org/10.1038/303492a0

Cline J. S., Hofstra A. H., Muntean J. L., Tosdal R.M. and Hickey K.A. 2005. Carlin-type gold deposits in Nevada: critical geologic characteristics and viable models. Economic Geology, 100th Anniversary Volume, 451–484, https://doi.org/10.5382/AV100.15

Cook, N.J., Ciobanu, C.L., Meria, D., Silcock, D. and Wade, B., 2013. Arsenopyrite-pyrite association in an orogenic gold ore: Tracing mineralization history from textures and trace elements. *Economic Geology*, *108*(6), pp.1273-1283.

Connolly, J. 1997. Devolatilization-generated fluid pressure and deformation- propagated fluid flow during prograde regional metamorphism. Journal of Geophysical Research: Solid Earth (1978–2012), 102, 18149-18173.

Corfu F., Gasser D., Chew D. M. 2014. New perspectives on the Caledonides of Scandinavia and related areas: introduction. Geological Society, London, Special Publications. Vol. 390 Pages 1 – 8. https://doi.org/10.1144/SP390.28

Corkhill C., Ixer R. A. F., Mason J. S., Irving D. & Pattrick, R. A. D. 2010. Polymetallic auriferous vein mineralization near Loch Tay, Perthshire, Scotland. Scottish Journal of Geology 46, 23–30.

Corti, C.W., Holliday, R.J. Commercial aspects of gold applications: From materials science to chemical science. Gold Bull 37, 20–26 (2004). https://doi.org/10.1007/BF03215513

Cox, S.F., 1987. Antitaxial crack-seal vein microstructures and their relationship to displacement paths. Journal of Structural Geology 9, 779±787.

Cox, S. F. 2005. Coupling between Deformation, Fluid Pressures, and Fluid Flow in Ore-Producing Hydrothermal Systems at Depth in the Crust. Economic Geology, 100th Anniversary Volume, 30-75.

Cox, S.F. 2010. The application of failure mode diagrams for exploring the roles of fluid pressure and stress states in controlling styles of fracture-controlled permeability enhancement in faults and shear zones. Geofluids, 10: 217-233. https://doi.org/10.1111/j.1468-8123.2010.00281.x

Cox, S.F., Etheridge, M.A., 1983. Crack-seal fibre growth mechanisms and their significance in the development of oriented layer silicate microstructures. Tectonophysics 92, 147-170.

Cox, S.F., Knackstedt, M.A., Braun, J., 2001. Principles of structural control on permeability and fluid flow in hydrothermal systems: Reviews in Economic Geology, v. 14, p. 1–24.

Cox, S., Wall, V., Etheridge, M. & Potter, T. 1991. Deformational and metamorphic processes in the formation of mesothermal vein-hosted gold deposits—examples from the Lachlan Fold Belt in central Victoria, Australia. Ore Geology Reviews, 6, 391-423.

Coward, M. P., 1980. The Caledonian thrust and shear zones of N. W. Scotland, *J. Struct. Geol. 2*, 11–17, 1980.

Craw, D., Windle, S. & Angus, P. Gold mineralization without quartz veins in a ductile-brittle shear zone, Macraes Mine, Otago Schist, New Zealand. Mineral. Deposita 34, 382–394 (1999). https://doi.org/10.1007/s001260050211

Craw, D., Upton, P., Yu, B.-S., Horton, T. & Chen, Y.-G. 2010. Young orogenic gold mineralisation in active collisional mountains, Taiwan. Mineralium Deposita, 45, 631-646.

Craw, D., Mackenzie, D. & Grieve, P. 2015. Supergene gold mobility in orogenic gold deposits, Otago Schist, New Zealand. New Zealand Journal of Geology and Geophysics, 58, 123-136.

Cumming, G. L. and Richards, J. R. 1975. Ore lead isotope ratios in a continuously changing earth. Earth and Planetary Science Letters, 28(2), pp.155-171.

Dalradian Resources, 2018. [Online]. Technical Report for the Curraghinalt Gold Project, Northern Ireland. [Accessed: November 2023].

de Ronde C. E. J., Faure K., Bray C. J., Whitford D. J.; 2000. Round Hill Shear Zone-Hosted Gold Deposit, Macraes Flat, Otago, New Zealand: Evidence of a Magmatic Ore Fluid. Economic Geology; 95 (5): 1025–1048. doi: https://doi.org/10.2113/gsecongeo.95.5.1025

de Ronde, C.E.J., Humphris, S.E., Höfig, T.W., Reyes, A.G. & the IODP Expedition 376 Scientists. 2019. Critical role of caldera collapse in the formation of seafloor mineralization: The case of Brothers volcano', *Geology*, 47(8), pp. 762–766. doi:10.1130/G46047.1.

Dempster, T. 1985. Uplift patterns and orogenic evolution in the Scottish Dalradian. Journal of the Geological Society, London, 142, 111–128, https://doi.org/10. 1144/gsjgs.142.1.0111

Deng, J., Wang, C.M., Bagas, L., Carranza, E.J.M., LU, Y.J., 2015. Cretaceous-Cenozoic tectonic history of the Jiaojia Fault and gold mineralization in the Jiaodong Peninsula, China: constraints from zircon U-Pb, illite K-Ar, and apatite fission track thermochronometry. Mineralium Deposita 50, 987- 1006.

Deng, J., Liu, X.F., Wang, Q.F., Dilek, Y., Liang, Y.Y., 2017. Isotopic characterization and petrogenetic modelling of early Cretaceous mafic diking-lithospheric extension in the North China Craton, eastern Asia. The Geological Society of America Bulletin 129, 1379-1407.

Dewey, J. F. and Mange, M. 1999. Petrography of Ordovician and Silurian sediments in the western Irish Caledonides: tracers of a short-lived Ordovician continent – arc collision orogeny and the evolution of the Laurentian Appalachian-Caledonian margin. Geological Society, London, Special Publications, 164, 55–107, https:// doi.org/10.1144/GSL.SP.1999.164.01.05

Dewey, J. F. and Strachan, R. A. 2003. Changing Silurian– Devonian relative plate motion in the Caledonides; sinistral transpression to sinistral transtension. Journal of the Geological Society, London, 160, 219–229, https://doi.org/10.1144/0016-764902-085

Dewey, J. F. 2005. Orogeny can be very short. *Proceedings of the National Academy of Sciences of the United States of America*, 102 (43), 15286–15293. https://doi.org/10.1073/pnas.0505516102

Dietrich, D. and Ramsay, J.G., 1980. Int. conf. *On the effect of deformation of rocks, Univ. of Gottingen, Gottingen*, pp.85-87.

Digimap, Edina, 2023. [Online]. [Accessed from 2019 to 2023]. Available from: https://digimap.edina.ac.uk/Dolejš, D. And Manning, C.E. 2010. Thermodynamic model for mineral solubility in aqueous fluids: theory, calibration and application to model fluid-flow systems. Geofluids, 10: 20-40. https://doi.org/10.1111/j.1468-8123.2010.00282.x

Dong, G. & Morrison, G. 1995. Adularia in epithermal veins, Queensland: morphology, structural state and origin. Mineralium Deposita, 30, 11-19.

Dong, G., Morrison, G., Jaireth, S., 1995. Quartz textures in epithermal veins, Queensland e classification, origin, and implication. Economic Geology 90, 1841-1856.

Dong, G.Y., and Zhou, T., 1996. Zoning in the Carboniferous-Lower Permian Cracow epithermal vein system, central Queensland, Australia: Mineralium Deposita, v. 31, p. 210–224.

Dongmo F. W. N., Chapman R. J., Bolarinwa A. T., Yongue R. F., Banks D. A., Olajide-Kayode J. O. 2018. Microchemical characterization of placer gold grains from the Meyos-Essabikoula area, Ntem complex, southern Cameroon. J Afr Earth Sci 1(151):189–201

Dowling, K., And Morrison, G. W., 1989, Application of quartz textures to the classification of gold deposits using North Queensland examples: Economic Geology Monograph 6, p. 342–355.

Dubé B., Gosselin P., Mercier-Langevin P., Hannington M. and Galley A. 2007. Gold-rich volcanogenic massive sulphide deposits. Geological Association of Canada, Mineral Deposits Division, Special Publication , 5, 75–94.

Durney, D.W., Ramsay, J.G., 1973. Incremental strains measured by syntectonic crystal growths. In: De Jong, K.A., Scholten, K. (Eds.), Gravity and Tectonics. Wiley, New York, pp. 67-96.

Elmer F. L., White R.W., Powell R. 2006. Devolatilization of metabasic rocks during greenschist–amphibolite facies metamorphism. Journal of Metamorphic Geology. Vol. 24, 2006. Pages 431-534

Energy & Mining, Government of South Australia, 2023. [Online]. [Accessed 21 December 2023]. Available from: https://www.energymining.sa.gov.au/industry/minerals-and-mining/mineral-commodities/gold

Erris Resources, 2020. Urlar-Calliachar observation data. Erris Resources Database.

Erris Gold Resources (former company website), 2020-2021. [Online]. [Accessed December 2022]

Ferry J. M. 1994; Role of fluid flow in the contact metamorphism of siliceous dolomitic limestones. *American Mineralogist* 1994; 79 (7-8): 719–736.

Ferron C.J., 2016. Recovery of gold as by-product from the base-metals industries. M.D. Adams (Ed.), Gold Ore Processing (second ed.), pp. 831-856.

Finch, E. G. & Tomkins, A. G. 2017. Pyrite-Pyrrhotite Stability in a Metamorphic Aureole: Implications for Orogenic Gold Genesis. Economic Geology, 112, 661.

Fisher, D. and Byrne, T. 1990. The character and distribution of mineralised fractures in the Kodiak Formation, Alaska: implications for fluid flow in an underthrust sequence. Journal of Geophysical Research,95, 9069–9080,https://doi.org/10.1029/JB095iB06p09069

Fisher, D. M., Brantley, S. L., 1992. Models of quartz overgrowth and vein formation: deformation and episodic fluid flow in an ancient subduction zone. Journal of Geophysical Research 97, 20043-20061.

Fougerouse, D., Micklethwaite, S., Tomkins, A.G., Mei, Y., Kilburn, M., Guagliardo, P., Fisher, L.A., Halfpenny, A., Gee, M., Paterson, D. & Howard, D.L., 2016. Gold remobilisation and formation of high grade ore shoots driven by dissolution–reprecipitation replacement and Ni substitution into auriferous arsenopyrite. *Geochimica et Cosmochimica Acta*, 178, pp. 143–159. https://doi.org/10.1016/j.gca.2016.01.018

Fougerouse, D., Reddy, S.M., Aylmore, M., Yang, L., Guagliardo, P., Saxey, D.W., Rickard, W.D.A. & Timms, N., 2021. A new kind of invisible gold in pyrite hosted in deformation-related dislocations. *Geology*, 49(10), pp.1225–1229. Available at: https://doi.org/10.1130/G49028.1

Fournier R. O. 1985. The behavior of silica in hydrothermal solution: Reviews in Economic Geology, v. 2, p. 45–61.

Fournier, R. O., Thompson, J.M., Cunningham, C.G., and Hutchinson, R.A., 1991, Conditions leading to a recent small hydrothermal explosion at Yellowstone National Park: Geological Society of America Bulletin, v. 103, p. 1114-1120.

Frelinger, S. N., Ledvina, M.D., Kyle, J.R. and Zhao, D. 2015. Scanning electron microscopy cathodoluminescence of quartz: principles, techniques and applications in ore geology. Ore Geology Reviews, 65, 840–852, https://doi.org/10.1016/j.oregeorev.2014.10.008

Fyfe, W. S. & Kerrich, R. 1976. Geochemical prospecting: extensive versus intensive factors. Journal of Geochemical Exploration, 6, 177-192.

Fyfe, W. S. 1978. Fluids In The Earth's Crust: Their Significance In Metamorphic, Tectonic And Chemical Transport Process, Elsevier.

Gaboury D. 2019. Parameters for the formation of orogenic gold deposits, Applied Earth Science, 128:3, 124-133, DOI: 10.1080/25726838.2019.1583310

Galantas Gold Corporation, 2020. [Online]. Controls on Mineralisation at the Galantas Gold Mine, Cavanacaw, Omagh, County Tyrone, Northern Ireland. [Accessed: June 2021].

Galley A., Hannington M. and Jonasson I. 2007. Volcanogenic massive sulphide deposits. Mineral Deposits of Canada Special Publication, 5, 141–146.

Gammons C. H. 1988. Studies in hydrothermal phenomena: (1)~The solubility of silver sulfide in aqueous sulfide solutions to 300 degrees Celsius; (2)~A paragenesis and fluid inclusion study of polymetallic vein mineralization in the Big Creek mining district, central Idaho. The Pennsylvania State University ProQuest Dissertations Publishing, 1988. 8909994.

Gammons, C. H. & Williams-Jones, A. E. 1995. Hydrothermal geochemistry of electrum; thermodynamic constraints. Economic Geology, 90, 420-432.

Gammons, C. H., Williams-Jones, A. E. 1997. Chemical mobility of gold in the porphyry-epithermal environment. Economic Geology 92: 45-59

Gammons, C. H, Yu, Y., Williams-Jones, A. E. 1997. The disproportionation of gold chloride complexes at 25 to 200°C. Geochimica et Cosmochimica Acta 61: 1971-1983

Garnett R. H. T. and Bassett N.C. 2005. Placer deposits. Society for Economic Geology, 100th Anniversary Volume, 813–844, https://doi.org/10.5382/AV100.25

Garofalo, P. S. & Ridley, J. R. 2014. Gold-transporting hydrothermal fluids in the Earth's crust: an introduction. Geological Society, London, Special Publications, 402.

Gartman, A., Hannington, M., Jamieson, J.W., Peterkin, B., Garbe-Schönberg, D., Findlay, A.J., Fuchs, S. & Kwasnitschka, T. 2018. 'Boiling-induced formation of colloidal gold in black smoker hydrothermal fluids', *Geology*, 46(1), pp. 39–42. doi:10.1130/G39492.1.

Gas'kov I. V., 2017. Major impurity elements in native gold and their association with gold mineralization settings in deposits of Asian folded areas. Russ GeolGeophys 58:1080–1092

Gauthier, L., Hagemann, S.G., Robert, F., Pickens, G., 2004. New constraints on the architecture and timing of the giant Golden Mile gold deposit, Kalgoorlie, Western Australia. In: Groves, D.I. (Ed.), SEG2004: Predictive Mineral Discovery under Cover, Extended Abstracts. Society of Economic Geologists, Conference= Series, pp. 353-356

Gebre-Mariam M., Hagemann S.G. and Groves D.I. 1995. A classification scheme for epigenetic Archaean lode-gold deposits. Mineralium Deposita, 30, 408–410, https://doi.org/10.1007/BF00202283

Godwin, C. I. and Sinclair, A. J. 1982. Average lead isotope growth curves for shale-hosted zinc-lead deposits, Canadian Cordillera. Economic Geology, 77, 675–690, https://doi.org/10.2113/gsecongeo.77.3.675

Godwin, C. I., Gabites, J. E. and Andrew, A. 1988. A galena lead isotope data base for the Canadian Cordillera, with a guide to its use by explorationists. British Columbia Geological Survey Branch, Mineral Resources Division, Paper, 1988-4.

Goldfarb R. J., Leach D. L., Pickthorn W. J., Paterson C. J. 1988. Origin of lode-gold deposits of the Juneau gold belt, southeastern Alaska. *Geology* 1988; 16 (5): 440–443. doi: https://doi.org/10.1130/0091-7613(1988)016<0440:OOLGDO>2.3.CO;2

Goldfarb R. J., Groves D.I. and Gardoll S. 2001. Orogenic gold and geologic time; a global synthesis. Ore Geology Reviews, 18, 1–75, https://doi.org/10.1016/S0169-1368(01)00016-6

Goldfarb, R. J., Baker, T., Dube, B., Groves, D. I., Hart, C. J. & Gosselin, P. 2005. Distribution, character, and genesis of gold deposits in metamorphic terranes. Economic Geology 100th Anniversary Volume, 407-450.

Goldfarb, R. J. & Groves, D. I. 2015. Orogenic gold: Common or evolving fluid and metal sources through time. Lithos, 233, 2-26.

Goldfarb, R. J. 2021. Lode gold deposits in time and space in Alderton, and Elias, S.A., editors, Encyclopedia of Geology, 2nd edition, volume 5, United Kingdom, Academic Press, p. 663-679.

Goldhaber, M.B., Church, S.E., Doe, B.R., Aleinikoff, J.N., Brannon, J.C., Podosek, F.A., Mosier, E.L., Taylor, C.D. and Gent, C.A. 1995. Lead and sulfur isotope investigation of Paleozoic sedimentary rocks from the southern Midcontinent of the United States; implications for paleohydrology and ore genesis of the Southeast Missouri lead belts. Economic Geology, 90(7), pp.1875-1910.

Götze, J., Plötze, M., Fuchs, H. and Habermann, D., 1999. Defect structure and luminescence behaviour of agate; results of electron paramagnetic resonance (EPR) and cathodoluminescence (CL) studies. *Mineralogical Magazine*, *63*(2), pp.149-163.

Götze, J., Plötze, M. & Habermann, D. 2001. Origin, spectral characteristics and practical applications of the cathodoluminescence (CL) of quartz – a review. Mineralogy and Petrology, 71, 225-250.

Götze, J., Plötze, M. & Trautmann, T. 2005. Structure and luminescence characteristics of quartz from pegmatites. American Mineralogist.

Götze, J. 2009. Chemistry, textures and physical properties of quartz – geological interpretation and technical application. Mineralogical Magazine, 73. 645–671. https://doi.org/10.1180/minmag.2009.073. 4.645

Götze, J. 2012. Application of cathodoluminescence microscopy and spectroscopy in geosciences. Microscopy and Microanalysis, 18, 1270- 1284.

Götze, J., Pan Y., Mueller., A. 2021. Mineralogy and mineral chemistry of quartz: A review. Mineralogical Magazine (2021), 85, 639–664 doi:10.1180/mgm.2021.72

Green Glen Minerals, 2023. [Online]. [Accessed 2021 to 2023]. Available from: https://greenglenminerals.com/

Grigor'ev D.P., 1965, Ontogeny of minerals : Jerusalem, Israel Program for Scientific Translations, 250 p.

Groves, D. I., Goldfarb, R. J., Gebre-Mariam, M., Hagemann, S. & Robert, F. 1998. Orogenic gold deposits: a proposed classification in the context of their crustal distribution and relationship to other gold deposit types. Ore geology reviews, 13, 7-27.

Groves, D. I., Goldfarb, R. J., Knox-Robinson, C. M., Ojala, J., Gardoll, S., Yun, G. Y., Holyland, P., 2000. Late-kinematic timing of orogenic gold deposits and significance for computer- based exploration techniques with emphasis on the Yilgarn Block, Western Australia. Ore Geology Reviews 17, 1-38.

Groves, D. I., Goldfarb, R. J., Robert, F. & Hart, C. J. 2003. Gold deposits in metamorphic belts: overview of current understanding, outstanding problems, future research, and exploration significance. Economic Geology, 98, 1-29.

Groves D. J., Santosh M. 2015. Province-scale commonalities of some world-class gold deposits: Implications for mineral exploration. Geosci. Front., 6 (3) (2015), pp. 389-399, 10.1016/j.gsf.2014.12.007

Groves, D. I. & Santosh, M. 2016. The giant Jiaodong gold province: The key to a unified model for orogenic gold deposits? Geoscience Frontiers, 7, 409-417.

Groves, D. I., Santosh M., Goldfarb R. J., Zhang L. 2018. Structural geometry of orogenic gold deposits: Implications for exploration of world-class and giant deposits. Geoscience Frontiers. Volume 9, Issue 4, July 2018, Pages 1163-1177

Groves, D.I., Santosh, M., Deng, J., Wang, Q., Yang, L. and Zhang, L., 2020. A holistic model for the origin of orogenic gold deposits and its implications for exploration. *Mineralium Deposita*, *55*(2), pp.275-292. https://doi.org/10.1007/s00126-019-00877-5

Hamers M. F., Drury M. R. 2011. Scanning electron microscope-cathodoluminescence (SEM-CL) imaging of planar deformation features and tectonic deformation lamellae in quartz. Meteorit. Planet. Sci., 46 (12) (2011), pp. 1814-1831

Hancock E. A., Thorne A.M. 2011. Mineralogy of lode and alluvial gold from the western Capricorn Orogen, Western Australia. Aus J Earth Sci 58:793–801

Hannington M.D., Poulsen K.H., Thompson J.F.H. and Sillitoe R.H. 1999. Volcanogenic gold in the massive sulfide environment. Reviews in Economic Geology , 8, 325–356.

Hannington, M., Harðardóttir, V., Garbe-Schönberg, Brown K. L. 2016. Gold enrichment in active geothermal systems by accumulating colloidal suspensions. *Nature Geosci* **9**, 299–302. https://doi.org/10.1038/ngeo2661

Harland W. B., Wright N. J. R., 1979. Alternate hypothesis for the pre-Carboniferous evolution of Svalbard Skr. Nor. Polarinst., 167 (1979), pp. 90-117

Hart, C. J. 2007. Reduced intrusion-related gold systems. Mineral Deposits of Canada: A synthesis of Major deposit types, district metallogeny, the Evolution of geological provinces, and exploration methods: Geological Association of Canada, Mineral Deposits Division, Special Publication, 95-112.

Hastie, E. C. G., Kontak, D. J. & Lafrance, B. 2020a. Gold remobilization: insights from Au deposits in the Swayze greenstone belt, Abitibi Subprovince, Canada. Econ. Geol. 115, 241–277.

Hastie, E. C. G., Schindler, M., Kontak, D.J., Lafrance. B., 2021. Transport and coarsening of gold nanoparticles in an orogenic deposit by dissolution–reprecipitation and Ostwald ripening. *Commun Earth Environ* 2, 57. https://doi.org/10.1038/s43247-021-00126-6

Haeussler P. J., Bradley D., Goldfarb R., Snee L., Taylor C., 1995. Link between ridge subduction and gold mineralization in southern Alaska. Geology, 23, 995-998.

Hedenquist, J. W., Arribas, R., And Gonzalez-Urien, E., 2000, Exploration for epithermal gold deposits: Reviews in Economic Geology, v. 13, p. 245–277.

Herrington, R. J. & Wilkinson, J. J. 1993. Colloidal gold and silica in mesothermal vein systems. Geology, 21, 539-542.

Herzig P. M., Becker K. P., Stoffers P., Bäcker H., Blum N. 1988. Hydrothermal silica chimney fields in the Galapagos Spreading Center at 86°W. Earth and Planetary Science Letters. Volume 89, Issues 3–4, August 1988, Pages 261-272

Hilgers, C., Koehn, D., Bons, P.D., Urai, J. L., 2001. Development of crystal morphology during uniaxial growth in a progressively widening vein: II. Numerical simulations of the evolution of anitaxial fibrous veins. Journal of Structural Geology 23, 873-885.

Hilgers, C., Urai, J.L., 2002a. Microstructural observations on natural syntectonic fibrous veins: implications for the growth process. Tectonophysics 352 (2002) 257–274.

Hilgers, C., Dilg-Gruschinski, K., Urai, J.L., 2004. Microstructural evolution of syntaxial veins formed by advective flow. Geology 32, 261-264.

Hill, N. J., Jenkin, G. R. T., Boyce, A. J., Sangster, C.J.S., Catterall, D.J., Holwell, D.A., Naden, J. & Rice, C.M. 2013. How the Neoproterozoic S-isotope record illuminates the genesis of vein gold systems: an example from the Dalradian Supergroup in Scotland. In: Jenkin, G.R.T., Lusty, P.A.J., McDonald, I., Smith, M.P., Boyce, A.J. & Wilkinson, J.J. (Eds.) Ore Deposits in an Evolving Earth. Geological Society, London, Special Publications, 393, 9.

Hill N. J. 2014. Development of a genetic model for targeting gold mineralisation in the Dalradian Supergroup, Scotland. Ph.D. thesis, University of Leicester.

Hochella Jr, M.F., Lower, S.K., Maurice, P.A., Penn, R.L., Sahai, N., Sparks, D.L. and Twining, B.S., 2008. Nanominerals, mineral nanoparticles, and earth systems. *science*, *319*(5870), pp.1631-1635.

Hodkiewicz, P. F., Weinberg, R. F., Gardoll, S. J., Groves, D. I. 2005. Complexity gradients in the Yilgarn Craton: Fundamental controls on crustal-scale fluid flow and the formation of world-class orogenic-gold deposits. *Australian Journal of Earth Sciences*, 52 (6) 831-841 doi:10.1080/08120090500304257

Holland, M., Urai, J.L., 2010. Evolution of anastomosing crack-seal vein networks in limestones: insights from an exhumed high-pressure cell, Jabal Shams, Oman Mountains. Journal of Structural Geology 32, 1279-1290

Hollister, L.S., 1970. Origin, mechanism, and consequences of compositional sector-zoning in staurolite. *American Mineralogist: Journal of Earth and Planetary Materials*, *55*(5-6), pp.742-766.

Holdsworth, R. E., Van Diggelen, E.W.E., Spiers, C.J., De Bresser, J.H.P., Walker, R.J., And Bowen, L., 2011. Fault rocks from the SAFOD core samples: Implications for weakening at shallow depths along the San Andreas fault, California: Journal of Structural Geology, v. 33, p. 132–144.

Holmes, A. 1946. An estimate of the age of the earth. Nature, 157, pp.680-684.

Hough, R. M., Butt, C. R. M. & Fischer-Bühner, J. 2009. The Crystallography, Metallography and Composition of Gold. Elements, 5, 297-302.

Hough, R. M., Noble, R. R. P. & Reich, M. 2011. Natural gold nanoparticles. Ore Geol. Rev. 42, 55–61

Hronsky, J. M., Groves, D. I., Loucks, R. R. & Begg, G. C. 2012. A unified model for gold mineralisation in accretionary orogens and implications for regional-scale exploration targeting methods. Mineralium Deposita, 47, 339-358.

Humphreys, F. J. & Hatherly, M. 2004a. Chapter 12 - Recrystallization Textures. In: HATHERLY, F. J. H. (ed.) Recrystallization and Related Annealing Phenomena (Second Edition). Oxford: Elsevier.

Humphreys, F. J. & Hatherly, M. 2004b. Chapter 9 - Recrystallization Of Two Phase Alloys. In: Hatherly, F. J. H. (ed.) Recrystallization and Related Annealing Phenomena (Second Edition). Oxford: Elsevier.

Huston, D. L., Bottrill, R. S., Creelman, R. A., Zaw, K., Ramsden, T. R., Rand, S. W., Gemmell, J. B., Jablonski, W., Sie, S. & Large, R. R. 1992. Geologic and geochemical controls on the mineralogy and grain size of gold-bearing phases, eastern Australian volcanic-hosted massive sulfide deposits. Economic Geology, 87, 542-563.

Huston, D.L. and Champion, D.C. 2023. Applications of Lead Isotopes to Ore Geology, Metallogenesis and Exploration. In: Huston, D. and Gutzmer, J. ed(s). Isotopes in Economic Geology, Metallogenesis and Exploration. Springer.

Huston, D.L., Champion, D.C., Morrison, G., Mass, R., Thorne, J.P., Carr, G., Beams, S., Bottrill, R., Chang, Z. S., Dhnaram, C., Downe, P.M., Forster, D.B., Gemmell, J.B., Lisitsin, V., McNeill, A. and Vicary, M. 2017. Spatial variations in lead isotopes, Tasman Element, eastern Australia. Townsville: James Cook University.

Hutton D. H. W. 1987. Strike-slip terranes and a model for the evolution of the British and Irish Caledonides. *Geological Magazine*. 1987;124(5):405-425. doi:10.1017/S0016756800017003

Hutton D. H. W., Mc Erlean M., 1991. Silurian and Early Devonian sinistral deformation of the Ratagain granite, Scotland: constraints on the age of Caledonian movements on the Great Glen fault system. Journal of the Geological Society, 148, 1-4.

Ixer, R. A., Pattrick, R. A. and Stanley, C. J. 1997 Geology, mineralogy and genesis of gold mineralization at Calliachar-Urlar Burn, Scotland; Transactions of the Institution of Mining and Metallurgy Section B-Applied Earth Science, 106, p.99-108.

Jacques J. M., Reavy R. J. 1994. Caledonian plutonism and major lineaments in the SW Scottish Highlands. Journal of the Geological Society of London, 151 (1994), pp. 955-969

Jaffey, A.H., Flynn, K.F., Glendenin, L.E., Bentley, W.C. and Essling, A.M. 1971. Precision Measurement of Half-Lives and Specific Activities of 235U and 238U. Physical Review C, 4(5), pp. 1889-1906.

Jébrak, M. 1997. Hydrothermal breccias in vein-type ore deposits: A review of mechanisms, morphology and size distribution. Ore Geology Reviews, 12, 111-134.

Jefferies, S. P., Holdsworth, R.E., Shimamoto, T., Takagi, H., Lloyd, G.E., And Spiers, J., 2006b, Origin and mechanical significance of foliated cataclastic rocks in the cores of crustal-scale faults: Examples from the Median Tectonic Line, Japan: Journal of Geophysical Research, v. 111, p. 1978- 2012.

Jenkin, G. R. T., Craw, D. & Fallick, A. E. 1994. Stable isotopic and fluid inclusion evidence for meteoric fluid penetration into an active mountain belt; Alpine Schist, New Zealand. Journal of Metamorphic Geology, 12, 429-444.

Joly, A., Porwal, A., McCuaig, T., Chudasama, B., Dentith, M. and Aitken, A. 2015. Mineral systems approach applied to GIS-based 2D-prospectivity modelling of geological regions: Insights from Western Australia. Ore Geology Reviews, 71, pp.673-702

Jourdan, A.L., Vennemann, T.W., Mullis, J., Ramseyer, K. and Spiers, C.J., 2009. Evidence of growth and sector zoning in hydrothermal quartz from Alpine veins. *European Journal of Mineralogy*, *21*(1), pp.219-231.

Katz, Y., Weinberger, R. and Aydin, A., 2004. Geometry and kinematic evolution of Riedel shear structures, Capitol Reef National Park, Utah. *Journal of structural geology*, *26*(3), pp.491-501.

Kamilli, R. J. 1998. Paragenesis. In: Marshall, C.P. and Fairbridge, R.W. (eds) Encyclopedia of Geochemistry. Springer, Dordrecht, 485–488, https://doi.org/10. 1007/1-4020-4496-8_240

Kerrich R., Fyfe W. S., 1981. The gold-carbonate association: Source of CO2 and CO2 fixation reactions in Archaean lode deposits Chem. Geol., 33, pp. 265-294

Kerrich R., Wyman D., 1990. Geodynamic setting of mesothermal gold deposits: An association with accretionary tectonic regimes. Geology, 18, 882-885

Knight, J. & Mctaggart, K. 1986. The composition of placer and lode gold from the Fraser River drainage area, southwestern British Columbia. Canadian Geology Journal of the CIM, 1, 21-30.

Knight, J. B., Morison, S. & Mortensen, J. 1999a. The relationship between placer gold particle shape, rimming, and distance of fluvial transport as exemplified by gold from the Klondike District, Yukon Territory, Canada. Economic Geology, 94, 635-648.

Knight, J. B., Mortensen, J. K. & Morison, S. R. 1999b. Lode and placer gold composition in the Klondike District, Yukon Territory, Canada; implications for the nature and genesis of Klondike placer and lode gold deposits. Economic Geology, 94, 649-664.

Knight J. B., Leitch C. H., 2001. Phase relations in the system Au–Cu–Ag at low temperatures, based on natural assemblages. Can Mineral 39: 889–905

Knight, E., Schneider, D. & Ryan, J. 2013. Thermochronology of the Yukon Tanana Terrane, West-Central Yukon: Evidence for Jurassic Extension and Exhumation in the Northern Canadian Cordillera. The Journal of Geology, 121, 371-400.

Krupp, R. E. & Weiser, T. 1992. On the stability of gold-silver alloys in the weathering environment. Mineralium Deposita, 27, 268-275.

Labrousse L., Hetényi G., Raimbourg H., Jolivet L., Andersen T. B. 2010. Initiation of crustal-scale thrusts triggered by metamorphic reactions at depth: Insight from a comparison between the Himalayas and Scandinavian Caledonides. Tectonics, 29 (2010), p. TC5002, 10.1029/2009TC002602

Landefeld, L.A., 1988. The geology of the Mother Lode gold belt, Sierra Nevada Foothills metamorphic belt, California. *Bicentennial Gold*, *88*, pp.167-172.

Lang, J. R. & Baker, T. 2001. Intrusion-related gold systems: the present level of understanding. Mineralium Deposita, 36, 477-489.

Lavelle, A. 2020a. Report on the Detailed Mapping of the Calliachar-Urlar Gold Prospect, Aberfeldy Scotland. Erris Gold Resources.

Lavelle, A. 2020b. Channel Sampling Results & Scout Drill Targets Lead Trial, 2020-2021. Erris Gold Resources.

Lawley C., Imber J., Selby D., 2013. Structural Controls on Orogenic Au Mineralization During Transpression: Lupa Goldfield, Southwestern Tanzania. Economic Geology, v. 108, pp. 1615–1640

Leach, D., Bradley, D., Lewchuk, M., Symons, D., de Marsily, G. and Brannon, J. 2001. Mississippi Valleytype lead–zinc deposits through geological time: implications from recent age-dating research. Mineralium Deposita, 36, 711–740, https://doi.org/10.1007/ s001260100208

Leake, R., Bland, D., Styles, M. & Cameron, D. 1991. Internal structure of Au-Pd-Pt grains from south Devon, England, in relation to low temperature transport and deposition. Transactions Of The Institution Of Mining And Metallurgy Section B-Applied Earth Science, 100, B159-B178.

Leake, R., Chapman, R., Bland, D., Condliffe, E. & Styles, M. 1997a. Microchemical characterization of gold from Scotland: Institution of Mining and Metallurgy Transactions, v. 106, sec. B. 102:65–82.

Leake, R. C., Cameron, D. G., Bland, D. J., Styles, M. T. and Fortey, N. J., 1997b. The potential for gold mineralisation in the British Permian and Triassic red beds and their contacts with underlying rocks.

Leake R. C., Chapman R. J., Bland D. J., Stone P., Cameron D. G., Styles M. T. 1998. The origin of alluvial gold in the Leadhills area of Scotland: evidence from internal chemical characteristics. J Explor Geochem 63:7–36

Lebrun, E., Thébaud, N., Miller, J., Roberts, M. and Evans, N. 2016. Mineralisation footprints and regional timing of the world-class Siguiri orogenic gold district (Guinea, West Africa). Mineralium Deposita, 52, 539–564, https://doi.org/10.1007/s00126-016-0684-6

Lehmann K., Berger A., Götte T., Ramseyer K., Wiedenbeck M. 2009. Growth-related trace element distribution in quartz overgrowths and crystals determined by EPMA-, SIMS-, CL- and charge contrast-imaging. Mineralogical Magazine, 73 (4) (2009), pp. 633-643

Leslie A. G., Smith M., Soper N. J., 2008. "Laurentian margin evolution and the Caledonian orogeny — A template for Scotland and East Greenland", The Greenland Caledonides: Evolution of the Northeast Margin of Laurentia, A.K. Higgins, Jane A. Gilotti, M. Paul Smith

Li, R., Wang, X., Yang, L., Zhang, B., Liu, Q. and Liu, D. 2020. The characteristic of microstructural deformation of gold bearing pyrite in Jiaodong: the links between nanoscale gold enrichment and crystal distortion. Ore Geology Reviews, 122, 103495, https://doi.org/10. 1016/j.oregeorev.2020.103495

Li, H., Wang, Q., Wenig, W., Dong, C., Yang, L., Wang, X. and Deng, J. 2022. Co-precipitation of gold and base metal sulfides during fluid boiling triggered by fault-valve processes in orogenic gold deposits. Ore Geology Reviews, 149, https://doi.org/10.1016/j.oregeorev. 2022.105090

Lindgren, W. 1899. The gold and silver veins of Silver City, De Lamar and other mining districts in Idaho: U.S. Geological Survey 20th Annual Report, v.3, p. 63-236.

Lindgren W., 1933. Mineral Deposits, 4th edition: New York, McGraw-Hill, 930 p.

Liu, H. & Beaudoin, G. 2021. Geochemical signatures in native gold derived from Aubearing ore deposits. Ore Geology Reviews, 132, 104066.

Liu, H., Beaudoin, G., Makvandi, S., Jackson, S. E. & Huang, X. 2021a. Multivariate statistical analysis of trace element compositions of native gold from orogenic gold deposits: Implication for mineral exploration. Ore Geology Reviews, 131, 104061.

Liu, J., Wang, A., Xia, H., Zhai, Y., Gao, L., Xiu, Q., Zhang, Z., Zhao, Z. & Cao, D., 2010. Cracking mechanisms during galena mineralization in a sandstone-hosted lead–zinc ore deposit: case study of the Jinding giant sulfide deposit, Yunnan, SW China. *Mineralium Deposita*, 45, pp.567–582. https://doi.org/10.1007/s00126-010-0294-7

Liu, Y., Zhao, Y., Xue, C., Yu, L., Chu, H. and Zhao, X. 2021b. The Changshagou gold deposit, Eastern Tianshan, NW China: orogenic gold mineralization overprinting a porphyry gold occurrence. Geological Society, London, Special Publications, 516, https:// doi.org/10.1144/SP516-2020-248

Lovering, T.G. 1972. Jasperold in the United States--its characteristics, origin, and economic significance: U.S. Geological Survey Professional Paper 710, 164 p

MacKenzie D. J., Craw, D. 2007. Contrasting hydrothermal alteration mineralogy and geochemistry in the auriferous Rise & Shine Shear Zone, Otago, New Zealand, New Zealand Journal of Geology and Geophysics, 50:2, 67-79, DOI: 10.1080/00288300709509822

Mackenzie, D., Craw, D., Cooley, M. & Fleming, A. 2010. Lithogeochemical localisation of disseminated gold in the White River area, Yukon, Canada. Mineralium Deposita, 45, 683-705.

Mackenzie, D., Craw, D. & Finnigan, C. 2015. Lithologically controlled invisible gold, Yukon, Canada. Mineralium Deposita, 50, 141-157.

Maltese, A. and Mezger, K. 2020. The Pb isotope evolution of Bulk Silicate Earth: Constraints from its accretion and early differentiation history. Geochimica et Cosmochimica acta, 271, pp.179-193.

Mao J., Wang Y., Li H., Pirajno F., Zhang C., Wang R., 2008. The relationship of mantle-derived fluids to gold metallogenesis in the Jiaodong Peninsula: Evidence from D–O–C–S isotope systematics. Ore Geology Reviews. V. 33, 3–4, p. 361-381

Mark, D., Rice, C., Fallick, A., Trewin, N., Lee, M., Boyce, A. and Lee, J. 2011. 40Ar/39Ar dating of hydrothermal activity, biota and gold mineralization in the Rhynie hot-spring system, Aberdeenshire, Scotland. Geochimica et Cosmochimica Acta, 75(2), pp.555-569.

Marshall, D. J. 1988. Cathodoluminescence of Geological Materials. Unwin Hyman, Boston.

Mendum, J. R.; Noble, S.R. 2010. Mid-Devonian sinistral transpression on the Great Glen Fault: The rise of the Rosemarkie Inlier and the Acadian Event in Scotland. Geol. Soc. Lond. 2010, 335, 161–187.

Mason, J., 1990. Photomicrographs of Calliachar Burn gold mineralisation, taken in January 1990. Unpublished report.

McCuaig T. C., Kerrich R., 1998. P-T-t-deformation-fluid characteristics of lode gold deposits: evidence from alteration systematics. Ore Geol. Rev., 12 (6), pp. 381-453, 10.1016/S0169-1368(98)80002-4

McCuaig, T.C., Beresford, S. and Hronsky, J. 2010. Translating the mineral systems approach into an effective exploration targeting system. Ore Geology Reviews, 38(3), pp.128-138.

Mcinnes, M., Greenough, J. D., Fryer, B. J. & Wells, R. 2008. Trace elements in native gold by solution ICPMS and their use in mineral exploration: A British Columbia example. Applied Geochemistry, 23, 1076-108

Mckerrow, W. S.; Niocaill C. M., Dewey J. F. 2000. The Caledonian orogeny redefined. J. Geol. Soc., 157 (6) (2000), pp. 1149-1154

Micklewhite, S., Sheldon H. A., Baker T., 2010. Active fault and shear processes and their implications for mineral deposit formation and discovery, Journal of Structural Geology, Volume 32, Issue 2. Pages 151-165, ISSN 0191-8141, https://doi.org/10.1016/j.jsg.2009.10.009.

Mikucki, E.J. 1998. Hydrothermal transport and depositional processes in Archean lode-gold systems: A review. Ore Geology Reviews, 13, 307-321.

Mills, S., Tomkins, A., Weinberg, R. and Fan, H. 2015. Implications of pyrite geochemistry for gold mineralisation and remobilisation in the Jiaodong gold district, northeast China. Ore Geology Reviews, 71, 150–168, https://doi.org/10.1016/j.oregeorev.2015. 04.022

Milot, J., Blichert-Toft, J., Sanz, M.A., Fetter, N., Télouk, P. and Albarede, F., 2021. The significance of galena Pb model ages and the formation of large Pb-Zn sedimentary deposits. *Chemical Geology*, *583*, p.120444.

Milnes, A.G., 1998. Alpine and Caledonide tectonics-a brief comparative study. *Gff*, *120*(2), pp.237-247.

Moles, N. R.; Chapman, R.J.; Warner, R.B. 2013. The significance of copper concentrations in natural gold alloy for reconnaissance exploration and understanding gold-depositing hydrothermal systems. Geochem. Explor. Environ. Anal., 13, 115–130

Moles, N.R. and Chapman, R.J., 2019. Integration of detrital gold microchemistry, heavy mineral distribution, and sediment geochemistry to clarify regional metallogeny in glaciated terrains: Application in the Caledonides of southeast Ireland. *Economic Geology*, *114*(2), pp.207-232.

Moncada, D., Mutchler, S., Nieto, A., Reynolds, T. J., Rimstidt, J. D. & Bodnar, R. J. 2012. Mineral textures and fluid inclusion petrography of the epithermal Ag–Au deposits at Guanajuato, Mexico: Application to exploration. Journal of Geochemical Exploration, 114, 20-35.

Morgan, P.G. 1925. The so-called "pseudomorphous" quartz of Tertiary gold-silver veins: Economic Geology, v. 20, p. 203-207.

Morrison, G. W., Rose, W. J. & Jaireth, S. 1991. Geological and geochemical controls on the silver content (fineness) of gold in goldsilver deposits. Ore Geology Reviews, 6, 333-364.

Mortensen, J. K.; Craw, D.; MacKenzie, D.J. 2022. Concepts and revised models for Phanerozoic orogenic gold deposits. In *Recent Advances in Understanding Gold Deposits: From Orogeny to Alluvium*; Torvela, T.M., Chapman, R.J., Lambert-Smith, J., Eds.; Special Publication: London, UK, Volume 516, pp. 15–46.

Mount, V. S., And Suppe, J., 1992. Present-day stress orientations adjacent to active strike-slip faults: Journal of Geophysical Research, v. 97, p. 11,995–12,013.

Mountain B. W., Wood S. A. 1988. Chemical controls on the solubility, transport and deposition of platinum and palladium in hydrothermal solutions: a thermodynamic approach. Econ Geol 83:492–510

Mueller, A. G.,Harris, L. B. & Lungan, A. 1988. Structural control of greenstone-hosted gold mineralization by transcurrent shearing: a new interpretation of the Kalgoorie mining district, western Australia. Ore Geology. Reviews 3, 359–87.

Mühe, R., Peucker-Ehrenbrink, B., Devey, C. W. and Garbe-Schönberg, D. 1997. On the redistribution of Pb in the oceanic crust during hydrothermal alteration. Chemical Geology, 137(1-2), pp.67-77.

Mügge, O., 1925. Über gehemtes Kristallwachstum. Zeitschrift für Kristallographie 62, 415-442.

Mügge, O., 1928. Über die Entstehung faseriger Minerale und ihrer Aggergationsformen. Neues Jahrbuch für Mineralogie, Geologie und Paläontologie 58A, 303-348.

Müller, A., Wiedenbeck, M., Van den Kerkhof, A.M., Kronz, A. and Simon, K. 2003. Trace elements in quartz – a combined electron microprobe, secondary ion mass spectrometry, laser-ablation ICP-MS, and cathodoluminescence study. European Journal of Mineralogy, 15, 747–763

Müller, A., Herrington, R., Armstrong, R., Seltmann, R., Kirwin, D.J., Stenina, N.G. and Kronz, A., 2010. Trace elements and cathodoluminescence of quartz in stockwork veins of Mongolian porphyry-style deposits. *Mineralium Deposita*, *45*(7), pp.707-727.

Naden, J.; Gunn, A.G.; Shepherd, T.J.. 2010. *Fluids and mineralisation in the Scottish Dalradian.* Nottingham, UK, British Geological Survey, 168pp. (OR/09/054) (Unpublished)

Neilson J. C, Kokelaar B. P., Crowley Q. G. 2009. Timing, relations and cause of plutonic and volcanic activity of the Siluro-Devonian post-collision magmatic episode in the Grampian Terrane, Scotland. J. Geol. Soc. Lond., 166 (2009), pp. 545-561

Nesbitt B. E., Muehlenbachs K.; 1991. Melange- and sediment-hosted gold-bearing quartz veins, Hodgkinson gold field, Queensland, Australia; discussion. *Economic Geology* 1991; 86 (1): 195–197. doi: https://doi.org/10.2113/gsecongeo.86.1.195

Neumayr, P., Hagemann, S. G. & Couture, J. F. 2000. Structural setting, textures, and timing of hydrothermal vein systems in the Val d'Or camp, Abitibi, Canada: implications for the evolution of transcrustal, second- and third-order fault zones and gold mineralization. Canadian Journal of Earth Sciences 37, 95–114.

Newton, R. C., Manning, C.E., 2010. Role of saline fluids in deep-crustal and upper mantle metasomatism: insights from experimental studies. Geofluids 10, 58 – 72.

Nollet, S., Urai, J.L., Bons, P.D., Hilgers, C., 2005. Numerical simulations of polycrystal growth in veins. Journal of Structural Geology 27, 217-230.

Northrup, P.A. and Reeder, R.J., 1994. Evidence for the importance of growth-surface structure to trace element incorporation in topaz. *American Mineralogist*, *79*(11-12), pp.1167-1175.

Okamoto, A., Kikuchi, T., Tsuchiya, N., 2008. Mineral distribution within polymineralic veins in the Sanbagawa belt, Japan: implications for mass transfer during vein formation. Contributions to Mineralogy and Petrology 156, 323-336

Okamoto, A., Tsuchiya, N., 2009. Velocity of vertical fluid ascent within vein forming fractures. Geology 37, 563-566.

Okamoto, A., Saishu, H., Hirano, N., Tsuchiya, N., 2010. Mineralogical textural variation in hydrothermal flow-through experiments: implications for quartz vein formation. Geochimica Cosmochimica Acta 74, 3692-3706.

Okamoto, A., Sekine, K., 2011. Textures of syntaxial quartz veins synthesized by hydrothermal experiments. Journal of Structural Geology 33, 1764-1775

Oliver, G. J. H. 2001. Reconstruction of the Grampian episode in Scotland: its place in the Caledonian Orogeny. Tectonophysics, 332, 23–49, https://doi.org/10.1016/ S0040-1951(00)00248-1

Oliver, N., Bons, P., 2001. Mechanisms of fluid flow and fluid-rock interaction in fossil metamorphic hydrothermal systems inferred from vein- and wall-rock patterns, geometry and microstructure. Geofluids 1, 137-162.

Oliver, G., Wilde, S. and Wan, Y. 2008. Geochronology and geodynamics of Scottish granitoids from the late Neoproterozoic break-up of Rodinia to Palaeozoic collision. Journal of the Geological Society, 165, 661–674, https://doi.org/10.1144/0016-76492007-105

Onasch C. M., Vennemann T. W.; 1995. Disequilibrium partitioning of oxygen isotopes associated with sector zoning in quartz. *Geology* 1995; 23 (12): 1103–1106. doi: https://doi.org/10.1130/0091-7613(1995)023<1103:DPOOIA>2.3.CO;2

Ord A., Oliver N. H. S. 1997. Mechanical controls on fluid flow during regional metamorphism: some numerical models. *Journal of Metamorphic Geology*, vol. 15, no. 3, pp. 345-359. https://doi.org/10.1111/j.1525-1314.1997.00030.x

Palacios, C., Hérail, G., Townley, B., Maksaev, V., Sepúlveda, F., De Parseval, P., Rivas, P., Lahsen, A. & Parada, M. A., 2001. The composition of gold in the Cerro Casale gold-rich porphyry deposit, Maricunga belt, northern Chile. The Canadian Mineralogist, 39, 907-915.

Palme, H. and O'Neill, H. 2003. Cosmochemical estimates of mantle composition. Treatise on Geochemistry, 2, pp.1-38.

Pal'yanova G., 2008. Physicochemical modeling of the coupled behavior of gold and silver in hydrothermal processes: gold fineness, Au/Ag ratios and their possible implications. Chem. Geol., 255, pp. 399-413

Pal'yanova, G.; Murzin, V.; Borovikov, A.; Karmanov, N.; Kuznetsov, S. 2021. Native gold in the chudnoe Au-Pd-ree deposit (Subpolar Urals, Russia): Composition, minerals in intergrowth and genesis. Minerals 2021, 11, 451.

Parnell, J., Earls, G., Wilkinson, J. J., Hutton, D. H. W., Boyce, A. J., Fallick, A. E., Ellam, R. M., Gleeson, S. A., Moles, N. R., Carey, P. F., Legg, I. & Carey, P. F. 2000. Regional Fluid Flow and Gold Mineralization in the Dalradian of the Sperrin Mountains, Northern Ireland. Economic Geology, 95, 1389-1416.

Parry, S.F., Noble, S.R., Crowley, Q.G. and Wellman, C.H., 2011. A high-precision U–Pb age constraint on the Rhynie Chert Konservat-Lagerstätte: time scale and other implications. *Journal of the Geological Society*, *168*(4), pp.863-872.

Passchier, C. W., Trouw, R.A.J., 1996. Microtectonics. Springer Verlag, Berlin.

Passchier, C. W., Trouw, R.A.J., 2005. Microtectonics, second ed. Springer-Verlag, Berlin, p. 366.

Pattrick, R. A. D. 1984. Sulphide mineralogy of the Tomnadashan copper deposit and the Corrie Buie lead veins, south Loch Tayside, Scotland. Mineralogical Magazine, 48, 85–91.

Peach B. N., Horne J., Gunn W., Clough C. T., Hinxman L. W., Teall J. J. H. 1907. The geological structure of the NW Highlands of Scotland Geol. Surv. Great Brit. Mem. (1907) (668 pp.)

Pearce, M. A., White, A. J. R., Fisher, L. A., Hough, R. M. & Cleverley, J. S. 2015. Gold deposition caused by carbonation of biotite during latestage fluid flow. Lithos, 239, 114-127.

Pearson, R. G. 1963. Hard and Soft Acids and Bases. Journal of the American Chemical Society, 85, 3533-3539.

Penniston-Dorland, S.C., 2001. Illumination of vein quartz textures in a porphyry copper ore deposit using scanned cathodoluminescence: Grasberg Igneous Complex, Irian Jaya, Indonesia. *American Mineralogist*, *86*(5-6), pp.652-666.

Perring C. S. et al. 1989. Criteria for the recognition of metamorphosed or altered lamprophyres: a case study from the Archaean of Kambalda, Western Australia. Precambrian Research. Vol. 43, Issue 3, May 1989, Pages 215-222, 225-237

Petrella, L., Thébaud, N., Fougerouse, D., Evans, K., Quadir, Z., Laflamme, C. 2020. Colloidal gold transport: a key to high-grade gold mineralization? Mineralium Depos. 55, 1–8

Petrella L, Thébaud N., Evans K., LaFlamme C., Occhipinti S., 2021. The role of competitive fluid-rock interaction processes in the formation of high-grade gold deposits. Geochim. Cosmochim. Acta, 313, pp. 38-54

Petrella, L., Thébaud, N., Fougerouse, D., Tattitch B., Martin L., Turner S., Suvorova A., Gain S. 2022. Nanoparticle suspensions from carbon-rich fluid make high-grade gold deposits. *Nat Commun* 13, 3795. https://doi.org/10.1038/s41467-022-31447-5

Phillips, G. N. & Powell, R. 2010. Formation of gold deposits: a metamorphic devolatilization model. Journal of Metamorphic Geology, 28, 689-718.

Pochon, A., Desaulty, A.-M., Bailly, L. & Lach, P. 2021. Challenging the traceability of natural gold by combining geochemical methods: French Guiana example. Applied Geochemistry, 129, 104952.

Pokrovski, G. S., Akinfiev, N. N., Borisova, A. Y., Zotov, A. V. & Kouzmanov, K. 2014. Gold speciation and transport in geological fluids: insights from experiments and physical-chemical modelling. Geological Society, London, Special Publications, 402, 9-70.

Pokrovski, G., Kokh, M., Proux, O., Hazemann J.L., Bazarkina, E., Testemale, D., Escoda C., Boiron, M.C., Blanchard, M., Aigouy, T. 2019. The nature and partitioning of invisible gold in the pyrite-fluid system. Ore Geol. Rev., 109, pp. 545-563

Putnis, A., 2009. Mineral replacement reactions. *Reviews in mineralogy and geochemistry*, *70*(1), pp.87-124.

Quilichini, A., Siebenaller, L., Teyssier, C. and Vennemann, T. 2016. Magmatic and meteoric fluid flow in the Bitterroot extensional detachment shear zone (MT, USA) from ductile to brittle conditions. Journal of Geodynamics, 101, 109–128, https://doi.org/10. 1016/j.jog.2016.05.006

Ramsay, J. G., 1980. The crack-seal mechanism of rock deformation. Nature 284, 135-139.

Ramsay, J. G., Huber, M., 1983. The Techniques of Modern Structural Geology. Volume 1: Strain Analysis. Academic Press, London.

Ramsay, J. G., Huber, M., 1987. The Techniques of Modern Structural Geology. Volume 2: Folds and Fractures. Academic Press, London.

Reed, M. H. Palandri, J, 2006. Sulfide Mineral Precipitation from Hydrothermal Fluids. Reviews in Mineralogy & Geochemistry Vol. 61, pp. 609-631

Renard, F., Andréani, M., Boullier, A.M., Labaume, P., 2005. Uncorrelated stress release variations in crustal rocks. In: Geological Society, London, Special Publications, vol. 243. 67e79.

Rhys, D.A., Lewis, P.D. and Rowland, J.V., 2020. Structural controls on ore localization in epithermal gold-silver deposits: a mineral systems approach.

Rice, C. M., Mark, D. F., Selby, D., Neilson, J. E. & Davidheiser-Kroll, B. 2016. Age and Geologic Setting of Quartz Vein-Hosted Gold Mineralization at Curraghinalt, Northern Ireland: Implications for Genesis and Classification. Economic Geology, 111, 127-150.

Ridley, J. R. & Diamond, L. W. 2000. Fluid chemistry of orogenic lode gold deposits and implications for genetic models. Gold in, 2000. 141-162.

Ridley, J., And Mengler, F., 2000. Lithological and structural controls on the form and setting of vein stockwork orebodies at the Mount Charlotte gold deposit, Kalgoorlie: Economic Geology, v. 95, p. 85–98.

Robb, L., 2020. *Introduction to Ore-Forming Processes* (2nd ed.). Wiley-Blackwell.

Robert, F., Poulson, H.K., Cassidy, K.F., Hodgson, J.C., 2005. Gold Metallogeny of the Superior and Yilgarn Cratons. Economic Geology 100th Anniversary Volume, pp. 1001-1033.

Robert, F., Brommecker, R., Bourne, B. T., Dobak, P.J., McEwan, C. J., Rowe, R. R., and Zhou, X., 2007, Models and exploration methods for major gold deposit types: Exploration 07, 5th Decennial International Conference on Mineral Exploration, Toronto, Canada, Proceedings, p. 691–711.

Roberts, J. L. and Treagus, J. E. 1977. Polyphase generation of nappe structures in the Dalradian rocks of the southwest Highlands of Scotland. Scottish Journal of Geology, 13, 237–254, https://doi.org/10.1144/ sjg13030237

Rogers A. F., 1917, A review of the amorphous minerals: The Journal of Geology, v. 25, p. 515–541.

Rogers G., Dunning G. R. 1991. Geochronology of appinitic and related granitic magmatism in the W highlands of Scotland: constraints on the timing of transcurrent fault movement. Journal of the Geological Society of London, 148 (1991), pp. 17-27

Rooney, A. D., Chew, D. M., And Selby, D. 2011. Re–Os geochronology of the Neoproterozoic–Cambrian Dalradian Supergroup of Scotland and Ireland: Implications for Neoproterozoic stratigraphy, glaciations and Re–Os systematics. Precambrian Research 185(3): 202–214

Rottier, B. and Casanova, V., 2021. Trace element composition of quartz from porphyry systems: A tracer of the mineralizing fluid evolution. *Mineralium Deposita*, *56*(5), pp.843-862.

Rusk, B. 2012. Cathodoluminescent textures and trace elements in hydrothermal quartz. Quartz: Deposits, Mineralogy and Analytics. Springer.

Rusk, B. 2014. Quartz cathodoluminescence: textures, trace elements, and geologic applications. Mineralogical Association of Canada: Short Course 45, 147–168.

Rusk, B. G., Reed, M.H., and Dilles, J.H., 2008a, Fluid Inclusion Evidence for Magmatic Hydrothermal Fluid Evolution in the Porphyry Copper-Molybdenum Deposit at Butte, Montana: Economic Geology, v. 103, no. 2, p. 307–334.

Rusk, B. G., Lowers, H. A. and Reed, M. H. 2008b. Trace elements in hydrothermal quartz: Relationships to cathodoluminescent textures and insights into vein formation. Geology, 36, 547-550.

Rusk, B., Koenig, A. & Lowers, H. 2011. Visualizing trace element distribution in quartz using cathodoluminescence, electron microprobe, and laser ablation-inductively coupled plasma-mass spectrometry. American Mineralogist, 96, 703-708.

Rutter, E. H., 1983. Pressure solution in nature, theory and experiment. Journal of the Geological Society 140, 725e740.

Ryan P. D., Soper N. J., Snyder D. B., England R. W., Hutton D. H. W. 1995 The Antrim–Galway Line: a resolution of the Highland Border Fault enigma of the Caledonides of Britain and Ireland. *Geological Magazine*. 1995; 132(2):171-184. doi:10.1017/S0016756800011730

Sahoo, P. R., Venkatesh, A. S. 2015. Constraints of mineralogical characterization of gold ore: Implication for genesis, controls and evolution of gold from Kundarkocha gold deposit, eastern India. Journal of Asian Earth Sciences, 97, Part A, 136-149.

Sales de Oliveira C. E., Pe-Piper G., Piper, Y. Zhang D. J. W., Corney R. 2017. Integrated methodology for determining provenance of detrital quartz using optical petrographic microscopy and cathodoluminescence (CL) properties. Mar. Petrol. Geol., 88 (2017), pp. 41-53

Sanchez, M. G., Allan, M. M., Hart, C. J. R., Mortensen, J. K., 2014. Structural and tectonic control on mineralization by magnetite-destructive faults in western Yukon and eastern Alaska. Geological Society of America Abstracts with Programs 46 (6), 462.

Sander, M. V. & Black, J. E. 1988. Crystallization and recrystallization of growth-zoned vein quartz crystals from epithermal systems; implications for fluid inclusion studies. Economic Geology, 83, 1052-1060.

Saunders, J. A. 1990. Colloidal transport of gold and silica in epithermal precious-metal systems: Evidence from the Sleeper deposit, Nevada. Geology, 18, 757-760.

Saunders, J. A., 1994, Silica and gold textures in bonanza ore of the Sleeper deposit, Humboldt County, Nevada: Evidence for colloids and implications for epithermal ore-forming processes: Economic Geology, v. 89, p. 628–638.

Saunders, J. A., Schoenly, P.A. 1995. Fractal Structure of Electrum Dendrites in Bonanza Epithermal Au-Ag Deposits. In: Barton, C.C., La Pointe, P.R. (eds) Fractals in the Earth Sciences. Springer, Boston, MA. https://doi.org/10.1007/978-1-4899-1397-5_13

Saunders J. A., Vikre P. J., Unger D. L., and Beasley L. 2010. Colloidal and physical transport textures exhibited by electrum and naumannite in bonanza epithermal veins from western USA, and their

significance (Conference paper). Great Basin evolution and metallogeny: Geological Society of Nevada, 2010 Symposium, May 14-22

Saunders, J. A., Vikre, P., Unger, D.L., Beasley, L., Steininger, R. and Pennell, W., 2011. Colloidal and physical transport textures exhibited by electrum and naumannite in bonanza epithermal veins from western USA, and their significance. In *Great Basin Evolution and Metallogeny. Geol. Soc. Nevada 2010 Symposium* (pp. 825-832).

Saunders, J. A., Hofstra, A.H., Goldfarb, R.J., and Reed, M.H., 2014, Geochemistry of Hydrothermal Gold Deposits, in Holland, H.D., and Turekian, K.K., eds., Treatise on Geochemistry: 2nd edn., v. 13, Oxford, Elsevier Ltd., p. 383–424.

Saunders, J. A. & Burke, M., 2017. Formation and aggregation of gold (electrum) nanoparticles in epithermal ores. *Minerals* 7, 163.

Savastano, L., Chapman, R., and Torvela, T. 2023. Metallogeny of gold (from in-situ to placer) in the Loch Tay area of Central Scotland. 17th SGA Biennial Meeting: Zurich, ETH Zurich.

Schrader, F. S., 1912. A reconnaissance of the Jarbidge, Contact, and Elk mountain mining districts, Elko County, Nevada: U.S. Geological Survey Bulletin 497, 62 p.

Schieferdecker, A.A.G., ed., 1959, Geological nomenclature: The Hague, Royal Geological and Mining Society of Netherlands, 512 p.

ScotGold Resources, 2023. [Online] Cononish Project. Available at: Cononish Project: Scotgold Resources Ltd [Accessed: December 2023]

Shah, S. A.; Shao, Y.; Zhang, Y.; Zhao, H.; Zhao, L. 2022. Texture and Trace Element Geochemistry of Quartz: A Review. *Minerals* 2022, *12*, 1042. https://doi.org/10.3390/min12081042

Shaw J., Torvela T., Cooper M. R., Leslie G., Chapman R. J., 2022. A progressive model for the development of the Cavanacaw Au–Ag–Pb vein deposit, Northern Ireland, and implications for the evolution and metallogeny of the Grampian Terrane. Journal of Structural Geology, V. 161, 2022, 104637

Shikazono N.; 1985. A comparison of temperatures estimated from the electrum-sphalerite-pyrite-argentite assemblage and filling temperatures of fluid inclusions from epithermal Au-Ag vein-type deposits in Japan. *Economic Geology*; 80 (5): 1415–1424. doi: https://doi.org/10.2113/gsecongeo.80.5.1415.

Shimizu, T., Matsueda, H., Ishiyama, D., and Matsubaya, O., 1998, Genesis of epithermal Au-Ag mineralization of the Koryu mine, Hokkaido, Japan: Economic Geology, v. 93, p. 303–325

Shimizu T. 2014. Reinterpretation of Quartz Textures in Terms of Hydrothermal Fluid Evolution at the Koryu Au-Ag Deposit, Japan. *Economic Geology* 2014; 109 (7): 2051–2065. doi: https://doi.org/10.2113/econgeo.109.7.2051

Shore, M. and Fowler, A.D., 1996. Oscillatory zoning in minerals; a common phenomenon. *The Canadian Mineralogist*, *34*(6), pp.1111-1126.

Sibson, R. H. 1981. 'Fluid flow accompanying faulting: Field evidence and models', in: Simpson, D.W. & Richards, P.G. (eds.) *Earthquake Prediction: An International Review* (Maurice Ewing Series, Vol. 4), American Geophysical Union, Washington, D.C., pp. 593–603. doi:10.1029/ME004p0593.

Sibson R. H., 1994. Crustal stress, faulting and fluid flow. m PARNELL, J. (ed.), 1994, Geofluids: Origin, Migration and Evolution of Fluids in Sedimentary Basins, 69 Geological Society Special Publication No. 78, 69-84.

Sibson, R. H., 2001. Seismogenic framework for hydrothermal transport and ore deposition. Society of Economic Geologists. Vol 14, pp. 25-50. https://doi.org/10.5382/Rev.14.02

Sibson, R. H., Moore, J.M. & Rankin, A.H. 1981. 'Seismic pumping: A hydrothermal fluid transport mechanism', Journal of the Geological Society, 138(6), pp. 701–714. doi:10.1144/gsjgs.138.6.0701.

Sibson, R. H., 1987. Earthquake rupturing as a mineralising agent in hydrothermal systems. *Geology*, 15(8), pp.701–704.

Sibson, R. H., Robert, F. & Poulsen, K. H. 1988. High-angle reverse faults, fluid-pressure cycling, and mesothermal gold-quartz deposits. Geology, 16, 551-555. doi: https://doi.org/10.1130/0091-7613(1988)016<0551:HARFFP>2.3.CO;2

Sillitoe, R. H., 1985. Ore-related breccias in volcanoplutonic arcs. *Economic Geology*, 80(6), pp. 1467–1514.

Sillitoe R. H. 2000. Gold-rich porphyry deposits: descriptive and genetic models and their role in exploration and discovery. SEG Reviews, 13, 315–345.

Sillitoe, R. 2010. Porphyry Copper Systems. Economic Geology, 105(1), pp.3-41.

Sillitoe, R.H., 2020. "Chapter 1: Gold Deposit Types: An Overview", Geology of the World's Major Gold Deposits and Provinces, Richard H. Sillitoe, Richard J. Goldfarb, François Robert, Stuart F. Simmons. https://doi.org/10.5382/SP.23.01.

Simmons, S. F., White, N. C. & John, D. A. 2005. Geological characteristics of epithermal precious and base metal deposits. Economic Geology 100th anniversary volume, 29, 485-522.

Simmons, S.F., Tutolo, B.M., Barker, S.L., Goldfarb, R.J. and Robert, F., 2020. Hydrothermal gold deposition in epithermal, Carlin, and orogenic deposits. Geology of the World's Major Gold Deposits and Provinces (Ch. 38), Sillitoe R. H., Goldfarb R. J., Robert F., Simmons S.

Slingerland R. 1984. Role of hydraulic sorting in the origin of fluvial placers. Journal of Sedimentary Research, 1, 137–150.

Smith D. G., 1996. Fractures and mineralisation in the Scottish Dalradian. Unpublished Ph.D. Thesis, University of Manchester.

Soper N. J., Strachan R. A., Holdsworth R. E., Gayer R. A., Greilung R. O. 1992. Sinistral transpression and the Silurian closure of Iapetus Journal - Geological Society (London), 149 (1992), pp. 871-880

Spear, F. S. & Wark, D. A. 2009. Cathodoluminescence imaging and titanium thermometry in metamorphic quartz. Journal of Metamorphic Geology, 27, 187-205.

Spence-Jones C. P., Jenkin, G.R.T., Boyce, A.J., Hill, N.J., Sangster, C.J.S. 2018. Tellurium, magmatic fluids and orogenic gold: an early magmatic fluid pulse at Cononish gold deposit, Scotland. Ore Geol Rev 102: 894–905

Spence-Jones C. P., 2021. Geochemical Signatures of Native Gold Alloys as a Tool for Understanding Auriferous Ore Deposits. Ph.D. thesis, University of Leeds.

Spooner, E. T. C., Fyfe, W.S. & Kerrich, R. 1987. 'Hydrothermal fluids and mineralization in metamorphic terranes', *USGS Research on Mineral Resources, 1987; Programs and Abstracts*, U.S. Geological Survey Circular 995, p. 57.

Sprunt, E. S., Dengler, L. A. & Sloan, D. 1978. Effects of metamorphism on quartz cathodoluminescence. Geology, 6, 305-308.

Spycher N. F. and Reed M. H., 1989; Evolution of a broadlands-type epithermal ore fluid along alternative P-T paths; implications for the transport and deposition of base, precious, and volatile metals. Economic Geology 1989; 84 (2): 328–359. doi: https://doi.org/10.2113/gsecongeo.84.2.328

Stacey, J. S. and Kramers, J.D. 1975. Approximation of terrestrial lead isotope evolution by a two-stage model. Earth and Planetary Science Letters, 26, 207–221, https://doi.org/10.1016/0012- 821X (75)90088-6

Standish, C., Dhuime, B., Chapman, R., Hawkesworth, C., Pike, A., 2014. The genesis of gold mineralisation hosted by orogenic belts: A lead isotope investigation of Irish gold deposits. Chem. Geol. 378–379, 40–51. https://doi.org/10.1016/j. chemgeo.2014.04.012.

Standish, C. D., Chapman, R. J., Moles, N. R., Walshaw, R. D., Sheridan, J. A., 2022. Archaeological applications of natural gold analyses. From: Torvela, T., Lambert-Smith, J. S. and Chapman, R. J. (eds) Recent Advances in Understanding Gold Deposits: from Orogeny to Alluvium. Geological Society, London, Special Publications, 516, https://doi.org/10.1144/SP516-2021-59

Stanton, R. and Russell, R. 1959. Anomalous leads and the emplacement of lead sulfide ores. Economic Geology, 54(4), pp.588-607.

Stefánsson, A. & Seward, T. M. 2004. Gold(I) complexing in aqueous sulphide solutions to 500°C at 500 bar. Geochimica et Cosmochimica Acta, 68, 4121-4143.

Stephenson D., Gould D., 1995. The Grampian Highlands British Regional Geology Series, HMSO, London (1995), p. 262 1995

Stephenson, D., Mendum, J.R., Fettes, D.J. & Leslie, A.G. 2013. The Dalradian rocks of Scotland: an introduction. In: Stephenson, D., Leslie, A.G., Mendum, J.R., Tanner, P.W.G. & Treagus, J.E. (Eds.) The Dalradian Rocks of Scotland. Proceedings of the Geologists' Association, 124, 3-82. https://doi.org/10.1016/j.pgeola.2012.06.002

Stewart, M., Holdsworth, R. E., & Strachan, R. A. 2000. Deformation processes and weakening mechanisms within the frictional-viscous transition zone of major crustal-scale faults: Insights from the Great Glen Fault Zone, Scotland. Journal of Structural Geology, 22(5), 543–560. https://doi.org/10.1016/S0191-8141(99)00164-9

Stewart M., Strachan R. A., Martin M. W., Holdsworth R. E., 2001. Constraints on early sinistral displacements along the Great Glen Fault Zone, Scotland: structural setting, U–Pb geochronology and emplacement of the syntectonic Clunes tonalite. Journal of the Geological Society of London, 158 (2001), pp. 821-830

Strachan, R. A., Smith, M., Harris, A.L. and Fettes, D.J., 2002. *The Northern Highland and Grampian Terranes*. In: Trewin, N.H. (ed.) *The Geology of Scotland*, 4th ed. Geological Society, London, pp.81–147.

Stuwe K., 1998. Tectonic constraints on the timing relationships of metamorphism, fluid production and gold-bearing quartz vein emplacement. Ore Geology Reviews 13 1998 219–228

Sun, S.S., Carr, G.R. and Page, R.W. 1996. A continued effort to improve lead-isotope model ages. AGSO Research Newsletter, 24, pp.19-20.

Tanner P. W. G., Sutherland S. 2007. The Highland Border Complex, Scotland: a paradox resolved. J. Geol. Soc., 164 (2007), pp. 111-116

Tanner P. W. G. 2008. Tectonic significance of the Highland Boundary Fault. Journal of the Geological Society, London, 165, 915-921.

Tanner, P.G., 2012. The giant quartz-breccia veins of the Tyndrum–Dalmally area, Grampian Highlands, Scotland: their geometry, origin and relationship to the Cononish gold–silver deposit. *Earth and Environmental Science Transactions of the Royal Society of Edinburgh*, *103*(1), pp.51-76.

Tanner, P., Thomas, C., Harris, A., Gould, D., Harte, B., Treagus, J., and Stephenson, D. 2013. The Dalradian rocks of the Highland Border region of Scotland. Proceedings of the Geologists' Association, 124, 215–262, https://doi.org/10.1016/j.pgeola.2012.07.013

Tanner P. W. G., 2014a. Structural controls and origin of gold–silver mineralization in the Grampian Terrane of Scotland and Ireland. Geol. Mag. 151 (6), pp. 1072–1094. c Cambridge University Press 2014. https://doi.org/10.1017/S0016756813001131

Tanner, G., 2014b. A kinematic model for the Grampian Orogeny, Scotland. Geological Society, London, Special Publications. Volume 390. Pages 467 – 511. https://doi.org/10.1144/SP390.

Tatsumoto, M., Knight, R.J. and Allegre, C.J. 1973. Time Differences in the Formation of Meteorites as Determined from the Ratio of Lead-207 to Lead-206. 180(4092), pp.1279-1283.

Tchalenko J. 1970. Similarities between shear zones of different magnitudes. Geological Society of America Bulletin 81, 1625–39.

Tera, F. and Carlson, R. W. 1999. Assessment of the Pb–Pb and U–Pb chronometry of the early solar system. Geochimica et Cosmochimica Acta, 63(11-12), pp.1877-1889.

Thomas H. V., Large R. R., Bull S. W., Maslennikov V., Berry R. F., Fraser R., Froud S., Moye R. 2011. Pyrite and Pyrrhotite Textures and Composition in Sediments, Laminated Quartz Veins, and Reefs at Bendigo Gold Mine, Australia: Insights for Ore Genesis. Economic Geology 106 (1): 1–31. doi: https://doi.org/10.2113/econgeo.106.1.1

Thompson J. F. H., Sillitoe R.H., Baker T., Lang J.R. and Mortensen J.K. 1999. Intrusion-related gold deposits associated with tungsten-tin provinces. Mineralium Deposita , 34, 197–217.

Tomkins, A. G. 2013a. A Biogeochemical Influence on the Secular Distribution of Orogenic Gold. Economic Geology, 108, 193-197.

Tomkins, A. G. 2013b. On the source of orogenic gold. Geology, 41, 1255-1256.

Tosdal R. M, Dilles J. H., Cooke D. R.; 2009. From Source to Sinks in Auriferous Magmatic-Hydrothermal Porphyry and Epithermal Deposits. Elements 2009; 5 (5): 289–295. doi: https://doi.org/10.2113/gselements.5.5.289

Tosdal, R.M., Wooden, J.L. and Bouse, R.M., 1999. Pb isotopes, ore deposits, and metallogenic terranes. In: Lambert, D. and Ruiz, J. ed(s). Application of Radiogenic Isotopes to Ore Deposit Research and Exploration. Society of Economic Geologists.

Torvela, T., Chapman, R., Lambert-Smith, J. 2022. An introduction to Recent Advances in Understanding Gold Deposits: from Orogeny to Alluvium: the importance of multi-method approaches and developing a characterisation. Recent Advances in Understanding Gold Deposits: from Orogeny to Alluvium, T. Torvela, J. S. Lambert-Smith, R. J. Chapman

Townley, B. K., Hérail, G., Maksaev, V., Palacios, C., De Parseval, P., Sepulveda, F., Orellana, R., Rivas, P. & Ulloa, C. 2003. Gold grain morphology and composition as an exploration tool: application to gold exploration in covered areas. Geochemistry: Exploration, environment, analysis, 3, 29-38.

Townsend, A., Yu, Z., Mcgoldrick, P. and Hutton, J. 1998. Precise lead isotope ratios in Australian galena samples by high resolution inductively coupled plasma mass spectrometry. Journal of Analytical Atomic Spectrometry, 13(8), pp.809-813.

Treagus J. E. 1991. Fault displacements in the Dalradian of the Central Highlands. Scottish Journal of Geology 27, 135–45.

Treagus, J. E.; Pattrick, R.A.D.; Curtis, S.F. 1999. Movement and mineralization in the Tyndrum fault zone, Scotland and its regional significance. J. Geol. Soc. 1999, 156, 591–604

UC Berkeley Rausser College of Natural Resource. Accessed 11 – Jan- 2024

Urai, J. L., Williams, P.F., Van Roermund, H.L.M., 1991. Kinematics of crystal growth in syntectonic fibrous veins. Journal of Structural Geology 13, 823-836.

Van den Kerkhof, A.M., Kronz, A., Simon, K. and Scherer, T. 2004. Fluid-controlled quartz recovery in granulite as revealed by cathodoluminescence and trace element analysis (Bamble sector, Norway). Contributions to Mineralogy and Petrology, 146, 637–652.

Van Noten, K., Muchez, P., Sintubin, M., 2011. Stress-state evolution of the brittle upper crust during compressional tectonic inversion as defined by successivequartz vein types (High-Ardenne slate belt, Germany). Journal of the Geological Society, London 168, 407-422

van Staal C. R., Dewey J. F., Mac Niocall C., McKerrow W. S. 1998. The Cambrian–Silurian tectonic evolution of the northern Appalachian and British Caledonides: history of a complex west and southwest Pacific-type segment of Iapetus. *Geol. Soc. Lond. Spec. Publ.* 143:199–242

Vearncombe, J.R., 1998. Shear zones, fault networks, and Archean gold. *Geology*, *26*(9), pp.855-858.

Velasquez, A. 2006. Trace element analysis of native gold by laser ablation ICP-MS: A case study in greenstone-hosted quartz-carbonate vein ore deposits, Timmins, Ontario.

Voisey, C. R., Willis, D., Tomkins, A.G., Wilson C.J.L., Micklethwaite, S., Salvemini F., Bougoure, J., Rickard W.D.A. 2020. Aseismic refinement of orogenic gold systems. Economic Geol. 115, 33–50

Vrolijk P., Myers G., 1990. Fluid pressure history in subduction zones: evidence from fluid inclusions in the Kodiak Accretionary Complex, Alaska. elibrary.pcu.edu.ph

Watling, R. J., Herbert, H. K., Delev, D. & Abell, I. D. 1994. Gold fingerprinting by laser ablation inductively coupled plasma mass spectrometry. Spectrochimica Acta Part B: Atomic Spectroscopy, 49, 205- 219.

Watson J. V. 1984. The ending of the Caledonian orogeny in Scotland J. Geol. Soc. Lond., 141 (1984), pp. 193-214

Webb, S., Torvela, T., Chapman, R., Selby, D. and Gooday, R. 2023. An integrated approach towards unravelling the gold mineralisation processes around Ardtalnaig, Scotland. ETH Zürich, 1 September. Zurich: Society for Geology Applied to Mineral Deposits, extended abstracts.

Webb, S., 2024. Understanding metallogeny around Loch Tay, Scotland: insights from isotope geochemistry and petrographic studies (Ph.D. thesis, University of Leeds).

Webb S., Torvela T. M., Chapman R. J., Savastano L. 2024. Textural mapping and building a paragenetic interpretation of hydrothermal veins, with a case study from an Au-Cu-Zn-Pb vein in Glen Almond, Loch Tay, Scotland. Geol. Soc., London, Special Publications Volume 541, https://doi.org/10.1144/SP541-2023-1

Webb, S., Torvela, T., Chapman, R., Savastano, L., Jamieson, R., Boyce, A., Tait, A., Hollis, S. and Pashley, V., 2025. Constraining the fluid sources of gold-bearing veins in orogenic belts using sulfur and lead isotopes: A case study from Loch Tay, Scotland (UK). *Ore Geology Reviews*, p.106619.

Wedepohl, K. and Hartmann, G. 1994. The composition of the primitive upper earth's mantle. In: Meyer HOA, Leonardos OH. eds. Kimberlites, related rocks and mantle xenoliths. Companhia de Pesquisa de Recursos Minerais, Rio de Janeiro, pp.486-495.

Weinberg R. F., Van der Borgh P., Bateman R. J., Groves D. I.; 2005 Kinematic History of the Boulder-Lefroy Shear Zone System and Controls on Associated Gold Mineralization, Yilgarn Craton, Western Australia. *Economic Geology*; 100 (7): 1407–1426. doi: https://doi.org/10.2113/gsecongeo.100.7.1407

Weinberg R. F., Becchio R., Farias P., Suzaño N., Sola A., 2018. Early Paleozoic accretionary orogenies in NW Argentina: Growth of West Gondwana. Earth-Sci. Rev., 187 (2018), pp. 219-247

White, D. E, Brannock, W.W., and Murata, K.J., 1956, Silica in hot-spring waters: Geochimica et Cosmochimica Acta, v. 10, p. 27-59.

Williams-Jones, A. E., Bowell, R. J. & Migdisov, A. A. 2009. Gold in Solution. Elements, 5, 281-287.

Wilson, C. 1994. Crystal growth during a single-stage opening event and its implications for syntectonic veins. Journal of Structural Geology, 16, 1283–1296, https://doi.org/10.1016/0191-8141(94) 90070-1

Wilson, C. J. L., Schaubs, P. M., and Leader, L. D. 2013. Mineral Precipitation in the Quartz Reefs of the Bendigo Gold Deposit, Victoria, Australia. Economic Geology, 108, 259-278.

Wiltschko D. V., Morse J. W. 2001; Crystallization pressure versus "crack seal" as the mechanism for banded veins. *Geology* 2001; 29 (1): 79–82. doi: https://doi.org/10.1130/0091-7613(2001)029<0079:CPVCSA>2.0.CO;2

Wind, S. C., Hannington, M. D., Schneider, D. A., Fietzke, J., Kilias, S. P. and Gemmell, J. B., 2023. Origin of hydrothermal barite in polymetallic veins and carbonate-hosted deposits of the Cyclades continental back arc. Economic Geology, 118(8), pp.1959–1994.

Woodcock, N. H. and Fischer, M., 1986. Strike-slip duplexes. *Journal of Structural Geology*, 8(7), pp.725–735.

Woodhead, J. and Hergt, J. 2000. Pb-isotope analyses of USGS reference materials. Geostandards Newsletter, 24(1), pp.33-38.

Wrighton, T. 2013. Placer Gold Microchemical Characterization And Shape Analysis Applied As An Exploration Tool In Western Yukon. Masters of Science, University of British Columbia.

Yang, L.-Q., Deng, J., Wang, Z.-L., Guo, L.-N., Li, R.-H., Groves, D. I., Danyushevsky, L. V., Zhang, C., Zheng, X.-L. and Zhao, H. 2016. Relationships Between Gold and Pyrite at the Xincheng Gold Deposit, Jiaodong

Peninsula, China: Implications for Gold Source and Deposition in a Brittle Epizonal Environment. Economic Geology, 111, 105-126.

Yardley, B. W. & Cleverley, J. S. 2013. The role of metamorphic fluids in the formation of ore deposits. Geological Society, London, Special Publications, 393, SP393. 5.

Yesares, L., Drummond, D.A., Hollis, S.P., Doran, A.L., Menuge, J.F., Boyce, A.J., Blakeman, R.J. and Ashton, J.H., 2019. Coupling mineralogy, textures, stable and radiogenic isotopes in identifying ore-forming processes in Irish-type carbonate-hosted Zn–Pb deposits. *Minerals*, *9*(6), p.335.

Yuan H., Yuan W., Cheng C., Liang P., Liu X., Dai M., Bao Z, Zong C., Chen K., Lai S. 2016. Evaluation of lead isotope compositions of NIST NBS 981 measured by thermal ionization mass spectrometer and multiple-collector inductively coupled plasma mass spectrometer.

Zezin D. Y., Migdisov A. A., Williams-Jones A. E., 2011. The solubility of gold in H2O–H2S vapour at elevated temperature and pressure. Geochim. Cosmochim. Acta, 75 (18), pp. 5140-5153

Zhang, Y., Schaub, P. M., Zhao, C., Ord, A., Hobbs, B. E. & Barnicoat, A. C., 2008. Fault-related dilation, permeability enhancement, fluid flow and mineral precipitation patterns: numerical models

Zheng, Y. F. and Hoefs, J., 1993. Effects of mineral precipitation on the sulfur isotope composition of hydrothermal solutions. *Chemical Geology*, *105*(4), pp.259-269.

Zhong, R., Brugger, J., Tomkins, A. G., Chen, Y. & Li, W. 2015. Fate of gold and base metals during metamorphic devolatilization of a pelite. Geochimica et Cosmochimica Acta, 171, 338-352.

Appendix

Appendix 1.

Intensely fractured outcrops – Upper Calliachar Burn

Mineralised 330-trending joints – Calliachar Burn

Pattern of joints in Lower Calliachar Burn

Channel trace – Lead Trial main vein outcrop

Supporting bespoke chart for section 7.2.4:

Dilational jogs scenario – case 1

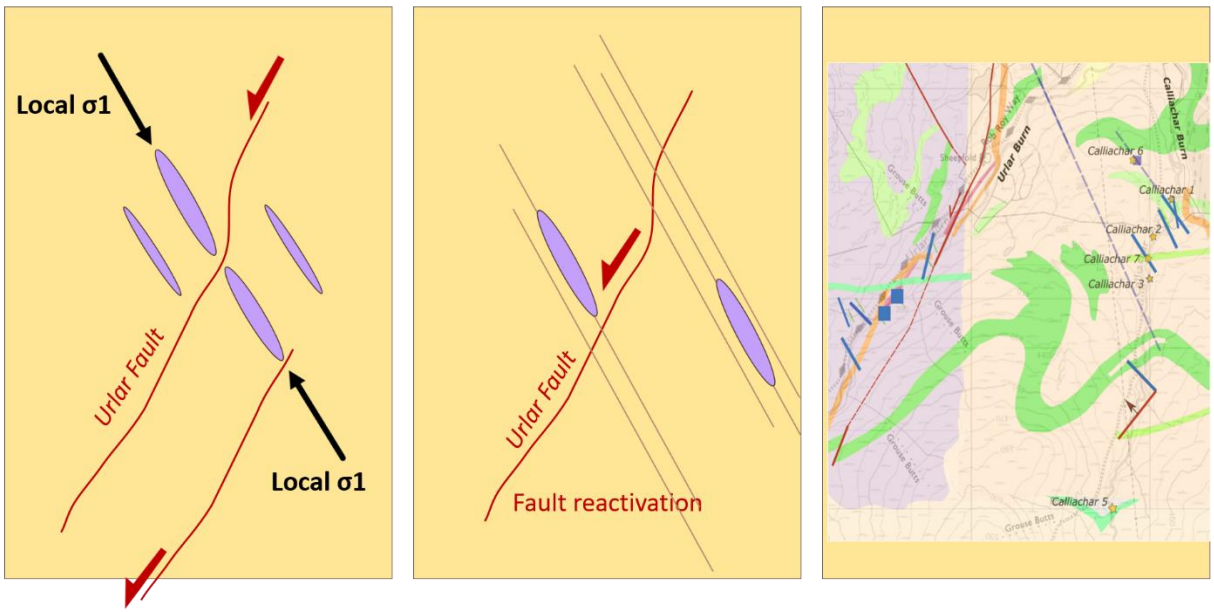

Appendix 2.

SEM-CL images – vein samples from Calliachar Burn

LSCL2, full montage (panorama) SEM map *– BSE and CL-Blue*

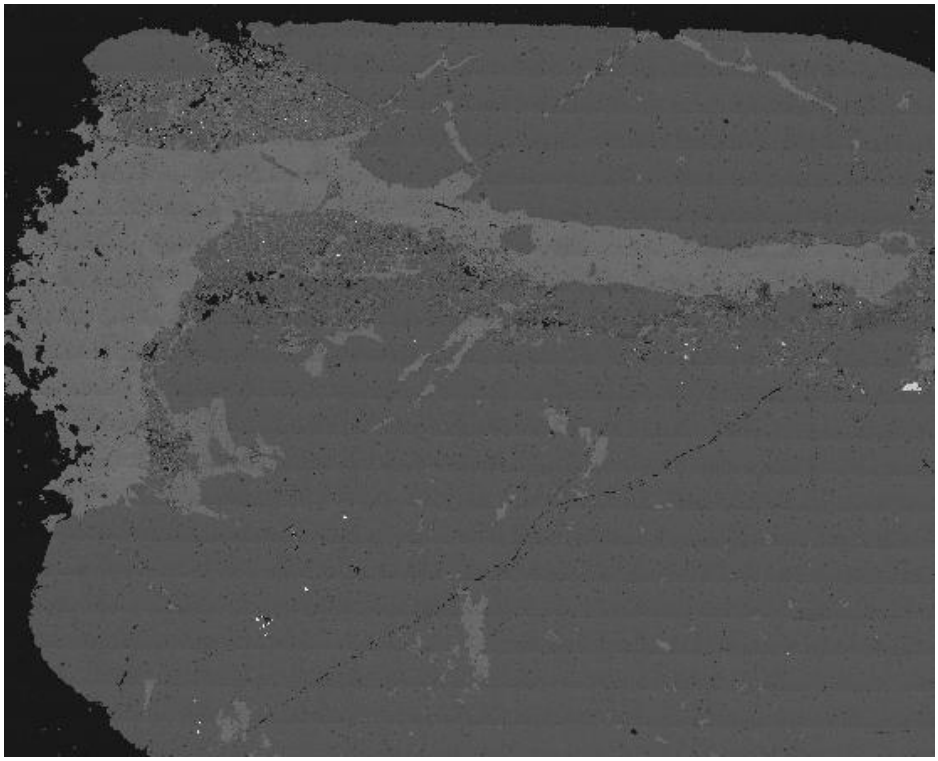

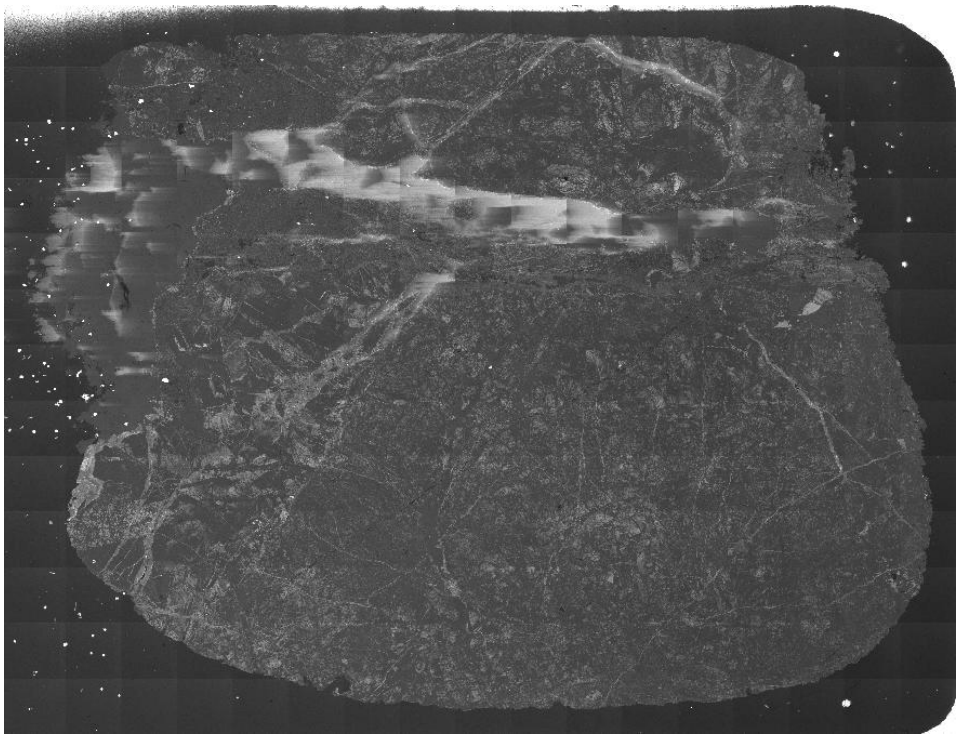

SEM-CL images – vein samples from the Lead Trial

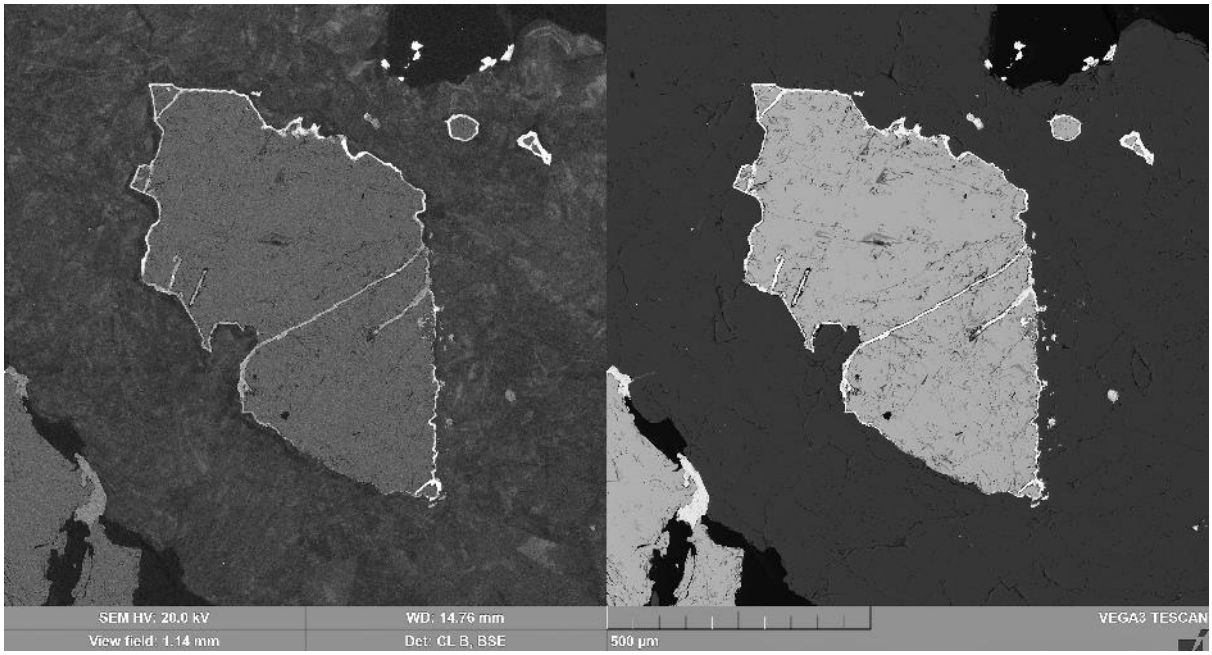

Sphalerite surrounded by quartz.

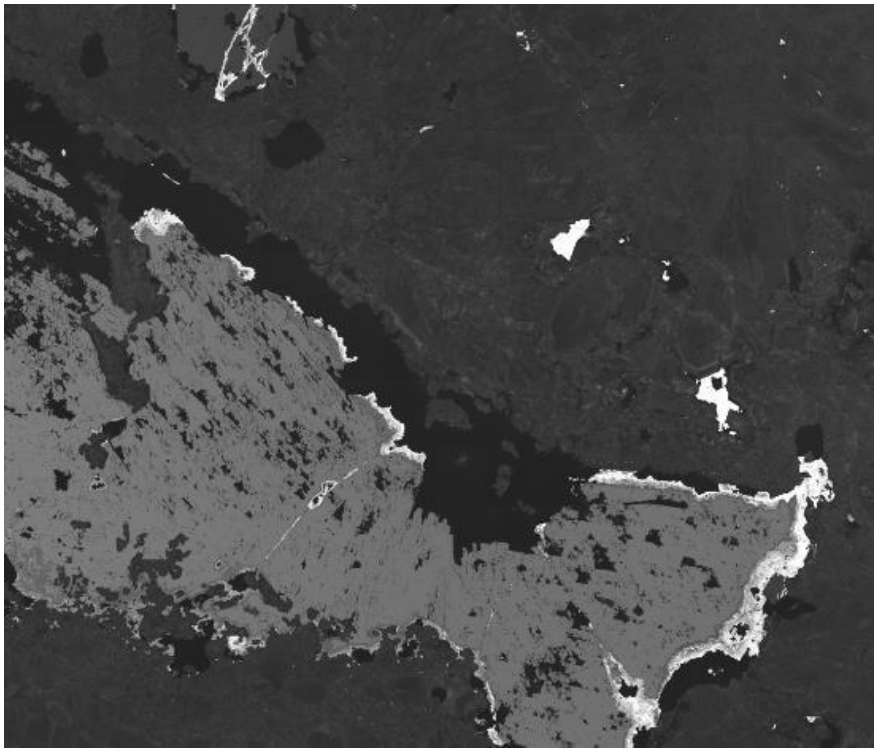

Galena surrounded by quartz.

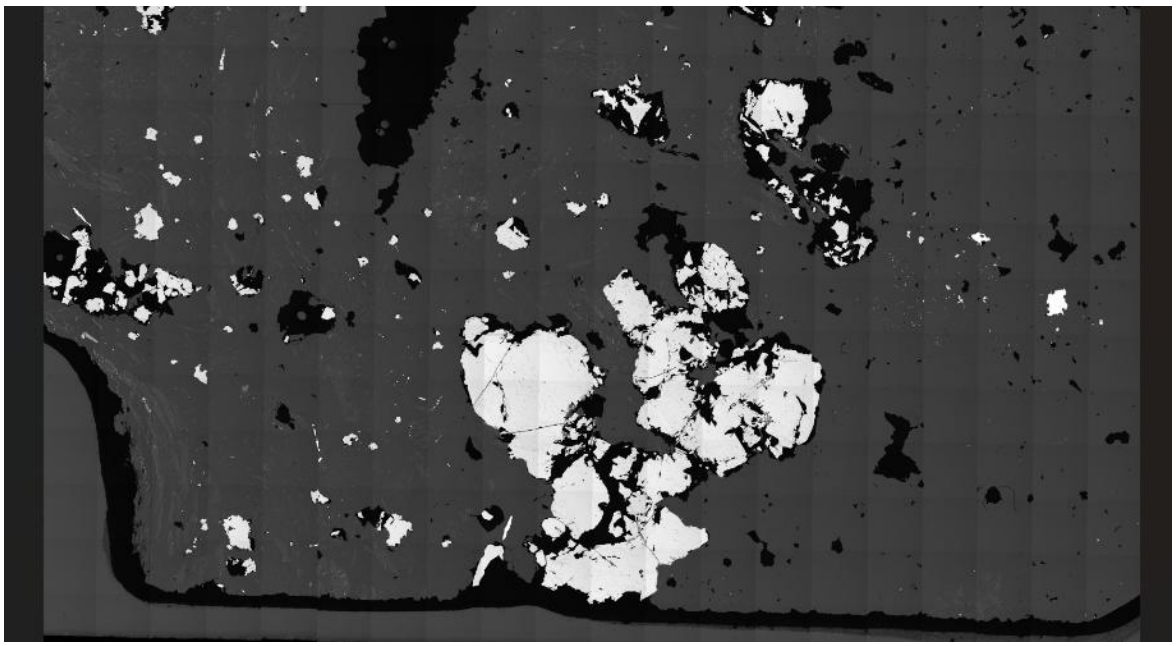

Sphalerite and quartz in the LSLTA2 thin section.

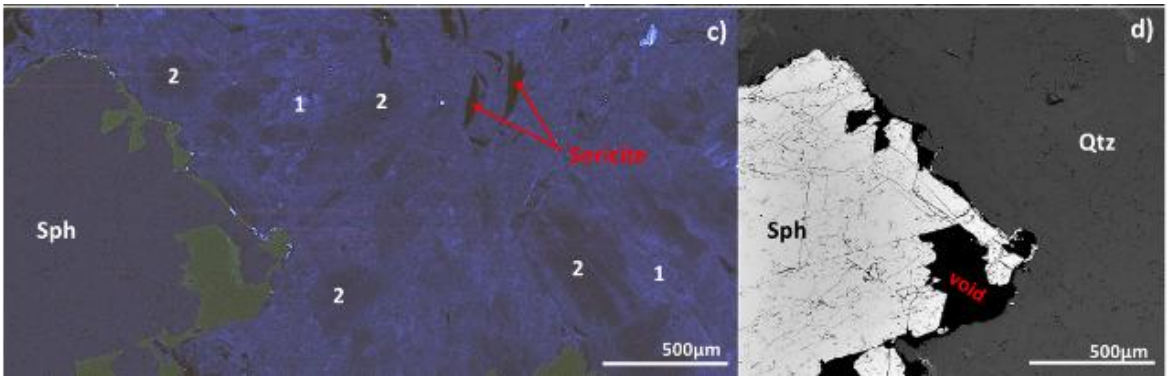

Sphalerite, quartz and sericite.

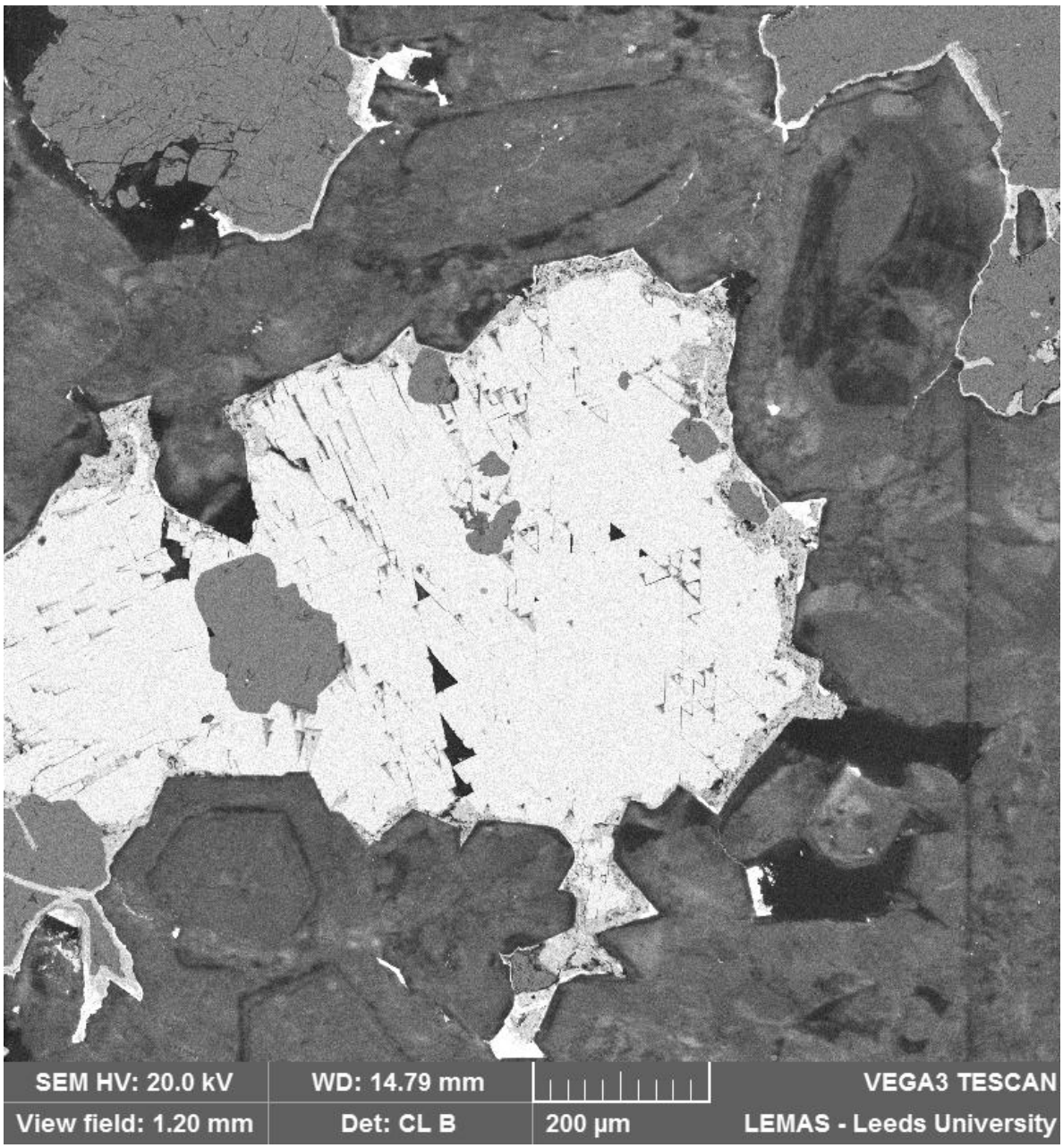

28461 thin section. Galena (bright, with cleavage), quartz (with visible zonation) and sphalerite.

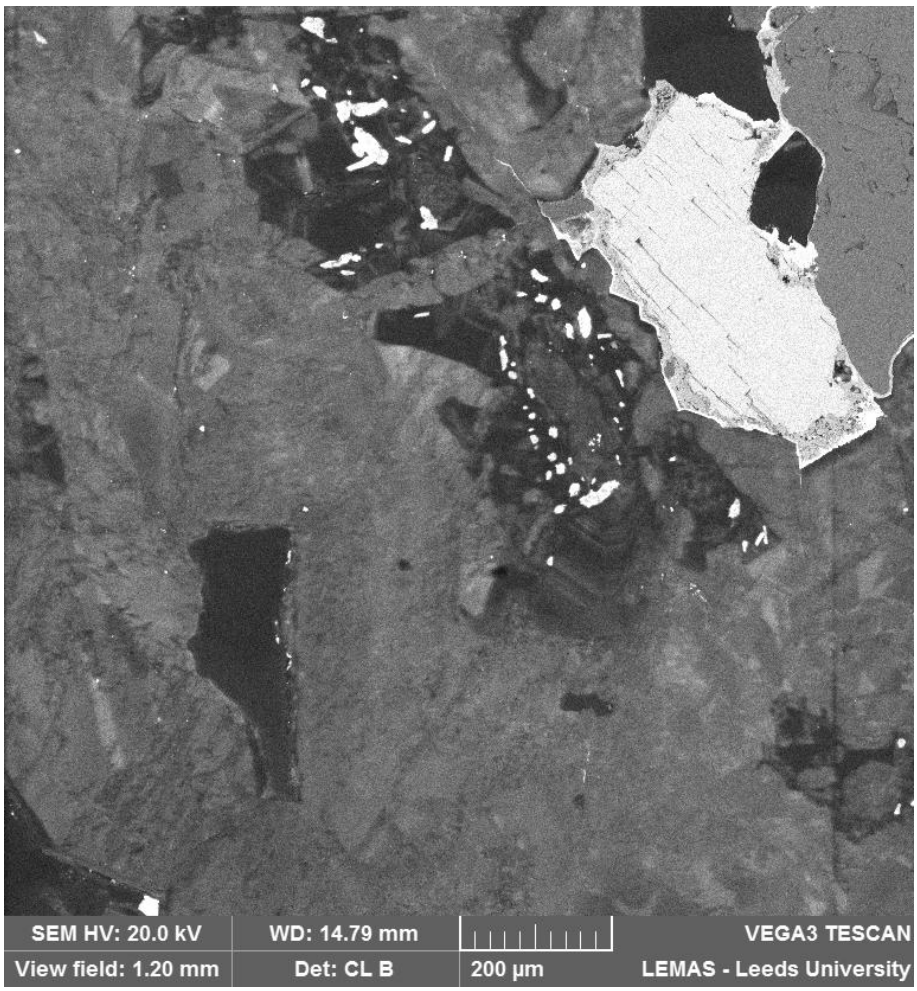
SEM HV: 20.0 kV
WD: 14.79 mm
VEGA3 TESCAN
View field: 1.20 mm
Det: CL B
200 µm
LEMAS - Leeds University

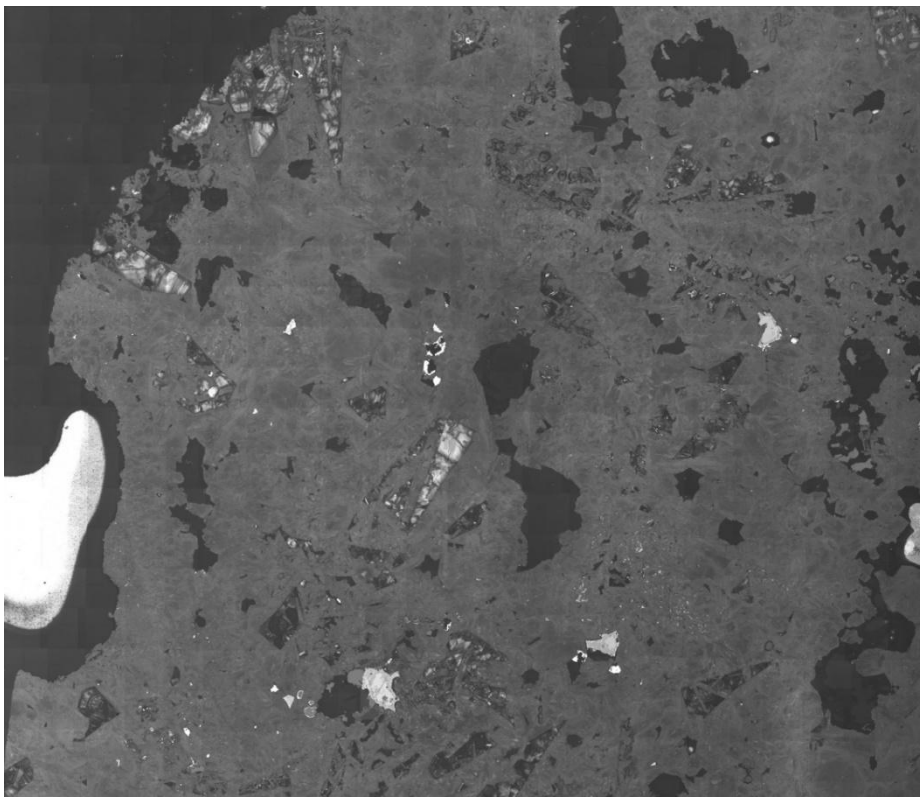

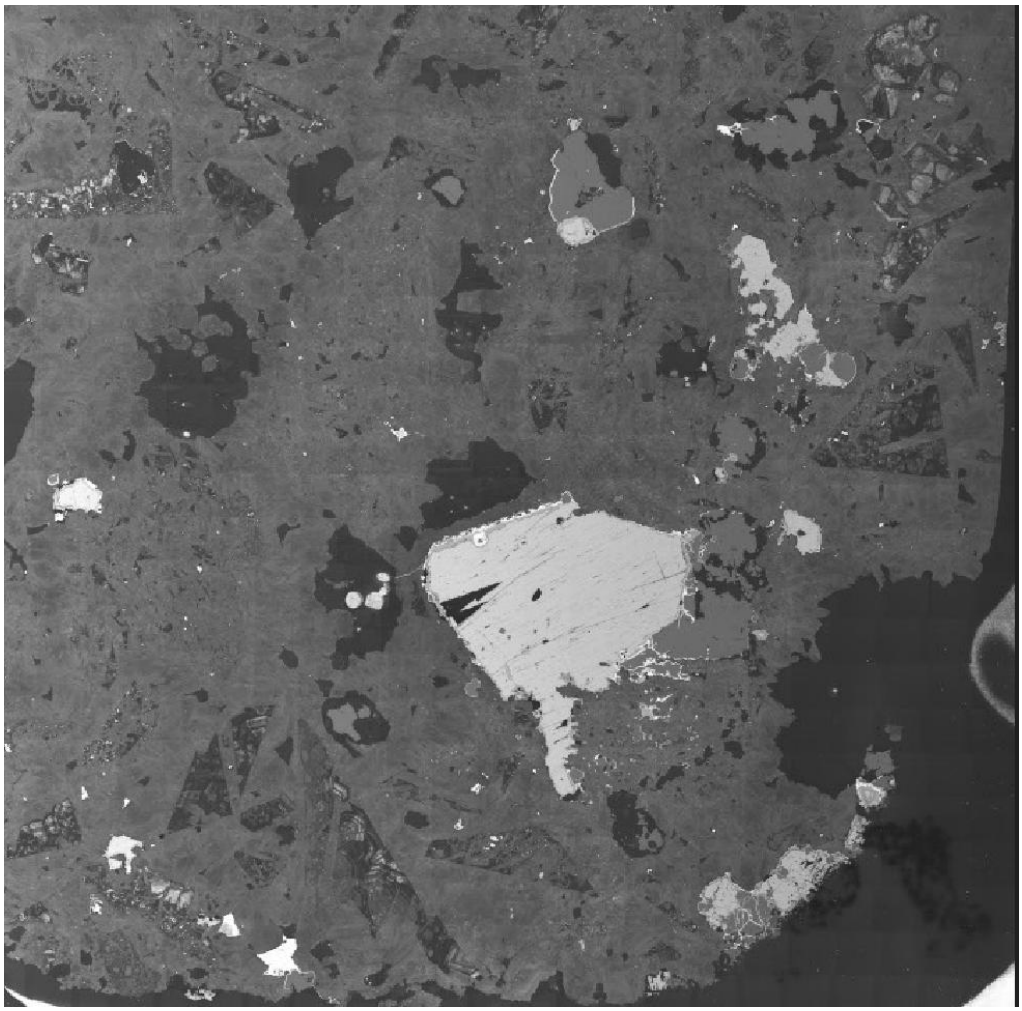

Coire Buidhe, LS2. *BSE panorama map.*

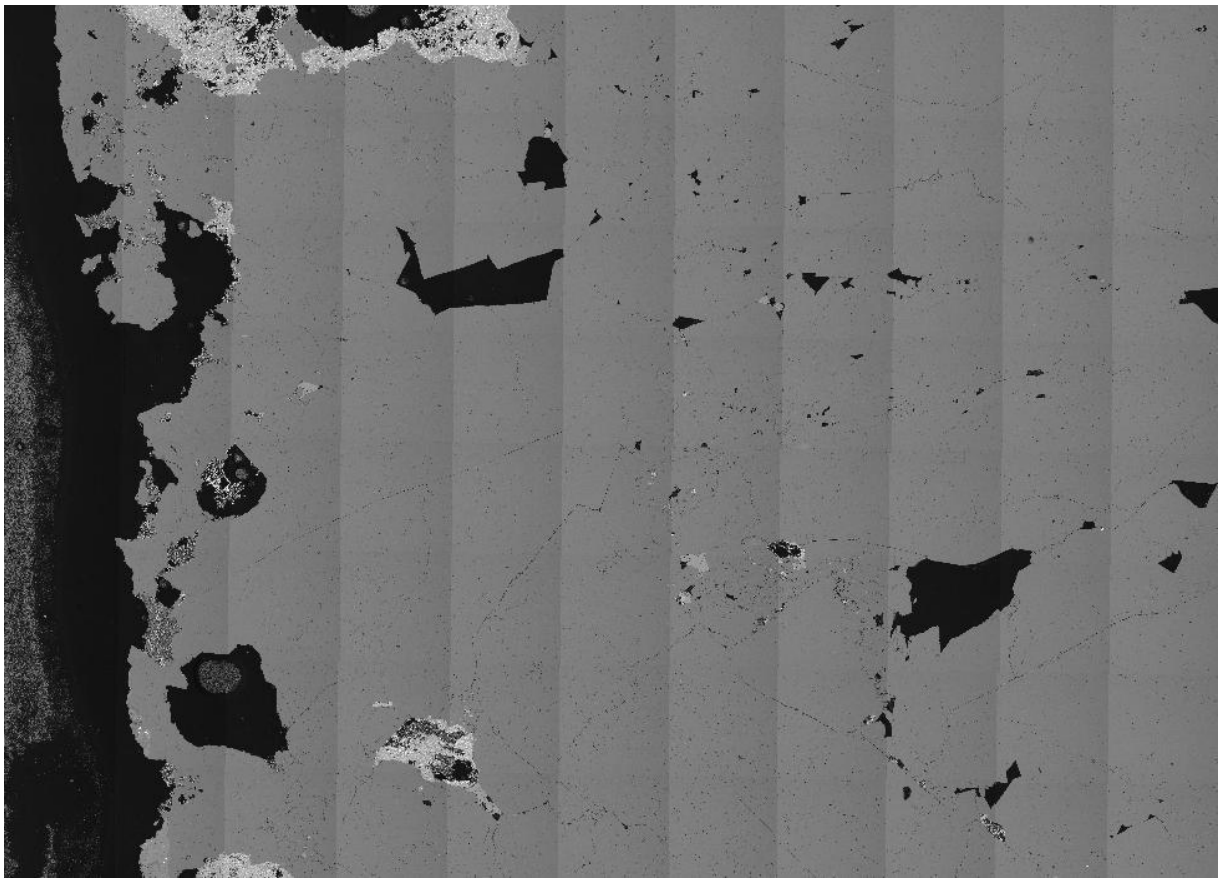

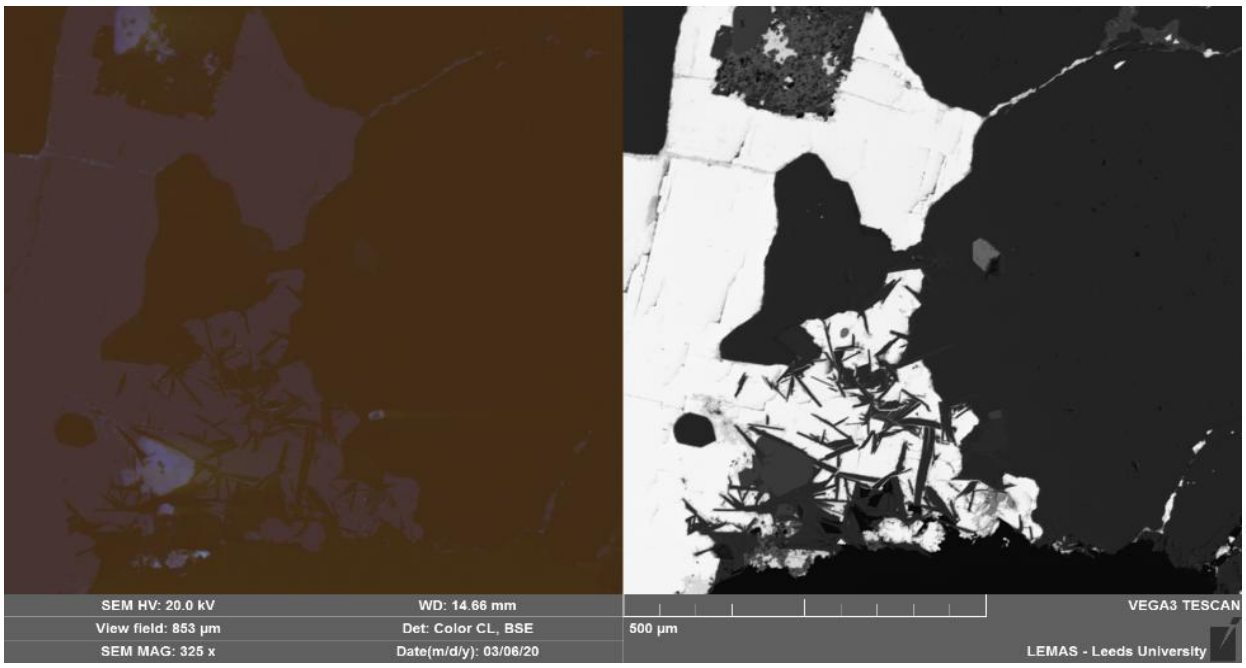

BSE image (right) displays the "presumed" lillianite (needle-shaped mineral)

Appendix 3.

LA-ICP-MS

Determination of the Limits Of Detection (LODs)

The detection limits (LODs) for the LA-ICP-MS analyses presented in this thesis can be estimated from the processed Sills output files. In these files, detection limits are reported as "less-than values", which are generated for both standards and unknown samples and may vary slightly between individual ablation runs.

To derive representative detection limits for each element, all reported less-than values obtained from the reference materials need to be compiled. The AuRM gold reference material was used for elements certified in the AuRM standard, whereas NIST SRM 610 and MASS-1 reference materials were used for elements not in AuRM. The reported less-than values can be averaged for each element to obtain a representative detection threshold expressed as a weight-to-weight (wt/wt) ratio.

These average detection thresholds can subsequently be converted into concentrations in parts per million (ppm) using the calibration from the standards. The resulting values can be adopted as the approximate analytical detection limits for each element.

The detection limit is defined as three times the standard deviation (3σ) of the gas blank signal. To provide a more reliable threshold for quantitative interpretation, a limit of quantification (LOQ) may also be considered, defined as ten times the detection limit ($10 \times DL$).

LA-ICP-MS reduced data (organised by sample locality)

Samples	Label	V51	Cr53	Mn55	Fe57	Co59	Ni60	Cu63	Zn66	As75	Se82	Mo95	Ag107	Cd111	Sn118	Sb121	Au197	Hg202	Tl205	Pb208	Bi209	Th232	U238	Rh103	Pd105	Re187	Ir193	Pt195	Te125
		µg/g	µg/g	µg/g	µg/g	µg/g	µg/g	µg/g	µg/g	µg/g	µg/g	µg/g	µg/g	µg/g	µg/g	µg/g	µg/g	µg/g	µg/g	µg/g	µg/g	µg/g	µg/g	µg/g	µg/g	µg/g	µg/g	µg/g	µg/g
Almond at hydro_10	RJC137-01_01							0.574162					336803			3.18771	601287.4	61905.85					0.020478						
Almond at hydro_10	RJC137-01_02a	0.374312		2.186197	189.77		0.51933	16.21962	1.35658				186904.5			0.405676	810121.1	2762.407		0.792479	0.300689	0.014828	0.012755						
Almond at hydro_10		12.70394		61.10854	4854.135	1.37577	9.750262	26.07448	40.2933	8.978747			198070.6			0.926147	794274.7	2613.137		21.73444	1.651382	2.606625	0.192588						
Almond at hydro_10	RJC137-01_02b						0.207891	10.04491					189440.3			0.767423	807694.6	2854.057											
Almond at hydro_10		1.61348		52.84429	1008.818	0.298809	1.051252	14.083	5.558663	6.655307			201017			0.573305	793974.1	3901.488		15.54965	0.089628	0.224342	0.069618						
Almond at hydro_10	RJC137-01_03							22.52135					254852.5			1.824106	743940.4	1182.725											
Almond at hydro_10	RJC137-01-04							17.83151					285177.8			2.345323	712555.4	2246.55		0.082507									
Almond at hydro_10	RJC137-01-06						0.310168	19.47443					240628.5			2.37005	756644.1	2705.314									0.005583		
Almond at hydro_10	RJC137-01-07							20.89871					260320.3			1.663977	737306.4	2350.813											
Almond at hydro_10	RJC137-01-09							23.51802					236657.1			60.31462	761053	2206.112											
Almond at hydro_10	RJC137-01-10						0.396011	5.376168				1.003438	374535.6	1.003438		0.16399	625372	82.59741											1.75838
Almond at hydro_10	RJC137-01-11							117.3056					84086.09				912291.7	3502.096							2.790073				
Almond at hydro_10	RJC137-01-12							13.5739					239796			11.79603	759679.9	498.6969									0.010685		
Almond at hydro_10	RJC137-01-13							157.4201					117512.2			0.5756	881559.8	769.9976											
Almond at hydro_10	RJC137-01-14	2.717678		13.5894	949.0016	0.803385	1.775127	12.27867	9.927214	0.773916			375882.2			12.99941	617191.3	5917.203	0.077616	4.525437	0.037819	0.569057	0.162263				0.006773		
Almond at hydro_10		40.29499	29.50571	258.3534	14441.67	7.725108	22.1137	60.69746	89.05663	13.17201		0.660456	380021.2	0.660456	1.210226	9.533392	601150.5	3808.15	0.185138	38.38341	0.170672	5.250134	1.559957				0.01077		
Almond at hydro_10	RJC137-01-16	77.91198	46.24807	116.4	14180.22	4.175433	20.68023	43.29962	124.6392	18.40063		0.48454	302603.7	0.48454	1.979346	1.537285	681435.2	1300.597	2.025926	19.38071		0.987884	0.349951				0.005657		1.270654
Almond at hydro_10	RJC137-01-17							114.5243				0.143818	96828.41	0.143818		0.119296	900193.2	2863.374			0.055863								
Almond at hydro_10	RJC137-01-18	0.136069		0.427373	36.30842		0.320596	11.85308					251974.3			11.08367	741083.5	6881.86		0.167516		0.01194					0.016977		
Almond 12 (auchnafree A3)	RJC137-04-02							2.912772					379353.2			5.355765	611600.3	9038.209									0.006842		
Almond 12 (auchnafree A3)	RJC137-04-03							7.539219					276029.7			21.81867	715996.2	7944.425											0.328436
Almond 12 (auchnafree A3)	RJC137-04-04	2.656817		6.574767	1805.849	0.150716	0.363814	59.74485	49.21412	142.3216		0.646102	180877.5	0.646102		1.100848	812173	4843.549		35.13174	0.144662	0.028173	0.104028		0.057565				1.199355
Almond 12 (auchnafree A3)								30.12335		4.503272			183021.6			1.145918	811787.2	5155.435											
Almond 12 (auchnafree A3)	RJC137-04-06							32.73608					227640.8			20.0318	769111.5	3194.977											
Almond 12 (auchnafree A3)	RJC137-04-07							5.327171					287349.9			31.90531	707500.4	5111.868			0.331602						0.008223		0.248681
Almond 12 (auchnafree A3)	RJC137-04-12							29.12453					211427.6			1.014586	785285	3257.268											
Almond 12 (auchnafree A3)	RJC137-04-14							13.75961					288696.8			9.123422	706829.9	4450.382					0.005479	0.019958					
Almond 12 (auchnafree A3)	RJC137-04-15	3.151255		25.97144	1439.268	0.438134	2.23707	46.02797	21.81576	3.246546			290219.1			9.84191	705140	3086.174		2.295282		0.203999	0.141947		0.093911				
Almond 12 (auchnafree A3)	RJC137-04-16	1.555086		8.468942	1169.401	0.148775	0.487377	61.66514	10.22133	3.69892			261900.4			1.151734	728398.6	8429.586		14.42603		0.146742	0.07828						
Almond 12 (auchnafree A3)	RJC137-04-17			0.389283			0.160993	125.1171					109418.9			0.154591	887495.6	2959.585							0.084848		0.007659		
Almond 12 (auchnafree A3)	RJC137-04-19							10.73994					259969.6			3.678846	721802.5	18213.53					0.009799						
Almond 12 (auchnafree A3)	RJC-136-6-01							36.55421					165058.4			8.773005	822141.8	12754.53											
Almond 12 (auchnafree A3)	RJC-136-6-02							79.76957	1.186477				140583.8			8.6464	854863.5	4463.13											
Almond 12 (auchnafree A3)	RJC-136-6-04							148.6806					89696.29			0.909213	886220.8	23932.98		0.036345									0.34482
Almond 12 (auchnafree A3)	RJC-136-6-06							71.48092	0.356391				152985.9			2.761695	843709.9	3229.526					0.010659						
Almond 12 (auchnafree A3)	RJC-136-6-09							471.514	0.612283				39784.98	0.764839		4.154	928900	30837.75							0.189361				
Almond 12 (auchnafree A3)	RJC-136-6-10a					0.019621		182.8809					54781.89		0.210607	1.438658	939591.8	5441.778											
Almond 12 (auchnafree A3)	RJC-136-6-10b							184.1573					53864.29			1.795232	929093.7	16856.08											
Almond 12 (auchnafree A3)	RJC-136-6-14a							12.89463					173595.3			4.718298	812578.4	13808.4			0.015328								0.33465
Almond 12 (auchnafree A3)	RJC-136-6-14b				9.447756			2.579278					177529.7			3.874122	806613.1	15840.94					0.030205						0.285665
Almond 12 (auchnafree A3)	RJC-136-6-15							2.821436					163087			1.496174	521883.3	315025.4											
Almond trib_11_near 5	RJC-135_17-01		0.723843			0.01227		25.10993	0.9168				240214.4	0.057205		6.729108	750174.5	9577.532	0.024121	0.04967									
Almond trib_11_near 5	RJC-135_17-02		0.721609					5.811192					364168.4	0.135394		4.384576	626924.5	8895.622	0.008006		0.017242		0.024019						0.445749
Almond trib_11_near 5	RJC-135_17-03	0.032683						7.462531	13.83746			0.040647	341020.5			5.095182	651989.4	6963.51		0.024575					0.058899				0.403384
Almond trib_11_near 5	RJC-135_17-04	0.00769	0.680334			0.0055		24.02627	0.918877			0.044464	274725	0.054896		3.221055	722218	3027.381											0.658767
Almond trib_11_near 5	RJC-136-13-01							34.2961		0.487652			75004.01				906563.1	18397.75	0.036713				0.024651						0.303299
Almond trib_11_near 5	RJC-136-13-02							22.8073					184693.7			15.24747	648859.3	166409		0.031877									
Almond at vein_5	RJC-135-15-1							19.1529				0.081227	190165.6			11.7271	785369	24434.51											
Almond at vein_5	RJC-135-15-2							72.033					77324.15			2.247064	897873.4	24727.21		0.05889							0.00783		
Almond at vein_5	RJC-135-15-3							26.86884					189007.5	0.20621		2.18472	805343.2	5620.001		0.042297	0.016334								
Almond at vein_5	RJC-135-15-4							29.04125					186007.3			3.805354	801555.2	12404.63		0.097442									
Almond at vein_5	RJC-135-15-5							36.73323		27.0733			165932.7	0.500241		43.42925	825645.6	8313.325		0.341188	0.083792								0.266783
Almond at vein_5	RJC-135-15-6							64.1597					133170.5			5.711845	859852.3	6905.693		1.445519	0.0324								0.18041
Almond at vein_5	RJC-135-15-7							49.64354		19.20015			154264.5	1.549306		12.2263	818333.4	27298.87		2.347404	17.8437								0.388974
Almond at vein_5	RJC-135-15-8			2.5034	56.73579			4.383419					192676.3			0.968055	803084.1	4174.81		0.083824		0.058482							
Almond at vein_5				28.29634	1911.259	1.543381	6.155751	20.43656	16.92475	7.556693			187510.3			1.204434	799853.8	10634	0.059827	3.834843	0.024593	0.850525	0.12128						
Almond at vein_5	RJC-135-15-10							39.25037	1.189749				188342.4			7.476116	801985.6	9623.403		0.357972					0.063049				0.257488
Almond at vein_5	RJC-135-15-11							9.39151					200519.4			1.608993	788714.2	10755.2											0.211689
Almond at vein_5	RJC-135-15-12							6.888113					213524.7			10.87567	756429.4	30028.16					0.01002						
Almond at vein_5	RJC-135-15-13							120.7065	0.570688				109140.9	7.686784		2.86766	808748.7	81978.51		0.034744	0.012453				0.045328				
Almond at vein_5	RJC-135-15-14			0.47349				93.62731					94686.52			0.107373	896829.4	8388.073		0.07129	0.043762	0.35196	0.038194		0.23905				1.010753
Almond at vein_5		1.764206		10.36153	314.476		0.146061	73.54432	0.458409	1.233669			95736.72				890727.6	13097.99		0.768678	0.14907	32.14876	1.3923		0.216104				1.020706
Almond at vein_5	RJC-135-15-15	0.076338			16.67297			25.55685				0.140668	156314.6				831558.1	12079.75		0.795897			0.10099						
Almond at vein_5	RJC-135-15-16							23.90127		0.490278			180914.5			7.328568	757657.9	61395.92											
Almond at vein_5	RJC-135-15-17							49.10683	0.360544				147402			1.434503	831351.6	21195.3											0.215854
Almond at vein_5	RJC-135-15-18							394.7024					78625.37				911182.1	9797.863											
Almond at vein_5	RJC-136-7-01							23.33342					166505.8			15.11134	743309.9	90145.84											
Almond at vein_5	RJC-136-7-02							38.84913					179399.5	0.249552		11.6175	798686.3	21863.5											
Almond at vein_5	RJC-136-7-03						0.104259	18.66672					208017.7			3.929085	788206.7	3752.864									0.00805		
Almond at vein_5	RJC-136-7-04							33.53001					185580			11.97402	798613.1	15761.38											
Almond at vein_5	RJC-136-7-05							22.71562		0.447358			186644.1			7.479323	807037.7	6287.145		0.104552									0.307249
Almond at vein_5	RJC-136-7-06							39.5717					173272			13.06554	812971.2	13704.12											
Almond at vein_5	RJC-136-7-07							74.96057					136193.2			8.6307	843259.2	20463.87											0.222609
Almond at vein_5	RJC-136-7-08							3.934896				0.128826	234276.5			5.199906	754688.6	11025.67											
Almond at vein_5	RJC-136-7-09	10.84615		64.35382	7667.465	0.914299	1.705881	362.1665	4.816086			0.392619	37766.6			0.080531	932310.5	21799.79		0.201183	0.041289	0.083273	0.035922	0.025388	3.670551			0.494893	5.790407
Almond at vein_5	RJC-136-7-10							21.43934					204948.8			19.63216	778115.9	16893.88											0.366894
Almond at vein_5	RJC-136-7-11							188.504					53703.12			0.291902	939094.5	7013.307			0.031862				0.196705				
Almond at vein_5	RJC-136-7-12							35.66623					191641.3			15.28749	805715.3	2592.146											0.33017
Almond at vein_5	RJC-136-7-13							22.368					161264.5			2.314665	822042.5	16668											0.372328
Almond at vein_5	RJC-136-7-14							44.94375					170584.4			18.18793	813899.5	15452.5							0.423929				
Almond at vein_5	RJC-136-7-15							49.25558		0.571058			168013.2			6.804537	818822.1	13108.07											

[322]

Samples	Label	V51	Cr53	Mn55	Fe57	Co59	Ni60	Cu63	Zn66	As75	Se82	Mo95	Ag107	Cd111	Sn118	Sb121	Au197	Hg202	Tl205	Pb208	Bi209	Th232	U238	Rh103	Pd105	Re187	Ir193	Pt195	Te125
		µg/g	µg/g	µg/g	µg/g	µg/g	µg/g	µg/g	µg/g	µg/g	µg/g	µg/g	µg/g	µg/g	µg/g	µg/g	µg/g	µg/g	µg/g	µg/g	µg/g	µg/g	µg/g	µg/g	µg/g	µg/g	µg/g	µg/g	µg/g
Calliachar_nugget	RJC137-10-03					0.079517		37.34684					241280.4			179.0159	757558.3	944.7826		0.075905									
Calliachar_nugget	RJC137-10-04	0.234202		0.516104	173.7512	0.950825	1.012609	8.247729	1.927784	10.36707			378552.3			31.32004	615812.2	5099.263		307.6678		0.122735	0.051123						
Calliachar_nugget	RJC137-10-06				21.27861			0.771402		1.520618			474988.7			0.700752	492859	32124.61		2.624618			0.013091						
Calliachar_nugget	RJC137-10-07							27.29922					251558			1.738435	740229.2	8183.757											
Calliachar_nugget	RJC137-10-08			0.374398	62.57543			0.755625					340643.1				635724.1	23566.7		2.378917			0.015431						
Calliachar_nugget		9.655419	7.539436	30.3162	5724.457	2.042598	9.276063	103.1927	76.99732	4.89069		0.263779	330353.5	0.263779		0.284946	629962.6	33677.33	0.155514	35.73303	0.090873	0.47772	0.578247						0.354484
Calliachar_nugget	RJC137-10-09							33.98882			3.553021		255017.5			163.2004	742151.5	2630.265											
Calliachar_nugget	RJC137-10-14							5.302815		3.609696			288470.4			53.31911	694758.3	16709.07											
Calliachar_nugget	RJC-138-03-1	0.363538	2.306274	0.847143	38.22135	0.041817	0.219691	11.7691	0.674389			0.031221	285709.1	0.052031		38.69357	707807.1	6390.477		0.035047		0.020274	0.014951						
Calliachar_nugget	RJC-138-03-2							6.814268				0.059924	371781.5			117.8398	619146.8	8949.454											
Calliachar_nugget	RJC-138-03-3	0.020643	0.521634			0.025466		12.63004				0.026377	276548.6			7.493457	722140.8	1290.065	0.007796					0.02443					
Calliachar_nugget	RJC-138-03-8					0.006863		45.47005				0.04209	168903.6	0.036372		16.27225	830212.2	822.7034							0.129943	0.011258			
Calliachar_nugget	RJC-138-03-10	0.046506	1.488874			0.000991		7.21323					305433.9	0.150607		47.04237	688114.9	6394.782	0.005153										0.510388
Calliachar_nugget	RJC-138-03-11	0.043851	1.102501			0.00229		7.227488					304542	0.205458		46.87309	689120.7	6281.389											0.516382
Calliachar_nugget	RJC-138-03-12					0.007327		44.43618				0.066518	166732.8	0.099354		3.453995	831202.4	2017.354								0.006574			
Calliachar_nugget	RJC-138-03-13							37.63459				0.061266	215620.4			16.17501	782862.8	1462.832			0.138828					0.007585			
Calliachar_nugget	RJC-138-03-14		0.327708					37.42709				0.050908	215522.8			16.08784	782964.7	1458.542			0.138331					0.00817			
Calliachar_nugget	RJC-138-03-15a	0.025818	0.246187		7.169287			31.55009					192900.1	0.202552		8.401156	805791.3	1260.942		0.070766						0.007678			
Calliachar_nugget	RJC-138-03-15b					0.006434		15.81276				0.030583	196986.9	0.035345		4.466946	801059.4	1934.416			0.074115								
Calliachar_nugget	RJC-138-03-18		2.775455			0.015902		28.09729			5.225465	0.051329	225531.6	0.187622		3.01939	771148.2	3280.813											
Calliachar_nugget	RJC-138-03-19	0.006885						27.31329				0.006969	257344.6	0.01101		30.77337	740670.6	1927.803	0.0126							0.018733			
Calliachar_nugget	RJC-138-03-20	0.172849		0.662476	58.49474		0.236635	14.5939	0.776248				262948.4	0.343386		5.764799	734945.8	2025.051	0.011516	0.083298									
Calliachar_nugget	RJC-138-03-21a	0.167942		0.679087	60.5659		0.255836	14.64423	0.78432				264014.7	0.314054		5.788009	733876.1	2026.293	0.01297	0.101412									
Calliachar_nugget	RJC-138-03-21b							21.66263					290108	0.06758		41.69701	704984.9	4844.198	0.011048										
Calliachar_nugget	RJC-138-03-26	0.053597	0.711999					16.01157					266257.6	0.284118		7.143068	727083.3	6634.891					0.005483			0.011094			
Calliachar_nugget	RJC-138-03-27	1.172782		1.374154	545.4152		1.355397	26.85186	10.26141				272432.4	0.377944		4.11645	714475.5	12500.38		0.758613		0.132542	0.07294						
Calliachar_nugget	RJC-138-03-28							2.480289				0.032424	424938.7	0.328678		139.0128	565157.3	9764.321											
Calliachar_2	RJC-136-14				10.45727			1.223425				0.384259	231754.2			18.08669	759945.3	8269.306		1.028655	0.012885						0.005683		
Calliachar_2	RJC-136-14							34.30012					160991.7			16.31872	716163.1	122794.3			0.015353								0.215866
Calliachar_2	RJC-136-14							146.9604					93268.25			12.54916	869603.3	36968.81											0.179546
Calliachar_2	RJC-136-14							19.31179					263408.1			253.094	733995.7	2323.729											
Calliachar_2	RJC-136-14							17.60308					230497.3			30.16506	733806.2	35648.71									0.005329		
Calliachar_2	RJC-136-14			0.328494				23.21632					236667			12.68217	729895.5	33401.08		0.042593	0.095917								
Calliachar_2	RJC137-12-01						0.187604	16.51852	1.094703				325924.2			50.85753	668510.2	5496.909									0.005595		
Calliachar_2	RJC137-12-03							48.31954	2.02918				192077.9			12.90923	806800.4	1058.123											0.334465
Calliachar_2	RJC137-12-04a					0.081393		22.26583	0.446442				265016.8			3.300155	733358	1598.961											
Calliachar_2	RJC137-12-04b							16.71682	11.31415				271986.3			2.073164	726591.6	1392.041											
Calliachar_2								8.883679					323790.3			1.955048	652166	24032.91											
Calliachar_2	RJC137-12-07							71.20199					128557.3			1.83323	870244.1	1125.62											
Calliachar_2	RJC137-12-08							5.268673					284395.8			2.859927	708876	6720.1											
Calliachar_2	RJC137-12-09							78.71737	0.298906				141212.5			2.309293	857827.4	878.7693											
Calliachar_2	RJC137-12-10							9.292934					133506.8			0.192383	865004.2	1479.018											
Calliachar_2	RJC137-12-11							21.12679	1.399765				285623			18.64275	701996.8	12339											
Calliachar_2	RJC137-12-14							46.63888	1.117967				230546.6			8.430203	768772.7	624.5096											
Calliachar_2	RJC137-11-01							6.438116	0.348693				406545.6			24.96963	585939.2	7483.163		0.154224	0.120925		0.008346				0.008017		
Calliachar_2	RJC137-11-02							21.04024					312618.4			85.91628	682328.2	4946.489											
Calliachar_2	RJC137-11-03	1.174653		845.6194	30123.57		0.217686	1.988112	3.072299				338638.4			9.207387	626104.9	4264.538		0.111189	0.107233								7.015563
Calliachar_2	RJC137-11-04							22.55344				0.135915	234683.1	0.135915		5.56155	762334.4	2954.076									0.006155		
Calliachar_2	RJC137-11-07					0.191536		15.61257	1.61754				306935.9			98.74796	687132.3	5814.419		0.136176			0.010874				0.008363		1.044852
Calliachar_2	RJC137-11-08							25.57747					258070.8			12.42003	732936.3	8954.893											
Calliachar_2	RJC137-11-10							130.7804					151752.6			9.67606	846721.8	1385.028		0.12022									
Calliachar_2	RJC137-11-11							19.27795	0.867209				294856.2			59.07397	701679.2	3385.332									0.016623		
Calliachar_2	RJC137-11-13							4.673761	1.056819				330732.6			1.662713	663288.4	5960.894		10.65491	0.048794						0.00754		
Calliachar_2	RJC137-11-15							40.59981					250788.9			100.9745	742485.3	6584.246											
Calliachar_2	RJC137-11-16							71.58441					146803.7			3.971043	852707.3	413.5056											
Calliachar_2	RJC137-11-17							85.01394					172498.7			49.28979	823698.7	3668.227						0.030252					
Calliachar_2					343.8927	2.448431	1.662934	120.5981	2.722913	41.40078			172272.9			46.76591	823559.6	3607.642		0.385954				0.0267					
Calliachar_2	RJC137-11-19				8.510868			0.728009					421584.8			337.6962	534618	43449.9					0.026015						0.334604
Calliachar_2	RJC137-11-20							54.70451					166392.1			2.475158	831210.3	2340.397											

Samples	Label	V51	Cr53	Mn55	Fe57	Co59	Ni60	Cu63	Zn66	As75	Se82	Mo95	Ag107	Cd111	Sn118	Sb121	Au197	Hg202	Tl205	Pb208	Bi209	Th232	U238	Rh103	Pd105	Re187	Ir193	Pt195	Te125
		µg/g	µg/g	µg/g	µg/g	µg/g	µg/g	µg/g	µg/g	µg/g	µg/g	µg/g	µg/g	µg/g	µg/g	µg/g	µg/g	µg/g	µg/g	µg/g	µg/g	µg/g	µg/g	µg/g	µg/g	µg/g	µg/g	µg/g	µg/g
Lead Trial	RJC-134-20-1							4.136843	6.703808				182656.5	0.173769		0.112072	816836.3	495.3187		0.14681									0.36103
Lead Trial	RJC-134-20-2					0.331209	0.175555	5.66829	0.718853			16.94384	188440	0.264744		13.54993	810528.4	906.6883		86.90669									0.367909
Lead Trial					34.54895	6.575723	3.994458	4.100128	0.702588	2.683959			196300.6			0.67827	802838.5	804.4052		1.404358									1.737722
Lead Trial	RJC-134-20-3	0.142987		1.0577	145.8846	0.025405	2.034721	25.37027	30.37429	0.754434	1.862142	0.497987	268624.9	14.8486		145.384	673248.3	52512.42	0.051513	5244.617	0.064595	0.04024	0.11842	0.054125					1.125293
Lead Trial	RJC-134-20-4							1.803793	0.667981			0.129635	208539.2			2.840101	790246.3	1208.515		0.270829									0.317443
Lead Trial	RJC-134-20-5	0.057526				0.063887		3.625812				0.351361	208879.9			3.287121	778309.6	12802.28		0.237394									0.585896
Lead Trial	RJC-134-20-6				9.175067			4.085958				0.200746	190011.5			0.180138	809379.1	594.8979		0.567882	0.009134								0.310728
Lead Trial	RJC-134-20-7				20.56975	0.417259	0.150443	2.477755	724.3608			1.274654	276299.7	3.698803		90.94939	678079.6	44772.01		3.624183									1.142434
Lead Trial	RJC-134-20-8					0.033833		3.251246	0.356966			0.220507	200413.5			9.674895	796887.5	2684.819		0.24675	0.013968			0.0111					0.36491
Lead Trial	RJC-134-20-9					0.044642		4.119046				0.523712	188446.7	0.19047		0.546604	810904.7	642.2345	0.021214	0.557954	0.012604								0.337281
Lead Trial	RJC-134-20-10			1.210868	8.971401	0.281538	0.400303	1.415118	22.25452			30.24295	325885.1			369.6853	625999	47558.61	0.04976	121.1455	0.142937		0.006502						1.534306
Lead Trial	RJC-134-20-11							3.97255	5.47108				198225.2			8.135187	795374.4	6381.609		0.286724									0.953117
Lead Trial				4.485348	831.1848	0.535123	0.266056	10.90096	2075.112	11.17171		0.497023	187989	9.737499		52.75605	799083.9	9736.723		190.9451			0.652055						2.080884
Lead Trial					186.5155	0.161619		4.665714	267.0882				195900	2.844936		10.91941	796170.1	7450.847		2.860178									3.938172
Lead Trial	RJC-134-20-12					0.170119		2.31748	682.3163			0.251527	341000.1	2.418652		95.63538	601199.4	57012.24		4.277642									0.875448
Lead Trial	RJC-134-20-13					0.044201		4.015849				0.287102	199470.7			10.98876	796186.9	4326.353		0.2402	0.053834		0.005923						0.432853
Lead Trial	RJC-134-20-14							5.532418				0.202042	199288.5			37.28681	795908.4	4758.942		0.519015									0.617772
Lead Trial	RJC-134-20-15			0.319935		0.023363		3.470378	63.9556			0.355939	201982.7			0.419789	797256.8	690.8083		0.683313	0.014092								0.427402
Lead Trial	RJC-134-20-16							3.839742				0.29902	201084.6			3.064914	797884.2	1023.363		0.324855									0.367924
Lead Trial								4.34647				0.134416	191271.6			0.712337	807984.7	737.9462		0.303172									0.297735
Lead Trial	RJC-134-20-17					0.250677		5.303507	1954.552				204289.5	15.35356		0.579334	792846.4	887.3506		0.693882									
Lead Trial	RJC-134-20-18a	0.071009		2.08926	1044.399	0.081354	0.287258	31.05674	242.612	17.93988		0.765473	187741.9	0.278555	0.156541	30.67487	804910.4	5462.05		514.2092	0.027555	0.093914	0.582653	0.012159					0.282355
Lead Trial	RJC-134-20-18b							4.52053				0.185041	181086.2	0.171444		0.694099	818209.4	698.1101		0.243462									0.518377
Lead Trial						0.229878	0.239885	4.452135	212.4746			0.155793	187074.1	1.359588		2.282245	810392.1	2311.228		0.406698	0.016895								0.921822
Lead Trial	RJC-134-20-19							4.404991					186893.1		0.215195	0.307761	812530.6	567.7662		3.265709			0.096049						0.24613
Lead Trial	RJC-134-20-21	0.378797		0.387514	150.4926	0.036929		35.11116	135.2634	4.001619	27.94038	0.336783	265598.5	0.572889		158.0101	692710.2	37854.4	0.023652	3321.639	0.238448	0.096342	0.632824					0.021516	1.609152
Lead Trial	RJC-134-20-22			4.283786	361.6665	9.464272	7.479394	167.0759	13624.73	2.40289		0.286485	191920.7	60.25655	0.165474	2.191919	793026.9	790.6587	0.048881	19.05156	0.009799		0.010923	0.019888					2.594163
Lead Trial	RJC-134-20-23							3.990336	11.46672			0.468194	199745.3			7.61516	798687	1541.904		1.931908	0.012815								0.310841
Lead Trial	RJC-134-20-24					0.033853		3.512083				0.423141	197562.3			6.812531	800482.6	1943.4		0.677529									0.280138
Lead Trial						0.047233	0.180091	6.489629	0.821703			3.003062	189438			7.073514	808636.6	1863.49		43.90176									0.380109
Lead Trial	RJC-134-20-25							3.457969	13.57418			0.269208	198281.4			1.068978	800717.6	981.9119		0.444975									0.317799
Lead Trial	RJC-134-20-2b					0.218341	0.919348	3.558276	0.987758	3.644391		85.95781	215146.7			191.1647	776754.1	7593.941		217.103			0.038106						1.712752
Lead Trial	RJC-134-20-5b			7.400293	77.65957	0.197813	0.120525	6.836777	133.3027	1.541119		9.172338	262537.8	0.821938		153.584	676163.1	55199.06	0.055076	5708.369	0.020711	0.011145	0.075708	0.064112					0.805777
Lead Trial	RJC-134-20-12b						0.08311	2.967726	0.624142			0.187449	218215.4			55.64654	765181	16543.09		0.185866									0.862155
Lead Trial	RJC-134-20-15b					0.064788		2.666445				0.687649	259496.6			82.45843	717589.9	22825.25	0.027316	1.686003	0.012552								0.662711
Lead Trial	RJC-134-20-19b	0.064991		9.378559	40.01053	0.748253	0.253082	8.695807	1306.911	0.776177		3.706866	228795.7	6.752948		171.1551	737235.3	31798.21		620.4649	0.024458	0.037302	0.045192						1.733116
Lead Trial	RJC-134-20-21b							4.164785				0.287095	197450.2			19.04409	797660.5	4864.56		0.741471									0.462249
Lead Trial						0.080201		3.878313	210.1663			0.160091	199558.5	1.302664		5.161567	798405.4	1814.306		0.539465									0.556286
Lead Trial	RJC-134-21-11							4.727868				0.214067	179365.9			2.616116	819870	756.1852		0.160523	0.03379								0.222452
Lead Trial					21.84359	0.487407	0.17435	6.008592	2644.326				183674.5	11.24415		2.339901	812950	686.0756		1.178804									1.842368
Lead Trial	RJC-134-21-12	0.066506		0.732368	78.97019	1.56981	0.234132	5.220147	8650.78	0.38246		0.762685	305260.3	35.45649		96.32447	637321.9	48505.18	0.047654	39.13883	0.008503		0.007406						2.931471
Lead Trial	RJC-134-21-13			0.63095		0.35628	0.246575	2.901874	347.3891			14.37674	283901	1.693705		65.29725	677284.3	37210.11		1170.31	0.070605								1.331192
Lead Trial	RJC-134-21-14							3.181713					208272.3			0.373629	790809.8	914.0471		0.093338	0.017113								0.214215
Lead Trial	RJC-134-21-15			0.272954	8.331569			2.474942	14.83755			1.71431	347251.5			208.6808	597352.2	55129.19		30.41178	0.010332								0.390209
Lead Trial	RJC-134-21-15b			8.59012		0.064015	0.08298	6.5823	6.430579			0.569224	196807.5			10.62701	797857.5	5257.598		44.05504			0.025262						0.354303
Lead Trial	RJC-134-21-16							4.099267	0.255359			0.168062	198844.3			9.229022	796917.5	4223.94		0.296604									0.221231
Lead Trial	RJC-134-21-17				283.3422	0.156197		235.9836	119.5618			7.408215	186305.3	0.625174		3.045684	812430.4	585.1203	0.02563	28.5186									0.550655
Lead Trial						0.060065		7.379603	488.04			0.55945	197603.1	2.749391		0.714524	801273.1	621.7366		1.854221									0.771041
Lead Trial								5.87429				0.421261	192026.7			0.28692	807385.9	580.376		0.444275									
Lead Trial	RJC-134-21-18							3.053824				0.278437	208879.9			2.206818	789533.8	1579.998		0.51744									0.276896
Lead Trial	RJC-134-21-19	0.133571		244.5266	49.26246	0.94243		110.2442	15.66965	2.301784		4.630627	313833.4	0.315291		186.7604	551469.8	108929.1	0.034808	25151.92	0.038854	0.047647	0.395654	0.212902					0.286671
Lead Trial	RJC-134-21-19b	2.793688		834.8654	511.8627	0.944707	0.352743	131.8151	76.89595	16.44978		9.5746	332524.2	0.284263		112.3026	565078.3	95238.4		5457.484	0.221324	0.457304	2.016629	0.054704					0.671804
Lead Trial	RJC-134-21-20			0.336429				3.26426					214302.4	0.140222		8.894901	782592.3	3090.224		2.108256	0.009709								0.295107

Samples	Label	V51	Cr53	Mn55	Fe57	Co59	Ni60	Cu63	Zn66	As75	Se82	Mo95	Ag107	Cd111	Sn118	Sb121	Au197	Hg202	Tl205	Pb208	Bi209	Th232	U238	Rh103	Pd105	Re187	Ir193	Pt195	Te125
		µg/g	µg/g	µg/g	µg/g	µg/g	µg/g	µg/g	µg/g	µg/g	µg/g	µg/g	µg/g	µg/g	µg/g	µg/g	µg/g	µg/g	µg/g	µg/g	µg/g	µg/g	µg/g	µg/g	µg/g	µg/g	µg/g	µg/g	µg/g
Ardtalnaig	RJC-134-10-1						0.125394	0.895629	0.38481			0.293456	333812.6	0.278901		39.59553	644963.1	21179.52		2.772856	0.018089		0.014967						0.407505
Ardtalnaig		0.322		1.971755	282.243	0.14005	2.564432	13.78375	17.9346	0.770375		0.17525	296572.3			45.01338	675538	27515.24		3.027232	0.016758	6.375996	0.05441					0.054111	
Ardtalnaig	RJC-134-10-2							454.1052					33750.34			0.259973	956310.2	9483.591		0.652454	0.749921				0.057483				
Ardtalnaig	RJC-134-10-3							7.584155	1.2425			0.439526	205894.9			10.64972	789005.6	5079.436		0.187321									
Ardtalnaig	RJC-134-10-4							12.01435				0.749192	127870.5	0.147951		0.528106	871224.8	890.3366		0.970049									
Ardtalnaig	RJC-134-10-5							12.52928				0.41339	132183.6			2.30127	866525.6	1274.923	0.028477	0.318925									0.246531
Ardtalnaig	RJC-134-10-5b							11.55731	0.340551			1.178447	125432			1.477633	873394.4	1157.971		0.809069	0.029794								
Ardtalnaig	RJC-134-10-6							46.1779					138109.2			0.370931	856858.7	4985.496		0.047673									
Ardtalnaig	RJC-135-18-02				33.55093	0.216979		2.300821				229.9604	242498.6			36.93098	755746.4	1173.604	1.946421	273.3906									3.086637
Ardtalnaig					218.7208	0.699444	0.978775	5.449668		7.433509		1050.607	260520.6			175.7924	735107.7	1618.654	7.466888	1282.222							0.010248		3.634688
Ardtalnaig	RJC-135-18-03							13.03496					123670.1			0.335068	874108.8	2207.62	0.026129	0.113294									
Ardtalnaig	RJC-135-18-04							756.7035					27603.31				970082.8	1557.023		0.019907				0.050827	0.086194				
Ardtalnaig	RJC-135-18-05							797.4822					30371.23				966472.1	1327.829		0.92628	626.0862								404.3945
Ardtalnaig	RJC-135-18-05b							870.9575					28930.7				968734.5	1463.86						0.028708					
Ardtalnaig		0.274191		0.685913	64.46718	0.049524	0.523871	808.6864	3.104427				31102.52				965803.3	2215.663		0.539504	0.018661		0.008614	0.046205	0.075011				
Ardtalnaig	RJC-135-18-06	0.245054		6.106761	144.6841	0.088286	0.397228	25.87268	1.4516	0.465608		5.741581	137385.7			5.481439	859911.6	2492.968	0.04832	16.95511	0.035746	0.150438	0.040451						1.955024
Ardtalnaig	RJC-138-1-01	1.351288		5.830575	673.5511	0.481339	7.263329	30.21957	33.99272	0.821471		7.291701	135901.7			3.774665	855354.5	7969.468	0.170398	8.52336	0.05107	0.446313	0.094035						0.442061
Ardtalnaig	RJC-138-1-02				16.35475			12.34608	0.313099			0.204716	139280.5			0.836774	856240	4449.383		0.07806									

Samples	Label	V51	Cr53	Mn55	Fe57	Co59	Ni60	Cu63	Zn66	As75	Se82	Mo95	Ag107	Cd111	Sn118	Sb121	Au197	Hg202	Tl205	Pb208	Bi209	Th232	U238	Rh103	Pd105	Re187	Ir193	Pt195	Te125
		µg/g	µg/g	µg/g	µg/g	µg/g	µg/g	µg/g	µg/g	µg/g	µg/g	µg/g	µg/g	µg/g	µg/g	µg/g	µg/g	µg/g	µg/g	µg/g	µg/g	µg/g	µg/g	µg/g	µg/g	µg/g	µg/g	µg/g	µg/g
Invergeldie	RJC137-9-01							293.4507					66079.85			1.351659	931491	2134.16							0.138251				
Invergeldie	RJC-137-09-02		0.032295			0.006285		213.8963				0.012975	90313.39	1.707332		0.44044	909196.7	273.3194							0.460389				
Invergeldie	RJC-137-09-03	1.161649	1.602466	20.07571	4141.866	0.91028	8.815042	21.4479	23.59041			1.259301	258097.5	0.074331		7.379721	734926	2698.95	0.016742	7.521539	0.327013	0.143497	0.4077						1.632647
Invergeldie	RJC-137-09-05	0.004106						23.51888					226525			2.869234	771034.5	2415.155											0.35905
Invergeldie	RJC-137-09-06	0.022197	2.301929					50.99777					174893.3	0.026174	0.344666	6.231395	815167.7	9879.005							0.103898				
Invergeldie	RJC-137-09-08					0.032073		45.96513	5.303211			0.030689	210984.7	0.062382		10.76356	787685.9	1268.854	0.009445						0.269599				
Invergeldie	RJC-137-09-09		1.237312					23.88236					265275.2	0.029263		1.364166	731585.5	3112.784	0.016978										
Invergeldie	RJC-137-09-10	0.005884						340.5505				0.07249	45270.35	0.330447		2.252793	954308.9	78.71074			0.113969				0.100284				
Invergeldie	RJC-137-09-11	0.06462		0.322224	26.15963	0.038097		22.21775	0.690912			0.016949	268368.8			3.10057	730384.4	1194.202		1.017143			0.006006						0.570268
Invergeldie	RJC-137-09-12a	1.894996		21.64656	960.8926	0.52469	0.742104	31.99741	5.261723	15.87996		0.065828	259399.7		0.242734	2.550041	738434.4	1092.109		30.78909	0.188019	0.049368	0.037569			0.01038			1.872495
Invergeldie	RJC-137-09-12b	1.41727	2.906385	4.405171	305.1817	0.354877	2.266297	35.92826	20.33562	1.139727		0.014285	216970.6			0.40053	781214.8	1400.049	0.021158	39.84935		0.052159	0.020129	0.013506					0.344594
Invergeldie	RJC-137-09-13		1.894732					123.5818	0.766505				136215.7	0.114099		0.493492	863211.8	445.6913						0.018752					
Invergeldie	RJC-137-09-14							41.40941					225948.2	0.160147		4.234529	771208.8	2797.726		0.029889			0.082933						
Invergeldie	RJC-137-09-15	54.60227	194.8868	242.1168	70442.54	16.42368	91.10178	418.4029	1802.464	1282.98		3.464852	256087	4.202334	1.52992	547.2184	661491	4784.173	0.362964	2392.399	79.30278	4.424034	4.165716	0.046333					51.62715
Invergeldie	RJC-137-09-16	4.652686	0.387323	16.4426	435.8449	0.794581	4.509144	112.1854	15.10498	1.825353			52237.85	0.452798		0.102573	946782.9	318.8344	0.056932	67.10987	0.050827	0.138529	0.218692		0.101055				0.469823
Invergeldie	RJC-137-09-17	0.031874						55.50507	1.488576				218517.2	0.245362		1.479175	780402	1022.427	0.00922							0.005471			
Invergeldie	RJC-137-09-18	9.734139	7.201745	91.77989	3180.066	4.100667	18.97836	73.1398	69.07369	18.01426		0.104302	151218.5	0.303796	0.288778	0.427731	844915.4	208.6132	0.457733	181.8952	0.217094	0.685859	0.70411						0.345895
Invergeldie	RJC-137-09-20				9.052667			17.00856		2.657629			270530.2	0.177828		3.379475	724427.2	5010.38					0.000165			0.018082			0.726649
Invergeldie		0.457882	0.158724	5.543886	1125.037	0.025726	0.51792	17.77147	4.691913	52.14293		0.135744	265456.8	0.108041		3.369583	728681.5	4649.456	0.005394	1.214825	0.155491	0.054796	0.29228		0.06483				0.405193
Invergeldie	RJC-137-09-21	2.505281	9.040308	25.69657	838.24	0.751322	4.62577	100.4794	22.20082	5.378384		0.272858	61452.8	3.217727	1.071697	1.845224	936968.8	405.6523	0.025295	155.496	0.833593	0.809499	0.214486						
Invergeldie	RJC-137-09-22	0.009096				0.008554		550.0961					58690.48	0.043083			940362.3	367.6734		0.043386	0.022007		0.001242		30.66673			0.106668	
Invergeldie		0.006147	0.13792	13.57714	37.81723	0.015198		576.8469	5.69576			0.009439	58981.19	0.283691			939976.1	354.485	0.02544	20.42102	0.665972		0.001977		30.8045			0.282933	
Invergeldie	RJC-137-09-23		2.66312				0.610504	149.0227	1.065957			0.013771	99927.17	0.083675		0.175437	899124.2	794.6334		0.380908									
Invergeldie	RJC-137-09-25	0.792313	5.529878	4.100264	971.3595	0.147699	0.966144	126.3716	9.200926	8.621067		0.073596	93099.2	0.406323		0.252811	904537.6	750.137	0.023874	483.4947	0.443199	0.143188	0.272591						0.818966
Invergeldie	RJC-137-09-16					0.020595		188.2395					44417.7				954749.2	644.7347							0.133654				
Invergeldie	RJC-137-09-18	0.060138		1.933336				47.5052	4.229903			0.078907	142016.6			0.420773	857557.3	371.4672		0.132457	0.24632								
Invergeldie	RJC-137-09-21					0.027709		138.9018					88175.51			4.206342	910629.1	1052.289									0.006493		
Invergeldie	RJC-137-09-22							554.7805					53808.22				944990.6	616.7784						0.033642	29.58346				
Invergeldie	RJC-137-09-23	0.042218						25.05418					203720.2			2.26467	792911.4	3340.787											0.322873
Invergeldie	RJC-137-09-03	9.126366	6.167387	63.34718	32758.27	4.48509	54.87511	50.86387	88.20178	140.3814		8.986015	231225.9	0.450197		35.11428	730094.9	5381.774	0.056362	63.19935	3.26625	1.215173	2.485303						6.924776
Invergeldie	RJC-137-09-09						0.113462	65.40453					170881.2			3.526939	823264.7	5785.043											
Invergeldie	RJC-137-09-10							24.3325	0.396155				254583.1			1.3578	739015.9	6374.949									0.005494		
Invergeldie	RJC-137-09-15	0.17408		0.62496	152.0557		0.602011	22.18841	7.323693	2.929636			252882			2.610658	726460.6	20460.38		8.233053	0.265529	0.015743	0.016274						
Invergeldie	RJC-138-2_01							16.81238					228217.8			1.60893	768813.5	2950.288											
Invergeldie	RJC-138-2_02							148.5433					103020.6			0.779349	892586.8	4243.244			0.016862								
Invergeldie	RJC-138-2_03							15.42037					253847.4			1.233059	743352.8	2782.557											0.410352
Invergeldie	RJC-138-2_04a							96.88607					130726.5			3.081661	821137.3	48035.93		0.340226						0.030615			
Invergeldie	RJC-138-2_04b							87.59474					142147.8			2.760101	838689.8	19072		0.025172									
Invergeldie	RJC-138-2_05							20.09786					219324.5				760729.5	19925.89		0.063945				0.017215					

Appendix 4.

Pb isotope raw data

STANDARDS USED IN THIS RUN

ID	Date	From	Notes	208Pb (voltage)	206Pb/204Pb	207Pb/204P	208Pb/204Pb	206Pb/204Pb (absolute error)	207Pb/204P (absolute error)	208Pb/204Pb (absolute error)
SRM981 (2)	30-Jun-20	International Standard	none	28.70	16.9352	15.4897	36.6941	0.000109	0.000118	0.000318
SRM981 (3)	30-Jun-20	International Standard	none	28.86	16.9352	15.4900	36.6940	0.000107	0.000111	0.000309
SRM981 (4)	30-Jun-20	International Standard	none	29.10	16.9355	15.4901	36.6944	0.000110	0.000116	0.000322
SRM981 (5)	30-Jun-20	International Standard	none	28.73	16.9354	15.4902	36.6942	0.000116	0.000120	0.000329
SRM981 (6)	30-Jun-20	International Standard	none	29.65	16.9350	15.4897	36.6932	0.000105	0.000115	0.000326
SRM981 (7)	30-Jun-20	International Standard	none	29.16	16.9349	15.4896	36.6925	0.000119	0.000126	0.000343
SRM981 (8)	30-Jun-20	International Standard	none	28.80	16.9348	15.4897	36.6929	0.000099	0.000114	0.000307
SRM981 (1)	1-Jul-20	International Standard	none	28.53	16.9356	15.4905	36.6948	0.000121	0.000126	0.000349
SRM981 (2)	1-Jul-20	International Standard	none	28.44	16.9352	15.4901	36.6942	0.000107	0.000118	0.000320
SRM981 (3)	1-Jul-20	International Standard	none	28.42	16.9352	15.4901	36.6941	0.000110	0.000118	0.000309
SRM981 (4)	1-Jul-20	International Standard	none	28.01	16.9352	15.4901	36.6944	0.000118	0.000113	0.000319
SRM981 (5)	1-Jul-20	International Standard	none	28.21	16.9353	15.4903	36.6946	0.000108	0.000115	0.000315
SRM981 (6)	1-Jul-20	International Standard	none	28.49	16.9350	15.4899	36.6938	0.000107	0.000115	0.000305
			AVERAGE (mean)		**16.9352**	**15.4900**	**36.6939**	**0.000110**	**0.000117**	**0.000321**
			JUAN ET AL. Certified Values		**16.940600**	**15.495700**	**36.7184**			
			Accuracy (%RD)		**-0.031974**	**-0.036731**	**-0.066589**			
			Correction factor		**1.000320**	**1.000367**	**1.000666**			
			2*stdev		**0.0005**	**0.0005**	**0.0014**			
			Precision (%RSD)		**0.0027**	**0.0032**	**0.0037**			

RAW DATA BELOW

ID	Date	From	Notes	208Pb (voltage)	206Pb/204Pb	207Pb/204P	208Pb/204Pb	206Pb/204Pb (absolute error)	207Pb/204P (absolute error)	208Pb/204Pb (absolute error)	Model age (Ma)	Mu value
LS1	1-Jul-20	**LS1** East of Loch Tay, up on the hill (not	Sample	26.80	17.3871	15.3808	37.5145	0.000118	0.000121	0.000349	493.1	9.0
LS2	1-Jul-20	**LS2** Mell nan Oighreag (in situ)	Sample	32.23	17.8285	15.4679	37.6736	0.000105	0.000107	0.000315	328.2	9.2
LS4a	30-Jun-20	**LS4** Urlar Burn (in situ)	Sample - repeat; galena digest	33.31	17.7509	15.4573	37.6390	0.000101	0.000106	0.000294	366.0	9.2
LS4b	30-Jun-20	**LS4** Urlar Burn (in situ)	Sample - repeat; galena digest	19.33	17.7504	15.4567	37.6376	0.000132	0.000128	0.000349	360.9	9.2
LS4c	30-Jun-20	**LS4** Urlar Burn (in situ)	Sample - repeat; galena digest	21.05	17.7503	15.4564	37.6366	0.000125	0.000120	0.000339	360.6	9.2
LS4d	30-Jun-20	**LS4** Urlar Burn (in situ)	Sample - repeat; galena digest	21.13	17.7506	15.4569	37.6379	0.000125	0.000124	0.000337	360.8	9.2
LS4x	30-Jun-20	**LS4** Urlar Burn (in situ)	Sample - repeat; solution	16.11	17.7500	15.4562	37.6366	0.000167	0.000159	0.000430	367.7	9.2
LS4y	30-Jun-20	**LS4** Urlar Burn (in situ)	Sample - repeat; solution	31.19	17.7509	15.4569	37.6387	0.000106	0.000104	0.000295	370.0	9.2
LS4z	30-Jun-20	**LS4** Urlar Burn (in situ)	Sample - repeat; solution	18.27	17.7508	15.4569	37.6387	0.000139	0.000144	0.000394	370.0	9.2
LS5	30-Jun-20	**LS5** Urlar Burn (in situ-downstream)	Sample	32.04	17.7686	15.4623	37.6555	0.000112	0.000118	0.000326	367.4	9.2
LS6	1-Jul-20	**LS6** Calliachar Burn (not in situ)	Sample	33.52	17.8675	15.4665	37.7390	0.000110	0.000115	0.000328	298.8	9.2
LS7	30-Jun-20	**LS7** Urlar Burn (not in situ)	Sample	19.53	17.7498	15.4541	37.6412	0.000128	0.000123	0.000335	364.7	9.2
LS8	30-Jun-20	**LS8** (probably Urlar Burn – not in situ)	Sample	32.06	17.6817	15.4413	37.5858	0.000112	0.000114	0.000316	394.8	9.2

CORRECTED (using values of Juan et al) DATA BELOW

ID	Date	From	Notes	208Pb (voltage)	206Pb/204Pb	207Pb/204P	208Pb/204Pb	206Pb/204Pb (absolute error)	207Pb/204P (absolute error)	208Pb/204Pb (absolute error)	Model age (Ma)	Mu value
LS1	1-Jul-20	**LS1** East of Loch Tay, up on the hill (not	Sample	26.80	17.3926	15.3864	37.5395	0.000118	0.000121	0.000349	498.1	9.0
LS2	1-Jul-20	**LS2** Mell nan Oighreag (in situ)	Sample	32.23	17.8342	15.4736	37.6987	0.000105	0.000107	0.000315	328.2	9.2
LS4a	30-Jun-20	**LS4** Urlar Burn (in situ)	Sample - repeat; galena digest	33.31	17.7566	15.4629	37.6641	0.000101	0.000106	0.000294	366.0	9.2
LS4b	30-Jun-20	**LS4** Urlar Burn (in situ)	Sample - repeat; galena digest	19.33	17.7560	15.4624	37.6627	0.000132	0.000128	0.000349	364.5	9.2
LS4c	30-Jun-20	**LS4** Urlar Burn (in situ)	Sample - repeat; galena digest	21.05	17.7560	15.4621	37.6617	0.000125	0.000120	0.000339	364.2	9.2
LS4d	30-Jun-20	**LS4** Urlar Burn (in situ)	Sample - repeat; galena digest	21.13	17.7562	15.4626	37.6630	0.000125	0.000124	0.000337	364.4	9.2
LS4x	30-Jun-20	**LS4** Urlar Burn (in situ)	Sample - repeat; solution	16.11	17.7557	15.4618	37.6617	0.000167	0.000159	0.000430	367.7	9.2
LS4y	30-Jun-20	**LS4** Urlar Burn (in situ)	Sample - repeat; solution	31.19	17.7566	15.4626	37.6637	0.000106	0.000104	0.000295	370.0	9.2
LS4z	30-Jun-20	**LS4** Urlar Burn (in situ)	Sample - repeat; solution	18.27	17.7565	15.4626	37.6638	0.000139	0.000144	0.000394	370.0	9.2
LS5	30-Jun-20	**LS5** Urlar Burn (in situ-downstream)	Sample	32.04	17.7743	15.4680	37.6806	0.000112	0.000118	0.000326	383.9	9.3
LS6	1-Jul-20	**LS6** Calliachar Burn (not in situ)	Sample	33.52	17.8732	15.4721	37.7642	0.000110	0.000115	0.000328	308.8	9.3
LS7	30-Jun-20	**LS7** Urlar Burn (not in situ)	Sample	19.53	17.7555	15.4597	37.6663	0.000128	0.000123	0.000335	381.0	9.2
LS8	30-Jun-20	**LS8** probably Urlar Burn (not in situ)	Sample	32.06	17.6874	15.4470	37.6108	0.000112	0.000114	0.000316	410.7	9.2

Note 1: David Van Acken who ran these said there is no SRM981 (1) analysis as machine conditions were changed after this was run (the standard was way off).

Note 2: I plotted the orange values as error, as the reproducibility of the standard was greater than that of the individual measurements (the reported absolute error)

Note 3: I corrected the data to the values for SRM981 reported by Juan et al. All the data shift together (you'll see this on the plot comparison). I published my Pb method in Yeseares et al. (2019; Minerals) and Walsh et al. (2019; Irish J of Earth Science)

Appendix 5.

Example of raw EPMA data

SAMPLE	Locality	NUMBER	TAKEOFF	KILOVOLT	CURREN	BEAMSIZE	Au WT%	Ag WT%	Hg WT%	Cu WT%	Pd WT%	TOTAL	Au CDL99	Ag CDL99	Hg CDL99	Cu CDL99	Pd CDL99	Au la (2,Li	Ag la (1,Pl	Hg mb (3,F	Cu ka (4,L	Pd la (5,Pl	DATETIME	Au STD_N	Ag STD_N	Hg STD_N	Cu STD_N	Pd STD_N	Au STD_N	Ag STD_N	Hg STD_N	Cu STD_N	Pd STD_N
Au_Alloy_Std		3	40	20	50	0	81.4462	18.3888	0.09723	0.03304	0.065159	100.03	0.087508	0.071458	0.110596	0.017361	0.056125	30	30	30	30	30	44263.76	7801	7801	7711	7708	7719	Au-Ag Allc	Au-Ag Allc	HgS	Cu_metal	Pd_metal
Au_Alloy_Std		4	40	20	50	0	81.1111	18.408	-0.08125	0.034094	0.097533	99.5695	0.087138	0.072247	0.116198	0.017331	0.055476	30	30	30	30	30	44263.77	7801	7801	7711	7708	7719	Au-Ag Allc	Au-Ag Allc	HgS	Cu_metal	Pd_metal
Au_Alloy_Std		5	40	20	50	0	81.2414	18.5169	0.055257	0.016767	0.070938	99.9013	0.087376	0.070859	0.11231	0.01744	0.057507	30	30	30	30	30	44263.77	7801	7801	7711	7708	7719	Au-Ag Allc	Au-Ag Allc	HgS	Cu_metal	Pd_metal
Au_Alloy_Std		6	40	20	50	0	80.9448	18.636	0.080201	0.026376	0.070222	99.7577	0.087484	0.070499	0.112396	0.017401	0.056786	30	30	30	30	30	44263.77	7801	7801	7711	7708	7719	Au-Ag Allc	Au-Ag Allc	HgS	Cu_metal	Pd_metal
RJC134_04_01	Sma Glen rough	7	40	20	50	0	82.4559	16.9172	0.311865	0.031701	0.085331	99.802	0.08734	0.070987	0.114345	0.017359	0.05717	30	30	30	30	30	44263.77	7801	7801	7711	7708	7719	Au-Ag Allc	Au-Ag Allc	HgS	Cu_metal	Pd_metal
RJC134_04_02	Sma Glen rough	8	40	20	50	0	94.8559	3.42525	0.862287	0.040195	0.079619	99.2633	0.088202	0.078472	0.123618	0.017289	0.061261	30	30	30	30	30	44263.77	7801	7801	7711	7708	7719	Au-Ag Allc	Au-Ag Allc	HgS	Cu_metal	Pd_metal
RJC134_04_03	Sma Glen rough	9	40	20	50	0	90.5379	8.3212	0.116333	0.056983	0.066386	99.0988	0.087378	0.075075	0.119353	0.017335	0.05959	30	30	30	30	30	44263.77	7801	7801	7711	7708	7719	Au-Ag Allc	Au-Ag Allc	HgS	Cu_metal	Pd_metal
RJC134_04_04	Sma Glen rough	10	40	20	50	0	74.3538	24.7461	0.401268	0.023055	0.103147	99.6274	0.086875	0.06957	0.111632	0.017297	0.052822	30	30	30	30	30	44263.77	7801	7801	7711	7708	7719	Au-Ag Allc	Au-Ag Allc	HgS	Cu_metal	Pd_metal
RJC134_04_05	Sma Glen rough	11	40	20	50	0	76.4216	23.1409	0.075504	0.022377	0.081551	99.7419	0.086737	0.068919	0.110828	0.01742	0.056628	30	30	30	30	30	44263.77	7801	7801	7711	7708	7719	Au-Ag Allc	Au-Ag Allc	HgS	Cu_metal	Pd_metal
RJC134_04_06	Sma Glen rough	12	40	20	50	0	79.7688	19.1628	0.189856	0.039731	0.107992	99.2692	0.087441	0.070353	0.112131	0.017356	0.05499	30	30	30	30	30	44263.77	7801	7801	7711	7708	7719	Au-Ag Allc	Au-Ag Allc	HgS	Cu_metal	Pd_metal
RJC134_04_07	Sma Glen rough	13	40	20	50	0	67.3626	31.7656	0.080027	0.027851	0.081414	99.3175	0.086663	0.065193	0.105783	0.017303	0.05106	30	30	30	30	30	44263.78	7801	7801	7711	7708	7719	Au-Ag Allc	Au-Ag Allc	HgS	Cu_metal	Pd_metal
RJC134_04_08	Sma Glen rough	14	40	20	50	0	67.3664	32.1092	0.10115	0.009058	0.047939	99.6337	0.086862	0.066113	0.105815	0.017425	0.053946	30	30	30	30	30	44263.78	7801	7801	7711	7708	7719	Au-Ag Allc	Au-Ag Allc	HgS	Cu_metal	Pd_metal
RJC134_04_09	Sma Glen rough	15	40	20	50	0	83.9485	15.5463	0.090564	0.027459	0.065612	99.6785	0.087372	0.073037	0.115133	0.017464	0.058546	30	30	30	30	30	44263.78	7801	7801	7711	7708	7719	Au-Ag Allc	Au-Ag Allc	HgS	Cu_metal	Pd_metal
RJC134_04_10	Sma Glen rough	16	40	20	50	0	75.1092	23.2	1.09123	0.02506	0.083939	99.5094	0.087462	0.071405	0.111565	0.017393	0.055204	30	30	30	30	30	44263.78	7801	7801	7711	7708	7719	Au-Ag Allc	Au-Ag Allc	HgS	Cu_metal	Pd_metal
RJC134_04_11	Sma Glen rough	17	40	20	50	0	92.1902	6.89753	0.099771	0.025147	0.121113	99.3338	0.08757	0.074079	0.120683	0.017344	0.058976	30	30	30	30	30	44263.78	7801	7801	7711	7708	7719	Au-Ag Allc	Au-Ag Allc	HgS	Cu_metal	Pd_metal
RJC134_04_12	Sma Glen rough	18	40	20	50	0	84.8516	14.1619	0.142701	0.02383	0.033545	99.2136	0.087377	0.073372	0.112965	0.017312	0.059759	30	30	30	30	30	44263.78	7801	7801	7711	7708	7719	Au-Ag Allc	Au-Ag Allc	HgS	Cu_metal	Pd_metal
RJC134_04_13	Sma Glen rough	19	40	20	50	0	93.0277	5.11192	0.161114	0.092249	0.052207	98.4452	0.087508	0.074661	0.116152	0.017276	0.061592	30	30	30	30	30	44263.78	7801	7801	7711	7708	7719	Au-Ag Allc	Au-Ag Allc	HgS	Cu_metal	Pd_metal
RJC134_04_14	Sma Glen rough	20	40	20	50	0	91.853	7.07147	0.078547	0.027883	0.067592	99.0985	0.088383	0.077391	0.119189	0.017386	0.060988	30	30	30	30	30	44263.78	7801	7801	7711	7708	7719	Au-Ag Allc	Au-Ag Allc	HgS	Cu_metal	Pd_metal
RJC134_04_15	Sma Glen rough	21	40	20	50	0	76.8117	22.1181	0.326242	0.034373	0.042096	99.3325	0.087003	0.070399	0.107484	0.017217	0.056485	30	30	30	30	30	44263.78	7801	7801	7711	7708	7719	Au-Ag Allc	Au-Ag Allc	HgS	Cu_metal	Pd_metal
RJC134_04_16	Sma Glen rough	22	40	20	50	0	84.5442	14.4362	-0.0216	0.033694	0.036804	99.0292	0.087212	0.072363	0.116046	0.017251	0.060485	30	30	30	30	30	44263.78	7801	7801	7711	7708	7719	Au-Ag Allc	Au-Ag Allc	HgS	Cu_metal	Pd_metal
RJC134_04_17	Sma Glen rough	23	40	20	50	0	79.655	19.8993	0.094023	0.021476	0.121117	99.7909	0.08704	0.070391	0.113708	0.017443	0.054735	30	30	30	30	30	44263.79	7801	7801	7711	7708	7719	Au-Ag Allc	Au-Ag Allc	HgS	Cu_metal	Pd_metal
RJC134_03_01	Sma Glen rough	24	40	20	50	0	91.4241	6.88901	0.084625	0.020876	0.075989	98.4946	0.087739	0.076797	0.119602	0.017286	0.060801	30	30	30	30	30	44263.79	7801	7801	7711	7708	7719	Au-Ag Allc	Au-Ag Allc	HgS	Cu_metal	Pd_metal
RJC134_03_02	Sma Glen rough	25	40	20	50	0	78.0561	21.327	0.122852	0.024914	0.061439	99.5923	0.087039	0.07097	0.111017	0.01735	0.055529	30	30	30	30	30	44263.79	7801	7801	7711	7708	7719	Au-Ag Allc	Au-Ag Allc	HgS	Cu_metal	Pd_metal
RJC134_03_03	Sma Glen rough	26	40	20	50	0	85.1623	12.604	0.35247	0.022052	0.110297	98.2511	0.086854	0.073681	0.115161	0.017377	0.057019	30	30	30	30	30	44263.79	7801	7801	7711	7708	7719	Au-Ag Allc	Au-Ag Allc	HgS	Cu_metal	Pd_metal
RJC134_03_04	Sma Glen rough	27	40	20	50	0	85.9453	13.1736	0.19867	0.031146	0.063862	99.4126	0.087436	0.072833	0.116038	0.017368	0.059426	30	30	30	30	30	44263.79	7801	7801	7711	7708	7719	Au-Ag Allc	Au-Ag Allc	HgS	Cu_metal	Pd_metal
RJC134_03_05	Sma Glen rough	28	40	20	50	0	65.0462	34.4373	-0.0655	0.007847	0.041361	99.4672	0.086433	0.065307	0.105376	0.017475	0.05325	30	30	30	30	30	44263.79	7801	7801	7711	7708	7719	Au-Ag Allc	Au-Ag Allc	HgS	Cu_metal	Pd_metal
RJC134_03_06	Sma Glen rough	29	40	20	50	0	69.169	30.4635	0.282137	0.031322	0.049669	99.9956	0.087126	0.066302	0.106779	0.017324	0.054603	30	30	30	30	30	44263.79	7801	7801	7711	7708	7719	Au-Ag Allc	Au-Ag Allc	HgS	Cu_metal	Pd_metal
RJC134_03_07	Sma Glen rough	30	40	20	50	0	75.3999	23.8492	-0.01865	0.010873	0.054212	99.2956	0.086764	0.068955	0.112179	0.017442	0.056651	30	30	30	30	30	44263.79	7801	7801	7711	7708	7719	Au-Ag Allc	Au-Ag Allc	HgS	Cu_metal	Pd_metal
RJC134_03_08	Sma Glen rough	31	40	20	50	0	80.4726	19.7151	0.088227	0.033694	0.053735	100.363	0.087648	0.070207	0.113854	0.017354	0.056935	30	30	30	30	30	44263.79	7801	7801	7711	7708	7719	Au-Ag Allc	Au-Ag Allc	HgS	Cu_metal	Pd_metal
RJC134_03_09	Sma Glen rough	32	40	20	50	0	86.8922	11.8225	0.24939	0.061525	0.107508	99.1331	0.087691	0.07412	0.117426	0.017315	0.057717	30	30	30	30	30	44263.8	7801	7801	7711	7708	7719	Au-Ag Allc	Au-Ag Allc	HgS	Cu_metal	Pd_metal
RJC134_03_10	Sma Glen rough	33	40	20	50	0	77.8732	21.3686	0.087024	0.014427	0.102177	99.4454	0.087293	0.070165	0.110769	0.017464	0.056289	30	30	30	30	30	44263.8	7801	7801	7711	7708	7719	Au-Ag Allc	Au-Ag Allc	HgS	Cu_metal	Pd_metal
RJC134_03_11	Sma Glen rough	34	40	20	50	0	79.7062	19.3334	0.142657	0.02828	0.061529	99.2721	0.087729	0.072386	0.110593	0.017361	0.055797	30	30	30	30	30	44263.8	7801	7801	7711	7708	7719	Au-Ag Allc	Au-Ag Allc	HgS	Cu_metal	Pd_metal
RJC134_03_12	Sma Glen rough	35	40	20	50	0	77.5109	20.5428	1.88607	0.03337	0.056554	100.03	0.087087	0.069843	0.113062	0.01732	0.057567	30	30	30	30	30	44263.8	7801	7801	7711	7708	7719	Au-Ag Allc	Au-Ag Allc	HgS	Cu_metal	Pd_metal
RJC134_03_13	Sma Glen rough	36	40	20	50	0	89.474	9.48094	0.083676	0.028194	0.106999	99.1738	0.087476	0.074853	0.119173	0.017377	0.058325	30	30	30	30	30	44263.8	7801	7801	7711	7708	7719	Au-Ag Allc	Au-Ag Allc	HgS	Cu_metal	Pd_metal
RJC134_03_14	Sma Glen rough	37	40	20	50	0	58.7494	39.6867	0.416964	0.016643	0.04955	98.9193	0.086152	0.064734	0.099811	0.017505	0.051636	30	30	30	30	30	44263.8	7801	7801	7711	7708	7719	Au-Ag Allc	Au-Ag Allc	HgS	Cu_metal	Pd_metal
RJC134_03_15	Sma Glen rough	38	40	20	50	0	70.6266	28.9214	0.106396	0.033613	0.084203	99.7722	0.086733	0.067822	0.10687	0.017376	0.055084	30	30	30	30	30	44263.8	7801	7801	7711	7708	7719	Au-Ag Allc	Au-Ag Allc	HgS	Cu_metal	Pd_metal
RJC134_03_16	Sma Glen rough	39	40	20	50	0	74.6445	25.1015	0.172142	0.013401	0.044498	99.976	0.086745	0.069268	0.108606	0.017431	0.055484	30	30	30	30	30	44263.8	7801	7801	7711	7708	7719	Au-Ag Allc	Au-Ag Allc	HgS	Cu_metal	Pd_metal
RJC134_03_17	Sma Glen rough	40	40	20	50	0	80.2703	19.0113	0.274051	0.035643	0.038398	99.6297	0.08662	0.069758	0.112093	0.017315	0.058022	30	30	30	30	30	44263.8	7801	7801	7711	7708	7719	Au-Ag Allc	Au-Ag Allc	HgS	Cu_metal	Pd_metal
RJC134_03_18	Sma Glen rough	41	40	20	50	0	85.5646	13.324	0.156734	0.026823	0.053102	99.1252	0.087864	0.073658	0.115858	0.01733	0.059201	30	30	30	30	30	44263.81	7801	7801	7711	7708	7719	Au-Ag Allc	Au-Ag Allc	HgS	Cu_metal	Pd_metal
RJC134_03_19	Sma Glen rough	42	40	20	50	0	90.3177	8.88641	0.198099	0.035227	0.033929	99.4713	0.087727	0.07498	0.121397	0.017419	0.061783	30	30	30	30	30	44263.81	7801	7801	7711	7708	7719	Au-Ag Allc	Au-Ag Allc	HgS	Cu_metal	Pd_metal
RJC134_03_20	Sma Glen rough	43	40	20	50	0	89.8337	9.73914	-0.01212	0.046953	0.085703	99.6933	0.087726	0.074393	0.121094	0.017375	0.058877	30	30	30	30	30	44263.81	7801	7801	7711	7708	7719	Au-Ag Allc	Au-Ag Allc	HgS	Cu_metal	Pd_metal
RJC134_03_21	Sma Glen rough	44	40	20	50	0	82.7721	16.6511	0.122508	0.028942	0.087481	99.6621	0.087168	0.072883	0.114327	0.017443	0.057954	30	30	30	30	30	44263.81	7801	7801	7711	7708	7719	Au-Ag Allc	Au-Ag Allc	HgS	Cu_metal	Pd_metal
RJC134_03_22	Sma Glen rough	45	40	20	50	0	81.815	16.9949	0.129111	0.024243	0.072208	99.0355	0.087181	0.072295	0.110222	0.01734	0.056795	30	30	30	30	30	44263.81	7801	7801	7711	7708	7719	Au-Ag Allc	Au-Ag Allc	HgS	Cu_metal	Pd_metal
RJC134_03_23	Sma Glen rough	46	40	20	50	0	86.4118	13.0412	0.029329	0.051701	0.11551	99.6496	0.087673	0.072965	0.117035	0.017315	0.057408	30	30	30	30	30	44263.81	7801	7801	7711	7708	7719	Au-Ag Allc	Au-Ag Allc	HgS	Cu_metal	Pd_metal
RJC134_03_24	Sma Glen rough	47	40	20	50	0	67.517	31.3011	0.39887	0.020953	0.092454	99.3304	0.086543	0.06561	0.105474	0.017347	0.053823	30	30	30	30	30	44263.81	7801	7801	7711	7708	7719	Au-Ag Allc	Au-Ag Allc	HgS	Cu_metal	Pd_metal
RJC134_03_25	Sma Glen rough	48	40	20	50	0	83.6223	16.2082	0.027279	0.029399	0.085776	99.973	0.087215	0.072091	0.114598	0.017391	0.058032	30	30	30	30	30	44263.81	7801	7801	7711	7708	7719	Au-Ag Allc	Au-Ag Allc	HgS	Cu_metal	Pd_metal
RJC134_05_01	Sma Glen Intermediate	49	40	20	50	0	85.2919	10.7978	0.114313	0.035875	0.070747	96.3107	0.087367	0.079216	0.123322	0.017179	0.057097	30	30	30	30	30	44263.81	7801	7801	7711	7708	7719	Au-Ag Allc	Au-Ag Allc	HgS	Cu_metal	Pd_metal
RJC134_05_02	Sma Glen Intermediate	50	40	20	50	0	79.1984	19.9697	0.219662	0.029376	0.034957	99.452	0.087446	0.071661	0.113896	0.0174	0.057333	30	30	30	30	30	44263.81	7801	7801	7711	7708	7719	Au-Ag Allc	Au-Ag Allc	HgS	Cu_metal	Pd_metal
RJC134_05_03	Sma Glen Intermediate	51	40	20	50	0	75.6313	24.3202	0.062891	0.022767	0.024674	100.062	0.086812	0.06705	0.108915	0.017378	0.057004	30	30	30	30	30	44263.82	7801	7801	7711	7708	7719	Au-Ag Allc	Au-Ag Allc	HgS	Cu_metal	Pd_metal

Example of a sheet from the Loch Tay gold compositional database

Population_ID	Block	Sub-Population	Grain	Phase	Phase_ID	Au	Ag	Cu	Hg	Pd	Total	Inclusion_1	Inclusion_2	Inclusion_3
Sma Glen_1	RJC103	3	1	1	Sma Glen_1_RJC103_3_1_1	74.6649	25.4162	0.040365	0.049554	0.059447	100.23			
Sma Glen_1	RJC103	3	2	1	Sma Glen_1_RJC103_3_2_1	73.0634	26.7419	0.021831	-0.01661	0.062157	99.8726			
Sma Glen_1	RJC103	3	3	1	Sma Glen_1_RJC103_3_3_1	72.3368	27.5864	0.016268	0.014639	0.108716	100.063	sp	ga	po
Sma Glen_1	RJC103	3	4	1	Sma Glen_1_RJC103_3_4_1	72.9293	26.4308	0.031781	0.1739	0.143948	99.7097			
Sma Glen_1	RJC103	3	5	1	Sma Glen_1_RJC103_3_5_1	71.6868	28.0393	0.010204	0.227331	0.127815	100.092			
Sma Glen_1	RJC103	3	6	1	Sma Glen_1_RJC103_3_6_1	74.452	21.7438	0.023025	4.64407	0.05236	100.915			
Sma Glen_1	RJC103	3	7	1	Sma Glen_1_RJC103_3_7_1	81.1763	17.6383	0.035296	0.172953	0.090808	99.1136			
Sma Glen_1	RJC103	3	8	1	Sma Glen_1_RJC103_3_8_1	73.5375	25.4834	0.014267	0.219568	0.000026	99.2547			
Sma Glen_1	RJC103	3	9	1	Sma Glen_1_RJC103_3_9_1	82.9729	16.522	0.019446	0.009168	0.126808	99.6504	ga		
Sma Glen_1	RJC103	3	10	1	Sma Glen_1_RJC103_3_10_1	76.5473	22.8266	0.013786	-0.01951	0.010726	99.3789			
Sma Glen_1	RJC101	2	1	1	Sma Glen_1_RJC101_2_1_1	81.4637	18.3662	-0.01848	0.272927	-0.10809	99.9763			
Sma Glen_1	RJC101	2	2	1	Sma Glen_1_RJC101_2_2_1	88.2951	11.7106	0.001679	0.225273	-0.07722	100.155			
Sma Glen_1	RJC101	2	3	1	Sma Glen_1_RJC101_2_3_1	83.5725	16.9301	-0.00205	0.111681	0.019616	100.632	NiAsS		
Sma Glen_1	RJC101	2	4	1	Sma Glen_1_RJC101_2_4_1	70.1291	29.0953	-0.00567	0.557733	-0.0144	99.762	NiFeAsS	CuFeAsS	
Sma Glen_1	RJC101	2	5	1	Sma Glen_1_RJC101_2_5_1	75.3293	24.7628	-0.00142	0.190481	0.013335	100.295			
Sma Glen_1	RJC101	2	6	1	Sma Glen_1_RJC101_2_6_1	69.3814	30.4103	-0.00527	0.261454	-0.03017	100.018			
Sma Glen_1	RJC101	2	7	1	Sma Glen_1_RJC101_2_7_1	80.5489	19.8636	0.002793	0.101926	0.063883	100.581			
Sma Glen_1	RJC101	2	8	1	Sma Glen_1_RJC101_2_8_1	93.7218	5.6144	0.062145	0.199752	0.017052	99.6151			
Sma Glen_1	RJC101	2	9	1	Sma Glen_1_RJC101_2_9_1	91.1593	8.46143	0.02902	0.239099	-0.01252	99.8764			
Sma Glen_1	RJC101	2	10	1	Sma Glen_1_RJC101_2_10_1	83.1962	16.8659	0.02171	0.005655	0.021608	100.111			
Sma Glen_1	RJC101	2	11	1	Sma Glen_1_RJC101_2_11_1	72.8655	27.0208	0.011471	0.326133	-0.02177	100.202			
Sma Glen_1	RJC101	2	12	1	Sma Glen_1_RJC101_2_12_1	85.0635	14.6004	0.010703	0.487183	-0.02618	100.136			
Sma Glen_1	RJC101	2	13	1	Sma Glen_1_RJC101_2_13_1	69.811	29.8832	0.012531	0.170369	-0.06913	99.808			
Sma Glen_1	RJC101	2	14	1	Sma Glen_1_RJC101_2_14_1	79.9984	20.2081	-0.00876	0.216337	-0.02562	100.388			
Sma Glen_1	RJC101	2	15	1	Sma Glen_1_RJC101_2_15_1	93.8102	5.64464	0.043932	0.249422	0.067677	99.8158			
Sma Glen_1	RJC101	2	16	1	Sma Glen_1_RJC101_2_16_1	91.7185	8.39555	0.02759	0.222403	0.064885	100.429			
Sma Glen_1	RJC101	2	17	1	Sma Glen_1_RJC101_2_17_1	82.8665	16.9251	0.002416	0.136004	-0.048	99.882			
Sma Glen_1	RJC101	2	18	1	Sma Glen_1_RJC101_2_18_1	75.9792	22.6179	-0.00067	1.35747	-0.06836	99.8856			
Sma Glen_1	RJC101	2	19	1	Sma Glen_1_RJC101_2_19_1	90.4799	9.17987	0.016944	0.405371	-0.10335	99.9788			